Universidade do Minho
Escola de Ciências

Fernando Ricardo da Silva Ferreira

Unveiling the integration of redox and bioelectric phenomena in vertebrate regeneration

outubro de 2019

Unveiling the integration of redox and bioelectric phenomena in vertebrate regeneration
Fernando Ricardo da Silva Ferreira
UMinho|2019

Funding

The thesis herein presented is grounded on a mixed Ph.D. studentship (Bolsa de Doutoramento) awarded to Ph.D. candidate Fernando Ferreira by Fundação para a Ciência e Tecnologia (FCT; SFRH/BD/87256/2012), using national and European funds from the Ministério da Educação e Ciência (MEC) and from the Fundo Social Europeu, respectively, in the ambit of the POPH – QREN – Tipologia 4.1 – Formação Avançada.

This studentship covered the student's wages abroad at University of California (UC), Davis in USA and the student's home institution tuition fees at Universidade do Minho in Braga, Portugal, for most of the programme time (4 years). The wages and tuition fees of the first year were covered by the student himself. The wages of most of the sixth year were covered by a short-term (8 months at 60% wage) contract with the UC Davis, as a Staff Research Associate, step II. The tuition fees of the extra trimester needed to submit the completed thesis was covered by the student himself.

The laboratorial work grounding the present thesis was supported by the following grants, ordered by type and not by time of use: National Institutes of Health (NIH; EB015737 and EY019101); Air Force Office of Scientific Research (AFOSR; FA9550-16-1-0052); and Unrestricted Grant from Research to Prevent Blindness, Inc., UC Davis, Ophthalmology.

FCT
Fundação para a Ciência e a Tecnologia
MINISTÉRIO DA EDUCAÇÃO E CIÊNCIA

POPH
QUALIFICAR É CRESCER.

QREN
QUADRO DE REFERÊNCIA ESTRATÉGICO NACIONAL
PORTUGAL 2007.2013

Governo da República Portuguesa

UNIÃO EUROPEIA
Fundo Social Europeu

Universidade do Minho
Escola de Ciências

Fernando Ricardo da Silva Ferreira

Unveiling the integration of redox and bioelectric phenomena in vertebrate regeneration

Tese de Doutoramento
Doutoramento em Biologia Molecular e Ambiental
Especialidade em Biologia Celular e Saúde

Trabalho efetuado sob a orientação do
Professor Doutor Min Zhao
e da
Professora Doutora Andreia Ferreira de Castro Gomes

outubro de 2019

DIREITOS DE AUTOR E CONDIÇÕES DE UTILIZAÇÃO DO TRABALHO POR TERCEIROS

Licença concedida aos utilizadores deste trabalho

ACKNOWLEDGMENTS

I longed for this moment! From class-born dreams to bench side turmoil, a decade went by. The quest was lengthy but not lonely... and now I shall thank (briefly; completed in Appendix XV) who was there.

I am grateful to my pedagogic supervisor, Prof. Andreia Gomes, for guiding me through the theoretical year and with all academic bureaucratises and for being my link to Universidade do Minho. Obrigado!

I am especially grateful to my scientific advisor, Prof. Min Zhao, for accepting a strange project and providing all the tools for its accomplishment beyond the original proposed aims. His relentless mentorship and his constant kind words are an example for how to support the students of science.

Beyond the mentorship of Prof. Min, three researches helped and worked with me the most, Guillaume Luxardi, Brian Reid and VijayKrishna Raghunathan. They introduced me to the Lab and trained me in the exquisite and routine techniques. Thank you for that and for the partnership.

As immediate but rather great lab companions and friends, who shared the ventures of the bench side idiosyncrasies and helped each other, I want to say Thank you! to Li Ma, Yunyun Shen and Kan Zhu. A friendly word too for those with whom I collaborated and/or shared the bench or office at times: Yan Li, Trisha Pfluger, Liang Guo, Yawei Yu and Yao-Hui Sun. Also, a kind word to all Zhao Lab members.

Another appreciation word to Eric Karplus, who helped me operate the novel SMOT technique. Special thanks to Alan Shipley, who never stopped supporting and, most enigmatically, believing in me!

***

Na língua herdada, os agradecimentos são devidos à família nuclear, à minha sobejamente querida e aos amigos do lado de cá. Dizer, da distância, que foi dificil é somente exercitar a redundância retórica. Aos pai Manuel e mãe Rosa, seis irmãos e oito irmãs, seis cunhados e cinco cunhadas, doze sobrinhos (um deles afilhado) e doze sobrinhas (uma delas afilhada), e, até, um sobrinho-neto!, o meu Obrigado!

Na bruma da escrita surgiu-se-me a minha sobejamente querida. De seu nome Gena, diva da mente humana e da música, refugiou-me numa ermida de escriba onde findei a Tese de Doutoramento! Assim, o meu Obrigado! à mãe Lúcia, irmã, futuro cunhado, avó e prima-afilhada da Gena.

A cura, à dedicatória desta tese, passou-se com a Gena a conceber o Jardim • *Vertigem (ir)reversível*, exposto no Festival Internacional de Jardins de Ponte de Lima, sob o tema "Jardins do Fim do Mundo".

Agradeço também à demais família, aos colegas e aos amigos que perceberam as minhas ausências.

STATEMENT OF INTEGRITY

I hereby declare having conducted this academic work with integrity. I confirm that I have not used plagiarism or any form of undue use of information or falsification of results along the process leading to its elaboration.

I further declare that I have fully acknowledged the Code of Ethical Conduct of the University of Minho.

RESUMO

Descoberta da integração de fenómenos redox e bioelétricos na regeneração de vertebrados

Regeneração, ou a capacidade de recuperar a forma e função em caso de lesão em larga escala, é um processo complexo. Múltiplas vias bioquímicas e biofísicas têm vindo a ser reveladas como importantes para a regeneração epimórfica. Entre elas, as espécies reativas de oxigénio (ROS) e a densidade de corrente elétrica (J_I) modulam a regeneração. No entanto, a relação entre os sinais bioquímicos e biofísicos durante a regeneração permanece evasiva. Aqui, investiga-se a interação entre os estados redox (parte bioquímica) e bioelétrico (parte biofísica) na regeneração caudal de girinos *Xenopus laevis*.

Uma regulação de duas vias das atividades bioelétricas pelos ROS é revelada. O fluxo de eletrões conduzido pelas NADPH oxidases (propriedade eletrogénica) despolariza o potencial de membrana (V_m), enquanto os ROS (propriedade catalítica) aumentam o potencial transepitelial (TEP) e revertem a J_I durante a regeneração. A depleção dos ROS por inibição da produção, eliminação ou bloqueio da sua difusão para o interior das células, mimetiza os TEP e J_I anormais do período refratário (não regenerativo). Crucialmente, a aplicação breve de peróxido de hidrogénio (H_2O_2) recupera (do decréscimo de ROS) e induz (do período refratário) regeneração, aumento do TEP e reversão do J_I. Assim, H_2O_2 é necessário à e suficiente para induzir a regeneração e para regular os TEP e J_I. Ensaios de epistasia mostram que os canais de Na^+ dependente de voltagem (Na_V) atuam a jusante de H_2O_2.

Um micro-ótrodo detalhado é usado para traçar o perfil espácio-temporal de fluxo de O_2 durante a regeneração. O perfil revela um aumento no influxo de O_2, após amputação, que se correlaciona com a regeneração. A inibição da produção de ROS, mas não a sua eliminação, diminui a magnitude do influxo. Assim, a produção de ROS é responsável pela maior parte da força motriz que impulsiona o O_2. Tanto o O_2 como os ROS contribuem para a pressão parcial de O_2, afetando a hipóxia e consequente estabilização do fator induzível pela hipóxia (HIF). Notavelmente, o bloqueio de HIF-1α impede a regeneração, enquanto a sua estabilização induz a regeneração no período refratário. A proteína de choque térmico (HSP) 90 é um potencial e a reversão do J_I é um *de facto* alvo a jusante de HIF-1α.

Em conjunto, estes resultados revelam a orquestração de atividades redox e bioelétricas e integram-nas durante a regeneração de um vertebrado. Estas descobertas poderão ser importantes para induzir a regeneração epimórfica no corpo humano, provavelmente a derradeira meta da medicina regenerativa.

Palavras-chave Fenómenos redox; Fenómenos bioelétricos; Integração; Regeneração; *Xenopus laevis*

ABSTRACT

Unveiling the integration of redox and bioelectric phenomena in vertebrate regeneration

Regeneration, or the ability to regain the form and function upon large-scale injury, is a complex process. Multiple biochemical and biophysical pathways and cues play a key role during epimorphic regeneration. Among them, reactive oxygen species (ROS) and electric current densities (J_I) modulate regeneration. However, the biochemical and biophysical crosstalk during regeneration remains elusive. Here, it is investigated the interplay between redox (biochemical part) and bioelectric (biophysical part) states during tail regeneration in *Xenopus laevis* tadpoles.

A two-way regulation of bioelectric activities by the required NADPH oxidase-mediated production of ROS is unveiled. NADPH oxidase-driven electron flow (electrogenic property) depolarizes the membrane potential (V_m), while produced ROS (catalytic property) increases the transepithelial potential (TEP) and reverses J_I during regeneration. Importantly, depletion of ROS levels by the inhibition of production, scavenging or blocking their diffusion into cells, mimics the abnormal TEP and J_I observed in the refractory (non-regenerative) period. Crucially, short-term application of hydrogen peroxide (H_2O_2) rescues (from depleted ROS) and induces (from the refractory period) regeneration, TEP increase and J_I reversal. Therefore, H_2O_2 is necessary for and sufficient to induce regeneration and to regulate TEP and J_I. Epistasis assays show that voltage-gated Na^+ channels (Na_V) act downstream of H_2O_2.

The stringently detailed micro-optrode is used to map the spatiotemporal oxygen (O_2) flux during regeneration. The profile reveals an increased and steady O_2 influx (an O_2 sink) immediately upon amputation that correlates with regeneration. Inhibition of ROS production, but not their scavenging, decreases the magnitude of O_2 influx. Therefore, ROS production accounts for most of the motive force driving O_2 flux. Both O_2 and ROS contribute to the local partial pressure of O_2, affecting hypoxia and consequent hypoxia-inducible factor (HIF) stabilization in the regeneration bud. Notably, blocking HIF-1α abrogates regeneration, while stabilizing its activity induces regeneration in the refractory period. Heat shock protein (HSP) 90 is a potential and J_I reversal is a *de facto* downstream target of HIF-1α activity.

Altogether, these results unveil the orchestration of redox and bioelectric activities and integrate them during a vertebrate model of regeneration. These discoveries might be important to induce epimorphic regeneration in the human body, probably the ultimate goal of regenerative medicine.

Keywords Redox phenomena; Bioelectric phenomena; Integration; Regeneration; *Xenopus laevis*

TABLE OF CONTENTS

INDEXES

Figures

Tables

Boxes

Equations

LISTS

Abbreviations

a. u.	Arbitrary units
AC	Alternating current
AEC	Apical epidermal cap
AER	Apical ectodermal ridge
AI	Artificial intelligence
AKT	Protein kinase B
APO	Apocynin
AQP	Aquaporin
ARE	Antioxidant responsive elements
ASET	Automated scanning electrode technique
BMP	Bone morphogenetic protein
BSA	Bovine serum albumin
BSS+	Artificial tear solution
BTS	*N*-benzyl-p-toluene sulfonamide
CaCC	Calcium-activated chloride channel
CCD	Charge-coupled device
CGD	Chronic granulomatous disease
CM-H_2DCFDA	Chloromethyl derivative of 2',7'-dichlorofluorescein dye
DAPI	4′,6-diamidino-2-phenylindole
DC	Direct current
dH_2O	Deionized water
DMOG	Dimethyloxallyl glycine
DMSO	Dimethyl sulfoxide
DO	Dissolved oxygen

d/h/minpa Days/hours/minutes post-amputation

DPI Diphenyleneiodonium

Duox1/2 Dual oxidase one/two

ECL Enhanced chemiluminescence reaction

ECM Extracellular matrix

eHSP90α Extracellularly secreted form of heat shock protein ninety

ERK Extracellular signal-regulated kinase

ex/em Excitation/emission wavelengths

FACS Fluorescence-activated cell sorting

FGF Fibroblast growth factor

fgf20 Gene of fibroblast growth factor twenty

GFP Green fluorescent protein

HEPES 4-(2-hydroxyethyl)-1-piperazineethanesulfonic acid

HIF-1α/1β Hypoxia-inducible factor one alpha/one beta

Hippo Protein kinase Hippo

HRE Hypoxia responsive elements

HSP90 Heat shock protein ninety

IGF1 Insulin-like growth factor one

IgG_1 Immunoglobulin G one antibody

IL-11 Interleukin-eleven

IT Information technology

IVF *In vitro* fertilization

JNK c-Jun N-terminal kinase

LED Light-emitting diode

Lyn SRC family kinase (SFK) Lyn

MAPK Mitogen-activated protein kinase

MCI MCI-186

MMR Marc's modified Ringer

MRI Magnetic resonance imaging

MRL Murphy Roths Large mouse strain

Msx1 Homeobox protein Msx one

NADPH Nicotinamide adenine dinucleotide phosphate

nAG Newt anterior gradient protein

Nanog Homeobox protein Nanog

Na_v or VGSC Voltage-gated sodium channel

NF-κB Nuclear factor kappa-light-chain-enhancer of activated B cells

Notch Transmembrane receptor protein Notch

Nox1/2/4/5 NADPH oxidase one/two/four/five

NS Non-significant

OCT Optimal cutting temperature

Oct3/4 Octamer-binding transcription factor three/four

OxyR Bacterial H_2O_2-sensitive transcription factor

PBS Phosphate-buffered saline

PCP Planar cell polarity pathway

PDGF Platelet-derived growth factor

PFA Paraformaldehyde

PHD Prolyl hydroxylase

PMT Photomultiplier

pro-MMP-2 Pro-matrix metalloproteinase two

PSt1 Proprietary oxygen-specific fluorophore

PZ Progress zone

R. bud Regeneration bud

RI Regeneration index

ROC Regeneration-organizing cell

ROI Region of interest

ROS Reactive oxygen species

Shh Sonic hedgehog protein

SMOT Scanning micro-optrode technique

SOD Superoxide dismutase

St. Stage

TBST Tris-buffered saline with Tween 20

TEP Transepithelial potential

TGF-β Transforming growth factor beta

VAS VAS2870

V-ATPase Vacuolar-type H^+-ATPase

VGEF Vascular endothelial growth factor

WE Wound epithelium

Wnt Wingless-related integration protein

17-DMAG Alvespimycin

2,4-DNP 2,4-Dinitrophenol

2-APB 2-Aminoethoxydiphenyl borate

2D Two dimensional

3D Three dimentional

3R Replacement, reduction and refinement of the guiding ethical principles

Symbols

Ag/AgCl	Silver/Silver chloride (measuring/reference) electrode
C_m	Capacitance of membrane
D	Diffusion coefficient of dissolved oxygen
e^-	Electron
EF or E	Electric field
E_{Na^+}	Electromotive force driving sodium ions
f	Frequency of regeneration phenotype
FMO(MFI)	Geometric mean fluorescence intensity of the fluorescence minus one (FMO)
FMO(SD)	Standard deviation of the FMO per experiment
I	Electric (ionic) current
I_{Na^+}	Current of sodium ions
J_I	Electric current density
J_{O_2}	Oxygen flux
n	Biological replicates
P* or *p	Statistical *P* or *p* value
p_{atm}	Atmospheric pressure
p_N	Standard atmospheric pressure
pH	Acid-base adimensional scale
pO_2	Partial pressure of oxygen
$p_w(T)$	Vapor pressure of water
Q	Ratio of oxygen in the gas mixture

r / r^2	Correlation coefficient/Coefficient of determination
$\mathbf{R}$	Resistance to electric (ionic) current
$\mathbf{R}_{Na^+}$	Resistance to sodium ions flux (synonymous of Na_V channels)
$\mathbf{S}_{H_2O_2}$	Switcher H_2O_2
$\mathbf{V}$	Voltage
$\mathbf{V}_M$	Molar volume
$\mathbf{V}_m$ **or** $\mathbf{V}_{mem}$	Membrane potential
x(MFI)	Geometric mean fluorescence intensity
$\mathbf{x}_{FMO}$**(MFI)**	Standardized geometric mean fluorescence intensity
xyz	Cartesian coordinate system
α**(T)**	Bunsen absorption coefficient
$[O_2]/\delta O_2$	Oxygen concentration/Concentration difference of dissolved oxygen
Δ**x or d**	Excursion of probe
λ	Wavelength
ρ	Resistivity
φ	Phase angle
∇	Gradient
$\propto$	Directly proportional

DISCLOSURES

The Ph.D. student declares that the theoretical (curricular) part of the thesis was entirely received at Universidade do Minho in Portugal and lasted a year; the practical (laboratorial) part was entirely performed in the Zhao lab at University of California (UC), Davis in USA and lasted four years and two months. A sole exception exists, where a subset of the data of oxygen flux measurements was performed in a short summer externship (two weeks) at Marine Biological Laboratory (MBL) in USA, where the optic-based scanning micro-optrode technique (SMOT) to quantify oxygen was originally learned; the thesis writing occurred in both (Minho and California, Davis) universities in two periods of the ultimate two years. Thesis was written by the Ph.D. student, as the original drafts of all first-author publications. Similarly, the vast majority of the laboratorial work was also performed by the Ph.D. student; additional contributions in experiments are detailed throughout thesis and reprinted publications.

The Ph.D. student also declares that the micro-optrode measurements were performed using turn-key systems provided free for use at MBL and loaned to the Zhao lab at UC Davis for no cost, by Applicable Electronics, LLC and Science Wares, Inc. The companies had no influence over the research (in design, execution or interpretation) nor its reporting; moreover, no restrictions on data sharing have been imposed.

The Ph.D. student further declares that the primary language of writing is English in the British native dialect, except for some reprints (media coverage, protocols, posters and publications (in American journals)), where American English is used instead. Portuguese is the native language (European native dialect) of the student and of the University where thesis is defended; therefore, the formal pages and a thesis abstract are in Portuguese. The same applies to some acknowledgments, dedications and quotations. Other languages – Latin, French, Spanish and Chinese (by order of appearance), were used solely in quotations. Latin words and expressions were also used in both the scientific and literary contexts. Finally, Greek symbols are used in the scientific context.

in Memoriam
mana Graça
eterna Saudade

For thine own blossom of all forging fire
He stole and gave to mortals; trespass grave
For which the Gods have called him to account,
That he may learn to bear Zeus' tyranny
And cease to play the lover of mankind.

Aeschylus *in* Prometheus Bound (*ca.* 430 B.C.E.)[1]

And ready-witted Prometheus he bound with inextricable bonds, cruel chains,
and drove a shaft through his middle, and set on him a long-winged eagle,
which used to eat his immortal liver; but by night the liver grew
as much again everyway as the long-winged bird devoured in the whole day.

Hesiod *in* Theogony (*ca.* 700 B.C.E.)[2]

Prometheus
Universidade do Minho
(José Rodrigues, 1992)

PROLOGUE

SYNOPSIS

Si nous osons quelquefois nous élever plus haut, que ce soit avec cette sage circonspection qui sied si bien à une vue aussi faible que la nôtre.

Jean d'Alembert *in* Encyclopédie, ou dictionnaire raisonné des sciences, des arts et des métiers (Discours Préliminaire des Éditeurs) (1751)[3]

Motivation

Nature is magnificent, so is scrutinizing it by science! Being a resolute student of nature, one reaches a point of despair: what drop to pursue in the ocean of wonder? The hard choice was based on a serendipity event. Learning about reactive oxygen species in the university classroom, brought caudal regeneration in lizards to mind; basically, oxygen would enter into the autotomizing site, be oxidized into reactive oxygen species, and alarm and trigger cells to undergo recovery. Regeneration then!

By its natural marvel and biomedical implications, regeneration field is self-motivating. Moreover, by its wide scope, regeneration allows a student to research a plethora of animal models, tissues, organs or structures, and many branches of biology, in addition to a putative integration with physical and even computational sciences.

Although the three centuries of modern research (rooted in the studies of R. Réaumur in crustaceans and A. Trembley in polyps), and the explosive cellular, genetic and molecular detailing of the process in the recent decades, there is a poor understanding – even poorer at the onset of this thesis – about the redox and bioelectric phenomena possibly underlining regeneration. Furthermore, virtually nothing was known about a possible crosstalk between redox and bioelectric phenomena in the context of animal regeneration.

This thesis therefore arose to bridge the chasms of knowledge in the apparently disparate fields of redox and bioelectric biology and humbly contribute to shed some lime light to these less recognizable subfields of regeneration.

Aims

In science, other than pure descriptive analyses, the designing of detailed, consecutive and consequential objectives *a priori* is a tentative exercise. Nevertheless, the general objective of this doctoral thesis is to unveil and demonstrate an effective integration and interplay between redox and bioelectric phenomena during regeneration. To achieve this core aim, we delineated the following descriptive and functional specific objectives, not necessarily sequential, using the *Xenopus laevis* tadpole tail as the animal regeneration model: (i) spatiotemporal profiling of bioelectric parameters – membrane potential (V_m), transepithelial potential (TEP), electric fields (EF) and electric current density (J_i) – during regeneration; (ii) spatiotemporal profiling of redox parameters – oxygen (O_2) flux, reactive oxygen species (ROS) and hypoxia imaging – during regeneration; (iii) understand the necessity and sufficiency for regeneration of candidate bioelectric and redox players: voltage-activated sodium channels (Na_V), hydrogen peroxide (H_2O_2) and hypoxia-inducible factor one alpha (HIF-1α); (iv) readout of the bioelectric parameters upon chemical modulation of the redox status and players; (v) ultimately, from compiled know-how, induce regeneration in the non-regenerative refractory period, by functional modulation of the combinatory interplay between bioelectric and redox states.

Outline

The thesis herein written to obtain the degree of *philosophiae doctor* (Ph.D.) is comprised of **PROLOGUE**, nine **CHAPTERS**, and **EPILOGUE** based on laboratorial research supported by **REFERENCES** of mostly peer-reviewed scientific literature, scientific books, and occasional journalistic articles, and supplemented by sixteen **APPENDIXES** of relevant and complimentary information and work.

In addition to outline the thesis, the current **PROLOGUE**: Synopsis, provides the motivation and aims of the doctorate, and the citations of the end products of research, *i.e.*, the indexed publications (also presents manuscripts and article writings).

In the **CHAPTER I**: General introduction, is surveyed the literature exposing the state of the art required for an integrative understanding of the fields researched in the experimental parts of the thesis. An in-depth focus is given to the fields of redox and bioelectric biology in the context of animal regeneration.

In the next **CHAPTER II**: *Changing the paradigm of redox biology in wound healing and regeneration: H_2O_2 at the core of the insurgence*, is a brief review manuscript, not submitted for indexed publication, that introduces and proposes a paradigm shift after covering the roles of redox players in wound healing and regeneration.

The **CHAPTER III**: *Developmental bioelectricity*, is a partial reprinted publication, a comprehensive academic-grade *Wikipedia* article, that thoroughly overviews the bioelectricity field, in particular in the wound healing and regeneration contexts.

In the **CHAPTER IV**: General hypothesis, is exposed the working hypothesis that was stringently tested during the thesis.

The **CHAPTER V**: General methodology, is detailed the purpose and fundament of the used physiological techniques – microelectrode, vibrating probe and micro-optrode – for a robust interpretation of the derived results. Routine and classic protocols are omitted in this chapter, as they appear in the equivalent section of the reprinted publications with stringent detail.

The **CHAPTER VI**: *Real-time physiological measurements of oxygen using a non-invasive self-referencing micro-optrode*, is a reprinted publication, a technical article where the micro-optrode technique is stringently explored and a detailed protocol derived for application, mainly, in animal physiology. The study starts with explanations on the calibration and on the validation of the method. Next, anticipated results are presented, beginning with O_2 measurements in classic physiological responses – such as respiration and bioenergetics, followed by original physiological responses – such as appendage regeneration. In the end, the study presents a dual micro-optrode mode which can be used to speed up recordings or measure two ionic or molecular species simultaneously.

The **CHAPTER VII**: *Early bioelectric activities mediate redox-modulated regeneration*, is a reprinted publication, a research article of the first part of the thesis, where an interplay between biochemical (specifically redox) and biophysical (specifically bioelectric) signals during regeneration is unveiled and demonstrated. The study starts with an extensive profiling of the spatiotemporal dynamics of extracellular bioelectricity (TEP, EF and J_I) and the temporal requirement for ROS production. It is then reported the effect of redox modulation on bioelectric activities. The study proceeds with rescue and gain of function attempts using exogenous H_2O_2 to restore bioelectric potency and therefore induce

regeneration. The study ends with the elucidation of candidate molecular (ion translocators) mechanisms behind the redox-bioelectric interplay.

The **CHAPTER VIII**: *Early redox activities modulate* Xenopus *tail regeneration*, is a reprinted publication, a research article of the second part of the thesis, where an integration of redox players – O_2, ROS and HIF-1α – during regeneration is explored and shown. The study starts with a complete mapping of the extracellular O_2 flux during regeneration, followed by the search for a correlation with the non-regenerative refractory period. Then it is studied whether the exogenous O_2 fuels required ROS production. Hypoxia and HIF-1α are analysed as downstream candidates of the local pO_2 variations potentially induced by O_2 flux and ROS production. The study ends with candidate molecular mechanisms for the unveiled redox integration that is necessary for and sufficient to induce regeneration.

In the final **CHAPTER IX**: General conclusion, is presented a summary of the drawn conclusions and final remarks that provide a snapshot of the scope of the work performed and evidence-based messages passed. It is also presented future perspectives to compile further evidences or deepen the understanding, especially the molecular mechanisms, of the core thesis that redox and bioelectric phenomena crosstalk in vertebrate regeneration. Chapter ends with literature-based digression and discussion on future, probably cohabiting, strategies to regain function in truncated humans, based either in biology and technology.

In the **EPILOGUE**: Finale, the title and scope of the thesis are re-evaluated to check overall integrity of the written text backing the defended thesis.

Publications

Grounding thesis

Ferreira, F. (2014). Changing the paradigm of redox biology in wound healing and regeneration: H_2O_2 at the core of the insurgence. *Chemical Biology of Oxidants and Free Radicals Course*. (University of California, Davis)

(Chapter II; not peer reviewed and unpublished)

Ferreira, F., Luxardi, G., Reid, B. and Zhao, M. (2016). Early bioelectric activities mediate redox-modulated regeneration. *Development*. **143**, 4582–4594.

(Chapter VII, Appendix VI)

Levin, M., Bates, E., Zhao, M. and Ferreira, F. (2018). Developmental bioelectricity. *Wikipedia*. (https://en.wikipedia.org/wiki/Bioelectricity)

(Chapter III; not peer reviewed)

Ferreira, F., Raghunathan, VK., Luxardi, G., Zhu, K. and Zhao, M. (2018). Early redox activities modulate *Xenopus* tail regeneration. *Nature Communications*. **9**, 1–15.

(Chapter VIII, Appendix VII)

Ferreira, F., Luxardi, G., Reid, B., Ma, L., Raghunathan, VK and Zhao, M. (2019). Real-time physiological measurements of oxygen using a non-invasive self-referencing micro-optrode. *Nature Protocols*. (In press)

(Chapter VI, Appendix V)

Beyond thesis scope

Luxardi, G., Reid, B., Ferreira, F., Maillard, P. and Zhao, M. (2015). Measurement of extracellular ion fluxes using the ion-selective self-referencing microelectrode technique. *Journal of visualized experiments (JoVE)*. **99**, 1–11.

(Appendix I)

Shen, Y., Pfluger, T., Ferreira, F., Liang, J., Navedo, M. F., Zeng, Q., Reid, B. and Zhao, M. (2016). Diabetic cornea wounds produce significantly weaker electric signals that may contribute to impaired healing. *Scientific Reports*. **6**, 1–11.

(Appendix II)

Sun, YH., Reid, B., Ferreira, F., Luxardi, G., Ma, L., Lokken, K., Zhu, K., Xu, G., Sun, Y., Ryzhuk, V., Guo, B., Lebrilla, C., Maverakis, E., Mogilner, A. and Zhao, M. (2019). Infection-generated electric field in gut epithelium drives bidirectional migration of macrophages. *PLoS Biology*. **17(4)**: e3000044. (Preprint in *bioRχiv*, doi: https://doi.org/10.1101/427294)

(Appendix III)

Ma, L., Ferreira, F., Reid, B., Guo, L. and Zhao, M. (2019). Optical microsensing reveals spatiotemporal oxygen dynamics in cornea that affect wound healing via reactive oxygen species.

(Appendix IV; manuscript in preparation; citation subject to change)

CHAPTER I

1. GENERAL INTRODUCTION

If there were no regeneration there could be no life. If everything regenerated there would be no death. All organisms exist between these two extremes (...) tend[ing] toward the latter end of the spectrum, never quite achieving immortality because this would be incompatible with reproduction.

Richard J. Goss *in* Principles of Regeneration (1969)

The why, when, where and how of regeneration are biological mysteries as old as modern science itself. Indeed, the birth of scientific experimentation coincided with the study of polyps regeneration by A. Trembley in 1740 (Dinsmore, 1991). Why regeneration ensue and why in some tissues and animals and not in others? How the existing part recognizes and restores just the lost part in precise size and proportion? How functional integration of new with old parts occur? These canonical questions and derived ones (Alvarado and Tsonis, 2006; Goss, 1969) find no straight answer in the research pursued; rather, that research opens original basic and applied avenues to see those questions from a novel and promising perspective.

1.1 Animal regeneration

1.1.1 Brief history

Before the rise of writing systems and modern science, it is virtually impossible to establish the origin of regeneration awareness, either of our own or of other animals. Nevertheless, prehistory parietal art from the upper Palaeolithic (50-10 ka B.C.E.) provides the first evidence of regeneration (or lack of it) with the negative silhouettes of human hands lacking finger parts. Written evidence appears in the ancient Greece mythology and in the philosophical works of Aristotle and Pliny. Infamous are the legends of the Hydra and of Prometheus. Hydra, a nine-headed serpent-like creature, could regenerate two heads for every one lost; and Prometheus, a Titan that Zeus punished to perpetuity for giving fire to humans, regenerated his liver overnight only to be eaten by an eagle at daytime (*vd.* page iv). By the might of Hercules, both regeneration myths ceased. Despite Aristotle's mention of animal limb regeneration, whether stone age humans and ancient Greeks actually knew about humans who could regenerate fingers and livers, respectively, one can only wonder; factual and scientific observations and

experimentation of regeneration was still far away in time (Carlson, 2007; Dinsmore, 1991; Morgan, 1901).

From the scientific inquiry triggered by anecdotal tales of seashore and riverbank fearers to the latest tinkering of molecular cues, just over three centuries of rich and compelling modern regeneration history have passed. "Nature gives back to the animal precisely and only that which it has lost, and she gives back to it all that it has lost." This quote is a sentence summary of the seminal publication starting the scientific study of regeneration. In 1712, R. Réaumur reported a detailed description of limb regeneration in freshwater crayfish, simultaneously elevating to science the folk tales pervading coastal and marginal people. Amid the preformation *vs.* epigenesis debate of the 18th century, Réaumur and others interpreted limb regeneration as the growth of an "egg" containing a preformed limb at the base of the limb. While captivating at first, further experiments revealing that limbs regenerate at multiple points thus requiring multiple "eggs", hindered preformation enthusiasm (Dinsmore, 1991; Reaumur, 1712). In 1740, A. Trembley brought decisive evidence in favour of epigenesis, besides avoiding the debate. While seeking an ultimate proof for the animal nature of polyps, Trembley instead discovered that whole new specimens regenerated from cut pieces. Elaborate experimentation created a seven-head creature leading him to call it *Hydra*, a fit eulogy to the Greek creature (Trembley, 1744a; Trembley, 1744b). Head regeneration also had theological and philosophical implications for the indivisibility of the "soul". The ambitious experimentation of Trembley established it as the *de facto* origin of the modern discipline of regeneration and even the broad experimental biology (Dinsmore, 1991).

Although one of the oldest biology fields, regeneration research has been progressing in waves of intense and moderate interest. Following Réaumur and Trembley path, an intense wave surfed Europe, and many organisms felt the scissors of researchers to unveil their regenerative prowess in detailed but gross observations: earthworms body and snails head by C. Bonnet in 1745 and 1777, respectively; earthworms body, snails head and amphibians (salamander and tadpoles) tail by Spallanzani in 1768; and planarians body by P. Pallas in 1774 (Bonnet, 1745; Bonnet, 1777; Carlson, 2007; Pallas, 1774; Spallanzani, 1768).

In the 19th century, cell theory and histologic techniques allowed for a finer understanding of regeneration. Evolutionary theory unveiled a new perspective to the field and raised questions about the monophyletic *vs.* polyphyletic nature of regeneration given its sparse distribution among animals (Bely

and Nyberg, 2010; Carlson, 2007; Dinsmore, 1991). The now ubiquitous nerve-dependency of regeneration was first discovered by T. Todd in newts in 1823, commencing the race to find the factor(s) underlying this neurotrophic phenomenon that still endures (Kumar and Brockes, 2012; Kumar et al., 2007; Singer, 1952; Todd, 1823). In pre-genetic era, T. Morgan published the landmark field book *Regeneration* in 1901, compiling his research on earthworms, planaria, crabs and fish, and, more importantly, organizing and categorising the field with critical definitions and classifications much needed (Morgan, 1901); his terminology remains actual. Morgan, an epigenetic and wholistic advocate, proposed that regeneration is a matter of internal organization of the whole (Dinsmore, 1991; Sunderland, 2010). Importantly, Morgan disproved Weismann's theory of regeneration by natural selection, specifically, that regenerative ability is a function of liability to injury (Morgan, 1898). Exception to this is the tail and appendages autotomy in lizards and arthropods, respectively, which is regarded as evolutionary adaptation to frequent tissue loss (Bely and Nyberg, 2010). Despite absent general liability basis, there is a general *utilitarian imperative* to regeneration, as R. Goss coined in his *Principles of Regeneration* (Goss, 1969). *I.e.*, regeneration proceeds only if inconsequent energetic expenditure is precluded, *e.g.*, there is no physiological significance in regenerating limbs or lens without neuronal connectivity in urodeles, or caps atop stalk without nucleated rhizoids in the protozoan *Acetabularia*. To frame polarity and patterning, Morgan introduced the gradient concept in regeneration, transformed into metabolic gradient by C. Child, and that later inspired A. Turing's reaction-diffusion model of pattern formation and L. Wolpert's positional information theory based on morphogen gradients draining into morphogenetic fields and regeneration territories (Child, 1907; Dinsmore, 1991; Morgan, 1905; Turing, 1952; Weiss, 1939; Wolpert, 1969).

Frustrated by the apparent lack of human regeneration, research entered a moderate wave in the 20th century. However, for understandable reasons, around World War II the tide shifted and arose an intense wave to induce limb regeneration on nonregenerative animals. The first success came in 1933, when Polezhaev stimulated frog limb regeneration by mechanical trauma (Polezhayev, 1933). Then, in 1954, on Todd's shoulders, M. Singer deviated the sciatic nerve to induce partial regeneration also in frog's limbs (Singer, 1954). Several other attempts were performed using chemical irritation, grafting, hormones, growth factors and electrical stimulation. At maximum, only partial regeneration was achieved in frogs, lizards, chicks, rats, among others (Carlson, 2007).

A bioelectric approach to regeneration was catalysed by A. Mathews' electric potential and polarity correlates in 1903 and by A. Monroy's measurement of an electric potential in amputated salamander limbs in 1941 (Mathews, 1903; Monroy, 1941; Zhao, 2018). On such grounds, in 1967, S. Smith implanted a bimetallic rod in nonregenerative frog's limb and partially induced regeneration with the generated small but physiologic current (Smith, 1967). With the introduction of the ultra-sensitive vibrating probe, to measure the tiny physiologic electric currents, around this time (Jaffe and Nuccitelli, 1974), bioelectric research boomed and radiated, and still holds promise in contemporary research (Adams et al., 2007; Borgens et al., 1977a; Borgens et al., 1977b; Ferreira et al., 2011; Hechavarria et al., 2010; Jenkins et al., 1996; Levin, 2007; Tseng and Levin, 2013) (Chapter VII, VIII).

Although rooted in earlier wound healing research (Sen and Roy, 2008), a redox approach to regeneration emerged only in the last few years and is revealing previously hidden mechanisms underlying regeneration in multiple tissues and structures of routine regeneration models, including zebrafish heart and fin, *Xenopus* tadpole tail, gecko tail, planarian body and more (Gauron et al., 2013; Han et al., 2014; Love et al., 2013; Niethammer et al., 2009; Pirotte et al., 2015; Zhang et al., 2016) (Chapter VI–VIII).

The molecular revolution, stem cells, tissue engineering, organ 3D printing and bionics have entered the 21st century regeneration research in strength, especially for the regenerative medicine subfield (Ambrose, 2017; Herr and Grabowski, 2011; Murphy and Atala, 2014; Ott et al., 2008). The 300 year-old scientific quest, or even dream, of achieving major human regeneration is approaching.

As made obvious by this brief historical overview, the corpus of regeneration research now fills dedicated textbooks in the life sciences libraries and influences both scientific and philosophic (*e.g.*, ethical prospects) endeavours.

1.1.2 Basic terminology and typology

By its historic and scientific roots in development, healing and reproduction, the definition of regeneration has been mutating over time. Synonyms of "regeneration" as "reproduction", "repair", "replacement", "renewal", "rearrangement" meant to be followed by "of lost parts", abounded in the 18th and 19th centuries literature (Dinsmore, 1991; Goss, 1969; Morgan, 1901). One important definition was put forth by D. Barfurth near the 20th century: regeneration is "the replacement of an organized whole from a part of the same." (Translated by and after (Morgan, 1901)). While elegant,

this definition failed to discard the fertilized egg that will become a body (Morgan, 1901). Both this definition and the views at the time encompassed physiological and pathological regeneration. *Physiological or homeostatic regeneration* is the natural turnover or replacement of used cells, tissues or body parts; and *pathological regeneration* – nowadays referred to as *reparative or facultative regeneration* – is the replacement of lost or damaged cells, tissues, organs, structures or body parts (Carlson, 2007; Poss, 2010).

Aiming to a virtually all-encompassing definition, in the field's seminal book, T. Morgan defined regeneration as "not only the replacement of a lost part, but also the development of a new, whole organism, or even a part of an organism, from a piece of an adult, or of an embryo, or of an egg. We must include also those cases in which the part replaced is less than the part removed, or even different in kind." (Morgan, 1901). Following his utilitarian imperative of regenerates (*vd.* section 1.1.1), R. Goss pragmatically defined regeneration "primarily as a device by which functional competence is recovered. Morphological restitution [perfect or imperfect] is only a means to this end." (Goss, 1969).

Developmental biology categorization branch regeneration with metamorphosis and aging as post-embryonic development. It goes further to define regeneration as "the reactivation of development in later life to restore missing tissues." (Gilbert, 2006). While fit for most natural occurrences, it does not bracket *in ovo*, *in utero*, embryonic and pre-metamorphic naturally occurring or artificially induced regeneration (Allan et al., 2006; Deuchar, 1975; Han et al., 2003; Morgan, 1901; Taylor et al., 1994).

To avoid such large and broad spectrum working definitions, Morgan and regenerationists ever since, systematically categorized regeneration to provide more discrete and accurate definitions. Crucially, Morgan introduced, in the same book, two fundamental categories: *epimorphic regeneration*, as the "cases of regeneration in which a proliferation of material precedes the development of a new part"; and *morphallaxis*, "in which a part is transformed directly into a new organism, or part of an organism without proliferation at the cut surfaces." (Morgan, 1901). Though respected in their essence, these definitions have evolved considerably. Presently, epimorphic regeneration refers to the replacement of an injured or automatized structure mediated by a regeneration bud or blastema; where the *blastema* is a mass of undifferentiated and proliferating cells (from dedifferentiation and/or from stem cells) arising at the onset of regeneration by epithelial-mesenchymal interactions and possessing intrinsic morphogenetic information that is responsible for the *de novo* formation of the lost part (Beck et al.,

2009; Carlson, 2007). A particular case of regeneration, *hypomorphic regeneration*, was termed specifically for the intrinsically deficient epimorphic regeneration forming an incompetent fibroblastema that typically produces a spike-like structure (Beck et al., 2009); the frog limb regeneration (Dent, 1962) is the textbook example. While far less studied than its counterpart, current morphallaxis definition relates more with the remodelling and repatterning of existing tissues to recover form than with proliferation itself, as limited proliferation occurs (Bely and Nyberg, 2010; Carlson, 2007).

Overall, the current textbook-like classification can be systematized as follows (Carlson, 2007; Poss, 2010). Upon injury, disease or autotomy, the cells, tissues, organs, structures and even the whole organism, undergo one of four major types of regeneration: (i) *homeostatic regeneration* – above defined, classic examples are skin and gut shedding, blood turnover, moulting and antler regeneration; (ii) *facultative regeneration* – above defined, that is subdivided in (a) *epimorphic regeneration* – above defined, classic examples are limb and tail regeneration in urodeles and pre-metamorphic anurans amphibians, lizard tail, planarian head and arthropod appendages; (b) *tissue regeneration* – similar to epimorphic one but without blastema formation, classic examples are muscle, bone, skin and heart; and (c) *cellular regeneration* – reconstitution of a damaged cell, examples include axons and regeneration in unicellular lifeforms as *Acetabularia*; (iii) *hypertrophy* – functional mass increase, can be (a) *compensatory* – when the increase occurs in the paired organ (mammalian kidneys and lungs cases) and (b) *regenerative* – when the increase occurs in the damaged organ itself (mammalian liver and pancreas cases); and (iv) *morphallaxis* – above defined, classic examples are necessarily simpler organisms, like planarias and hydroids.

Occasionally, regeneration occurs though the combination of epimorphosis and morphallaxis, namely in the fission of planarias. As here highlighted, invertebrate asexual reproduction, especially fission in protozoa, planaria, some starfish and annelids, share physiologic and molecular mechanisms with regeneration, blurring the line separating reproduction and regeneration, as it happened in the 18th century beginnings of regeneration biology (Bely and Nyberg, 2010; Carlson, 2007; Sánchez Alvarado, 2000).

Henceforth, sole focus will be given to epimorphic regeneration as it is the type studied using the *Xenopus laevis* (Daudin, 1802) tadpole tail regeneration as the selected regeneration model (*vd.* section 5.1).

1.1.3 Asymmetrical distribution upon basal origin

Prior to evolutionary theory, regeneration marvelled and perplexed developmental and regenerative biologists for the dramatic irregularity of its distribution among the animal kingdom. Natural selection itself, however, did not solve the problem, only allowed for a more comprehensive assessment of regeneration by the inclusion of ecological context, developmental basis and evolutionary history. Virtually all animals, from unicellular protozoans to multicellular mammals, regenerate; however, the degree of their ability to regenerate varies hugely. The efficiency distribution of epimorphic regeneration differs at the organismal, ontogenetic and phylogenetic levels (Bely and Nyberg, 2010; Fröbisch et al., 2015; Sánchez Alvarado, 2000).

Within the organism itself, regeneration fidelity shifts spatially. Such region-specificity is well illustrated in lizards. While automatized tails regenerate well morphologically and perfectly behaviourally, the amputated limbs only undergo hypomorphic regeneration (Alibardi, 2010). Another example are some annelids that regenerate the tail but not the head (Bely and Sikes, 2010). Reasons for the intraorganismal variability may include liability to structure loss and decoupling of regeneration from asexual reproduction (Bely and Nyberg, 2010).

Ontogenetically, regeneration efficiency differs with development and age. Anurans, like *Xenopus* spp., are the canonical examples here. While pre-metamorphic tails and limbs perfectly regenerate, post-metamorphic limbs only form spikes (hypomorphs) (Beck et al., 2009; Muneoka et al., 1986). Among the amniotes, birds and mammals, but not reptiles, have a higher epimorphic-like regenerative capacity in embryonic than in adult life (Alibardi, 2010; Deuchar, 1976; Han et al., 2003; Taylor et al., 1994). The exact reasons behind this temporal variability are elusive; yet, some evidence-supported hypotheses have been suggested, notably the correlation with the immune response and development (Fukazawa et al., 2009; Godwin and Brockes, 2006; Mescher and Neff, 2005).

Phylogenetically, regeneration is sparse and of dubious, apparently inexistent, pattern in their distribution (Sánchez Alvarado, 2000). Sometimes, closely related species have huge differential regenerative ability, such as in the body regeneration of annelids (Bely and Sikes, 2010). Generally, however, the simpler the organism (lower animals), the higher the regenerative capability. For instance, most whole animal (metazoan) regeneration cases, from small original pieces, come from planaria and hydra, specimens of the lower *taxa* Platyhelminthes and Cnidaria, respectively. Increasing complexity drains regeneration to morphogenetic fields, known as regeneration territories, where large-scale

amputation or autotomy regenerates solely the lost structure and not a full animal (Carlson, 2007). The most studied case of this are the so-called kings of regeneration, the urodeles, that have territories to regenerate jaws, lens, limbs, tail and crest via epimorphosis (Han et al., 2005; Weiss, 1939). Other *taxa* with considerable epimorphic regeneration territories include the protostomes Mollusca (siphon, tentacles and head), Annelida (head and tail) and Arthropoda (appendages) (Carlson, 2007). Other deuterostomes have allocated considerable epimorphic regeneration territories; fish regenerate damaged fins, tails and barbells (Akimenko et al., 2003; Goss, 1956), and reptiles regenerate automatized tails (Alibardi, 2010). In between Platyhelminthes and Amphibia, there are fairly complex animals such as starfish and sea stars (Echinodermata) who can still regenerate a full animal from a lost part, *i.e.*, the arm, either amputated or automatized. Although in Echinodermata full arm regeneration is relatively widespread, the whole animal regeneration is limited (Carnevali, 2006). As we reach extreme animal complexity in birds and mammals regeneration ability falls sharply and there are only residual regeneration territories in adult life. Research in bird regeneration is utterly rachitic and other than *in ovo* studies, not much is known about their abilities to regenerate, for instance, digit tips (Satoh et al., 2010). A tiny subset of mammals – rabbit, cat, super-healing mouse (MRL strain) and African spiny mouse – regenerate ear holes but not tips. The reasons behind such regeneration gift are absolutely elusive. This reportedly blastema-based regeneration restores cartilage and skin and even hair and sebaceous glands to the lost hole (Seifert et al., 2012; Williams-Boyce et al., 1986). The digit tip regeneration in foetal, neonatal and juvenile mammals, including humans where it was discovered, is the pinnacle of mammalian epimorphic regeneration and what has given hope to trigger limb regeneration in humans (Douglas, 1972; Han et al., 2005; Illingworth, 1974). This type of regeneration depends on the residual bed nail presence, probably due to the expression of the homeobox gene *Msx1* next to it, which regulates BMP signalling to induce regeneration (Han et al., 2003; Reginelli et al., 1995; Yu et al., 2010).

The sparse distribution could point to a polyphyletic origin, but in fact regeneration is likely monophyletic, *i.e.*, only evolved once. Indeed, regeneration is so basal that its origin probably coincided with the origin of multicellularity. Despite poor comparative genetic evidence, supporting this symplesiomorphy is the homology of regeneration mechanisms across phyla, both cellular and molecular, such as wound healing and blastema formation, nerve-dependency and Wnt signalling (*vd.* section 1.1.4) (Bely and Nyberg, 2010; Brockes and Kumar, 2008; Korschelt, 1927; Sánchez

Alvarado, 2000). Regeneration is thought to have originated as an epiphenomenon of development, *i.e.*, derived by the accessibility to the developmental program of the lost structure (Bely and Nyberg, 2010). Once originated, three mechanisms or hypotheses can explain its maintenance: selection (fitness and adaptation), pleiotropy or phylogenetic inertia. Sublethal predation is the commonest cause of triggered regeneration, thus the adaptative hypothesis by selection is the most widespread reason for maintained regeneration, having automatizing species at its core. Pleiotropy explains non-adaptive regeneration, when regeneration is tightly connected with other phenomenon, like asexual reproduction. Phylogenetical inertia hypothesize that current regeneration is not adaptative nor kept by pleiotropy; it is there simply because it was in their ancestries. This might be the case of some annelids (Bely and Nyberg, 2010).

What explains the maintenance of regeneration can also explain its loss. Thus, regeneration might have been loss by neutral or negative selection, or indirect selection via trade-offs with other important traits. Among the various disparate ecological and physiological selective pressures are energetic costs, lifespan, structure redundancy (*e.g.*, spider legs), decreased liability risk, increased resistance to injury (*e.g.*, skeleton development), infection risk and immune system development and evolution (*e.g.*, anurans) (Bely and Nyberg, 2010; Godwin and Brockes, 2006). Regeneration could also be lost by pleiotropy breakdown in annelids (Bely and Sikes, 2010). An elegant hypothesis for the amniotes loss of limb regeneration via this process, suggests that, to regenerate, the limb needs to primarily develop as a self-organized, semiautonomous module without interactions with transient structures, as is the case of urodeles (Galis et al., 2003).

Altogether, to grasp the drastically uneven distribution of regeneration at organism, ontogeny and phylogeny grounds, it is required to recall the ecological, evolutionary and developmental histories of the animal – the eco-evo-devo approach –, understand their differential weight and only then sense might be established for particular species (Bely and Nyberg, 2010; Fröbisch et al., 2015; Sánchez Alvarado, 2000).

1.1.4 Blurring with development and wound healing

Two long-standing canonical questions pervade the regeneration field: Is regeneration a wound healing without scarring? and Is regeneration a recapitulation of development? For self-explanatory reasons, the former question solely applies to tissue regeneration and not to epimorphic regeneration; *i.e.*, when a

blastema mediates regeneration the issue no longer applies. Naturally, epimorphic regeneration – as every other type of regeneration – requires wound healing of the damaged surface, but in epimorphosis type, the goal is to allow and instruct for a mesenchymal-like blastema to form under the healed epithelium (*vd.* details below). Notably, generic wounds – and not only amputation-derived wounds – can induce regeneration, showing that missing tissue context is what distinguishes them (Owlarn et al., 2017). For the latter question, following the main hypothesis for the origin of regeneration – an epiphenomenon of development – inherently mandates regeneration as largely a recapitulation of development (Bely and Nyberg, 2010). Notwithstanding, from the eons since its origin, regeneration-specific events evolved in disparate degrees in different animals. Nature tends to be excruciating economic, optimizing processes by selection and whenever possible co-opting what exists to create, or better, to derive something new. Convergent evolution of molecular pathways underlying limb and appendage development is a case of such economy or efficiency. Co-opted from development, regeneration has its main morphogenetic problems solved *a priori* by simply accessing the default blueprint (Nacu and Tanaka, 2011). Thus, the main problem becomes one of deployment of the developmental program, upon damage detection.

Mostly from the chick model, vertebrate limb development is cellularly and molecularly well established (Gilbert, 2006). Briefly, a limb bud composed of an apical ectodermal ridge (AER) and a mesenchymal progress zone (PZ) interact to morphogenetically grow the limb. FGF and Shh signalling from the AER and PZ, respectively, regulate development and define the proximodistal (P/D) and dorsoventral (D/V) axes. Anteroposterior (A/P) axis is controlled by BMP signalling, while retinoic acid (RA) further defines the PD structures (Zeller et al., 2009). In the signature regeneration model – urodele limb – equivalents to AER and PZ exist, the apical epidermal cap (AEC) and the blastema (Stocum, 2017). Classic grafting and transplantation experiments, between developing and regenerating limbs, showed their functional equivalence. Removal of AER or AEC or replacement with fully differentiated skin precludes development or regeneration, respectively, by the blockade of epithelial-mesenchymal communication with the underlying PZ or blastema, respectively (Brockes and Kumar, 2008; Nacu and Tanaka, 2011; Zeller et al., 2009). FGF, BMP and RA were also found to be pivotal to regeneration (Mercader et al., 2005; Nacu et al., 2016; Slack et al., 2004). The limb bud and tailbud typically regenerate in vertebrates, hence their analogy to the blastema; however and intriguingly, the *Xenopus* tailbud does not regenerate, despite its ability to regenerate the limb bud (Beck, 2015). The skin

grafting experiment revealed an essential trait of regeneration. The wound healing must not be terminal; rather, produce a transient epidermal structure that actively feedbacks with the underlying mesenchyme to permit (re)development to proceed.

This brief blurring of development, wound healing and regeneration is by no means complete but it is sufficient to highlight the trimodality of the process of regeneration: first, detect injury and transiently heal; second, generate a blastema via wound epithelium signals, and third, deploy default development. Although most epimorphic regeneration produces a (near) perfect replica of the original, some cases do not, like the lizard tail (Clause, 2006). In these cases, the fidelity of the recapitulation of development is not perfect and can be due to developmental or evolutionary constrains (*vd.* section 1.1.3).

1.1.5 General phenomenology and basic mechanisms

Despite its wide distribution, epimorphic regeneration follows some common phenomenology and mechanisms (Fig. I.1). The textbook example used to expose those rules – shared by different animals and tissues – is the amphibian limb regeneration, first described by Spallanzani in 1768 (Carlson, 2007; Dinsmore, 1991; Spallanzani, 1768). Most regenerationists categorize regeneration into three phases or modules: wound healing, blastema formation and redevelopment. Although successive, a natural overlapping between the phases takes place. This overlapping is indeed important, as active feedback exists between the structures and emanating molecular players within each phase (Fig. I.1a) (*vd.* section 1.1.4).

Upon limb amputation, key injury-responsive biochemical and biophysical cues sense and probably trigger epimorphic regeneration. Among the recently unveiled non-genetic biochemical signals are redox players, such as, O_2, ROS and HIF-1α (*vd.* section 1.2). Bioelectric players, such as, membrane and transepithelial potentials, and electric currents and fields, have been recently (re)discovered biophysical cues (*vd.* section 1.3). Within seconds, the retraction of soft tissues and nerves, and the contraction of blood vessels precede scar-free wound closure. Hours later, centripetal epithelial migration from wound edges covers the amputation surface. In larger cross-sectional wounds, a day or two may be required to complete the wound closure without a basement membrane (Carlson, 2007; Stocum, 2017). This pre-regeneration healing is similar to non-regenerating epithelial healing (Owlarn et al., 2017), but then an apical epidermal cap is formed, initiating its communication with the

underlying tissues, leading to the formation of a mesenchymal blastema. The healing itself is a long-standing essential factor in regeneration, as its blockage or the flapping and grafting of mature skin precludes regeneration (Ho and Whitman, 2008; Mescher, 1976). Interestingly, the skin-like structures impair important behaviours for regeneration, such as altered electric currents (Altizer et al., 2002; Reid et al., 2009) and disruption of epithelial-mesenchymal crosstalk (Lee et al., 2009). Moreover, the wound epithelium provides morphogenetic information for regeneration (Campbell and Crews, 2008; Endo et al., 2004).

The tissue breakdown and macrophage-mediated debridement and (histolysis and phagocytosis) (Godwin et al., 2013), limited immunomodulation (*e.g.*, inflammation) (Godwin and Brockes, 2006), remodelling of the extracellular matrix (ECM) via metalloproteinases (Vinarsky et al., 2005) and mitotic activation (*e.g.*, via thrombin) are permissive to canonical epithelial-mesenchymal interactions at the onset of blastema implementation (Fig. I.1b). This is the timing where decision making on whether to follow a regenerative program is taken; however, compared to the other phases, this phase was the least studied for decades (Carlson, 2007). Last decade efforts – including the ones presented in this thesis – have been bringing crucial findings, unveiling key limiting and stimulating factors of regeneration. By definition, a stimulating factor of regeneration is also a limiting one; the opposite is not necessarily true. Among those early factors, apoptosis-induced proliferation (Diwanji and Bergmann, 2018) with Wnt downstream (Chera et al., 2009) and ROS upstream (Fogarty et al., 2016), macrophage infiltration (Godwin et al., 2013), Wnt, FGF, Shh and BMP signalling (Beck et al., 2003; Lin and Slack, 2008; Lin et al., 2013; Nacu et al., 2016; Yokoyama et al., 2000), ROS (Love et al., 2013; Niethammer et al., 2009), HIF-1α (Zhang et al., 2015), membrane potential (Adams et al., 2007; Durant et al., 2017), electric currents and fields (Jenkins et al., 1996; Reid et al., 2009), all modulate dramatically the regeneration efficiency in different regeneration models.

Fig. I.1 Epimorphic regeneration in invertebrates and vertebrates. **a** General regeneration-specific phases: wound healing and blastema formation; redevelopment phase is then deployed. **b** General mechanisms. Adapted from Alvarado and Tsonis, 2006.

The origin of cells to the blastema has troubled scientists for centuries, especially due to the shifting dogma of cellular plasticity (Carlson, 2007; Dinsmore, 1991). In invertebrates, pre-existing stem cells (widespread neoblasts in planaria) are the sole contributor to the blastema. However, in vertebrates the issue is far more complicated and different species and tissues have different contributors to the blastema cell pool. Generally, both stem cells and mature cell dedifferentiation provide blastemal cells; however, the exact extent of their contribution remain elusive (Tanaka and Reddien, 2011). For instance, in adult newt limb regeneration, muscle dedifferentiation contributes to the blastemal mass; however, in axolotl and larval newt, satellite cells contribute instead (Kragl et al., 2009; Lo et al., 1993; Sandoval-Guzmán et al., 2014). Msx1 and mitogenic thrombin are required for myofibres cellularization and posterior proliferation, respectively, in adult urodeles (Kumar et al., 2004; Tanaka et al., 1999). Regenerating nerve fibres reach the AEC prior to blastema establishment; however, early blastema is relatively avascular and therefore potentially hypoxic (refer to Chapter VIII). Deviated nerves supplemented with contralateral skin grafts, or hyperinnervation induce the formation of an accessory

limb in axolotl and improve regeneration in adult *Xenopus*, respectively (Endo et al., 2004; Mitogawa et al., 2018). A quest to find growth/trophic factors to resolve the canonical nerve-dependency of limb regeneration, led to the discovery of the nerve-dependent newt anterior gradient (nAG) protein (Kumar et al., 2007). Other previously found candidates included, among others, transferrin and FGF2 (Kumar and Brockes, 2012). Initially expressed in Schwann cells, nAG is then expressed in the wound epithelium where it contributes to blastemal cell proliferation. nAG rescues denervated blastemas leading to complete regeneration (Kumar et al., 2007). Moreover, limb denervation during development results in continuous expression of nAG, providing a molecular explanation to the insofar paradoxical aneurogenic limb regeneration (Kumar et al., 2011). Intriguingly, nAG is a thioredoxin, thus linking neuronal and redox activities, two previously separated pathways of regeneration (Meda et al., 2018). The growth factors FGF10 and FGF2, expressed in blastema and in nerves and epithelium, respectively, are necessary for regeneration. In fact, FGF10 is even sufficient to induce partial regeneration in nonregenerative *Xenopus* limb by regulating *Shh* and *Msx1* expression (Lin et al., 2013; Yokoyama et al., 2000; Yokoyama et al., 2001).

With maturation, the now vascularized and well innervated blastema undergoes morphogenesis – patterning via cell determination and differentiation – grossly seen by precartilaginous blueprints later turned into bone where differentiating muscle attach (Brockes and Kumar, 2008; Carlson, 2007). The fate of blastemal cells was another historical puzzle in the regeneration field. Growing on older suggestions, contemporary genetic-based fate mapping has generically settled that appendage regeneration in different species occurs via proliferation and differentiation of lineage-restricted cells (Kragl et al., 2009; Nacu and Tanaka, 2011; Tanaka and Reddien, 2011). In other words, the blastema is a mass of similar-looking heterogeneous cells that retain memory of their cellular origin.

In adult urodeles, as the morphogenesis and patterning within the redevelopment phase approaches its end, the regenerated limb is a smaller copy of the contralateral intact limb. Hence, in the following weeks overall growth occurs until regular dimensions are attained. Larval amphibians almost dispense this growth period (Carlson, 2007). The well-studied major signalling and patterning pathways densely used throughout development, also have pervasive roles in this phase of regeneration – which falls beyond the scope of this thesis – as reviewed elsewhere (Brockes and Kumar, 2008; Chen and Poss, 2017; Nacu and Tanaka, 2011; Zeller et al., 2009).

This overview of the expanding field of regeneration is necessarily insufficient. Although some of the described details naturally differ across tissues and species (*vd.* section 1.1.6), the general phenomenology and basic mechanisms are broadly conserved (Alvarado and Tsonis, 2006; Miller et al., 2019) (Fig. I.1). After the classical anatomical, morphological and histological descriptions (Carlson, 2007; Dinsmore, 1991), the cellular, molecular and genetic basis of regeneration has been detailed in the last few decades, as well reviewed elsewhere (Brockes and Kumar, 2008; Chen and Poss, 2017; Nacu and Tanaka, 2011; Tanaka and Reddien, 2011). In addition to the always attractive molecular basis, regeneration is being dissected at the redox (Coffman and Su, 2019; Diwanji and Bergmann, 2018; Meda et al., 2018), bioelectrical (McCaig et al., 2005; McLaughlin and Levin, 2018), mechanical (Chiou and Collins, 2018), hormonal (Herrera-Rincon et al., 2018) and immunological (Julier et al., 2017; Mescher and Neff, 2005) basis.

1.1.6 Specifics of *Xenopus laevis* tadpole tail regeneration

Beyond urodeles, research using anurans of the genus *Xenopus* escaped their embryonic development confinement and became established regeneration models. The tadpole's (prospective) tail of *X. laevis* was first used as a regeneration model in 1975 to assess the regenerative ability of embryos (Deuchar, 1975). However, the use of anurans as regeneration models goes back to the very beginning of this research field, in the 18th century, with the experiments of L. Spallanzani published in his classic *Prodromo* (Spallanzani, 1768; Tsonis and Fox, 2009) (*vd.* section 1.1.1).

The *X. laevis* tadpole tail is comprised of epidermis, muscle, vasculature, connective tissues, somites, notochord, peripheral nerves and spinal cord (Fig. I.2a). Although originated from different developmental lineages, these tissues somehow orchestrate whole and functional tail regeneration in just a week (or up to three weeks, depending on tadpole's age). As for the urodeles textbook case (*vd.* section 1.1.5), regeneration can be divided into three successive but overlapping phases or modules: wound healing, regeneration bud formation and regenerative outgrowth (Beck et al., 2009; Li et al., 2016; Tseng and Levin, 2008).

In the wound healing phase, a scar-free wound epithelium covers the amputation plane within 6 h. The cells of basal layer of the epidermis are the responsible for this. The TGF-β pathway is the earliest of the canonical signalling pathways to be expressed (within 15 min) and its inhibition precludes healing and, therefore, regeneration. Initially expressed in the basal layer, TGF-β pathway is then expressed

throughout regeneration, regulating – in addition to wound epithelium – regeneration bud formation and cell proliferation (Ho and Whitman, 2008). A marvellous recent finding showed the existence of regeneration-organizing cells (ROC), using single-cell RNA sequencing (Aztekin et al., 2019). These cells, present in the epidermis during tail development, migrate to the amputation plane to form a competent wound epithelium. ROC removal leads to no regeneration and ROC grafting induces ectopic structures. ROC secretes ligands of canonical signalling pathways, including FGF, BMP and Wnt, therefore controlling downstream regeneration efficiency. Interestingly, inhibition of TGF-β pathway and ROS production preclude ROC migration, putting ROS and TGF-β pathway upstream of ROC (Aztekin et al., 2019).

Tadpole tail has fluctuating regenerative abilities in function of developmental stage or age. Specifically, in the pre-metamorphic stages 45-47 (Nieuwkoop and Faber, 1967) regeneration, for unknown reasons, fails to occur, leading to wound closure with a thicker, skin-like, epidermis (Beck et al., 2003). Not surprisingly, this refractory period is being used to readily compare cues with regenerative competing tadpoles and to perform pivotal gain-of-function assays (Li et al., 2016). Intriguingly, ROC cells do not migrate in the refractory period to form a regeneration-inducing wound epithelium (Aztekin et al., 2019).

Probably triggered and sustained by signals and growth factors from the wound epithelium, the blastema-equivalent regeneration bud is formed around 24 h. It comprises undifferentiated mesenchymal cells with one insofar identified stem cell type, satellite cells (Chen et al., 2006). The bud also includes degenerating muscles, a neural ampulla (spinal cord bisection closure) and precursor cells at the terminus of the notochord (Gargioli and Slack, 2004; Slack et al., 2004) (Fig. I.2b). Interleukin-11 (IL-11) and probably Msx1 induce and maintain the undifferentiated state of the bud, therefore facilitating cell proliferation within it (Beck et al., 2003; Tsujioka et al., 2017). ROS, electric currents, V-ATPase and apoptosis are required for regeneration and are upstream cues regulating master signalling pathways. Amputation-induced, long-term, sustained production of ROS modulate cell proliferation, Wnt and FGF signalling, all important for a proper activity of the regeneration bud (Lin and Slack, 2008; Love et al., 2013). Epidermis-driven electric current variations upon amputation and during regeneration are required for regeneration (Reid et al., 2009). Sodium is the major component of this current and modulates cell proliferation, axonal patterning, Notch and Msx1 (Tseng et al., 2010). The affected signalling pathways, together with Wnt and FGF (downstream of Wnt) are activated

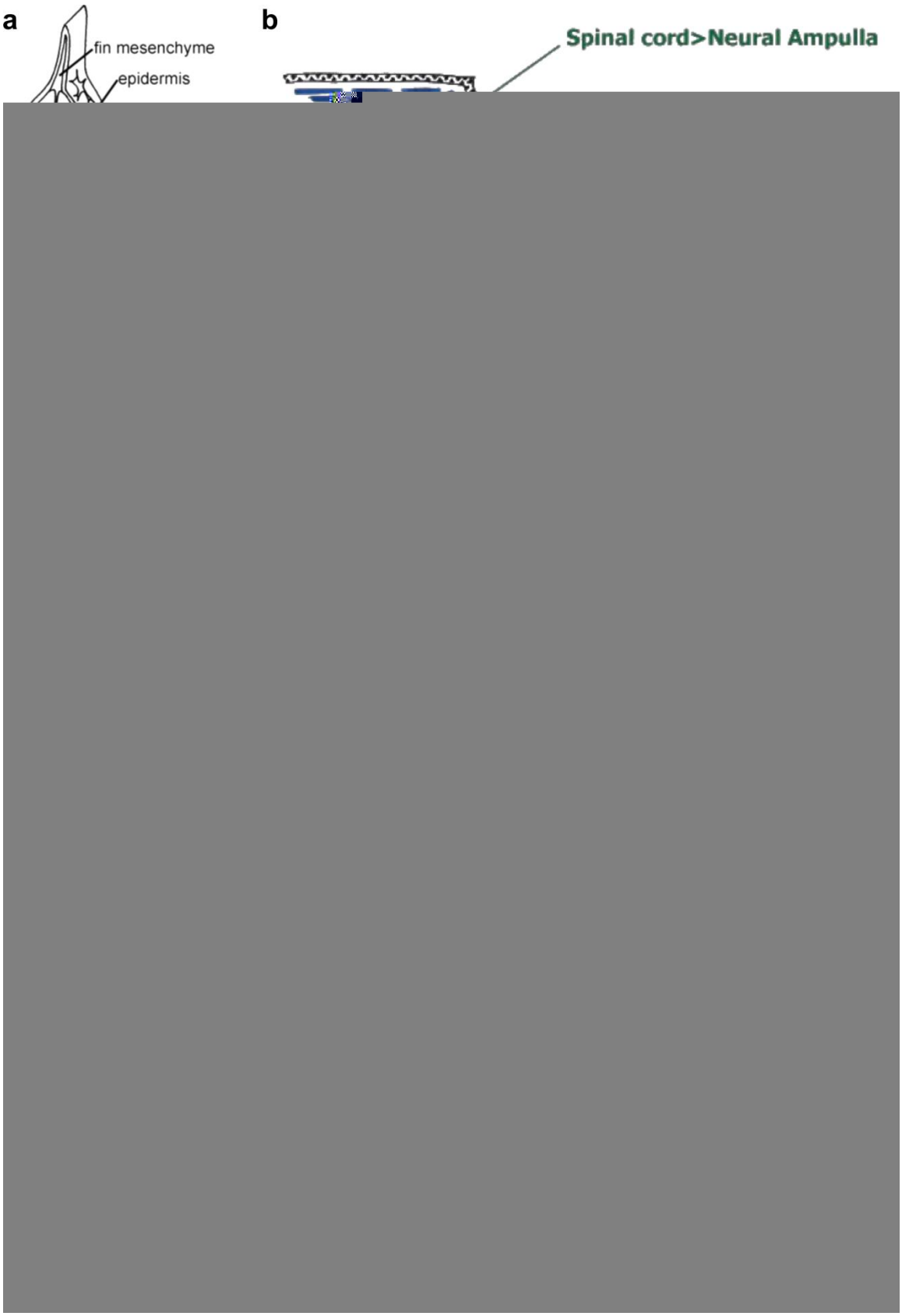

Fig. I.2 Regeneration of *Xenopus laevis* tadpole tail. **a** Tail tissues (transversal section). **b** Wound epithelium and regeneration bud (longitudinal section). **c** Signals and pathways. Adapted from Beck et al., 2009 (**a**), Gargioli and Slack, 2004 (**b**), and Li et al., 2016 (**c**).

1.2 Redox phenomena in regeneration

Redox biology is a broad field inside the biochemical discipline. In the context of regeneration, it encompasses oxygen (O_2) itself, reactive oxygen species (ROS), pro-oxidants (other than ROS), antioxidants (enzymatic and non-enzymatic), hypoxia, normoxia and hyperoxia, and the hypoxia-inducible factors (HIF). Other players are typically linked with these.

Having wound healing and regeneration as the underlying process, the origins of redox signalling and stress, the O_2 effects beyond bioenergetics, the shift of paradigm in redox biology, the HIF as more than an O_2 threshold alarm, and the redox control of signalling pathways required for regeneration were explored and copiously detailed next in the unpublished brief review manuscript (Chapter II).

Being written prior to this thesis published findings, the most recent references regarding the redox phenomena in regeneration can be found in the Introduction and Discussion sections of the reprinted publications (Chapter VI–VIII).

1.3 Bioelectric phenomena in regeneration

Bioelectricity is a broad field inside the biophysical discipline. In the context of regeneration, it includes membrane and transepithelial potentials, electric current density and electric fields. Other players are typically linked with these.

With a focus on wound healing and regeneration, the origins of bioelectric signals and cues, the terminology and definitions, the brief history, the methodological approaches and the role of bioelectricity in regeneration were stringently surveyed and explained next in the published academic-grade *Wikipedia* article (Chapter III).

CHAPTER II

2. *CHANGING THE PARADIGM OF REDOX BIOLOGY IN WOUND HEALING AND REGENERATION: H_2O_2 AT THE CORE OF THE INSURGENCE*

Mudam-se os tempos, mudam-se as vontades,
Muda-se o ser, muda-se a confiança;
Todo o mundo é composto de mudança,
Tomando sempre novas qualidades.

Luís de Camões *in* Rimas (Mudam-se os tempos, mudam-se as vontades) (1595; *postumus*)[4]

2.1 Manuscript overview

With a targeted and careful analysis of the literature, it was briefly reviewed the roles of oxidants and free radicals in wound healing and regeneration, framing them into a paradigm shift. The old paradigm is stemmed on the oxidizing power of ROS, perpetuating chain reactions that are harmful to life's constituents (DNA, proteins and lipids). During evolution, the cells hijacked this deleterious capacity of ROS to fight back invading pathogens via the oxidative burst. This defence mechanism is mediated by phagocytic NADPH oxidases that produce massive amounts of ROS to kill pathogens and avoid infections, further contributing to the dogmatic view of ROS as inherently toxic (Lambeth and Neish, 2014).

The paradigm started to shift when non-phagocytic NADPH oxidases were discovered, proving that ROS cannot be solely deleterious. Detailed studies showed that, when in minute amounts, different ROS, especially H_2O_2, are of crucial importance for cell signalling and behaviour. Following studies showed that ROS are required for wound healing beyond the combat of infections. Indeed, injury-induced ROS production preceded oxidative burst that occurred later from immune cells attracted to the wound site by the earlier ROS. More recently, a role in regeneration has also been recognized (Coffman and Su, 2019).

Together, such cumulative evidence presses for the changing of the paradigm in wound healing and regeneration, where ROS have pleiotropic roles dependent on a tight regulation of dosage and exposure during healing. The new paradigm, I argue, is on the way to become established and will provide new

opportunities to address wound healing and regeneration research. Some of those opportunities are deeply explored in the research and technical publications that followed this theoretical endeavour (Chapter VI–VIII).

This brief review manuscript, not submitted for indexed publication, was written as the main grading task for the course *Chemical Biology of Oxidants and Free Radicals*. Attendance to the course occurred as an officious student, without grading or certificate. The course was instructed by Prof. Ph.D. Jason Eiserich in the Spring Quarter of 2014 at University of California, Davis.

2.2 Manuscript contributions

F.F. conceived, outlined and wrote the brief review manuscript.

2.3 Manuscript reprint

Vide infra.

Changing the paradigm of redox biology in wound healing and regeneration: H_2O_2 at the core of the insurgence

Fernando Ferreira[1,2,*]

[1]Department of Dermatology, Institute for Regenerative Cures, University of California, Davis, CA, USA.

[2]Departamento de Biologia, Centro de Biologia Molecular e Ambiental (CBMA), Universidade do Minho, Braga, Portugal.

*** Corresponding Author**

Fernando Ferreira, M.Sc.

fdasilvaferreira@ucdavis.edu

Keywords: Reactive oxygen species; hydrogen peroxide; signaling; regeneration; paradigm

(2014)

Abstract

Throughout evolution organisms were constantly subjected to wounding and even amputations. Immune defense and signaling mechanisms should have evolved to avoid infection and to recover (at least partially) homeostasis, structure and function. Therefore the processes of wound healing and regeneration were subjected to selective pressure and became dormant (with differential ontogenetic and phylogenetic efficiency) in post-embryonic development. Due to reactive oxygen species (ROS) ability to oxidize virtually everything and perpetuate chain reactions, they were traditionally viewed as predominantly harmful to life. The elucidation of respiratory or oxidative burst and the discovery of phagocytic NADPH oxidases to kill bacteria and avoid infection, further rooted such view. The paradigm started to change with the discovery of non-phagocytic NADPH oxidases and its implications to cell signaling and later to wound healing. More recently, robust evidences showing a rapid and sustained hydrogen peroxide gradient prior to immune cells arrival to wound site and the requirement of ROS to regeneration are pressing for the change in paradigm. With the presentation and discussion of several seminal and emergent breakthrough studies, this brief review intends to argue that a change in paradigm of ROS in wound healing and regeneration is on way to become established. This change will allow a leap forward in the understanding of processes as complexes as wound healing and regeneration and may unveil new directions for basic research and clinical application.

Overview of ROS in wounds

The effects of ROS on regeneration are only now being unveiled; consequently, there are not many studies to cover. The seminal ones will be extensively discussed in the following sections. Wound healing is indeed the first step in the process of regeneration, also comprising two more phases: formation of the blastema – a mesenchyme-like structure responsible for the restoration of the missing parts, and redevelopment (Slack et al., 2004; Poss, 2010). Therefore, a brief overview of the effects of main ROS in wounds is important. For a more detailed review, other literature is recommended (Tandara and Mustoe, 2004; Sen and Roy, 2008).

In the path of oxidation to water, diatomic oxygen accepts four electrons in a sequential one electron reaction. First it is formed superoxide anion ($O_2^{\bullet-}$), then hydrogen peroxide (H_2O_2), next hydroxyl radical ($^{\bullet}OH$), and finally water (H_2O) (Fig. 1; Thannickal and Fanburg, 2000). Several enzymes catalyze these reactions, like the superoxide dismutase (SOD) that dismutates $O_2^{\bullet-}$ in H_2O_2. All of these ROS can at some point play a role during wound healing (Sen and Roy, 2008); however, my focus will be on H_2O_2. Intriguingly, the highest concentration of H_2O_2 in fluids was measured in wound fluids. A concentration as high as 0.1-0.3 mM of H_2O_2 was detected in wounds, pointing to possible key roles in the healing process (Roy et al., 2006).

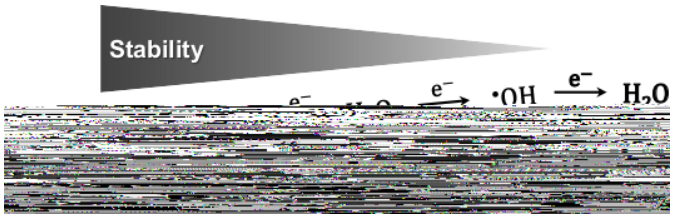

Fig. 1 | Simplified nonstoichiometric scheme of the four-electron oxidation of diatomic oxygen to water and grossly opposite gradients of stability and reactivity of generated reactive oxygen species (ROS). The first one electron reaction forms superoxide anion ($O_2^{\bullet-}$) from diatomic oxygen (O_2); the second one electron reaction generates hydrogen peroxide (H_2O_2) from $O_2^{\bullet-}$; the third one electron reaction forms hydroxyl radical ($^{\bullet}OH$) from H_2O_2; finally water (H_2O) is produced in the fourth one electron reaction from $^{\bullet}OH$. $O_2^{\bullet-}$ is a weak oxidant (and even a weak reductant) and relatively stable, whereas $^{\bullet}OH$ is highly and indiscriminately reactive and very unstable; H_2O_2 presents intermediate stability and reactivity.

Wound healing can be divided in hemostasis, inflammation, epithelization and vascularization (Sen and Roy, 2008); H_2O_2 plays a pivotal roles in all of these phases. H_2O_2 was identified as a second messenger in the collagen-induced platelet aggregation key to blood clot formation. Catalase inhibited the platelet aggregation in a dose-response way (Pignatelli et al., 1998). In

relation to inflammation, it is widely known the role of ROS formed after phagocytosis to kill pathogens. Furthermore it is now known that a gradient of H_2O_2 from non-phagocytic cells attracts immune cells to wound margin (Niethammer et al., 2009; Moreira et al., 2010; Love et al., 2013). This discovery was against the paradigm that ROS are produced entirely by immune cells in wounds and constitute the change in paradigm highlighted in this review (further discussion below). ROS are increasingly being associated with the cell migration (Hurd et al., 2012) required for epithelization. Keratinocyte migrates with membrane protrusions stimulated by insulin-like growth factor 1 (IGF1) and ROS production downregulates IGF1 receptor (Haase et al., 2003; Higashi et al., 2005). Extracellular matrix remodeling is important for cell migration. Importantly, the sustained production of H_2O_2 induced the activation of pro-matrix metalloproteinase 2 (pro-MMP2) (Yoon et al., 2002). Further, ROS appear to be an intermediate in direct current electric field-induced migration (electrotaxis) *in vitro* (Li et al., 2012; 2013). Oxygen availability and tension is a well-recognized regulator of *de novo* formation of blood vessels (vasculogenesis), mainly through hypoxia-inducible factor (HIF-1α) activation of the vascular endothelial growth factor (VEGF) (Kaelin and Ratcliffe, 2008). However, an HIF-1α-independent VEGF expression was observed in human keratinocytes, stimulated instead by H_2O_2 in micromolar range and in a dose-response way (100-500 μM) (Sen et al., 2002). Moreover, since ROS can induce HIF-1α activation (Bonello et al., 2007), a HIF-1α-dependent VEGF expression remains an open possibility. Altogether these studies present evidence that ROS intervene in all phases of wound healing, rendering them candidates for basic research and for drug development to clinical application.

What makes H_2O_2 a special ROS?

During the four electrons sequential oxidation of oxygen, the stability and reactivity grossly follow opposite directions; stability decreases and reactivity increases with higher oxidation number. Two electrons and a dismutase reaction transform the original O_2 into H_2O_2, which is roughly in the middle of the path (Fig. 1). Moreover, when compared to the other ROS, H_2O_2 (i) is not charged; (ii) is not a radical; (iii) have an intermediate oxidation number; (iv) is a moderate oxidant; and (v) is transformed by catalase disproportionation into water and O_2 without the expense of reduction equivalents (Bienert et al., 2007; Lambeth and Neish, 2014). These result in a relatively good stability and reactivity in physiological conditions. Altogether, with H_2O_2 biological versatility, tissue diffusion and cell membrane permeability, these are the

characteristics that make H_2O_2 a special ROS for different processes of cell signaling and a candidate for paracrine tissue signaling (Veal et al., 2007; Niethammer et al., 2009). Additionally, H_2O_2 *per se* is relatively insensitive to non-enzymatic antioxidants, given to cells a fine tuning regulation of its breakdown via enzymes like catalase.

Regarding membrane permeability, an important note should be addressed. Although H_2O_2 permeates cell membrane (Bienert et al., 2006) it was recently shown that most of the H_2O_2 diffuses through aquaporins, possibly due to chemical similarity with water (Bienert et al., 2007; Miller et al., 2010). This is not a disadvantage, but rather another advantage. Aquaporins are ubiquitous in different cells, suggesting the existence of a further level of regulation for H_2O_2 levels in and out the cell. Such regulation is pivotal since the ROS signaling-to-damaging transition is dose-dependent.

Other advantage that makes H_2O_2 special is the actual ways to produce ROS. Without chemical or physical damaging agents, ROS can be originated *in vivo* mainly by leak of mitochondria's oxidative phosphorylation and by enzymatic production. Most of these produce the first product of one electron reaction with O_2, $O_2^{\bullet-}$. But then either by spontaneous or by SOD in mitochondria, cytoplasm or extracellularly, $O_2^{\bullet-}$ is converted into H_2O_2 (Thannickal and Fanburg, 2000). Indeed the NADPH oxidases Dual oxidases 1 and 2 (Duox1 and 2) produce directly H_2O_2. $O_2^{\bullet-}$ is a weak oxidant and weak reductant and membrane impermeant (Lambeth and Neish, 2014); thus, a significant percentage of the available ROS for signaling purposes might actually be H_2O_2. In the other hand, hydroxyl radicals are highly unstable and react virtually with everything, creating secondary radicals which may perpetuate dangerous chain reactions (Thannickal and Fanburg, 2000). Because of this, $^{\bullet}OH$ do not possess significant diffusion in space, making it a poorer candidate to paracrine signaling. Nevertheless, the role of other ROS, mainly $O_2^{\bullet-}$, cannot be strictly excluded and indeed studies indicate their importance (*e.g.*, Li et al., 2012; 2013).

H_2O_2: from wound disinfectant to wound paracrine factor

First identified role: oxidative burst in wounds

Upon wounding, integrity and barrier is lost and the site is accessible to a wide range of microbes. An unspecific, broad spectrum antibiotic might have been then under selective pressure to either avoid potentially dangerous infections and also as an early step to recover

homeostasis. Being harmful, ROS were likely co-opted over evolution as disinfectant mechanism in the innate immune defense. Leucocytes such as neutrophils and macrophages migrate toward recent wound sites, engulf bacteria through phagocytosis and generate ROS into the phagosome to kill the pathogens. NADPH oxidases, mainly Nox2, localized in the phagosome membrane oxidize oxygen to $O_2^{\bullet-}$ and in a Nox2-independent one electron reaction form H_2O_2. H_2O_2 can be then halogenated with chloride to form hypochlorous acid (HOCl). H_2O_2, $O_2^{\bullet-}$ and HOCl can directly or by induction of other mechanisms (like protease attraction) kill bacteria (Decoursey and Ligeti, 2005). Because of the high levels of oxygen consumed to produce superoxide (100-fold increase) this process, described in the first half of the 20th century, became known as respiratory burst and more recently as oxidative burst (Baldridge and Gerard, 1932; Bedard and Krause, 2007). Functional deleterious mutations in the oxidase components of the oxidative burst lead to hereditary chronic granulomatous disease (CGD), rendering the patient susceptible to infection, being lethal if not treated. The phagocyte NADPH oxidase was discovery with the first reported case of CGD (Berendes et al., 1957; Bedard and Krause, 2007).

This well-studied process was classically viewed as the responsible for the entire ROS observed in wound, but a recent set of studies have shown that a tissue-scale gradient of H_2O_2 is formed before the arrival of the very first leucocyte to the wound margin (Niethammer et al., 2009; Moreira et al., 2010; Love et al., 2013). These discoveries shook the field and demanded a change in the paradigm of ROS in wound healing and regeneration.

The paradigm change: transition to wound sensing and wound signaling

Usually, in science change occurs through small steps over long periods of time. It can be said that the turning point in the redox biology, to start looking at ROS as much more than simple disinfectants in wounds, was with the discovery of NADPH oxidases isoforms in non-phagocytic cells. With genomic tools available, Nox1 was the first recognized isoform (Suh et al., 1999). If ROS, mainly $O_2^{\bullet-}$ and H_2O_2, were intentionally produced not to kill pathogens, then they must have other physiological functions. After this and other seminal discoveries (Bedard and Krause, 2007), many pivotal roles in cell signaling have been associated with ROS (Thannickal and Fanburg, 2000). One of those discoveries occurred in a study of wound healing in larval zebrafish. Niethammer and colleagues (2009) used a promising approach to specifically image H_2O_2, the genetically encoded ratiometric sensor HyPer (Belousov et al., 2006). The sensor has

a bacterial H_2O_2-sensitive transcription factor OxyR fused to a fluorescent protein. The reversible cysteine oxidation of OxyR allows dynamic measuring of intracellular H_2O_2. With this technique the authors reported, for the first time, that H_2O_2 was produced in the wound before the arrival of leucocytes from local blood vessels (Fig. 2). Starting at ~3 min after wounding and peaking at ~20 min, a sustained increase in H_2O_2 levels extended from the wound edge in a decreasing gradient 100-200 µm towards the main body of the larvae. An average of 4-6 leukocytes arrived at the wound edge within the first 42 min after wounding. By disrupting H_2O_2 production with the flavoprotein inhibitor diphenyleneiodonium (DPI) and the oxidase assembly inhibitor VAS2870, the authors showed that the gradient of H_2O_2 attracts the leucocytes to the wound edge (Fig. 2). By genetic modulation, ROS was shown to be produced by by the Duox1 and/or 2 located at the tail-fin epithelial cells around the wound, further pointing to H_2O_2 as the main ROS chemoattracting immune cells (Niethammer et al., 2009). The study did not clarify what trigger Duox and whether the gradient was generated by a point source followed by diffusion, by a Duox tissue gradient, or by a catalase reverse tissue gradient.

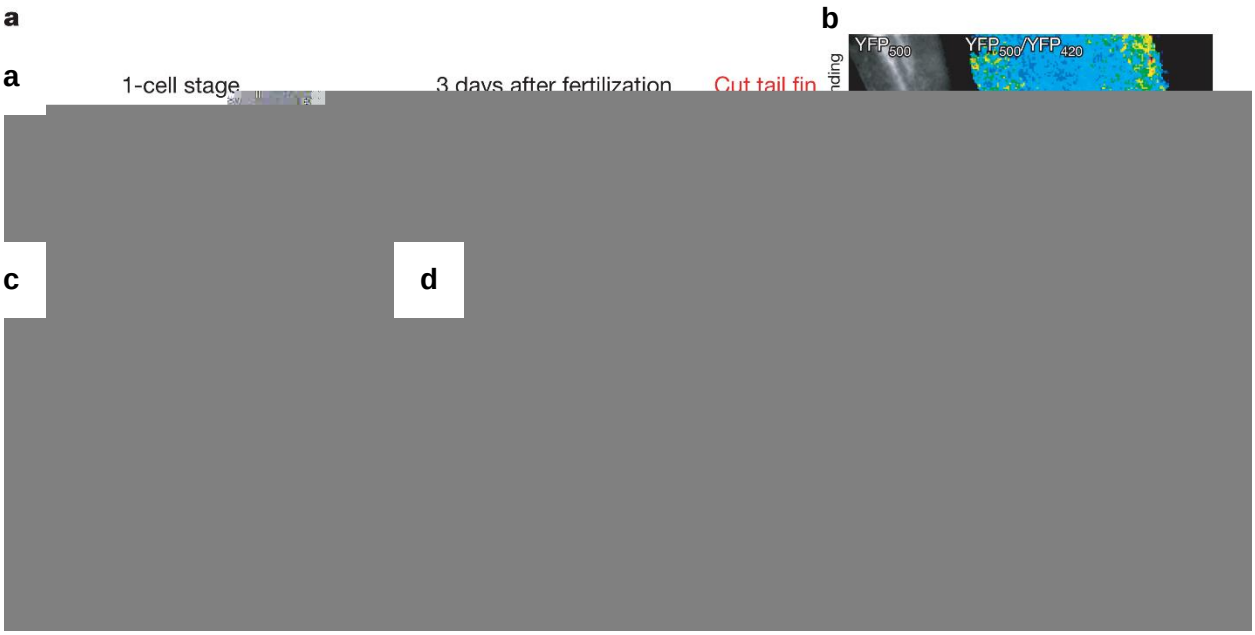

Fig. 2 | Wound edge H_2O_2 production upon wounding in zebrafish larvae tail fin. (**a**) Experimental procedure. (**b**) HyPer imaging after wounding. Relative [H_2O_2] is inferred from the YFP500/YFP420 excitation ratio of HyPer. (**c**) Temporal [H_2O_2] profile in a 10-30 µm broad region of interest along the wound edge. Arrival of first leukocyte at wound (solid red line) ± s.d. (dashed red line) is shown. An average of 4-6 leukocytes arrived at the wound edge within 42 min after wounding. (**d**) [H_2O_2] profile in different times after wounding by distance from wound edge. Pseudocolor calibration bars: HyPer ratio (YFP500/YFP420); scale bars: 100 µm. Adapted from Niethammer et al., 2009.

Before this study, it was already known that the wound microenvironment has at least two sources of ROS: (i) transient delivery of high amounts via oxidative burst by phagocytic cells; and *(ii)* sustained delivery of low amounts by enzymes of the NADPH oxidase family present in cells such as the fibroblasts, keratinocytes and endothelial cells (Sen and Packer, 1996; Roy et al., 2006). However, Niethammer et al. (2009) ordered these sources by proving, for the first time, the existence of wound sensing by a tissue-scale H_2O_2 pattern established and sustained before the oxidative burst. The other seminal evidence provided by this study is that H_2O_2 acts as a paracrine factor that attracts leucocytes via a tissue-scale gradient. Therefore, the argued change in paradigm in redox biology has its pinnacle in wound healing.

Follow-up studies in the same animal model have shown that the SRC family kinase (SFK) Lyn acts as a redox sensor in the leading edge of neutrophils, guiding their migration in response to H_2O_2 gradient (Wittmann et al., 2012; Yoo et al., 2011, 2012). In *Drosophila* wounding similar approaches further support these views, by showing the chemoattractant effect of H_2O_2 to immune cells (Moreira et al., 2010). Following these discoveries, topical application of H_2O_2 in a mice excision wound model enhanced angiogenesis and wound closure at 10 mM but retarded wound closure at 166 mM (Loo et al., 2012). This study recalls the pivotal importance for a correct balance in the redox state.

Notwithstanding, many open questions remain to be answered. One of the most important is whether the tissue gradient has roles beyond attracting leucocytes. Most likely yes, pleiotropic context- and time-dependent functions appear to be the case, as it was shown by a study presenting evidence for ROS requirement to a process more complex than wound healing, epimorphic regeneration (Love et al., 2013).

H_2O_2: a new master regulator in epimorphic regeneration

With the rapid, sustained and robust gradient of H_2O_2 upon wounding, could it be a sensor alarming that something is wrong? And could it be necessary to wound healing or regeneration? Such questions did not remain unanswered for long. Recurring also to HyPer to image H_2O_2, Love and colleagues (2013) showed that an amputation-induced gradient of H_2O_2 and its maintenance is necessary for tadpole tail regeneration in *Xenopus* (Fig. 3). First, the authors confirmed the observations that the ROS was generated by local cells and not by migrating phagocytic cells. Using pharmacological approaches, the authors demonstrated that the

gradient was generated by the family of NADPH oxidases, and with its inhibition by DPI or apocynin (APO) regeneration was abolished. To check for roles of H_2O_2 other than chemoattracting leucocytes, the authors stained for master signaling pathways and cell behavior long assumed as necessary for and in some cases even sufficient to induce regeneration (Lin and Slack, 2008; Slack et al., 2004). Wnt/β-catenin signaling, *fgf20* and proliferation were all showed as downstream to H_2O_2.

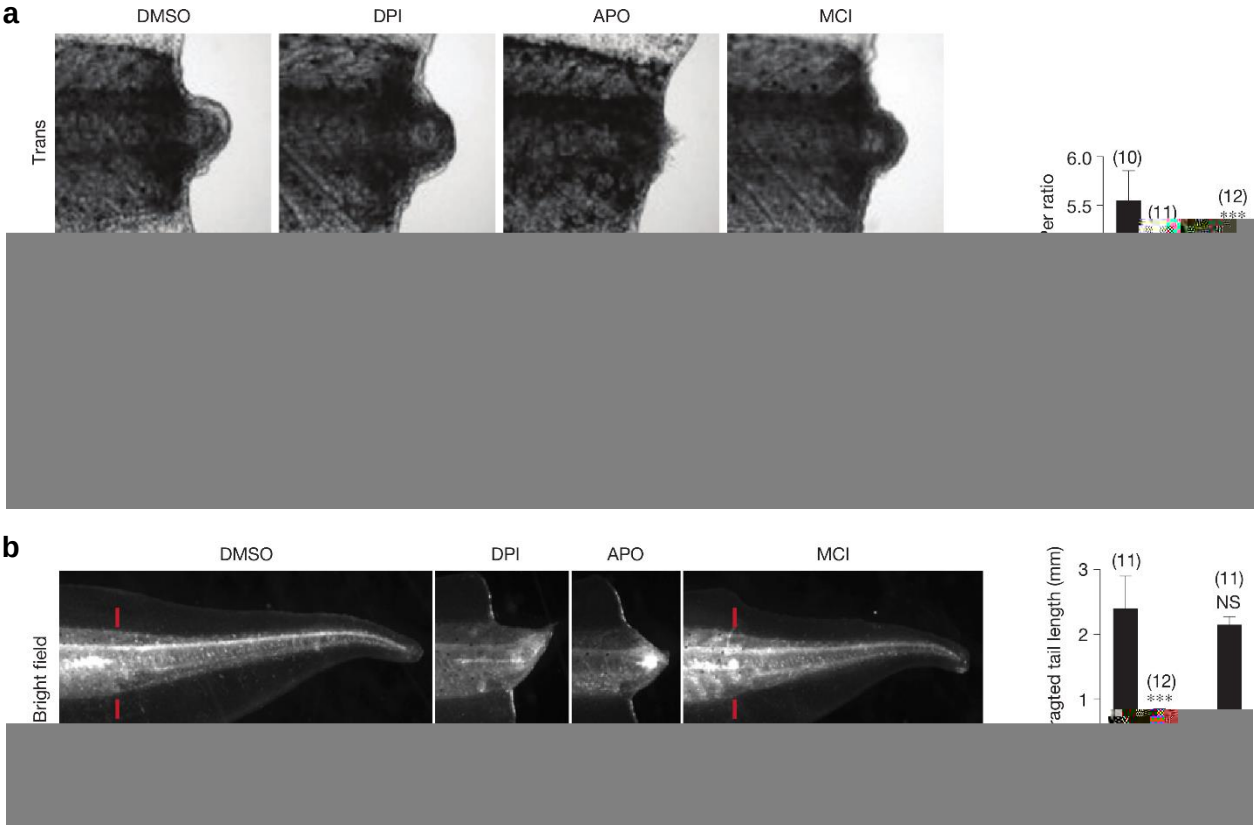

Fig. 3 | Decreasing ROS levels pharmacologically impairs *Xenopus* tadpole tail regeneration. (**a**) Representative transillumination (Trans) and HyPer imaging and relative [H_2O_2] quantification of tadpole tails treated with DMSO, NADPH oxidase assembly inhibitors DPI (2 μM) and apocynin (APO, 200 μM) or antioxidant MCI-186 (200 μM) treatments at 12 h post-amputation (hpa). (**b**) Images and relative [H_2O_2] quantification of tadpoles that were exposed to DMSO, DPI, APO or MCI-186 (the same doses as above) until 72 hpa and photographed at 7 days pa in normal medium. Error bars indicate s.d. of the mean of (n) specimens. The red lines indicate the plane of amputation. ***P* <0:01; ****P* <0:001; non-significant (NS), *P* >0:05. Adapted from Love et al., 2013.

After this seminal evidence, a new study in adult zebrafish caudal fin regeneration presented further evidences of the pivotal role of ROS in epimorphic regeneration and also in wound healing (Gauron et al., 2013). Although the main message is again that ROS are necessary to

regeneration, the impact of this study is important since it was the first on an adult model of wound healing and regeneration. Further, new downstream pathways to ROS signaling necessary for regeneration was unveiled. ROS production was shown to induce two different parallel pathways, apoptosis and JNK signaling, that impacts epidermal cell proliferation and are required for the formation of the blastema – a mesenchyme-like structure responsible for the restoration of the missing parts. Also, ROS was shown to stimulate pluripotency marker expression via apoptosis regulation (Gauron et al., 2013).

In short, several properties highlighted by these studies points to the born of a new promising master regulator of epimorphic regeneration. Maybe the most important properties are the time- and dose-responses to the amputation, both congruent with a very upstream positioning of ROS in the regeneration process. The immediate (in the minute scale) and sustained production of ROS upon amputation makes it a putative candidate as a trigger of the whole process. It is important to note here that a single-compound trigger of regeneration has been sought for decades without success. Following HyPer calibration, Niethammer et al. (2009) calculated ~0.5-50 µM of H_2O_2 at the wound edge, likely within the physiological range for signaling. Indeed, *in vitro* chemotaxis of neutrophils and vascular smooth muscle was shown with 10 µM of H_2O_2 (Klyubin et al., 1996; Li et al., 2000). The other important effects of amputated-induced ROS are in proliferation, apoptosis and signaling pathways, all know to be necessary for regeneration (Slack et al., 2004). However, the mechanism of how ROS, most likely H_2O_2, modulates directly or indirectly these cell behaviors and signaling pathways remains elusive, warrant further studies in epimorphic regeneration models.

What can H_2O_2 do for wound healing and regeneration?

Cell behavior control and master signaling pathways regulation

Due to the goal of recover function and homeostasis, wound healing and regeneration are processes that at some point seem to recapitulate development. Indeed, regeneration is commonly referred to as post-embryonic development (Gilbert, 2006). Thus, the control of cell behaviors and master signaling pathways is pivotal for a correct healing and outgrowth. In short, cell behaviors include proliferation (cell number), migration (cell position) and differentiation (cell state). Therefore, the rationale is simple, if H_2O_2 regulate these individual behaviors, then it is more likely to have a significant role in the overall process of regeneration.

References

Baldridge, C.W., and Gerard, R.W. (1932). The extra respiration of phagocytosis. Am J Physiol -- Leg. Content *103*, 235–236.

Bedard, K., and Krause, K.-H. (2007). The NOX family of ROS-generating NADPH oxidases: physiology and pathophysiology. Physiol. Rev. *87*, 245–313.

Belousov, V. V, Fradkov, A.F., Lukyanov, K.A., Staroverov, D.B., Shakhbazov, K.S., Terskikh, A. V, and Lukyanov, S. (2006). Genetically encoded fluorescent indicator for intracellular hydrogen peroxide. Nat. Methods *3*, 281–286.

Berendes, H., Bridges, R.A., and Good, R.A. (1957). A fatal granulomatosus of childhood: the clinical study of a new syndrome. Minn. Med. *40*, 309–312.

Bienert, G.P., Schjoerring, J.K., and Jahn, T.P. (2006). Membrane transport of hydrogen peroxide. Biochim. Biophys. Acta *1758*, 994–1003.

Bienert, G.P., Møller, A.L.B., Kristiansen, K. a, Schulz, A., Møller, I.M., Schjoerring, J.K., and Jahn, T.P. (2007). Specific aquaporins facilitate the diffusion of hydrogen peroxide across membranes. J. Biol. Chem. *282*, 1183–1192.

Bonello, S., Zähringer, C., BelAiba, R.S., Djordjevic, T., Hess, J., Michiels, C., Kietzmann, T., and Görlach, A. (2007). Reactive oxygen species activate the HIF-1alpha promoter via a functional NFkappaB site. Arterioscler. Thromb. Vasc. Biol. *27*, 755–761.

Burdon, R.H. (1995). Superoxide and hydrogen peroxide in relation to mammalian cell proliferation. Free Radic. Biol. Med. *18*, 775–794.

Carlson, B.M. (2007). Principles of Regenerative Biology (London: Academic Press).

Ceradini, D.J., Kulkarni, A.R., Callaghan, M.J., Tepper, O.M., Bastidas, N., Kleinman, M.E., Capla, J.M., Galiano, R.D., Levine, J.P., and Gurtner, G.C. (2004). Progenitor cell trafficking is regulated by hypoxic gradients through HIF-1 induction of SDF-1. Nat. Med. *10*, 858–864.

Decoursey, T.E., and Ligeti, E. (2005). Regulation and termination of NADPH oxidase activity. Cell. Mol. Life Sci. *62*, 2173–2193.

Dickinson, B.C., Peltier, J., Stone, D., Schaffer, D. V, and Chang, C.J. (2011). Nox2 redox signaling maintains essential cell populations in the brain. Nat. Chem. Biol. *7*, 106–112.

Gauron, C., Rampon, C., Bouzaffour, M., Ipendey, E., Teillon, J., Volovitch, M., and Vriz, S. (2013). Sustained production of ROS triggers compensatory proliferation and is required for regeneration to proceed. Sci. Rep. *3*, 2084.

Gilbert, S.F. (2006). Developmental Biology (Sinauer Associates Inc.; 8th edition).

Haase, I., Evans, R., Pofahl, R., and Watt, F.M. (2003). Regulation of keratinocyte shape, migration and wound epithelialization by IGF-1- and EGF-dependent signalling pathways. J. Cell Sci. *116*, 3227–3238.

Higashi, Y., Peng, T., Du, J., Sukhanov, S., Li, Y., Itabe, H., Parthasarathy, S., and Delafontaine, P. (2005). A redox-sensitive pathway mediates oxidized LDL-induced downregulation of insulin-like growth factor-1 receptor. J. Lipid Res. *46*, 1266–1277.

Hurd, T.R., DeGennaro, M., and Lehmann, R. (2012). Redox regulation of cell migration and adhesion. Trends Cell Biol. *22*, 107–115.

Jaiswal, J.K. (2001). Calcium – how and why? J. Biosci. *26*, 357–363.

Kaelin, W.G., and Ratcliffe, P.J. (2008). Oxygen sensing by metazoans: the central role of the HIF hydroxylase pathway. Mol. Cell *30*, 393–402.

Klyubin, I. V, Kirpichnikova, K.M., and Gamaley, I.A. (1996). Hydrogen peroxide-induced chemotaxis of

mouse peritoneal neutrophils. Eur. J. Cell Biol. *70*, 347–351.

Lambeth, J.D., and Neish, A.S. (2014). Nox enzymes and new thinking on reactive oxygen: a double-edged sword revisited. Annu. Rev. Pathol. *9*, 119–145.

Lane, N. (2004). Oxygen: The Molecule that Made the World (Oxford University Press).

Li, F., Wang, H., Li, L., Huang, C., Lin, J., Zhu, G., Chen, Z., Wu, N., and Feng, H. (2012). Superoxide plays critical roles in electrotaxis of fibrosarcoma cells via activation of ERK and reorganization of the cytoskeleton. Free Radic. Biol. Med. *52*, 1888–1896.

Li, F., Chen, T., Hu, S., Lin, J., Hu, R., and Feng, H. (2013). Superoxide Mediates Direct Current Electric Field-Induced Directional Migration of Glioma Cells through the Activation of AKT and ERK. PLoS One *8*, e61195.

Li, W., Liu, G., Chou, I.N., and Kagan, H.M. (2000). Hydrogen peroxide-mediated, lysyl oxidase-dependent chemotaxis of vascular smooth muscle cells. J. Cell. Biochem. *78*, 550–557.

Lin, G., and Slack, J.M.W. (2008). Requirement for Wnt and FGF signaling in Xenopus tadpole tail regeneration. Dev. Biol. *316*, 323–335.

Loo, A.E.K., Wong, Y.T., Ho, R., Wasser, M., Du, T., Ng, W.T., and Halliwell, B. (2012). Effects of hydrogen peroxide on wound healing in mice in relation to oxidative damage. PLoS One *7*, e49215.

Love, N.R., Chen, Y., Ishibashi, S., Kritsiligkou, P., Lea, R., Koh, Y., Gallop, J.L., Dorey, K., and Amaya, E. (2013). Amputation-induced reactive oxygen species are required for successful Xenopus tadpole tail regeneration. Nat. Cell Biol. *15*, 222–228.

Miller, E.W., Dickinson, B.C., and Chang, C.J. (2010). Aquaporin-3 mediates hydrogen peroxide uptake to regulate downstream intracellular signaling. Proc. Natl. Acad. Sci. U. S. A. *107*, 15681–15686.

Moreira, S., Stramer, B., Evans, I., Wood, W., and Martin, P. (2010). Prioritization of competing damage and developmental signals by migrating macrophages in the Drosophila embryo. Curr. Biol. *20*, 464–470.

Niethammer, P., Grabher, C., Look, A.T., and Mitchison, T.J. (2009). A tissue-scale gradient of hydrogen peroxide mediates rapid wound detection in zebrafish. Nature *459*, 996–999.

Passos, J.F., von Zglinicki, T., and Kirkwood, T.B.L. (2007). Mitochondria and ageing: winning and losing in the numbers game. Bioessays *29*, 908–917.

Pignatelli, P., Pulcinelli, F.M., Lenti, L., Paolo Gazzaniga, P., and Violi, F. (1998). Hydrogen Peroxide Is Involved in Collagen-Induced Platelet Activation. Blood *91*, 484–490.

Poss, K.D. (2010). Advances in understanding tissue regenerative capacity and mechanisms in animals. Nat. Rev. Genet. *11*, 710–722.

Ray, P.D., Huang, B.-W., and Tsuji, Y. (2012). Reactive oxygen species (ROS) homeostasis and redox regulation in cellular signaling. Cell. Signal. *24*, 981–990.

Roy, S., Khanna, S., Nallu, K., Hunt, T.K., and Sen, C.K. (2006). Dermal wound healing is subject to redox control. Mol. Ther. *13*, 211–220.

Sen, C.K., and Packer, L. (1996). Antioxidant and redox regulation of gene transcription. FASEB J. *10*, 709–720.

Sen, C.K., and Roy, S. (2008). Redox signals in wound healing. Biochim. Biophys. Acta *1780*, 1348–1361.

Sen, C.K., Khanna, S., Babior, B.M., Hunt, T.K., Ellison, E.C., and Roy, S. (2002). Oxidant-induced vascular endothelial growth factor expression in human keratinocytes and cutaneous wound healing. J. Biol. Chem. *277*, 33284–33290.

Simon, M.C., and Keith, B. (2008). The role of oxygen availability in embryonic development and stem cell function. Nat. Rev. Mol. Cell Biol. *9*, 285–296.

Slack, J.M.W., Beck, C.W., Gargioli, C., and Christen, B. (2004). Cellular and molecular mechanisms of regeneration in Xenopus. Philos. Trans. R. Soc. Lond. B. Biol. Sci. *359*, 745–751.

Suh, Y.A., Arnold, R.S., Lassegue, B., Shi, J., Xu, X., Sorescu, D., Chung, A.B., Griendling, K.K., and Lambeth, J.D. (1999). Cell transformation by the superoxide-generating oxidase Mox1. Nature *401*, 79–82.

Sundaresan, M., Yu, Z.-X., Ferrans, V.J., Irani, K., and Finkel, T. (1995). Requirement for Generation of H(2)O(2) for Platelet-Derived Growth Factor Signal Tran sduction. Science (80-.). *270*, 296–299.

Tandara, A. a, and Mustoe, T. a (2004). Oxygen in wound healing--more than a nutrient. World J. Surg. *28*, 294–300.

Thannickal, V.J., and Fanburg, B.L. (2000). Reactive oxygen species in cell signaling. Am. J. Physiol. Lung Cell. Mol. Physiol. *279*, L1005-28.

Urao, N., and Ushio-Fukai, M. (2013). Redox regulation of stem/progenitor cells and bone marrow niche. Free Radic. Biol. Med. *54*, 26–39.

Urao, N., McKinney, R.D., Fukai, T., and Ushio-Fukai, M. (2012). NADPH oxidase 2 regulates bone marrow microenvironment following hindlimb ischemia: role in reparative mobilization of progenitor cells. Stem Cells *30*, 923–934.

Veal, E. a, Day, A.M., and Morgan, B. a (2007). Hydrogen peroxide sensing and signaling. Mol. Cell *26*, 1–14.

Wittmann, C., Chockley, P., Singh, S.K., Pase, L., Lieschke, G.J., and Grabher, C. (2012). Hydrogen peroxide in inflammation: messenger, guide, and assassin. Adv. Hematol. *2012*, 541471.

Yoneyama, M., Kawada, K., Gotoh, Y., Shiba, T., and Ogita, K. (2010). Endogenous reactive oxygen species are essential for proliferation of neural stem/progenitor cells. Neurochem. Int. *56*, 740–746.

Yoo, S.K., Starnes, T.W., Deng, Q., and Huttenlocher, A. (2011). Lyn is a redox sensor that mediates leukocyte wound attraction in vivo. Nature *480*, 109–112.

Yoo, S.K., Freisinger, C.M., LeBert, D.C., and Huttenlocher, A. (2012). Early redox, Src family kinase, and calcium signaling integrate wound responses and tissue regeneration in zebrafish. J. Cell Biol. *199*, 225–234.

Yoon, S.-O., Park, S.-J., Yoon, S.Y., Yun, C.-H., and Chung, A.-S. (2002). Sustained production of H(2)O(2) activates pro-matrix metalloproteinase-2 through receptor tyrosine kinases/phosphatidylinositol 3-kinase/NF-kappa B pathway. J. Biol. Chem. *277*, 30271–30282.

Zhao, M. (2009). Electrical fields in wound healing-An overriding signal that directs cell migration. Semin. Cell Dev. Biol. *20*, 674–682.

Zhao, M., Song, B., Pu, J., Wada, T., Reid, B., Tai, G., Wang, F., Guo, A., Walczysko, P., Gu, Y., et al. (2006). Electrical signals control wound healing through phosphatidylinositol-3-OH kinase-gamma and PTEN. Nature *442*, 457–460.

CHAPTER III

3. *DEVELOPMENTAL BIOELECTRICITY*

Hic ego incredibili sum studio , & cupiditate incensus idem experiundi , & quod occultum in re esset in lucem proferendi . (...) Phænomenon eadem omnino ratione contigit ; vehementes nimirum contractiones in singulos artuum musculos , perinde ac si tetano præparatum animal esset correptum , eodem ipso temporis momento inducebantur , quo scintillæ extorquerentur .

Luigi Galvani *in* De Viribus Electricitatis In Motu Musculari Commentarius (1791)[5]

3.1 Article overview

A comprehensive review of developmental bioelectricity was written in a collaborative effort among the field's experts for an academic-grade, highly referenced, review-like *Wikipedia* page (not peer reviewed). My writing focused on the history, terminology and role of bioelectricity in wound healing and regeneration.

Life is intrinsically electrical; from the spark in fertilization to brain activity, biology is permeated by electricity. Developmental bioelectricity delves into the minute, sustained, slowly-changing and long-lasting electric variations occurring mainly in non-excitable cells and that are able to regulate signalling, behaviour and patterning in all phases of development (McLaughlin and Levin, 2018). The unity of bioelectricity is the ion, a charged atom that generates an electric current or field whenever in net movement. The basic structure of bioelectricity is the cell membrane, a lipid bilayer scattered by protein ion translocators, originating an essential in/out discontinuum and compartmentalization. In cell pools, the gap junctions allow not only cell-cell communication, but also work as electrical synapses (Mathews and Levin, 2017). Bioelectrically, the polarized epithelium is an expansion of the cell membrane, and is therefore a capacitor too; however, typically the cells have an inside negative potential and the epithelia have an inside positive potential. Owing to the electrochemical gradients, the cells and epithelia are *de facto* biological batteries. Therefore, the inside/outside potential distinction has obvious implications upon wounding: in the cell case, an inward current is measured, whereas in the epithelium case, there is an outward current instead (Fig. III.1) (Borgens et al., 1989; Levin, 2007; McCaig et al., 2005).

Draft:Bioelectricity

From Wikipedia, the free encyclopedia

In biology, **developmental bioelectricity** is the regulation of cell and tissue processes, behaviors, and patterning as the result of electric communications. The charge carrier in bioelectricity is the ion (charged atom), and an electric current and field is generated whenever a net ion flux occur.

Contents

motion, senses, nutrient transport, toxins clearance, and signaling in homeostatic and disease/injury conditions. Upon stimuli or barrier breaking (*short-circuit*) of the membrane, ions powered by the voltage gradient (*electromotive force*) diffuse or leak, respectively, through the cytoplasm and interstitial fluids (*conductors*), generating measurable electric currents – net ion fluxes – and fields. Some ions (such as calcium) and molecules (such as hydrogen peroxide) modulate targeted translocators to produce a current or to enhance, mitigate or even reverse an initial current, being *switchers*[3, 4].

Brief history: the pioneers

The modern roots of developmental bioelectricity can be traced back to the entire 18th century. Several seminal works stimulating muscle contractions using Leyden jars culminated with the publication of classical studies by Luigi Galvani in 1791 (*De viribus electricitatis in motu musculari*) and 1794. In these, Galvani thought to have uncovered intrinsic electric-producing ability in living tissues or “animal electricity”. Allessandro Volta argued about his 1791 work, showing that the frog’s leg muscle twitching was due to a static electricity generator and from dissimilar metals contact. Interestingly, the latter incept on Volta the basics for his battery (voltaic pile). Addressing Volta remarks, Galvani showed, in the 1794 study, twitching without metal electricity by touching the leg muscle with a deviating cut sciatic nerve, definitively showing “animal electricity”. Unknowingly, Galvani with this and related experiments discovered the injury current (ion leakage driven by the intact membrane/epithelial potential) and injury potential (potential difference between injured and intact membrane/epithelium). The injury potential was, in fact, the electrical source behind the leg contraction, as realized in the next century[5, 6].

Methodology: electrode-based techniques

The gold standard techniques to quantitatively extract electric dimensions from living specimens, ranging from cell to organism levels, are the glass microelectrode (or micropipette), the vibrating (or self-referencing) voltage probe and the vibrating ion-selective microelectrode. The former is inherently invasive and the two latter are non-invasive, but all are ultra-sensitive and fast-responsive sensors extensively used in a plethora of physiological conditions in widespread biological models[3, 6–9].

The glass microelectrode was developed in the 1940’s to study the action potential of excitable cells, deriving from the seminal work by Hodgkin and Huxley in the giant axon squid[10, 11]. It is simply a liquid salt bridge connecting the biological specimen with the electrode, protecting tissues from

leachable toxins and redox reactions of the bare electrode. Owing to its low impedance, low junction potential and weak polarization, silver electrodes are standard transducers of the ionic into electric current that occurs through a reversible redox reaction at the electrode surface[12].

The vibrating probe was introduced in biological studies in the 1970's[13]–[15]. The voltage-sensitive probe is electroplated with platinum to form a capacitive black tip ball with large surface area. When vibrating in an artificial or natural DC voltage gradient, the capacitive ball oscillates in a sinusoidal AC output. The amplitude of the wave is proportional to the measuring potential difference at the frequency of the vibration, efficiently filtered by a lock-in amplifier that boosts probe's sensitivity[15]–[17].

The vibrating ion-selective microelectrode was first used in 1990 to measure calcium fluxes in various cells and tissues[18]. The ion-selective microelectrode is an adaptation of the glass microelectrode, where an ion-specific liquid ion exchanger (ionophore) is tip-filled into a previously silanized (to prevent leakage) microelectrode. Also, the microelectrode vibrates at low frequencies to operate in the accurate self-referencing mode. Only the specific ion permeates the ionophore, therefore the voltage readout is proportional to the ion concentration in the measuring condition. Then, flux is calculated using the Fick's first law[16], [19].

Emerging optic-based techniques, for example, the pH optrode (or optode), which can be integrated into a self-referencing system may become an alternative or additional technique in bioelectricity laboratories. The optrode does not require referencing and is insensitive to electromagnetism[20], simplifying system setting up and making it a suitable option for recordings where electric stimulation is simultaneously applied.

On the technologies to apply exogenous electric currents and fields there are the voltage DC and AC apparatus integrated with agarose salt bridges[21]. These devices generate countless combinations of voltage magnitude and direction, pulses and frequencies. Such fine-tuning allows researchers to meet cell's criteria. Currently, lab-on-a-chip mediated application of electric fields is gaining ground in the field with the possibility to allow high-throughput screening assays of the large combinatory outputs[22].

Role in animal regeneration

In the early 20th century, Albert Mathews seminally correlated regeneration of a cnidarian polyp with the potential difference between polyp and stolon surfaces, and affected regeneration by imposing countercurrents. Amedeo Herlitzka, following on the wound electric currents footsteps of his mentor, du Bois-Raymond, theorized about electric currents playing an early role in regeneration, maybe initiating cell proliferation[5]. Using electric fields overriding endogenous ones, Marsh and Beams

astoundingly generated double-headed planarians and even reversed the primary body polarity entirely, with tails growing where a head previously existed[23]. After these seed studies, variations of the idea that bioelectricity could sense injury and trigger or at least be a major player in regeneration have spurred over the decades until the present day. A potential explanation lies on resting potentials (primarily V_{mem} and TEP), which can be, at least in part, dormant sensors (alarms) ready to detect and effectors (triggers) ready to react to local damage[4], [24]–[26].

Following up on the relative success of electric stimulation on non-permissive frog leg regeneration using an implanted bimetallic rod in the late 1960's[27], the bioelectric extracellular aspect of amphibian limb regeneration was extensively dissected in the next decades. Definitive descriptive and functional physiological data was made possible owing to the development of the ultra-sensitive vibrating probe and improved application devices[15]. Amputation invariably leads to a skin-driven outward current and a consequent lateral electric field setting the cathode at the wound site. Although initially pure ion leakage, an active component eventually takes place and blocking ion translocators typically impairs regeneration. Using biomimetic exogenous electric currents and fields, partial regeneration was achieved, which typically included tissue growth and increased neuronal tissue. Conversely, precluding or reverting endogenous electric current and fields impairs regeneration[14], [28]–[30]. These studies in amphibian limb regeneration and related studies in lampreys and mammals[31], combined with those of bone fracture healing[32], [33] and *in vitro* studies[34], led to the general rule that migrating (such as keratinocytes, leucocytes and endothelial cells) and outgrowing (such as axons) cells contributing to regeneration undergo electrotaxis towards the cathode (injury original site). Congruently, an anode is associated with tissue resorption or degeneration, as occurs in impaired regeneration and osteoclastic resorption in bone[30], [32], [35]. Although the efforts, the promise for a significant epimorphic regeneration in mammals remains elusive.

References

[1] N. Lane, J. F. Allen, and W. Martin, "How did LUCA make a living? Chemiosmosis in the origin of life.," *Bioessays*, vol. 32, no. 4, pp. 271–80, Apr. 2010.

[2] N. Lane and W. F. Martin, "The origin of membrane bioenergetics.," *Cell*, vol. 151, no. 7, pp. 1406–16, Dec. 2012.

[3] G. Luxardi, B. Reid, P. Maillard, and M. Zhao, "Single cell wound generates electric current circuit and cell membrane potential variations that requires calcium influx.," *Integr. Biol.*, vol. 6, no. 7, pp. 662–72, 2014.

[4] F. Ferreira, G. Luxardi, B. Reid, and M. Zhao, "Early bioelectric activities mediate redox-modulated regeneration," *Development*, no. November, p. dev.142034, 2016.

[5] C. E. Dinsmore, *A history of regeneration research: milestones in the evolution of a science*. New York: Cambridge University Press, 1991.

[6] C. D. McCaig, A. M. Rajnicek, B. Song, and M. Zhao, “Controlling cell behavior electrically: current views and future potential.,” *Physiol. Rev.*, vol. 85, no. 3, pp. 943–78, Jul. 2005.

[7] J. G. Kunkel, S. Cordeiro, Y. J. Xu, A. M. Shipley, and A. José, “The use of non-invasive ion-selective microelectrode techniques for the study of plant development,” in *Plant Electrophysiology*, 2006, pp. 109–137.

[8] J. Monteiro, R. Aires, J. D. Becker, A. Jacinto, A. C. Certal, and J. Rodríguez-León, “V-ATPase proton pumping activity is required for adult zebrafish appendage regeneration,” *PLoS One*, vol. 9, no. 3, pp. 1–11, 2014.

[9] Y. Shen *et al.*, “Diabetic Cornea Wounds Produce Significantly Weaker Electric Signals That May Contribute To Impaired Healing,” *Sci. Rep.*, vol. 6, no. January, pp. 1–11, 2016.

[10] A. L. Hodgkin and A. F. Huxley, “Action potentials recorded from inside a nerve fibre,” *Nature*, vol. 144, no. 3651, pp. 710–711, Oct. 1939.

[11] J. Graham and R. W. Gerard, “Membrane potentials and excitation of impaled single muscle fibers,” *J. Cell. Comp. Physiol.*, vol. 28, no. 1, pp. 99–117, Aug. 1946.

[12] Y. Zhao, S. Inayat, D. A. Dikin, J. H. Singer, R. S. Ruoff, and J. B. Troy, “Patch clamp technique: review of the current state of the art and potential contributions from nanoengineering,” *Proc. Inst. Mech. Eng. Part N J. Nanoeng. Nanosyst.*, vol. 222, pp. 1–11, 2009.

[13] R. B. Borgens, J. W. Vanable, and L. F. Jaffe, “Role of subdermal current shunts in the failure of frogs to regenerate.,” *J. Exp. Zool.*, vol. 209, no. 1, pp. 49–56, 1979.

[14] R. B. Borgens, J. W. Vanable, and L. F. Jaffe, “Bioelectricity and regeneration: large currents leave the stumps of regenerating newt limbs.,” *Proc. Natl. Acad. Sci. U. S. A.*, vol. 74, no. 10, pp. 4528–32, Oct. 1977.

[15] L. F. Jaffe and R. Nuccitelli, “An ultrasensitive vibrating probe for measuring steady extracellular currents,” *J. Cell Biol.*, vol. 63, no. 6, pp. 614–628, 1974.

[16] A. M. Shipley and J. A. Feijó, “The use of the vibrating probe technique to study steady extracellular currents during pollen germination and tube growth,” in *Fertilisation in Higher Plants: molecular and cytological aspects*, 1999, pp. 235–250.

[17] B. Reid, R. Nuccitelli, and M. Zhao, “Non-invasive measurement of bioelectric currents with a vibrating probe.,” *Nat. Protoc.*, vol. 2, no. 3, pp. 661–9, Jan. 2007.

[18] W. M. Kühtreiber and L. F. Jaffe, “Detection of Extracellular Calcium Gradients with a Calcium-specific Vibrating Electrode digital version can attain a noise level of less than,” *J. Cell Biol.*, vol. 110, no. May, pp. 1565–1573, 1990.

[19] G. Luxardi, B. Reid, F. Ferreira, P. Maillard, and M. Zhao, “Measurement of extracellular ion fluxes using the ion-selective self-referencing microelectrode technique.,” *J. Vis. Exp.*, no. 99, p. e52782, 2015.

[20] M. R. Chatni, G. Li, and D. M. Porterfield, “Frequency-domain fluorescence lifetime optrode system design and instrumentation without a concurrent reference light-emitting diode.,” *Appl. Opt.*, vol. 48, no. 29, pp. 5528–36, Oct. 2009.

[21] B. Song, Y. Gu, J. Pu, B. Reid, Z. Zhao, and M. Zhao, “Application of direct current electric fields to cells and tissues in vitro and modulation of wound electric field in vivo,” *Nat. Protoc.*, vol. 2, no. 6, pp. 1479–1489, 2007.

[22] S. Zhao *et al.*, “ElectroTaxis-on-a-Chip (ETC): an integrated quantitative high-throughput screening platform for electrical field-directed cell migration,” *Lab Chip*, vol. 14, no. 22, pp. 4398–4405, 2014.

[23] G. Marsh and H. W. Beams, “Electrical control of morphogenesis in regenerating dugesia tigrina. I. Relation of axial polarity to field strength,” *J. Cell. Comp. Physiol.*, vol. 39, no. 2, pp. 191–213, Apr. 1952.

[24] D. T. Lykken, “Square-wave analysis of skin impedance,” *Psychophysiology*, vol. 7, no. 2, pp. 262–275, 1971.

[25] A. T. Barker, L. F. Jaffe, and J. W. Vanable, “The glabrous epidermis of cavies contains a powerful battery.,” *Am. J. Physiol.*, vol. 242, no. 3, pp. R358–R366, 1982.

[26] R. B. Borgens, “Are limb development and limb regeneration both initiated by an integumentary wounding? A hypothesis.,” *Differentiation*, vol. 28, no. 2, pp. 87–93, 1984.

[27] S. D. Smith, “Induction of partial limb regeneration in Rana pipiens by galvanic stimulation.,” *Anat. Rec.*, vol. 158, no. 1, pp. 89–97, 1967.

[28] L. S. Jenkins, B. S. Duerstock, and R. B. Borgens, “Reduction of the current of injury leaving the amputation inhibits limb regeneration in the red spotted newt.,” *Dev. Biol.*, vol. 178, no. 2, pp. 251–62, Sep. 1996.

[29] R. B. Borgens, J. W. Vanable, and L. F. Jaffe, “Bioelectricity and regeneration. I. Initiation of frog limb regeneration by minute currents.,” *J. Exp. Zool.*, vol. 200, no. 3, pp. 403–416, 1977.

[30] R. B. Borgens, J. W. Vanable, and L. F. Jaffe, “Small artificial currents enhance Xenopus limb regeneration,” *J. Exp. Zool.*, vol. 207, pp. 217–226, 1979.

[31] R. B. Borgens, K. R. Robinson, J. W. Vanable, and M. E. McGinnis, *Electric Fields in Vertebrate Repair: Natural and Applied Voltages in Vertebrate Regeneration and Healing*. New York: Alan R. Liss, 1989.

[32] I. Yasuda, “Mechanical and electrical callus.,” *Ann. N. Y. Acad. Sci.*, vol. 238, pp. 457–65, 1974.

[33] E. Fukada and I. Yasuda, “On the Piezoelectric Effect of Bone,” *J. Phys. Soc. Japan*, vol. 12, no. 10, pp. 1158–1162, Oct. 1957.

[34] M. Zhao *et al.*, “Electrical signals control wound healing through phosphatidylinositol-3-OH kinase-gamma and PTEN.,” *Nature*, vol. 442, no. 7101, pp. 457–60, Jul. 2006.

[35] B. M. Carlson, *Principles of Regenerative Biology*. London: Academic Press, 2007.

CHAPTER IV

4. GENERAL HYPOTHESIS

ALL THIS IS A DREAM. Still examine it by a few experiments.
Nothing is too wonderful to be true, if it be consistent with the laws of nature;
and in such things as these, experiment is the best test of such consistency.

Michael Faraday *in* Diary (1849)

4.1 Putative assumptions

All cells and most tissues, organs and structures have an in/out discontinuum guaranteed by a membrane or epithelium, respectively. Beyond compartmentalization and physicochemical protection and communication, these barriers control ionic, atomic and molecular transport. This transport is tightly regulated and directional, using passive and active mechanisms to reach physiological steady states that typically renders cell's cytoplasm electronegative and tissue's subepithelium electropositive in relation to the extracellular milieus (Fig. III.1), and assures a continuous supply of O_2 to cells (Brahimi-Horn and Pouysségur, 2007; Randall et al., 2001).

Pre-regenerative injury or disease disrupts barrier's integrity creating an in/out continuum that instantaneously leak ions, oxygen, and other atoms and molecules by passive diffusion down the respective electrical and/or chemical gradients. Typically, an injury – by the charge separation and distribution (Levin, 2007) – induces an influx of cations (net inward electric current) in cells and an efflux of cations (net outward electric current) in tissues (McCaig et al., 2005) (Fig. III.1). In both cell and tissue injuries – by the differential partial pressure of O_2 (Brahimi-Horn and Pouysségur, 2007) – it is predicted an influx of O_2.

4.2 Seminal questions

Framing the simplistic assumptions within a straightforward thought experiment of an amputated vertebrate limb or tail, two seminal and generic questions arise: (i) could the expected passive influx of oxygen increase or otherwise fuel ROS levels and regulate local hypoxia, alarming for amputation and triggering regeneration?, and (ii) could the instantaneous and simultaneous movement of oxygen and ions translates into a redox-bioelectric interplay mediating regeneration?

4.3 Tentative corollaries

The assumptions and questions were drained into a general hypothesis decoupled in two specific hypotheses at the onset of the current thesis. The general hypothesis proposes an *integrative interplay between redox and bioelectric phenomena mediating vertebrate regeneration*. The specific hypotheses take the key players of redox and bioelectric phenomena and subject them to crosstalk testing in the context of *Xenopus laevis* tadpole tail regeneration (Fig. IV.1). Owing to technical availability and expertise, the specific hypotheses were anachronic in relation to the seminal questions order.

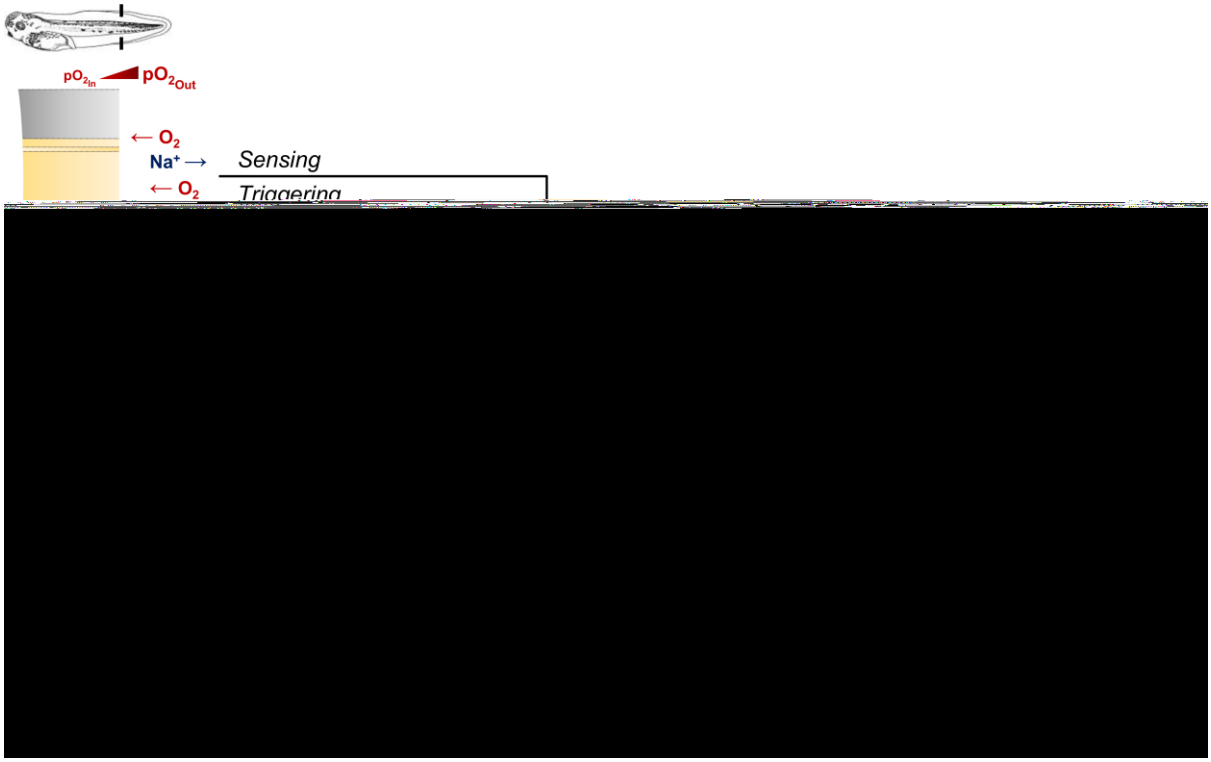

Fig. IV.1 Graphic hypothesis: redox-bioelectric integrative interplay mediates vertebrate epimorphic regeneration.

Firstly, is tested a *two-way regulation hypothesis* (Chapter VII) derived from the following refined question: do ROS modulate regeneration via the regulation of V_m, TEP, EF and/or J_I that are known to be necessary for regeneration? The etymology and substance of this hypothesis is rooted on the dual property of NADPH oxidases, *i.e.*, electrogenic and catalytic. Holoenzyme-driven electron flow – electrogenic property – depolarizes V_m and produced ROS, especially H_2O_2, – catalytic property – regulate TEP, EF and J_I and subsequently modulate regeneration.

Secondly, is tested a *sequential hypothesis* (Chapter VIII) where an injury-induced O_2 influx fuels local ROS production, setting a permissive pO_2 microenvironment, *i.e.*, hypoxia, in the regeneration bud to stabilize HIF-1α and subsequently modulate regeneration. For a deeper link with the previous hypothesis, it is added a new *sequence* where HIF-1α regulates a key bioelectric phenomenon required for regeneration, *i.e.*, J_I.

CHAPTER V

5. GENERAL METHODOLOGY

Le premier était de ne recevoir jamais aucune chose pour vraie, que je ne la connusse évidemment être telle: c'est-à-dire, d'éviter soigneusement la précipitation et la prévention; et de ne comprendre rien de plus en mes jugements, que ce qui se présenterait si clairement et si distinctement à mon esprit, que je n'eusse aucune occasion de le mettre en doute.

René Descartes *in* Discours de la Méthode Pour bien conduire sa raison, et chercher la vérité dans les sciences (1637)[6]

The materials and methods used to generate the raw data and, consequently, derive the results and support the conclusions, are described in detail in the equivalent section and also in figure captions of the reprinted publications and respective supplementary information (Chapter VI–VIII).

In this chapter, it is explained the purpose and fundament of the biophysical techniques used, not only to legitimate, but mainly to facilitate the comprehension of the subsequently organized results. The routine and classic protocols and methodologies used – animal handling and surgery; fin wound healing, tail regeneration and ectopic tail induction assays; optical and confocal microscopy imaging; pharmacological modulations; Western blotting; immunohistochemistry; flow cytometry; and statistical analyses; as well as minor procedures in the technical publication (Chapter VI) – are omitted in this chapter as stringent description is provided in the reprinted publications' equivalent section and supplementary information. Moreover, detailed stepwise protocols are provided for some of the routine assays – Western blotting, immunohistochemistry and flow cytometry – performed (Appendix XIII).

5.1 Regeneration model

5.1.1 Purpose

Xenopus laevis (Daudin, 1802) tail regeneration at tadpole phase (developmental stage 40-41; Nieuwkoop and Faber, 1967) was used as the regeneration model to answer the original and emergent questions addressed throughout the research plan (Fig. V.1). Although not a classical regeneration

model – those being mainly urodeles, planaria and hydras – *X. laevis* has gained ground in the field for its versatility and resourcefulness (Beck et al., 2009).

Frog's oocyte wounding, mouse's (*Mus musculus* (Linnaeus, 1758)) skin wounding and rat's (*Rattus norvegicus* (Fischer de Waldheim, 1803)) corneal wounding were the other experimental organism models sporadically used for dedicated questions related to the findings achieved using the tadpole tail regeneration model. Therefore, further details on those are not provided in this chapter; sufficient description is provided in the reprinted publications' equivalent section and supplementary information.

5.1.2 Fundament

For any given biological question, there is an ideal target experimental model. This cheap version of the Krogh principle (Krogh, 1929; Lindstedt, 2014) unveiled *X. laevis* tadpole tail regeneration as the suited research model for the unfolding of this thesis. Four key criteria were considered for this Kroghinian selection: (i) intrinsic capability of the model to empirically address the research hypotheses; (ii) availability and, even better, expertise on the model in the hosting laboratory; (iii) *a priori* use of the model to achieve at least some fairly similar research goals; and (iv) potentiality for extrapolation (to other biological contexts and species closer to the human paradigm) and for basic-to-applied translation.

To different extents, all the criteria were met and pointed to the chosen model. The seminal and core hypothesis grounding this thesis was to test whether and, if so, how the redox and bioelectric states integrate during regeneration (Chapter IV). This model (together with the close species *X. tropicalis*) had been previously used by the hosting and other laboratories to independently study redox (right prior to experimental commencement) (Love et al., 2013) and bioelectric phenomena during regeneration (Adams et al., 2007; Reid et al., 2009; Tseng et al., 2010). By itself, this would suffice to test on *Xenopus*, but more reasons exist. The tadpole tail is a complex vertebrate appendage, comprising tissues as muscle and spinal cord, making it a prime biomedical model. Besides the amniotes-like intricacies, tails are fully developed for amputation – a very simple surgical procedure – only 3 days post-fertilization, and perfectly regenerate within only a week (Fig. V.1); tadpoles used are only 7-12 mm length and are readily available in large numbers (either by in-house or inexpensive commercial breeding), allowing for huge and rapid dose-exposure pharmacological screenings; tadpoles are easy to handle and culture in regular saline-filled Petri dishes, dispensing food and circulating water; and tails

Proceedings in *X. laevis* housing, handling, experimentation, pharmacology and euthanasia were reviewed and approved by the local (mainly at the University of California, Davis, but also at the Marine Biological Laboratory) Institutional Animal Care and Use Committees (IACUC). Protocol nos are listed in the reprinted publications' equivalent section.

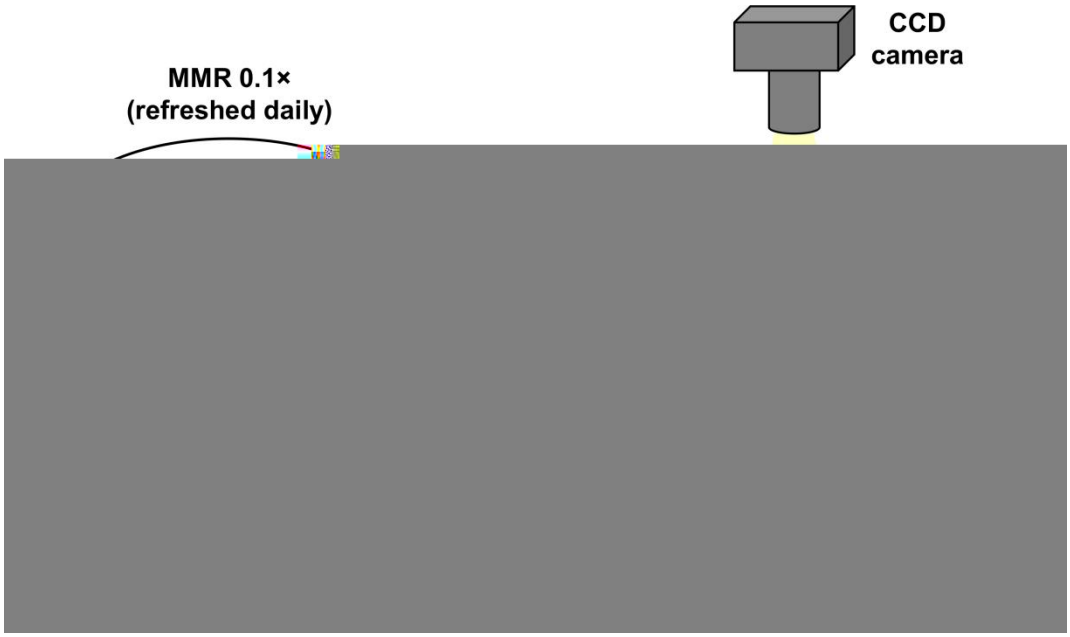

Fig. V.1 Epimorphic regeneration assay. St., stage of development.

5.2 Vibrating probe

5.2.1 Purpose

Physiologic or endogenous electric currents are typically minute, steady and long-lasting. They are commonly found in the extracellular milieu of wounds and in developing embryos. Therefore, to profile and to investigate the extracellular net electric current density dynamics during *X. laevis* tadpole tail regeneration requires an ultra-sensitive and fast-responsive sensor. The gold standard to achieve this non-invasively is the vibrating (or self-referencing) voltage probe (Fig. V.2). This probe was first applied to biological studies in the 1970s, essentially by L. Jaffe, R. Nuccitelli, R. Borgens and J. Vanable (Borgens et al., 1977b; Borgens et al., 1979a; Jaffe and Nuccitelli, 1974). Nonetheless, other than automation and digitalization, the core equipment and biophysical fundament remains unchanged.

5.2.2 Fundament

Ions in conductive aqueous milieus move, producing electric currents with both direction and magnitude, when an electrochemical gradient is established, either physically (*e.g.*, imposed electric fields) or biologically (*e.g.*, during action potentials). In physiologic contexts, an electrochemical gradient is (i) passive, set by a momentary continuum in two previously discrete ion compartments with different ion strengths, *e.g.*, ion leakage upon barrier breaking; (ii) active, set by ion translocators with or without energy consumption, *e.g.*, potential build-up after wounding; or (iii) a combination of both, *e.g.*, when epithelial barrier is leaky and significant movement of ions occur via the paracellular route in addition to via membrane translocators.

Regardless of its origin and sustenance, an ion-based electric current has associated an electric field and corresponding voltage difference (potential drop). This potential is what is detected by the vibrating probe that has an enough signal-to-noise ratio. The voltage-sensitive probe is an insulated and sharpened stainless steel wire, platinum-electroplated at the exposed tip to deposit a large surface area and capacitive black ball. The ball diameter defines the spatial resolution that is high (micrometre range); as everything works in electric principles, temporal resolution is also high (millisecond range). The probe vibrates one dimensionally at a frequency between 100-200 Hz by a piezoelectric bender, over an excursion of one ball diameter. In the presence of an artificial (for calibration) or a natural DC voltage gradient, the charge in the capacitive vibrating ball oscillates in a sinusoidal AC output with an amplitude proportional to the voltage difference and with a frequency of the vibration (Jaffe and Nuccitelli, 1974; Reid and Zhao, 2011; Reid et al., 2007; Shipley and Feijó, 1999) (Fig. V.2). The probe's signal is detected by a lock-in amplifier that filters out frequencies other than frequency of vibration. This technological improvement increased the sensitivity in around three orders of magnitude compared against the stationary probe, approximating it to the level of electronic noise (nanovolt range) and allowing accurate measurements of tiny electric currents (nanoampere range) (Borgens, 1982; Borgens et al., 1989; Reid et al., 2007; Shipley and Feijó, 1999). Vibration at the frequencies used do not meaningfully disturb local gradients, neither create stirring artefacts, because voltage is instantaneous.

a

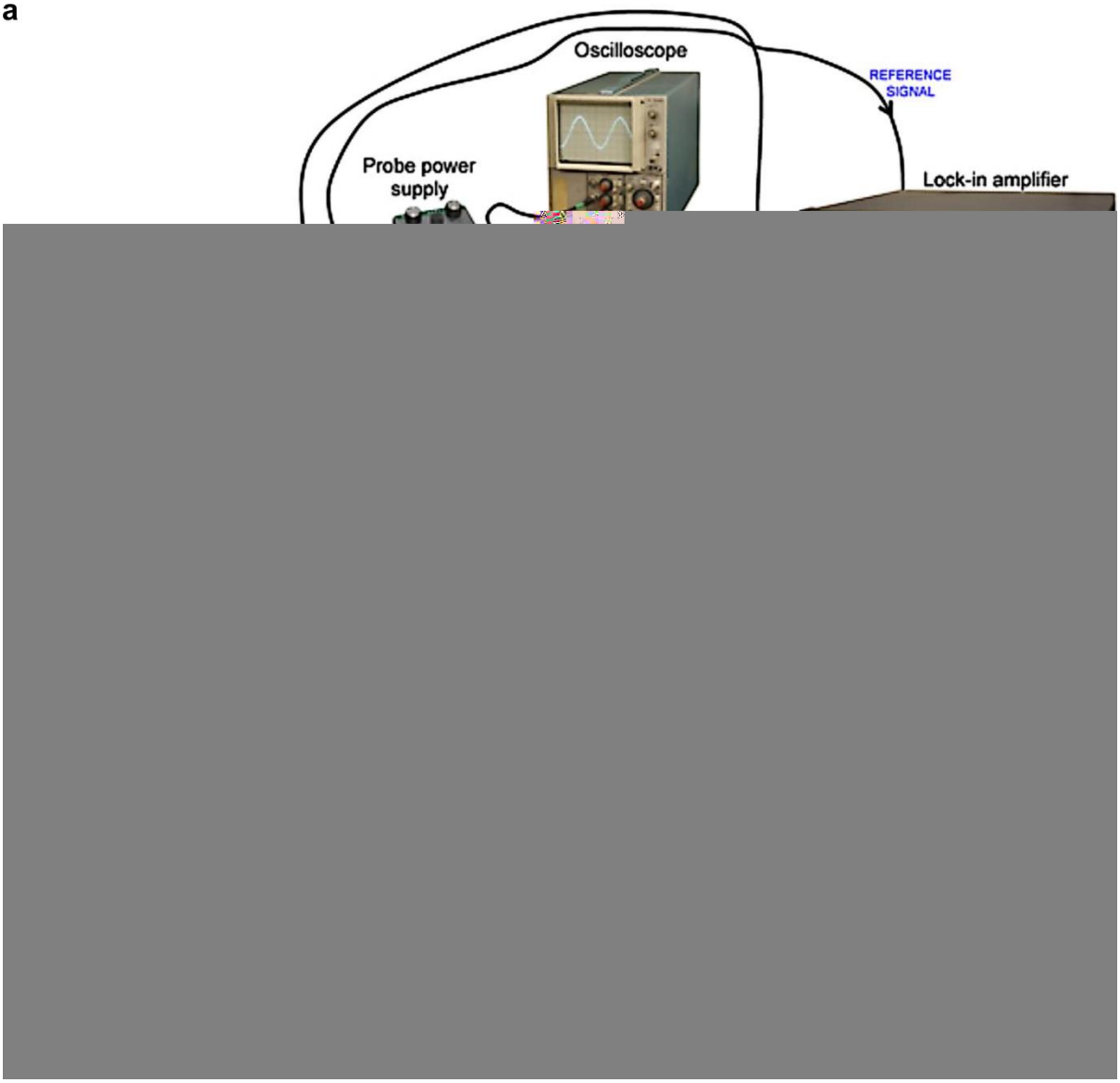

Fig. V.2 Vibrating voltage probe measurement. **a** Equipment and circuit (adapted from Reid and Zhao, 2011). **b** Biophysical principle. DC, direct current; AC, alternating current; A, amplitude of wave; V, voltage, J_I, electric current density; $\propto$, directly proportional; f, frequency of wave; $f_{vib.}$, frequency of voltage probe vibration.

The electric current density is calculated from the measured voltage difference using the calibration values that calibrate the probe following the Ohm's law,

$$J_I = \frac{E}{\rho} = \frac{V}{d \times \rho} \quad \text{(Eq. V.1)},$$

where J_I is the electric current density (μA cm^{-2}), E is the electric field (V cm^{-1}), ρ is the resistivity of the medium (Ω cm), V is the measured voltage by the probe (V), and d is the excursion (cm). The

we minimized the time to collect the data. The introduction of the sharp glass microelectrode, co-opted from glass micropipettes used for micromanipulation of bacteria and microinjection of living cells, was a milestone in electrophysiology (Bretag, 2017). Although no more than liquid salt bridges electrically connecting the tissue with the electrode, microelectrodes permitted to impale smaller cells other than the squid giant axon (up to 1 mm in diameter), and protected biological tissues from leachable toxics from bare electrodes (*e.g.*, Ag^+) and from redox and other chemical metal-induced reactions that could alter local physiology. Also, the smaller tip diameters increased the electrode resistance generating more consistent data due to the consequently increased signal-to-noise ratio (Zhao et al., 2009). Furthermore, we used small tip diameter electrodes to mitigate dialysis (electrode content draining into tissue). The electrolyte with high sodium content was used for the same reason, analogously to the use of high potassium content in V_m measurements.

Measurements rely in a basic voltage-sensitive circuit: a reference bare Ag/AgCl electrode in the medium and a measuring glass microelectrode (back-filled with electrolyte and with an Ag/AgCl electrode) connected to a high impedance headstage voltmeter that measures, after signal amplification, the voltage difference between the two electrodes (Fig. V.3). Recordings are performed after voltage offset to 0 mV (zeroing) prior to impalement. Together with the high content of sodium in the electrolyte, zeroing the microelectrodes mitigates the effects of liquid junction potentials (Barry and Lynch, 1991). Therefore, the voltage difference direction and magnitude equal the voltage of the measuring microelectrode.

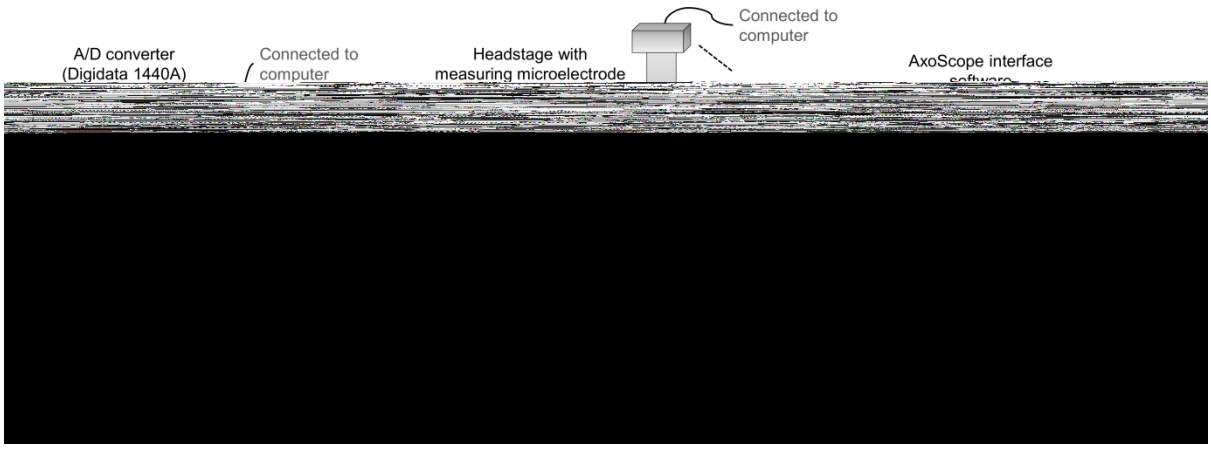

Fig. V.3 Glass microelectrode equipment and circuit for measurements.

Ag/AgCl electrodes are standard transducers of the ionic into electric current in electrophysiology as they have low impedance, low junction potential (electrode (metal) and electrolyte (saline) interface), weak polarization and are relatively low cost. The transduction occurs via a reversible redox reaction at the electrode surface that wares off the AgCl layer. For this reason, Ag/AgCl electrodes are routinely dipped in sodium hypochlorite (commercial bleach) to recoat the electrode with the AgCl layer, allowing stable recordings (Zhao et al., 2009).

As in the voltage probe technique, proper grounding was carefully maintained and a Faraday cage and 'wall' was used to further eliminate electromagnetic interference.

5.4 Micro-optrode

5.4.1 Purpose

The micro-optrode was used to profile and to investigate the extracellular O_2 flux dynamics mainly during *X. laevis* tadpole tail regeneration, but also during fin wound healing and in mouse and oocyte wounds. The optic-based technique was further applied to other measurements in order to prove its accuracy and versatility.

5.4.2 Fundament

The technical publication – reprinted next – exhaustively fundaments and elucidates the micro-optrode technique (Chapter VI).

CHAPTER VI

ABSTRACT

Reactive molecular oxygen (O_2) plays important roles in bioenergetics and metabolism, and is implicated in biochemical pathways underlying angiogenesis, fertilization, wound healing and regeneration. Here we describe how to use the Scanning Micro-Optrode Technique (SMOT) to measure extracellular fluxes of dissolved O_2. The self-referencing O_2-specific micro-optrode (also termed micro-optode and optical fibre microsensor) is a tapered optical fibre with an O_2-sensitive fluorophore coated onto the tip. The O_2 concentration is quantified by fluorescence quenching of the fluorophore emission upon excitation with blue-green light. The micro-optrode presents high spatial (<50 μm) and temporal (11 s) resolutions with improved signal-to-noise ratio in the picomole range. In this protocol, we provide step-by-step instructions for micro-optrode calibration, validation,

INTRODUCTION

Organisms have adapted to the reactive oxic environment and most live forms currently depend on diatomic or molecular oxygen, or dioxygen (O_2), especially because of bioenergetics and metabolism[1,2]. O_2 is a powerful oxidant and once adapted as the final electron acceptor in the oxidative phosphorylation (cellular aerobic respiration), the energy output dramatically increased[3]. This gave life degrees of freedom that permitted unprecedented and massive complexification, diversification and radiation of species[4,5]. Also, O_2 has being adapted for cell signalling and behaviour, whether related with bioenergetics, or not[6,7]. O_2 plays a key role in tracheal branching and lung development[8,9], vasculogenesis and angiogenesis[10], placentation[11], brain development[12], maintenance of pluripotency in stem cells niches[13], and in tumors[14,15]. Further, O_2 is important for cell migration, proliferation and differentiation[11,16,17], wound healing[18–20], and, more recently, regeneration[21–24]. Many of these functions are not controlled directly or strictly by molecular oxygen, but by master players of O_2 homeostasis and physiology: reactive oxygen species (ROS) and hypoxia-inducible factors (HIF). ROS are the products of the serial oxidation of O_2 to water (H_2O) in a four-electron gain. Most ROS are unstable and extremely reactive, perpetuating chain reactions that are noxious for cells[25,26]. Therefore, enzymatic and non-enzymatic antioxidant strategies evolved and are now ubiquitous in most life forms. The pro-oxidant/antioxidant balance in cells and in the extracellular milieu is indeed crucial for both the signalling and destructive powers of ROS[25]. As life grew dependent on O_2, sensing its deprivation (so-called hypoxia) became essential to allow immediate actions for cellular or organismal survival. HIF are not only O_2 sensors but also transcription factors, regulating the expression of hundreds of genes related to bioenergetics and other processes and functions[27]. This brief overview demonstrates that studying O_2 dynamics is of pivotal significance across biological sciences. Therefore, technologies and methods to reliably and accurately quantify O_2[28] are an indispensable research tool for investigators.

In a recent study, we demonstrated the integrated role that the three core players of molecular oxygen homeostasis – O_2 itself, ROS and HIF – play in *Xenopus laevis* tail regeneration. Using an optic-based probe (optrode), we were able to directly measure an O_2 influx following tail amputation. We showed that theO_2 influx correlates with the regeneration of the tadpole tails and is dependent on both ROS production and HIF-1α stabilization[24]. The O_2 concentration was

quantified by fluorescence quenching of the O_2-sensitive fluorophore located at the tip of the optrode.

There is an increasing interest in optic-based measurements as a mainstream tool to quantify molecular oxygen flux, and the validated protocol herein intends not only to offer a basic, user-friendly solution to reliably measure physiologically meaningful O_2 fluxes, but also to stimulate investigators into the exploration of the redox phenomena in biology.

Overview of the Procedure

In this Protocol, we describe the step-by-step procedures for quantifying O_2 using the Scanning Micro-Optrode Technique (SMOT) and provide example applications and data from various model organisms. We measure O_2 fluxes in *X. laevis* oocytes, epithelium, gills and tails, rat cornea and mouse skin. The procedure consists of 5 key stages: in the first two stages, we describe how to calibrate (Steps 1-6) and validate (Steps 7-13) the optrode; in the third stage (Step 14), we instruct how to setup data acquisition; in the fourth stage (Steps 15-27), we provide detailed experimental measurements; and in the fifth stage (Steps 28-29), we delineate strategies for data analysis.

Development of the fluorescence quenching-based method

The seed of the optrode-based method described in this Protocol was the mathematical formulation for fluorescence quenching by Stern and Volmer in 1919[29] (see **Box 1**). Since O_2 has been shown to be one of the best fluorescence quenchers[30,31], its measurement using optic-based sensors was a natural alternative, as well as step forward, further elicited to address the polarographic electrode pitfalls. The seminal studies for optical sensing of O_2 occurred in the 1930s when a fluorometer detected trace amounts of O_2 from a gaseous sample flowing through fluorophore-coated silica particles[30,32,33]. Developments in the 1960-70s led to the inclusion of optical fibres, marking the emergence and the coining of optrodes (linguistic analogy with electrodes) or optodes (from Greek's "optical way")[32,34,35]. Some 30 years after Clark's polarographic electrode milestone, a functionally-equivalent optrode was used to similarly measure mammalian blood partial pressure of oxygen (pO_2)[36]. O_2 was initially quantified as a

function of fluorescence amplitude (intensity), with the introduction of concurrent quantification via fluorescence decay time (lifetime) in 1988[37] (see **Box 1**). The sensor developments culminated in staple micro-optrodes in the l990s, tested and used mainly in aquatic microbial biology[38–42].

The next advance was the incorporation of self-referencing capabilities within the optrode system in the mid-2000s[43]. Technological advancements in optical fibres, light sources (including light-emitting diodes, LED), photodiodes, cameras, motion control and software, decreased expenses and improved the sensor system, progressing it to the modern, herein-described, state[44]. These developments broadened the use of optrodes to measure O_2 fluxes, with an emphasis on plant physiology, where various research and technical essays appeared[28,43,45–50]. Our research studies, however, focus on animal physiology and are carried out using SMOT to measure the extracellular fluxes of dissolved O_2 (**Fig. 1a**). The self-referencing O_2-specific micro-optrode quantifies the analyte concentration by quenching of the fluorescence emitted by an O_2-sensitive fluorophore excited with blue-green light (λ=505 nm; Fig. 1b,c)[31].

Comparison with other approaches to quantify physiological O_2

A wealth of established and emerging alternative technologies and methods are being used to measure or image O_2 dynamics[28,32]. Approaches based on redox (*e.g.*, Clark electrode), optical (*e.g.*, optrodes, planar sensor foils and sensor cartridges in a plate reader (Agilent's Seahorse)), molecular (*e.g.*, molecular probes (Luxcel Biosciences' MitoImage™), nanosensors and quantum dots) and microscopy (*e.g.*, electron paramagnetic resonance and fluorescence resonance energy transfer) measurements and imaging yield different outcomes in the qualitative to quantitative spectrum[28,32,47,51–56].

The approach described in this Protocol allows for quantitative determination of extracellular O_2 fluxes using a non-invasive self-referencing micro-optrode. The key alternative approach to this is the classic Clark-type (polarographic) microelectrode[52,57]. Polarographic microelectrodes are electrochemical-based sensors that were used for the majority of the seminal and classical studies of O_2 homeostasis and physiology, including respirometry[28,57,58]. The first of these electrodes was developed in 1953 to measure the pO_2 in blood and has, since, been improved and adapted into various forms[53,59]. Polarographic electrodes are based on redox reactions

consuming the analyte. The probe is polarized to reduce O_2, quantifying O_2 concentration as a function of the generated current (linear relationship). Local (sensor tip microenvironment) electric field generation and/or disturbance (due to polarized electrode) and chemical disturbance (due to analyte consumption) are significant disadvantages, especially for large sensors, which require stirring of the aqueous medium at constant speed to maintain diffusion equilibrium. In addition, temporal signal drift (due to diffusion-limited O_2 consumption at sensor), probe fouling, electromagnetic interference, and less sensitivity (*i.e.*, low detection limit) in low O_2 environments comprise the main disadvantages of polarographic electrodes (**Table 1**)[28,57,60]. Probe miniaturization, and the introduction, development and establishment of the self-referencing modality mitigated these problems[57,61–65], but did not discourage the research of concurrent and improved alternatives.

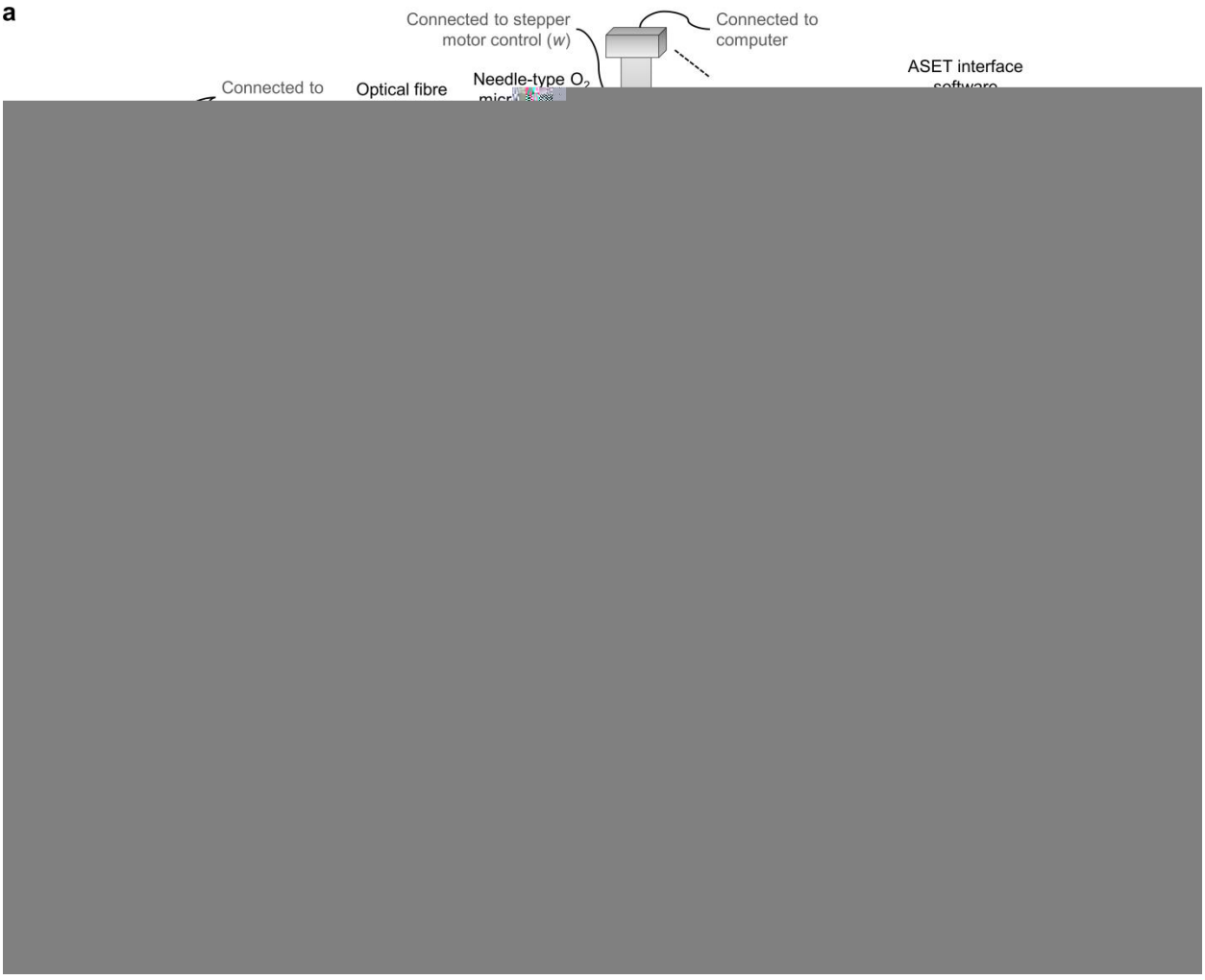

Figure 1 | Scanning Micro-Optrode Technique (SMOT). (**a**) Schematic representation of the SMOT system and circuitry. A pulse of fluorescent light travels down the optical fibre and then travels back up the fibre where its signal is converted to an electronic signal by the photomultiplier tube (PMT) housed in the micro-optrode amplifier. (**b**) Needle-type oxygen-specific micro-optrode. A tapered glass optical fibre with a tip diameter of <50 µm is housed in a stainless needle 40 mm long and with 0.8 mm outer diameter. The blocker is an adaptation in the syringe to hold and protect the micro-optrode inside the needle after use. Inset: schematic depiction and detail of the oxygen-sensitive sensor tip with the coated PSt1 fluorophore (solid state matrix). (**c**) Schematic of the fundamentals of the fluorescence quenching-based oxygen measurement by SMOT (details in **Box 1**). (**d**) Experimental design of representative specimens (two most used by us to test the system). Top: *Xenopus laevis* tadpole tail; bottom: *X. laevis* oocyte. Detail of near (full colour) and far (semi-transparent colour) positions of micro-optrode during excursion. Negative values are net influx and positive values are net efflux (applies to subsequent figures). Tadpole tail scheme (lateral view) is displayed in the same orientation as the whole organism anteroposterior (A/P), dorsoventral (D/V) and left-right (L/R) axes (middle scheme; applies to subsequent figures). The oocytes scheme (lateral view) is displayed in the animal (a) to vegetal (v) pole orientation (applies to subsequent figures). Sizes in schemes are relative and proportional approximations, except for the computer, which is zoomed out, and for the micro-optrode, which is zoomed in for clarity (applies to subsequent figures).

Limitations of the Approach

Depending on the application, some advantages of the approach may inadvertently become a limitation. A clear example is the higher spatial resolution of micro-optrodes, which permits the pinpointing of O_2 fluxes in a fraction of a cell. However, if the goal is to map a large part of the cell or tissue simultaneously upon treatment, then imaging methods may be better suited than the technique herein described.

Since the micro-optrode is housed in a needle, it allows the researcher to safely impale the micro-optrode into readily accessible or superficial tissues (*e.g.*, solid tumours), organs (*e.g.*, skin and eye) or body fluids (*e.g.*, blood). However, deeper or fragile tissues or organs (*e.g.*, bone tumour, heart and brain) may be out of the impalement range without further invasive surgery. Isolation of the tissue/organ of interest (*ex vivo* assays) from the organism may be required to overcome the accessibility limitation.

Further, the technique assumes that the sample or animal is immobilized to mitigate noise and to prevent artifactual recordings. Therefore, physical or chemical immobilization procedures are required, which may confer a limitation in certain experimental designs. However, this limitation is also shared by other available techniques.

BOX 1 | FUNDAMENTALS OF THE FLUORESCENCE LIFETIME-BASED OXYGEN MEASUREMENT

The SMOT system quantifies oxygen (in liquid or gas phases measurement) via fluorescence quenching, with high spatial and temporal resolutions (**Table 1**). By definition, fluorescence quenching is a process where the fluorescence intensity of a sample diminishes. Numerous physicochemical interactions can produce quenching; among them is the collisional (or dynamic) quenching by which the O_2 analyte is quantified. In this interaction, a fluorophore (fluorescence emitter) and a quencher collide, during the lifetime of the excited state, leading to energy transfer from the former to the latter that quenches the fluorescence intensity[28,31,32]. O_2 is a well-known and common collisional quencher that can be quantified by many fluorophores[30,31]. We utilize ready-to-use micro-optrodes that rely on the proprietary fluorophore PSt1 (commercially available from PreSens), which is a proprietary transition metal complex coated as a solid state matrix into the optical fibre tapered tip. PSt1 is excited by blue-green light (λ=505 nm) from a LED source. In the absence of O_2, the sensor emits fluorescence; in the presence of O_2 there is, instead, energy transfer by collision that quenches the fluorescence emission and energizes O_2 from the ground (triplet) to the excited (singlet) state, without consuming it (**Fig. 1c**). The quenching degree is directly proportional to the O_2 content, providing a reliable measurement.

Both fluorescence amplitude (intensity) and decay time (lifetime) decrease in the presence of O_2. The relationship between oxygen concentration, and fluorescence intensity and lifetime is described by the Stern-Volmer equation[29,31]:

$$\frac{F_0}{F} = \frac{\tau_0}{\tau} = 1 + K_{SV} \times [O_2], \quad (1)$$

where F_0/F is the fluorescence intensity in the absence and presence of O_2, respectively; τ_0/τ is the fluorescence decay in the absence and presence of O_2, respectively; K_{SV} is the Stern-Volmer constant and $[O_2]$ is the O_2 (quencher) concentration.

The interface software ASET (see **Box 3**) calculates O_2 concentration using the fluorescence lifetime-based method (phase-modulation or frequency-domain), instead of the fluorescence intensity-based method. For accurate measurements, the fluorescence intensity-based method increases the excitation energy (*i.e.*, laser/light intensity); however, this enhanced sensitivity leads to a significant increase in the fluorophore photobleaching and, consequently, shorter sensor longevity. The sensitivity/photobleaching/longevity trade-off, in addition to frequent calibration because of noise and drift in excitation sources, leaned the design of the current system in favour of the frequency-domain lifetime-based method[28,32,37,45,77]. This method relies on the O_2-dependent phase angle shift. Phase angle is a measure of the time delay in the emitted fluorescence caused by the decay of the fluorophore when excited by a frequency-modulated light (sine wave; **Fig. 2b**). The relationship between phase angle and decay time is described by the following equation[45]:

$$\tan \varphi = 2 \times f_{mod} \times \tau, \quad (2)$$

where φ is the phase angle and f_{mod} is the modulation frequency.

Finally, O_2 concentration is derived using a modified Stern-Volmer equation:

$$\frac{\tan \varphi_0}{\tan \varphi} = \frac{\tau_0}{\tau} = 1 + K_{SV} \times [O_2]. \quad (3)$$

The relationship between the phase angle and O_2 concentration is nonlinear for the pO_2 0-100% full range and is inversely proportional[28,31,78]. However, for the pO_2 0-32% range, relationship is almost perfectly linear (generally r^2>0.999). This range encompasses the physiologically meaningful O_2 tensions; consequently, a two-point calibration (sulfite- or N_2(*g*)-purged and O_2-saturated water) suffices to calibrate the micro-optrode[45,47,49].

In specific terms, the ASET software communicates with the electronic firmware that has an embedded microprocessor that automatically and in real-time calculates pO_2 (%). Calculation follows the above detailed fluorescence lifetime-based method via Stern-Volmer equation based on a measurement of phase angle shift relative to calibration values obtained (at known temperature and barometric pressure) for the sensor being used. The ASET software provides extractable raw data of the oxygen content in percent (%) units (see **Box 4**).

Applications of the Approach

The turn-key SMOT system employing a ready-to-use micro-optrode (**Fig. 1**; see **Box 1**), as well as alternative systems for the measurement and study of oxygen dynamics, are currently in a number of laboratories generating physiologically reliable data, especially in plant models[43,45–47,49]. Systems are also used in non-biological studies, like in metal corrosion[66]. With proper mounting, tuning and calibration, SMOT is a very versatile technique and easy to adapt to disparate laboratory environments and research goals. Commercially available micro-optrodes can take different and even customizable configurations (*e.g.*, for flow through recordings or to be incorporated in catheters), further increasing the versatility and potential uses of the technique. Moreover, the SMOT system can be readily adapted to incorporate perfusion, incubation and/or advanced imaging systems if desired, broadening its scope of applicability even more.

In our laboratory, we set up a '*Bioelectric and Redox Sensor Facility*', with the micro-optrode sensor (together with microelectrode-based sensors) at its core, mainly to study animal wound healing and regeneration, but also other physiological phenomena. Recently, we carried out research, successfully applying this technique, to study the O_2 dynamics during *Xenopus laevis* tadpole tail regeneration[24]. Representative and comprehensive examples of this and other research are presented in the **Anticipated results** section.

In addition to the non-invasive capabilities, the micro-optrode has invasive potentialities in the static mode of measurement (see **Experimental design** section). The metal needle can easily impale disparate tissues/organs, injecting the micro-optrode into previously inaccessible

measurement regions. Examples that we are testing include reading intravenous pO_2 in rat tail and intraocular pO_2 in non-human primate (**Supplementary Figure 1a,b**). Replacing the needle, a broken pulled capillary can provide a hole for the micro-optrode itself. We are testing this to measure intratissue pO_2 in the tadpole regeneration bud (**Supplementary Figure 1c**). Further, the micro-optrode itself can impale softer samples. Researchers can adapt these potentialities and apply in their fields with relative ease. We also applied successfully the micro-optrode in a gas phase measurement (see **Box 2**), an advantage over the polarographic microelectrode (**Table 1**) that proves micro-optrode versatility and widens its usability.

There are many other applications and potentialities for the micro-optrode, either in biological or non-biological contexts, for example: manure, sediment and biofilm profiling, package control, metal corrosion and many others too numerous to test or list here (*e.g.*, see micro-optrode manufacturer's large database: www.presens.de/knowledge/publications).

BOX 2 | LIQUID *VS.* GAS PHASE MEASUREMENT

An advantage of the micro-optrode over the polarographic microelectrode (**Table 1**) is that the micro-optrode can acquire measurements in the gas phase. Due to research purposes and specimen constraints we measured all samples in the liquid phase; however, we successfully tested this possibility in a wounded mouse skin recording (right). Note the similar plateaus after flux stabilization (liquid phase: −46.90±0.71; gas phase: −50.45±1.60; p=0.09 (unpaired Student's t test, two-tailed p value)). For more robust and reproducible data collection, the airflow surrounding the measuring chamber must be dramatically limited, and the humidity must also be controlled.

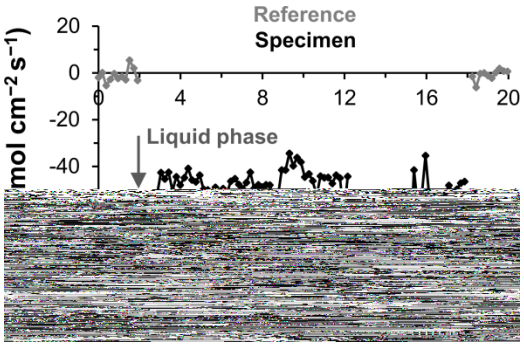

TABLE 1 | Advantages and disadvantages of oxygen flux measurement with micro-optrode *vs.* polarographic microelectrode.

Property*	**Micro-optrode**	**Polarographic microelectrode**
Sensing mechanism	Collisional (or dynamic) fluorescence quenching by O_2	O_2 chemical reduction at 0.7 V
Temporal resolution	11 s single micro-optrode[a]; 2 s dual micro-optrode[a]	<1 s

Figure 3 | Dual micro-optrode mode. (**a**) Schematic representation of the setup for the dual micro-optrode measurement, compared against the single micro-optrode. (**b,c**) Validation of the dual micro-optrode mode using an N_2 artificial sink. Curve fitted to a linear regression (inset in **c**) after logarithmic (log) transformation, demonstrating exponential drop of flux with distance, as expected. (**d**) Values were similar to single micro-optrode mode measuring the same N_2 bubble, further validating the dual mode. References and each distance (5, 10, 20, 40, 80, 160, 320 and 640 µm) from sink are delimited by a discontinuity in the solid lines. (**e-g**) Potentialities of the dual micro-optrode. (**e**) Dual micro-optrodes for pO_2 and pH operating in the near and far excursion mode. (**f**) Non-invasive simultaneous measurement of endogenous fluxes of O_2 and protons (H^+). pH micro-optrode flashing colour is pseudocoloured in green for distinction (actual light used is blue). (**g**) Invasive simultaneous measurement of endogenous intratissue pO_2 and pH. Dual micro-optrodes operating in the static mode. Scheme is a transverse section of a blood vessel (*e.g.*, from heated rat tail).

Additional data acquisition modes. The single and dual micro-optrode modes were typically operated as manual linear scans. However, automatic 2D and 3D line and grid scanning can be pre-programed in the ASET software to automatically profile an immobile sample, depending on research needs and specimens used. We tested and used these modes successfully in enucleated rat eyes, because of

MATERIALS

BIOLOGICAL MATERIALS

CRITICAL The examples shown in the Anticipated Results of this Protocol are listed below. In addition, we have tested rat tail and enucleated non-human primate eye (gifted by the California National Primate Research Center), and we anticipate that our Protocol should be compatible with *in vivo* and *ex vivo* tissues or organs readily accessible to the micro-optrode (ideally in a minimally or non-invasive way). The protocol cannot be used *in vivo* on deeper or very sensitive tissues or organs, unless an invasive surgery is made with utmost care.

Xenopus laevis (Daudin, 1802) oocytes and tadpoles. Pre-sorted oocytes were acquired from Xenopus 1 (www.xenopus1.com) and tadpoles were acquired from National Xenopus Resource (NXR; www.mbl.edu/xenopus) or Xenopus Express (www.xenopus.com)

Mus musculus (Linnaeus, 1758) skin. Mice with 8 week-old, male, BKS.Cg-*Dock7*^{m} +/+ *Lepr*^{db}/J heterozygous (non-diabetic) were acquired from The Jackson Laboratory (www.jax.org)

Rattus norvegicus (Berkenhout, 1769) eye. Rats with 7-8 weeks-old, male, Sprague-Dawley were acquired from Envigo (https://insights.envigo.com) or Charles River (https://www.criver.com)

CAUTION Any experiments involving aforementioned live animals conformed to relevant Institutional and National regulations. The experiments shown in this protocol using tadpoles were approved by the Marine Biological Laboratory (MBL; Woods Hole) (protocol no. 14-59) and the University of California (UC), Davis Institutional Animal Care and Use Committees (IACUC; protocol no. 18601). The procedures using rodents were approved by UC Davis IACUC (protocol nos 16766 and 17876)

REAGENTS

Deionized water (dH_2O)

Sodium bisulfite (mixture of $NaHSO_3$ and $Na_2S_2O_5$) (Sigma-Aldrich, Corp., cat. no. 243973)

CAUTION Acute oral toxicity; serious eye damage; acute aquatic toxicity; avoid contact with skin and eyes; do not store near acids; use personal protective equipment

Compressed $N_2(g)$ 100% cylinder. **CAUTION** Pressurized gas cylinder should be handled properly

Sodium chloride (NaCl; Sigma-Aldrich, Corp., Corp., cat. no. S7653)

Calcium chloride dihydrate ($CaCl_2 \cdot 2H_2O$; Sigma-Aldrich, Corp., cat. no. 223506)

Potassium chloride (KCl; Sigma-Aldrich, Corp., cat. no. P9333)

Magnesium chloride hexahydrate ($MgCl_2 \cdot 6H_2O$; Sigma-Aldrich, Corp., cat. no. MN-9272)

HEPES (Sigma-Aldrich, Corp., cat. no. H3375)

Sodium hydroxide (NaOH; Sigma-Aldrich, Corp., cat. no. 221465) **CAUTION** Causes severe skin burns and eye damage; avoid inhalation of vapour or mist; store in acids/bases cabinet; use personal protective equipment

Dimethyl sulfoxide (DMSO; Sigma-Aldrich, Corp., cat. no. D2650) **CAUTION** May be harmful if inhaled, swallowed or absorbed through skin; may cause eye irritation; keep away from sources of ignition; avoid contact with DMSO-containing toxic reagents, because DMSO readily transports them through skin; use personal protective equipment

N-benzyl-p-toluene sulfonamide (BTS; Tocris Bioscience, cat. no. 1870)

Hydrogen peroxide solution 30% (w/w) in H_2O (H_2O_2; Sigma-Aldrich, Corp., cat. no. H1009) **CAUTION** Acute oral toxicity; skin corrosion; serious eye damage; acute and chronic aquatic toxicities; keep away from sources of ignition; use personal protective equipment

Paraformaldehyde (PFA; Sigma-Aldrich, Corp., cat. no. P6148) **CAUTION** Acute oral toxicity; skin corrosion; serious eye damage; acute and chronic aquatic toxicities; keep away from sources of ignition; use personal protective equipment

2,4-Dinitrophenol (2,4-DNP; Sigma-Aldrich, Corp., D198501) **CAUTION** Toxic if swallowed, in contact with skin or if inhaled; may cause damage to organs through prolonged or repeated exposure; very toxic to aquatic life; use personal protective equipment

Potassium cyanide (KCN; Sigma-Aldrich, Corp., 60178) **CAUTION** Fatal if swallowed, in contact with skin or if inhaled; very toxic to aquatic life with chronic effects; use personal protective equipment

Sodium azide (NaN_3; Sigma-Aldrich, Corp., S2002) **CAUTION** Fatal if swallowed or in contact with skin; very toxic to aquatic life with chronic effects; use personal protective equipment

Compressed CO_2(*g*) 100% cylinder. **CAUTION** Pressurized gas cylinder should be handled properly

Artificial tear solution (BSS+; Alcon Laboratories, cat. no. 0065080050)

Hair removal cream (Church & Dwight, Inc., Nair)

Phosphate-buffered saline (PBS; Amresco, Inc., cat. no. E404)

Ethanol 95% (v/v) (EMD Millipore, Corp., cat no AX0441-03) **CAUTION** Causes severe eye and moderate skin irritation; causes respiratory tract irritation; highly flammable liquid and vapour; store in flammables cabinet; use personal protective equipment

EQUIPMENT

CRITICAL The Scanning Micro-Optrode Technique (SMOT) turn-key system can be divided into three subsystems: hardware, software and microsensor. The core components of the hardware are obtained via Applicable Electronics, LLC (www.applicableelectronics.com); the acquisition software is provided by Science Wares, Inc. (www.sciencewares.com); and the microsensor is acquired from PreSens, GmbH (www.presens.de). All components for the technique and measurements are listed below.

SMOT system, hardware

Single channel micro-optrode amplifier and light-emitting diode (LED) source (OA-1), with built-in photomultiplier (PMT), the light-to-electric signal transducer (Science Wares, Inc.)

Computerized motion control, four axis micro-stepper system (CMC-4), with programmable step, direction and speed. Fourth axis (*w*) is for microscope focus function (Applicable Electronics, LLC)

3D motorized micropositioners (Science Wares, Inc., cat. no. Model 3DMM) with extra focus motor

Upright zoom scope (1-14× magnification), with motorized focus (75 mm travel) and long working distance (typically >5 cm, increase or decrease depending on sample dimensions) (Applicable Electronics, LLC). This built-in optics can be readily and easily disassembled and substituted by compound, upright, inverted or any other type of microscope without

compromising compatibility with the acquisition software (ASET). The ASET-controlled motorized focus capability might be lost depending on the microscope

Horizontal zoom or other scope can also substitute or be added to the built-in vertical zoom scope for further or enhanced imaging. In another SMOT system, we added a Dino-Lite digital microscope (AnMo Electronics, Corp., cat. no. AM4013MTL) horizontally-oriented in some experimental designs. Imaging monitoring can be performed with the ASET software following the installation of an update

Colour USB digital camera, 1.3 megapixel (IDS µEYE, GmbH; www.en.ids-imaging.com, cat. no. Model UI-1240LE): for image capture and time-lapse and real-time video acquisition

Desktop computer

Analog-to-digital (A/D) board (National Instruments (NI), Corp., cat. no. PCI NI-6229) with breakout box/cables

Motion control board (NI, Corp., cat. no. PCI NI-7332)

Digital video interface (NI, Corp., cat. no. NI-IMAQ)

LCD flat screen video monitors: two linked as extended screen with one for acquisition software panel and another for sample visualization software panel

Micro-optrode holder: assembled with stainless-steel mounting posts and post clamps (Newport, Corp., cat. nos. M-MCA-2, M-MSP-1, M-MSP-2), and a syringe holder (Science Wares, Inc., cat. no. MOH2) mounted onto the 3D motorized micropositioners

Second micro-optrode micropositioner and holder: small 3D manual micropositioner (Narishige, Inc., cat. no. M-44) with a syringe holder (Science Wares, Inc., cat. no. MOH1) mounted onto the 3D motorized micropositioners (only for dual micro-optrode mode)

3D sample holder: flat square sample holder (Applicable Electronics, LLC) mounted onto a 3D manual micropositioner (Line Tool Company, cat. no. Model A), permitting high degrees of freedom for sample positioning

Vibration-isolation active-air tabletop with M6 tapped holes (Kinetic Systems, Inc.; www.kineticsystems.com, cat. no. Model 2212), where micropositioners, scope and sample holder are mounted. Place the vibration-isolation tabletop onto a working table or bench. In

another SMOT system, we use a heavy marble table topped with a M6 tapped holes metal platform (Edmund Optics, Inc.; www.edmundoptics.com, cat. no. 55-251). Alternatively, other suitable anti-vibration table/tabletop can be used

SMOT system, software

Automated Scanning Electrode Technique (ASET) interface software, version LV4, LabView application (Science Wares, Inc.): entirely automates the SMOT system for data, metadata and imaging acquisition

SMOT system, microsensor

Needle-type oxygen-specific micro-optrode (NTH-PSt1-L2.5-TS-NS20/0.4-NOP or NTH-PSt1-L5-TS-NS40/0.8-NOP): for the latter, the most used, a stainless-steel needle of 40 mm length and 0.8 mm outer diameter houses the tapered glass optical fibre with a tip diameter of <50 µm (PreSens, GmbH, cat. no. 200000062 or 200000069, respectively). Alternatively, micro-optrodes can be manufactured in-house from pulled glass optical fibre with embedded fluorophore onto the tip as detailed elsewhere[43,45]

Additional equipment

LED cold light source (Genesee Scientific, Corp., cat. no. 59-500). Alternatively, an optical fibre ring illuminator or other light source, compatible with the research needs, can be used

Tabletop thermometer (RadioShack, Corp., cat. no. 63-1035)

Aquarium air pump and airstone, with silicon tubing connection

AC power line conditioner (Tripp Lite, cat. no. Model LC1800), with voltage regulation and surge protection, connected to local outlet

Power strip with switch, connected to the AC power line conditioner and to which all equipment is connected

Experimental measurements equipment

Personal protective equipment (lab coats, gloves, googles and masks), for the handling of and experimentation with harmful reagents/solutions

Plastic Pasteur pipette 5 ml (Globe Scientific, Inc., cat. nos. 137030 and 137018), for the sorting of oocytes and tadpoles, and for sample and media transfer

60 and 100 mm Petri dishes (Genesee Scientific, Corp., cat. nos. 32-105 and 32-107, respectively), for the sorting and manipulation of oocytes and tadpoles, and for the making of calibration, dissecting and measuring chambers

6 well non-treated plates (Genesee Scientific, Corp., cat. no. 25-100), for tadpoles incubation

Nylon mesh (800 μm pore size; Dynamic Aqua-Supply, Ltd, cat. no. NTX750)

Nickel-chromium wire

Epoxy resin (VWR, LLC, cat. no. 500043-451)

Glass pipette puller (Narishige, Inc., cat. no. PC-10)

Straight microelectrode holders (Warner Instruments, LLC, cat. no. QSW-A15P)

Borosilicate glass capillaries without filament (WPI, Inc., cat. no. TW150-4)

Glass beads (Sigma-Aldrich, Corp., cat. no. 18406)

2 mm biopsy punch (Miltex, Inc., cat. no. 33–31)

Scalpels (blade no. 10, Feather Safety Razor, Co.; blade no. 15, Henry Schein, Inc.)

Premier edge microsurgical knife (Oasis, Inc., cat. no. PE 3015-3)

Fine spring scissors (Fine Science Tools, Inc.)

Acrylic cube with opening lid

Silicon tubing and tubing adapters

N_2 flowmeter regulator

CO_2 pressure compensation flowmeter (Western Medica, cat. no. M1-940-12FM)

Magnetic stand (WPI, Inc., cat. no. Model 10), to hold the 3D manual micropositioner

3D manual micropositioner (WPI, Inc., cat. no. Model KITE-R), for the manipulation of the pulled glass pipette that wounds oocytes

Temperature control equipment (optional, depending on the experimental design): for example, temperature probes, heating pads, heated stages, temperature controllers, or even an enclosed environmental chamber. Temperature monitoring can be performed with the ASET software following the installation of an update

Dissecting microscope: for the sorting of oocytes and tadpoles, glass pipette preparation, wounding of oocytes, tadpole fin and rat eyes, and for the amputation of tadpole tails

Data analysis software

Excel (Office 2016; Microsoft, Corp.): for data analysis and visualization

Template Excel worksheet (Supplementary Data 1): for automated data analysis and visualization

ImageJ (v. 1.47u; National Institutes of Health; https://imagej.nih.gov/ij): for image visualization and treatment (set scale bars and measure sizes)

GIMP (v. 2.8.16; The GIMP Development Team; https://www.gimp.org): for image visualization and non-manipulative editing (recolour, resize and crop)

Prism (v. 5.02; GraphPad Software, Inc.; www.graphpad.com/scientific-software/prism): for inferential statistics

REAGENT SETUP

CRITICAL We routinely use the calibration solutions described below. The measuring solutions can be used instead of the standard dH_2O, because O_2 solubility is affected by salinity[68]. However, the media salinity levels used (as well as others routinely used in biological research) are very low to have any mensurable effect on flux calculations. If the measurement medium composition is unknown (*e.g.*, proprietary media) or if some components are known/suspected to chelate or otherwise affect ambient pO_2, it is advised to compare calibrations using such medium *vs.* standard dH_2O. In the case of a consistent significant difference, calibrate

the micro-optrode using the measurement medium. It is important to note that the calibration relies on anoxic and normoxic pO_2; therefore, solutions made either with dH_2O or medium must have those O_2 concentrations. To guarantee this, a pre-calibrated micro-optrode can be used to assess the pO_2 of the calibration solutions under test. Alternatively, the calibration solutions can be prepared as recommended in the instruction manual of the micro-optrode manufacturer.

Anoxic (pO_2 0%) calibration solution. Prepare the saturated reducing agent sodium bisulfite (mixture of $NaHSO_3$ and $Na_2S_2O_5$) 0.2 or 2 M in deionized water (dH_2O). The 0.2 and 2 M sodium bisulfite solutions remain anoxic for at least 6 months and 2 years, respectively, if properly stocked. **CAUTION** Use appropriate protective personal equipment for the making and handling of the sodium bisulfite solution. **CRITICAL** To avoid solution oxygenation over time, keep stock container tightly closed and with little to no air inside; however, surplus sodium bisulfite is an efficient anoxic buffer.

Alternative anoxic calibration solution. Anoxic solution may also be prepared by aerating ~20 ml of dH_2O for 30 min using an airstone connected to a compressed nitrogen gas cylinder ($N_2(g)$ 100%). If measuring solutions instead of dH_2O, use this procedure for the anoxic calibration of the micro-optrode. **CAUTION** Pressurized gas cylinder should be handled properly. **CRITICAL** Shorter aeration time might not generate a totally anoxic solution. Container can be a centrifuge tube (50 ml) or other with a narrow entry (*e.g.*, Erlenmeyer flask). **CRITICAL** Use the O_2-purged solution immediately after preparation. The solution cannot be stored because it oxygenates quickly; *e.g.*, in an open Petri dish (60 mm), pO_2 reaches ~1-4% at 5 min after aeration, ~15% at 10 min and already ~19-20% – almost complete reoxygenation – at 30 min.

Normoxic (pO_2 20.95%) calibration solution. Aerate ~20 ml of dH_2O for ~20 min using an airstone connected to an aquarium air pump. If measuring solutions instead of dH_2O, use this procedure for the normoxic calibration of the micro-optrode. **CRITICAL** Shorter aeration time might not generate a totally saturated solution. Container can be a centrifuge tube (50 ml) or other with a narrow entry (*e.g.*, Erlenmeyer flask). Agitate container or stir liquid <30 s to

preclude supersaturated solution. **CRITICAL** Use the air-saturated solution immediately after preparation. The solution cannot be stored because it will quickly reach a non-saturated equilibrium with local (container or environmental) atmosphere.

Experimental measurements solutions. Prepare a stock solution of MMR (oocytes and tadpoles media) 10× by mixing reagents in dH_2O for the following concentrations: NaCl 1 M, $CaCl_2 \cdot 2H_2O$ 20 mM, KCl 20 mM, $MgCl_2 \cdot 6H_2O$ 10 mM, and HEPES 50 mM. Adjust pH to 7.1–7.2 with NaOH 1 M (pellets dissolved in dH_2O). Sterilize by autoclaving and store at room temperature (21-23 °C). Prepare the working media of MMR 1× (oocytes) or 0.1× (tadpoles) by 1:10 and 1:100 dilutions in dH_2O, respectively.

Prepare a stock solution of BTS 50 mM (tadpoles immobilizing solution) in DMSO and store at −20 °C in aliquots. Prepare the working concentration of BTS 50 µM by 1:1000 dilution in MMR 0.1×.

Prepare a stock solution of H_2O_2 1 M in dH_2O and store at 4 °C. Prepare the working concentration of H_2O_2 1, 2 and 10 mM (O_2 efflux inducer) by dilution in MMR 1×.

Prepare PFA 4% (w/v) by mixing weighted powder in pre-heated PBS 1× (60 °C) and store at −20 °C in aliquots.

Prepare stocks for drugs 2,4-DNP (in DMSO), KCN and NaN_3 (in dH_2O) and store at −20 °C in aliquots. Prepare the working concentrations of 2,4-DNP 50 and 100 µM, KCN 1 mM, and NaN_3 2 mM by dilution in MMR 0.1×.

Prepare BSS+ (rat eye medium) by injecting the 20 ml of Part II vial into the 480 ml of Part I bottle, using the provided vacuum transfer device. Use within 6 h after preparation or store at 4 °C.

Prepare PBS 1× (mouse skin medium) by dissolving the tablets in dH_2O, Store at room temperature.

Micro-optrode cleaning and sterilization solutions. Prepare H_2O_2 3% (v/v) by a 1:10 dilution in dH_2O of the bulk reagent or prepare ethanol 75% (v/v) by dilution of bulk ethanol in dH_2O. These solutions are optional, prepared depending on the experimental design.

EQUIPMENT SETUP

SMOT system setup. Our SMOT system is schematized in **Fig. 1**. SMOT is a turn-key system available from Applicable Electronics, LLC (www.applicableelectronics.com), which also provide loose parts and technical (presential or remote) assistance. SMOT is entirely controlled and automatized by the ASET software available from Science Wares, Inc. (www.sciencewares.com) for sensor operation and for data, metadata and imaging acquisition. ASET fully operates the movement and activity of the micro-optrode acquired from PreSens, GmbH (www.presens.de). Of the two available sensor tip configurations, we acquired the tapered sensor tip, which best fulfils our research requirements and probably those of most physiological studies. Compared with the flat-broken sensor tip (diameter of 140 µm), the tapered sensor has higher spatial and temporal resolutions, but lower robustness and light stability (higher photobleaching) and higher signal drift. The spatial resolution of the SMOT system is dependent on the micro-optrode tip diameter, <50 µm. If required, the micro-optrode manufacturer (PreSens) might select probes with elevated spatial resolution. The temporal resolution of SMOT is dependent on the sampling rules (see **Box 3**), but can be up to 2 s. Importantly, SMOT can be integrated with other systems to allow simultaneous measurements (using multiple sensors) of disparate phenomena, including (but not limited to) electric currents, potentials (both membrane and transepithelial), ion fluxes, pH and hydrogen peroxide (H_2O_2). Some of these potentialities are expanded below. Indeed, Applicable Electronics offers the service to integrate most of these techniques within the same physical and digital environment. Moreover, ASET interface software can be readily programmed and customized to integrate such disparate data recordings.

Other companies that provide complete sensor systems, parts and accessories include (but are not limited to) PreSens, GmbH (www.presens.de/products/o2) and World Precision Instruments, Inc. (WPI; www.wpiinc.com/product-listers/oxygen-sensors). PreSens commercializes, in addition to the mentioned micro-optrode, the amplifier/meter (*e.g.*, Microx 4) and the interface software

(*e.g.*, Datamanager). WPI, Inc. commercializes the amplifier (*e.g.*, OxyMicro), the micro-optrode (*e.g.*, MicroTip) and the interface software (*e.g.*, OxyMicro Software). Younger USA, LLC (www.youngerusa.com) commercializes a turn-key microelectrode-based system (Non-invasive Micro-test Technology; *e.g.*, NMT100) with interface software (*e.g.*, Non-invasive Ion & Molecule Flux Measurement Software), to which a third-party micro-optrode can probably be integrated.

Calibration chambers. Unaltered 60 mm Petri dishes half-filled with the anoxic and normoxic solutions.

Dissecting/measuring chamber (oocytes). In-house made chamber consisting of a 60 mm Petri dish with a ~1 cm^2 nylon mesh glued with epoxy resin to the centre of dish bottom. The mesh holds still the oocytes during measurements and during the wounding using a pulled and tip broken glass pipette[24,69]. Half-filled with MMR 1× supplemented with different reagents (fixative or drugs) according to the experimental conditions.

Dissecting chambers (tadpoles). Unaltered 60 mm Petri dishes, for tadpole fin wounding and half tail amputation, using a 2 mm biopsy punch and a blade no. 10 scalpel, respectively. Half-filled with MMR 0.1× supplemented with BTS 50 μM for chemical immobilization[21,24].

Rodent euthanasia chamber. Acrylic cube with opening lid, connected with silicon tubing to a fixated $CO_2(g)$ cylinder attached with a flowmeter regulator. For rats and mice euthanasia (5-10 min), confirmed with cervical dislocation, according to local IACUC guidelines[70].

Dissecting bench (rodents). A 50×50 cm coated paper taped onto laboratory bench, for enucleation of rat eyes using fine spring scissors and mouse skin wounding using a blade no. 15 scalpel. Square surface is cleaned and sterilized with ethanol 75% (v/v) before and after procedures[70].

Measuring chamber (tadpoles). In-house made chamber consisting of a 60 mm Petri dish with a ~10×2 mm plastic strip onto a small plastic square (provides height to facilitate probe access) welded (with melting plastic) to the centre of dish bottom. The strip holds still the tadpole (chemically immobilized with BTS) during measurements. Half-filled with MMR 0.1× supplemented with BTS 50 µM for chemical immobilization and additional reagents (drugs) according to the experimental conditions[21,24].

Measuring chamber (rat eyes). In-house made chamber consisting of a 60 mm Petri dish with two wire loops glued with epoxy to the dish bottom. The wire loops end in small diameter circles (at the centre of dish) that hold still the eyeball during measurements and corneal wounding by scraping ~2 mm^2 of epithelium using a microsurgical knife. Half-filled with BSS+[70,71].

Measuring chamber (mice skin). Unaltered 100 mm Petri dish half-filled with PBS 1×.

Measuring chambers (all). We usually cut a piece of the 60 mm Petri dish edge to increase the degrees of freedom of the moving micro-optrode. If required, chamber can be sterilized, adapted and/or treated for microscopic or other experimental design specifications. Common examples include the replacement of the plastic bottom by a light-friendly glass patch, coating with fibronectin and sterilizing by ultraviolet light.

PROCEDURE

Micro-optrode calibration. TIMING 30 min

CRITICAL Calibration of the micro-optrode is done with a conventional two-point calibration of dissolved pO_2 0 and 20.95% (**Fig. 2a-c**). Calibrations should be bracket by the calibration values range provided in the manufacture's inspection sheet for the acquired micro-optrode. After extensive use, values may normally differ (see also **Step 27**). Alternatively, the calibration can be performed as recommended by the instruction manual or video tutorial of the micro-optrode manufacturer (www.presens.de/support-services/videos).

1| Set the experimental temperature into the ASET software. **CRITICAL STEP** Temperature affects O_2 diffusion[72] and is a parameter inserted in the equations to derive O_2 flux value (see **Box 4**). Moreover, the micro-optrode is temperature-sensitive; therefore, temperature during calibration should be the same as during measurements for data accuracy. **CRITICAL STEP** We typically verify and set the temperature every time at the beginning of calibration., because laboratory rooms commonly have a negligible temperature variation. For alternative amplifiers with built-in temperature compensation (temperature sensor to offset variation) this critical step is dispensed. **TROUBLESHOOTING**

2| Extend the micro-optrode from the housing needle by removing the protectives cap and blocker off the syringe and pushing the plunger. **CRITICAL STEP** To prevent breaking the sensing tip, first immerse the needle in dH_2O for 5-10 minutes before extending the micro-optrode. This is to dilute and wash away any possible salt crystals or other debris remaining inside the needle from previous use. **TROUBLESHOOTING**

3| Half-fill a Petri dish with the pO_2 0% (anoxic) calibration solution, immerse the micro-optrode (avoid immersing the needle) and wait 1 min for stabilization. Acquire the phase angle of the fluorescence signal using the 'Calibration' tab in ASET. **CRITICAL STEP** The micro-optrode is temperature-sensitive; ensure that the setup is calibrated using calibration solutions that are at the same temperature as the desired experimental temperature. **CRITICAL STEP** If intended measurements will be gaseous (in air) instead of dissolved pO_2 (in liquid), then calibrate in gaseous state ($N_2(g)$ 100% and atmospheric pO_2 20.95%) (also see **Box 2**). **TROUBLESHOOTING**

4| Discard solution and rinse micro-optrode with dH_2O. When using the sodium bisulfite 2 M, the solution can be saved into a new container for reuse. Do not reuse often (not more than 5-10 times), because the O_2 buffering capacity of the solution decreases with every new contact with atmospheric air (either by container opening or during the new calibration).

5| Repeat **Steps 3 and 4** for the pO_2 20.95% (normoxic) calibration solution. **TROUBLESHOOTING**

6| Save the calibration measurements. The two-point calibration curve and linear slope are automatically calculated and incorporated by the ASET software to instantaneously derive pO_2 values and gradients during measurements (see **Box 4**). **CRITICAL STEP** One-time calibration

is enough for at least a day of measurements. We made a performance proof, *i.e.*, we tested the calibration shift after a full day of measurements (for the case, 12 recordings of ~30 min each; discontinuous sensor illumination or flashing). Phase angle shift before and after measurements was −0.02 ° for pO_2 0% and −0.3 ° for pO_2 20.95%. These differences are negligible; therefore, we usually calibrate every new day of measurements to promote repeatability and reproducibility. The manufacturer recommends recalibration after 8 h continuous sensor illumination or more than 18,000 data points. If the micro-optrode is replaced, a new calibration is required.

Micro-optrode validation. TIMING 1.5 h

CRITICAL We recommend validating the micro-optrode with a conventional artificial sink, N_2(*g*) 100% (**Fig. 2d,e**). We further validate using a natural sink (tadpole gills; **Fig. 2f,g**) and an induced natural source (H_2O_2-induced in oocytes; **Fig. 2d**). Note that purchased micro-optrodes are validated by default by the manufacturing companies, these steps being just a supplementary verification of the micro-optrode efficiency in the in-house system to promote repeatability and reproducibility.

7| Due to the large O_2 gradient generated by the artificial sink, this also permits to attest for a large signal-to-noise ratio and to determine the extracellular diffusion limit of O_2 and therefore define the microenvironment in which physiological activities might happen (typically <1 mm; **Fig. 2b-g**).

8| Heat pull a glass capillary using the puller and gently break the tip to increase its diameter (>50 µm).

9| Connect the N_2(*g*) 100% cylinder to the capillary using silicone tubing and tubing adapters.

10| Mount the artificial sink capillary in a microelectrode holder attached to a micropositioner.

11| Immerse the micro-optrode and artificial sink capillary in a Petri dish filled with dH_2O.

12| Open the gas cylinder to pressurize the capillary until a N_2 bubble is formed in its tip. Let the sink gradient from bubble stabilize for at least 5 min. **TROUBLESHOOTING**

13| Record (details below) and plot fluxes as a function of the distance (**Fig. 2e**). Theoretically, the anoxic sink generates a local chemical gradient driving O_2 influx. Empirically, if the sensor measures, in its excursion, lower O_2 concentration near the bubble than far, and if the difference is a net influx, then the micro-optrode is validated for its ability and efficiency to correctly detect the magnitude and direction of O_2 fluxes. **PAUSE POINT** One-time validation is enough for each micro-optrode.

Data acquisition setup. TIMING 1-3 h

14| Define the sampling rules for data acquisition in ASET, according to target specimen (see **Box 3** for a detailed description of the different sampling rules).

Experimental measurements. TIMING 1 h

15| Prepare the biological specimen according to the experimental condition (fixate and wound oocytes and tadpoles, amputate tadpole tails, enucleate rat eyes and wound mouse skin) and immobilize sample in the specimen-specific, in-house made, measuring chamber[21,24,69,70]. Immobilization (physical and/or chemical) should not compromise normal physiological activity and should grant free access and sufficient degrees of freedom to the moving micro-optrode.

16| Let the specimen equilibrate to the desired temperature, in case temperature-control is used. In our studies, the measurements are performed at room temperature; however, temperature can be set and monitored using widespread equipment (*e.g.*, heating pads, heated stages, temperature controllers or enclosed environmental chamber), according to sample, model and/or research needs. Such equipment can be integrated into the SMOT rig system that also allows the connection of a temperature probe. The ASET software can be updated to monitor temperature during experiment. **CRITICAL STEP** The temperature used for the experimental conditions should be the same as during calibration (**Steps 1-3**).

17| Place the sample under the zoom scope, focus the camera on the region of interest (ROI) of the specimen and carefully immerse the micro-optrode in the chamber away from the specimen (>>1 mm) for reference (also known as blank, buffer or background) measurements. **CRITICAL STEP** The results of many artificial and natural sources and sinks demonstrate that 1 mm

perpendicular to the sample is usually a safe distance where gradients are resolved (**Fig. 2e,g**). Sometimes, owing to the geometry of the specimen, a longer perpendicular distance might be required. For that reason, we set our reference position to >>1 mm (typically ~5 mm). **TROUBLESHOOTING**

18| Let medium stabilize for ~1 min. Optionally, press the 'Baseline' button in the 'Chart' tab of ASET to offset ("zerify") any residual gradient. **CRITICAL STEP** Medium in the chamber must be still (without ripples) to prevent noise and the dissipation of extracellular gradients. An anti-vibration table mitigates mechanical vibrations. To guarantee mechanical isolation, ensure that the rig is not touching the walls of the room and avoid proximity with freezers or other vibration-producing equipment. To guarantee airflow isolation, avoid proximity with air conditioner exit and hoods. If avoidance of airflows is not possible, isolate (cover) the measuring rig. Even the slightest vibration might move light samples in the microscale, increasing noise and therefore time to reach a stable reference signal.

19| Start recording (the probe starts vibrating) at the reference position using the 'Chart' tab of ASET. Record at the reference position until a stable plateau is reached. Usually, 10 data points or up to 2 min of recording are enough. Alternatively, press 'Reference' button in ASET to save a one-time reference value that will be automatically subtracted to each specimen gradient value; this will save time in post-acquisition analysis, but provides a less accurate baseline value (see **Box 4**). **TROUBLESHOOTING**

20| Stop recording (the probe stops vibrating) and move the micro-optrode near to the specimen and focus it in the *z* plane with the target ROI. With default settings, the velocity of the ASET-controlled microstepping does not cause meaningful medium disturbance. If settings are changed and/or disturbance occurs, let medium re-stabilize. **TROUBLESHOOTING**

21| Position the micro-optrode ~10 µm away from and perpendicularly to the ROI surface, using the ASET-controlled microstepping. **CAUTION** The micro-optrode tip is fragile, thus, when near the specimens, move sensor with caution and in small steps to avoid damaging or breaking the tip. Although fragile, for soft specimens (*e.g.*, soft tissues), the micro-optrode tip is robust enough to withstand touching them and can even penetrate the samples without breaking. **CRITICAL STEP** To obtain the most accurate data and to maximize the signal recorded, especially in weak gradients, the micro-optrode should be positioned as close as possible and

Data analysis. TIMING 15 min

28| Extract the raw data from the ASET program and analyse it using Excel. We use an in-house developed worksheet template (Excel file), pre-loaded with automatic formulas and plots in series, to calculate and visualize O_2 percentages, concentrations and fluxes in around 1 min in few steps (available as Supplementary Data 1). See **Box 4** for a detailed description of the data analysis procedure.

29| Perform statistical analysis as appropriate. *E.g.*, paired Student's *t* test to quantitatively compare different experimental conditions. The statistical analysis used in this Protocol is detailed in the figure captions.

BOX 4 | STEPWISE FLUX CALCULATIONS

For each new experiment, the ASET program creates, by default, two comma-separated values files (.cvs) compatible with Excel: one stores exclusively raw data, and the other stores metadata (such as calibration details and imaging times) and annotations (log entries). Both files are saved automatically and continuously until the end of the experiment. Using the calibration and phase angle shift of acquired data, the ASET software automatically calculates and saves raw data as percent pO_2 (see **Box 1**). The data and information from the program files are then extracted to an in-house developed worksheet template (Excel file), pre-loaded with automatic formulas and plots in series, to calculate and visualize O_2 percentages, concentr

where $[O_2]$ is the oxygen concentration (μM); p_{atm} is the atmospheric pressure (1013.25 mbar at sea level); $p_W(T)$ is the vapor pressure of water (26.507 mbar at 22 °C (mean room temperature)); p_N is the standard atmospheric pressure (1013.25 mbar); $\frac{2}{\frac{0.2095}{100}}$ is ratio of O_2 in the gas mixture (referred elsewhere[45] as Q); 0.2095 is the volume content of oxygen in air; $\alpha(T)$ is the Bunsen absorption coefficient (29.908 $cm^3(O_2)$ cm^{-3} at 22 °C) and V_M is the molar volume (22.414 l mol^{-1}). The temperature-dependent parameters $p_W(T)$ and $\alpha(T)$ are calculated/obtained using standard curves/tables consulted in the micro-optrode manufacturer's instruction manual. If the temperature changes, these parameters require update.

The $[O_2]$ is then converted to pmol cm^{-3} by a net 1000 factor multiplication and included in the Fick's first law to calculate the fluxes:

$$_2 (\quad\quad\quad\quad^{-2}\ ^{-1}) = - \quad \times \frac{}{}^2, \quad (5)$$

where J_{O_2} is the oxygen flux (pmol cm^{-2} s^{-1}); D is the diffusion coefficient of dissolved O_2 (2.42×10^{-5} cm^2 s^{-1} at 25 °C[79]); δO_2 is the concentration difference (pmol cm^{-3}) and δx is the excursion (0.003 cm).

The analysed data is now in flux units. Reference is averaged and subtracted to each specimen flux data point. Finally, specimen flux is averaged to provide a single flux value per sampling locus (ROI). Negative values mean net influx (O_2 entering the animal tissue) and positive values mean net efflux (O_2 exiting the animal tissue).

TIMING

Steps 1-6, micro-optrode calibration: 30 min (one-time per day of measurements), plus one-time 15 min to make the pO_2 0% solution

Steps 7-13, micro-optrode validation: 1.5 h (one-time per micro-optrode) for the N_2 artificial sink

Step 14, data acquisition setup: 5 min for ASET software setup. Sampling rules optimization (see **Box 3**) requires preliminary data acquisition to test the rules, thus timing is dependent on experimental design. It took us 1 h to optimize sampling rules using amputated tadpoles, which became 3 h because of the use of multiple biological replicates

Steps 15-27, experimental measurements: 30 min (one-time) for the making of the dissecting and measurement chambers; 5-45 min for sample preparation, depending on specimen and condition; measurements timing is dependent on the experimental design. *E.g.*, for gills measurements (single ROI), 7 min per tadpole, and for wounded cornea profile (multiple ROI: wound edges, centre and sides), 30 min per eye

Steps 28,29, data analysis: 1-2 h (one-time) for template Excel worksheet (preconfigure and format multiple sheets with instructions, formulas and plots); <10 s per raw data file for extraction of data into the worksheet (copy and paste); 1 min per raw data file for flux calculation and visualization; 1-5 min for ROI selection, outliers removal (*e.g.*, noise prior to signal stabilization, transient spikes, *etc.*) and mean calculation, according the number of ROI and trace noise; and 5-10 min for statistical analysis

TROUBLESHOOTING

Troubleshooting assistance can be found in **Table 2**.

TABLE 2 | Troubleshooting table.

Step	Problem	Possible reason	Solution
1	Too disparate signal in same day/same sample conditions	Temperature change or fluctuation	Recalibrate micro-optrode at the different temperature; dial new temperature at calibration into ASET software
2	No signal	The sensor tip is broken	Acquire a new sensor or pull and re-coat used sensor with fluorophore[43,45]. Avoid salt crystallization or trapped debris inside needle by careful rinsing with dH_2O after use
3	Low calibration phase angle for pO_2 0%	The calibration solution has been exposed to air	Make new pO_2 0% solution and minimize air exposure time and keep stock container tightly closed
5	High calibration phase angle for pO_2 20.95%	Unsaturated calibration solution	Aerate for no less than 20 min
12	N_2 continuous bubbling	Opening of the capillary is too large or flowmeter allows too much pressure to reach the capillary	Make a new capillary with smaller tip diameter or reduce the pressure in the flowmeter
17	Ripples in the medium	Manual zooming generating mechanical vibrations in the system	Ensure to use automatic ASET-controlled zooming (*w* motor microstepping) that prevent mechanical vibrations. If using alternative scopes, also try to use automatic zooming (*e.g.*, via joystick)

19	Unstable reference	The optrode was too close to the sample	Increase distance to at least ≥0.5 mm
20	Unstable signal and/or high noise	The medium and/or sample was disturbed	Allow stabilization (~1 min) of the medium. Move or isolate SMOT system rig from mechanical vibrations and airflow
22	Compromised sample/experiment	Soft tissue disruption by micro-optrode touching or micro-optrode is broken	Prepare a new sample or acquire a new micro-optrode. When close to the sample, reduce motor microstepping to 5-20 µm/step to prevent accidental sample disruption or sensor tip breakage
24	Reference values take more time than usual to return to original baseline	Disturbed media and/or dirty sensor tip with attached debris of the sample	Allow stabilization (~1 min) of the medium. Gently pipette medium at sensor tip to remove debris from fluorophore; allow re-stabilization. After experiment rinse with dH_2O and wash with liquid soap if required. Often, however, even a dirty tip yields reliable data, because of the robust fluorescence quenching-based sensing mechanism
27	Micro-optrode do not retract	Salt crystallization or otherwise dirty housing needle blocks retraction	Do no force plunger; it may lead to tip breaking. Immerge needle in dH_2O for 5-10 min to dissolve and/or drain debris inside needle

ANTICIPATED RESULTS

For a holistic overview of the micro-optrode capabilities and potentialities in animal physiology, we followed a multi-level analysis – from cellular to appendage levels –, in disparate animal models – from lower to higher vertebrates –, recording various physiological responses.

A *de novo* mounted turn-key SMOT system (**Fig. 1**) ought to be validated. The micro-optrode full operationally is a proxy validation of the entire setup (**Fig. 2**). Using an artificial sink ($N_2(g)$ bubble at capillary tip), a natural sink (tadpole gills), and a natural source (H_2O_2-iduced O_2 efflux in oocytes) we validated the micro-optrode as per O_2 flux direction and magnitude efficient detection. The O_2 influx decreases as the micro-optrode moves away the sink (**Fig. 2d-f**),

Figure 4 | Multi-level oxygen flux as a marker for physiological status and viability. Measurement of endogenous oxygen fluxes in control and fixated (PFA 4% overnight) *X. laevis* oocytes (cell level) (**a**-**c**), tadpole epithelium (tissue level) (**d**-**f**) and tadpole gill (organ level) (**g**-**i**). (**a,d,g**) Experimental design. Measurements were acquired in MMR 1× (oocytes) or 0.1× (tadpoles; applies to subsequent figures). Gill measurements were from the middle gill of left axis (white *). Tadpole drawing (lateral view) is displayed in the same orientation as the whole organism A/P, D/V and L/R axes (bottom right scheme; applies to subsequent figures). Scale bars: ~0.5 mm in **a** and **d**, and ~100 µm in **g**. (**b,e,h**) Representative results. Top plots: control; bottom plots: fixated. *y* axis titles in **b** plot also applies to **e** and **h** plots. *x* axis title in bottom plots also applies to top plots. (**c,f,i**) Distributions and statistics. *y* axis titles in **c** plot also applies to **f** and **i** plots. Data are presented using dot plots with mean lines. Statistical comparisons were performed using the unpaired Student's *t* test (two-tailed *p* value). NS, non-significant; **, $p<0.01$; ***, $p<0.001$. *n* biological replicates indicated in brackets. All procedures involving animals were approved by the relevant Institutional and National regulatory boards.

After validating the technique, we started to apply the micro-optrode (in single mode) as a way to verify the physiological integrity and viability of specimens (**Fig. 4**). To achieve this, we performed PFA-based fixation of specimens and measure O_2 fluxes at cell (oocytes; **Fig. 4a,b**), tissue (tadpole epithelium; **Fig. 4d,e**) and organ (tadpole gill; **Fig. 4g,h**) levels. Compared against viable specimens, the fixation vanished the fluxes ($p<0.01$) that became identical to reference baseline ($p>0.05$; **Fig. 4c,f,i**).

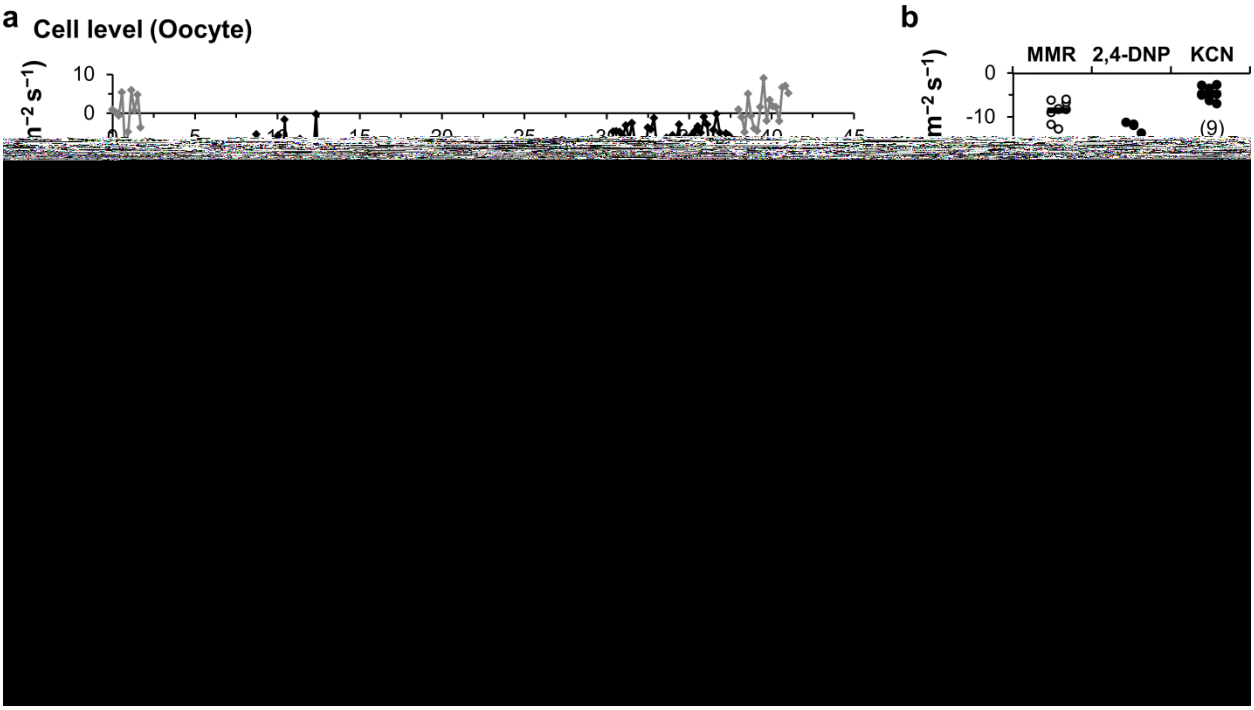

Finally, we show comprehensive results of the O_2 dynamics in wound healing and regeneration (**Fig. 7**), extracted mainly from the original data recently published[24]. We performed wounds from cellular to organ level, respectively, in oocytes (**Fig. 7a**), tadpole epithelium (**Fig. 7d**), rat cornea (**Fig. 7g**) and mouse skin (**Fig. 7j**), and measured the effect on O_2 influx magnitude. Also, we amputated half of tadpole tails (appendage level; **Fig. 7m**) to demonstrate a concomitant shift in O_2 fluxes. Interestingly, wounding or amputation resulted in a sustained increased of O_2 influx in cell (p<0.001; **Fig. 7b,c**), tissue (p<0.05; **Fig. 7e,f**), organ (p<0.05; **Fig. 7k,l**) and appendage (p<0.05; **Fig. 7n,o**) levels. Exception was in the corneal wounding where influx decreased instead (p<0.05; **Fig. 7h,i**). We showed that the elevated influx is caused by barrier breaking and to fuel ROS production, important for healing and regeneration[24]. In the case of rat cornea, the lower magnitude is probably due to the virtual absence of epithelial cells (scrapped off until stroma); we are following up this line of research in a new study.

BOX 5 | OSCILLATORY BEHAVIOUR

Oxygen is a major player in metabolic and signalling pathways; therefore, it might display or be subjected to oscillatory behaviour[74–76]. Intriguingly, we noticed that in many recordings the O_2 flux appears to stabilize in an oscillatory rather than in a flat plateau. Oscillations with a frequency (f) range of 4-8 mHz (2-4 min period (T; peak-to-peak time)) were not uncommon (right, representative result of a wounded tadpole epithelium). Owing to our research goals, we usually acquired data in the same sampling locus (ROI) for 2-5 min. Thus, we could not robustly study oscillations and definitively identify false positive and false negative readouts[24]. However, with an increase in recording time, this technique is perfectly suitable to study oscillations.

Intriguingly, many recordings, in the different animal models used, appear to present oscillations in the O_2 fluxes (see **Box 5**). The oscillatory behaviour may be the result or an epiphenomenon of the O_2 key role in bioenergetics and metabolism (*e.g.*, mitochondrial activity), and signalling pathways (*e.g.*, Ca^{2+})[47,74–76]. Future studies using this technique directed to research O_2 flux

oscillations may uncover fundamental aspects of the cell and oxic biology. Furthermore, the technique may become part of the life sciences toolkit to assist researchers in their findings.

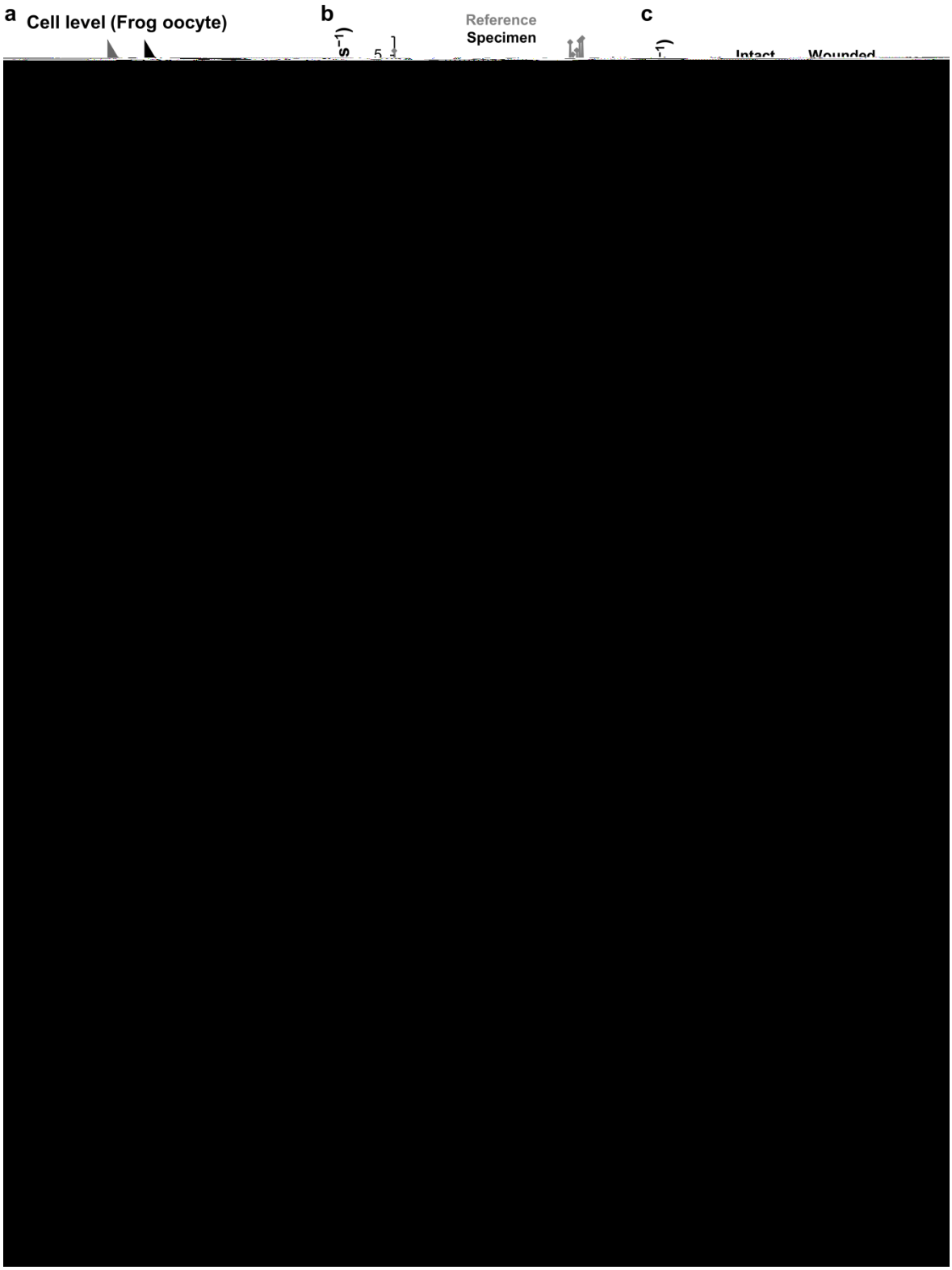

Figure 7 | Multi-level oxygen flux in wound healing and regeneration. Measurement of endogenous oxygen fluxes in intact and wounded or amputated *X. laevis* oocytes (cell level) (**a**-**c**)**,** tadpole epithelium (tissue level) (**d**-**f**), rat corneal epithelium (tissue level) (**g**-**i**), mouse skin (organ level) (**j**-**l**) and tadpole tail (appendage level) (**m**-**o**). (**a,d,g,j,m**) Experimental design. Measurements were acquired in artificial tear solution (BSS+; rat cornea) or phosphate buffered saline (PBS 1×; mouse skin). For the measurements we used isolated whole eyes enucleated from euthanized 7-8 weeks-old male Sprague-Dawley rats and euthanized 8 week-old male BKS.Cg-*Dock7*^{m} +/+ *Lepr*^{db}/J heterozygous (non-diabetic) mice. Eye photomicrograph and scheme (lateral view) are displayed in the temporal (T) to nasal (N) axis orientation. e: edge; c: centre; s: side. Mouse photomicrograph and scheme (top view) are displayed in the same orientation as the whole organism A/P, D/V and L/R axes (bottom right scheme). Scale bars: ~0.5 mm in **a** and **d**, and ~1 mm in **g**, **j** and **m**. (**b,e,h,k,n**) Representative results. Wounding and amputation times annotated. (**c,f,i,l,o**) Distributions and statistics. Data of **c**, **f**, **l** and **o** were originally published in[24]; complete spatiotemporal profiling of **f** and **o** can be found in the same study. Data are presented using dot plots with mean lines. Statistical comparisons were performed using the paired Student's *t* test (two-tailed *p* value for oocytes and one-tailed *p* value for mice) and unpaired Student's *t* test (one-tailed *p* value for rat). NS, non-significant; *, $p<0.05$; **, $p<0.01$. *n* biological replicates indicated in brackets. All procedures involving animals were approved by the relevant Institutional and National regulatory boards.

In conclusion, we describe here a powerful research tool – optic-based measurement of oxygen dynamics – with high sensitivity, and temporal and spatial resolutions, which investigators can use without excessive expenditure and training.

REPORTING SUMMARY

Additional information on the experimental design is available in the Nature Research Reporting Summary linked to this article.

DATA AVAILABILITY

The (structured and representative) data that support and use the approach are embedded in this protocol. Extended data are available in the support research paper[24]. In addition, other relevant data (discrete and numerical) are available from the corresponding authors upon reasonable request.

AUTHOR CONTRIBUTIONS STATEMENTS

F.F. designed and optimized the protocol. G.L. provided training in the oocyte wounding. B.R. provided the intact and wounded rat eyes. L.M. executed some experiments. F.F. performed the physiological measurements and analysed the data. M.Z. provided the funds for experiments and manuscript. All authors contributed to the scientific discussions and study design as appropriate. F.F. wrote the manuscript. B.R., VK.R. and M.Z. edited the manuscript. All authors read, commented and accepted the final manuscript.

ACKNOWLEDGMENTS

We apologize to all the studies that were not mentioned by space or context limitations. This work was supported by two NIH (EY019101 and R21EB015737), an AFOSR (FA9550-16-1-0052) and, in part, by an Unrestricted Grant from Research to Prevent Blindness, Inc., University of California (UC), Davis, Ophthalmology. F.F. was supported by Fundação para a Ciência e Tecnologia (FCT) grant SFRH/BD/87256/2012. We thank Dr. Andreia Gomes (Departamento de Biologia, CBMA, Universidade do Minho, Portugal) for support. We are grateful to Prof. Andrew L. Miller (Department of Biology, Hong Kong University of Science and Technology, China), Dr. Marko Horb (Director of the NXR, MBL) and Dr. Esther Pearl (NXR, MBL), and Mr. Alan M. Shipley (Applicable Electronics, LLC) for generously hosting F.F.'s visit to MBL (Summer season 2014), for help in providing access to local research facilities and materials (SMOT and tadpoles (NXR RRID: SCR_013731) included), and for helpful comments. We are also grateful to Mr. Christopher A. Shipley, owner of Applicable Electronics, LLC, for having the courtesy to loan a SMOT system to the Zhao lab. Special thanks to Mr. Eric Karplus (Science Wares, Inc.), designer and programmer of the SMOT, for providing software, technical assistance and support for its efficient installation and operation. We appreciate the input given by Mr. Alan M. Shipley and Mr. Eric Karplus to establish an efficient protocol in the Zhao lab. We are further thankful to Mr. Eric Karplus for helping with the mathematics and interpretation behind the equations used to calculate O_2 flux. We are grateful to Dr. Yawei Yu (Department of Molecular & Cell Biology, UC Berkeley) for generously providing glass beads and for helpful discussion. We appreciate the technical information about micro-optrodes provided by Ms. Sandra Kerschensteiner and Dr. Christian Huber (PreSens, GmbH). We thank Dr. Yunyun Shen (Department of Dermatology, UC Davis; Department of Occupational and Environmental Health, Zhejiang University, China) for kindly dispensing the euthanized mice. We thank Zhao lab members for helpful discussions.

COMPETING INTERESTS STATEMENT

The authors F.F. and M.Z. declare the existence of a non-financial competing interest. The measurements were performed using turn-key systems provided free for use at MBL and loaned to the Zhao lab at no cost, by Applicable Electronics, LLC and Science Wares, Inc. The companies had no influence over the research (design, execution and interpretation), or its reporting; no restrictions on data sharing have been imposed. The other authors declare no competing interests.

US, 2006). doi:10.1007/978-0-387-46312-4_8
32. Wang, X. & Wolfbeis, O. S. Optical methods for sensing and imaging oxygen: materials, spectroscopies and applications. *Chem. Soc. Rev.* **43**, 3666–3761 (2014).
33. Kautsky, H. & Hirsch, A. Interactions of excited dye molecules and oxygen. *Ber Dtsch Chem Ges.* **64**, 2677–2686 (1931).
34. Lübbers, D. W. & Opitz, N. The pCO2/pO2-optode: a new probe for measurement of pCO2 or pO2 in fluids and gases. *Zeitschrift fur Naturforschung. Sect. C, Biosci.* **30**, 532–533 (1975).
35. Wolfbeis, O. S. & Weidgans, B. M. Fiber optic chemical sensors and biosensors: a view back. in *Optical Chemical Sensors. NATO Science Series II: Mathematics, Physics and Chemistry* (eds. Baldini, F., Chester, A., Homola, J. & Martellucci, S.) 17–44 (Springer, Dordrecht, 2006). doi:10.1007/1-4020-4611

Death Dis. **8**, e2853 (2017).
57. Land, S. C., Porterfield, D. M., Sanger, R. H. & Smith, P. J. The self-referencing oxygen-selective microelectrode: detection of transmembrane oxygen flux from single cells. *J. Exp. Biol.* **202**, 211–8 (1999).
58. Lamboursain, L., St-Onge, F. & Jolicoeur, M. A Lab-Built Respirometer for Plant and Animal Cell Culture. *Biotechnol. Prog.* **18**, 1377–1386 (2002).
59. Severinghaus, J. W. The Invention and Development of Blood Gas Analysis. *Anesthesiology* **97**, 253–256 (2002).
60. Xiong, L. & Compton, R. G. Amperometric gas detection: A review. *Int. J. Electrochem. Sci.* **9**, 7152–7181 (2014).
61. Kühtreiber, W. M. & Jaffe, L. F. Detection of Extracellular Calcium Gradients with a Calcium-specific Vibrating Electrode digital version can attain a noise level of less than. *J. Cell Biol.* **110**, 1565–1573 (1990).
62. Jaffe, L. F. & Nuccitelli, R. An ultrasensitive vibrating probe for measuring steady extracellular currents. *J. Cell Biol.* **63**, 614–628 (1974).
63. Kunkel, J. G., Cordeiro, S., Xu, Y. J., Shipley, A. M. & José, A. The use of non-invasive ion-selective microelectrode techniques for the study of plant development. in *Plant Electrophysiology* 109–137 (2006). doi:10.1007/978-3-540-37843-3_5
64. Zisman, W. A. A new method of measuring contact potential differences in metals. *Rev. Sci. Instrum.* **3**, 367–370 (1932).
65. Porterfield, D. M. Measuring metabolism and biophysical flux in the tissue, cellular and sub-cellular domains: recent developments in self-referencing amperometry for physiological sensing. *Biosens. Bioelectron.* **22**, 1186–96 (2007).
66. Taryba, M. G., Montemor, M. F. & Lamaka, S. V. Quasi-simultaneous Mapping of Local Current Density, pH and Dissolved O2. *Electroanalysis* **27**, 2725–2730 (2015).
67. Chu, C.-S. & Su, C.-J. Optical fiber sensor for dual sensing of H2O2 and DO based on CdSe/ZnS QDs and Ru(dpp)32+ embedded in EC matrix. *Sensors Actuators B Chem.* **255**, 1079–1086 (2018).
68. Jamnongwong, M., Loubiere, K., Dietrich, N. & Hébrard, G. Experimental study of oxygen diffusion coefficients in clean water containing salt, glucose or surfactant: Consequences on the liquid-side mass transfer coefficients. *Chem. Eng. J.* **165**, 758–768 (2010).
69. Luxardi, G., Reid, B., Ferreira, F., Maillard, P. & Zhao, M. Measurement of extracellular ion fluxes using the ion-selective self-referencing microelectrode technique. *J. Vis. Exp.* e52782 (2015). doi:10.3791/52782
70. Shen, Y. *et al.* Diabetic Cornea Wounds Produce Significantly Weaker Electric Signals That May Contribute To Impaired Healing. *Sci. Rep.* **6**, 1–11 (2016).
71. Reid, B., Nuccitelli, R. & Zhao, M. Non-invasive measurement of bioelectric currents with a vibrating probe. *Nat. Protoc.* **2**, 661–9 (2007).
72. Han, P. & Bartels, D. M. Temperature Dependence of Oxygen Diffusion in H2O and D2O. *J. Phys. Chem.* **100**, 5597–5602 (1996).
73. Lopes, A. S., Lane, M. & Thompson, J. G. Oxygen consumption and ROS production are increased at the time of fertilization and cell cleavage in bovine zygotes. *Hum. Reprod.* **25**, 2762–2773 (2010).
74. Stringari, C. *et al.* In Vivo Single-Cell Detection of Metabolic Oscillations in Stem Cells. *Cell Rep.* **10**, 1–7 (2015).
75. Cai, H. *et al.* Nucleocytoplasmic Shuttling of a GATA Transcription Factor Functions as a Development Timer. *Science (80-.).* **343**, 1249531 (2014).
76. Feijó, J. A. *et al.* Cellular oscillations and the regulation of growth: The pollen tube paradigm. *BioEssays* **23**, 86–94 (2001).
77. Lakowicz, J. R. Frequency-Domain Lifetime Measurements. in *Principles of Fluorescence Spectroscopy* 157–204 (Springer US, 2006). doi:10.1016/0925-4005(96)80051-7
78. Demas, J. N., DeGraff, B. A. & Xu, W. Modeling of Luminescence Quenching-Based Sensors: Comparison of Multisite and Nonlinear Gas Solubility Models. *Anal. Chem.* **67**, 1377–1380 (2005).
79. Lide, D. R. *CRC Handbook of Chemistry and Physics*. *CRC Press* (2005). doi:978-1466571143

The results published show an orchestration between bioelectric and redox activities during regeneration, which can be harvested to induce regeneration in non-regenerative conditions.

7.2 Publication contributions

From publication's equivalent section: "F.F. and M.Z. conceived the study. F.F., G.L. and M.Z. designed the experiments. F.F. performed the experiments and analysed the results. G.L. and B.R. provided

2016. Published by The Company of Biologists Ltd Development (2016) 143, 4582-4594 doi:10.1242/dev.142034

Early bioelectric activities mediate redox-modulated regeneration

Fernando Ferreira[1,2,*], Guillaume Luxardi[1], Brian Reid[1] and Min Zhao[1,3,*]

ABSTRACT

Reactive oxygen species (ROS) and electric current modulate regeneration; however, the interplay between biochemical and biophysical signals during regeneration remains poorly understood. We investigate the interaction between redox and bioelectric activities during tail regeneration in *Xenopus laevis* tadpole. We show that inhibition of NADPH oxidase-mediated production of ROS, or cancelling or blocking their diffusion into cells, impairs regeneration and controls the membrane potential, transepithelial potential (TEP) and electric current density (J_I) during regeneration. Depletion of ROS mimics the altered TEP and J_I observed in the non-regenerative refractory period. Short-term application of hydrogen peroxide (H_2O_2) rescues (from depleted ROS) and induces (from the refractory period) regeneration, TEP increase and J_I reversal. H_2O_2 is therefore necessary and sufficient to induce regeneration and to regulate TEP and J_I. Epistasis analysis shows that voltage-gated Na^+ channel acts downstream of H_2O_2 to modulate regeneration. Altogether, these results suggest a novel mechanism for regeneration via redox-bioelectric orchestration.

KEY WORDS: NADPH oxidases, Reactive oxygen species, Membrane potential, Transepithelial potential, Electric current density, Voltage-gated Na^+ channels, Regeneration, ***Xenopus laevis***

INTRODUCTION

Understanding large-scale repair via regeneration is a fundamental issue in basic biology and regenerative medicine. Biochemical signals, such as Wnt and BMP pathways, have been extensively studied and have been shown to control regeneration (Alvarado and Tsonis, 2006; Stoick-Cooper et al., 2007). Reactive oxygen species (ROS), especially hydrogen peroxide (H_2O_2), are suggested to act as signaling cues in the wound microenvironment (Sen and Roy, 2008; Veal et al., 2007). Upon wounding, the *Drosophila* embryo (Moreira et al., 2010), zebrafish larva (Niethammer et al., 2009) and *Xenopus* tadpole (Love et al., 2013) produce a H_2O_2 gradient that precedes the oxidative burst. This gradient, in fact, attracts immune cells toward the wound edges. In addition, a redox sensor has been identified in the leading edge of neutrophils (Wittmann et al., 2012; Yoo et al., 2011, 2012) and topical application of low doses of H_2O_2 enhances wound closure in mice (Loo et al., 2012). Importantly, ROS are required for the regeneration of planarian head and tail (Pirotte et al., 2015), zebrafish caudal fin (Gauron et al., 2013) and heart (Han et al., 2014), *Xenopus* tadpole tail (Love et al., 2013), and gecko tail (Zhang et al., 2016).

In addition to ROS, biophysical signals such as the dynamic bioelectric activities measured during regeneration have been proposed to act as signaling cues (Levin, 2007; McCaig et al., 2005). It has been shown that transepithelial potential (TEP)-driven electric current densities (J_I) correlate with and are required for regeneration in amphibians (Borgens et al., 1977b; Jenkins et al., 1996; Nawata, 2001; Reid et al., 2009). Electrical stimulation induces some regeneration in non-permissive adult frog and rat limbs (Becker, 1972; Borgens et al., 1977a; Leppik et al., 2015; Smith, 1967). Moreover, engineered devices (Golding et al., 2016) partially induce mouse digit tip regeneration (Hechavarria et al., 2010) and are in clinical trials to improve paraplegia (Shapiro et al., 2005). Re-emerging bioelectric studies are revealing transduction mechanisms. V-ATPase-mediated repolarization of membrane potential (V_m) and voltage-gated Na^+ channel (VGSC or Na_V) 1.2-mediated sodium influx are necessary for and sufficient to induce *X. laevis* tadpole tail regeneration (Adams et al., 2007; Tseng et al., 2010). V-ATPase proton efflux activity correlates with regeneration rate and ability in zebrafish caudal fin regeneration (Monteiro et al., 2014). H^+/K^+-ATPase-mediated V_m depolarization modulates planarian head regeneration (Beane et al., 2011). In addition, ion and V_m dynamics correlate with axolotl larvae tail regeneration (Özkucur et al., 2010).

Interestingly, redox and bioelectric activities control the expression and activity of signaling pathways, such as Wnt, FGF, BMP and Notch, in addition to cell behaviors, such as proliferation, apoptosis and innervation, which are required for regeneration (Adams et al., 2007; Gauron et al., 2013; Han et al., 2014; Love et al., 2013; Monteiro et al., 2014; Tseng et al., 2010). Redox (ROS) and bioelectric [V_m, TEP, electric fields (EF) and J_I] states therefore affect regeneration. But how do these signals integrate? Do they act in parallel or in series during regeneration? *Xenopus laevis* tadpole tail regeneration provides an ideal model with which to address these questions (Love et al., 2013; Reid et al., 2009). The tail comprises epidermis, muscle, blood vessels and spinal cord, making it a prime model for biomedical research (Beck et al., 2009; Deuchar, 1975). In addition, the fluctuating regenerative abilities of tails through developmental stages offer unique opportunities to study regeneration-deficient tails, in the refractory period (Beck et al., 2003), using the same model organism.

RESULTS

Do ROS modulate regeneration via the regulation of V_m, TEP, EF and/or J_I, all of which are known to be required for regeneration? At the cellular level, NADPH oxidases in the cell membrane catalyze electron transfer from cytoplasmic NADPH to extracellular molecular O_2, generating ROS and depolarizing V_m (Demaurex and Petheö, 2005; Lambeth and Neish, 2014). This dual property – electrogenic and catalytic – of NADPH oxidases led us to hypothesize a two-way regulation: (1) the activity of NADPH

[1]Department of Dermatology, Institute for Regenerative Cures, University of California, Davis, CA 95817, USA. [2]Departamento de Biologia, Centro de Biologia Molecular e Ambiental (CBMA), Universidade do Minho, Braga 4710, Portugal. [3]Department of Ophthalmology, Institute for Regenerative Cures, University of California, Davis, CA 95817, USA.

*Authors for correspondence (fdasilvaferreira@ucdavis.edu; minzhao@ucdavis.edu)

M.Z., 0000-0002-2500-3035

Received 9 July 2016; Accepted 21 October 2016

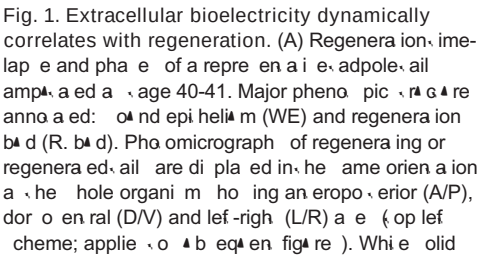

Fig. 1. Extracellular bioelectricity dynamically correlates with regeneration. (A) Regenera ion, ime-lap e and pha e of a repre en a i e, adpole, ail amp, a ed a , age 40-41. Major pheno pic , r g re anno a ed: o nd epi heli m (WE) and regenera ion b d (R. b d). Pho omicrograph of regenera ing or regenera ed, ail are di pla ed in, he ame orien a ion a , he hole organi m ho ing an eropo , erior (A/P), dor o en ral (D/V) and lef -righ (L/R) a e (op lef cheme; applie , o b eq en fig re). Whi e olid

phase pleiotropic effects during regeneration and NADPH oxidase-mediated ROS production is, to our knowledge, potentially the earliest biochemical limiting factor of regeneration.

NADPH oxidase-driven electron flow depolarizes V_m in the regeneration bud at 6 hpa

Cellular bioelectricity has previously been characterized in the same *X. laevis* model (Adams et al., 2007) and in axolotl larvae (Özkucur et al., 2010). These studies showed a robust V_m depolarization in the bud at 6 hpa that should repolarize by 24 hpa for complete regeneration (Adams et al., 2007). However, the origin of depolarization is unknown. V_m depolarization (Adams et al., 2007) and H_2O_2 concentration (Love et al., 2013) appear to overlap spatiotemporally. Activity of NADPH oxidases generates an electron flow that depolarizes V_m in immune cells that can be used as a direct quantification of holoenzyme activity (Demaurex and Petheö, 2005).

De elopmen (2016) 143, 4582-4594 doi:10.1242/de .142034

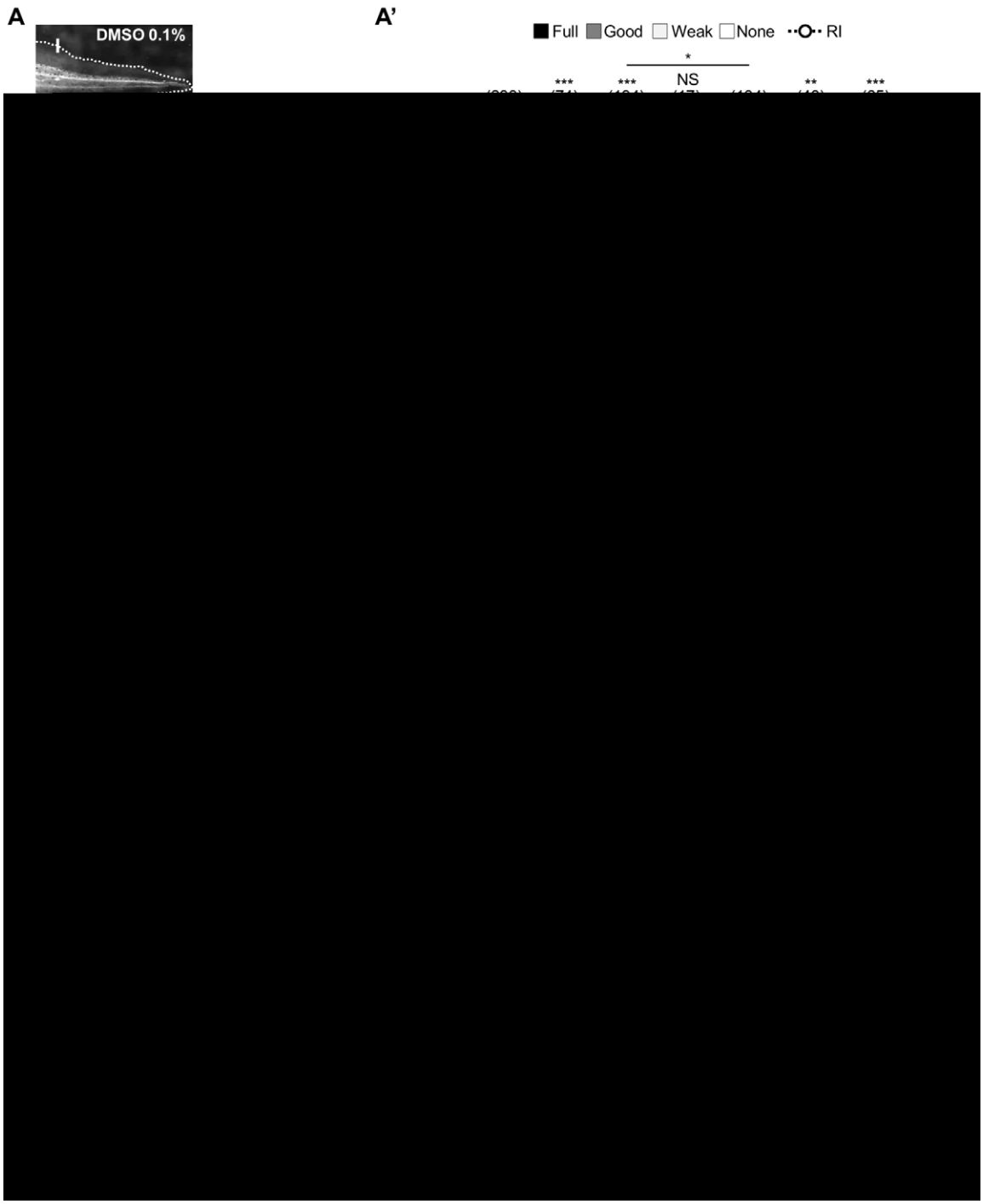

Fig. 2. Electrogenic property of NADPH oxidases is necessary for V_m depolarization and catalytic property for regeneration, TEP increase and J_I reversal. (A,A′) Lo and re ca e of regenera ion b ROS and H_2O_2 mod la ion. (A) Repre en a i e 7 dpa, ail from ehicle-con rol (DMSO 0.1%) and pharmacologicall , rea ed, adpole . Whi e line : amp , a ion plane. (A′) Qa ali a i e and qa an i a i e anal e of regenera ion efficienc for he differen condi ion , e , ed. RI, regenera ion inde . (B,B′) Ac i i of NADPH o ida e per e depolari e V_m. (B) Repre en a i e, ail nder, ran mi, ed ligh (op panel) and fl ore cence imaging (bo, om panel) of membrane po en ial- en i i e d e $DiBAC_4(3)$ in ehicle con rol and af er pharmacological, rea men a 6 hpa. Green arro head, V_m depolari a ion (rela i el po i i e) in, he b d; red arro head, no V_m depolari a ion in, he b d. (B′) Semi-qa an i a i e anal i of V_m for, he differen condi ion , e , ed. (C,D) Pharmacological lo and re ca e of regenera ion are correla ed i h aria ion of TEP (C) and J_I (D). In D, freq encie of ca ren re er al (mean percen age of in ard J_I, diamond) al o correla ed i h pharmacological, rea men . *P<0.05 er J_I magni de; $^{\#}P$<0.05 er J_I re er al ; **,$^{\#\#}P$<0.01; ***,$^{\#\#\#}P$<0.001. a., arbi rar ni . Scale bar : 1 mm; n al e are indica ed in bracke .

To test whether the activity of NADPH oxidases induced the V_m depolarization, we blocked them with DPI and imaged V_m with the membrane potential-sensitive dye $DiBAC_4(3)$ (Fig. S8A). DPI-treated tails at 6 hpa were, as in vehicle controls, still depolarized in the bud in relation to the rest of the tail (bud≫shoulder>trunk; Fig. S8A′), but had a significantly decreased depolarization (46% reduction, n=20, P=0.033; Fig. 2B,B′). Consequently, the spatial A/P gradient was also reduced (Fig. S8A′).

De elopmen (2016) 143, 4582-4594 doi:10.1242/de .142034

period (DMSO stage 40-41: −0.10±0.065 µA cm^{-2}, 82.34±6.27% reversal, *n*=23; DMSO stage 45-46+H_2O_2: 0.68±0.296 µA cm^{-2}, 43.81±11.18% reversal, *n*=37; *P*=0.013; Fig. 3C, Fig. S10B). H_2O_2 significantly decrease J_I magnitude in 81% to a still outward current (from 3.64±0.897, *n*=31, to 0.68±0.296 µA cm^{-2}, *n*=37, *P*=0.003; Fig. 3C). Importantly, current reversals increased threefold (from 14.29±7.19 to 43.81±11.18%, *P*=0.044; Fig. 3C).

We then attempted to induce ectopic tail formation during the regenerative period. Upon dorsal incisions, H_2O_2 treatment for 24 h slightly induced significant ectopic (abnormal or complete) tail formation (up to a frequency of 19%) in a dose-independent way (Fig. S15). Altogether, short-term exposure to low-dose H_2O_2 is sufficient to induce regeneration, TEP increase and J_I reversal during the refractory period, in addition to inducing ectopic tail formation in the regenerative period.

Regeneration efficiency correlates linearly with TEP magnitude and J_I reversals

Following the parallel responses of regeneration, TEP and J_I to the different conditions used, we tested whether bioelectricity predicts regeneration efficiency. Plotting all conditions together showed a significant linear correlation of regeneration efficiency with TEP magnitude (*r*=0.74, *P*=0.036; Fig. S14) and with the frequency of J_I reversals (*r*=0.86, *P*=0.006; Fig. 4).

Voltage-gated Na^+ channels are required for H_2O_2-modulated regeneration

To unveil the mechanisms by which H_2O_2 modulates regeneration, we searched for ion translocators that ideally affect regeneration and bioelectricity. $Na_V1.2$ is required for *X. laevis* tadpole tail regeneration via Na^+ influx control (Tseng et al., 2010). Therefore, we tested whether Na_V channels act downstream of H_2O_2 using complementary epistasis assays. First, we verified that the inhibition of Na_V channels impairs regeneration. As expected (Tseng et al., 2010), the Na_V inhibitor tricaine (Frazier and

Fig. 3. Exogenous H_2O_2 is sufficient to induce regeneration, TEP increase and J_I reversal during the refractory period. (A,A′) Ind g ion of regenera ion b e ogeno H_2O_2. (A) Repre en a i e 7 dpa ail from adpole amp a ed d ring he regenera i e (age 40-41) or refrac or period (age 45-46). Vehicle-con rol (DMSO 0.1%) and H_2O_2 rea ed (50 M n il 24 hpa) re l are ho n. Whi e olid line , amp a ion plane. Scale bar: 1 mm. (A′) Qua ali a i e and qua an i a i e anal e of regenera ion efficienc for he differen condi ion e ed. RI, regenera ion inde ; a.u., arbi rar ni . (B,C) E ogeno H_2O_2-media ed ind g ion of regenera ion i correla ed i h aria ion of TEP (B) and J_I (C). In C, freq encie of c rren re er al (mean percen age of in ard J_I, diamond) al o correla ed i h pharmacological rea men . *P<0.05 er J_I magni de; #P<0.05 er J_I re er al ; **, ##P<0.01; ***,###P<0.001. Hori on al a i label in C al o appl o A′,B. *n* al e are indica ed in bracke .

Fig. 4. Regeneration efficiency is directly proportional to J_I reversals. Compila ion of he differen condi ion e ed. Da a of regenera ion inde are from Fig 2A′, 3A′ and da a of freq enc of J_I re er al are from Fig 2D, 3C. Mo cro ed da a are ma ched ibling . Solid line, linear regre ion (r^2=0.75); *r*, correla ion coefficien .

De elopmen (2016) 143, 4582-4594 doi:10.1242/de .142034

Fig. 5. H_2O_2 modulates regeneration via voltage-gated Na^+ (Na_V) channels. (A,A′) Na_V channel inhibi ion i h ricaine impaired regenera ion. (A) Repre en a i e 7 dpa ail rea ed i h ehicle (DMSO 0.1%) or ricaine (250 or 150 M) from amp a ion or n il 24 hpa. (A′) Qua ali a i e and qua an i a i e anal e of regenera ion efficienc for he differen condi ion e ed. (B,B′) Na_V channel ac i a ion i h aconi ine re ca ed DPI-impaired regenera ion. (B) Repre en a i e 7 dpa ail rea ed i h ehicle (DMSO 0.1% and DMSO 0.2%) or DPI (1 M), alone or i h aconi ine (1 M), n il 24 hpa. (B′) Qua ali a i e and qua an i a i e anal e of regenera ion efficienc for he differen condi ion e ed. (C,C′) Na_V channel inhibi ion aboli hed H_2O_2-ind ced regenera ion in he refrac or period. (C) Repre en a i e 7 dpa ail amp a ed from adpole d ing he regenera i e (age 40-41) or refrac or (age 45-46) period . Tail ere rea ed n il 24 hpa i h ehicle, i h H_2O_2 (50 M) alone, or i h H_2O_2 (50 M) pl ricaine (150 M). (C′) Qua ali a i e and qua an i a i e anal e of regenera ion efficienc for he differen condi ion e ed. Primar e ical a i ile in A′ al o applie o B′,C′; econdar e ical a i ile in C′ al o applie o A′,B′. RI, regenera ion inde ; a.u., arbi rar ni . Whi e olid line , amp a ion plane. Scale bar , 1 mm; *n* al e are indica ed in bracke .

Narahashi, 1975) significantly impaired regeneration (250 µM: RI reduced from 277, n=59, to 113, n=45, P<0.0001; 250 µM until 24 hpa: RI reduced to 202, n=64, P=0.008). A lower dose (150 µM) had less penetrant effects (Fig. 5A,A′). Next, we designed the epistasis assays: (1) rescue DPI-impaired regeneration using the Na_V activator aconitine; and (2) loss H_2O_2-induced regeneration in the refractory period using the Na_V inhibitor tricaine.

Treatment with aconitine (Ameri, 1998) until 24 hpa significantly rescued DPI-impaired regeneration (Fig. 5B,B′). Aconitine increased 3.6-fold the frequency of tails with full phenotypes in relation to DPI-treated tails (from 9 to 34%) and decreased by ∼80% the frequency of none phenotypes (from 34 to 7%). Overall, regeneration was significantly rescued (RI from 105, n=57, to 179, n=56, P<0.0001; Fig. 5B,B′). Interestingly, aconitine (in the µM range) was lethal in the absence of DPI, pointing to antagonistic competition.

Treatment with tricaine until 24 hpa significantly impaired H_2O_2-induced regeneration (Fig. 5C,C′). Tricaine virtually eliminated full phenotypes in relation to H_2O_2-treated tails (from 30 to 2%) and increased 3.4-fold the frequency of none phenotypes (from 17 to 57%). Overall, regeneration was significantly lost (RI from 168, n=135, to 65, n=55, P<0.0001; Fig. 5C,C′). Therefore, Na_V channels act downstream of H_2O_2 and mediate H_2O_2-modulated regeneration – a new mechanism.

DISCUSSION

Bioelectric and, more recently, redox activities have been shown, independently, to modulate regeneration in widespread models: planaria (Beane et al., 2011; Pirotte et al., 2015), zebrafish (Gauron et al., 2013; Monteiro et al., 2014) and amphibians (Love et al., 2013; Reid et al., 2009). Seeking a biochemical and biophysical integration, we aimed to determine whether and how these pervasive activities interact during regeneration.

Redox-modulated regeneration is mediated by early bioelectric activities

Do ROS modulate regeneration via regulation of bioelectric activities that are known to be required for regeneration? Our results support the two-way regulation hypothesis proposed to address this question. First we mapped the spatiotemporal dynamics of extracellular

bioelectricity (Fig. 1, Figs S2-S5) and the temporal requirement for NADPH oxidase-mediated ROS production (Fig. 2A,A′, Fig. S7). These profiles identified the bud at 6 hpa as key to testing the proposed hypothesis, owing to its bioelectric state. Next, we blocked NADPH oxidases and imaged V_m. We found that V_m depolarization resulted from NADPH oxidase activity per se (Fig. 2B,B′). This supported the first part of the two-way regulation hypothesis, arguing that the electrogenic property of NADPH oxidases is the mechanism by which V_m depolarization occurs. As depolarization is not required for regeneration (Adams et al., 2007), we then focused on the extracellular bioelectricity. Drug-depleted ROS levels decreased TEP and prevented or postponed J_I reversal, maintaining a steady outward current at 6 hpa (Fig. 2C,D). This mimicked the altered TEP and J_I measured during the refractory period (Fig. S11). Exogenous H_2O_2 rescued and induced regeneration, TEP and J_I (Figs 2, 3). It also induced ectopic tail formation (Fig. S15). Regeneration efficiency was directly proportional to TEP increase and J_I reversals (Fig. 4, Fig. S14). These results supported the second part o1.6s1s28.31(ss)]TJ-23.805-1.1.7(5f)]TJh(a)2.4(7(ing)-183e9.8(t)-06.S56

part in both TEP and J_I suggests that inward current magnitude should go beyond TEP recovery.

Homeostatic (from 48 hpa)

Ion fluxes should now be mainly for housekeeping functions, as TEP and J_I return to uncut baseline, resolving EF. Uncut and complete regeneration tails have an inside-positive TEP and a small inward J_I, in agreement with the salt uptake (osmoregulatory) function of amphibian skin (Koefoed-Johnsen and Ussing, 1958). Remarkably, TEP recovers to the new stage-specific level, not to the level before amputation (Fig. S2C),

two-thirds of the reversed current. However, neither ion nor translocator modulations were able to actually maintain the outward current (Reid et al., 2009). Remarkably, using non-ionic modulation, we either prevented or postponed current reversal in the bud at 6 hpa, mimicking the refractory period. This led to a dramatic inhibition of regeneration. We showed that H_2O_2 diffuses into the cell and stimulates the reversal. Thus, in an electrical equivalent circuit, we propose that H_2O_2 is a switcher that permits Na^+-carried current to diffuse into the stump (Fig. 6B). In the same model, Tseng et al. unveiled part of the molecular basis for Na^+ influx, the channel $Na_V1.2$ (Tseng et al., 2010). We found that H_2O_2 acts upstream of the Na_V channel family. Future work is necessary to reveal the mechanism of this activation, which can be indirect (e.g. redox-sensitive pathways or gene transcription of channels proteins/regulators) or direct (e.g. oxidation of channels cysteine residues, if available) (Fig. 6A). $Na_V1.2$ is present by 18 hpa in the bud, accumulating cations there (Tseng et al., 2010). The mismatch with our measured reversal at 6 hpa might imply other Na_V channel(s) in action, possibly in the wound epithelium. This would complete the path of Na^+ from outside to bud, as barrier restoration prevents most ion leakage and reduces paracellular flux. In principle, however, some Na^+ transporter(s) should be present in the wound epithelium to move the ions against the electrochemical gradient. The sharp TEP increase until 6 hpa supports this and might suggest the ubiquitous Na^+/K^+-ATPase as a candidate (Dubé et al., 2010). Thus, it is possible that H_2O_2 (or other ROS) modulates additional ion translocators (Ma, 2011; Matalon et al., 2003). Exogenous H_2O_2 rescued and induced regeneration and induced ectopic tails, suggesting that H_2O_2 provides indispensable morphogenetic information. H_2O_2 robustly rescued and induced TEP increase and J_I reversal at 6 hpa. Therefore, we propose that H_2O_2-switched current reversal is a hallmark of regeneration. As a limiting and stimulating factor of regeneration, this hallmark can be used as a diagnostic characteristic of regeneration and as a marker and prognosis of its efficiency (Fig. 4). Furthermore, it can be used to promote regeneration in regenerative-deficient animals.

J_I reversal prior to blastema formation was also seen in newt limbs (unquantified frequency, apparently occasional due to net outward current) (Borgens et al., 1977b) and tails (Nawata, 2001), and in *X. laevis* tadpole limb regeneration (G.L., unpublished). Reversal in newt tails was assumed to be a return to baseline (Nawata, 2001), despite the higher magnitude than before amputation. Surface potential measurements revealed stump potential reversal (from positive to negative) prior to blastema formation in urodels, but not in non-permissive anuran limb regeneration (Becker, 1961; Rose and Rose, 1974), showing a correlation with regeneration. However, another study found potential reversal in both taxa (Lassalle, 1979). We measured instead transepithelial potentials that, apart from sporadic reversals, had no overall mean reversal. Short-range $EF_{Shoulder \rightarrow Bud}$ presented more reversal frequency (21%) than did long-range $EF_{Trunk \rightarrow Bud}$ (9%) at 6 hpa (increasing thereafter; Fig. S3C), indicating the predominance of local reversal (in the bud). Indeed, in newt limbs, the surface potential reversal occurred only a short distance from the amputation plane (Rose and Rose, 1974). The small and soft bud hindered the spatial resolution required to fully characterize local reversals. Unambiguous current reversal supports the short-range potential and EF reversals in the bud. Altogether, our results showed a close correlation between reversals, bud formation and regeneration (Figs 4, 6, 7).

How can the H_2O_2-switched current reversal mechanistically impact regeneration? Cell migration precedes proliferation (Adams et al., 2007) and is essential for wound closure in the first phase of regeneration (Beck et al., 2009). Thus, the early and vectorial J_I reversal suggests migration as a prime candidate. However, other cell behaviors are not excluded. Cumulative evidence shows that endogenous or exogenous EF act as guiding cues for migration during wound healing (McCaig et al., 2005; Zhao et al., 1996, 2006). Importantly, most cells, including keratinocytes and neurons, migrate or grow towards the cathode (Song, 2004; Sun et al., 2013). ROS-depleted and refractory period tails at 6 hpa had a sustained outward J_I that led to lower bud TEP and higher short-range EF, establishing a long-term cathode at amputation plane (Figs 2C, 3B, Figs S11, S16A). Therefore, we postulate that a non-reversed J_I by 6 hpa might lead to cell overmigration. In short, cells are deluded into behaving as if the wound was still open (Fig. S16B). Wound epithelium from the refractory period is thicker than regenerative *X. laevis* tadpole tails (Beck et al., 2003; Reid et al., 2009; Tseng et al., 2010). Mature skin flapped or grafted to amputated newt limbs or children's fingertips blocks regeneration (Illingworth, 1974; Mescher, 1976). Interestingly, these skin-like structures have altered currents (Altizer et al., 2002; Reid et al., 2009) (Fig. S11) and might disrupt epithelial-mesenchymal crosstalk (Lee et al., 2009), both of which are important for regeneration. Thereby, cell overmigration might produce a non-permissive refractory-like wound epithelium. This might explain why J_I reversal by 24 hpa in MCI- and $AgNO_3$-treated tails (Fig. S8C) was not sufficient for regeneration (Fig. 2A,A′). Although we cannot exclude direct ROS-induced chemotaxis (Hurd et al., 2012; Pan et al., 2011), ROS-modulated electrotaxis might be the major cue (Zhao, 2009). This rationale could apply to axonal sprouting and to axonal growth (electrotropism). Neuronal presence is a long-recognized limiting and stimulating factor in regeneration (Kumar and Brockes, 2012; Sidman and Singer, 1951). Importantly, applied currents enhance nerve growth and regeneration in adult frogs (Borgens et al., 1979). Observed J_I reversal per se or the establishment of a steady inward current might be independent cues. Reversal can be a transitory electric pole discretely sensed by cells. Therefore, J_I reversal may fine-tune (mitigate) migration of cells and axonal growth, setting the conditions for or triggering bud initiation around 6 hpa and subsequent proliferation and *de novo* tail formation. Indeed, a permissive epithelium neuronally supplied (Thornton, 1954) is the basis of the accessory limb formation in axolotls (Endo et al., 2004). H_2O_2-induced ectopic tails might thus result from bioelectric effects on neuronal tissue.

Towards a comprehensive model of redox and bioelectric integration during regeneration

We aimed to conceptualize a comprehensive model that integrates redox and bioelectric states during regeneration (Fig. 7). We showed that NADPH oxidase-mediated ROS production is pleiotropic (early on it affects morphogenesis; later on it affects growth) and is required immediately upon amputation. Thus, an elusive ultra-fast signal needs to trigger the activity of NADPH oxidases. Probably the fastest injury-induced signals are bioelectric in nature. Exogenous EF activate NADPH oxidases in cells *in vitro* (Chatterjee et al., 2012; Li et al., 2013). Thus, we propose that endogenous EF activate NADPH oxidases (Fig. 7). Another candidate is Ca^{2+} signaling. Wounding induces fast Ca^{2+} influx and Ca^{2+} flashes in *X. laevis* oocytes and *Drosophila* embryo, respectively (Luxardi et al., 2014; Razzell et al., 2013). Importantly, those flashes activate a NADPH oxidase (Duox). Excitingly, this points to a feedback module, where bioelectric signals (primary EF and/or Ca^{2+}) might activate redox signals (NADPH oxidases and generated H_2O_2) that in turn regulate bioelectricity (V_m, TEP,

Supplementary information

Supplementary information available online at http://dev.biologists.org/lookup/doi/10.1242/dev.142034.supplemental

References

Adams, D. S., Masi, A. and Levin, M. (2007). H+ pump-dependent change in membrane voltage are an early mechanism necessary and sufficient to induce Xenopus tail regeneration. *Development* 134, 1323-1335.

Altizer, A. M., Stewart, S. G., Albertson, B. K. and Borgens, R. B. (2002). Skin flap inhibits both the current of injury at the amputation surface and regeneration of the hind limb in newts. *J. Exp. Zool.* 293, 467-477.

Alvarado, A. S. and Tsonis, P. A. (2006). Bridging the regeneration gap: genetic insights from diverse animal models. *Nat. Rev. Genet.* 7, 873-884.

Ameri, A. (1998). The effects of Aconitum alkaloids on the central nervous system. *Prog. Neurobiol.* 56, 211-235.

Bankers-Fulbright, J. L., Gleich, G. J., Kephart, G. M., Kita, H. and O'Grady, S. M. (2003). Regulation of eosinophil membrane depolarization during NADPH oxidase activation. *J. Cell Sci.* 116, 3221-3226.

Barker, A. T., Jaffe, L. F. and Vanable, J. W. (1982). The glabrous epidermis of cavies contains a powerful battery. *Am. J. Physiol.* 242, R358-R366.

Beane, W. S., Morokuma, J., Adams, D. S. and Levin, M. (2011). A chemical genetic approach reveals H,K-ATPase-mediated membrane voltage is required for planarian head regeneration. *Chem. Biol.* 18, 77-89.

Beck, C. W., Christen, B. and Slack, J. M. W. (2003). Molecular pathways needed for regeneration of spinal cord and muscle in a vertebrate. *Dev. Cell* 5, 429-439.

Beck, C. W., Izpisúa Belmonte, J. C. and Christen, B. (2009). Beyond early development: Xenopus as an emerging model for the study of regenerative mechanisms. *Dev. Dyn.* 238, 1226-1248.

Becker, R. O. (1961). The bioelectric factors in amphibian-limb regeneration. *J. Bone Jt. Surg.* 43, 643-656.

Becker, R. O. (1972). Stimulation of partial limb regeneration in rats. *Nature* 235, 109-111.

Bienert, G. P. and Chaumont, F. (2014). Aquaporin-facilitated transmembrane diffusion of hydrogen peroxide. *Biochim. Biophys. Acta* 1840, 1596-1604.

Borgens, R. B. (1984). Are limb development and limb regeneration both initiated by an integumentary wounding? Ann. Rev. Physiol. *Differentiation* 28, 87-93.

Borgens, R. B., Vanable, J. W. and Jaffe, L. F. (1977a). Bioelectricity and regeneration. I. Initiation of frog limb regeneration by minute current. *J. Exp. Zool.* 200, 403-416.

Borgens, R. B., Vanable, J. W. and Jaffe, L. F. (1977b). Bioelectricity and regeneration: large currents leave the stump of regenerating newt limb. *Proc. Natl. Acad. Sci. USA* 74, 4528-4532.

Borgens, R. B., Vanable, J. W. and Jaffe, L. F. (1979). Small artificial currents enhance Xenopus limb regeneration. *J. Exp. Zool.* 207, 217-226.

Chatterjee, S., Browning, E. A., Hong, N., DeBolt, K., Sorokina, E. M., Liu, W., Birnbaum, M. J. and Fisher, A. B. (2012). Membrane depolarization is the trigger for PI3K/Akt activation and leads to the generation of ROS. *AJP Hear. Circ. Physiol.* 302, H105-H114.

Demaurex, N. and Petheö, G. L. (2005). Electron and proton transport by NADPH oxidase. *Philos. Trans. R. Soc. Lond. B. Biol. Sci.* 360, 2315-2325.

Deuchar, E. M. (1975). Regeneration of the tail bud in Xenopus embryo. *J. Exp. Zool.* 192, 381-389.

Dubé, J., Rochette-Drouin, O., Lévesque, P., Gauvin, R., Roberge, C. J., Auger, F. A., Goulet, D., Bourdages, M., Plante, M., Germain, L. et al. (2010). Restoration of the transepithelial potential of tissue-engineered human skin in vitro and during the wound healing process in vivo. *Tissue Eng. Part A* 16, 3055-3063.

Endo, T., Bryant, S. V. and Gardiner, D. M. (2004). A stepwise model system for limb regeneration. *Dev. Biol.* 270, 135-145.

Frazier, D. T. and Narahashi, T. (1975). Tricaine (MS-222): effects on ionic conductance of squid axon membrane. *Eur. J. Pharmacol.* 33, 313-317.

Garland, S. P., Wang, R. Y., Raghunathan, V. K., Lam, K. S., Murphy, C. J., Russell, P., Sun, G. and Pan, T. (2014). Photopatternable and photoactive hydrogel for on-demand generation of hydrogen peroxide in cell culture. *Biomaterials* 35, 1762-1770.

Gauron, C., Rampon, C., Bouzaffour, M., Ipendey, E., Teillon, J., Volovitch, M. and Vriz, S. (2013). Sustained production of ROS triggers compensatory proliferation and is required for regeneration to proceed. *Sci. Rep.* 3, 2084.

Golding, A., Guay, J. A., Herrera-Rincon, C., Levin, M. and Kaplan, D. L. (2016). Astronable silk hydrogel device for studying limb regeneration in adult Xenopus Laevis. *PLoS ONE* 11, e0155618.

Han, P., Zhou, X.-H., Chang, N., Xiao, C.-L., Yan, S., Ren, H., Yang, X.-Z., Zhang, M.-L., Wu, Q., Tang, B. et al. (2014). Hydrogen peroxide primes heart regeneration with a derepression mechanism. *Cell Res.* 24, 1091-1107.

Hechavarria, D., Dewilde, A., Braunhut, S., Levin, M. and Kaplan, D. L. (2010). BioDome regenerative tissue culture for biochemical and biophysical stimulation of tissue regeneration. *Med. Eng. Phys.* 32, 1065-1073.

Hurd, T. R., DeGennaro, M. and Lehmann, R. (2012). Redox regulation of cell migration and adhesion. *Trends Cell Biol.* 22, 107-115.

Illingworth, C. M. (1974). Trapped fingers and amputated fingertip in children. *J. Pediatr. Surg.* 9, 853-858.

Jaffe, L. F. (1981). The role of ionic currents in establishing developmental patterns.

Otomo, E. (2003). Effec of a no el free radical ca enger, edara one (MCI-186), on ac e brain infarc ion. Randomi ed, placebo-con rolled, do ble-blind d a mi icen er . *Cerebrovasc. Dis.* 15, 222-229.
Owusu-Ansah, E., Yavari, A., Mandal, S. and Banerjee, U. (2008). Di ing mi ochondrial re rograde ignal con rol he G1-S cell c cle checkpoin . *Nat. Genet.* 40, 356-361.
Özkucur, N., Epperlein, H.-H. and Funk, R. H. W. (2010). Ion imaging d ring a olo l ail regenera ion in i o. *Dev. Dyn.* 239, 2048-2057.
Pan, Q., Qiu, W.-Y., Huo, Y.-N., Yao, Y.-F. and Lou, M. F. (2011). Lo le el of h drogen pero ide im la e corneal epi helial cell adhe ion, migra ion, and o nd healing. *Invest. Ophthalmol. Vis. Sci.* 52, 1723-1734.
Pirotte, N., Stevens, A.-S., Fraguas, S., Plusquin, M., Van Roten, A., Van Belleghem, F., Paesen, R., Ameloot, M., Cebrià, F., Artois, T. et al. (2015). Reac i e o gen pecie in planarian regenera ion: an p ream nece i for correc pa erning and brain forma ion. *Oxid. Med. Cell. Longev.* 2015, 1-19.
Razzell, W., Evans, I. R., Martin, P. and Wood, W. (2013). Calci m fla he orche ra e he o nd inflamma or re pon e hro gh da o ac i a ion and h drogen pero ide relea e. *Curr. Biol.* 23, 424-429.
Reid, B., Nuccitelli, R. and Zhao, M. (2007). Non-in a i e mea remen of bioelec ric c rren i h a ibra ing probe. *Nat. Protoc.* 2, 661-669.
Reid, B., Song, B. and Zhao, M. (2009). Elec ric c rren in Xenop adpole ail regenera ion. *Dev. Biol.* 335, 198-207.
Rose, M. S. and Rose, F. C. (1974). Elec rical die on normall regenera ing, on X-ra ed, and on dener a ed limb mp of Tri ra . *Growth* 38, 363-380.
Sen, C. K. and Roy, S. (2008). Redo ignal in o nd healing. *Biochim. Biophys. Acta* 1780, 1348-1361.
Serena, E., Figallo, E., Tandon, N., Cannizzaro, C., Gerecht, S., Elvassore, N. and Vunjak-Novakovic, G. (2009). Elec rical im la ion of h man embr onic em cell : cardiac differen ia ion and he genera ion of reac i e o gen pecie . *Exp. Cell Res.* 315, 3611-3619.
Shapiro, S., Borgens, R., Pascuzzi, R., Roos, K., Groff, M., Purvines, S., Rodgers, R. B., Hagy, S. and Nelson, P. (2005). O cilla ing field im la ion for comple e pinal cord inj r in h man : a pha e 1 rial. *J. Neurosurg. Spine* 2, 3-10.
Sidman, R. L. and Singer, M. (1951). S im la ion of forelimb regenera ion in he ne , Tri ra iride cen , b a en or ner e ppl i ola ed from he cen ral ner o em. *Am. J. Physiol.* 165, 257-260.
Simons, J. M., 't Hart, B. A., Ip Vai Ching, T. R. A. M., Van Dijk, H. and Labadie, R. P. (1990). Me abolic ac a ion of na ral phenol in o elec i e o ida i e b r agoni b ac i a ed h man ne rophil . *Free Radic. Biol. Med.* 8, 251-258.
Smith, S. D. (1967). Ind c ion of par ial limb regenera ion in Rana pipien b gal anic im la ion. *Anat. Rec.* 158, 89-97.
Song, B., Zhao, M., Forrester, J. and McCaig, C. (2004). Ner e regenera ion and o nd healing are im la ed and direc ed b an endogeno elec rical field in i o. *J. Cell Sci.* 117, 4681-4690.
Stoick-Cooper, C. L., Moon, R. T. and Weidinger, G. (2007). Ad ance in ignaling in ex ebra e regenera ion a a prel de o regenera i e medicine. *Genes Dev.* 21, 1292-1315.
Sugiura, T., Tazaki, A., Ueno, N., Watanabe, K. and Mochii, M. (2009). Xenop Wn -5a ind ce an ec opic lar al ail a inj red i e, gge ing a cr cial role for noncanonical Wn ignal in ail regenera ion. *Mech. Dev.* 126, 56-67.
Sun, Y., Do, H., Gao, J., Zhao, R., Zhao, M. and Mogilner, A. (2013). Kera oc e fragmen and cell ili e compe ing pa h a o mo e in oppo i e direc ion in an elec ric field. *Curr. Biol.* 23, 569-574.
Tandon, N., Cimetta, E., Villasante, A., Kupferstein, N., Southall, M. D., Fassih, A., Xie, J., Sun, Y. and Vunjak-Novakovic, G. (2014). Gal anic micropar icle increa e migra ion of h man dermal fibrobla in a o nd-healing model ia reac i e o gen pecie pa h a . *Exp. Cell Res.* 320, 79-91.
ten Freyhaus, H., Huntgeburth, M., Wingler, K., Schnitker, J., Bäumer, A. T., Vantler, M., Bekhite, M. M., Wartenberg, M., Sauer, H. and Rosenkranz, S. (2006). No el No inhibi or VAS2870 a en a e PDGF-dependen moo h m cle cell chemo a i , ba no prolifera ion. *Cardiovasc. Res.* 71, 331-341.
Thornton, C. S. (1954). The rela ion of epidermal inner a ion o limb regenera ion in Ambl oma lar ae. *J. Exp. Zool.* 127, 577-601.
Tseng, A.-S. and Levin, M. (2013). Cracking he bioelec ric code: Probing endogeno ionic con rol of pa ern forma ion. *Commun. Integr. Biol.* 6, 1-8.
Tseng, A.-S., Beane, W. S., Lemire, J. M., Masi, A. and Levin, M. (2010). Ind c ion of ex ebra e regenera ion b a ran ien odi m c rren . *J. Neurosci.* 30, 13192-13200.
Veal, E. A., Day, A. M. and Morgan, B. A. (2007). H drogen pero ide en ing and ignaling. *Mol. Cell* 26, 1-14.
Verkman, A. S., Anderson, M. O. and Papadopoulos, M. C. (2014). Aq aporin : impor an ba el i e dr g arge . *Nat. Rev. Drug Discov.* 13, 259-277.
Wittmann, C., Chockley, P., Singh, S. K., Pase, L., Lieschke, G. J. and Grabher, C. (2012). H drogen pero ide in inflamma ion: me enger, g ide, and a a in. *Adv. Hematol.* 2012, 541471.
Yoo, S. K., Starnes, T. W., Deng, Q. and Huttenlocher, A. (2011). L n i a redo en or ha media e le koc e o nd a rac ion in i o. *Nature* 480, 109-112.
Yoo, S. K., Freisinger, C. M., LeBert, D. C. and Huttenlocher, A. (2012). Earl redo , Src famil kina e, and calci m ignaling in egra e o nd re pon e and i e regenera ion in ebrafi h. *J. Cell Biol.* 199, 225-234.
Zhang, Q., Wang, Y., Man, L., Zhu, Z., Bai, X., Wei, S., Liu, Y., Liu, M., Wang, X., Gu, X. et al. (2016). Reac i e o gen pecie genera ed from kele al m cle are req ired for gecko ail regenera ion. *Sci. Rep.* 6, 1-11.
Zhao, M. (2009). Elec rical field in o nd healing—an o erriding ignal ha direc cell migra ion. *Semin. Cell Dev. Biol.* 20, 674-682.
Zhao, M., Agius-Fernandez, A., Forrester, J. V. and McCaig, C. D. (1996). Orien a ion and direc ed migra ion of c l red corneal epi helial cell in mall elec ric field are er m dependen . *J. Cell Sci.* 109, 1405-1414.
Zhao, M., Song, B., Pu, J., Wada, T., Reid, B., Tai, G., Wang, F., Guo, A., Walczysko, P., Gu, Y. et al. (2006). Elec rical ignal con rol o nd healing hro gh pho pha id lino i ol-3-OH kina e-gamma and PTEN. *Nature* 442, 457-460.

Supplementary Information

Supplementary Figures

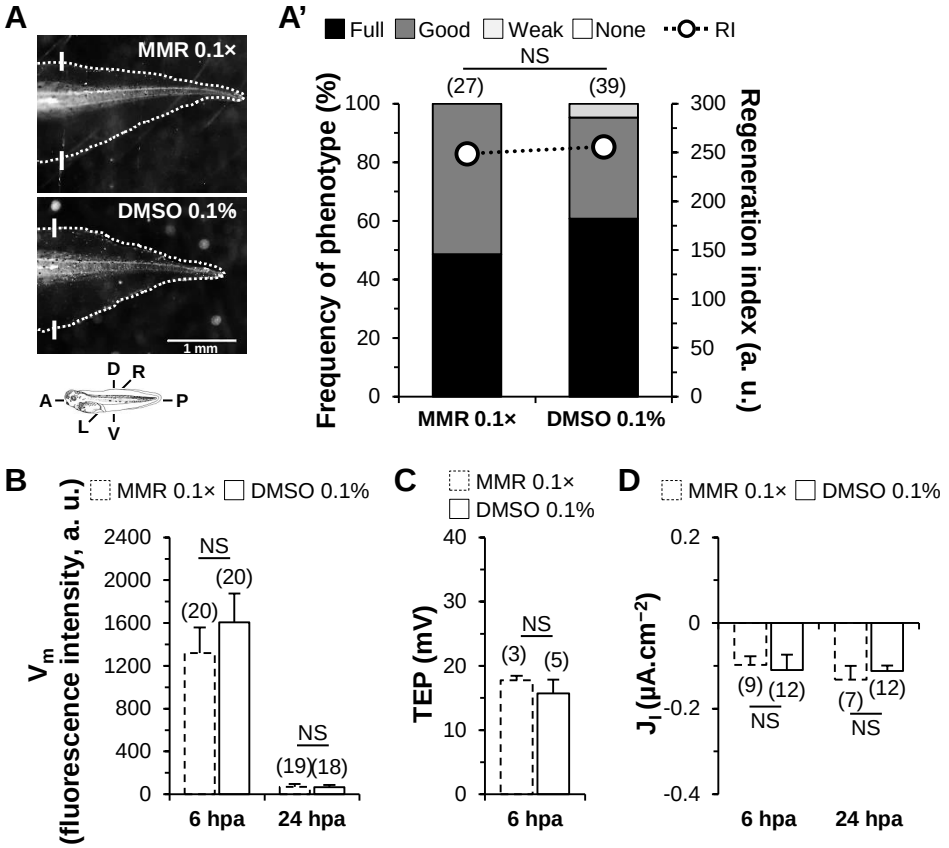

n specimens indicated in brackets.

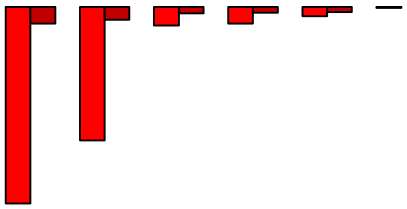

δx) were obtained from tail photomicrographs (details to follow). ROIs are the same as those shown in Fig. S2A. (B) Specific equations used to calculate lateral EF from TEP data of Fig. S2C. Distances (denominators) were challenging to measure because the microelectrode tip was virtually invisible once impaled and because the tail/tadpole commonly moved place due to the microelectrode impalement (inherently mechanical). Thus, even taking consecutive photomicrographs, it was hard to accurately measure the distances between the three ROIs every time impaled. To overcome this, we used the very consistent regeneration bud length at 6 hpa as a relative size reference and then defaulted to measure TEP for bud at its half and for trunk at 2.5Ĭ the 6 hpa bud size, starting from the shoulder. Shoulder was therefore at distance 0 mm. In this way, for all tails we just needed to take one photomicrograph of the bud and measure its length for each tadpole. Then we calculated the mean of all 6 hpa buds and fixed that value (0.134Ñ0.009 mm, n=24) for ωؤ شد خ نى نجى لي For ʻOʼǪ ذ شس ز ºخ ئخ شد equation denominator, the bud/new trunk length was always directly measured at all time-points and then halved to represent the distance from shoulder to bud. (C) Spatiotemporal profile of lateral EF during regeneration in vehicle-control (DMSO 0.1%). Frequencies of potential/EF reversals (total percentage of TEP_{Trunk}<TEP_{Bud}*, hence anode (positive pole) at bud) are given under condition bars for* $EF_{Trunk\ Ÿ\ Bud}$*. Data of* $EF_{Trunk\ Ÿ\ Bud}$ *are the same as those shown in Fig. 1C. NA: not applicable; n specimens indicated in brackets.*

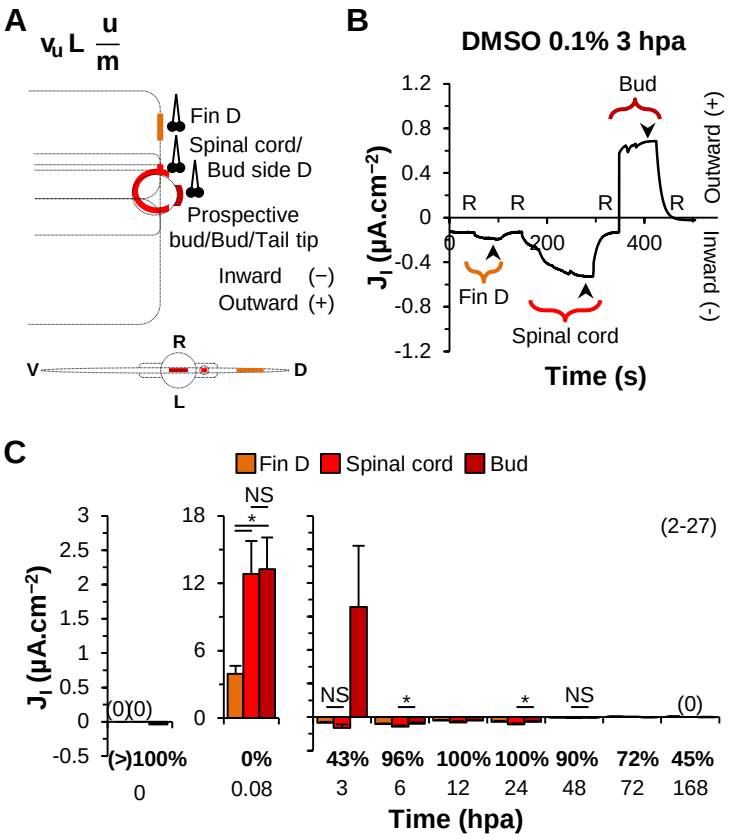

I: electric current;A: area. (B) Representative result from raw data. J_I was recorded until stable peak was reached (<1 minute). R: reference position measurement (>>1mm from tail surface); arrowhead: extracted plateau peak value. (C) Spatiotemporal profile of J_I during regeneration in vehicle-control (DMSO 0.1%). Frequencies of current reversals (total percentage of inward J) are given under condition bars for bud. Data of regeneration bud are the same as those shown in Fig. 1D. n specimens indicated in brackets.

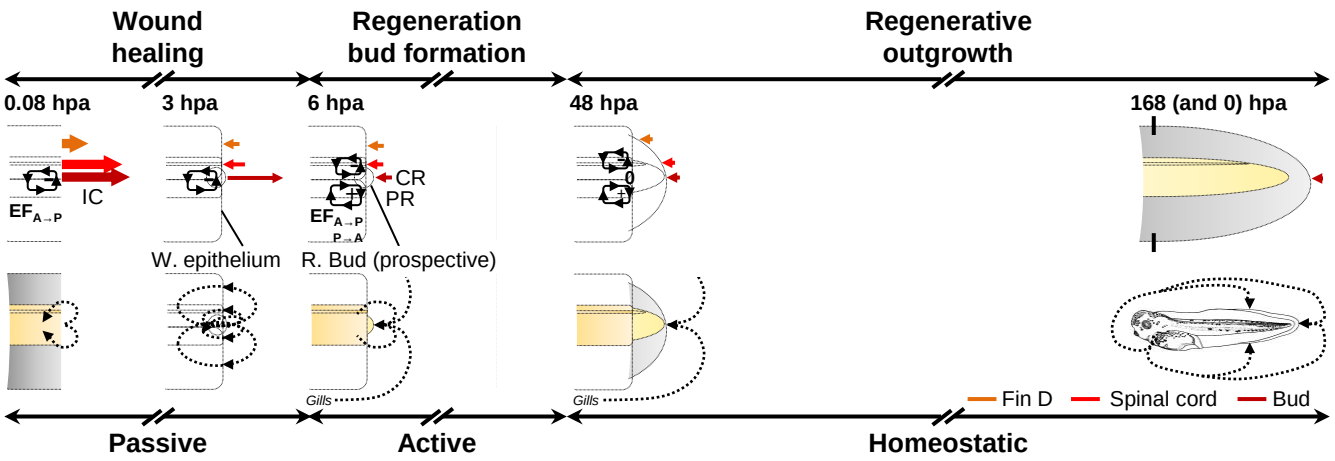

et al., 2009). Profiles are divided into three phases according to the bioelectric activity: passive, active and homeostatic. ROIs are the same as those shown in Fig. S4A. Colored solid arrows: net outward (left arrow) or inward (right arrow) current density; black solid arrows: simplified electric field lines; black dotted arrows: simplified current field (circuit) lines. Arrows are not at absolute scale, but present the relative spatiotemporal directions and magnitudes of the currents and circuit loops and fields. Key: A: anterior; P: posterior; IC: injury current; CR: current reversal; PR: potential reversal; W. epithelium: wound epithelium; R. bud: regeneration bud Black solid lines: amputation plane.

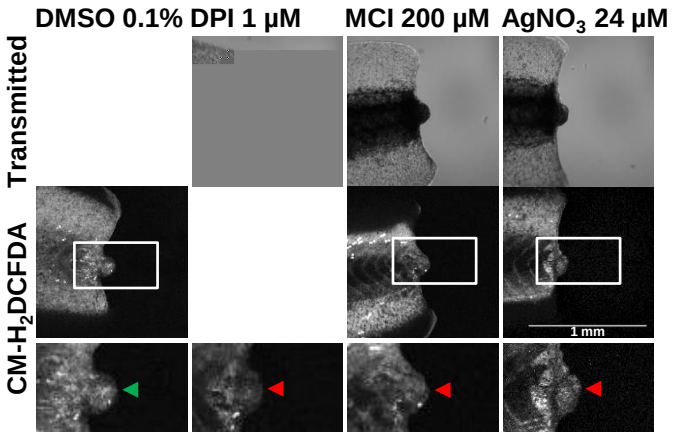
DMSO 0.1%
DPI 1 µM
MCI 200 µM
AgNO3 24 µM
Transmitted
CM-H2DCFDA
1 mm

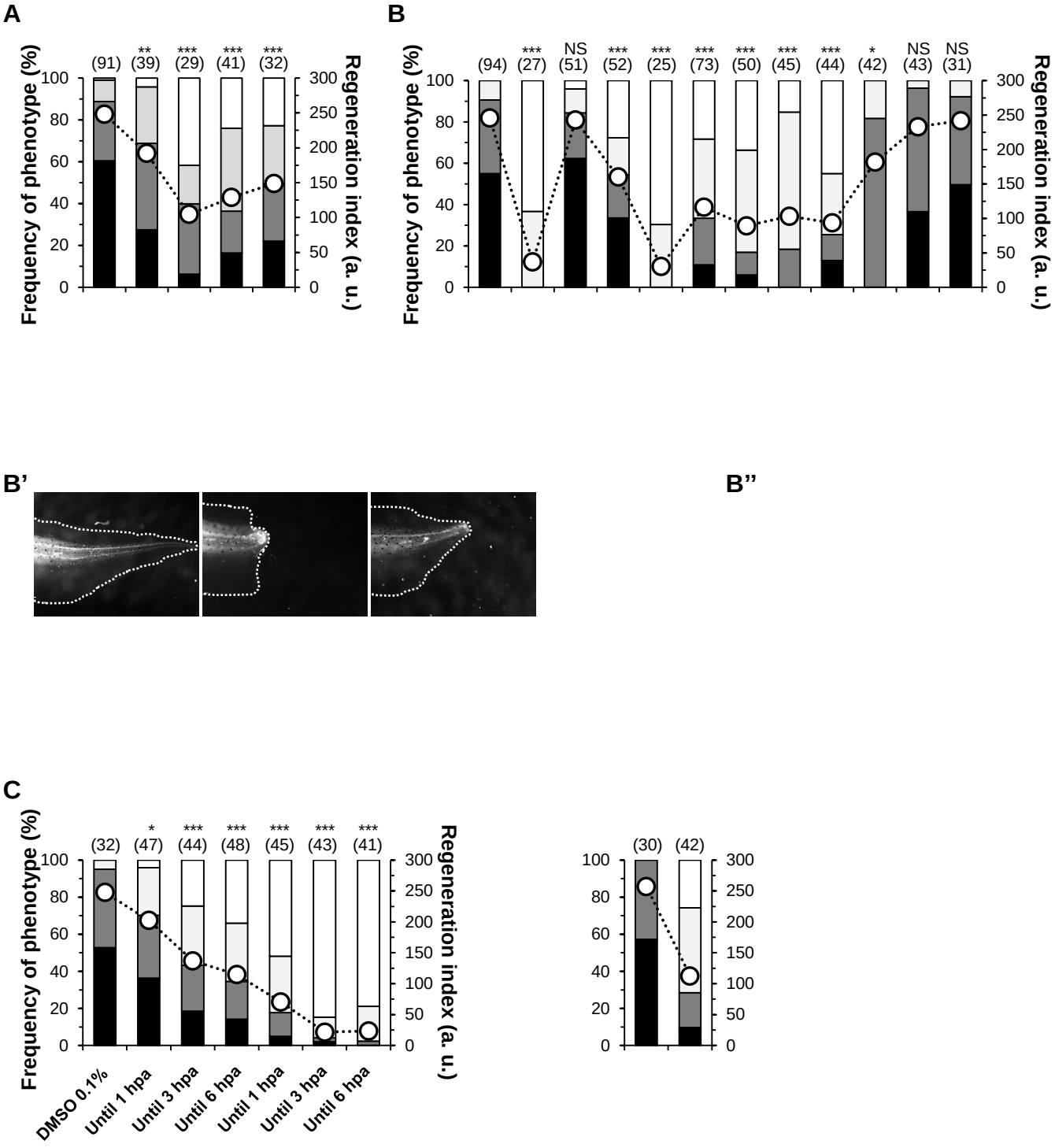
A
B
B'
B''
C
Frequency of phenotype (%)
Regeneration index (a. u.)
(91) (39) (29) (41) (32)
** *** *** ***
(94) (27) (51) (52) (25) (73) (50) (45) (44) (42) (43) (31)
*** NS *** *** *** *** *** * NS NS
(32) (47) (44) (48) (45) (43) (41)
* *** *** *** *** ***
(30) (42)
DMSO 0.1%
Until 1 hpa
Until 3 hpa
Until 6 hpa
Until 1 hpa
Until 3 hpa
Until 6 hpa

n

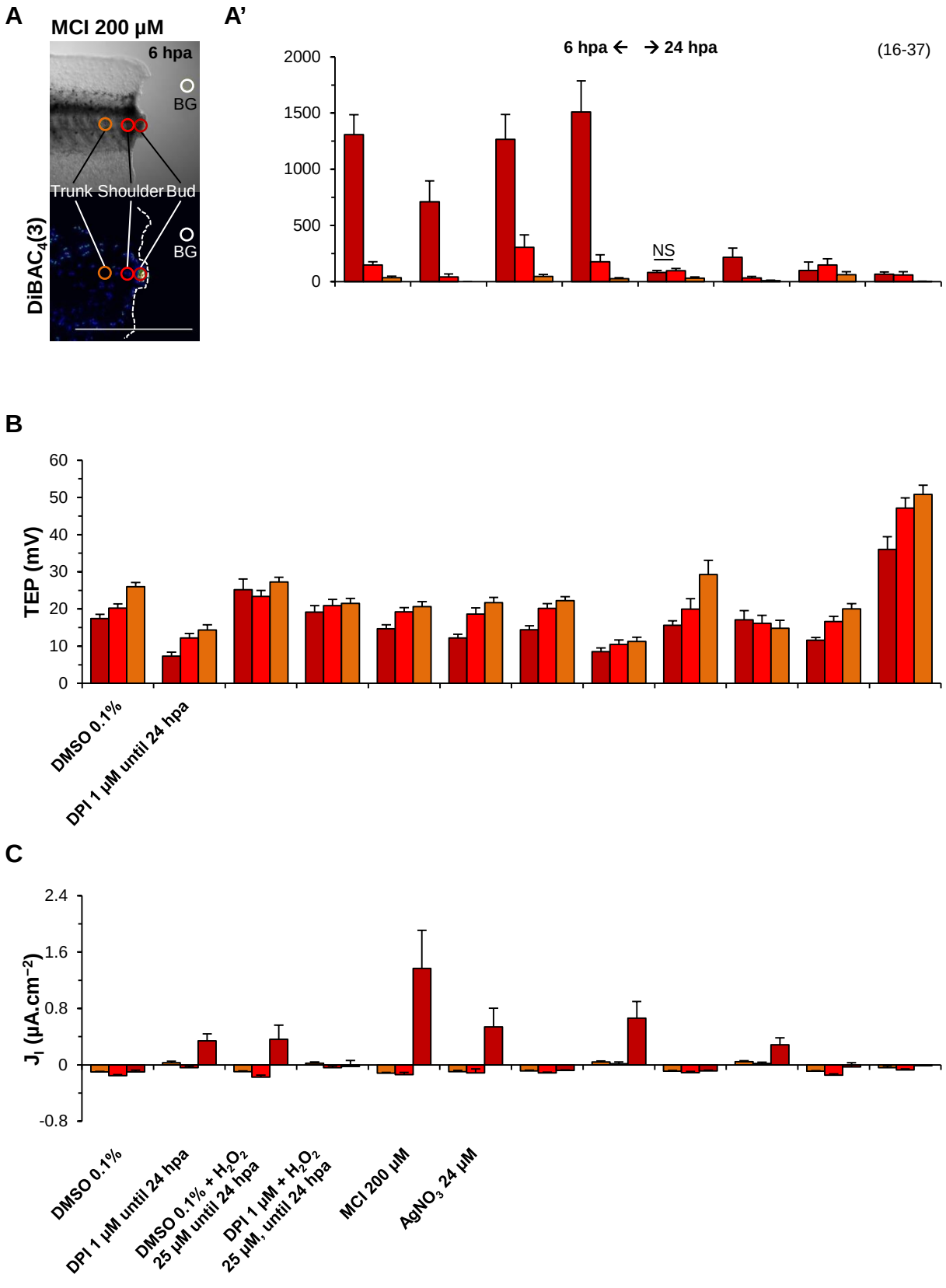
A
MCI 200 µM
6 hpa
BG
Trunk
Shoulder
Bud
BG
DiBAC4(3)
A'
6 hpa ← → 24 hpa
(16-37)
2000
1500
1000
500
0
NS
B
TEP (mV)
60
50
40
30
20
10
0
DMSO 0.1%
DPI 1 µM until 24 hpa
C
JI (µA.cm−2)
2.4
1.6
0.8
0
-0.8
DMSO 0.1%
DPI 1 µM until 24 hpa
DMSO 0.1% + H2O2 25 µM until 24 hpa
DPI 1 µM + H2O2 25 µM, until 24 hpa
MCI 200 µM
AgNO3 24 µM

per se

n

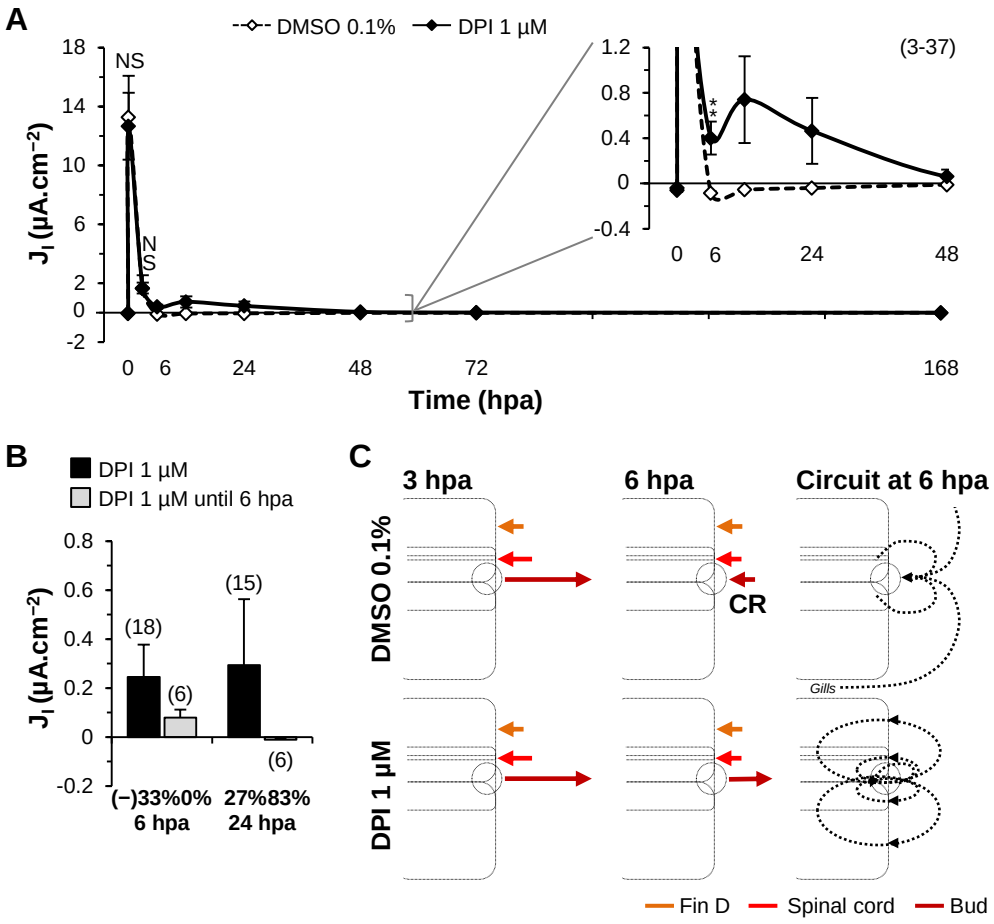

n specimens indicated in brackets.

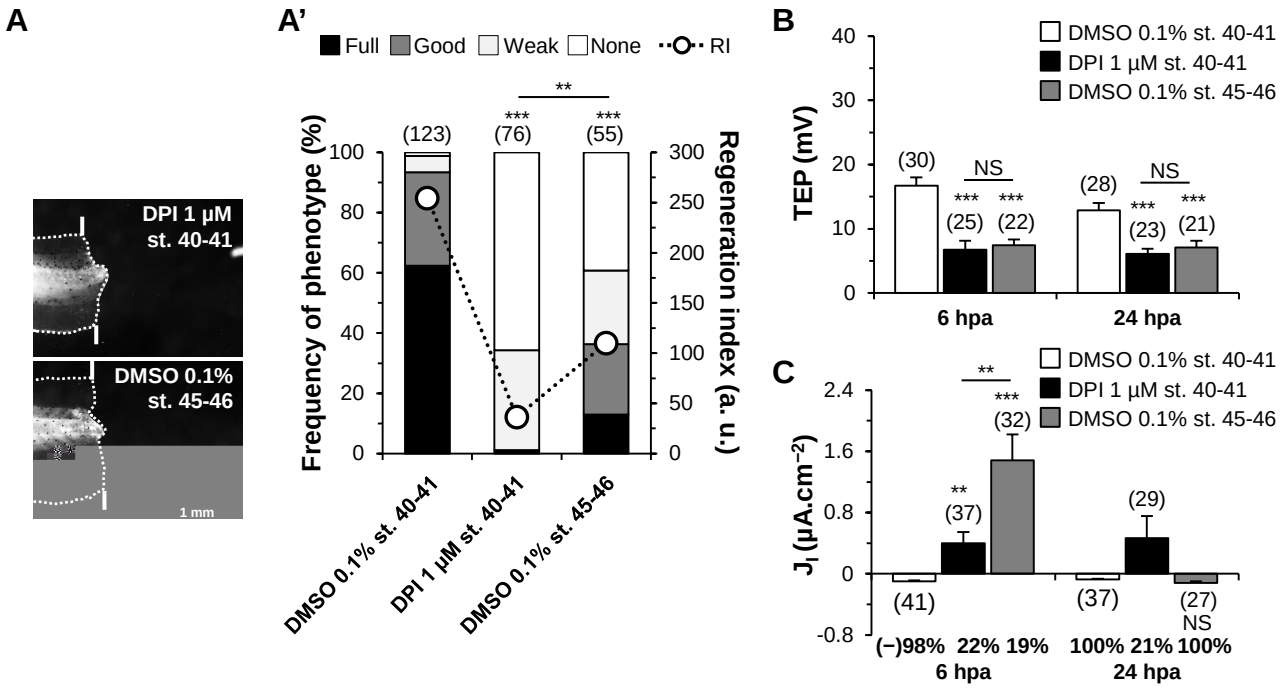

n specimens indicated between brackets.

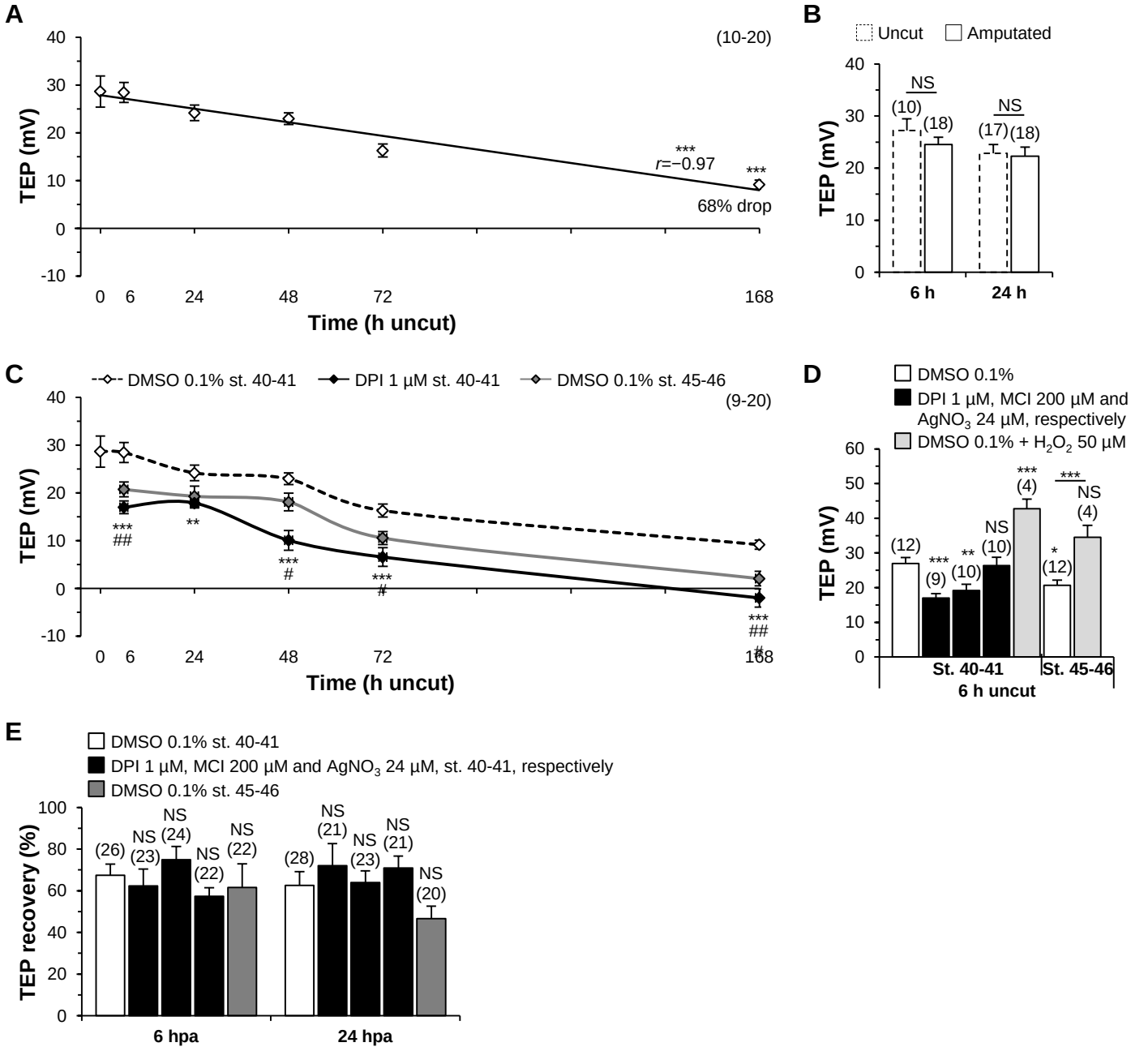

)LJ 526 PRGXODWRU\ DPSOLWXGH DQG DPSOLWXGH UHFRYHU\ SHUG***per se affect TEP in a regeneration-unspecific way. (A) Temporal profile of TEP during development in vehicle-control (DMSO 0.1%). Uncut trunk TEP is ontogeny-dependent,*** *i.e., inversely proportional to developmental time (r= ī0.97, P=0.0009). TEP significantly decreases up to 68% (n=17, P<0.0001) in a linear way (r^2=0.95) as tadpole develops in the same time-window of regeneration (7 days). Solid line: linear regression; r: correlation coefficient. (B) Trunk TEP baseline is amputation-independent and regeneration-unspecific in vehicle-control. (C) Temporal profile of TEP during development in depleted ROS (DPI 1 >M) and refractory period (vehicle-control) conditions. TEP baseline shifts in the*

vs. DPI 1 ÕM st. 40-41; #: vs. DMSO 0.1% st. 45-46. (D) Representative uncut time-point (6 h). Depleted ROS levels and amputation in refractory period shift TEP baseline the same way as bud subjected to the same conditions. Most data of DMSO 0.1% st. 40-41 and st. 45-46, and all data of DPI 1 ÕM are from C. (E) Depleted ROS levels and amputation in refractory period do not affect TEP recovery. This is the consequence of a similar shift in direction and magnitude of bud and trunk TEP in these conditions. n specimens indicated in brackets.

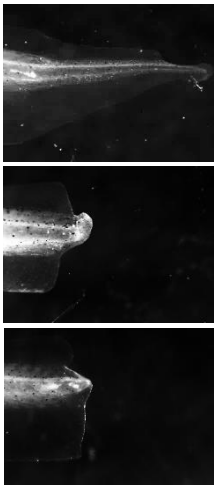

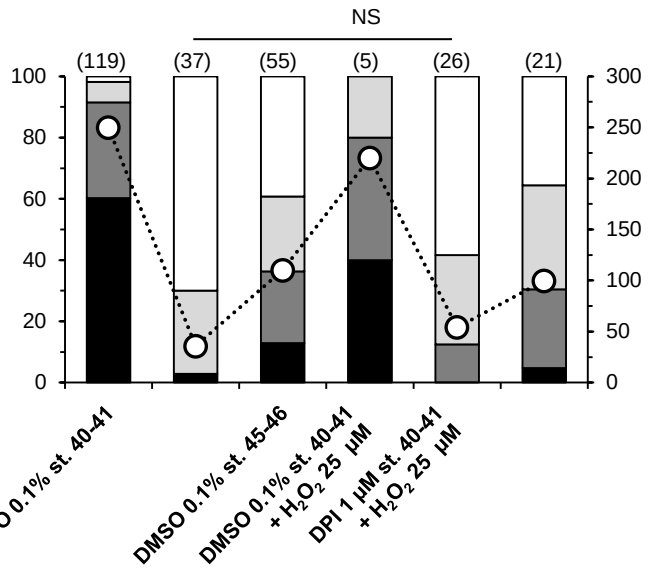

)LJ 16 (RHEXV [HQRSXV 2 ORVVDEDW\ WRUHFWH DQ QFH UHJHQHUDWRQ SUHVHQW WKURXJK UHJHQHUDWRQ $ 5HSUHVHQWDWLYH IRUP WDDSSXWHG IURP WDGSRROHV UHJHQHUDWRU RUHIDFWRU\ SHURGXDEUHWUHDWHGHFRQURO062 RU SRUPDFRORJLFDO WUHDWPHQW WKH ROG OHVDPSXWDWRQSODHVDOH EDP \$ 4XDOLWDWLDQ TXQWLWDWLDQDOVLV RIUHJHQHUDWRQIIHFWRUWKGLUHQW FRQGLWRQV UHJHQHUDWRQ[DX DUEWUDU\ *Values specimens indicated in brackets.*

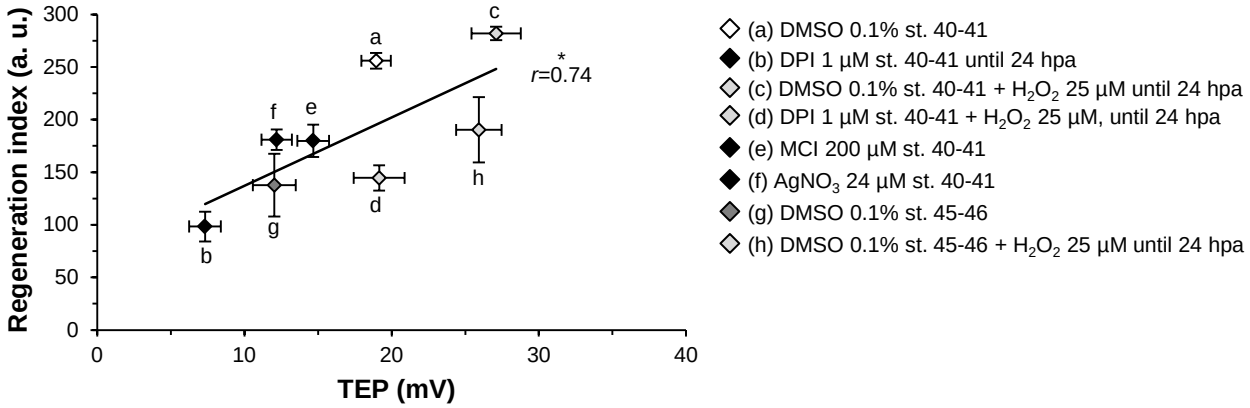

r^2=0.55); r: correlation coefficient (P=0.036).

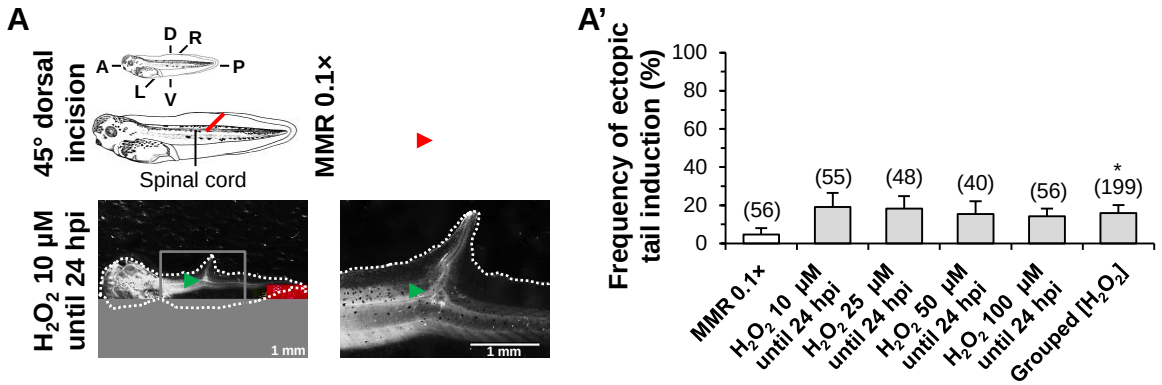

)LJ 6 (RFHQW 2 QFHVHFWRSE DEQUPDO RUFRPSOHWH WDLVRQGRUVO EQ
HHUQWK SDQO FRUG $ 7RSUW SDEO FKPDWE WDGSRDHW GHSEWQWK
HSHUPHQVDOGHQWRWKDQHGEQ %RWWRPUWDQWRSDQERWWSDQHQWSUHVQVDWH
GDVRWEQVDV QFRQVUQO 1DQ WSOHPHQVHGVKUHSUHVQVDWHGRUHVQVDWH
WD RWSRWEQVDV QFRQVUQO %RWWRPOHIWSDEO FORW WRFHFWDQQERWWRPUWSDEO
DUURWDGEQVHQSRQVLVHFWRSE WDLQFWRQ 1RWHWWHFWRSE WDLQFWRQ
DUURWDGEQVHQSRQVLVHFWRSE WDLQFWRQ 1RWHWWHFWRSE WDLQFWRQ SUHVQVHFWQ
WUFWRWHVLVHFWUQDQIQQ SHQVDWEQOORZGIORZ 6FDOHEDUPP $ (FWRSE
WDLQFWRQVGRVQHSHQHQW7WWFDW DWQHDWIRUWUPHSRWH RWVQ
UHODWLVOGRZVWUDEQRI + 2)UHTXHQRI DEQUPDO RU FRPSOHWH HFWRSE WDLQDWW
DXPHQWHGQ *ca. 10-15% above the ca. 5% baseline frequency of control. Exogenous H_2O_2 (tested 50 and 200 >M) loses ability to induce ectopic tails when present throughout 7 days (data not shown). n specimens indicated in brackets.*

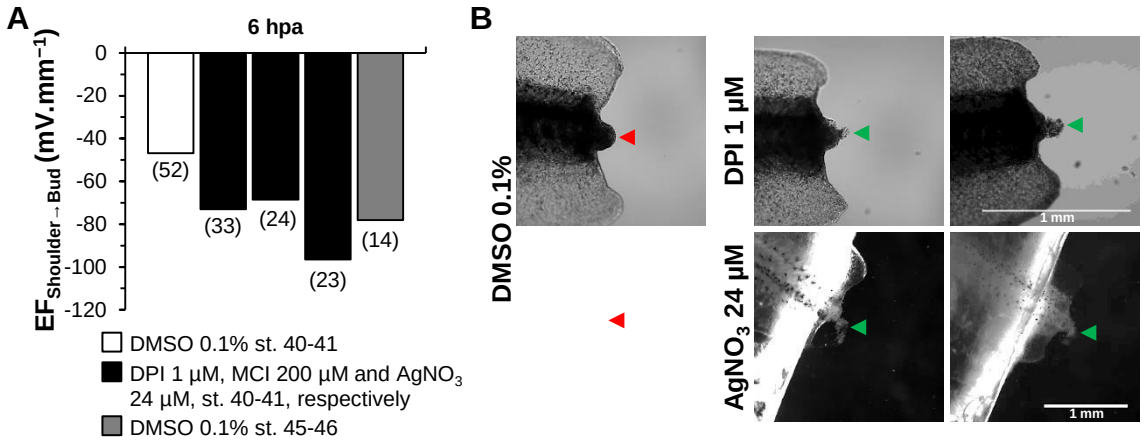

n specimens indicated in brackets.

2018. Published by The Company of Biologists Ltd Development (2018) 145, dev168625. doi:10.1242/dev.168625

CORRECTION

Correction: Early bioelectric activities mediate redox-modulated regeneration (doi: 10.1242/dev.142034)

Fernando Ferreira, Guillaume Luxardi, Brian Reid and Min Zhao

There was an error in Development (2016) **143**, 4582-4594 (doi: 10.1242/dev.142034).

The following text was omitted from the Funding section:

This work was also supported by the Air Force Office of Scientific Research (FA9550-16-1-0052).

The authors apologise to readers for this mistake.

CHAPTER VIII

8. *EARLY REDOX ACTIVITIES MODULATE* XENOPUS *TAIL REGENERATION*

(...) though pure dephlogisticated air might be very useful as a medicine, it might not be so proper for us in the usual healthy state of the body; for, as a candle burns out much faster in dephlogisticated than in common air, so we might, as may be said, live out too fast *(...)*

Joseph Priestley *in* Experiments and Observations on Different Kinds of Air (1775)

8.1 Publication overview

After the elucidation that ROS modulate regeneration by means of bioelectric activities, we further focus on the redox state during regeneration. It is well known that oxygen availability and tension modulate cell signalling and cell behaviour in disparate physiological conditions. Hypoxia – low partial pressure of O_2 – plays a critical role in angiogenesis, development, stem cells status and cancer activity. Hypoxia implications are essentially mediated by HIF-1α, the master regulator of O_2 homeostasis. HIF-1α is important for wound healing and it was shown, recently, to be necessary for mouse ear hole regeneration.

However, the interplay between O_2, ROS, hypoxia and HIF-1α during regeneration remains utterly obscure. Therefore, in this publication, we attempt to integrate those redox players, using the *Xenopus laevis* tadpole tail as the regeneration model. *Addenda* to and poster versions of the publication are provided (Appendix VII, X, XII)

We successfully report an early integration between O_2 and ROS that modulate regeneration. We unveil that the injury-induced influx of exogenous O_2 correlates with regeneration progression and efficiency, fuelling the production of the required ROS. Together, O_2 influx and ROS production tune the local pO_2 microenvironment to hypoxia, stabilizing HIF-1α. Temporal requirement assays reveal that HIF-1α is necessary for regeneration within the first 3 hours post-amputation. Drug-induced stabilization of HIF-1α induces regeneration in the non-regenerative refractory period. Modulation of ROS production and scavenging show that ROS do not stabilize HIF-1α directly but indirectly via hypoxia. An epistasis assay further supports this view. Searching for downstream mechanisms, we find that regeneration requires HSP90 in the same time-window of HIF-1α, and that electric current reversal – a hallmark of

regeneration identified in the previous publication (Chapter VII) – requires HIF-1α activity. Together, these suggested HSP90 as a putative and J_I reversal as a *de facto* downstream targets of HIF-1α to modulate regeneration.

The results published show a crosstalk between and integration of redox players to coordinate regeneration. The findings hold important implications for translational medicine.

8.2 Publication contributions

From publication's equivalent section: "F.F., VK.R., G.L. and M.Z designed the experiments. F.F. performed most experiments and analysed the data and results. F.F., VK.R. and K.Z. performed and analysed the Western blots. F.F. and G.L. performed the flow cytometry; G.L. analysed the flow cytometry. VK.R. and G.L. helped to interpret overall results. F.F., VK.R., G.L. and M.Z. outlined the manuscript. F.F. wrote the manuscript. All authors edited the manuscript."

8.3 Publication reprint

Vide infra.

nature COMMUNICATIONS

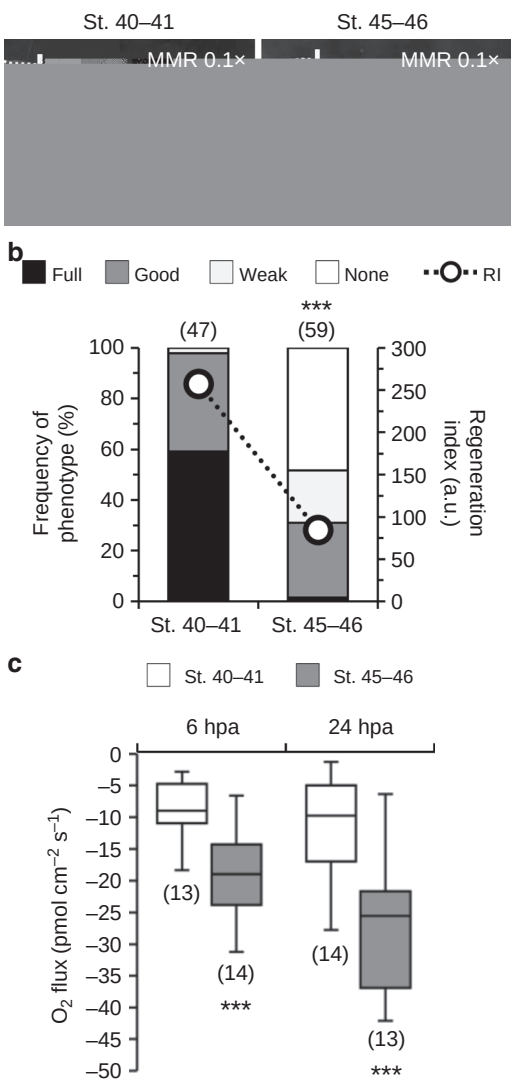

Fig. 2 Extracellular O_2 in ux predicts regeneration ef ciency. a Representative tails at 7 dpa in MMR 0.1× from tadpoles amputated in regenerative (st. 40–41) or refractory period (st. 45–46). White solid lines: amputation plane; scale bar: 1 mm. b Qualitative and quantitative analyses of regeneration ef ciency for the different conditions tested. RI regeneration index; a.u. arbitrary units. c O_2 ux measured in two different time-points in the bud of regenerative or refractory period tadpoles. Statistical analyses were performed by Fisher's exact test b, or unpaired Student's t-test (both two-tailed p-value) c. The data are presented as median ± min to max (with outliers). n biological replicates indicated in brackets. ***$p < 0.001$

$p = 0.033$; Supplementary Fig. 5d–f). Collectively, the similarity in responses observed regardless of the wound model and site suggest that elevated O_2 influx is a conserved response to injury. This applies to the cases where an O_2 gradient and consequent O_2 sink can be established upon wounding.

Exogenous O_2 fuels ROS production that is required for regeneration. To identify mechanisms underlying the correlation between O_2 influx and regeneration efficiency, we determined whether ROS production is dependent on the influx of exogenous O_2, i.e., of O_2 not from the circulatory system (endogenous O_2). For this, using diphenyleneiodonium (DPI) we inhibited the NADPH oxidase family[27] and measured the extracellular O_2 fluxes in regenerative tadpoles. We and others have demonstrated that DPI decreases ROS production during tail regeneration[6,8]. First, we verified the necessity of ROS in regeneration. DPI-treated tadpoles had a 12-fold reduction in the frequency of full phenotypes (from 73 to 6%); whereas, the frequency of none phenotypes increased from 0 to 31%. Consistent with previous studies[6,8], overall regeneration was significantly abolished (RI reduced from 273, $n = 19$, to 106, $n = 16$, $p < 0.0001$; Fig. 3a, b).

DPI-treated tadpoles showed a significant decrease in O_2 influx both at 6 hpa (114% reduction, from -12.03 ± 1.24, $n = 15$, to -5.63 ± 1.11 pmol cm^{-2} s^{-1}, $n = 16$, $p = 0.0006$; Fig. 3c) and 24 hpa (172% reduction, from -17.43 ± 2.12 pmol cm^{-2} s^{-1}, $n = 14$, to -6.40 ± 1.01 pmol cm^{-2} s^{-1}, $n = 17$, $p = 0.0002$; Fig. 3c).

Next, we investigated whether depletion of ROS had a similar effect in O_2 influx in the refractory period. Previously, we demonstrated that hydrogen peroxide (H_2O_2) is the key ROS necessary for and sufficient to induce regeneration[8], leading us to hypothesize that ROS production is deficient in refractory period tails. To determine if this was indeed true, we performed semi-quantitative imaging of ROS using HyPer transgenic tadpoles that have a constitutive genetically encoded H_2O_2-specific sensor[28]. Refractory period tadpoles presented significantly lower H_2O_2 levels than regenerative tadpoles at both 6 and 24 hpa (Supplementary Fig. 7a–c), proving the assumption. The use of a general ROS-sensitive dye in wild-type tadpoles also showed a reduction in overall ROS levels in the refractory period, validating HyPer results (Supplementary Fig. 7d, e). We next hypothesized that, due to lower H_2O_2 levels, DPI would not robustly affect the magnitude of O_2 influx. Indeed, treatment with DPI for 6 hpa did not significantly affect O_2 influx in comparison to vehicle-control (from -20.63 ± 1.71, $n = 17$, to -19.07 ± 2.22 pmol cm^{-2} s^{-1}, $n = 14$, $p = 0.576$; Fig. 3d) in refractory period tails. However, treatment with DPI for 24 hpa significantly decreased O_2 influx (43% reduction, from -21.34 ± 1.88, $n = 14$, to -14.93 ± 0.83 pmol cm^{-2} s^{-1}, $n = 15$, $p = 0.006$; Fig. 3d). This reduction in influx was fourfold lesser than the reduction observed with regenerative tadpoles (172%), further highlighting that ROS production in the refractory period was deficient.

To decouple enzymatic ROS production from ROS per se, we used the antioxidant trolox and quantified regeneration and measured the O_2 flux in the regenerative period. We and others demonstrated that antioxidant decrease ROS production and impair tail regeneration[6,8]. Similarly, trolox impaired regeneration in this study. The frequency of full phenotypes almost halved (1.7-fold decrease, from 69 to 40%) and the frequency of none phenotypes increased from 0 to 17%. Overall, regeneration was significantly impaired (RI reduced from 264, $n = 83$, to 180, $n = 96$, $p < 0.0001$; Fig. 3e, f). Trolox-treated tadpoles showed non-significant shifts in O_2 influx at 6 hpa (from -8.92 ± 2.09, $n = 8$, to -9.50 ± 1.56 pmol cm^{-2} s^{-1}, $n = 11$, $p = 0.824$; Fig. 3g) or 24 hpa (from -18.42 ± 2.10 pmol cm^{-2} s^{-1}, $n = 10$, to -17.09 ± 2.27 pmol cm^{-2} s^{-1}, $n = 10$, $p = 0.671$; Fig. 3g).

Altogether, ROS is a probable pathway by which O_2 influx correlates with regeneration efficiency in the regenerative tadpoles, but not likely in the refractory period tadpoles due to intrinsically impaired ROS levels.

HIF-1α is necessary for and suf cient to induce regeneration. Next, we sought downstream effectors capable of mediating ROS-driven O_2 influx and regeneration. Steady and long-term O_2 influx and ROS production are likely to influence the pO_2 in the bud. Thus, we tested whether the master mediator of hypoxia, HIF-1α, is necessary for regeneration. For this, we used echinomycin, a small-molecule DNA-binding inhibitor that precludes HIF-1α from binding to HRE, thus inhibiting its action[29].

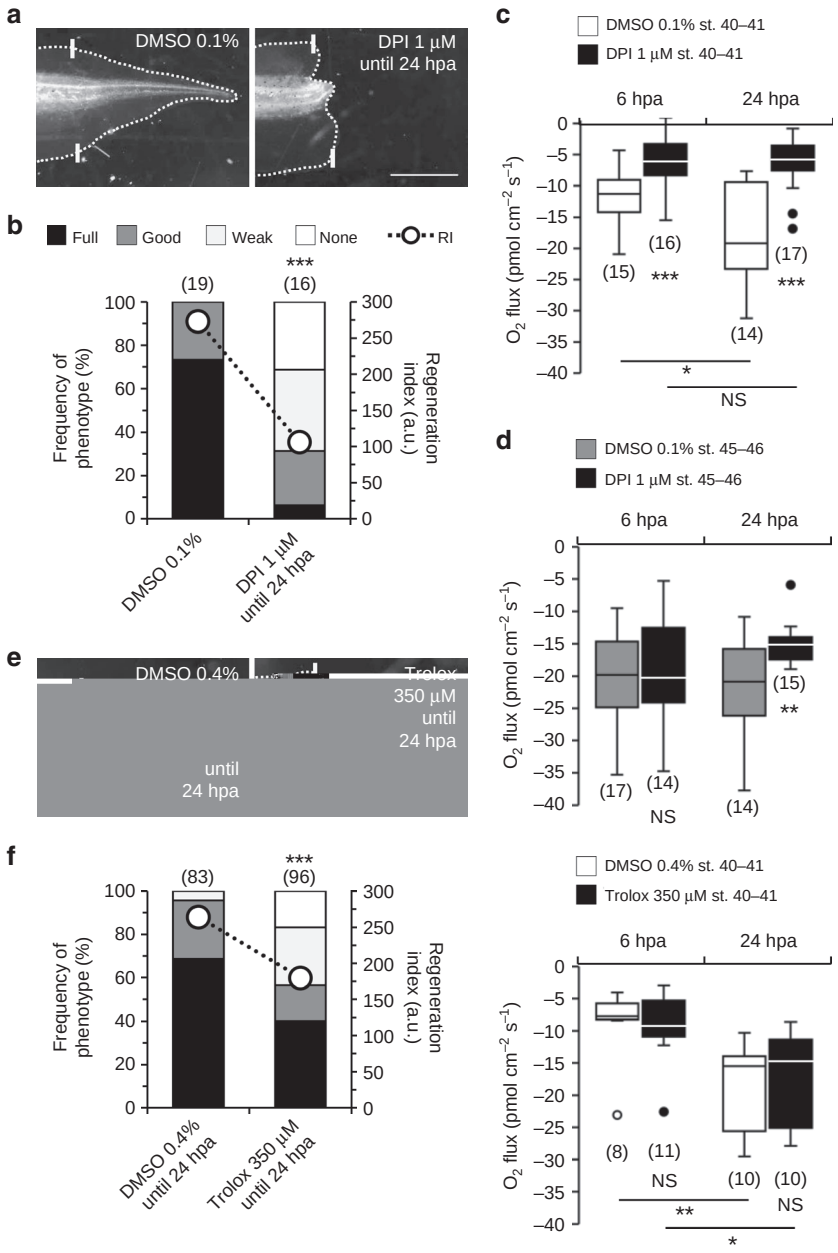

Fig. 3 Exogenous O_2 fuels ROS production that is necessary for regeneration. a–d O_2 in ux fuels ROS production in regenerative but not likely in refractory period tadpoles. a Representative tails at 7 dpa in vehicle-control and pharmacological treatment from tadpoles amputated at st. 40–41. b Qualitative and quantitative analyses of regeneration ef ciency for the different conditions tested. Most tadpoles from O_2 ux measurements. RI regeneration index. Stacked bars legend applies to f. O_2 ux measured in two different time-points in the bud of vehicle-control and pharmacological treatment from tadpoles amputated in regenerative c or refractory period d. e–g The magnitude of O_2 in ux is independent of ROS per se. e Representative tails at 7 dpa in vehicle-control and pharmacological treatment from tadpoles amputated at st. 40–41. f Qualitative and quantitative analyses of regeneration ef ciency for the different conditions tested. Tadpoles from O_2 ux measurements included in quanti cation. g O_2 ux measured in two different time-points in the bud of vehicle-control and pharmacological treatment from tadpoles amputated at st. 40–41. White solid lines: amputation plane; scale bar: 1 mm; a.u. arbitrary units. Statistical analyses were performed by Fisher's exact test b, f, or unpaired Student's t-test (both two-tailed p-value) c, d, g. Data are presented as median ± min to max (with outliers). n biological replicates indicated in brackets. NS non-signi cant; *$p < 0.05$; **$p < 0.01$; ***$p < 0.001$

Echinomycin-treated tadpoles had dramatically abrogated regeneration presenting only weak (tadpoles with incomplete or abnormal tail regeneration; 11% frequency) and none (89% frequency) phenotypes. Overall, RI reduced from 248 ($n = 48$) to 11 ($n = 55$, $p < 0.0001$; Fig. 4a, b). The first 24 hpa are more likely to present regeneration-specific events (Fig. 1c). Thus, we next performed an extensive exposure screen to determine the exact time-window of requirement for HIF-1α. First, we exposed the tadpoles to echinomycin for 24 hpa. This treatment was as penetrant as continuous exposure to HIF-1α inhibitor throughout regeneration (RI reduced to 19, $n = 48$, $p < 0.0001$; Fig. 4b). A refined exposure showed that echinomycin until 15 minpa was still equally penetrant with only 10% weak phenotypes and the remainder 90% presenting a none phenotype (RI reduced from 228, $n = 47$, to 10, $n = 47$, $p < 0.0001$; Fig. 4a, c). The complementary approach showed that echinomycin either from 1 or 2 hpa until the end of regeneration (7 days) impaired regeneration in an exposure-dependent way. Specifically,

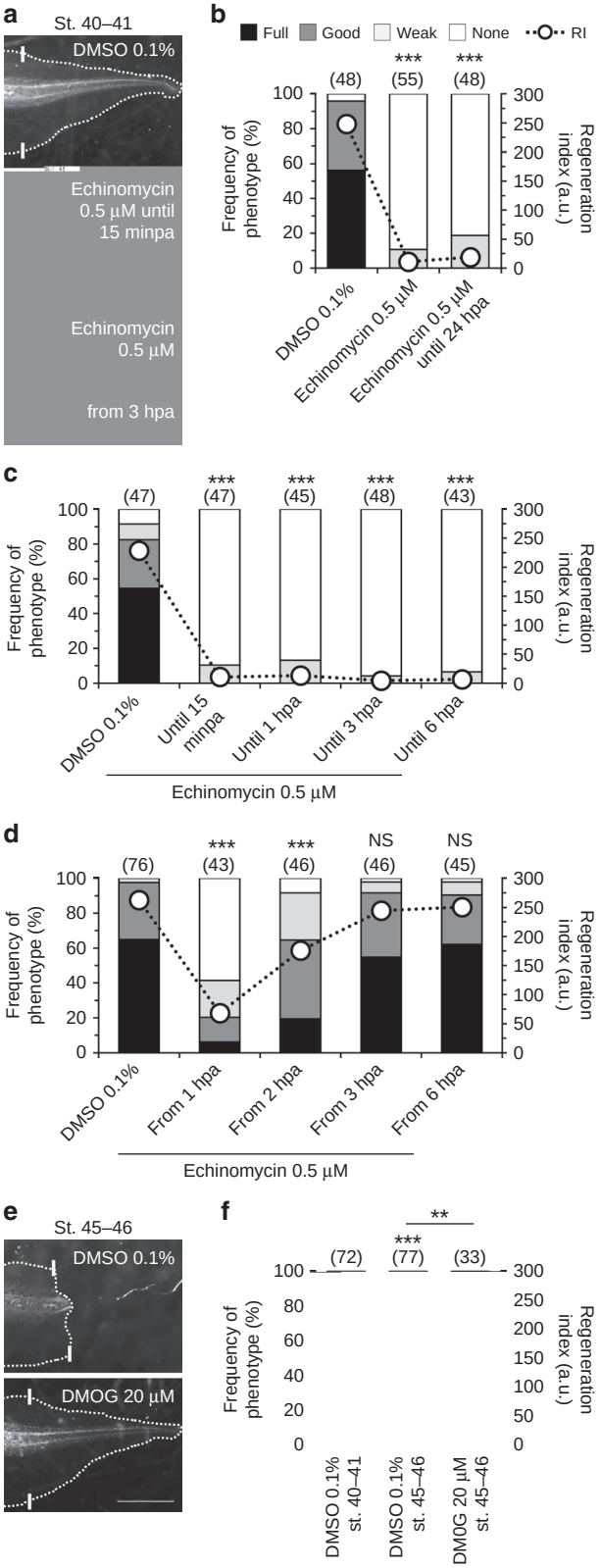

Fig. 4 HIF-1 is necessary for and sufficient to induce regeneration. a–d Loss of regeneration by HIF-1 inhibition and temporal requirement for HIF-1 activity during regeneration. a Representative tails at 7 dpa in vehicle-control and pharmacological treatment from tadpoles amputated at st. 40–41. b–d Qualitative and quantitative analyses of regeneration efficiency for the different conditions tested. RI regeneration index. Stacked bars legend in b applies to c, d, and f. e, f Induction of regeneration by HIF-1 stabilization. e Representative tails at 7 dpa in vehicle-control and pharmacological treatment from tadpoles amputated in refractory period. f Qualitative and quantitative analyses of regeneration efficiency for the different conditions tested. White solid lines: amputation plane; scale bar: 1 mm; a.u. arbitrary units. Statistical analyses were performed by Fisher's exact test (two-tailed p-value). n biological replicates indicated in brackets. NS non-significant; **$p < 0.01$; ***$p < 0.001$

treatment with echinomycin from 2 hpa decreased the frequency of full phenotypes by 3.4-fold (from 65 to 19%) and increased the frequency of none phenotypes from 0 to 8% (RI reduced from 263, $n = 76$, to 176, $n = 46$, $p < 0.0001$; Fig. 4d). Treatment with echinomycin from 3 hpa or beyond did not significantly impair regeneration. From 3 hpa, the frequency of full phenotypes slightly decreased (from 65 to 55%) and the frequency of good phenotypes (tail regeneration with minor defects) slightly increased (from 33 to 37%) in comparison to vehicle-control (RI from 263, $n = 76$, to 244, $n = 46$, $p = 0.347$; Fig. 4a, d). These results suggest that HIF-1α is essential for regeneration within the first 3 hpa.

Secondary validation of these results was performed using the alternative drug chetomin, a small-molecule transcription inhibitor of HIF-1α[30]. Chetomin also robustly inhibited regeneration and supported the observation that early stabilization of HIF-1α is essential for regeneration (Supplementary Fig. 9a, b). Drug-enhanced stabilization of HIF-1α with the PHD inhibitor dimethyloxallyl glycine (DMOG)[31] showed no effect in regenerative tadpoles (Supplementary Fig. 9a, c).

Next, we attempted to induce regeneration in the refractory period by stabilizing HIF-1α with DMOG. Compared with vehicle-control, DMOG-treated tadpoles almost doubled the frequency of full phenotypes (1.8-fold increase, from 8 to 14%) and decreased the frequency of none phenotypes by fivefold (from 33 to 7%). Overall, regeneration was significantly induced in refractory period by stabilization of HIF-1α (RI from 110, $n = 77$, to 170, $n = 33$, $p = 0.007$; Fig. 4e, f, Supplementary Fig. 9d) demonstrating the importance of HIF-1α stability. Short-term exposure to DMOG (until 24 hpa) did not induce regeneration, despite a slight increase in RI (to 126, $n = 56$, $p = 0.326$; Supplementary Fig. 9e).

Collectively, data demonstrate that HIF-1α is necessary for and sufficient to induce regeneration, suggesting HIF-1α as a candidate pathway downstream of ROS and by which O_2 influx correlates with regeneration efficiency in both regenerative and refractory period tadpoles.

Hypoxia correlates with HIF-1α stabilization that in turn regulates regeneration. Highest HIF-1α activity was delimited within 1 hpa. Subsequently, we tested whether ROS and refractory period affect hypoxia and HIF-1α stabilization in that time-window. First, using the hypoxia marker pimonidazole[32], we determined the level of hypoxia in the wound epithelium and prospective regeneration bud under all conditions. For a semi-quantitative analysis, cells proximal to the amputation plane were dissociated for flow cytometry. DPI-treated tadpoles had a significant reduction (by 41%) in the overall hypoxia compared with vehicle-control ($n = 3$ flows of 60 specimens, $p = 0.027$; Fig. 5a, b). In the refractory period, hypoxia was dramatically reduced by 70%, compared with the stage control ($n = 3$ flows of 60 specimens, $p = 0.032$; Fig. 5a, b, Supplementary Fig. 13d–f). No significant difference in hypoxia was observed in tadpoles with drug-stabilized HIF-1α (Fig. 5b, Supplementary Fig. 13g).

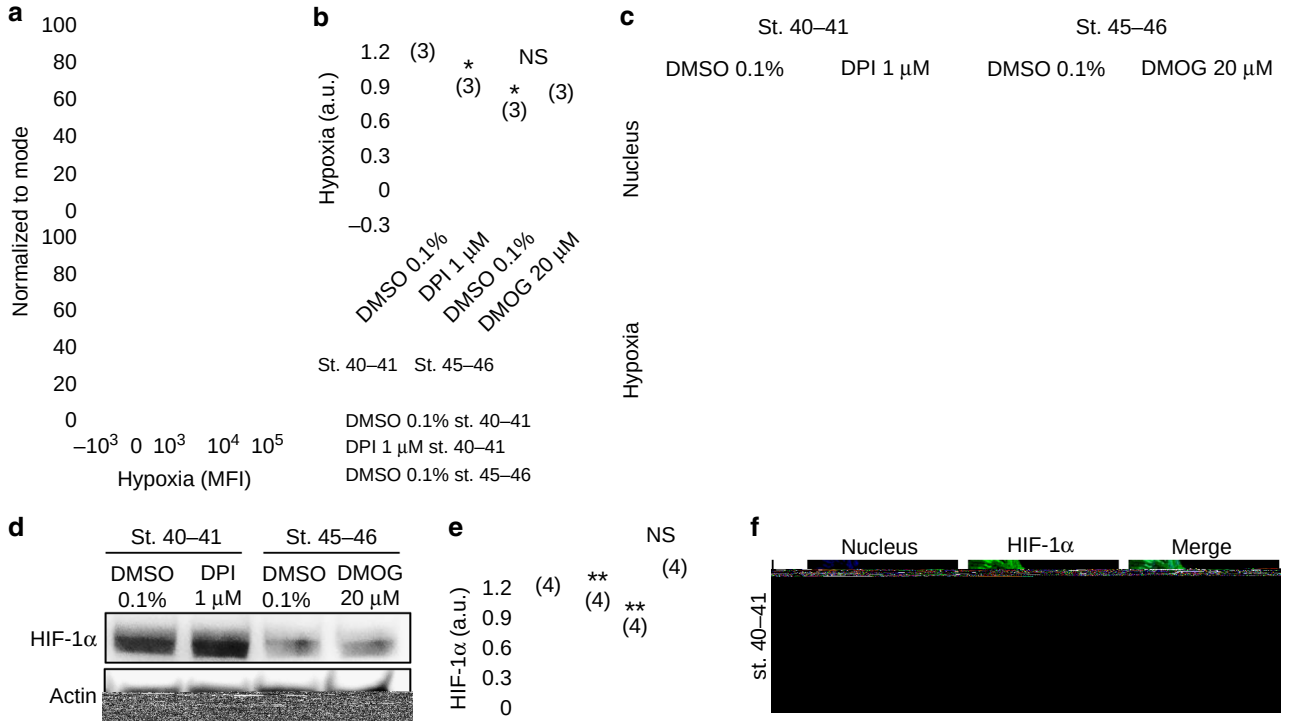

Fig. 5 Hypoxia and HIF-1

Hypoxia was then spatially resolved using the same marker by confocal microcopy. The wound epithelium was hypoxic but maximal hypoxia occurred in the prospective regeneration bud. Hypoxia was less penetrant in the DPI-treated tadpoles. In the refractory period, hypoxia was virtually absent in the tails of both vehicle-control and drug-stabilized HIF-1α tadpoles (Fig. 5c).

Next, we investigated the stabilization and localization of HIF-1α in the different conditions at 1 hpa. For a semi-quantitative analysis of HIF-1α levels, tail explants were collected for western blotting[33,34]. DPI-treated tadpoles significantly decreased HIF-1α stability levels by 20% compared with the vehicle-control ($n = 4$ blots of 120 specimens, $p = 0.007$; Fig. 5d, e, Supplementary Fig. 14). DPI decreased both hypoxia and HIF-1α stability, suggesting that ROS might not directly stabilize HIF-1α. To test this, we performed three assays: treated tadpoles with ROS scavenger trolox and determined (i) hypoxia and (ii) HIF-1α stability levels; and (iii) treated tadpoles with NADPH oxidases inhibitor at a dosage higher by one order of magnitude (DPI 10 µM until 1 hpa) and determined HIF-1α stability levels. Treatment with trolox neither affected hypoxia nor HIF-1α levels (Supplementary Fig. 15a–c), and treatment with the higher dose of DPI did not decrease HIF-1α levels proportionately (Supplementary Fig. 15d, e). In the refractory period, HIF-1α levels were dramatically decreased in half (51%), compared with the stage control ($n = 4$ blots of 120 specimens, $p = 0.001$; Fig. 5d, e). DMOG-treated tadpoles had a 36% non-statistically significant increase in HIF-1α stability compared with vehicle-control st. 45–46 ($n = 4$ blots of 120 specimens, $p = 0.343$; Fig. 5d, e). This effect may probably have been more penetrant and significant if exposure to DMOG were larger than 1 h (other studies typically use 6 or 24 h)[31]. Intriguingly, both uncut and amputated whole tadpoles had drastic differences in HIF-1α stability levels, which were far higher in regenerative than in refractory period tadpoles (Supplementary Fig. 16). These point to an age-dependent stability pattern that might have implications in developmental phenomena beyond regeneration.

HIF-1α was then spatially resolved using confocal microcopy. We showed that HIF-1α was highly stabilized in the wound epithelium and prospective regeneration bud. Importantly, co-localization with the nucleus inferred robust transcriptional activity (Fig. 5f).

Collectively, data demonstrate strong correlations between hypoxia penetrance and HIF-1α stability levels necessary for regeneration. Further, data show that ROS stabilizes HIF-1α indirectly, i.e., via hypoxia.

HIF-1α does not act downstream of ROS to modulate regeneration. To further integrate ROS and HIF-1α, we investigated whether ROS acts upstream of HIF-1α to modulate regeneration.

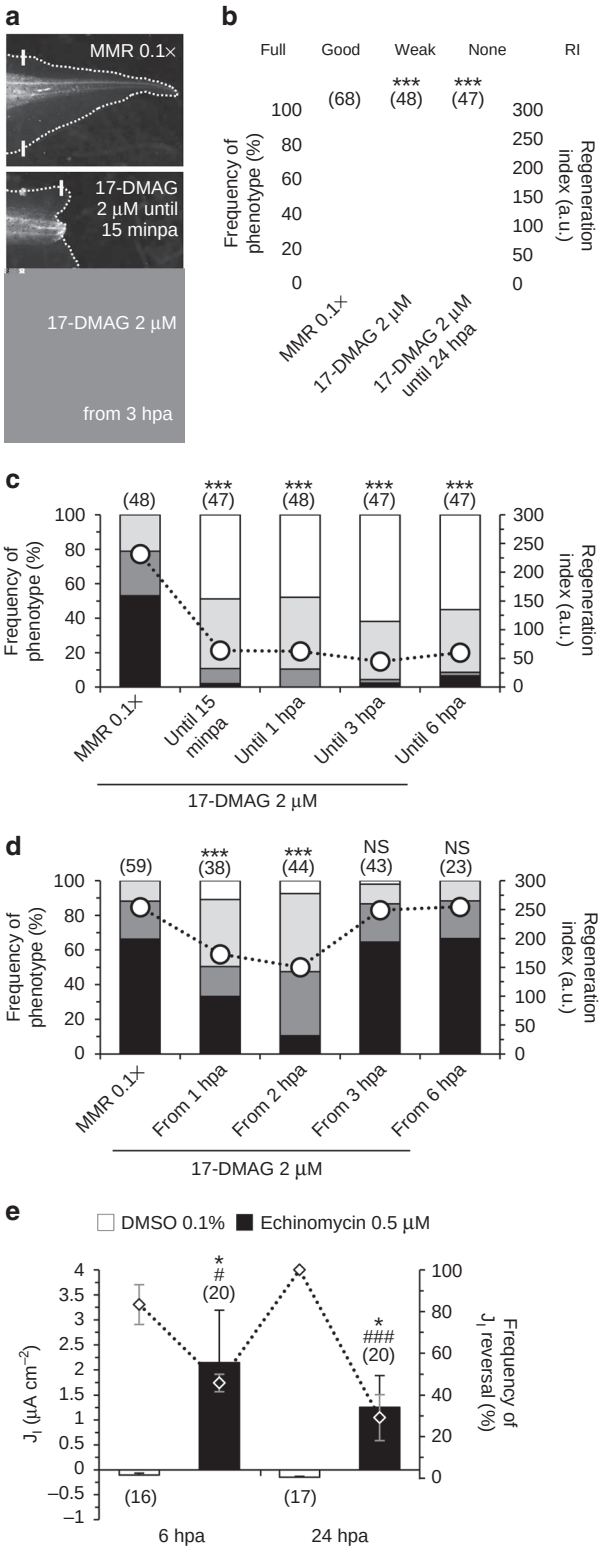

Fig. 7 HSP90 is a putative and J_I reversal is a de facto downstream targets of HIF-1 . a–d Loss of regeneration by HSP90 inhibition and temporal requirement for HSP90 activity during regeneration. a Representative tails at 7 dpa in control and pharmacological treatment from tadpoles amputated at st. 40–41. b–d Qualitative and quantitative analyses of regeneration ef ciency for the different conditions tested. White solid lines: amputation plane; scale bar: 1 mm. RI regeneration index; a.u. arbitrary units. Stacked bars legend in b applies to c and d. e HIF-1 regulates the J_I reversal hallmark. J_I in regeneration bud measured in two different time-points in vehicle-control and echinomycin-treated tadpoles amputated at st. 40–41. Statistical analyses were performed by Fisher's exact test b–d; e #, vs. J_I reversals), or unpaired Student's t-test (both two-tailed p-value) (e: *, vs. J_I magnitude). The data are presented as mean ± s.e.m. n biological replicates indicated in brackets. NS non-signi cant; */#$p < 0.05$; ***/###$p < 0.001$

influx was independent of ROS per se, excluding a feedback loop between reagent (O_2) and product (ROS). Inhibition of HIF-1α dramatically abolished regeneration, while its stabilization induced regeneration in the refractory period. Hypoxia correlated with HIF-1α stability levels, whose co-localization in the prospective bud underlies regeneration efficiency. Experiments modulating ROS production and scavenging demonstrated that ROS did not stabilize HIF-1α directly but indirectly via hypoxia. An epistasis assay confirmed that HIF-1α did not act downstream of ROS to modulate regeneration. Finally, we analyzed candidate downstream targets of HIF-1α. HSP90 was found to be necessary for regeneration in the same time-window as HIF-1α, and HIF-1α activity was required for electric current reversal. Together, these suggested HSP90 as a putative (correlative) and J_I reversal as a de facto (causative) downstream targets of HIF-1α to modulate regeneration. Altogether, the results provide evidence for an instantaneous injury-induced O_2 sink that fuels required ROS production and together stabilize HIF-1α by hypoxia to modulate regeneration possibly via HSP90 and J_I reversal. This sequence of events is postulated as a mechanism of action (Fig. 8, Supplementary Fig. 19).

Intriguingly, while recording, many O_2 flux measurements appear to stabilize in an oscillatory rather than in a flat plateau. O_2 oscillations with a period ranging between ~2 and 4 min (frequency between ~4 and 8 mHz) were relatively common (Supplementary Fig. 6). This study was not designed to address O_2 oscillations (which likely require longer recordings, e.g., of 30 min); nonetheless, they might be an epiphenomenon of oscillations in metabolism (e.g., mitochondrial activity) or signaling (e.g., Ca^{2+}), and/or might be an intrinsic signaling cue[39,40]. That being said, NAD(P)H metabolite concentration is oscillatory[41]. NADPH donates an electron to O_2 to generate a ROS; therefore, it is feasible to speculate that O_2 oscillations might be, at least in part, the result of oscillatory O_2 oxidation, since exogenous O_2 fuels ROS. The roles of O_2 oscillations in general and during regeneration in particular warrant future work (Supplementary Fig. 6)[42,43].

The existence of O_2-specific plasmalemmal translocators (passive or active) is unknown. Aquaporin-1 has been identified as a non-selective translocator of O_2[44]; however, anatomic and physiologic intricacies such as the rete mirabile in fish swim bladder, point to no active (against gradient) O_2 transmembrane transporters. Thus, with or without a barrier, the O_2 flux follows passive diffusion in a supply-demand way. Injury disrupts local vasculature and together with infection, inflammation, oxidative burst, cell migration, and cell proliferation, comprise the factors leading to chronic wound hypoxia[45,46]. This established rationale may lead to a paradox where large amounts of O_2 are being consumed in multiple fronts without an efficient blood supply. In wound and regeneration models, ROS have been shown to precede oxidative burst; in fact, ROS attract the immune cells responsible for the oxidative burst[6,47,48]. Further, ROS has been consistently demonstrated as essential for regeneration[3–8]. The same studies showed that ROS production is a steady and long-lasting response to injury, creating an additional burden for O_2 demand, further highlighting the paradox. Therefore, we

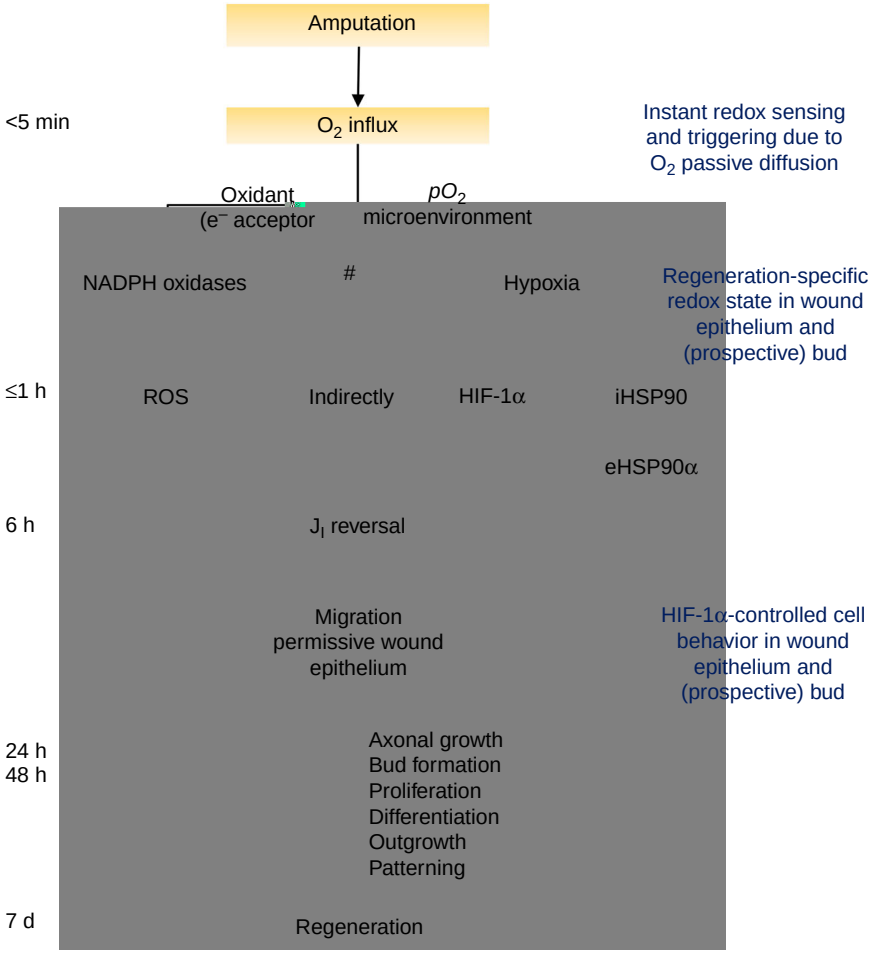

Fig. 8 Stepwise model integrating redox state activities during regeneration. Instantaneous injury-induced O_2 in ux fuels ROS production and together tune a permissive pO_2 microenvironment—hypoxia—for HIF-1 stabilization. Early time-window up to 6 hpa is focused, because is when the magnitude of O_2 in ux correlates with regeneration and when required ROS and HIF-1 activities occur. ROS per se do not feedback with the magnitude of O_2 in ux. ROS do not directly stabilize HIF-1 but do so indirectly by regulating hypoxia in the bud owing to local O_2 consumption and O_2 in ux demand (Supplementary Fig. 19). We infer that intracellular HSP90 is at least partially required for early hypoxia-induced stabilization of HIF-1 , resulting in the secretion of eHSP90 . 6 hpa is also the time-point of the hallmark J_I reversal, an accurate predictor of regeneration ef ciency that mediates redox-modulated regeneration. HIF-1 regulates J_I reversal, pointing to an integration of HIF-1 with the bioelectric state, in series or in parallel with ROS. Mechanistically, HIF-1 modulates regeneration via HSP90/eHSP90 and J_I reversal presumptive effect on cell migration migration to form the wound epithelium and/or regeneration bud. iHSP90: intracellular HSP90; eHSP90 : extracellular HSP90 . Solid line arrows: demonstrated; dotted line arrows: hypothesized/probable. # mechanism schematized in Supplementary Fig. 19; * demonstrated in ref. [8]

theorized that exogenous O_2 fuels local ROS production in the regeneration bud. Indeed, using reverse analysis methodology, we showed that at least half to two-thirds of the required ROS production in regenerative tadpoles depends on influx of exogenous O_2 into the bud. Instant ROS production might prevent an acute hyperoxia, which would derive from the observed instant and steady O_2 influx. Nonetheless, some level of acute hyperoxia or injury oxidation is not entirely excluded, and it could, for example, contribute to localized cell death. The use of an antioxidant proved that production, not ROS per se, decreased O_2 influx causally. Moreover, unaltered O_2 influx in antioxidant-treated tadpoles showed that ROS do not feedback with the magnitude of O_2 influx, suggesting that NADPH oxidases activity is the major driving force for O_2 flux. Other motive forces (cumulative) are likely to be proliferation and bud maturation at 24 hpa, since a peak in O_2 influx was noted at this time-point. Our data does not entirely exclude the possibility of O_2-induced ROS production as previously observed[49]. Thus, it is likely that exogenous O_2 modulates regeneration by fueling required ROS production, making O_2 a potential target to enhance regeneration, in addition to its routine applications in chronic wounds[50–52].

The higher O_2 influx in the refractory period was independent of its deficient ROS production. This raises two important questions: how the higher O_2 influx mechanistically abolishes regeneration? and, why an elevated O_2 influx occurs during the refractory period when ROS production is lower? For the first question, we postulated that a higher O_2 influx leads to a non-hypoxic bud. This non-permissive oxic microenvironment degrades HIF-1α, subsequently abolishing regeneration. Our data on the quantification and imaging of hypoxia and HIF-1α substantiate this rationale. For the second question, we inferred that depleted ROS production and negligible proliferation and bud maturation, point to less demand for O_2. Nurturing the paradox, refractory period tails have a wound epithelium thicker than regenerative tadpoles[24,53,54] and hence may be less permeable to O_2. Size does not explain the robust influx though. Altogether, the driving causes for the regeneration-dependent higher O_2 influx

by local (University of California, Davis) Institutional Animal Care and Use Committee (protocol no. 16766).

Tail regeneration assay. Half of the tail of randomized normal tadpoles, equilibrated to room temperature and immobilized in myosin inhibitor N-benzyl-p-toluene sulfonamide (BTS; Tocris Bioscience, cat. no. 1870) 50 μM, was amputated with a scalpel (blade no. 10; Feather Safety Razor) (Fig. 1a). Experimental conditions were refreshed daily and tail photomicrographs were taken at 7 days post-amputation (dpa). Regeneration efficiency was scored using the regeneration index (RI), calculated from the frequencies (f) of the outcome predefined phenotypes using the following equation[23,53]:

$$RI = (f_{Full} \times 3) + (f_{Good} \times 2) + (f_{Weak} \times 1) + (f_{None} \times 0), \quad (1)$$

RI ranges from 0 (if all none) to 300 (if all full), in arbitrary units. For guidance, when RI is 250 it represents virtually unimpaired regeneration; and, when RI is 100 it represents drastically impaired regeneration. Over length or area, RI provides an advantageous measure of the morphogenetic quality (axes outgrowth and patterning) of regenerated tails.

Fin wound healing assay. Randomized normal tadpoles (st. 40–41) equilibrated to room temperature and immobilized were wounded using a 2 mm biopsy punch (Miltex, cat. no. 33–31) that removed a rounded portion of the dorsal fin (at A/P axis intersection; Supplementary Fig. 4a,b). Healing was followed and photomicrographed as in the amputated tails. Wound area was measured using ImageJ (http://rsbweb.nih.gov/ij/) and treated using Excel (Microsoft).

Oocytes wounding. Oocytes equilibrated to room temperature were wounded using a heat-pulled glass capillary with a broken tip (diameter of ~75 μm) mounted on a manual micromanipulator and impaled through the oocyte membrane[26]. Wounds were made around the center of the animal pole. A nylon mesh (800 μm pore size; nitex mesh) glued to the Petri dish provided support and immobilization to the oocytes during capillary impalement and optrode measurements (Supplementary Fig. 5a).

Mice skin wounding. Killed mice were kindly dispensed by Yunyun Shen (UC Davis; Department of Occupational and Environmental Health, Zhejiang University, China), after eyes removal for unrelated purposes[65]. A square patch of hair from the back (dorsal axis) was removed with hair remover cream (Nair). Naked skin was cleaned with ethanol 75% and washed with deionized water prior to wounding. A full thickness skin wound of <1 cm length was made at around the L/R and A/P axes intersection using a scalpel (blade no. 15; Henry Schein) (Supplementary Fig. 5d).

Pharmacologic modulations. DPI (Sigma-Aldrich, cat. no. D2926) 1 and 10 mM, trolox (Cayman Chemical, cat. no. 10011659) 80 mM, echinomycin (Cayman Chemical, cat. no. 11049) 0.5 mM, chetomin (Cayman Chemical, cat. no. 14437) 0.5 mM, and DMOG (Cayman Chemical, cat. no. 71210) 20 and 100 mM were stocked in dimethyl sulfoxide (DMSO; Sigma-Aldrich, cat. no. D2650) at −20 °C. 17-DMAG (Selleckchem, Cat. no. S1142) 765 μM was stocked in phosphate-buffered saline (PBS; HyClone, cat. no. SH30264) at −20 °C. Working solutions—drugs and vehicle (DMSO) reconstituted in MMR 0.1×—were freshly prepared prior to application via immersion (bath), in the doses and exposures specified. Extensive randomized dose-exposure screenings were designed for a final DMSO concentration of typically 0.1% (Supplementary Figs. 8, 10–12, 17). For delimited exposures, drugs were washed in and to the respective control (MMR 0.1×) or vehicle-control (DMSO 0.1%). Tadpoles treated with the light-sensitive drug 17-DMAG were followed in the dark. Dosage and exposure used did not meaningfully affect development or mortality (Supplementary Figs. 8, 10–12, 17). However, long-term exposure (throughout regeneration) to 17-DMAG resulted in increased mortality after 6 dpa. Therefore, tail photomicrographs were taken at 6 dpa, exclusively for this case. This change does not compromise data reliability, because tails at 6 or 7 dpa have the regeneration phenotype equally well defined. Matched sibling controls were performed for every drug treatment used in all readouts.

Optrode measurement. Extracellular net dissolved O_2 flux (J_{O_2}) was measured non-invasively with a self-referencing O_2-selective optrode. This probe is a pulled optical fiber with a solid state O_2-sensitive fluorophore coating in the tip. O_2 is quantified by fluorescence quenching after excitation of the fluorophore with blue–green light (= 505 nm) from a LED source[66]. System has high spatial (~20–50 μm) and temporal (~2 s) resolutions. Unlike polarographic electrodes, optrode does not consume O_2 in the measurement and has the capacity to measure in the gas phase. Our measurements were performed always in the liquid phase (experimental condition specified). Ready-to-use needle-type housing optrodes (PreSens, NTH-PSt1-L5-TS-NS40) were incorporated into the turn-key system scanning micro-optrode technique (SMOT; Applicable Electronics).

Prior to measurements, a two-point calibration of the optrode was performed in 0 and 20.95% pO_2 solutions. 0% pO_2 was achieved with saturated sodium bisulfite (mixture of $NaHSO_3$ and $Na_2S_2O_5$; Sigma-Aldrich, cat. no. 243973) 2 M and 20.95% pO_2 was achieved with bubbled deionized water; for the bubbling was used

and mean pixel intensity was measured from a circular ROI placed in the (prospective) regeneration bud and in the background (annotated in Supplementary Fig. 7a). After background subtraction, a final pixel intensity value was achieved for both 405/515 and 488/515 nm spectra. The values obtained with ex/em at 405/515 nm were always very low (thus considered as background fluorescence) and did not shift across conditions (ROS/H_2O_2/amputation); although fluorescence intensities varied markedly across conditions in the 488/515 nm ex/em spectra. Thus, a ratio of intensities at [488/515 nm] to [405/515 nm] would have resulted in very large values that may falsely be perceived artefactual. Therefore, for clarity, we only present the values for fluorescence obtained with ex/em at 488/515 nm and considered the fluorescence values in the ex/em at 405/515 nm spectra as background intensities in this study. The acquisition settings were kept constant across experiments to allow for ready cross comparison. Technical negative controls (for autofluorescence and wavelength selectivity), transgenesis' negative control (i.e., no HyPer expression) and experimental positive control (high H_2O_2) gave conservative expected readouts (Supplementary Fig. 7a). Data and metadata were acquired and extracted using FluoView (Olympus) and treated using ImageJ and Excel.

ROS **fl**uorescence imaging. ROS was imaged and semi-quantified using the vital dye chloromethyl derivative of 2',7'-dichlorofluorescein (CM-H_2DCFDA; Molecular Probes; cat. no. C6827) in wild-type tadpoles. Stock dye was freshly prepared in anhydrous DMSO (Sigma-Aldrich, cat. no. 276855) at 1 mM. Tadpoles were incubated at room temperature in the dark in fresh CM-H_2DCFDA 10 µM for 1 h. Dye was washed out prior to fluorescence imaging. Individually immobilized tadpoles at the specified condition were placed in a small Petri dish under a fluorescence upright microscope (Zeiss Lumar V12) with attached monochromatic CCD camera (Zeiss AxioCam MRm). Tails were imaged using the GFP (488 nm) filter set channeling the light from a metal halide lamp of a fluorescence illumination system (EXFO X-Cite 120). Fluorescent images were pseudo-colored in gray and mean pixel intensity was measured from a rectangular ROI englobing the whole-imaged tail and a circular ROI in the background (Supplementary Fig. 7d). After background subtraction, a final pixel intensity value was achieved for the GFP channel. The acquisition settings were kept constant across experiments to allow for ready cross comparison. Technical negative controls (for autofluorescence and wavelength selectivity) and experimental positive control (high H_2O_2) gave conservative expected readouts (Supplementary Fig. 7d). Data and metadata were acquired and extracted using AxioVision software (Zeiss) and treated using ImageJ and Excel.

Flow cytometry. Hypoxia was semi-quantified by flow cytometry (fluorescence-activated cell sorting, FACS) of dissociated cells from tail explants[70] using the marker pimonidazole (Hypoxyprobe, cat, no. HP2-100Kit). In hypoxia or pO_2 less than 1.1% (8 mmHg or 11 hPa) at 22 °C (mean room temperature), pimonidazole is reductively activated, forming stable adducts with thiol-containing proteins where antibody binds. Tadpoles were incubated in pimonidazole HCl 300 µM for 1 h and, per condition, 20 tail explants (0.5 mm proximal to amputation plane) were incubated in 1 ml of dissociation solution composed of DNase I 100 U ml^{-1} (Roche, cat. no. 4716728001) and Liberase 0.25 mg ml^{-1} (Roche, cat. no. 5401119001) (in PBS), at 28 °C for ~30 min. Cells were washed (FACS buffer: bovine serum albumin (BSA) 1% in PBS) and live/dead stained (Aqua stain; Life Technology, cat no. L34965) at room temperature for 30 min. After fixation (formaldehyde 3.7% in PBS), cells were incubated in mouse IgG_1 anti-pimonidazole fluorescein (FITC)-conjugated monoclonal antibody 1:50 (in FACS buffer) at room temperature for 1 h. Cells were passed through a 35 µm cell strainer (Corning, 352235) and 20,000 to 25,000 cells were analyzed on a BD LSRFortessa flow cytometer (BD Biosciences). Geometric mean fluorescence intensities (MFI) were calculated per condition after gating live single cells (Supplementary Fig. 13a–c). Across experiments, MFI were standardized (Supplementary Fig. 13h, j) using the equation:

$$x_{FMO}(MFI) = \frac{x(MFI) - FMO(MFI)}{FMO(SD)}, \quad (4)$$

where x_{FMO}(MFI) is the standardized geometric mean fluorescence intensity of hypoxia per experiment, x(MFI) is the geometric mean fluorescence intensity of hypoxia per experiment, FMO(MFI) is the geometric mean fluorescence intensity of the fluorescence minus one (FMO) per experiment and FMO(SD) is the standard deviation of the FMO per experiment. Standardization method was then applied per condition to obtain final geometric MFI value. Data were acquired using FACSuite (BD Biosciences) and treated using FlowJo (FlowJo).

Immunohistochemistry. Hypoxia was imaged by immunofluorescence of marker pimonidazole in cryosections, as recommended by marker's manufacturer. Tadpoles were incubated in pimonidazole HCl 300 µM for 1 h, fixed in paraformaldehyde (PFA) 4% at 4 °C for 2 h, dehydrated in sucrose 30% (in PBS) at 4 °C overnight and embedded in optimal cutting temperature (OCT) compound for sectioning in a cryotome. Slides with 5 µm sections were rehydrated and permeabilized (Tris-buffered saline with Tween 20 0.1%, TBST) for 10 min, blocked (goat serum 10% in PBS, plus Tween 20 0.1%) at 37 °C for 1 h and incubated in mouse IgG_1 anti-pimonidazole FITC-conjugated monoclonal antibody 1:50 (in blocking solution) at room temperature for 1 h. After washings (TBST), slides were incubated with DAPI (Novus Biologicals, cat. no. NBP2-31156) 1:1000 (in PBS) for 5 min and mounted (Fluoromount-G; SouthernBiotech, cat. no. 0100-01).

HIF-1α was spatially imaged by immunofluorescence in cryosections. Slides were obtained and treated as above with a difference in the blocking solution (goat serum 10% in PBS, plus Triton X-100 0.3%). Slides were incubated in rabbit anti-HIF-1α primary polyclonal antibody (Abcam, cat. no. ab2185) 1:500 (in blocking solution) at 4 °C overnight. After washings (TBST), slides were incubated in goat anti-rabbit IgG (H + L) Alexa Fluor 488-conjugated secondary antibody (Jackson ImmunoResearch Laboratories, cat. no. 111-545-144) 1:200 (in blocking solution) at room temperature for 1 h, stained with DAPI and mounted.

Slides were imaged using UPLSAPO 20×/NA 0.75 and PLAPO 40×WLSM/NA 0.90 (water) objectives (Olympus) mounted in an inverted Olympus FV1000 confocal microscope. Excitation wavelengths were 405 nm for DAPI and 488 nm for FITC/Alexa Fluor 488. The imaging settings were kept constant across conditions and experiments to allow reliable cross comparison. Control slides without antibodies had conservative readouts; however, owing to autoflorescence in the 488 nm excitation, up to the first quarter of the fluorescence intensity signal was excluded. Several independent experiments were performed. Data and metadata were acquired and extracted using FluoView (Olympus) and treated using ImageJ (http://rsbweb.nih.gov/ij/) and Excel.

Western blotting. HIF-1α stability levels were semi-quantified by western blotting[33,34]. Per condition, 30 tail explants (0.5 mm proximal to amputation plane) were incubated for 30 min on ice and homogenized in 75 µl of cold lysis solution composed of RIPA buffer (Thermo Scientific, cat. no. 89900) with a protease inhibitor mix (Halt cocktail 3× and EDTA 1× (Thermo Scientific, cat. no. 78430), calpain inhibitor I 260 µM (Cayman Chemical, cat. no. 14921) and MG-132 5 µM (Selleckchem, cat. no. S2619)). For whole tadpoles' analysis, we used 5 tadpoles lysed in 100 µl lysis solution. Samples (40 µg; DC protein assay; Bio-Rad, cat. no. 5000111) were loaded into 4–12% Novex gels (Invitrogen, cat. no. XP04120) for electrophoresis. Following transfer, nitrocellulose membranes (Invitrogen, cat. no. LC2001) were washed (TBST), blocked (fetal bovine serum 10%, SuperBlock 10% (Thermo Scientific, cat. no. 37515), fish gelatin 3% (VWR, cat. no. M319), sodium azide 0.02%, in PBS, pH 7.4) at 37 °C for 1 h and incubated in rabbit anti-HIF-1α polyclonal/mouse IgG_1 anti-actin monoclonal primary antibodies (Abcam, cat. no. ab2185/Invitrogen, cat. no. MA5-11869) 1:250/1:2000 (in blocking solution) at 4 °C overnight. Membranes were incubated in goat anti-rabbit IgG (H+L)/goat anti-mouse IgG (H+L) horseradish peroxidase-conjugated secondary antibodies (Abcam, cat. no. ab205718/KPL, cat. no. 474-1806) 1:1000/1:10000 (in blocking solution) at 37 °C for 1 h, washed and detected by enhanced chemiluminescence (ECL) reaction (Advansta, cat. no. K-12045). Nuclear HIF-1α lysate (5 µg; Abcam, cat. no. ab180880) was used to validate the selected anti-HIF-1α antibody. Data were acquired and extracted using VisionWorks (UVP) and treated using ImageJ and Excel.

Vibrating probe measurement. Extracellular net electric current density (J_I) was measured non-invasively with a vibrating probe[8]. Prior to measurements, a platinum-electroplated probe (~30 µm ball diameter) vibrating at 100–200 Hz was calibrated in the experimental conditions by an applied J_I of 1.5 µA cm^{-2}. Recording procedure was as in the optrode measurements, with minor changes. Currents were acquired until a plateau peak was reached in the various ROI and times indicated, typically in <1 min. To mitigate the electromagnetic noise, we used a Faraday 'wall' (grounded aluminum-wrapped cardboard) covering the microscope. Data were acquired and extracted using WinWCP V4 (Strathclyde Electrophysiology Software) and treated using Excel.

Statistical analysis. Blinding was not employed in data acquisition, treatment, or statistical analysis. Statistical inference tests were used as appropriate and are annotated in figure captions. Pre-tests were conducted for normality (Kolmogorov-Smirnov, Shapiro-Wilk and/or D'Agostino and Pearson tests) and equal variances (F test) assumptions. If assumptions were not verified, the large sampling mitigated normality influence and the Welch's correction addressed unequal variances. Data are presented as mean ± s.e.m., with sample size (n, biological replicates or blots (Western) and flows (cytometry) of tens of tadpoles) indicated in figures and text. Data are additionally presented as median ± min to max (with outliers) in the case of boxplots. At least two independent batches of tadpoles or oocytes were used per readout (rare exceptions solely in Supplementary Fig. 1d, 15a,b). Differences were considered significant when $p < 0.05$ and level of significances were as follow: NS non-significant; *$p < 0.05$; **$p < 0.01$; and ***$p < 0.001$. Data treatment and visualization were performed using Excel, except for flow cytometry data where were used FlowJo and R (The R Foundation for Statistical Computing). Statistical tests were performed using GraphPad Prism 5 (GraphPad Software).

Data availability

The data (structured or treated, representative, and raw) that support the findings of this study are embedded in the paper and its Supplementary Information. Additionally, all

other relevant data (discrete and numerical) are available and unrestricted from the corresponding authors upon reasonable request.

Received: 23 March 2017 Accepted: 10 September 2018
Published online: 16 October 2018

References

1. Alvarado, A. S. & Tsonis, P. A. Bridging the regeneration gap: genetic insights from diverse animal models. Nat. Rev. Genet. 7, 873–884 (2006).
2. Beck, C. W., Izpisúa Belmonte, J. C. & Christen, B. Beyond early development: Xenopus as an emerging model for the study of regenerative mechanisms. Dev. Dyn. 238, 1226–1248 (2009).
3. Pirotte, N. et al. Reactive oxygen species in planarian regeneration: an upstream necessity for correct patterning and brain formation. Oxid. Med. Cell.Longev. 2015, 1–19 (2015).
4. Gauron, C. et al. Sustained production of ROS triggers compensatory proliferation and is required for regeneration to proceed. Sci. Rep. 3, 2084

58. Bonello, S. et al. Reactive oxygen species activate the HIF-1alpha promoter via a functional NFkappaB site. Arterioscler. Thromb. Vasc. Biol. 27, 755–761 (2007).
59. Minet, E. et al. Hypoxia-induced activation of HIF-1: role of HIF-1α-Hsp90 interaction. FEBS Lett. 460, 251–256 (1999).
60. Kubis, H.-P., Hanke, N., Scheibe, R. J. & Gros, G. Accumulation and nuclear import of HIF1 alpha during high and low oxygen concentration in skeletal muscle cells in primary culture. Biochim. Biophys. Acta 1745, 187–195 (2005).
61. Li, W. et al. Extracellular heat shock protein-90α: linking hypoxia to skin cell motility and wound healing. EMBO J. 26, 1221–1233 (2007).
62. Ceradini, D. J. et al. Progenitor cell trafficking is regulated by hypoxic gradients through HIF-1 induction of SDF-1. Nat. Med. 10, 858–864 (2004).
63. McCaig, C. D., Rajnicek, A. M., Song, B. & Zhao, M. Controlling cell behavior electrically: current views and future potential. Physiol. Rev. 85, 943–978 (2005).
64. Guo, X. et al. The galvanotactic migration of keratinocytes is enhanced by hypoxic preconditioning. Sci. Rep. 5, 1–13 (2015).
65. Shen, Y. et al. Diabetic cornea wounds produce significantly weaker electric signals that may contribute to impaired healing. Sci. Rep. 6, 1–11 (2016).
66. Lakowicz, J. R. Principles of Fluorescence Spectroscopy, 277–330 (Springer, US, 2006).
67. Chatni, M. R., Li, G. & Porterfield, D. M. Frequency-domain fluorescence lifetime optrode system design and instrumentation without a concurrent reference light-emitting diode. Appl. Opt. 48, 5528–5536 (2009).
68. Mishina, N. M. et al. in Methods in Enzymology (eds. Cadenas, E. & Packer, L.) 526, 45–59 (Elsevier Inc., Amsterdam, 2013).
69. Pearl, E. J., Grainger, R. M., Guille, M. & Horb, M. E. Development of Xenopus resource centers: the national Xenopus resource and the european Xenopus resource center. Genesis 50, 155–163 (2012).
70. Tsujioka, H., Kunieda, T., Katou, Y., Shirahige, K. & Kubo, T. Unique gene expression profile of the proliferating Xenopus tadpole tail blastema cells deciphered by rna-sequencing analysis. PLoS ONE 10, 1–15 (2015).

Acknowledgements

This work was supported by a NIH EY019101, an AFOSR (FA9550-16-1-0052) and, in part, by an Unrestricted Grant from Research to Prevent Blindness, Inc., University of California (UC), Davis, Ophthalmology. F.F. was supported by Fundação para a Ciência e Tecnologia (FCT) grant SFRH/BD/87256/2012 (majority of work) and by a staff research associate position in the laboratory (minority of work). We thank Dr. Andreia Gomes (Departamento de Biologia, CBMA, Universidade do Minho, Portugal) for support. We are grateful to Dr. Andrew L. Miller (Department of Biology, Hong Kong University of Science and Technology, China), Dr. Marko Horb (Director of the NXR, MBL) and Dr. Esther Pearl (NXR, MBL), and Mr. Alan M. Shipley (Applicable Electronics, LLC.) for generously hosting F.F.'s visit to MBL (Summer season 2014), for help in providing access to local research facilities and materials (SMOT and tadpoles (NXR RRID: SCR_013731) included), and for helpful comments. We are also grateful to Mr. Christopher A. Shipley, owner of Applicable Electronics, LLC., for having the courtesy to loan a SMOT system to the Zhao lab, and special thanks to Mr. Eric Karplus (Science Wares, Inc.), designer and programmer of the SMOT, for providing software, technical assistance and support for its efficient installation and operation. We are further grateful to Mr. Eric Karplus for helping with the mathematics and interpretation behind the equations used to calculate O_2 flux. We are thankful to Dr. Christopher Murphy (Department of Ophthalmology and Vision Sciences, UC Davis (R01 EY016134 and P30 EY12576)) and Dr. Paul Russell (Department of Surgical and Radiological Sciences, UC Davis) lab for kindly providing 17-DMAG and western blotting reagents and equipment for the experiments. We are also thankful to Iman Jalilian (Department of Surgical and Radiological Sciences, UC Davis) and Elias Barriga (Department of Cell and Developmental Biology, University College London, UK) for helpful comments about the western blotting technique. We thanks to Dr. Yunyun Shen (Department of Dermatology, UC Davis; Department of Occupational and Environmental Health, Zhejiang University, China) for kindly dispensing the euthanized mice and Dr. Li Ma (Department of Dermatology, UC Davis; Skin and Cosmetic Research Department, Shanghai Skin Disease Hospital, China) for helpful comments on the immunohistochemistry technique. We are grateful to Zhao lab members for helpful discussion.

Author contributions

F.F., VK.R., G.L. and M.Z. designed the experiments. F.F. performed most experiments and analyzed the data and results. F.F., VK.R. and K.Z. performed and analyzed the western blots. F.F. and G.L. performed the flow cytometry; G.L. analyzed the flow cytometry. VK.R. and G.L. helped to interpret overall results. F.F., VK.R., G.L. and M.Z. outlined the manuscript. F.F. wrote the manuscript. All authors edited the manuscript.

Additional information

Supplementary Information accompanies this paper at https://doi.org/10.1038/s41467-018-06614-2.

Competing interests: The authors F.F. and M.Z. declare the following competing interests. The optrode measurements were acquired using turn-key systems provided free for use at MBL and loaned to the Zhao lab at no cost, by Applicable Electronics, LLC and Science Wares, Inc. The companies had no influence over the research, in design, execution, interpretation, or its reporting. No restrictions on data sharing have been imposed. The remaining authors declare no competing interests.

Reprints and permission information is available online at http://npg.nature.com/reprintsandpermissions/

Publisher's note: Springer Nature remains neutral with regard to jurisdictional claims in published maps and institutional affiliations.

Early redox activities modulate *Xenopus* tail regeneration

Fernando Ferreira[1,2,*], VijayKrishna Raghunathan[3-5], Guillaume Luxardi[1], Kan Zhu[1] & Min Zhao[1,6,*]

(Integrating redox activities during regeneration)

[1]Department of Dermatology, Institute for Regenerative Cures, University of California, Davis, CA, USA.
[2]Departamento de Biologia, Centro de Biologia Molecular e Ambiental (CBMA), Universidade do Minho, Braga, Portugal.
[3]Department of Basic Sciences, University of Houston, TX, USA.
[4]The Ocular Surface Institute, College of Optometry, University of Houston, TX, USA.
[5]Department of Biomedical Engineering, Cullen College of Engineering, University of Houston, TX, USA.
[6]Department of Ophthalmology, Institute for Regenerative Cures, University of California, Davis, CA, USA.
*Corresponce: F.F., email: id3955@alunos.uminho.pt; M.Z., email: minzhao@ucdavis.edu.

Supplementary Figures

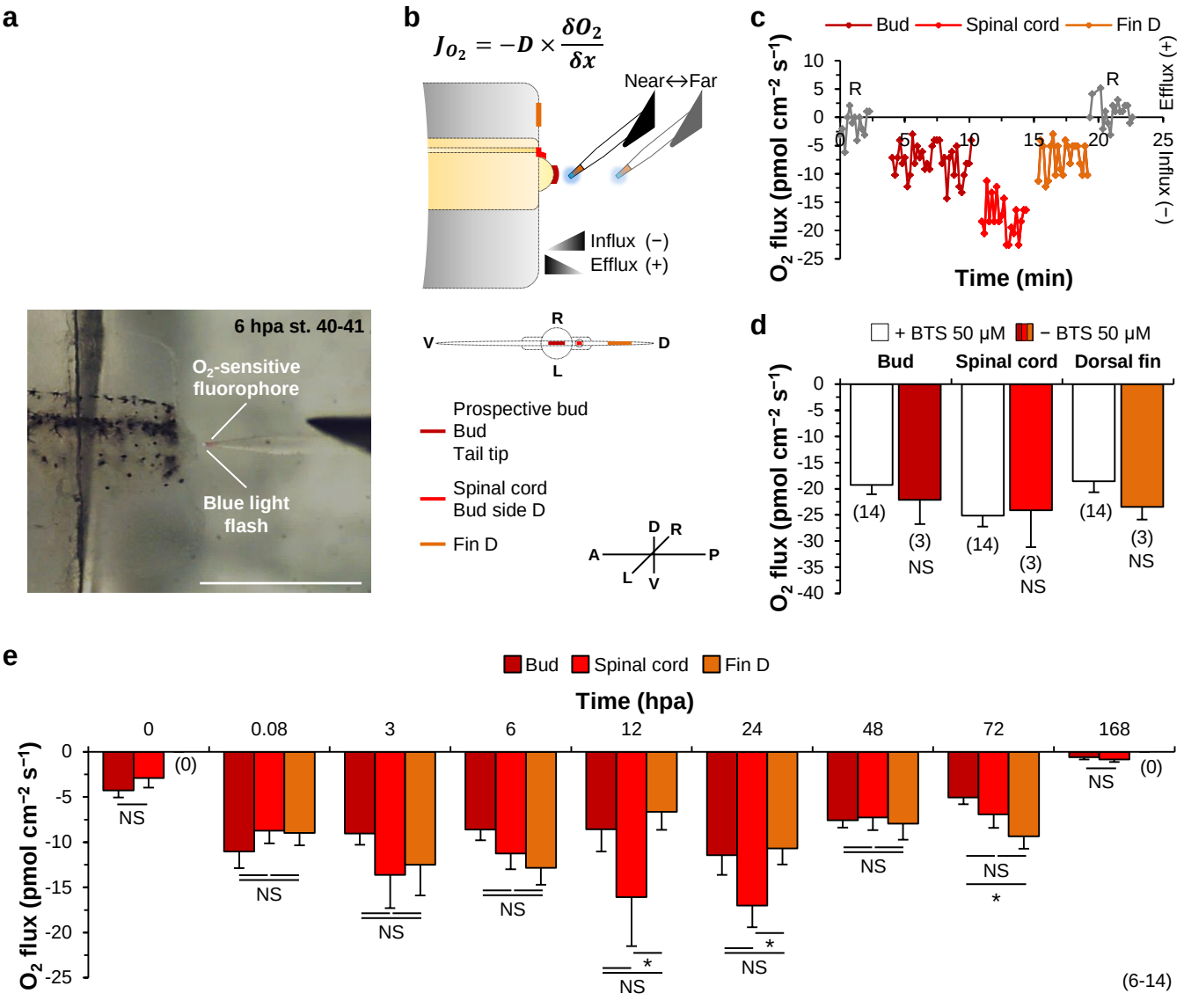

Supplementary Figure 1 | Spatiotemporal profile of extracellular O_2 flux during tail regeneration. (**a**,**b**) Experimental design, regions of interest (ROIs) and flux equation (Fick's first law detailed in Methods) for the O_2 flux profiling. Bottom panel in **a**

dorsal fins had larger O_2 influxes than regenerated dorsal (and ventral) ones at 72 hpa. Since the profiling is to elucidate regeneration, we excluded the non-regenerated dorsal fin data at 72 hpa (3 out of 9). Statistical analyses were performed by unpaired Student's *t*-test (two-tailed *p* value). Data are presented as mean±s.e.m. *n* biological replicates indicated in brackets. NS, non-significant; *, $p<0.05$.

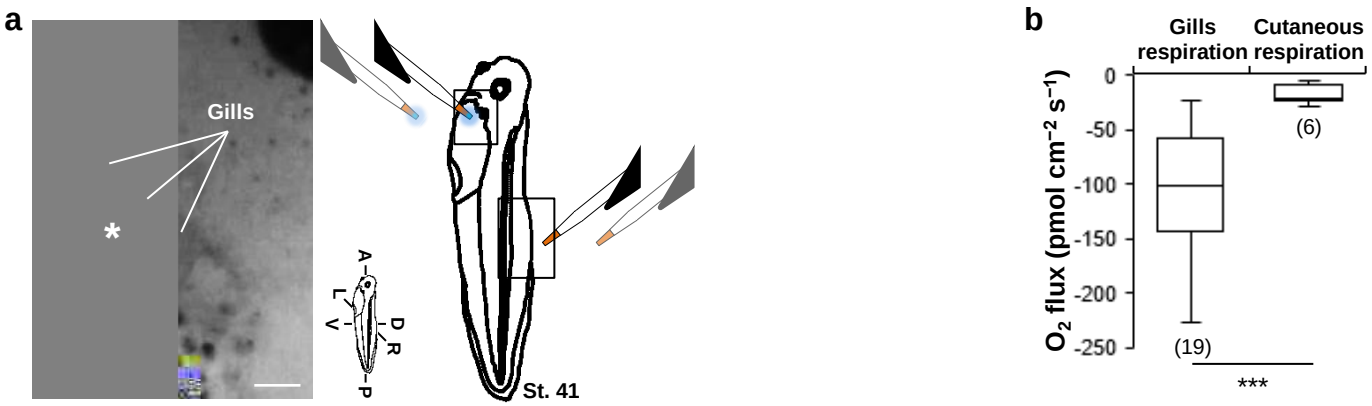

Supplementary Figure 2 | Modalities of respiration in tadpoles. (**a**,**b**) Tadpoles uptake O_2 through gills and cutaneous surfaces with different magnitudes. (**a**) Center: Experimental design. Right and left panels: representative gills and dorsal fin close ups of rectangles in center. Gill measurements were taken in the middle gill of left axis (white *). Scale bars: ~100 μm in right panel and ~0.5 mm in left panel. (**b**) O_2 influx in the two respiration surfaces (in MMR 0.1×). Data of cutaneous respiration are from Supplementary Fig. 4e, being siblings of part of the gills respiration data. Statistical analyses were performed by unpaired Student's *t*-test (two-tailed *p* value). Data are presented as median±min to max (with outliers). *n* biological replicates indicated in brackets. ***, $p<0.001$.

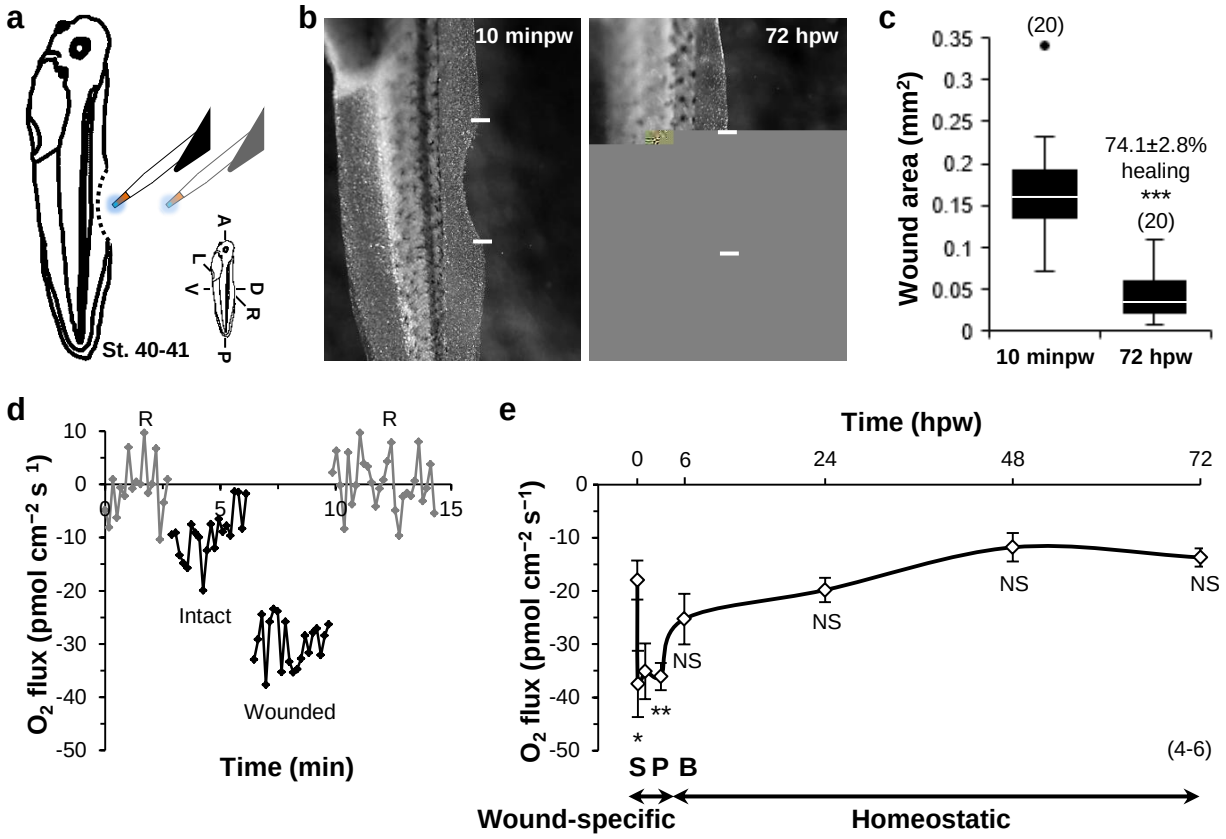

Supplementary Figure 4 | Temporal profile of extracellular O_2 flux during wound healing. (**a**) Experimental design. (**b**) Representative dorsal fins after wounding (10 min) and healing (72 h) (in DMSO 0.1%). White solid lines: wound edges; scale bar: 1 mm. (**c**) Area of unhealed and percentage of healed fin. After 72 hpw there was no significant fin healing (72 hpw: 0.055±0.016 mm^2; 120 hpw: 0.054±0.018 mm^2; n=5, p=0.968). (**d**) Representative result (MMR 0.1× 0 and 5 minpw). (**e**) Temporal profile of O_2 flux during wound healing (in MMR 0.1×). Profile is descriptively divided into three parts: S, slope – instantaneous; P, plateau – until 3 hpw; and B, baseline – after 3 hpw; comprising two phases: wound-specific and homeostatic. Statistical analyses were performed by unpaired Student's t-test (two-tailed p value). Data are presented as median±min to max (with outliers) (**c**), or mean±s.e.m. (**e**). n biological replicates indicated in brackets. NS, non-significant; *, p<0.05; **, p<0.01; ***, p<0.001.

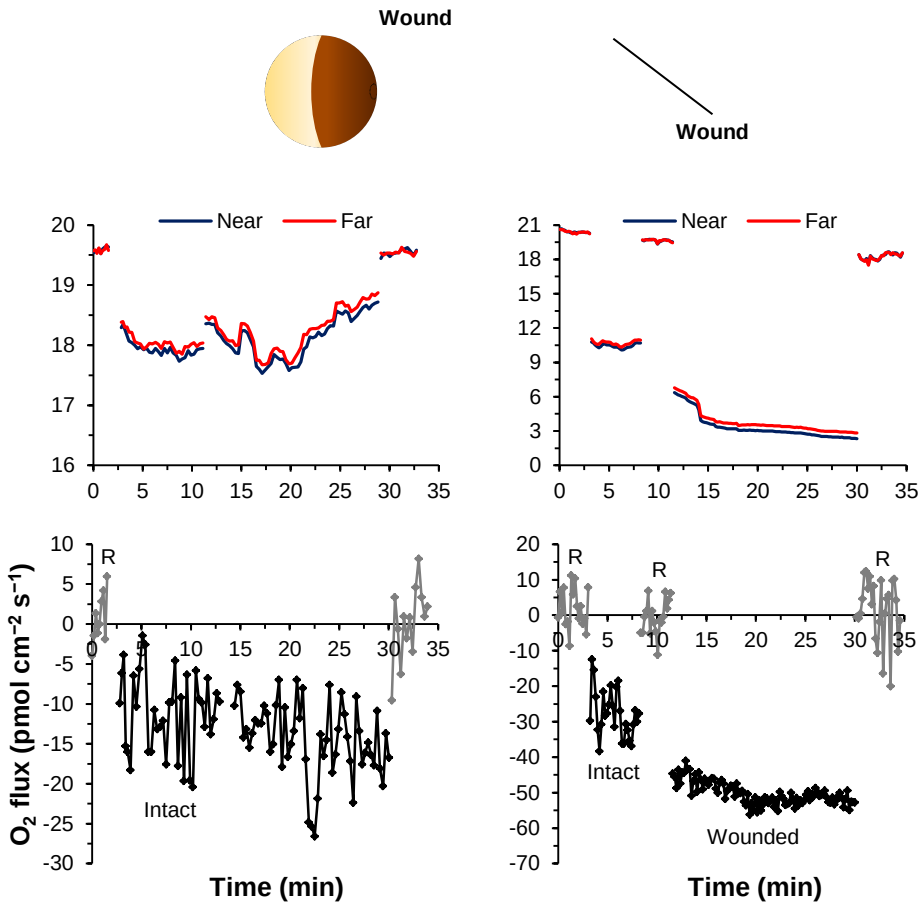
d
Wound
Wound
Near
Far
Near
Far
R
R
R
Intact
Intact
Wounded
Time (min)
Time (min)
O2 flux (pmol cm−2 s−1)

c

f

closer to equilibrium. Therefore, the O_2 gradient established upon wounding is much smaller in oocytes than in mice skin, generating a much less penetrant O_2 sink. Reference (R), intact and wounded measurements (labels in bottom plots) are delimited by a discontinuity in the solid lines. *x* axis title in bottom plots applies to top plots; *y* axis titles in **b** apply to **e**. (**c**,**f**) O_2 influxes elevate upon wounding in oocytes (29% increase; p=0.003) and in mice skin (61% increase; p=0.033). Statistical analyses were performed by paired Student's *t*-test (two-tailed p value for **c**, or one-tailed p value for **f**). Data are presented as median±min to max (with outliers). *n* biological replicates indicated in brackets. *, p<0.05; **, p<0.01.

and far poles; bottom plots: O_2 flux calculated using the difference of near and far poles values (δO_2) from top plots (after conversion to O_2 concentration as detailed in Methods). References (R) do not appear to present oscillations, excluding noise and drift as causes for the measured oscillations. Reference and ROI measurements (legend and label in bottom plots) are delimited by a discontinuity in the solid lines. *x* axis title in bottom plots applies to top plots; *y* axis titles in **a**/**c** apply to **b**/**d**. Injury-specific peak O_2 sinks – *i.e.*, minimum reference level minus maximum specimen level – are annotated. O_2 sink drastically decreases with fin healing in **d**; same occurs during regeneration as decreased O_2 influx proves (Fig. 1b,c). (**e**) Schematic plots depicting the apparently more common oscillation profile observed in **a**-**d** and in all other recordings acquired. Right plot: O_2 static at near and far poles; left plot: O_2 flux calculated from right plot (after conversion to O_2 concentration). The oscillation profile seems counter-intuitive, because when O_2 sink is larger O_2 flux is smaller and *vice-versa*. Thereby, O_2 static and O_2 flux oscillations (waves) are in antiphase, *i.e.*, crests in left plot are troughs in right plot and *vice-versa*. Other apparently less common oscillation profiles were also note. More exhaustive and robust qualitative and quantitative analyses of oscillations and putative oscillations were not performed. Such analyses would have required a specific experimental design. The most important design requirement would have been the increase of sampling time (*e.g.*, to 30 min per ROI) to be able to encompass more oscillation cycles (periods) and to clearly identify potential false positives and false negatives. As described in Methods, we recorded the fluxes usually for 2-5 min per ROI; as the representative oscillations attest, 2 min is a probable minimal threshold to detect a single period, therefore many plots could not be analyzed to robustly study oscillations. For these reasons, we avoided to calculate means±SEMs and instead selected cases that seem to represent the range of the reasonably identifiable oscillations. Thereby, for the period, the range seems to be around 2-4 min and for the frequency, the range seems to be around 4-8 mHz. Equation: frequency (*f*) is the multiplicative inverse (reciprocal) of the period (*T*) and *vice-versa*. Annotated periods and frequencies were calculated by averaging most or all crest-to-crest and trough-to-trough times for each plot (*e.g.*, the 3 crests and 3 troughs in bottom **d** provided 4 peak-to-peak time values that when averaged gave a period of 2.5 min and a frequency of 6.7 mHz).

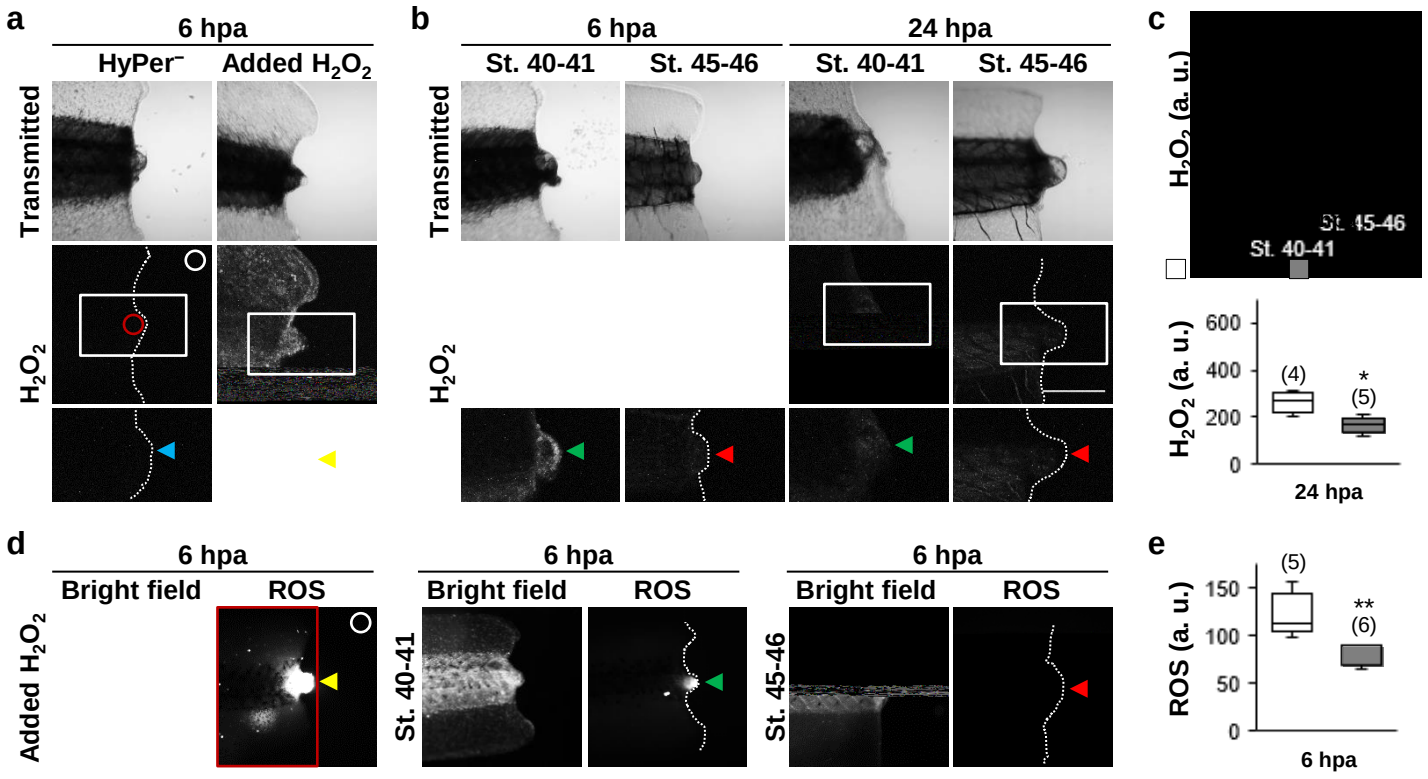

Supplementary Figure 7 | Refractory period tadpoles have lower ROS/H_2O_2 levels in the bud. (**a**) Controls validating the measurement of H_2O_2 using HyPer transgenic tadpoles. Representative tails under transmitted light (top panels) and fluorescence imaging (488/515 excitation/emission nm; middle and bottom panels) (applies to **b**). Transgenesis' negative control (*i.e.*, no HyPer expression; left panels) was devoid of any measurable fluorescence (blue arrowhead) and experimental positive control (H_2O_2 1 mM added to bath for 15 min; right panels) had very strong fluorescence (yellow arrowhead), validating the measurement system. Several tadpoles presented similar readouts at both 6 and 24 hpa in st. 40-41. (**b**,**c**) HyPer transgenic tadpoles during different regenerative periods. (**b**) Representative tails in regenerative (st. 40-41) and refractory (st. 45-46) periods at 6 and 24 hpa. Bottom panels: close up of corresponding rectangles in middle panels. (**c**) Semi-quantitative analysis of H_2O_2 levels (background subtracted; white circular ROI in **a**) in both conditions in the bud (red circular ROI in **a**) at 6 and 24 hpa. Refractory period H_2O_2 levels are 122 and 59% lower than regenerative levels at 6 and 24 hpa, respectively (p=0.032 in both). Box and whiskers plots legend applies to **e**. (**d**,**e**) Secondary validation of HyPer results using the ROS-sensitive dye CM-H_2DCFDA in wild-type tadpoles. (**d**) Representative tails under bright field (left panels) and fluorescence imaging (GFP channel; right panels) in regenerative (st. 40-41) and refractory (st. 45-46) periods at 6 hpa. Yellow arrowhead: very high ROS levels in the prospective regeneration bud; green arrowhead: high ROS/H_2O_2 levels in the (prospective) bud; red arrowhead: low ROS/H_2O_2 levels in the (prospective) bud; scale bars: 0.5 mm. (**e**) Semi-quantitative analysis of ROS levels (background subtracted; white circular ROI in **c**) in both conditions in the whole imaged tail (red rectangular ROI in **c**) at 6 hpa. Refractory period ROS levels are 46% lower than regenerative levels at 6 hpa (p=0.004). a. u.: arbitrary units. Statistical analyses were performed by non-parametric Mann Whitney test. Data are presented as median±min to max (with outliers). *n* biological replicates indicated in brackets. *, p<0.05; **, p<0.01.

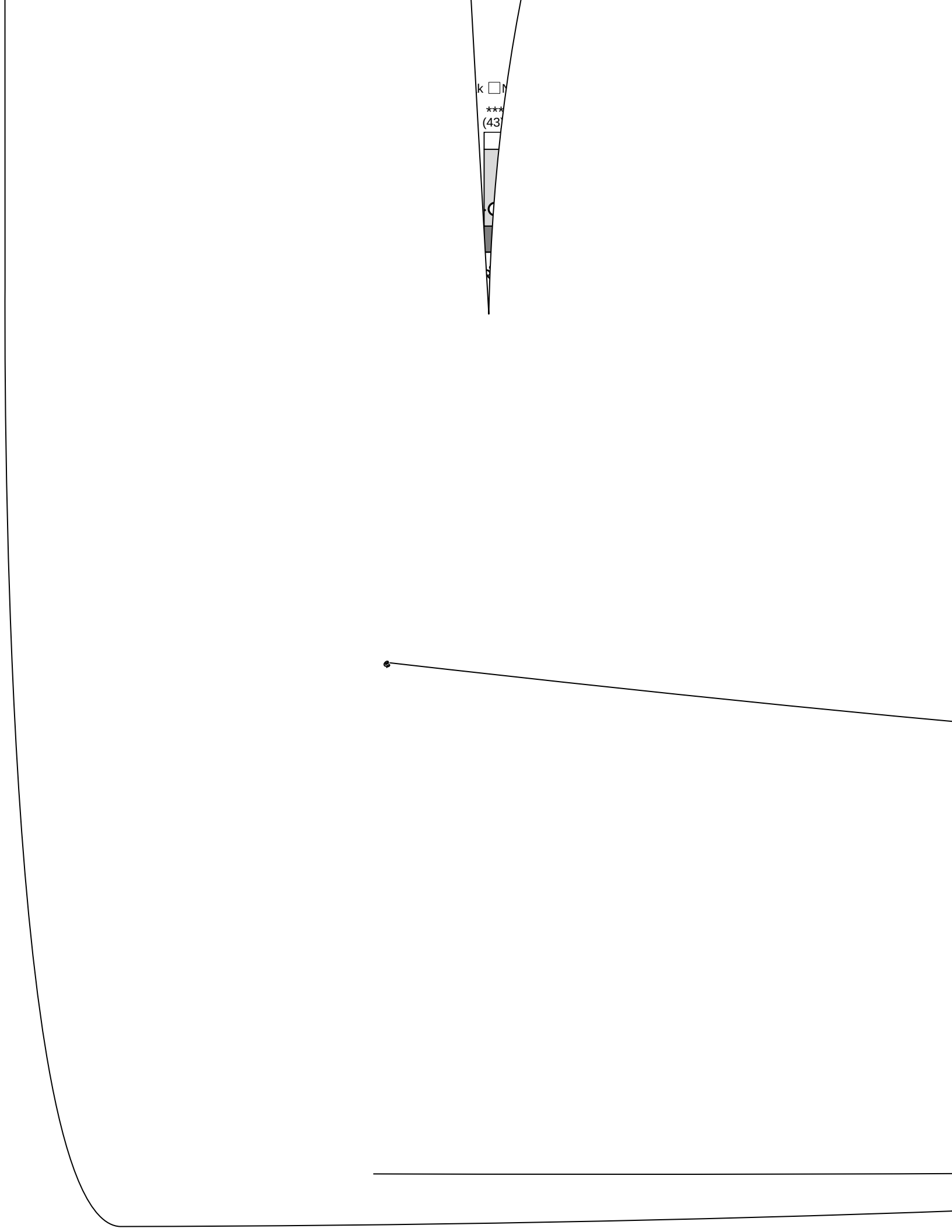

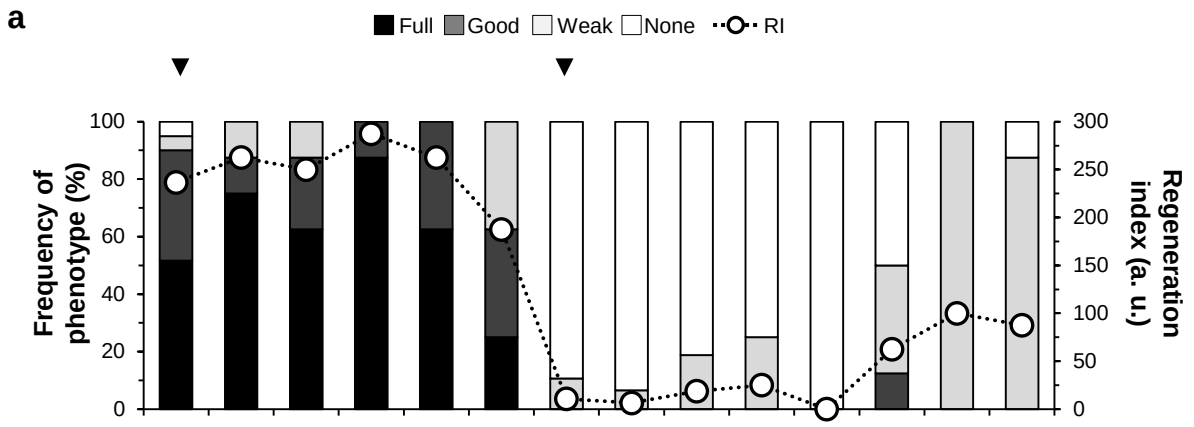
a
Full
Good
Weak
None
RI
Frequency of phenotype (%)
Regeneration index (a. u.)
100
80
60
40
20
0
300
250
200
150
100
50
0

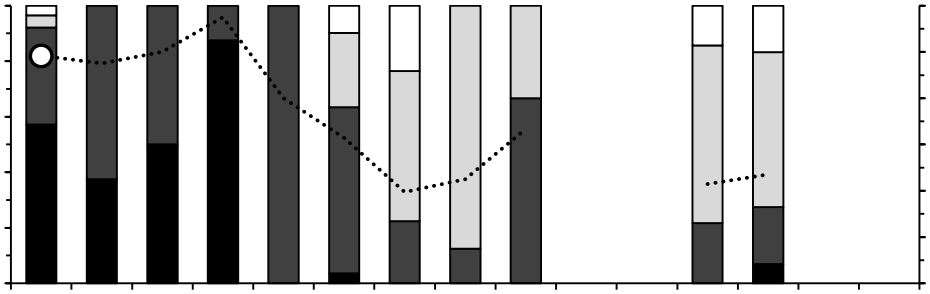

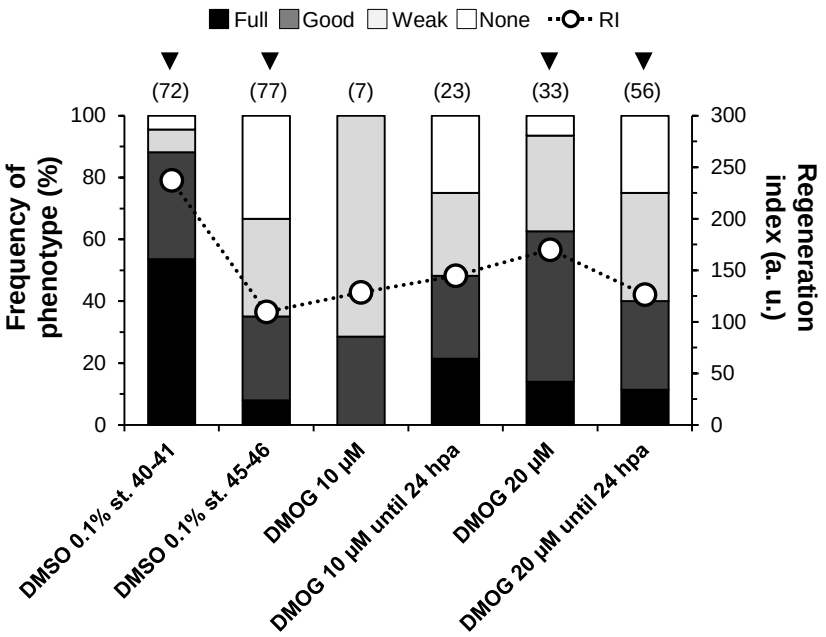

Supplementary Figure 12 | Dose-exposure screening to fine-tune pharmacological treatments during regeneration: DMOG. Selection was based on the maximal penetrance with minimal observable toxicity and developmental side defects. Black arrowheads: selected dose-exposures and respective vehicle-controls. RI: regeneration index; a. u.: arbitrary units. *n* biological replicates indicated in brackets.

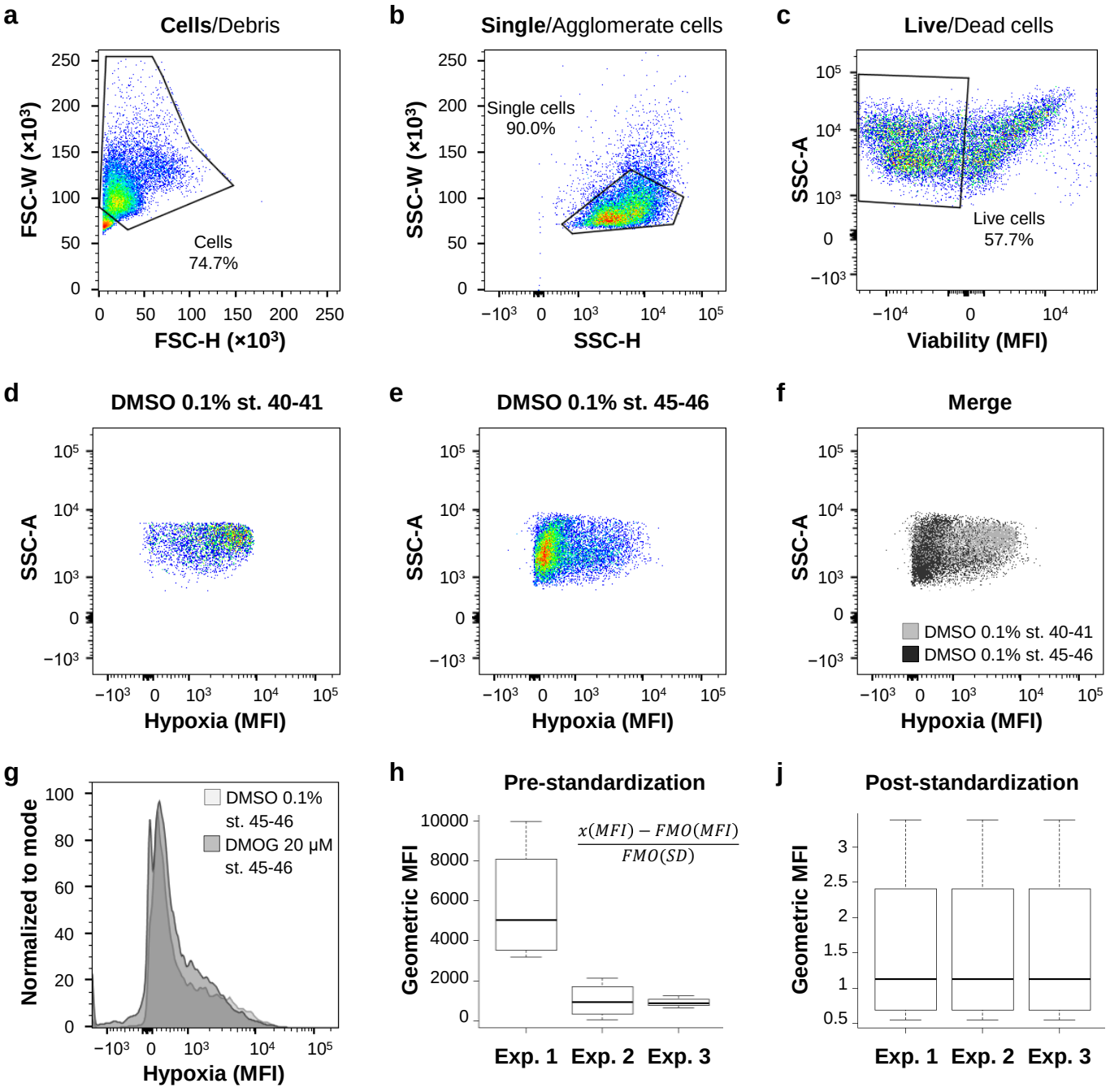

Supplementary Figure 13 | Stepwise data analysis of flow cytometry. (**a**-**c**) Representative flow cytograms of sequential gating. Debris (**a**), cell fragments and agglomerates (**b**), and dead cells (Aqua blue positive) (**c**) were excluded to gate live single cells. (**d**-**f**) Post-gating representative flow cytograms of cells analyzed in the fluorescein (FITC) channel. Merged data in **f** is the same as that shown in the bottom panel of Fig. 5a, presented as discriminated cells instead of histogram. FSC: forward scatter pulse; SSC: side scatter pulse; W: width; H: height; A: area; MFI: mean fluorescence intensity. (**g**) HIF-1α stabilizing drug does not induce hypoxia in the refractory period at 1 hpa. (**h**,**j**) Standardization of independent flow cytometry experiments for robust cross comparison. Inset in **h**: standardization equation (details in Methods). Distribution of fluorescence intensity per experiment pre- (**h**) and post-standardization (**j**). Exp.: experiment.

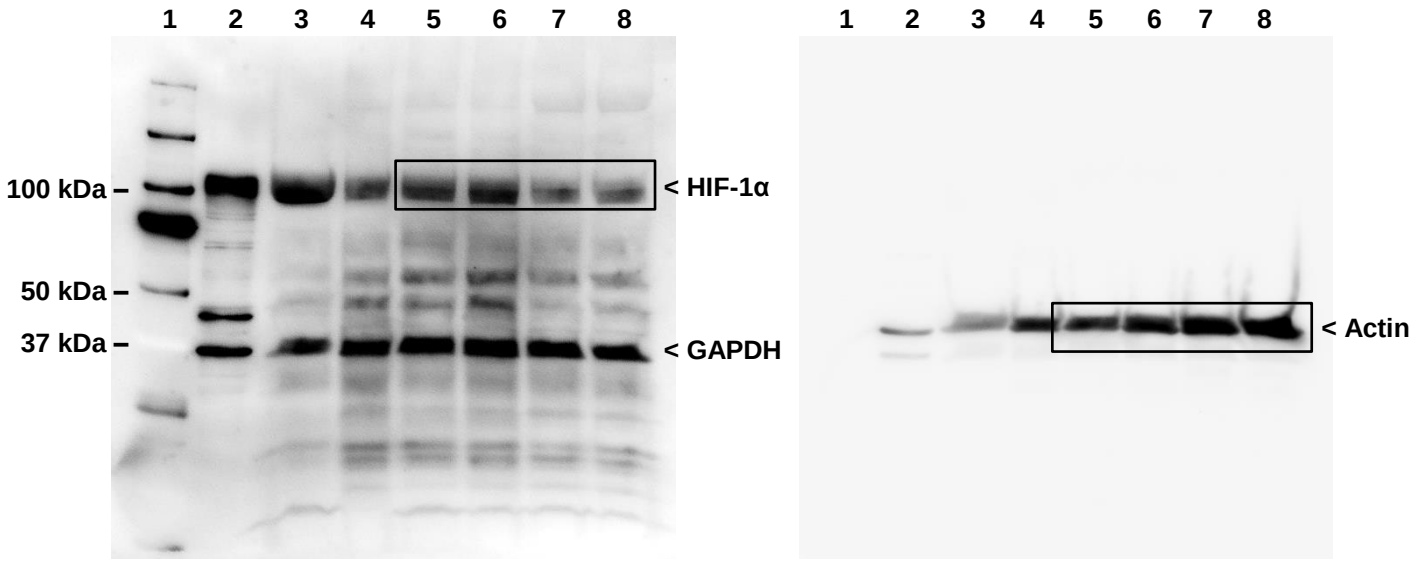

Lanes

1. Ladder
2. HIF-1α lysate (5 µg)
3. DMSO 0.1% st. 40-41, 1 huncut (whole tadpole)
4. DMSO 0.1% st. 45-46, 1 huncut (whole tadpole)
5. DMSO 0.1% st. 40-41, 1 hpa
6. DPI 1 µM st. 40-41, 1 hpa
7. DMSO 0.1% st. 45-46, 1 hpa
8. DMOG 20 µM st. 45-46, 1 hpa

Supplementary Figure 14 | Uncropped membranes of Western blotting against HIF-1α. Black rectangles mark the cropped membrane used in Fig. 5. Technical positive control (HIF-1α lysate in lane 2) validates selected antibody and respective specificity. GAPDH was initially used as reference protein; however, later reblotting of the membranes with actin antibody (right membrane) revealed less variability among lanes.

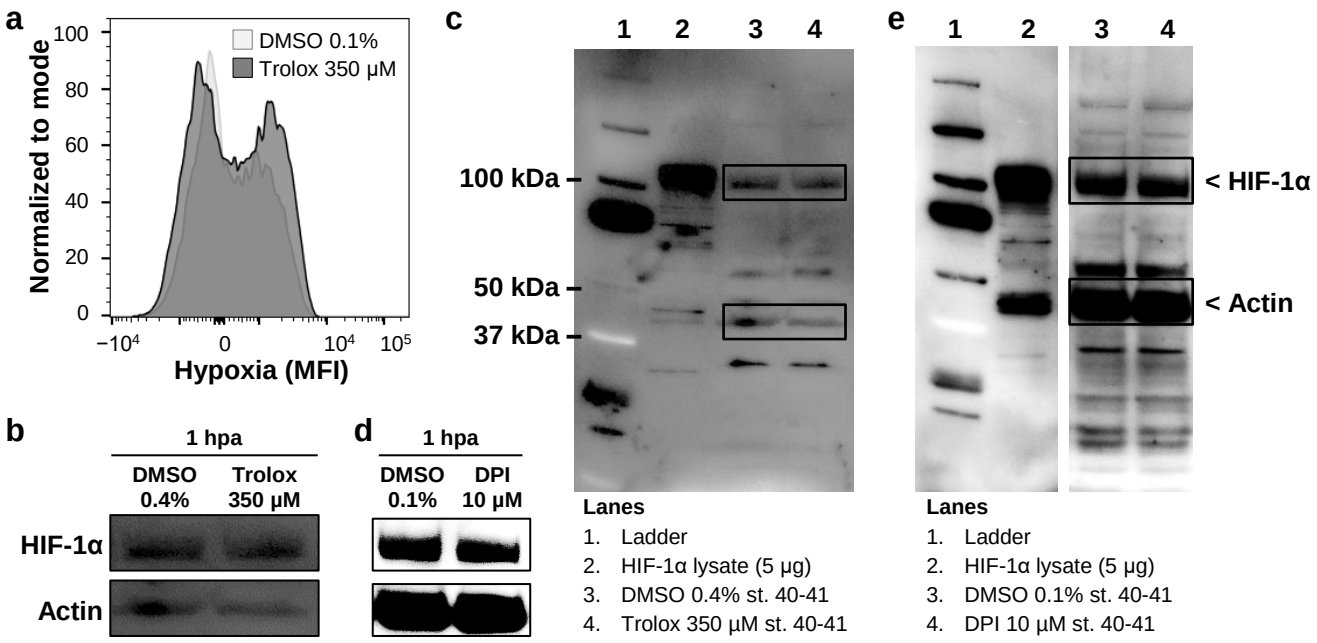

Supplementary Figure 15 | ROS *per se* neither affect hypoxia nor stabilize HIF-1*α*. Flow cytogram (**a**) and Western blotting (**b**) of DMSO 0.1%/0.4% st. 40-41 *vs.* trolox 350 µM st. 40-41 at 1 hpa. MFI: mean fluorescence intensity. (**d**) Western blotting showing that a ten-fold increase in the inhibition of ROS production does not proportionally decrease HIF-1α stability levels. This modulation of ROS production and scavenging implies that ROS do not directly stabilize HIF-1α. (**c**,**e**) Uncropped membrane. Black rectangles mark the cropped membrane used in **b** and **d**, respectively. Technical positive control (HIF-1α lysate) in lanes 2.

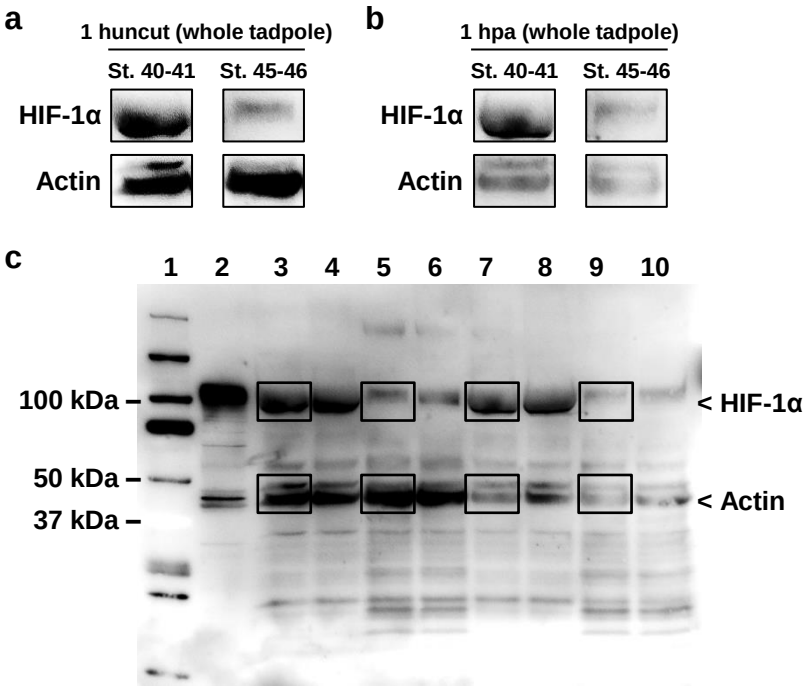

Lanes

1. Ladder
2. HIF-1α lysate (5 µg)
3. DMSO 0.1% st. 40-41, 1 huncut (whole tadpole)
4. DPI 1 µM st. 40-41, 1 huncut (whole tadpole)
5. DMSO 0.1% st. 45-46, 1 huncut (whole tadpole)
6. DMOG 20 µM st. 45-46, 1 huncut (whole tadpole)
7. DMSO 0.1% st. 40-41, 1 hpa (whole tadpole)
8. DPI 1 µM st. 40-41, 1 hpa (whole tadpole)
9. DMSO 0.1% st. 45-46, 1 hpa (whole tadpole)
10. DMOG 20 µM st. 45-46, 1 hpa (whole tadpole)

Supplementary Figure 16 | Age-dependent (stage-specific) HIF-1α stabilization predicts regeneration efficiency. (**a**-**c**) Western blotting against HIF-1α. HIF-1α stability levels are far higher in regenerative (st. 40-41) than in refractory (st. 45-46) period tadpoles. Differential trend is similar in both uncut (**a**) and amputated (**b**) whole tadpoles. Independent Western blots gave consistent readouts; *e.g.*, compare lanes 3 *vs.* 4 in Supplementary Fig. 14. Other, unstudied, developmental or physiological effects of HIF-1α stability disparity in the intriguing refractory period warrant future research. (**c**) Uncropped membrane. Black rectangles mark the cropped membrane used in **a** and **b**. Technical positive control (HIF-1α lysate) in lane 2.

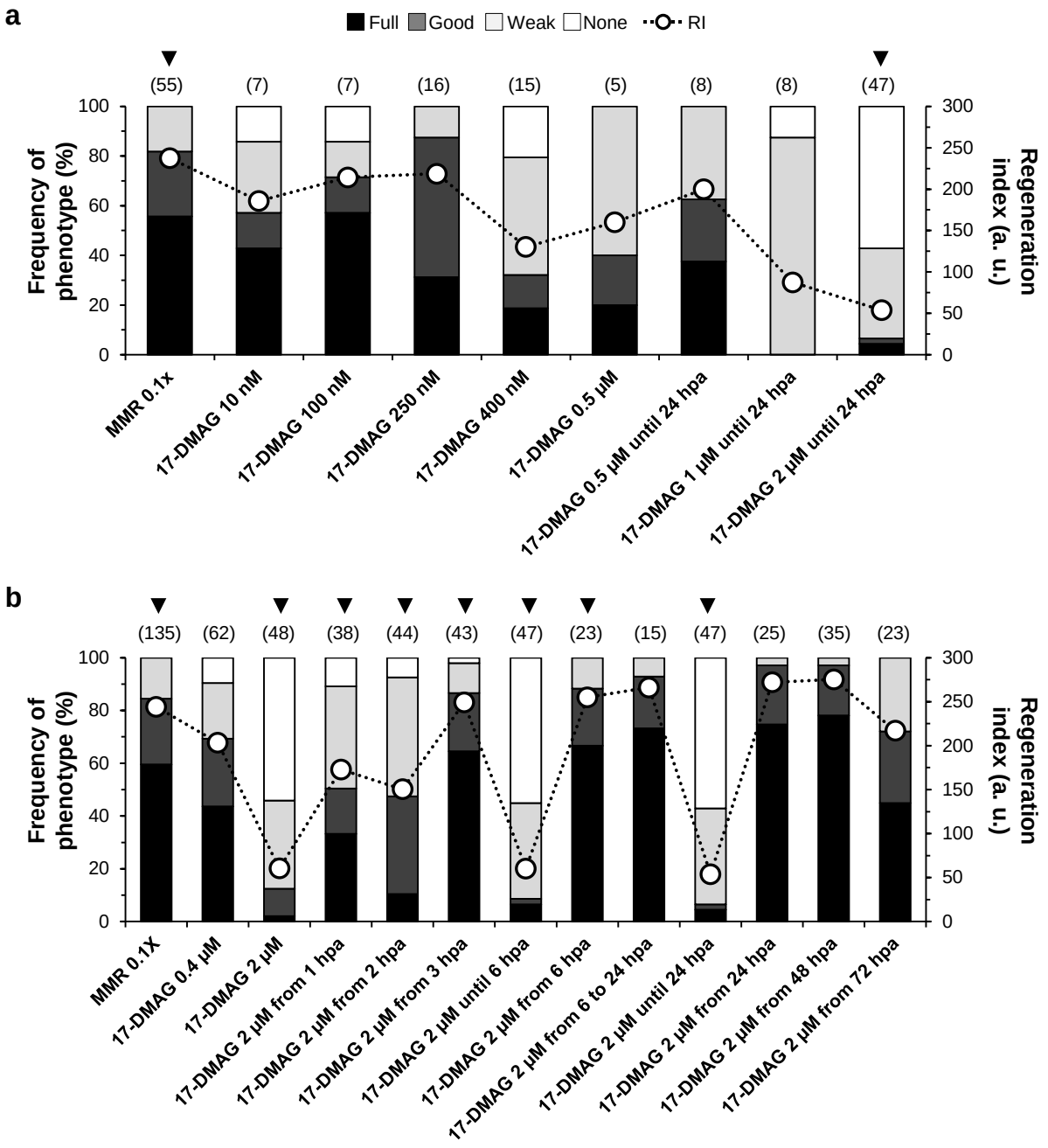

Supplementary Figure 17 | Dose-exposure screening to fine-tune pharmacological treatments during regeneration: 17-DMAG. (**a**) Gross screening. (**b**) Refined screening. Selection was based on the maximal penetrance with minimal observable toxicity and developmental side defects. Black arrowheads: selected dose-exposures and respective control. RI: regeneration index; a. u.: arbitrary units. *n* biological replicates indicated in brackets.

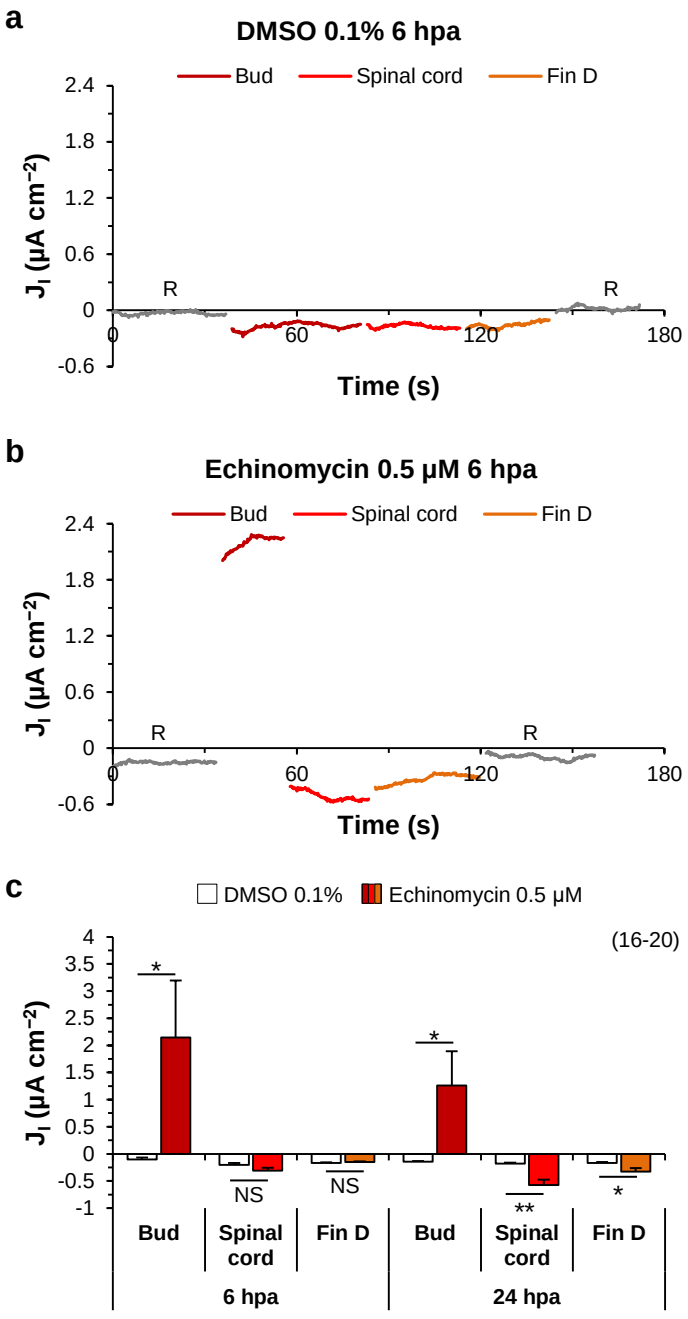

Supplementary Figure 18 | HIF-1α regulates the J_I reversal hallmark in a spatial-dependent way. (**a**,**b**) Representative results. The conventional current flow – direction defined by the flux of positive charge – is used, hence positive values are net outward and negative are net inward currents. Reference (R) and ROI measurements are delimited by a discontinuity in the solid lines. (**c**) Spatial profile of J_I measured in two different time-points in vehicle-control and echinomycin-treated tadpoles amputated at st. 40-41. Data of regeneration bud are the same as those shown in Fig. 7e. Statistical analyses were performed by unpaired Student's *t*-test (two-tailed p value). Data are presented as mean±s.e.m. *n* biological replicates indicated in brackets. NS, non-significant; *, $p<0.05$; **, $p<0.01$.

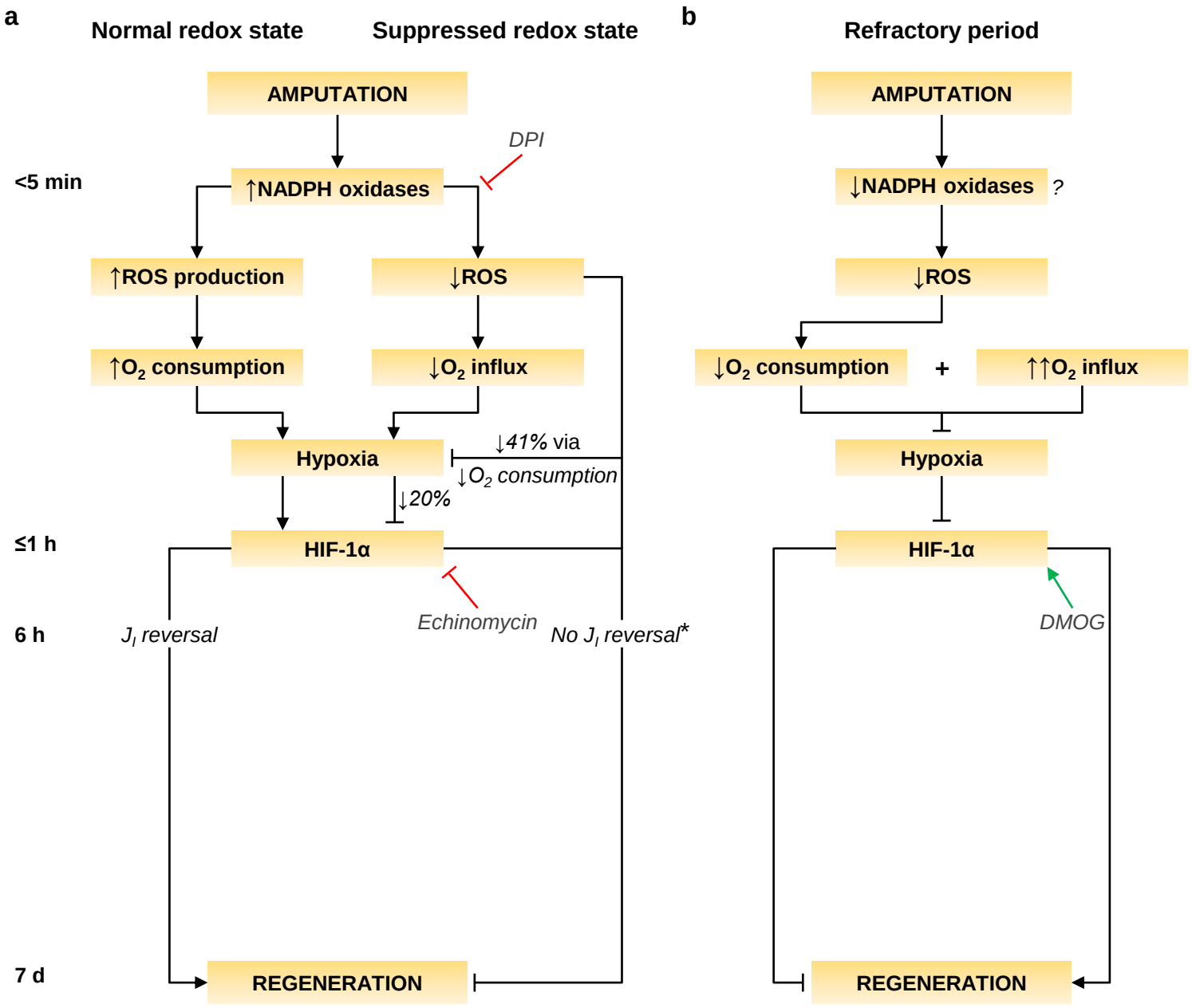

Supplementary Figure 19 | Stepwise model integrating redox state activities during regeneration. (**a**) Early antagonistic ROS production levels generate (and/or contribute to) and sustain considerable local hypoxia. Evidence-based mechanism explaining how either ROS production presence or absence generate (and/or contribute to) hypoxia. In normal redox state (left text boxes), the NADPH oxidase-mediated ROS production consumes O_2 locally, decreasing local pO_2. In suppressed redox state, NADPH oxidase inactivity demands less O_2 influx, decreasing local pO_2. Other hypoxia-generating sources, *e.g.*, vasculature disruption, are not excluded and are probably cumulative. Downstream hypoxia stabilizes HIF-1α that modulates regeneration *via* J_I reversal. However, ROS also modulates J_I reversal, impairing regeneration through this pathway, despite the presence of considerable hypoxia and HIF-1α stability (Fig. 5a-e). HIF-1α and ROS might regulate J_I reversal in series or in parallel. *: ROS effect on J_I reversal demonstrated in[5]. (**b**) Tadpoles amputated in the refractory period produce low levels of ROS (likely due to lower NADPH oxidases activity), therefore consuming less O_2 than regenerative tadpoles. In addition, these tails have a larger O_2 influx. Together, low consumption and high influx, increases local pO_2, disrupting hypoxia (Fig. 5a). Without hypoxia, HIF-1α undergoes degradation, impairing regeneration. DMOG mimics hypoxia, stabilizing HIF-1α that, in turn, induces regeneration. Timing in **a** applies to **b**. Italic dark grey font: drugs; green closed arrow: pharmacological activation; red bar arrow: pharmacological inhibition.

Supplementary References

1. Nieuwkoop, P. D. & Faber, J. *Normal table of Xenopus laevis (Daudin)*. (Amsterdam: North-Holland, 1967).
2. Beck, C. W., Christen, B. & Slack, J. M. W. Molecular pathways needed for regeneration of spinal cord and muscle in a vertebrate. *Dev. Cell* **5,** 429–39 (2003).
3. Reid, B., Song, B. & Zhao, M. Electric currents in Xenopus tadpole tail regeneration. *Dev. Biol.* **335,** 198–207 (2009).
4. Tseng, A.-S., Beane, W. S., Lemire, J. M., Masi, A. & Levin, M. Induction of vertebrate regeneration by a transient sodium current. *J. Neurosci.* **30,** 13192–200 (2010).
5. Ferreira, F., Luxardi, G., Reid, B. & Zhao, M. Early bioelectric activities mediate redox-modulated regeneration. *Development* **143,** 4582–4594 (2016).

CHAPTER IX

9. GENERAL CONCLUSION

The important thing is not to stop questioning. Curiosity has its own reason for existence. One cannot help but be in awe when he contemplates the mysteries of eternity, of life, of the marvellous structure of reality. It is enough if one tries merely to comprehend a little of this mystery each day. Never lose a holy curiosity.

Albert Einstein *in* Life magazine (Old Man's Advice to Youth: 'Never Lose a Holy Curiosity') (1955)

9.1 Concluding remarks

Regeneration, or the ability to recover form and regain function after injury or disease, is a multifactorial process of utmost complexity (Carlson, 2007). The regeneration type emphasized throughout this thesis – epimorphosis – is undoubtedly a fascinating and intriguing phenomenon; testifying a regenerating limb or tail is a certificate of nature's genius. While the renaissance in regeneration research brought molecular insight into classic and emergent organism models, much remained elusive regarding the redox and bioelectric aspects of regeneration, and virtually nothing was known about their integration and interplay, if any.

To unveil the putative redox and bioelectric hidden mysteries of regenerative biology, in the commencement of this study it was hypothesized, in general, that a redox-bioelectric integrative interplay orchestrates vertebrate regeneration. Sprouting from this, two specific hypotheses arose for testing such bistate interaction using the *X. laevis* tadpole tail as a vertebrate regeneration model. First, a two-way regulation hypothesis, rooted on the electrogenic and catalytic properties of NADPH oxidases, where an O_2-oxidizing electron flow depolarizes V_m and produced ROS, in turn, regulate TEP, EF and J_I to modulate regeneration. Second, a sequential hypothesis, where an O_2 influx fuels local ROS production setting a HIF-1α-stabilizing hypoxia to modulate regeneration (Chapter IV). The results compiled robustly support both hypotheses (Chapter VII, VIII).

The comprehensive descriptive analysis – spatiotemporal profiling of extracellular bioelectricity (TEP, EF and J_I), showed a dynamic correlation of bioelectricity with regeneration progression and identified the regeneration bud at 6 hpa as key for the two-way regulation hypothesis testing. The extensive functional analysis – scanning the temporal requirement for NADPH oxidase-mediated ROS production,

showed multi-phase pleiotropic effects during regeneration (morphogenesis early; growth later) and suggested ROS as the earliest biochemical limiting factor of regeneration. Blocking NADPH oxidases decreased the depolarization-sensitive fluorescence intensity of the vital dye $DiBAC_4(3)$, unveiling the origin of the important V_m bud depolarization. Depletion of ROS levels decreased TEP magnitude and prevented or postponed J_I reversal, mimicking the altered bioelectricity in the refractory period. Short-term exposure to exogenous H_2O_2 normalized TEP magnitude and switched J_I reversal in non-regenerative conditions and, consequently, rescued and induced regeneration. Exogenous H_2O_2 was sufficiently inductive to form ectopic tails in fin injuries severing the spinal cord during the regenerative period. Molecularly, epistasis assays showed that H_2O_2 regulates Na_V channels in order to modulate regeneration. Altogether, the convergent results highlighted the redox-bioelectric interplay during regeneration and revealed mediation by early bioelectric activities of redox-modulated regeneration.

Using the optic-based probe micro-optrode (Chapter VI), the comprehensive descriptive analysis – spatiotemporal profiling of extracellular O_2 flux, showed a dynamic correlation of O_2 influx (an O_2 sink) with regeneration progression and identified the regeneration bud at 6 and 24 hpa as key for the sequential hypothesis testing. A lower O_2 influx magnitude was measured in the refractory period, exposing also a correlation with regeneration efficiency. Wound healing measurements in disparate animal models showed that the O_2 sink is an instantaneous and conserved response to injury. Inhibiting NADPH oxidases decreased the magnitude of O_2 influx, proving that exogenous O_2 (*i.e.*, not from the circulatory system) fuels the vital ROS production for downstream modulation of regeneration. Using an antioxidant drug, O_2 influx magnitude was revealed insensitive to ROS *per se*, excluding feedback between reagent (O_2) and product (ROS). Blocking HIF-1α activity virtually completely abrogated regeneration, while stabilizing its activity induced regeneration in the refractory period. Imaging and measurement of hypoxia revealed marked local hypoxia, especially in the regenerating bud of regenerative animals. The hypoxia was the result of ROS production, since NADPH oxidases inhibition decreased the level of hypoxia. Congruently with the excessive O_2 influx, refractory period had almost absent hypoxia. The hypoxia robustly correlated with HIF-1α stabilization and ROS *per se* did not stabilize HIF-1α. Attempting to further integrate HIF-1α and ROS, it was carried an epistasis assay. HIF-1α did not act downstream of ROS to modulate regeneration, backing hypoxia imaging results. Seeking a molecular insight downstream to HIF-1α, HSP90 was shown to be required for regeneration in the same time-window as HIF-1α, suggesting HSP90 as a putative (correlative) downstream target of

HIF-1α. Both HIF-1α and HSP90 are virtually immediately required for regeneration, pairing with ROS as the earliest biochemical limiting factors for regeneration; all discovered in the studies grounding this thesis. Altogether, the elucidative results demonstrated an integration of O_2, ROS and HIF-1α, unveiling a modulation of regeneration by the orchestration of early redox activities.

After successfully addressing the core of both specific hypotheses, one last critical experiment was compulsory aiming to integrate both publications' findings into a broader view. Regeneration is a multifactorial process with intricate interactions among canonical and non-canonical signalling pathways (Slack et al., 2004), and, as current studies unveiled, with interplay between apparently disparate states, redox and bioelectric. Compelling evidences from the empirical work provided robust explanations for the very upstream interplay between O_2, ROS and HIF-1α, and between ROS and bioelectricity. Since O_2 fuelled ROS, a link was missing between the master regulator of O_2 homeostasis – HIF-1α – and bioelectricity.

Seeking for the missing link, it was blocked HIF-1α activity and measured the electric current density when the hallmark J_I reversal occurs, *i.e.*, at 6 hpa. Thrillingly, the J_I reversal was prevented with a strong penetrance, proving causality. Therefore, J_I reversal is a *de facto* (causative) downstream target of HIF-1α. This crucial discover, included in the end of Chapter VIII's publication, ties loose ends allowing an evidence-based early stepwise phenomenology in regeneration, a *redox-bioelectric continuum model of regeneration* (Fig. IX.1), which can be described, in synthesis, as follows: amputation-induced barrier breaking generates outward currents (probably mainly Na^+ efflux) and O_2 influx. O_2 transforms into ROS, specifically H_2O_2, that at 6 hpa switches current reversal (to inward). O_2 and ROS tune the pO_2 microenvironment stabilizing HIF-1α, which in turn also regulate J_I reversal, in series or in parallel with H_2O_2. H_2O_2, Na_V (*i.e.*, Na^+ influx) and HIF-1α are required for and even sufficient to induce regeneration. Mechanistically, a prime candidate for the J_I reversal effect on regeneration is cell migration as it closes the wound, precedes proliferation, innervation and differentiation, and requires a vector cue (Adams et al., 2007; Beck et al., 2009; Zhao et al., 2006). Although not robustly tested, circumstantial evidences (shown in publications' supplementary information) and literature suggest that H_2O_2, Na_V and HIF-1α are important for cell migration (Brackenbury et al., 2008; Guo et al., 2015; Li et al., 2007; Pan et al., 2011). Therefore, these players may orchestrate, attracting essential cells (including neuronal cells) to form the wound epithelium and to populate the regeneration bud, subsequently reaching near-perfect regeneration. Other redox- and

bioelectric-regulated cell signalling and cell behaviour processes such as regulation of required signalling pathways (Beck et al., 2003; Lin and Slack, 2008); cytokines and progenitor cells chemotaxis (Ceradini et al., 2004); stemness control and pluripotency regulators (Oct3/4, Notch and Wnt) (Gustafsson et al., 2005; Kaidi et al., 2007; Zhang et al., 2015); proliferation, differentiation and innervation (Adams et al., 2007; Blackiston et al., 2009; Borgens et al., 1979b; Kumar and Brockes, 2012; Singer, 1952; Tseng et al., 2010), and more are evidently not excluded and most likely play roles during regeneration as discussed more lengthy in publications' discussion.

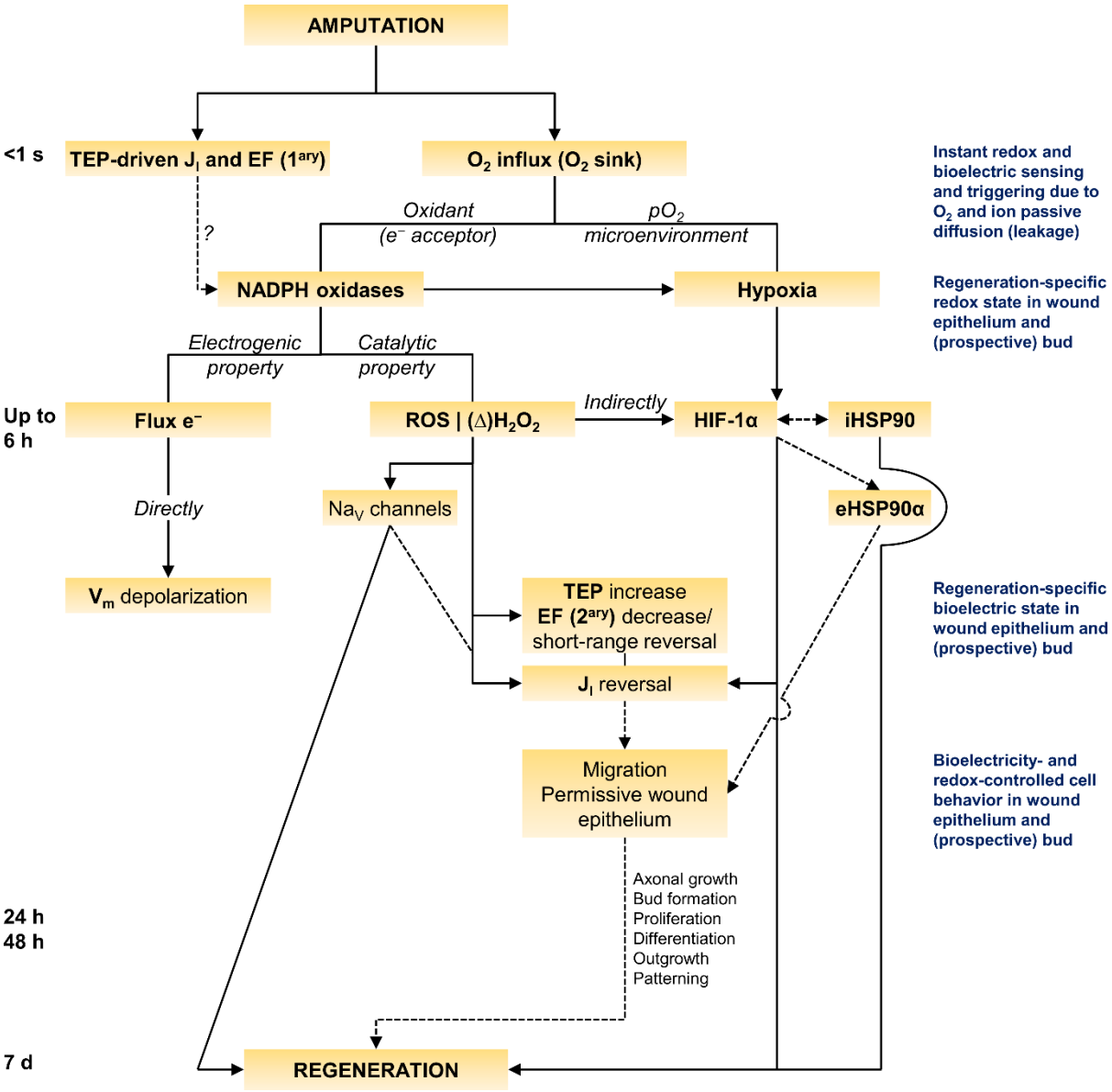

Fig. IX.1 Redox-bioelectric continuum model of regeneration. Solid line arrows: demonstrated; dotted line arrows: hypothesized/probable.

In conclusion, the thesis successfully answered the seminal questions, supporting the proposed hypotheses, partially using a cutting-edge optic-based technology. The work performed reveals and demonstrates a robust interplay between biochemical (redox) and biophysical (bioelectric) signals and an integration of the redox players – O_2, ROS and HIF-1α – during regeneration. Early and very upstream redox and bioelectric activities interact, resulting in pervasive and penetrant effects on the regeneration outcome. In the vital effort to find, gather and test limiting and stimulating factors of regeneration, this thesis unveils novel and reinforce known targets – V_m, TEP, J_I, EF, O_2, ROS, H_2O_2, aquaporins, hypoxia, HIF-1α and HSP90 – and suggest a time period – early on – to attempt to induce regeneration in deficient or poor regenerating animal models and eventually in humans with higher hopes.

9.2 Future perspectives and opportunities

Reductionist approaches have led to impressive discoveries and knowledge gain in science, especially fruitful in the detailing of intricate and elaborate networks of metabolic and signalling pathways. In this thesis, however, a more holistic-like approach was followed, merging apparently disparate research fields into the regeneration context. This approach can also be prolific in insight generation (Chao and Inoue, 2003; Lecuit and Lenne, 2007; Serena et al., 2009; Tandon et al., 2014). Any holistic approach necessarily requires interdisciplinary valences, which are not easy to obtain without collaborations in the highly specialized research laboratories. This may account, at least partially, for the lack of interdisciplinary studies in regeneration and elsewhere. In the current study, for the first time, it was orchestrated together the redox biology and bioelectricity fields during regeneration with interesting and even captivating results.

Besides the seminal interdisciplinary work, far more is needed for an in-depth and comprehensive holistic view of the regeneration process (Fig. IX.2). One immediate question popping-up after the work completion, is whether bioelectricity-modulated redox activities also occur during regeneration? Since ROS are immediately required for regeneration and bioelectric shifting is among the fastest injury-induced signals, it is hypothesized that primary EF (Chatterjee et al., 2012; Li et al., 2012; Li et al., 2013) and/or Ca^{2+} (Razzell et al., 2013) activate the NADPH oxidases (Chapter VII). A small-scale project was already designed to test this; briefly, it will be applied physiologically meaningful EF and

measured the ROS output in the regenerating tail. Preliminary results of this critical experiment excitingly support the hypothesis (Data not shown).

For the (near) future, towards a higher level of mechanistic understanding, it will be mandatory to merge the acquired insights with the molecular state repertoire, *i.e.*, to integrate the redox and bioelectric players with the canonical and non-canonical signalling pathways known to be necessary for and in some cases even sufficient to induce regeneration. Among those pathways are the Wnt, BMP, Notch, FGF, Shh and TGF (Beck et al., 2003; Ho and Whitman, 2008; Lin and Slack, 2008; Sugiura et al., 2009; Taniguchi et al., 2014).

Signalling pathways are often transduced into cell behaviours; therefore, those should be also integrated for a fluid top-down elucidation of regeneration. With the preliminarily results (circumstantial evidences) already compiled, an initial focus could be given to cell migration (Chapter VII, VIII). That cells respond to exogenous and endogenous EF, both *in vitro* and *in vivo*, is presently well established (McCaig et al., 2005). Applied EF open or close *in vitro* scratch and *ex vivo* corneal wounds (Zhao et al., 2006). Neuronal tissue accumulates upon electric stimulation of non-regenerating adult frogs (Borgens et al., 1979b). However, the intricacies of electrotaxis during the entire regeneration process require further study. Also, how ROS (Li et al., 2012; Li et al., 2013) and hypoxia/HIF-1α (Guo et al., 2015) might affect or regulate the endogenous regeneration-specific EF remains elusive.

The recent identification of regeneration-organizing cells (ROC) was a thrilling finding (Aztekin et al., 2019). Epidermis-related ROC cells migrate towards the amputation plane only in regenerative tadpoles, where they activate canonical signalling pathways. Intriguingly, ROC cells do not migrate when NADPH oxidase-mediated ROS production is inhibited (Aztekin et al., 2019). This means that early ROS may somehow guide ROC migration. Electrotaxis of ROC cells – not tested in the study – is a must test experiment for the near future. Taking the discoveries within this thesis (Chapter VII, VIII), it is tempting to suggest that ROS-switched electric currents may drive and guide ROC migration.

After cell migration, focus might be given to apoptosis, proliferation, differentiation and innervation, essential behaviours for *Xenopus* spp. tadpole tail regeneration (Adams et al., 2007; Love et al., 2013; Tseng et al., 2007; Tseng et al., 2010). As above, goal is always to integrate with the redox and bioelectric states.

Another future research direction is the accommodation of other states, in addition to the above-mentioned molecular state, within the redox-bioelectric model of regeneration. Probably, the more important are the mechanical (Golding et al., 2016; Tsutsumi et al., 2016), the neuronal (Filoni and Paglialunga, 1990; Gaete et al., 2012; Meda et al., 2018; Mitogawa et al., 2014; Taniguchi et al., 2008), the hormonal (Herrera-Rincon et al., 2018; Marshall et al., 2019) and the immunological (Fukazawa et al., 2009; Godwin et al., 2013; Mescher and Neff, 2005; Paré et al., 2017) states (Fig. IX.2). In fact, preliminary, but robust, critical experiments were already performed regarding the mechanical state, showing that mechanosensitive channels, specifically stretch-activated channels, are significantly required not only for regeneration but also for the hallmark J_I reversal (unpublished; Appendix XIV). This finding, once more, put J_I reversal as a core phenomenon in regeneration, linking all states analysed.

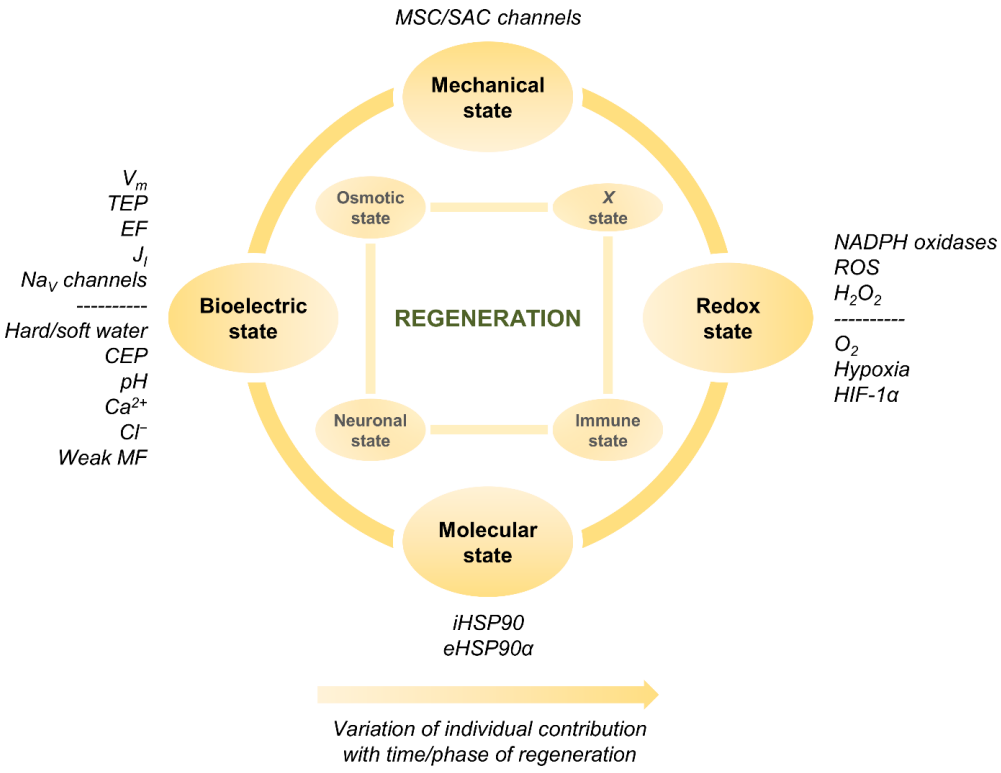

Fig. IX.2 Regeneration: a holistic view, or the path for a unifying theory in regeneration. Outer circle: studied and integrated (at least partially; Chapter VII, VII; Appendix XIV); inner square: to be studied and integrated. *X* stands for other state(s), *e.g.*, hormonal state.

The empirical work and advanced hypotheses intended to unveil the fundaments, the basics, behind regeneration. It was not the intention to have a practical or clinical agenda guiding the course of the performed research. Although not applied research, the basic research performed is, nonetheless, on

fields – regenerative biology and medicine – that eager for novel insights and targets in order to enhance and/or stimulate the very limited and circumscribed regenerating abilities of the human body (Alvarado and Tsonis, 2006). Therefore, any future perspective and opportunity, no matter how far in time still, would be incomplete if a bench to bedside possibility was not included. Obviously, prior to that, compulsory intermediate steps need to be followed. Among the first ones is to verify the findings in different regeneration models, especially in adults; then, poor regenerating animals, including mammals, should be tested with the gained knowledge. Possible approaches would be the application of engineered devices and/or gels (Churchill et al., 2019; Golding et al., 2016; Hechavarria et al., 2010; Herrera-Rincon et al., 2018; Shapiro et al., 2005) simultaneously boosting, until a permissive level is reached, the endogenous redox and bioelectric activities, especially earlier after amputation. For instance, an engineered crème could be a hydrogel with controlled release of O_2 (Harrison et al., 2007) and H_2O_2 (Garland et al., 2014) and packed with galvanic microparticles (Tandon et al., 2014).

9.3 Glimpse into a putative future: cohabiting "regeneration" strategies

Intrigued by folk tales and anecdotal reports of mainly fishermen about regenerating lobsters, crabs and crayfish, R. Réaumur performed the first systematic experiments on regeneration. The year was 1712 and he scientifically demonstrated regeneration of crayfish claws, commencing the modern study of regeneration (Dinsmore, 1991; Réaumur, 1712). Three centuries accumulating massive multilevel knowledge have passed; yet, epimorphic regeneration stimulation in humans remains painfully elusive (Carlson, 2007). What is the situation point? Is it a utopic dream to expect near-perfect limb regeneration in humans? Will a lost arm ever regrows or be replaced aesthetically and functionally?

To address these questions, below are classified and summarized the putative envisioned "regeneration" strategies that can eventually compete in the future – unfortunately hard to precise – to provide the best solution for truncated or mutilated humans to regain the form and function of lost organs or structures (Table IX.1). Strategies might not likely be ripe for clinical application simultaneously and include approaches purely based on regenerative biology or medicine, and beyond biology. Although designed for epimorphic regeneration of limbs, strategies might also be applied to other regeneration targets, such as the heart. Ideally, people and patients will have the opportunity to choose the "regeneration" treatment following the physician advices, according their condition, and the advantages and disadvantages of each cohabiting strategy.

Table IX.1 Summary of the envisioned strategies to "regenerate" or regain the form and function of lost organs or structures in truncated or mutilated humans.

Selected parameters	Strategy		
	***In situ* regeneration**	***Ex situ* regeneration**	**Bionics**
Approaches	Biomimetic Inducers (triggers) Recapitulate development AI-aided or AI-generated	Biomimetic Perfusion-decellularization 3D Bioprinting Xenoculture AI-aided or AI-generated	Biomimetic Biomechatronics AI-aided or AI-generated
Cancer risk	Medium to high	Low to medium	None
Immunorejection	Absent	Absent to mild	Absent to mild
Morphology	Near-perfect	Identical to near-perfect	Progressively biomimetic
Functionality	Near-perfect	Identical to near-perfect	Progressively identical
Timing	Months to years	Weeks to months	Days to weeks
Status	Old field Basic and applied research No patient application	Emergent field Basic and applied research No patient application	Emergent field Basic and applied research Patient application
Clinical access*	Distant	Medium	Close

* Tentative relative temporal ordering based on the interpretation of analysed literature.

9.3.1 *In situ* regeneration

Probably the most ambitious and hard to achieve strategy to regenerate human structures efficiently is by stimulating latent regenerative abilities or inducing them anew, likely recapitulating development (Nacu and Tanaka, 2011). The *in situ* regeneration strategy derives from epimorphic regeneration of highly regenerative animals, such as anuran and urodele amphibians, and fish (Stoick-Cooper et al., 2007). As it intends to find stimulating factors in those animals this is a biomimicry-based strategy.

On a theoretical basis, humans should retain the required framework for efficient limb regeneration. This assertion is based on five lines of evidence: (i) regeneration reactivates developmental pathways and processes (Gardiner et al., 2002); (ii) foetal and neonatal digit tips of mice regenerate, sharing processes with amphibian's blastema-based regeneration (Han et al., 2003; Han et al., 2008; Reginelli et al., 1995); (iii) foetal and postnatal fingertips of humans regenerate similarly with mice, essentially in children (Douglas, 1972; Illingworth, 1974), with cases in adults (Bossley, 1975); (iv) growth factor treatment induces regeneration in non-regenerating mouse digits (Yu et al., 2010); and (v) alligator tails regenerate, excluding human limb cross-sectional area as a limiting factor (Han et al., 2005).

Anuran amphibians lose the regenerative ability post metamorphosis, making them the standard model for stimulation experiments. Importantly, similar experiments are typically performed in mammals. These experiments can be organized in six main points (Carlson, 2007): (i) regeneration-promoting tissue implants or extracts (Malinin and Deck, 1958); (ii) dedifferentiation-inducing mechanical trauma or chemical irritation (Polezhayev, 1946; Rose, 1944); (iii) increased neuronal supply and factors (Kumar et al., 2007; Sidman and Singer, 1951); (iv) scarring avoidance (Schotté and Wilber, 1958) (v) supplemented growth factors and molecules (Ferreira et al., 2016; Ferreira et al., 2018; Yokoyama et al., 2001; Yu et al., 2010); and (vi) electric stimulation and control (Borgens et al., 1977a; Ferreira et al., 2016; Ferreira et al., 2018; Hechavarria et al., 2010; Smith, 1967; Tseng et al., 2010). Practically all of these attempts produced partial regeneration in both amphibians and mammals. Although with modest success, the efforts suggest regenerative latency that could be more efficiently harvested once a more holistic understanding of regeneration allows for multifactorial stimulatory attempts.

The major risk, and so disadvantage, of *in situ* regeneration would be cancer induction, because proliferation and (de)differentiation would occur at high levels (Oviedo and Beane, 2009). Other disadvantage would be the time required for complete regeneration. The core advantage would be the identical and symmetrical regeneration, in both physiological function and aesthetical appearance.

9.3.2 *Ex situ* regeneration

Another ambitious strategy to successfully regenerate the human body is by *in vitro* cell seeding and tissue culture forming or completing the desired structure to be implanted. The *ex situ* regeneration strategy grounds on the shoulders of the cell, tissue and organ culture, the tissue engineering and the stem cells decades old research (Ambrose, 2017; Berthiaume et al., 2011; Cai et al., 2004; Carrel and Burrows, 1911; Till and McCulloch, 1961), and in the more recent induced pluripotent stem cells (iPS) (Singh et al., 2015; Takahashi and Yamanaka, 2006; Zhou et al., 2008) and additive manufacturing or 3D bioprinting (Boland et al., 2003; Murphy and Atala, 2014; Wilson and Boland, 2003) technologies.

The structure culture strategy can be accomplished by three main approaches that, although promising, are in their infancy: (i) the 'ghost structure' approach, where the intended organ or structure (autologous or heterologous) to be replaced is decellularized, exposing the ECM "skeleton". This endogenous or native scaffold is kept on a bioreactor continuously perfusing oxygen, nutrients and growth factors to feed the receptor's seeded stem, progenitor or differentiated autologous cells. Cells

autonomously self-organize and form the complete structure (He and Callanan, 2013). This approach successfully produced, at least partially, functional rodent heart, pancreas, lung and liver (Goh et al., 2013; Ott et al., 2008; Ott et al., 2010; Uygun et al., 2010), and a rat and monkey limb (Jank et al., 2015); (ii) the *de novo* and scaffold-mediated structure bioprinting, where autologous cells and biomaterials are layered by an adapted printer to produce the intended structure entirely or over a structure-like sacrificial scaffold (Murphy and Atala, 2014). This approach has generated transplantable tissues, and simple or hollow organs, including skin, bone, cartilage, blood vessels, heart components, brain tissue, ear and bladder (Atala et al., 2006; Hockaday et al., 2012; Jank et al., 2015; Kang et al., 2016; Lozano et al., 2015; Norotte et al., 2009); however, proper vascularization and innervation are major barriers to produce complex and solid organs, like the kidney and heart (Munaz et al., 2016; Murphy and Atala, 2014); and (iii) the emergent structure xenoculture, where receptor's stem cells are microinjected into donor's embryo (Wu et al., 2017; Yamaguchi et al., 2017), to produce transplantable human-animal chimeric organs, in species size-compatible with humans, like pigs.

The key advantages of this strategy are cancer risk avoidance and quicker regeneration (except for the xenoculture), while the major disadvantages are the need for ultraprecise microsurgery transplantation, the finding of proper donors and possible transplant immunorejection (especially for the xenoculture).

9.3.3 Bionics

Adapting the definition of regeneration to simply a "process that regain form and function upon insult", it is possible to go beyond regenerative biology and take advantage of the prolific information (digital) revolution (Makridakis, 1995; Turing, 1937) to obtain regeneration. The bionics strategy emerges from the prosthetics (ten Kate et al., 2017), biomimicry (Hwang et al., 2015) and robotic (Hockstein et al., 2007) researches. Bionics – perhaps a portmanteau of 'biology' and 'electronics' – intends to deliver robotic (mechatronic) structures biologically immerged, supplemented and enhanced.

Currently, bionics – or more specifically, biomechatronics (physiology merged with mechatronics) – has a quick bench-to-bedside translation to replace lost arms, legs, hands and feet in a personalized way. Indeed and besides its infancy, of all the strategies herein classified, bionics seems to be on the vanguard to provide aesthetically and functionality competent and very satisfactory treatments. Several recent milestones support this assertion and include: (i) bionic ankle-foot prosthesis that, for the first time, permitted biomechanical and physiological normalization with a natural leg (*i.e.*, gait as if with

own leg) (Herr and Grabowski, 2011); (ii) autonomous power systems, allowing active prosthetics (Herr and Grabowski, 2011; Windrich et al., 2016); (iii) neuromuscular interface microchips, allowing real time autonomous adjustment of prosthetics response (Hoover et al., 2012); (iv) emulation of natural sensation with skin-like receptors (Tee et al., 2015); and (v) harvesting of natural control with a surgical paradigm shift in amputations and microprocessors connecting brain to structure (Hochberg et al., 2012; Ortiz-Catalan et al., 2014; Srinivasan et al., 2017). The promise of bionic strategies goes beyond limb rescue, applying to internal organ function recovery (Cook et al., 2015; El-Khatib et al., 2017).

Notably, the bionics strategy might present several advantages over purely regenerative biology-based ones. The most striking is cancer prevention: no biological regrow, no cancer risk. This introduces the second advantage, time: after biometric and biomechanical evaluation, typically by magnetic resonance imaging (MRI), robotic indenters and *post hoc* modelling of biologic counterparts, bionic replacements can be manufactured quicker than regrown structures. The possibility to a fully-sensitive autologous or artificial skin coverture still warrants more and deeper research to become reality. Similarly, neuromuscular interface systems have few degrees of freedom in spatiotemporal resolutions (responsiveness and accuracy in gross and fine movements). Therefore, first generations (already available or in research) bionic limbs will be less sensitive and less motile than natural (regrown) ones. Additionally, the use of electric-based systems and possible ferromagnetic materials makes bionics incompatible with MRI, a powerful diagnostic and therapeutic medical tool.

9.3.4 Artificial intelligence-generated discovery

In 2009, the 50 millionth scientific article was published since the seminal French *Le Journal des Sçavans* and English *Philosophical Transactions* proto-journals were launched in 1665 (Jinha, 2010). Of about 30 thousand scholarly peer-reviewed journals active, the annual output is estimated to be roughly 2.5 million articles, with a mean annual growth rate of 6% (Ware and Mabe, 2015). Thus, the text and data to be searched and analysed or 'mined' by a student or scientist is cumbersome. In addition to big text/data, interdisciplinary, holistic and systems biology research will likely become more common and transversal (Brigandt, 2013; Chuang et al., 2010; Renwick, 2016; Somvanshi and Venkatesh, 2014), producing new and enlarging old massive and intricate networks and feedbacks of signals, factors, processes and behaviours. Altogether, the need of assistance from powerful information technologies (IT) in research is a pressing reality of an increasingly demanding science.

By the year 2030, it is estimated that 20–40% of all jobs, in several G8 economies, are at risk owing to automation from robotics and artificial intelligence (AI) (PwC, 2017). Another report estimates that 49% of all work activities are suitable for immediate automation, by adapting the current technological catalogue (Manyika et al., 2017). While in the past, most was low skilled labour substitutions, now and in the future, with the information and AI (r)evolutions (Makridakis, 1995; Makridakis, 2017; Turing, 1950), high skilled labour is also prone for replacement, including that of a scientist (World Economic Forum, 2016). In fact, the year 2004 marks the commencing of AI-generated scientific knowledge. An AI-brained robot scientist scanned the scientific literature, formulated original hypotheses, tested them experimentally and discovered novelty in yeast's genomics, outperforming in time and resources human scientists (King et al., 2004; King et al., 2009). More recently, also going through the core stages of research, another robot scientist discovered some candidate drugs against malaria (Williams et al., 2015). The sole stage yet out of AI reach is coherent, hardcore and reliable scientific writing. Notwithstanding, as AI-generated journalistic pieces (*e.g.*, Automated Insights' Wordsmith, Narrative Science's Quill and The Washington Post's Heliograf), and non-fiction and fiction books (*e.g.*, Philip Parker's patented algorithms) prove (Clerwall, 2014; Podolny, 2015), scientific writing is also prone to automation. Thought-provoking reviews, hypotheses and research articles, or even Ph.D. theses might be authored or co-authored in the future by advanced AI automated scientific writers. AI capabilities will first be, more likely, applied to aid and then automate the peer review publishing process to screen and expedite science communication and divulgation (BioMed Central, 2017).

Therefore, AI-based research – either AI-aided and/or AI-generated – might be, besides its actual immaturity, a potential and important source of discovery in all domains and fields of science, and regeneration is no exception. Cooperation and even competition among human and robot scientists will probably drive research a new leap forward. With AI assistance or discovery, humans might have an ultimate chance to, using the above strategies, regenerate or regain function of lost body parts.

9.3.5 Merged strategies

As often occurs in clinical practice, treatment strategies might be merged for idiosyncratic reasons or opportunities. A foreseeable one, for instance, would be *in situ* regeneration facilitated and/or accelerated with the use of biomimetic acellular substrates or native ECM scaffolds, or with the grafting of autologous tissues cultured *in vitro*.

EPILOGUE

FINALE

No divino impudor da mocidade,
Nesse êxtase pagão que vence a sorte,
Num frémito vibrante de ansiedade,
Dou-te o meu corpo prometido à morte!

Florbela Espanca *in* Charneca em flor (Volúpia) (1931; *postumus*)[7]

A 'book' of this sort – an academic thesis – must end recalling the title for a final test of its accuracy, after the multitude of pages attempting to support it. *Unveiling the integration of redox and bioelectric phenomena in vertebrate regeneration*, the Ph.D. thesis title. The presented and defended work (i) does unveil a previously unknown process in regeneration, the redox-bioelectric interplay, and (ii) does integrate, as holistically as possible, the redox (biochemical) and bioelectric (biophysical) activities, either discretely and in conjugation, in the context of vertebrate epimorphic regeneration (*Xenopus laevis* tadpole tail as model).

Hopefully, this work will set the stage for a more widespread use of interdisciplinary approaches for the study of animal regeneration, aiming for a higher level of mechanistic detailing and integration that might result in promising translational medicine opportunities.

REFERENCES

CITATIONS

Cuando algunos sentimos la tentación de despreciar demasiado a nuestros semejantes,
nos basta para reconciliarnos con ellos contemplar una biblioteca como ésta,
llena de monumentos elevados por la grandeza del hombre.

Arturo Pérez-Reverte *in* Hombres buenos (2015)[8]

The references cited in the publications and manuscripts are embedded in their equivalent section and therefore are not included in this list, unless cited outside the publications. For this reason, naturally, many references are duplicated.

Adams, D. S., Masi, A. and Levin, M. (2007). H+ pump-dependent changes in membrane voltage are an early mechanism necessary and sufficient to induce Xenopus tail regeneration. *Development* **134**, 1323–35.

Adams, D. S., Tseng, A.-S. and Levin, M. (2013). Light-activation of the Archaerhodopsin H(+)-pump reverses age-dependent loss of vertebrate regeneration: sparking system-level controls in vivo. *Biol. Open* **2**, 306–13.

Akimenko, M.-A., Marí-Beffa, M., Becerra, J. and Géraudie, J. (2003). Old questions, new tools, and some answers to the mystery of fin regeneration. *Dev. Dyn.* **226**, 190–201.

Alibardi, L. (2010). Regeneration in Reptiles and Its Position Among Vertebrates. In *Morphological and Cellular Aspects of Tail and Limb Regeneration in Lizards*, pp. 1–49. Berlin: Springer-Verlag.

Allan, C. H., Fleckman, P., Fernandes, R. J., Hager, B., James, J., Wisecarver, Z., Kyle Satterstrom, F., Gutierrez, A., Norman, A., Pirrone, A., et al. (2006). Tissue response and Msx1 expression after human fetal digit tip amputation in vitro. *Wound Repair Regen.* **14**, 398–404.

Altizer, A. M., Stewart, S. G., Albertson, B. K. and Borgens, R. B. (2002). Skin flaps inhibit both the current of injury at the amputation surface and regeneration of that limb in newts. *J. Exp. Zool.* **293**, 467–477.

Alvarado, A. S. and Tsonis, P. A. (2006). Bridging the regeneration gap: genetic insights from diverse animal models. *Nat. Rev. Genet.* **7**, 873–84.

Ambrose, C. T. (2017). An amended history of tissue culture: Concerning Harrison, Burrows, Mall, and Carrel. *J. Med. Biogr.* 096777201668503.

Atala, A., Bauer, S. B., Soker, S., Yoo, J. J. and Retik, A. B. (2006). Tissue-engineered autologous bladders for patients needing cystoplasty. *Lancet* **367**, 1241–1246.

Aztekin, C., Hiscock, T. W., Marioni, J. C., Gurdon, J. B., Simons, B. D. and Jullien, J. (2019). Identification of a regeneration-organizing cell in the Xenopus tail. *Science (80-.).* **364**, 653–658.

Barry, P. H. and Lynch, J. W. (1991). Liquid junction potentials and small cell effects in patch-clamp analysis. *J. Membr. Biol.* **121**, 101–117.

Beane, W. S., Tseng, A.-S., Morokuma, J., Lemire, J. M. and Levin, M. (2012). Inhibition of planar cell polarity extends neural growth during regeneration, homeostasis, and development. *Stem Cells Dev.* **21**, 2085–94.

Beck, C. W. (2015). Development of the vertebrate tailbud. *Wiley Interdiscip. Rev. Dev. Biol.* **4**, 33–44.

Beck, C. W., Christen, B. and Slack, J. M. W. (2003). Molecular pathways needed for regeneration of spinal cord and muscle in a vertebrate. *Dev. Cell* **5**, 429–39.

Beck, C. W., Christen, B., Barker, D. and Slack, J. M. W. (2006). Temporal requirement for bone morphogenetic proteins in regeneration of the tail and limb of Xenopus tadpoles. *Mech. Dev.* **123**, 674–688.

Beck, C. W., Izpisúa Belmonte, J. C. and Christen, B. (2009). Beyond early development: Xenopus as an emerging model for the study of regenerative mechanisms. *Dev. Dyn.* **238**, 1226–48.

Bely, A. E. and Nyberg, K. G. (2010). Evolution of animal regeneration: re-emergence of a field. *Trends Ecol. Evol.* **25**, 161–70.

Bely, A. E. and Sikes, J. M. (2010). Latent regeneration abilities persist following recent evolutionary loss in asexual annelids. *Proc. Natl. Acad. Sci. U. S. A.* **107**, 1464–9.

Berthiaume, F., Maguire, T. J. and Yarmush, M. L. (2011). Tissue Engineering and Regenerative Medicine: History, Progress, and Challenges. *Annu. Rev. Chem. Biomol. Eng.* **2**, 403–430.

BioMed Central (2017). *What might peer review look like in 2030?*

Blackiston, D. J., McLaughlin, K. a and Levin, M. (2009). Bioelectric controls of cell proliferation: ion channels, membrane voltage and the cell cycle. *Cell Cycle* **8**, 3519–28.

Boland, T., Mironov, V., Gutowska, A., Roth, E. a and Markwald, R. R. (2003). Cell and Organ Printing 2: Fusion of Cell Aggregates in Three-Dimensional Gels. *Anat. Rec. A. Discov. Mol. Cell. Evol. Biol.* **272**, 497–502.

Bonnet, C. (1745). *Traité d'insectologie*. Paris: Duvand Librairie.

Bonnet, C. (1777). Expériences sur la régénération de la tête du limaçon terrestre. *J. Phys.* **10**, 165–179.

Borgens, R. B. (1982). What is the role of naturally produced electric current in vertebrate regeneration and healing. *Int. Rev. Cytol.* **76**, 245–298.

Borgens, R. B., Vanable, J. W. and Jaffe, L. F. (1977a). Bioelectricity and regeneration. I. Initiation of frog limb regeneration by minute currents. *J. Exp. Zool.* **200**, 403–416.

Borgens, R. B., Vanable, J. W. and Jaffe, L. F. (1977b). Bioelectricity and regeneration: large currents leave the stumps of regenerating newt limbs. *Proc. Natl. Acad. Sci. U. S. A.* **74**, 4528–32.

Borgens, R. B., Vanable, J. W. and Jaffe, L. F. (1979a). Role of subdermal current shunts in the failure of frogs to regenerate. *J. Exp. Zool.* **209**, 49–56.

Borgens, R. B., Vanable, J. W. and Jaffe, L. F. (1979b). Small artificial currents enhance Xenopus limb regeneration. *J. Exp. Zool.* **207**, 217–226.

Borgens, R. B., Robinson, K. R., Vanable, J. W. and McGinnis, M. E. (1989). *Electric Fields in Vertebrate Repair: Natural and Applied Voltages in Vertebrate Regeneration and Healing*. (ed. Borgens, R. B.), Robinson, K. R.), Vanable, J. W.), and McGinnis, M. E.) New York: Alan R. Liss.

Bossley, C. J. (1975). Conservative treatment of digit amputations. *N. Z. Med. J.* **82**, 379–80.

Brackenbury, W. J., Djamgoz, M. B. A. and Isom, L. L. (2008). An Emerging Role for Voltage-Gated Na+ Channels in Cellular Migration: Regulation of Central Nervous System Development and Potentiation of Invasive Cancers. *Neurosci.* **14**, 571–583.

Brahimi-Horn, M. C. and Pouysségur, J. (2007). Oxygen, a source of life and stress. *FEBS Lett.* **581**, 3582–91.

Bretag, A. H. (2017). The glass micropipette electrode: A history of its inventors and users to 1950. *J. Gen. Physiol.*

Brigandt, I. (2013). Integration in biology: Philosophical perspectives on the dynamics of interdisciplinarity. *Stud. Hist. Philos. Sci. Part C Stud. Hist. Philos. Biol. Biomed. Sci.* **44**, 461–465.

Brockes, J. P. and Kumar, A. (2008). Comparative aspects of animal regeneration. *Annu. Rev. Cell Dev. Biol.* **24**, 525–549.

Cai, J., Weiss, M. L. and Rao, M. S. (2004). In search of "stemness." *Exp. Hematol.* **32**, 585–598.

Campbell, L. J. and Crews, C. M. (2008). Wound epidermis formation and function in urodele amphibian limb regeneration. *Cell. Mol. Life Sci.* **65**, 73–9.

Carlson, B. M. (2007). *Principles of Regenerative Biology*. London: Academic Press.

Carnevali, C. (2006). Regeneration in Echinoderms: repair, regrowth, cloning. *ISJ* **3**, 64–76.

Carrel, A. and Burrows, M. T. (1911). Cultivation of Tissues in Vitro and Its Technique. *J. Exp. Med.* **XIII**, 387–406.

Ceradini, D. J., Kulkarni, A. R., Callaghan, M. J., Tepper, O. M., Bastidas, N., Kleinman, M. E., Capla, J. M., Galiano, R. D., Levine, J. P. and Gurtner, G. C. (2004). Progenitor cell trafficking is regulated by hypoxic gradients through HIF-1 induction of SDF-1. *Nat. Med.* **10**, 858–64.

Chao, E. Y. S. and Inoue, N. (2003). Biophysical stimulation of bone fracture repair, regeneration and remodelling. *Eur. Cell. Mater.* **6**, 72–84; discussion 84-5.

Chatterjee, S., Browning, E. A., Hong, N., DeBolt, K., Sorokina, E. M., Liu, W., Birnbaum, M. J. and Fisher, A. B. (2012). Membrane depolarization is the trigger for PI3K/Akt activation and leads to the generation of ROS. *AJP Hear. Circ. Physiol.* **302**, H105–H114.

Chen, C.-H. and Poss, K. D. (2017). Regeneration Genetics. *Annu. Rev. Genet.* **51**, 63–82.

Chen, Y., Lin, G. and Slack, J. M. W. (2006). Control of muscle regeneration in the Xenopus tadpole tail by Pax7. *Development* **133**, 2303–13.

Chera, S., Ghila, L., Dobretz, K., Wenger, Y., Bauer, C., Buzgariu, W., Martinou, J.-C. and Galliot, B. (2009). Apoptotic cells provide an unexpected source of Wnt3 signaling to drive hydra head regeneration. *Dev. Cell* **17**, 279–89.

Child, C. M. (1907). An analysis of form-regulation in Tubularia. *Arch. für Entwicklungsmechanik der Org.* **23**, 445–456.

Chiou, K. and Collins, E. M. S. (2018). Why we need mechanics to understand animal regeneration. *Dev. Biol.* **433**, 155–165.

Chuang, H.-Y., Hofree, M. and Ideker, T. (2010). A Decade of Systems Biology. *Annu. Rev. Cell Dev. Biol.* **26**, 721–744.

Churchill, C. D. M., Winter, P., Tuszynski, J. A. and Levin, M. (2019). EDEn–Electroceutical Design Environment: Ion Channel Tissue Expression Database with Small Molecule Modulators. *iScience* **11**, 42–56.

Clause, A. R. (2006). Caudal Autotomy and Regeneration in Lizards. **973**, 965–973.

Clerwall, C. (2014). Enter the Robot Journalist. *Journal. Pract.* **8**, 519–531.

Coffman, J. A. and Su, Y.-H. (2019). Redox regulation of development and regeneration. *Curr. Opin. Genet. Dev.* **57**, 9–15.

Cook, J. A., Shah, K. B., Quader, M. A., Cooke, R. H., Kasirajan, V., Rao, K. K., Smallfield, M. C., Tchoukina, I. and Tang, D. G. (2015). The total artificial heart. *J. Thorac. Dis.* **7**, 2172–80.

Dent, J. N. (1962). Limb regeneration in larvae and metamorphosing individuals of the South African clawed toad. *J. Morphol.* **110**, 61–77.

Deuchar, E. M. (1975). Regeneration of the tail bud in Xenopus embryos. *J. Exp. Zool.* **192**, 381–390.

Deuchar, E. M. (1976). Regeneration of amputated limb-buds in early rat embryos. *J. Embryol. Exp. Morphol.* **35**, 345–354.

Dinsmore, C. E. (1991). *A history of regeneration research: milestones in the evolution of a science*. (ed. Dinsmore, C. E.) New York: Cambridge University Press.

Diwanji, N. and Bergmann, A. (2018). An unexpected friend — ROS in apoptosis-induced compensatory proliferation: Implications for regeneration and cancer. *Semin. Cell Dev. Biol.* **80**, 74–82.

Douglas, B. S. (1972). Conservative management of guillotine amputation of the finger in children. *J. Paediatr. Child Health* **8**, 86–89.

Durant, F., Morokuma, J., Fields, C., Williams, K., Adams, D. S. and Levin, M. (2017). Long-Term, Stochastic Editing of Regenerative Anatomy via Targeting Endogenous Bioelectric Gradients. *Biophys. J.* **112**, 2231–2243.

El-Khatib, F. H., Balliro, C., Hillard, M. A., Magyar, K. L., Ekhlaspour, L., Sinha, M., Mondesir, D., Esmaeili, A., Hartigan, C., Thompson, M. J., et al. (2017). Home use of a bihormonal bionic pancreas versus insulin pump therapy in adults with type 1 diabetes: a multicentre randomised crossover trial. *Lancet* **389**, 369–380.

Endo, T., Bryant, S. V and Gardiner, D. M. (2004). A stepwise model system for limb regeneration. *Dev. Biol.* **270**, 135–45.

Ferreira, F., Thorsteinsdóttir, S. and Certal, C. (2011). Regeneração da barbatana caudal em peixe-zebra (Danio rerio): uma perspectiva biofísica. *Repos. ULisboa*.

Ferreira, F., Luxardi, G., Reid, B. and Zhao, M. (2016). Early bioelectric activities mediate redox-modulated regeneration. *Development* **143**, 4582–4594.

Ferreira, F., Raghunathan, V., Luxardi, G., Zhu, K. and Zhao, M. (2018). Early redox activities modulate Xenopus tail regeneration. *Nat. Commun.* **9**, 1–15.

Ferreira, F., Luxardi, G., Reid, B., Ma, L. and Raghunathan, V. (2019). Real-time physiological measurements of oxygen using a non- invasive self-referencing micro-optrode. *Nat. Protoc.* **(In press)**,.

Filoni, S. and Paglialunga, L. (1990). Effect of denervation on hindlimb regeneration in Xenopus laevis larvae. *Differentiation* **43**, 10–9.

Fogarty, C. E., Diwanji, N., Lindblad, J. L., Tare, M., Amcheslavsky, A., Makhijani, K., Brückner, K., Fan, Y. and Bergmann, A. (2016). Extracellular Reactive Oxygen Species Drive Apoptosis-Induced Proliferation via Drosophila Macrophages. *Curr. Biol.* **26**, 575–584.

Fröbisch, N. B., Bickelmann, C., Olori, J. C. and Witzmann, F. (2015). Deep-time evolution of regeneration and preaxial polarity in tetrapod limb development. *Nature* **527**, 231–234.

Fukazawa, T., Naora, Y., Kunieda, T. and Kubo, T. (2009). Suppression of the immune response potentiates tadpole tail regeneration during the refractory period. *Development* **136**, 2323–7.

Gaete, M., Muñoz, R., Sánchez, N., Tampe, R., Moreno, M., Contreras, E. G., Lee-Liu, D. and Larraín, J. (2012). Spinal cord regeneration in Xenopus tadpoles proceeds through activation of Sox2-positive cells. *Neural Dev.* **7**, 13.

Galis, F., Wagner, G. P. and Jockusch, E. L. (2003). Why is limb regeneration possible in amphibians but not in reptiles, birds, and mammals? *Evol. Dev.* **5**, 208–20.

Gardiner, D. M., Endo, T. and Bryant, S. V (2002). The molecular basis of amphibian limb regeneration: integrating the old with the new. *Semin. Cell Dev. Biol.* **13**, 345–52.

Gargioli, C. and Slack, J. M. W. (2004). Cell lineage tracing during Xenopus tail regeneration. *Development* **131**, 2669–2679.

Garland, S. P., Wang, R. Y., Raghunathan, V. K., Lam, K. S., Murphy, C. J., Russell, P., Sun, G. and Pan, T. (2014). Photopatternable and photoactive hydrogel for on-demand generation of hydrogen peroxide in cell culture. *Biomaterials* **35**, 1762–1770.

Gauron, C., Rampon, C., Bouzaffour, M., Ipendey, E., Teillon, J., Volovitch, M. and Vriz, S. (2013). Sustained production of ROS triggers compensatory proliferation and is required for regeneration to proceed. *Sci. Rep.* **3**, 2084.

Gilbert, S. F. (2006). *Developmental Biology*. Eighth. Sinauer Associates Inc.; 8th edition.

Godwin, J. W. and Brockes, J. P. (2006). Regeneration, tissue injury and the immune response. *J. Anat.* **209**, 423–32.

Godwin, J. W., Pinto, A. R. and Rosenthal, N. A. (2013). Macrophages are required for adult salamander limb regeneration. *Proc. Natl. Acad. Sci.* **110**, 9415–9420.

Goh, S.-K., Bertera, S., Olsen, P., Candiello, J. E., Halfter, W., Uechi, G., Balasubramani, M., Johnson, S. A., Sicari, B. M., Kollar, E., et al. (2013). Perfusion-decellularized pancreas as a natural 3D scaffold for pancreatic tissue and whole organ engineering. *Biomaterials* **34**, 6760–72.

Golding, A., Guay, J. A., Herrera-Rincon, C., Levin, M. and Kaplan, D. L. (2016). A Tunable Silk Hydrogel Device for Studying Limb Regeneration in Adult Xenopus Laevis. *PLoS One* **11**, 1–23.

Goss, R. J. (1956). An experimental analysis of taste barbel regeneration in the catfish. *J. Exp. Zool.* **131**, 27–49.

Goss, R. J. (1969). *Principles of Regeneration.* New York: Academic Press.

Graham, J. and Gerard, R. W. (1946). Membrane potentials and excitation of impaled single muscle fibers. *J. Cell. Comp. Physiol.* **28**, 99–117.

Guo, X., Jiang, X., Ren, X., Sun, H., Zhang, D., Zhang, Q., Zhang, J. and Huang, Y. (2015). The Galvanotactic Migration of Keratinocytes is Enhanced by Hypoxic Preconditioning. *Sci. Rep.* **5**, 1–13.

Gustafsson, M. V., Zheng, X., Pereira, T., Gradin, K., Jin, S., Lundkvist, J., Ruas, J. L., Poellinger, L., Lendahl, U. and Bondesson, M. (2005). Hypoxia requires Notch signaling to maintain the undifferentiated cell state. *Dev. Cell* **9**, 617–628.

Han, M., Yang, X., Farrington, J. E. and Muneoka, K. (2003). Digit regeneration is regulated by Msx1 and BMP4 in fetal mice. *Development* **130**, 5123–5132.

Han, M., Yang, X., Taylor, G., Burdsal, C. a, Anderson, R. a and Muneoka, K. (2005). Limb regeneration in higher vertebrates: developing a roadmap. *Anat. Rec. B. New Anat.* **287**, 14–24.

Han, M., Yang, X., Lee, J., Allan, C. H. and Muneoka, K. (2008). Development and regeneration of the neonatal digit tip in mice. *Dev. Biol.* **315**, 125–35.

Han, P., Zhou, X.-H., Chang, N., Xiao, C.-L., Yan, S., Ren, H., Yang, X.-Z., Zhang, M.-L., Wu, Q., Tang, B., et al. (2014). Hydrogen peroxide primes heart regeneration with a derepression mechanism. *Cell Res.* **24**, 1091–107.

Harrison, B. S., Eberli, D., Lee, S. J., Atala, A. and Yoo, J. J. (2007). Oxygen producing biomaterials for tissue regeneration. *Biomaterials* **28**, 4628–4634.

Hayashi, S., Ochi, H., Ogino, H., Kawasumi, A., Kamei, Y., Tamura, K. and Yokoyama, H. (2014). Transcriptional regulators in the Hippo signaling pathway control organ growth in Xenopus tadpole tail regeneration. *Dev. Biol.* **396**, 31–41.

He, M. and Callanan, A. (2013). Comparison of methods for whole-organ decellularization in tissue engineering of bioartificial organs. *Tissue Eng. Part B. Rev.* **19**, 194–208.

Hechavarria, D., Dewilde, A., Braunhut, S., Levin, M. and Kaplan, D. L. (2010). BioDome regenerative sleeve for biochemical and biophysical stimulation of tissue regeneration. *Med. Eng. Phys.* **32**, 1065–1073.

Herr, H. M. and Grabowski, A. M. (2011). Bionic ankle–foot prosthesis normalizes walking gait for persons with leg amputation. *Proc. R. Soc. London B Biol. Sci.*

Herrera-Rincon, C., Golding, A. S., Moran, K. M., Harrison, C., Martyniuk, C. J., Guay, J. A., Zaltsman, J., Carabello, H., Kaplan, D. L. and Levin, M. (2018). Brief Local Application of Progesterone via a Wearable Bioreactor Induces Long-Term Regenerative Response in Adult Xenopus Hindlimb. *Cell Rep.* **25**, 1593-1609.e7.

Ho, D. M. and Whitman, M. (2008). TGF-β signaling is required for multiple processes during Xenopus tail regeneration. *Dev. Biol.* **315**, 203–216.

Hochberg, L. R., Bacher, D., Jarosiewicz, B., Masse, N. Y., Simeral, J. D., Vogel, J., Haddadin, S., Liu, J., Cash, S. S., van der Smagt, P., et al. (2012). Reach and grasp by people with tetraplegia using a neurally controlled robotic arm. *Nature* **485**, 372–375.

Hockaday, L. A., Kang, K. H., Colangelo, N. W., Cheung, P. Y. C., Duan, B., Malone, E., Wu, J., Girardi, L. N., Bonassar, L. J., Lipson, H., et al. (2012). Rapid 3D printing of anatomically accurate and mechanically heterogeneous aortic valve hydrogel scaffolds. *Biofabrication* **4**, 035005.

Hockstein, N. G., Gourin, C. G., Faust, R. A. and Terris, D. J. (2007). A history of robots: from science fiction to surgical robotics. *J. Robot. Surg.* **1**, 113–8.

Hodgkin, A. L. and Huxley, A. F. (1939). Action potentials recorded from inside a nerve fibre. *Nature* **144**, 710–711.

Hoover, C. D., Fulk, G. D. and Fite, K. B. (2012). The Design and Initial Experimental Validation of an Active Myoelectric Transfemoral Prosthesis. *J. Med. Device.* **6**, 011005.

Hwang, J., Jeong, Y., Park, J. M., Lee, K. H., Hong, J. W. and Choi, J. (2015). Biomimetics: forecasting the future of science, engineering, and medicine. *Int. J. Nanomedicine* **10**, 5701–13.

Illingworth, C. M. (1974). Trapped fingers and amputated finger tips in children. *J. Pediatr. Surg.* **9**, 853–858.

Jaffe, L. F. and Nuccitelli, R. (1974). An ultrasensitive vibrating probe for measuring steady extracellular currents. *J. Cell Biol.* **63**, 614–628.

Jank, B. J., Xiong, L., Moser, P. T., Guyette, J. P., Ren, X., Cetrulo, C. L., Leonard, D. A., Fernandez, L., Fagan, S. P. and Ott, H. C. (2015). Engineered composite tissue as a bioartificial limb graft. *Biomaterials* **61**, 246–256.

Jenkins, L. S., Duerstock, B. S. and Borgens, R. B. (1996). Reduction of the current of injury leaving the amputation inhibits limb regeneration in the red spotted newt. *Dev. Biol.* **178**, 251–62.

Jinha, A. (2010). Article 50 million: An estimate of the number of scholarly articles in existence. *Learn. Publ.* **23**, 258–263.

Julier, Z., Park, A. J., Briquez, P. S. and Martino, M. M. (2017). Promoting tissue regeneration by modulating the immune system. *Acta Biomater.* **53**, 13–28.

Kaidi, A., Williams, A. C. and Paraskeva, C. (2007). Interaction between beta-catenin and HIF-1 promotes cellular adaptation to hypoxia. *Nat Cell Biol* **9**, 210–217.

Kakebeen, A. D. and Wills, A. E. (2019). More Than Just a Bandage: Closing the Gap Between Injury and Appendage Regeneration. *Front. Physiol.* **10**, 81.

Kang, H.-W., Lee, S. J., Ko, I. K., Kengla, C., Yoo, J. J. and Atala, A. (2016). A 3D bioprinting system to produce human-scale tissue constructs with structural integrity. *Nat Biotech* **34**, 312–319.

King, R. D., Whelan, K. E., Jones, F. M., Reiser, P. G. K., Bryant, C. H., Muggleton, S. H., Kell, D. B. and Oliver, S. G. (2004). Functional genomic hypothesis generation and experimentation by a robot scientist. *Nature* **427**, 247–252.

King, R. D., Rowland, J., Oliver, S. G., Young, M., Aubrey, W., Byrne, E., Liakata, M., Markham, M., Pir, P., Soldatova, L. N., et al. (2009). The Automation of Science. *Science (80-.).* **324**,.

Koefoed-Johnsen, V. and Ussing, H. H. (1958). The nature of the frog skin potential. *Acta Physiol. Scand.* **42**, 298–308.

Korschelt, E. (1927). *Regeneration und transplantation*. Berlin: Gebrüder Borntraeger.

Kragl, M., Knapp, D., Nacu, E., Khattak, S., Maden, M., Epperlein, H. H. and Tanaka, E. M. (2009). Cells keep a memory of their tissue origin during axolotl limb regeneration. *Nature* **460**, 60–65.

Krogh, A. (1929). The progress of physiology. *Am. J. Physiol.* **90**, 243–251.

Kumar, A. and Brockes, J. P. (2012). Nerve dependence in tissue, organ, and appendage regeneration. *Trends Neurosci.* **35**, 691–9.

Kumar, A., Velloso, C. P., Imokawa, Y. and Brockes, J. P. (2004). The Regenerative Plasticity of Isolated Urodele Myofibers and Its Dependence on Msx1. *PLoS Biol.* **2**, e218.

Kumar, A., Godwin, J. W., Gates, P. B., Garza-Garcia, a A. and Brockes, J. P. (2007). Molecular basis for the nerve dependence of limb regeneration in an adult vertebrate. *Science (80-.).* **318**, 772–7.

Kumar, A., Delgado, J.-P., Gates, P. B., Neville, G., Forge, A. and Brockes, J. P. (2011). The aneurogenic limb identifies developmental cell interactions underlying vertebrate limb regeneration. *Proc. Natl. Acad. Sci. U. S. A.* **108**, 13588–93.

Lambeth, J. D. and Neish, A. S. (2014). Nox enzymes and new thinking on reactive oxygen: a double-edged sword revisited. *Annu. Rev. Pathol.* **9**, 119–45.

Lecuit, T. and Lenne, P.-F. (2007). Cell surface mechanics and the control of cell shape, tissue patterns and morphogenesis. *Nat. Rev. Mol. Cell Biol.* **8**, 633–44.

Lee, Y., Hami, D., De Val, S., Kagermeier-Schenk, B., Wills, A. a, Black, B. L., Weidinger, G. and Poss, K. D. (2009). Maintenance of blastemal proliferation by functionally diverse epidermis in regenerating zebrafish fins. *Dev. Biol.* **331**, 270–80.

Levin, M. (2007). Large-scale biophysics: ion flows and regeneration. *Trends Cell Biol.* **17**, 261–70.

Levin, M. (2014). Molecular bioelectricity: how endogenous voltage potentials control cell behavior and instruct pattern regulation in vivo. *Mol. Biol. Cell* **25**, 3835–3850.

Levin, M., Bates, E., Zhao, M. and Ferreira, F. (2018). Developmental Bioelectricity. *Wikipedia*.

Li, W., Li, Y., Guan, S., Fan, J., Cheng, C.-F., Bright, A. M., Chinn, C., Chen, M. and Woodley, D. T. (2007). Extracellular heat shock protein-90alpha: linking hypoxia to skin cell motility and wound healing. *EMBO J.* **26**, 1221–1233.

Li, F., Wang, H., Li, L., Huang, C., Lin, J., Zhu, G., Chen, Z., Wu, N. and Feng, H. (2012). Superoxide plays critical roles in electrotaxis of fibrosarcoma cells via activation of ERK and reorganization of the cytoskeleton. *Free Radic. Biol. Med.* **52**, 1888–96.

Li, F., Chen, T., Hu, S., Lin, J., Hu, R. and Feng, H. (2013). Superoxide Mediates Direct Current Electric Field-Induced Directional Migration of Glioma Cells through the Activation of AKT and ERK. *PLoS One* **8**, e61195.

Li, J., Zhang, S. and Amaya, E. (2016). The cellular and molecular mechanisms of tissue repair and regeneration as revealed by studies in Xenopus. *Regeneration* **3**, 198–208.

Lin, G. and Slack, J. M. W. (2008). Requirement for Wnt and FGF signaling in Xenopus tadpole tail regeneration. *Dev. Biol.* **316**, 323–35.

Lin, G., Chen, Y. and Slack, J. M. W. (2013). Imparting regenerative capacity to limbs by progenitor cell transplantation. *Dev. Cell* **24**, 41–51.

Lindstedt, S. (2014). Krogh 1929 or "The Krogh principle". *J. Exp. Biol.* **217**, 1640–1.

Lo, D. C., Allen, F. and Brockest, J. P. (1993). *Reversal of muscle differentiation during urodele limb regeneration*.

Love, N. R., Chen, Y., Ishibashi, S., Kritsiligkou, P., Lea, R., Koh, Y., Gallop, J. L., Dorey, K. and Amaya, E. (2013). Amputation-induced reactive oxygen species are required for successful Xenopus tadpole tail regeneration. *Nat. Cell Biol.* **15**, 222–8.

Lozano, R., Stevens, L., Thompson, B. C., Gilmore, K. J., Gorkin, R., Stewart, E. M., in het Panhuis, M., Romero-Ortega, M. and Wallace, G. G. (2015). 3D printing of layered brain-like structures using peptide modified gellan gum substrates. *Biomaterials* **67**, 264–273.

Luxardi, G., Reid, B., Maillard, P. and Zhao, M. (2014). Single cell wound generates electric current circuit and cell membrane potential variations that requires calcium influx. *Integr. Biol.* **6**, 662–72.

Luxardi, G., Reid, B., Ferreira, F., Maillard, P. and Zhao, M. (2015). Measurement of extracellular ion fluxes using the ion-selective self-referencing microelectrode technique. *J. Vis. Exp.* e52782.

Makridakis, S. (1995). The forthcoming information revolution. Its impact on society and firms. *Futures* **27**, 799–821.

Makridakis, S. (2017). The forthcoming Artificial Intelligence (AI) revolution. Its impact on society and firms. *Futures* **90**, 46–60.

Malinin, T. and Deck, J. D. (1958). The effects of implantation of embryonic and tadpole tissues into adult frog limbs. I. Regeneration after amputation. *J. Exp. Zool.* **139**, 307–327.

Manyika, J., Chui, M., Miremadi, M., Bughin, J., George, K., Willmott, P. and Dewhurst, M. (2017). *A future that works: Automation, employment, and productivity*. Chicago.

Marshall, L. N., Vivien, C. J., Girardot, F., Péricard, L., Scerbo, P., Palmier, K., Demeneix, B. A. and Coen, L. (2019). Stage-dependent cardiac regeneration in Xenopus is regulated by thyroid hormone availability. *Proc. Natl. Acad. Sci. U. S. A.* **116**, 3614–3623.

Mathews, A. P. (1903). Electrical polarity in the hydroids. *Am. J. Physiol.* **8**, 294–299.

Mathews, J. and Levin, M. (2017). Gap junctional signaling in pattern regulation: Physiological network connectivity instructs growth and form. *Dev. Neurobiol.* **77**, 643–673.

McCaig, C. D., Rajnicek, A. M., Song, B. and Zhao, M. (2005). Controlling cell behavior electrically: current views and future potential. *Physiol. Rev.* **85**, 943–78.

McLaughlin, K. A. and Levin, M. (2018). Bioelectric signaling in regeneration: Mechanisms of ionic controls of growth and form. *Dev. Biol.* **433**, 177–189.

Meda, F., Rampon, C., Dupont, E., Gauron, C., Mourton, A., Queguiner, I., Thauvin, M., Volovitch, M. and Joliot, A. (2018). Nerves, H2O2 and Shh: Three players in the game of regeneration. *Semin. Cell Dev. Biol.* **80**, 65–73.

Mercader, N., Tanaka, E. M. and Torres, M. (2005). Proximodistal identity during vertebrate limb regeneration is regulated by Meis homeodomain proteins. *Development* **132**, 4131–4142.

Mescher, A. L. (1976). Effects on adult newt limb regeneration of partial and complete skin flaps over the amputation surface. *J. Exp. Zool.* **195**, 117–128.

Mescher, A. L. and Neff, A. W. (2005). Regenerative capacity and the developing immune system. *Adv. Biochem. Eng. / Biotechnol.* **93**, 39–66.

Miller, B. M., Johnson, K. and Whited, J. L. (2019). Common themes in tetrapod appendage regeneration: a cellular perspective. *Evodevo* **10**, 11.

Mitogawa, K., Hirata, A., Moriyasu, M., Makanae, A., Miura, S., Endo, T. and Satoh, A. (2014). Ectopic blastema induction by nerve deviation and skin wounding: a new regeneration model in Xenopus laevis. *Regeneration* **1**, 26–36.

Mitogawa, K., Makanae, A. and Satoh, A. (2018). Hyperinnervation improves Xenopus laevis limb regeneration. *Dev. Biol.* **433**, 276–286.

Mochii, M., Taniguchi, Y. and Shikata, I. (2007). Tail regeneration in the Xenopus tadpole. *Dev. Growth Differ.* **49**, 155–161.

Monroy, A. (1941). Ricerche sulle correnti elettriche derivabili dalla superficie del corpo di. Tritoni adulti normali e durante la rigenerazione degli arti e della coda. *Pubbl. della Stn. Zool. di Napoli* **18**, 265–281.

Morgan, T. H. (1898). Regeneration and liability to injury. *Zool. Bull.* **1**, 287–300.

Morgan, T. H. (1901). *Regeneration*. New York: Macmillan.

Morgan, T. H. (1905). "Polarity" considered as a phenomenon of gradation of materials. *J. Exp. Zool.* **2**, 495–506.

Munaz, A., Nguyen, N.-T., Vadivelu, R. K., St. John, J., Barton, M. and Kamble, H. (2016). Three-Dimensional Printing of Biological Matters. *J. Sci. Adv. Mater. Devices* **1**, 1–17.

Muneoka, K., Holler-Dinsmore, G. and Bryant, S. V. (1986). Intrinsic control of regenerative loss in Xenopus laevis limbs. *J. Exp. Zool.* **240**, 47–54.

Murphy, S. V and Atala, A. (2014). 3D bioprinting of tissues and organs. *Nat Biotech* **32**, 773–785.

Nacu, E. and Tanaka, E. M. (2011). Limb regeneration: a new development? *Annu. Rev. Cell Dev. Biol.* **27**, 409–40.

Nacu, E., Gromberg, E., Oliveira, C. R., Drechsel, D. and Tanaka, E. M. (2016). FGF8 and SHH substitute for anterior–posterior tissue interactions to induce limb regeneration. *Nature* **533**, 407–410.

Neher, E. and Sakmann, B. (1976). Single-channel currents recorded from membrane of denervated frog muscle fibres. *Nature* **260**, 799–802.

Niethammer, P., Grabher, C., Look, A. T. and Mitchison, T. J. (2009). A tissue-scale gradient of hydrogen peroxide mediates rapid wound detection in zebrafish. *Nature* **459**, 996–9.

Nieuwkoop, P. D. and Faber, J. (1967). *Normal table of Xenopus laevis (Daudin)*. Amsterdam: North-Holland.

Norotte, C., Marga, F. S., Niklason, L. E. and Forgacs, G. (2009). Scaffold-free vascular tissue engineering using bioprinting. *Biomaterials* **30**, 5910–5917.

Ortiz-Catalan, M., Håkansson, B. and Brånemark, R. (2014). An osseointegrated human-machine gateway for long-term sensory feedback and motor control of artificial limbs. *Sci. Transl. Med.* **6**,.

Ott, H. C., Matthiesen, T. S., Goh, S.-K., Black, L. D., Kren, S. M., Netoff, T. I. and Taylor, D. a (2008). Perfusion-decellularized matrix: using nature's platform to engineer a bioartificial heart. *Nat. Med.* **14**, 213–221.

Ott, H. C., Clippinger, B., Conrad, C., Schuetz, C., Pomerantseva, I., Ikonomou, L., Kotton, D. and Vacanti, J. P. (2010). Regeneration and orthotopic transplantation of a bioartificial lung. *Nat. Med.* **16**, 927–933.

Oviedo, N. J. and Beane, W. S. (2009). Regeneration: The origin of cancer or a possible cure? *Semin. Cell Dev. Biol.* **20**, 557–64.

Owlarn, S., Klenner, F., Schmidt, D., Rabert, F., Tomasso, A., Reuter, H., Mulaw, M. A., Moritz, S., Gentile, L., Weidinger, G., et al. (2017). Generic wound signals initiate regeneration in missing-tissue contexts. *Nat. Commun.* **8**, 1–13.

Pallas, P. S. (1774). *Spicilegia zoologica: quibus novae imprimis et obscurae animalium species iconibus, descriptionibus atque commentariis illustrantur*. Berolini: Prostant Apud Gottl.

Palmer, L. G. and Andersen, O. S. (2008). The two-membrane model of epithelial transport: Koefoed-Johnsen and Ussing (1958). *J. Gen. Physiol.* **132**, 607–12.

Pan, Q., Qiu, W.-Y., Huo, Y.-N., Yao, Y.-F. and Lou, M. F. (2011). Low levels of hydrogen peroxide stimulate corneal epithelial cell adhesion, migration, and wound healing. *Invest. Ophthalmol. Vis. Sci.* **52**, 1723–34.

Paré, J.-F., Martyniuk, C. J. and Levin, M. (2017). Bioelectric regulation of innate immune system function in regenerating and intact Xenopus laevis. *npj Regen. Med.* **2**, 15.

Pirotte, N., Stevens, A., Fraguas, S., Plusquin, M., Roten, A. Van, Belleghem, F. Van, Paesen, R., Ameloot, M., Cebrià, F., Artois, T., et al. (2015). Reactive Oxygen Species in Planarian Regeneration : An Upstream Necessity for Correct Patterning and Brain Formation. *Oxid. Med. Cell. Longev.* **2015**, 1–19.

Podolny, S. (2015). If an Algorithm Wrote This, How Would You Even Know? *New York Times*.

Polezhayev, L. W. (1933). Concerning the renewal of regenrative capacity in tailless amphibians (Russian). *Biol Zhur* **2**, 357–367.

Polezhayev, L. W. (1946). The loss and restoration of regenerative capacity in the limbs of tailless amphibia. *Biol. Rev. Camb. Philos. Soc.* **21**, 141–147.

Poss, K. D. (2010). Advances in understanding tissue regenerative capacity and mechanisms in animals. *Nat. Rev. Genet.* **11**, 710–22.

PwC (2017). Up to 30% of existing UK jobs could be impacted by automation by early 2030s, but this should be offset by job gains elsewhere in economy.

Randall, D., Burggren, W. and French, K. (2001). *Eckert animal physiology: mechanisms and adaptations.* 5th ed. New York: W.H. Freeman and Co.

Razzell, W., Evans, I. R., Martin, P. and Wood, W. (2013). Calcium flashes orchestrate the wound inflammatory response through duox activation and hydrogen peroxide release. *Curr. Biol.* **23**, 424–429.

Reaumur, R.-A. F. de (1712). Sur les diverses reproductions qui se font dans les écrevisses, les omars, les crabes, etc. et entr'autres sur celles de leurs jambes et de leurs écailles. *Mem. Acad. Roy. Sci.* 223–245.

Réaumur, R.-A. F. de (1712). Sur les diverses reproductions qui se font dans les Ecrevisse, les Omars, les Crabes, etc. et entr'autres sur celles de leurs Jambes et de leurs Ecailles. *Mem. Acad. Roy. Sci.* 223–245.

Reginelli, A. D., Wang, Y. Q., Sassoon, D. and Muneoka, K. (1995). Digit tip regeneration correlates with regions of Msx1 (Hox 7) expression in fetal and newborn mice. *Development* **121**, 1065–76.

Reid, B. and Zhao, M. (2011). Measurement of bioelectric current with a vibrating probe. *J. Vis. Exp. JoVE* 1–6.

Reid, B., Nuccitelli, R. and Zhao, M. (2007). Non-invasive measurement of bioelectric currents with a vibrating probe. *Nat. Protoc.* **2**, 661–9.

Reid, B., Song, B. and Zhao, M. (2009). Electric currents in Xenopus tadpole tail regeneration. *Dev. Biol.* **335**, 198–207.

Renwick, C. (2016). Biology, social science and history: interdisciplinarity in three directions. *Palgrave Commun.* **2**, 1–5.

Rose, M. S. (1944). Methods of initiating limb regeneration in adult anura. *J. Exp. Zool.* **95**, 149–170.

Sánchez Alvarado, A. (2000). Regeneration in the metazoans: Why does it happen? *BioEssays* **22**, 578–590.

Sandoval-Guzmán, T., Wang, H., Khattak, S., Schuez, M., Roensch, K., Nacu, E., Tazaki, A., Joven, A., Tanaka, E. M. and Simon, A. (2014). Fundamental Differences in Dedifferentiation and Stem Cell Recruitment during Skeletal Muscle Regeneration in Two Salamander Species. *Cell Stem Cell* **14**, 174–187.

Satoh, A., Makanae, A. and Wada, N. (2010). The apical ectodermal ridge (AER) can be re-induced by wounding, wnt-2b, and fgf-10 in the chicken limb bud. *Dev. Biol.* **342**, 157–68.

Schotté, O. E. and Wilber, J. F. (1958). Effects of Adrenal Transplants upon Forelimb Regeneration in Normal and in Hypophysectomized Adult Frogs. *J. Exp. Zool.* **6**, 247–269.

Seifert, A. W., Kiama, S. G., Seifert, M. G., Goheen, J. R., Palmer, T. M. and Maden, M. (2012). Skin shedding and tissue regeneration in African spiny mice (Acomys). *Nature* **489**, 561–5.

Sen, C. K. and Roy, S. (2008). Redox signals in wound healing. *Biochim. Biophys. Acta* **1780**, 1348–61.

Serena, E., Figallo, E., Tandon, N., Cannizzaro, C., Gerecht, S., Elvassore, N. and Vunjak-Novakovic, G. (2009). Electrical stimulation of human embryonic stem cells: Cardiac differentiation and the generation of reactive oxygen species. *Exp. Cell Res.* **315**, 3611–3619.

Shapiro, S., Borgens, R., Pascuzzi, R., Roos, K., Groff, M., Purvines, S., Rodgers, R. Ben, Hagy, S. and Nelson, P. (2005). Oscillating field stimulation for complete spinal cord injury in humans: a phase 1 trial. *J. Neurosurg. Spine* **2**, 3–10.

Shen, Y., Pfluger, T., Ferreira, F., Liang, J., Navedo, M. F., Shen, Q., Reid, B. and Zhao, M. (2016). Diabetic Cornea Wounds Produce Significantly Weaker Electric Signals That May Contribute To Impaired Healing. *Sci. Rep.* **6**, 1–11.

Shipley, A. M. and Feijó, J. A. (1999). The use of the vibrating probe technique to study steady extracellular currents during pollen germination and tube growth. In *Fertilisation in Higher Plants: molecular and cytological aspects*, pp. 235–250.

Sidman, R. L. and Singer, M. (1951). Stimulation of forelimb regeneration in the newt, Triturus viridescens, by a sensory nerve supply isolated from the central nervous system. *Am. J. Physiol.* **165**, 257–260.

Singer, M. (1952). The influence of the nerve in regeneration of the amphibian extremity. *Q. Rev. Biol.* **27**, 169–200.

Singer, M. (1954). Induction of regeneration of the forelimb of the postmetamorphic frog by augmentation of the nerve supply. *J. Exp. Zool.* **126**, 419–471.

Singh, V. K., Kalsan, M., Kumar, N., Saini, A., Chandra, R., Bianchi, M. E. and Vita, U. (2015). Induced pluripotent stem cells: applications in regenerative medicine, disease modeling, and drug discovery. *Front. Cell Dev. Biol.* **3**, 1–18.

Slack, J. M. W., Beck, C. W., Gargioli, C. and Christen, B. (2004). Cellular and molecular mechanisms of regeneration in Xenopus. *Philos. Trans. R. Soc. Lond. B. Biol. Sci.* **359**, 745–51.

Slack, J. M. W., Lin, G. and Chen, Y. (2008). The Xenopus tadpole: a new model for regeneration research. *Cell. Mol. Life Sci.* **65**, 54–63.

Smith, S. D. (1967). Induction of partial limb regeneration in Rana pipiens by galvanic stimulation. *Anat. Rec.* **158**, 89–97.

Somvanshi, P. R. and Venkatesh, K. V (2014). A conceptual review on systems biology in health and diseases: from biological networks to modern therapeutics. *Syst. Synth. Biol.* **8**, 99–116.

Spallanzani, L. (1768). *Prodromo di un'opera da imprimersi sopra le riproduzioni animali*. Modena: Giovanni Montanari.

Srinivasan, S. S., Carty, M. J., Calvaresi, P. W., Clites, T. R., Maimon, B. E., Taylor, C. R., Zorzos, A. N. and Herr, H. (2017). On prosthetic control: A regenerative agonist-antagonist myoneural interface. *Sci. Robot.* **2**,.

Stocum, D. L. (2017). Mechanisms of urodele limb regeneration. *Regeneration* **4**, 159–200.

Stoick-Cooper, C. L., Moon, R. T. and Weidinger, G. (2007). Advances in signaling in vertebrate regeneration as a prelude to regenerative medicine. *Genes Dev.* **21**, 1292–315.

Sugiura, T., Tazaki, A., Ueno, N., Watanabe, K. and Mochii, M. (2009). Xenopus Wnt-5a induces an ectopic larval tail at injured site, suggesting a crucial role for noncanonical Wnt signal in tail regeneration. *Mech. Dev.* **126**, 56–67.

Sun, Y., Reid, B., Ferreira, F., Luxardi, G., Ma, L., Lokken, K. L., Zhu, K., Xu, G., Sun, Y., Ryzhuk, V., et al. (2019). Infection-generated electric field in gut epithelium drives bidirectional migration of macrophages. *PLoS Biol.* **17**, e3000044.

Sunderland, M. E. (2010). Regeneration: Thomas Hunt Morgan's window into development. *J. Hist. Biol.* **43**, 325–61.

Takahashi, K. and Yamanaka, S. (2006). Induction of Pluripotent Stem Cells from Mouse Embryonic and Adult Fibroblast Cultures by Defined Factors. *Cell* **126**, 663–676.

Tanaka, E. M. and Reddien, P. W. (2011). The Cellular Basis for Animal Regeneration. *Dev. Cell* **21**, 172–185.

Tanaka, E. M., Drechsel, D. N. and Brockes, J. P. (1999). Thrombin regulates S-phase re-entry by cultured newt myotubes. *Curr. Biol.* **9**, 792–9.

Tandon, N., Cimetta, E., Villasante, A., Kupferstein, N., Southall, M. D., Fassih, A., Xie, J., Sun, Y. and Vunjak-Novakovic, G. (2014). Galvanic microparticles increase migration of human dermal fibroblasts in a wound-healing model via reactive oxygen species pathway. *Exp. Cell Res.* **320**, 79–91.

Taniguchi, Y., Sugiura, T., Tazaki, A., Watanabe, K. and Mochii, M. (2008). Spinal cord is required for proper regeneration of the tail in Xenopus tadpoles. *Dev. Growth Differ.* **50**, 109–20.

Taniguchi, Y., Watanabe, K. and Mochii, M. (2014). Notochord-derived hedgehog is essential for tail regeneration in Xenopus tadpole. *BMC Dev. Biol.* **14**, 27.

Taylor, G. P., Anderson, R., Reginelli, A. D. and Muneoka, K. (1994). FGF-2 induces regeneration of the chick limb bud. *Dev. Biol.* **163**, 282–284.

Tee, B. C.-K., Chortos, A., Berndt, A., Nguyen, A. K., Tom, A., McGuire, A., Lin, Z. C., Tien, K., Bae, W.-G., Wang, H., et al. (2015). A skin-inspired organic digital mechanoreceptor. *Science (80-.).* **350**,.

ten Kate, J., Smit, G. and Breedveld, P. (2017). 3D-printed upper limb prostheses: a review. *Disabil. Rehabil. Assist. Technol.* **12**, 300–314.

Till, J. E. and McCulloch, E. A. (1961). A direct measurement of the radiation sensitivity of normal mouse bone marrow cells. *Radiat. Res.* **14**, 213–22.

Todd, T. J. (1823). On the process of reproduction of the members of the aquatic salamander. *Q. J. Sci. Lit. Arts* **16**, 84–96.

Trembley, A. (1744a). Observations and experiments upon the freshwater polypus (Translated from the French by P. H. Z.). *Philos. Trans.* **42**, iii–xi.

Trembley, A. (1744b). *Mémoires pour servir à l'histoire d'un genre de polypes d'eau douce, à bras en forme de cornes*. Leiden: Verbeek.

Tseng, A.-S. (2017). Seeing the future: using Xenopus to understand eye regeneration. *genesis* **55**, e23003.

Tseng, a.-S. and Levin, M. (2008). Tail Regeneration in Xenopus laevis as a Model for Understanding Tissue Repair. *J. Dent. Res.* **87**, 806–816.

Tseng, A.-S. and Levin, M. (2012). Transducing Bioelectric Signals into Epigenetic Pathways During Tadpole Tail Regeneration. *Anat. Rec. Adv. Integr. Anat. Evol. Biol.* **295**, 1541–1551.

Tseng, A.-S. and Levin, M. (2013). Cracking the bioelectric code: Probing endogenous ionic controls of pattern formation. *Commun. Integr. Biol.* **6**, 1–8.

Tseng, A., Adams, D. S., Qiu, D., Koustubhan, P. and Levin, M. (2007). Apoptosis is required during early stages of tail regeneration in Xenopus laevis. *Dev. Biol.* **301**, 62–69.

Tseng, A.-S., Beane, W. S., Lemire, J. M., Masi, A. and Levin, M. (2010). Induction of vertebrate regeneration by a transient sodium current. *J. Neurosci.* **30**, 13192–200.

Tseng, A.-S., Carneiro, K., Lemire, J. M. and Levin, M. (2011). HDAC Activity Is Required during Xenopus Tail Regeneration. *PLoS One* **6**, e26382.

Tsonis, P. a and Fox, T. P. (2009). Regeneration according to Spallanzani. *Dev. Dyn.* **238**, 2357–63.

Tsujioka, H., Kunieda, T., Katou, Y., Shirahige, K., Fukazawa, T. and Kubo, T. (2017). interleukin-11 induces and maintains progenitors of different cell lineages during Xenopus tadpole tail regeneration. *Nat. Commun.* **8**, 495.

Tsutsumi, R., Yamada, S. and Agata, K. (2016). Functional joint regeneration is achieved using reintegration mechanism in Xenopus laevis. *Regeneration* **3**, 26–38.

Turing, A. M. (1937). On Computable Numbers, with an Application to the Entscheidungsproblem. *Proc. London Math. Soc.* **s2-42**, 230–265.

Turing, A. M. (1950). I.-Computing machinery and intelligence. *Mind* **LIX**, 433–460.

Turing, A. M. (1952). The Chemical Basis of Morphogenesis. *Philos. Trans. R. Soc. Lond. B. Biol. Sci.* **237**, 37–72.

Uygun, B. E., Soto-Gutierrez, A., Yagi, H., Izamis, M.-L., Guzzardi, M. A., Shulman, C., Milwid, J., Kobayashi, N., Tilles, A., Berthiaume, F., et al. (2010). Organ reengineering through development of a transplantable recellularized liver graft using decellularized liver matrix. *Nat. Med.* **16**, 814–820.

Vinarsky, V., Atkinson, D. L., Stevenson, T. J., Keating, M. T. and Odelberg, S. J. (2005). Normal newt limb regeneration requires matrix metalloproteinase function. *Dev. Biol.* **279**, 86–98.

Ware, M. and Mabe, M. (2015). *The STM Report: An overview of scientific and scholarly journal publishing*. The Hague.

Weiss, P. A. (1939). *Principles of development*. New York: Henry Holt & Co.

Williams-Boyce, P. K., Daniel, J. C. and Jr (1986). Comparison of ear tissue regeneration in mammals. *J. Anat.* **149**, 55–63.

Williams, K., Bilsland, E., Sparkes, A., Aubrey, W., Young, M., Soldatova, L. N., De Grave, K., Ramon, J., de Clare, M., Sirawaraporn, W., et al. (2015). Cheaper faster drug development validated by the repositioning of drugs against neglected tropical diseases. *J. R. Soc. Interface* **12**,.

Wilson, W. C. and Boland, T. (2003). Cell and organ printing 1: Protein and cell printers. *Anat. Rec.* **272A**, 491–496.

Windrich, M., Grimmer, M., Christ, O., Rinderknecht, S. and Beckerle, P. (2016). Active lower limb prosthetics: a systematic review of design issues and solutions. *Biomed. Eng. Online* **15**, 5–19.

Wolpert, L. (1969). Positional information and the spatial pattern of cellular differentiationt. *Theor. Biol* **25**, 1–47.

World Economic Forum (2016). *The Future of Jobs Employment, Skills and Workforce Strategy for the Fourth Industrial Revolution*. Cologny.

Wu, J., Platero-Luengo, A., Sakurai, M., Sugawara, A., Gil, M. A., Yamauchi, T., Suzuki, K., Bogliotti, Y. S., Cuello, C., Morales Valencia, M., et al. (2017). Interspecies Chimerism with Mammalian Pluripotent Stem Cells. *Cell* **168**, 473-486.e15.

Yamaguchi, T., Sato, H., Kato-Itoh, M., Goto, T., Hara, H., Sanbo, M., Mizuno, N., Kobayashi, T., Yanagida, A., Umino, A., et al. (2017). Interspecies organogenesis generates autologous functional islets. *Nature* **542**, 191–196.

Yokoyama, H., Yonei-Tamura, S., Endo, T., Izpisúa Belmonte, J. C., Tamura, K. and Ide, H. (2000). Mesenchyme with fgf-10 expression is responsible for regenerative capacity in Xenopus limb buds. *Dev. Biol.* **219**, 18–29.

Yokoyama, H., Ide, H. and Tamura, K. (2001). FGF-10 stimulates limb regeneration ability in Xenopus laevis. *Dev. Biol.* **233**, 72–9.

Yu, L., Han, M., Yan, M., Lee, E.-C., Lee, J. and Muneoka, K. (2010). BMP signaling induces digit regeneration in neonatal mice. *Development* **137**, 551–559.

Zeller, R., López-Ríos, J. and Zuniga, A. (2009). Vertebrate limb bud development: moving towards integrative analysis of organogenesis. *Nat. Rev. Genet.* **10**, 845–858.

Zhang, Y., Strehin, I., Bedelbaeva, K., Gourevitch, D., Clark, L., Leferovich, J., Messersmith, P. B. and Heber-Katz, E. (2015). Drug-induced regeneration in adult mice. *Sci. Transl. Med.* **7**, 1–11.

Zhang, Q., Wang, Y., Man, L., Zhu, Z., Bai, X., Wei, S., Liu, Y., Liu, M., Wang, X., Gu, X., et al. (2016). Reactive oxygen species generated from skeletal muscles are required for gecko tail regeneration. *Sci. Rep.* **6**, 1–11.

Zhao, M. (2018). Perspective on Bioelectrics—an underappreciated and fertile field in biology. In *Ahead of the Curve: Hidden breakthroughs in the biosciences (Volume 2)* (ed. Levin, M.) and Adams, D.), pp. 3-3-3–6. Bristol: IOP Publishing.

Zhao, M., Song, B., Pu, J., Wada, T., Reid, B., Tai, G., Wang, F., Guo, A., Walczysko, P., Gu, Y., et al. (2006). Electrical signals control wound healing through phosphatidylinositol-3-OH kinase-gamma and PTEN. *Nature* **442**, 457–60.

Zhao, Y., Inayat, S., Dikin, D. A., Singer, J. H., Ruoff, R. S. and Troy, J. B. (2009). Patch clamp technique: review of the current state of the art and potential contributions from nanoengineering. *Proc. Inst. Mech. Eng. Part N J. Nanoeng. Nanosyst.* **222**, 1–11.

Zhao, B., Tumaneng, K. and Guan, K.-L. (2011). The Hippo pathway in organ size control, tissue regeneration and stem cell self-renewal. *Nat. Cell Biol.* **13**, 877–883.

Zhou, Q., Brown, J., Kanarek, A., Rajagopal, J. and Melton, D. A. (2008). In vivo reprogramming of adult pancreatic exocrine cells to β-cells. *Nature* **455**, 627–632.

APPENDIXES

I. *MEASUREMENT OF EXTRACELLULAR ION FLUXES USING THE ION-SELECTIVE SELF-REFERENCING MICROELECTRODE TECHNIQUE*

万物并育而不相害，道并行而不相悖。
孔子 *in* 中庸，子思 (*ca.* 500 B.C.E.)[8]

Publication overview

Following a publication using the ion-selective self-referencing microelectrode technique (Luxardi et al., 2014), a laboratory co-worker was invited by the *Journal of visualized experiments (JoVE)* to submit a technical manuscript with video recording about that technique. It is an electrophysiology technique based on a classic glass microelectrode with an ion-selective ionophore in its tip, allowing the measurement of specific ion fluxes. The publication details the steps required to derive and calibrate the special microelectrodes, validate the technique and present representative data and respective analysis and presentation.

Publication contributions

The publication has not a section detailing the author contributions and since I am not the first author, I will only mention my contribution to this publication. I helped in the designing and planning of the artificial source assay (Fig. 2D) and in the writing and editing of the corresponding section ('3. Validation of the Ion-selective Microelectrode Technique'). Also, I contributed with discussion of the methodology and results, to manuscript revision and editing, and to addressing peer review comments.

Publication reprint

Vide infra.

Video Article

Measurement of Extracellular Ion Fluxes Using the Ion-selective Self-referencing Microelectrode Technique

Guillaume Luxardi[1], Brian Reid[1], Fernando Ferreira[1,2], Pauline Maillard[3], Min Zhao[1,4]

[1]Department of Dermatology, Institute for Regenerative Cures, University of California, Davis

[2]Departamento de Biologia, Centro de Biologia Molecular e Ambiental, Universidade do Minho

[3]Department of Neurology and Center for Neuroscience, University of California, Davis Imaging of Dementia and Aging Laboratory

[4]Department of Ophthalmology, Institute for Regenerative Cures, University of California, Davis

Correspondence to: Guillaume Luxardi at gluxardi@ucdavis.edu

URL: http://www.jove.com/video/52782
DOI: doi:10.3791/52782

Keywords: Cellular Biology, Issue 99, ion-selective, self-referencing, microelectrode, extracellular ion fluxes, *in vivo* measurements

Date Published: 5/3/2015

Citation: Luxardi, G., Reid, B., Ferreira, F., Maillard, P., Zhao, M. Measurement of Extracellular Ion Fluxes Using the Ion-selective Self-referencing Microelectrode Technique. *J. Vis. Exp.* (99), e52782, doi:10.3791/52782 (2015).

Abstract

Cells from animals, plants and single cells are enclosed by a barrier called the cell membrane that separates the cytoplasm from the outside. Cell layers such as epithelia also form a barrier that separates the inside from the outside or different compartments of multicellular organisms. A key feature of these barriers is the differential distribution of ions across cell membranes or cell layers. Two properties allow this distribution: 1) membranes and epithelia display selective permeability to specific ions; 2) ions are transported through pumps across cell membranes and cell layers. These properties play crucial roles in maintaining tissue physiology and act as signaling cues after damage, during repair, or under pathological condition. The ion-selective self-referencing microelectrode allows measurements of specific fluxes of ions such as calcium, potassium or sodium at single cell and tissue levels. The microelectrode contains an ionophore cocktail which is selectively permeable to a specific ion. The internal filling solution contains a set concentration of the ion of interest. The electric potential of the microelectrode is determined by the outside concentration of the ion. As the ion concentration varies, the potential of the microelectrode changes as a function of the log of the ion activity. When moved back and forth near a source or sink of the ion (*i.e.* in a concentration gradient due to ion flux) the microelectrode potential fluctuates at an amplitude proportional to the ion flux/gradient. The amplifier amplifies the microelectrode signal and the output is recorded on computer. The ion flux can then be calculated by Fick's law of diffusion using the electrode potential fluctuation, the excursion of microelectrode, and other parameters such as the specific ion mobility. In this paper, we describe in detail the methodology to measure extracellular ion fluxes using the ion-selective self-referencing microelectrode and present some representative results.

Video Link

The video component of this article can be found at http://www.jove.com/video/52782/

Introduction

All animal cells are surrounded by a lipid bilayer membrane which separates the cytoplasm from the outside environment. The cell maintains an electrical membrane potential, negative inside, by active transport of ions[1]. The membrane potential is a stored energy source which the cell can utilize to operate various molecular devices in the membrane[2]. Neurons and other excitable cells have large membrane potentials. Rapid opening of sodium channels collapses the membrane potential (depolarization) and produces the action potential which is transported along the length of the neuron[2]. Aside from these rapid electrical changes, many tissues and organs generate and maintain significant long-term electrical potentials. For example, skin and corneal epithelia generate and maintain trans-epithelial potentials and extracellular electric currents by directional pumping of ions (mainly sodium and chloride)[3].

While measurements of endogenous extracellular electric current using the vibrating probe[4-6] and measurements of membrane or trans-epithelial potentials using the microelectrode system[7-10] allow measurement of the electric parameters of cell membranes and epithelial cell layers, they give no indication of the ion species involved.

Microelectrodes with selective ionophore can measure specific ion concentration in solution. Ion gradients or flux could be measured with two or more electrodes at different positions. However, the intrinsic voltage drift of each probe would be different, causing inaccurate measurements or even detection of a gradient that was not present. A single electrode used in "self-referencing" mode whereby it moves at low frequency between two points solves this problem. Now the ion flux can be seen against the background of a relatively slow and stable signal drift (see **Figure 3B**).

The ion-sensitive measuring system uses ion-selective self-referencing microelectrodes to detect small extracellular fluxes of ions close to tissues or single cells. The system consists of an amplifier which processes the signal from the microelectrode and a micro stepper motor and driver to control the motion of the microelectrode. The ion-selective microelectrode and the reference electrode that close the circuit are connected to the amplifier via a headstage pre-amplifier (**Figure 1A**). Computer software determines the parameters of the microelectrode movement (frequency, distance) and also records the output of the amplifier. The stepper motor controls the microelectrode movement via

a three-dimensional micropositioner. A low frequency vibrating ion-selective microelectrode was first developed in 1990 to measure specific calcium flux[11]. As well as calcium, commercially accessible ionophore cocktails are now available to make microelectrodes sensitive to sodium, chloride, potassium, hydrogen, magnesium, nitrate, ammonium, fluoride, lithium or mercury.

Basically, the self-referencing ion-selective microelectrode technique converts the activity of a specific ion dissolved in a solution into an electric potential, which can be measured by a voltmeter. The ionophore cocktail is an immiscible liquid (organic, lipophilic) phase with ion-exchange properties. The ionophore selectively complexes (binds) specific ions reversibly and transfers them between the aqueous solution contained in the microelectrode (electrolyte) and the aqueous solution in which the microelectrode is immersed (**Figure 1D**). This ion transfer leads to an electrochemical equilibrium and a variation of the electric potential between the microelectrode and the reference electrode is measured by the voltmeter. The voltage is proportional to the logarithm of the specific ion activity according to the Nernst equation allowing the calculation of the ion concentration (**Figure 2A** and **B**).

At present, several systems allow measurement of ion flux using a similar concept or principle. For example, the Scanning Ion-selective Electrode Technique (SIET)[12,13] or the Microelectrode Ion Flux Estimation (MIFE) technique developed by Newman and Shabala[14-16] are commercially available and widely used by the research community in order to determine specific ion fluxes occurring at cell membrane and tissue across a variety of animal, plant and single living cell models. Ion-selective microelectrodes have been used to measure hydrogen, potassium and calcium flux across plant roots[17], chloride flux in rat cerebral arteries[18] and in pollen tubes[19], hydrogen flux in skate retinal cells[20], calcium flux in mouse bone[21], various ion fluxes in fungal hyphae[22] and in rat cornea[23], and finally calcium flux during single cell wound healing[12,24]. See also the following review for detailed information on ion-selective self-referencing microelectrodes[25].

The following article describes in detail how to prepare and perform measurement of endogenous extracellular ion fluxes using the ion-selective self-referencing microelectrode technique at the single cell level.

Protocol

1. Ion-selective Self-referencing Microelectrode Preparation

1. Preparation of ion-selective microelectrode
    1. Heat pull thin walled borosilicate capillaries without filament (1.5 mm outer diameter, 1.12 mm inner diameter) using a microelectrode puller.
    Note: This gives tips 3-4 µm in diameter. Smaller tips have higher resistance which makes microelectrodes more susceptible to electronic noise and is also associated with a slower response to a change in ion concentration. Useful information can be found in the paper published by Smith *et al.*[26].
    2. Silanize the electrodes to render the inner surface hydrophobic to aid retention of the lipophilic ionophore cocktail. Place the microelectrodes in a metal rack and heat O/N in an oven at >100 °C to dry them. The rack is a metal plate with 2 mm diameter holes drilled part of the way through. Place the electrodes in the holes tip upwards with a 250 ml glass beaker over them.
    3. In the morning, turn the oven off and while wearing insulated gloves, carefully remove the metal rack with the electrodes and beaker in place. Close the oven door to retain the heat.
    4. Wear latex or nitrile gloves, lab coat and eye protection. With a plastic Pasteur pipette, place a drop of silanization solution I at the base of each electrode (keep the beaker in place; use the pouring lip for pipette access). The silanization solution is vaporized by the hot plate and silanizes the inside of the electrodes. Use a chemical extractor fume hood for this stage. Place the rack/beaker/electrodes back in the hot oven for a few hours to allow any remaining silanization solution to evaporate.
    Note: For safety reasons, do not turn the oven back on. Place a label on the oven indicating it must not be switched on as it may contain harmful and flammable vapor.
    5. After cooling, store the microelectrodes in a microelectrode storage jar inside a glass desiccator with 400 g of desiccant. Microelectrodes can be stored thus for many weeks.
    Note: An alternative silanization method is described in Smith *et al.*[26]
    6. Back-fill the microelectrode with 50 to 100 µl (a length of about 1 cm) of a solution containing 100 mM of the ion to be measured (see **Table 1** and **Figure 1B**). Use a disposable plastic Pasteur pipette heat pulled in a Bunsen burner to a fine filament. Rinse the pipette in dH_2O afterward to prevent blockage.
    Note: Alternatively, adjust the ion concentration of the backfilling solution to match the concentration of ion in the external solution[27].
    7. Observe the microelectrode under a dissecting microscope to ensure the absence of air bubbles.
        1. If bubbles are present tap the microelectrode lightly with a finger nail while holding the electrode vertically (tip down) and/or push the bubbles out the tip by applying back pressure using a syringe modified with a silicone tube replacing the needle.
    8. Tip-fill the microelectrode with 15 to 20 nl (a length of 30-50 µm) of ion-specific ionophore cocktail (see **Table 1**). Place a small droplet of ionophore cocktail on the short edge of a microscope slide. Observe the microelectrode tip under a dissecting microscope and move it toward the microscope slide until the microelectrode tip touches the ionophore cocktail for only about half a sec. Draw the ionophore cocktail into the microelectrode by capillary pressure.
    Note: Avoid a long column of ionophore cocktail as this increases the probe's electrical resistance which can make it susceptible to electronic interference (noise) and also slows the response time.
    9. Mount the microelectrode in a straight microelectrode holder with a gold 1 mm male connector and AgCl(Ag^+) wire (**Figure 1B**).
    10. Attach the microelectrode holder to the head stage mounted on a three-dimensional computer-controlled electronic micropositioner (**Figure 1A**).
    11. Place the microelectrode tip in measuring solution appropriate for the sample to be measured (physiological saline, culture medium, *etc.*) to allow the microelectrode to stabilize for an hr or two, or even overnight.
2. Preparation of the reference electrode

1. Reference electrodes (**Figure 1C**) are the same capillaries as above. Cut the capillary with a diamond pencil into 5 cm lengths and fire-polished at each end for 1-2 sec in a Bunsen flame.
2. Fill these electrodes with ~200 µl of a 3 M solution of NaCl, CH_3CO_2K (potassium acetate) or KCl with 2% agarose. Choose the solution depending on the ion to be measured (the reference electrode should not contain the ion being measured; see **Table 1**). Mix the agarose and the solution and heat to almost boiling in a microwave. Stir to dissolve the agarose (the solution goes clear).
3. Attach the reference electrode to a plastic Pasteur pipette and draw the hot solution into the capillary.
4. Drop the electrode into cold 3 M NaCl, CH_3CO_2K or KCl solution and store in this 3 M solution in sealed tubes prior to use. Discard any reference electrodes with air bubbles.
5. Mount the reference electrode in a straight microelectrode holder (pre-filled with 3 M solution) with an AgCl(Ag^+) pellet inside and a gold 2 mm male connector (**Figure 1C**) and attach the electrode and holder onto a manual micro-positioner mounted on a magnetic stand.

2. Ion-selective Self-referencing Microelectrode Calibration

1. Preparing calibrating solutions containing the ion of interest as in the reference solution; see **Table 1**. Bracket the concentration that is in the solution the sample will be in (*e.g.* culture media, physiological saline). That is, one calibration solution must contain a lower concentration of ion than in the measuring solution, and one higher.
    1. For example, use saline that contains 1 mM of K^+. To bracket this concentration, dissolve KCl powder in deionized water to a concentration of 10, 1 and 0.1 mM in serial dilutions. Use these calibration solutions. Alternatively, use at least two of these solutions.

2. Immerse the ion-selective microelectrode and the reference electrode in each calibration solution and let the voltage value stabilize for 1 to 3 min before recording the corresponding voltage using the dedicated software (see **Table 1**).
3. As the software saves the data (amplifier output) as a txt file, copy the data into a spreadsheet file. Plot the microelectrode output (mV) against the logarithm of the molar ion concentration (**Figure 2A**).
4. Apply a linear regression and calculate the Nernst slope, intercept and R^2 value. Accept the microelectrode if the Nernst slope is 58 ± 11 mV/decade for monovalent ions and 29 ± 11 mV/decade for divalent ions (for cations, the Nernst slope is positive, for anions it is negative). Additionally, good microelectrodes should have a strong linear correlation (R^2 >0.9; **Figure 2B**).
   Note: The mV output of the amplifier used here gives mV reading with a tenfold gain. Values have to be divided by a factor of ten.
5. Use the linear regression formula to convert the raw mV output of the microelectrode into actual ion concentration (**Figure 2B**).

3. Validation of the Ion-selective Microelectrode Technique

1. Preparing an artificial source
    1. Artificial source capillaries are the same capillaries as above. Heat pull the capillary using a microelectrode puller as in step 1.1.1.
    2. Backfill these capillaries with 200 µl of a 1 M solution of NaCl, KCl, $CaCl_2$2 H_2O or pH 4 buffer. Choose the artificial source solution depending on the ion to be measured (see **Table 1**).
       Note: Alternatively, pull electrodes with bigger tip diameter (~20 µm) and tip-fill with the same solutions but containing 0.5-1% agarose (agarose will prevent any bulk flow of solution).
    3. Mount the artificial source capillary on a micromanipulator and immerse it in the solution used to measure the flux of the ion in the samples. Leave the artificial source in the solution for 30 min to 1 hr to allow stabilization of the gradient.

2. Validation of the ion-selective microelectrode
    1. Immerse the ion-selective microelectrode about one centimeter away from the artificial source capillary in the solution used to measure the flux of ion on the samples and close the circuit with the reference electrode as before. Let the voltage value stabilize for 1 to 3 min before recording the corresponding voltage using the dedicated software for 1 to 2 min. This value corresponds to the buffer value (in literature also referred as reference, background or blank value).
    2. Move the ion-selective microelectrode to about 5 µm from the artificial source and let the voltage value stabilize for 1 to 3 min before recording the corresponding voltage using the software for 1 to 2 min.
    3. Repeat the above procedure by placing the ion selective microelectrode at 10, 20, 40, 80, 160, 320, 640 and 1280 µm away from the artificial source capillary.
    4. Extract the data as a txt file and copy the values into a spreadsheet file.

3. Calculate the ion concentration corresponding to the mV values in the same way as for the calibration values. Plot the value.
   Note: If an ion flux is present, the microelectrode detects a difference in ion concentration between the two positions **(Figure 3B**). If the artificial source contains more ions of the species measured than the solution, the concentration should be higher close to the source than far away, validating the ability of the ion-selective microelectrode to correctly detect the direction of an ion flux (in this case efflux; for an artificial sink, with lower specific ion concentration than measuring medium, it should be influx).
    1. Calculate the ion flux using Fick's law of diffusion: $J = c\ \mu\ (dc/dx)$ where c is the ion concentration in the solution (mol cm^{-3}), μ is the ion mobility (mol cm N^{-1} sec^{-1}), and dc is the concentration difference over distance dx (cm) (**Figure 2C**). Ion flux data are usually presented in *pmol* cm^{-2} s^{-1} *or nmol* cm^{-2} sec^{-1}.
       Note: An alternative method of ion flux calculation described by Smith *et al.*[26]. can be used. Main differences include the use of the diffusion coefficient instead of the ion mobility and the subtraction of the background ion flux (also voltage drift or correction factor) calculated from measurement of ion flux in saline solution without sample.
    2. Plot the mean of the ion fluxes of each step against the distance from the source (**Figure 2D**). Moving away from the source, observe an exponential decrease of the flux value validating the ability of the ion-selective microelectrode to sense different magnitude of ion fluxes.
    3. Do the artificial source validation once for each specific ion intended to be recorded in order to validate its correct direction and magnitude measurements with a large signal-to-noise ratio.

Note: Ion flux measurement of the buffer without samples indicates the background level or noise. Typically, buffer measurement shows no clear fluctuation of the ion concentration leading to very small flux that displays variable directions.

4. Preparation of Measuring Chamber

Note: Before experiments, consider the sample to be measured and how the sample is to be mounted and immobilized for microelectrode measurements.

1. For *Xenopus laevis* oocyte measurements cut a 1 cm square of an 800 µm nylon mesh (nitex mesh) and glue it into a plastic Petri dish (**Figure 1E**).

5. Ion Flux Measurement

1. Measure the ion concentration present in the buffer used to perform the measurements on the sample in the same way as for the calibration solution. *X. laevis* oocytes require Mark's Modified Ringer (MMR). Dissolve NaCl, KCl, CaCl, MgCl and HEPES into deionized water to reach a final concentration of (mM): 100 NaCl, 2 KCl, 2 CaCl, 1 MgCl and 5 HEPES. Adjust the pH of the buffer to 7.5 using NaOH.
2. Place the sample into the measuring chamber and bring the ion-selective microelectrode close to the sample (about 10 µm away) using the micropositioner to define the close position of the microelectrode (**Figure 3A**).
3. Start the low frequency (0.3 Hz) excursion (100 µm) of the microelectrode between the close position and a position away from the sample (distant) using the dedicated software. Ensure that the movement of the microelectrode is perpendicular to the surface of the sample.
   Note: The excursion of the microelectrode can be set on the software. Large excursion increases the gradient read allowing an easier detection of small fluxes during the measurement while lengthens the sampling interval and decreases the temporal resolution. See **Figure 3A** for an example.
4. Start the recording using the software. The microelectrode pauses at each position and the electric potential in mV is recorded on the computer. Obtain measurements for at least 2 min, allowing signal stabilization. For short time-lapse experiments, record potential variations at the position of interest for the whole time course.
5. Extract the data as a txt file and copy the values into a spreadsheet file.
6. Calculate the ion concentration corresponding to the mV values in the same way as for the calibration values. Plot the value.
   Note: If an ion flux is present, the microelectrode detects a difference in ion concentration between the two positions (**Figure 3B**).
7. Calculate the ion flux using Fick's law of diffusion as before (step 3.3.1).
8. Repeat the buffer measurement before measuring a new sample and repeat the procedure of flux measurement and calculation for every new sample.

6. Statistical Analysis and Data Presentation

1. Test the independent effects of the position and/or of the time on ion fluxes under the control condition using an ANCOVA model with mixed effects[28].
   Note: Analysis of covariance (ANCOVA) is a general linear model that mixes regular ANOVA and regression by allowing both categorical and continuous measures to be used as independent variables. In addition, in the presence of correlated errors induced by repeated measures per individual and eventual nested effects, mixed effects models are used to model accurate estimates of both fixed and random effects.
2. Calculate pairwise comparisons using Student *t*-test between group levels with Bonferroni correction for multiple testing[28].
3. Generate boxplots to summarize ion flux measurements according to position and time. Include *p* values from the pairwise Student *t* described above (**Figure 3D**) and indicate significance levels of *p* values as follows: *: $p < 0.05$; **: $p < 0.01$; ***: $p < 0.001$[29]

Representative Results

We have previously shown that calcium influx appears after single cell wounding[24]. We therefore asked whether other ion fluxes occur upon single cell wounding. We used the *X. laevis* oocyte, a well-established model for single cell wound healing[30-34] and electrophysiological recording[24,35-39]. Interestingly, potassium ions are more concentrated inside *X. laevis* oocytes (about 110 mM)[40] than in the extracellular solution used (in MMR 1x: 1 mM) suggesting an efflux of potassium upon wounding. In order to confirm that hypothesis, we measured the potassium flux during the course of *X. laevis* oocyte cell membrane healing using the ion-selective self-referencing microelectrode.

To wound the oocyte, first pull a capillary electrode with a large tip size (~50 µm). Attach the electrode to a straight electrode holder and mount on a manual micro-positioner. Wound the oocyte by touching the membrane with the electrode tip[24]. Soon after wounding we detected a large efflux of potassium (up to 250 nmol cm^{-2} sec^{-1}; **Figure 3B**-**D**). As the membrane wound healed, this flux diminished, returning to unwounded flux values seen in the intact membrane (~5 nmol cm^{-2} sec^{-1}) when the wound healed (up to 16 min after wounding; **Figure 3B**-**D**). ANCOVA revealed a significant effect of time after wounding on potassium flux measurements ($p < 0.001$). *Post hoc* analyses revealed significantly increased potassium efflux at 1-2 min ($p < 0.001$) and at 5-6 min ($p < 0.05$), but not at 15-16 min after wounding when compared to intact cell membrane condition (**Figure 3D**). We concluded that upon single cell wounding, an efflux of potassium appears at the level of the wound that decrease during the course of healing.

Ion	Ionophore cocktail	Electrolyte solution (100 mM)	Reference solution (3 M)	Artificial source solution (1 M)
Ca^{2+}	Calcium Ionophore I Cocktail A (cat# 21048)	$CaCl_2$ $2H_2O$	KCl	$CaCl_2$ $2H_2O$
Na^+	Sodium Ionophore II Cocktail A (cat# 71178)	NaCl	KCl	NaCl
Cl^-	Chloride Ionophore I Cocktail A (cat# 24902)	NaCl	CH_2CO_2K (Potassium Acetate)	NaCl
K^+	Potassium Ionophore I Cocktail A (cat# 60031)	KCl	NaCl	KCl
H^+	Hydrogen Ionophore I Cocktail A (cat#95291)	pH 7.0	KCl	pH 4.0

Table 1: Examples of commonly used ionophore cocktails. Also shown are appropriate solutions to place in the microelectrodes, for the artificial source and to perform calibration. Catalog numbers are from Sigma-Aldrich.

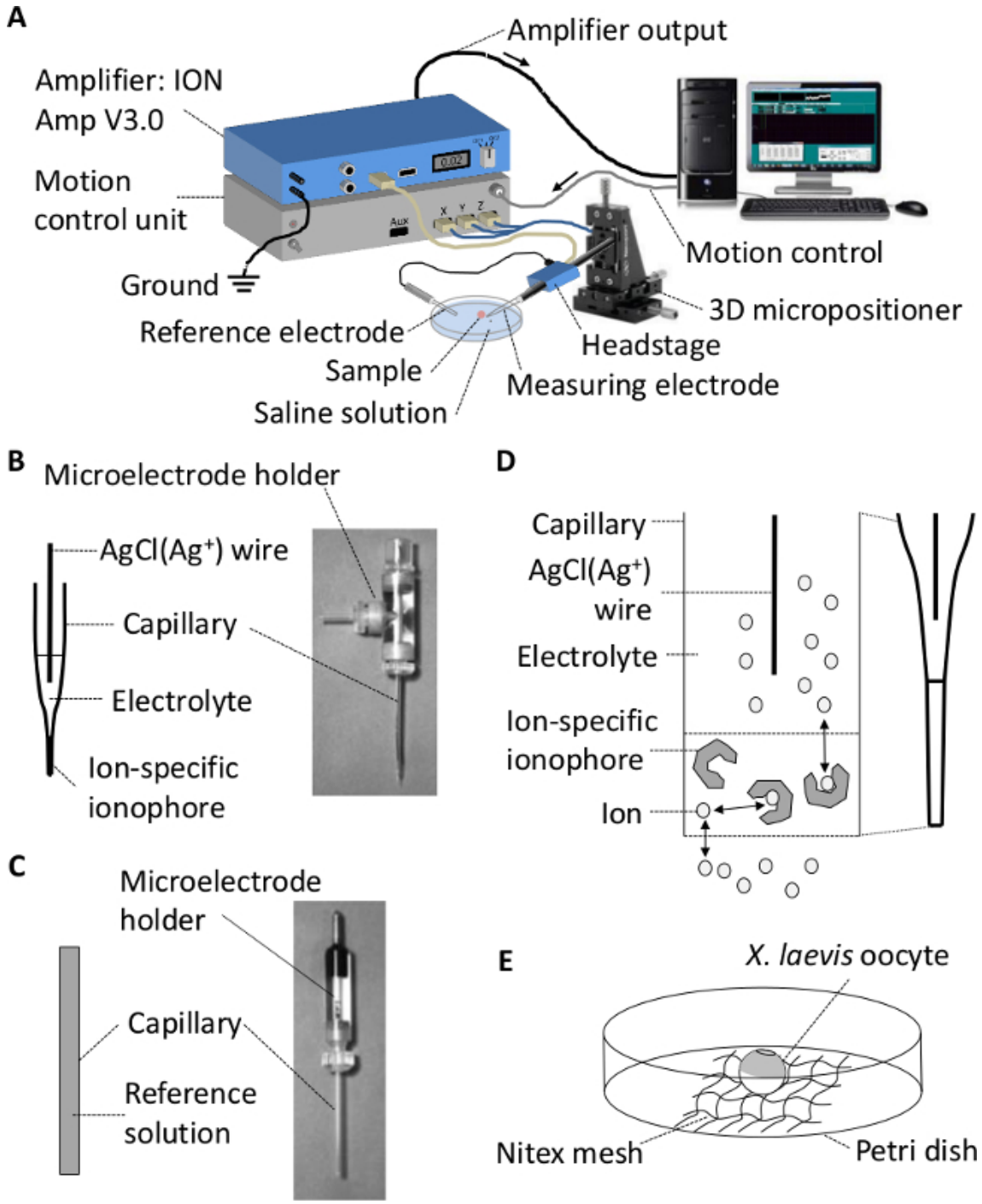

Figure 1: Ion-selective microelectrodes. (**A**) Schematic representation of the ion-selective self-referencing microelectrode system. (**B**) Ion-selective microelectrode. (**C**) Reference electrode. (**D**) Ion exchange between the external solution and the microelectrode via the ionophore. (**E**) Scheme of the measuring chamber used for *X. laevis* oocyte.

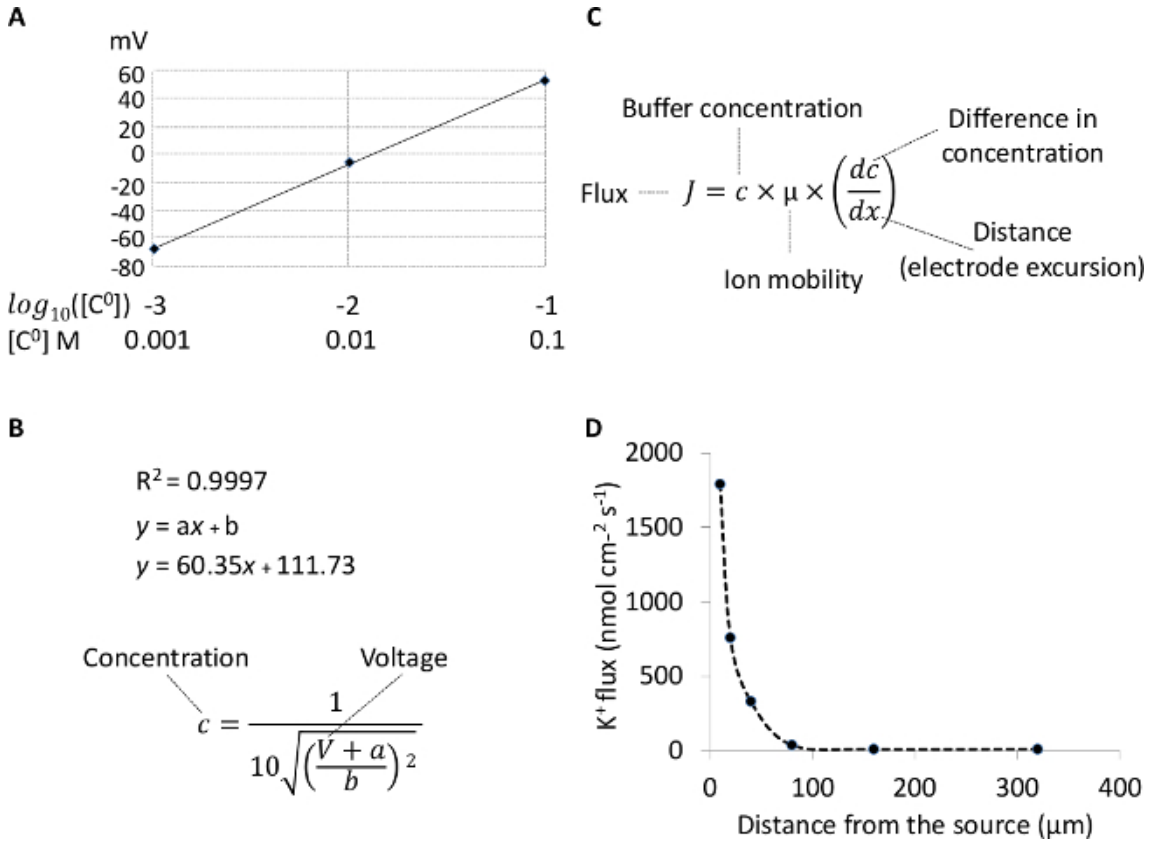

Figure 2: Ion-selective microelectrodes calibration, artificial source and flux calculation. (**A**) Calibration curve. (**B**) Equation of the calibration curve and calculation of the ion concentration. (**C**) Calculation of the ion flux. (**D**) Ion flux measured at specific distances from the artificial source (1 M KCl).

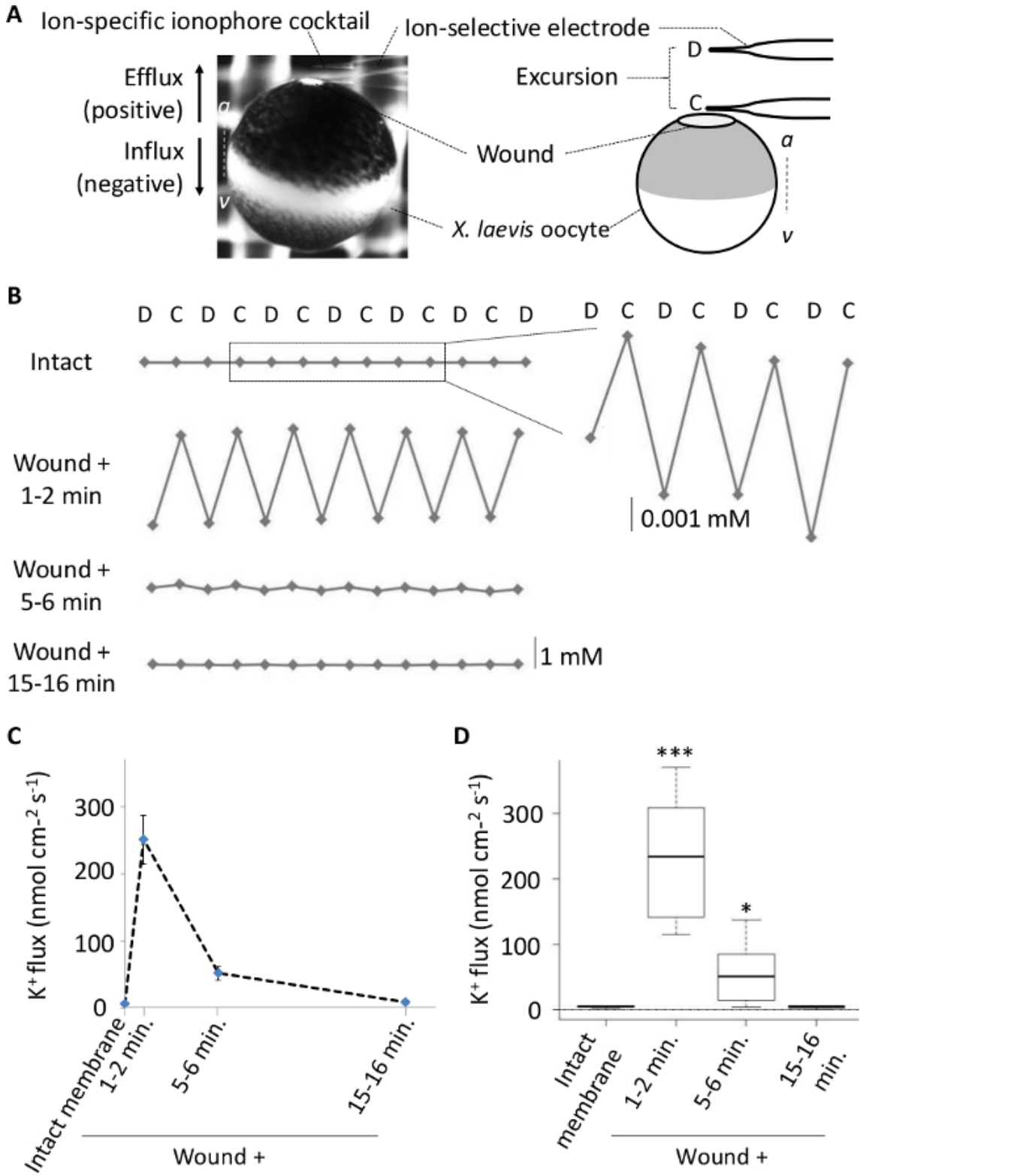

Figure 3: Evolution of the potassium flux at *X. laevis* oocyte wound during healing. (**A**) Photograph and illustration of the excursion of the ion-selective microelectrode measuring ion concentration at *X. laevis* oocyte wound; the dashed line between ''a'' and ''v'' represents the animal–vegetal axis. (**B**) Illustration of the variation of potassium ion concentration at *X. laevis* oocyte wound during healing. (**C**) Scatter (xy) plot showing the mean and the standard error of potassium flux measurement at the level of the wound at different time during *X. laevis* oocyte wound healing. (**D**) Boxplot showing potassium flux measurement at the level of the wound at different time during *X. laevis* oocyte wound healing (n = 16; p values indicated as follow: *: p <0.05; ***: p <0.001).

Discussion

The most critical steps for successful measurement of extracellular ion fluxes *in vivo* are: the reduction of the noise, the correct fabrication of the ion-selective microelectrodes and reference electrode, and the positioning of the sample and both electrodes.

In order to minimize the noise, the recording system should be in an earthed (grounded) Faraday cage preferably with a metal-topped (vibration isolation) table which is also earthed. In addition, the microscope chassis should also be earthed. Sources of electric noise include the light source. A fiber-optic 'fan-less' light source causes minimal electric noise. Finally, keeping the silver wire and pellet in the microelectrode holders chlorided also minimizes noise (dip in sodium hypochlorite bleach and rinse in dH_2O).The presence of air bubbles in the ion-selective microelectrode or in the reference electrode will result in measurement failure as the conductivity of the microelectrode will be nil or compromised. Thus, it is crucial to verify the electrodes under the microscope before mounting them on the holders. See the protocol for detailed procedure to remove air bubbles. The correct positioning of both the sample and the microelectrodes are required in order to ensure reliable and reproducible results. The measurement of ion flux is dependent on the excursion of the microelectrode and its position relative to the sample. It is important to identify precisely the area of interest that will be measured on the sample and position the microelectrode to have a perpendicular movement from the sample. Any excursion of the microelectrodes in a way that is not perpendicular to the sample will result in altered ion fluxes measurements and increased variability among samples.

Ionophore cocktails dedicated to measure specific ions, for example potassium, may also sense the presence of other ions, such as sodium. In the case that the measuring solution contains a high amount of a competing ion for the ionophore cocktail, it is important to determine the selectivity of the ionophore cocktail by using the artificial source experiment. Here, the solution used to culture *X. laevis* oocytes (MMR) contains a high concentration of sodium. Thus, it is important to assess whether the potassium ionophore cocktail used also senses sodium. By using the potassium ionophore cocktail filled microelectrode, we can attempt to measure a sodium flux using an artificial source that contains high sodium concentration (1 M NaCl; see **Table 1**) keeping the same measuring solution. The chemical gradient favors the efflux of sodium, but ideally no sodium flux should be detected by the potassium-specific ionophore cocktail. If a significant flux is measured, the experimental condition should be optimized. For example, the concentration of the competing ion could be lowered down to the point the microelectrode does not sense it anymore, while this may affect the sodium flux across the plasma membrane leading to potential interference during potassium flux measurements. Ideally, a correcting factor calculated from the artificial source experiment can be applied to the data, or another ionophore cocktail can be tested. Ion flux measurements using the ion-selective self-referencing microelectrode allow the measurement of ion fluxes occurring at cells and tissue in aqueous solution. Measurements of ion fluxes in cells or tissues that are normally in contact with an air environment requires the presence of a solution that is not naturally present in their environment and that can alter the ion flux and exchange that occurs under normal conditions. Specific attention has to be made to define the content of such solution and minimize the deviation from the original, physiological environment. The spectrum of ions that can be measured by the ion-selective self-referencing microelectrode technique depends on the availability and existence of specific ionophore cocktails selective to the ion of interest.

Ion flux measurements performed with the ion-selective self-referencing microelectrode are done in solution, usually near the surface of cells or tissues, allowing the non-invasive measurement of extracellular ion fluxes. This method does not allow the measurement of ion fluxes inside tissues, between cell and intercellular space. The ion-selective self-referencing microelectrode is not the only method that allows measurement of ion fluxes *in vivo*. An alternative new method uses fluorescent bioelectricity reporters[41] which enables the measurement of ion fluxes that are not possible using microelectrodes. These dyes permit measurements of ions fluxes inside tissues and cells and can achieve subcellular localization. This technique can acquire spatial information of the ion flux inside tissues and cells but not ion exchange between the tissue and the extracellular space. Furthermore, the fluorescent bioelectricity reporters usually generate semi-quantitative data. The use of microelectrode-based technology to measure ion fluxes is still valid and necessary and brings additional information to the use of fluorescent bioelectricity reporters, making them complementary rather than competing techniques. In addition, interesting recent developments include amperometric self-referencing detectors of oxygen, nitric oxide and neurotransmitters dopamine and glutamate[42,43]. Amperometric sensing is based on a chemical reaction at the sensor tip. New fiber-optic microelectrodes (“optrodes”) have been developed to measure non-invasively metabolic oxygen flux[34,35] and pH[44] with high selectivity and sensitivity[45,46]. There is now also an enzyme-based nanoparticle-coated probe sensitive to glucose[47].

We have seen that the ion-selective self-referencing microelectrode enables measurements of extracellular ion fluxes *in vivo*. Ions are not only exchanged between the cells/tissues and extracellular space but also between cells and tissues within living organisms. It is important to combine this technique with others such as fluorescent bioelectricity reporters in order to appreciate the spatial resolution of the ion fluxes inside tissues in addition to the actual measurements of the ion fluxes near its surface. In addition, ion fluxes represent an important part of the bioelectric state that defines cells and tissues together with cell membrane potential, trans-epithelia potential or extracellular electric currents. It is important, in addition to the measurement of ion fluxes, to measure, in combination, cell membrane and trans-epithelia potential as well as extracellular electric currents[24].

Disclosures

The authors declare that they have no competing financial interests.

Acknowledgements

This work was supported by National Science Foundation grant MCB-0951199, and in part by the NIH grant EY01910, California Institute of Regenerative Medicine grants RB1-01417 and by the Fundação para a Ciência e Tecnologia (FCT) grant SFRH/BD/87256/2012.

References

1. Weber, W. M., Liebold, K. M., Clauss, W. Amiloride-sensitive Na+ conductance in native Xenopus oocytes. *Biochimica et biophysica acta.* **1239**, 201-206 (1995).
2. McCaig, C. D., Song, B., Rajnicek, A. M. Electrical dimensions in cell science. *Journal of cell science.* **122**, 4267-4276 (2009).
3. Zhao, M. Electrical fields in wound healing-An overriding signal that directs cell migration. *Seminars in cell & developmental biology.* **20**, 674-682 (2009).
4. Jaffe, L. F., Nuccitelli, R. An ultrasensitive vibrating probe for measuring steady extracellular currents. *The Journal of cell biology.* **63**, 614-628 (1974).
5. Reid, B., Nuccitelli, R., Zhao, M. Non-invasive measurement of bioelectric currents with a vibrating probe. *Nature protocols.* **2**, 661-669 (2007).
6. Reid, B., Zhao, M. Measurement of bioelectric current with a vibrating probe. *Journal of visualized experiments : JoVE.* (2011).
7. Neher, E., Sakmann, B. Single-channel currents recorded from membrane of denervated frog muscle fibres. *Nature.* **260**, 799-802 (1976).
8. Moore, J. W. The patch clamp: single-channel recording. *Science.* **224**, 50-51 (1984).
9. Brown, A. L., Johnson, B. E., Goodman, M. B. Patch clamp recording of ion channels expressed in Xenopus oocytes. *Journal of visualized experiments.* (2008).
10. McCaig, C. D., Robinson, K. R. The ontogeny of the transepidermal potential difference in frog embryos. *Developmental biology.* **90**, 335-339 (1982).
11. Kuhtreiber, W. M., Jaffe, L. F. Detection of extracellular calcium gradients with a calcium-specific vibrating electrode. *The Journal of cell biology.* **110**, 1565-1573 (1990).
12. The use of the vibrating probe technique to study steady extracellular currents during pollen germination and tube growth. *Fertilisation in Higher Plants: molecular and cytological aspects.* Cai, G., Cresti, M., Moscatelli, A. 235-252 Springer-Verlag (1999).
13. Kunkel, J. G., Xu, Y., Shipley, A. M., Feijó, J. A. The use of non-invasive ion-selective microelectrode techniques for the study of plant development. *Plant Electrophysiology – Theory and Methods. (ed Volkov AG.* 109-137 Springer-Verlag Berlin Heidelberg (2006).
14. Ordonez, N. M., Shabala, L., Gehring, C., Shabala, S. Noninvasive microelectrode ion flux estimation technique (MIFE) for the study of the regulation of root membrane transport by cyclic nucleotides. *Methods in molecular biology.* **1016**, 95-106 (2013).
15. Tegg, R. S., Melian, L., Wilson, C. R., Shabala, S. Plant cell growth and ion flux responses to the streptomycete phytotoxin thaxtomin A: calcium and hydrogen flux patterns revealed by the non-invasive MIFE technique. *Plant & cell physiology.* **46**, 638-648 (2005).
16. Newman, I. A. Ion transport in roots: measurement of fluxes using ion-selective microelectrodes to characterize transporter function. *Plant, cell & environment.* **24**, 1-14 (2001).
17. Kochian, L. V., Shaff, J. E., Kuhtreiber, W. M., Jaffe, L. F., Lucas, W. J. Use of an extracellular, ion-selective, vibrating microelectrode system for the quantification of K(+), H (+), and Ca (2+) fluxes in maize roots and maize suspension cells. *Planta.* **188**, 601-610 (1992).
18. Doughty, J. M., Langton, P. D. Measurement of chloride flux associated with the myogenic response in rat cerebral arteries. *The Journal of physiology.* **534**, 753-761 (2001).
19. Messerli, M. A., Smith, P. J., Lewis, R. C., Robinson, K. R. Chloride fluxes in lily pollen tubes: a critical reevaluation. *The Plant journal : for cell and molecular biology.* **40**, 799-812 (2004).
20. Molina, A. J., *et al.* Neurotransmitter modulation of extracellular H+ fluxes from isolated retinal horizontal cells of the skate. *The Journal of physiology.* **560**, 639-657 (2004).
21. Marenzana, M., Shipley, A. M., Squitiero, P., Kunkel, J. G., Rubinacci, A. Bone as an ion exchange organ: evidence for instantaneous cell-dependent calcium efflux from bone not due to resorption. *Bone.* **37**, 545-554 (2005).
22. Lew, R. R. Ionic currents and ion fluxes in Neurospora crassa hyphae. *Journal of experimental botany.* **58**, 3475-3481 (2007).
23. Vieira, A. C., *et al.* Ionic components of electric current at rat corneal wounds. *PloS one.* **6**, e17411 (2011).
24. Luxardi, G., Reid, B., Maillard, P., Zhao, M. Single cell wound generates electric current circuit and cell membrane potential variations that requires calcium influx. *Integrative biology : quantitative biosciences from nano to macro.* **6**, 662-672 (2014).
25. Smith, P. J. S., Sanger, R. H., Messerli, M. A. *Electrochemical Methods for Neuroscience.* Michael, A. C., Borland, L. H. (2007).
26. Smith, P. J., Hammar, K., Porterfield, D. M., Sanger, R. H., Trimarchi, J. R. Self-referencing, non-invasive, ion selective electrode for single cell detection of trans-plasma membrane calcium flux. *Microscopy research and technique.* **46**, 398-417 (1999).
27. Messerli, M. A., Smith, P. J. Construction theory, and practical considerations for using self-referencing of Ca(2+)-selective microelectrodes for monitoring extracellular Ca(2+) gradients. *Methods in cell biology.* **99**, 91-111 (2010).
28. Chambers, J., Hastie, T., Pregibon, D. Ch. 48. *Compstat.* Momirović, K., Mildner, V. 317-321 Physica-Verlag HD (1990).
29. Chambers, J. M., Cleveland, W. S., Kleiner, B., Tukey, P. A. *Graphical methods for data analysis.* Wadsworth & Brooks/Cole (1983).
30. Burkel, B. M., Benink, H. A., Vaughan, E. M., von Dassow, G., Bement, W. M. A Rho GTPase signal treadmill backs a contractile array. *Developmental cell.* **23**, 384-396 (2012).
31. Bement, W. M., Mandato, C. A., Kirsch, M. N. Wound-induced assembly and closure of an actomyosin purse string in Xenopus oocytes. *Current biology : CB.* **9**, 579-587 (1999).
32. Mandato, C. A., Bement, W. M. Contraction and polymerization cooperate to assemble and close actomyosin rings around Xenopus oocyte wounds. *The Journal of cell biology.* **154**, 785-797 (2001).
33. Benink, H. A., Bement, W. M. Concentric zones of active RhoA and Cdc42 around single cell wounds. *The Journal of cell biology.* **168**, 429-439 (2005).
34. Simon, C. M., Vaughan, E. M., Bement, W. M., Edelstein-Keshet, L. Pattern formation of Rho GTPases in single cell wound healing. *Molecular biology of the cell.* **24**, 421-432 (2013).
35. Petersen, C. C., Dupont, G. The initiation of a calcium signal in Xenopus oocytes. *Cell calcium.* **16**, 391-403 (1994).
36. Horisberger, J. D., Lemas, V., Kraehenbuhl, J. P., Rossier, B. C. Structure-function relationship of Na,K-ATPase. *Annual review of physiology.* **53**, 565-584 (1991).
37. Miledi, R. A calcium-dependent transient outward current in Xenopus laevis oocytes. *Proceedings of the Royal Society of London. Series B, Containing papers of a Biological character. Royal Society.* London, England, 491-497 (1982).
38. Miledi, R., Parker, I. Chloride current induced by injection of calcium into Xenopus oocytes. *The Journal of physiology.* **357**, 173-183 (1984).

39. Parker, I., Miledi, R. A calcium-independent chloride current activated by hyperpolarization in Xenopus oocytes. *Proceedings of the Royal Society of London. Series B, Containing papers of a Biological character. Royal Society.* **233**, 191-199 (1988).
40. Costa, P. F., Emilio, M. G., Fernandes, P. L., Ferreira, H. G., Ferreira, K. G. Determination of ionic permeability coefficients of the plasma membrane of Xenopus laevis oocytes under voltage clamp. *The Journal of physiology.* **413**, 199-211 (1989).
41. Adams, D. S., Levin, M. General principles for measuring resting membrane potential and ion concentration using fluorescent bioelectricity reporters. *Cold Spring Harbor protocols.* **2012**, 385-397 (2012).
42. Porterfield, D. M. Measuring metabolism and biophysical flux in the tissue, cellular and sub-cellular domains: recent developments in self-referencing amperometry for physiological sensing. *Biosensors.* **22**, 1186-1196 (2007).
43. McLamore, E. S., *et al.* A self-referencing glutamate biosensor for measuring real time neuronal glutamate flux. *Journal of neuroscience methods.* **189**, 14-22 (2010).
44. Yin, M., *et al.* Highly sensitive and fast responsive fiber-optic modal interferometric pH sensor based on polyelectrolyte complex and polyelectrolyte self-assembled nanocoating. *Analytical and bioanalytical chemistry.* **399**, 3623-3631 (2011).
45. Chatni, M. R., Porterfield, D. M. Self-referencing optrode technology for non-invasive real-time measurement of biophysical flux and physiological sensing. *The Analyst.* **134**, 2224-2232 (2009).
46. McLamore, E. S., Jaroch, D., Chatni, M. R., Porterfield, D. M. Self-referencing optrodes for measuring spatially resolved, real-time metabolic oxygen flux in plant systems. *Planta.* **232**, 1087-1099 (2010).
47. McLamore, E. S., *et al.* A self referencing platinum nanoparticle decorated enzyme-based microbiosensor for real time measurement of physiological glucose transport. *Biosensors & bioelectronics.* **26**, 2237-2245 (2011).

II. *DIABETIC CORNEA WOUNDS PRODUCE SIGNIFICANTLY WEAKER ELECTRIC SIGNALS THAT MAY CONTRIBUTE TO IMPAIRED HEALING*

Publication overview

For this publication (also for unrelated projects), I was collaborating actively by measuring the TEP in intact and wounded corneas, healthy and diabetic, of *ex vivo* eyes from rats and mice. The aim was to test whether the electric fields, directly calculated from TEP, were correlative with disease and with healing efficiency. Albeit promising, due to difficulties to interpret and to integrate the results into the study, these data were not published. The aim was successfully and robustly achieved using a vibrating probe. Overall, the findings of this study resonate with those of my doctorate, namely the general conclusion that injury-induced electric signals have an active role in the progress and efficiency of the healing. Moreover, the study unveiled that diabetic wounds may have impaired healing because of the weaker electric fields produced, which are known to guide cell migration during healing. In fact, high glucose compromised electrotaxis in human corneal epithelial cells *in vitro*. Such findings are of clinical relevance, suggesting electric signals as a new and targetable player to enhance chronic and non-healing wounds.

Publication contributions

From publication's equivalent section: "Y.S., T.P., B.R. and F.F. performed the experiments and acquired the data, M.F.N. provided LFD and HFD fed mice and contributed to the revision of the manuscript, Q.Z. provided some financial support and participated in analysis and interpretation of data. J.L. contributed to the revision of the manuscript and analysis of data. M.Z., B.R. and Y.S. conceived and designed the study. Y.S., B.R. and M.Z. wrote the manuscript."

More specifically, I (F.F.) contributed to the wound healing assay (Fig. 4) and to the scheme shown in Fig. 7. Moreover, I contributed with discussion of the methodology and results, to manuscript revision and editing, and to addressing peer review comments.

Publication reprint

Vide infra.

SCIENTIFIC REPORTS

OPEN

Diabetic cornea wounds produce significantly weaker electric signals that may contribute to impaired healing

Received: 14 January 2016
Accepted: 04 May 2016
Published: 10 June 2016

Yunyun Shen[1,2], Trisha Pfluger[1], Fernando Ferreira[1,3], Jiebing Liang[4], Manuel F. Navedo[5], Qunli Zeng[2], Brian Reid[1] & Min Zhao[1,6]

Wounds naturally produce electric signals which serve as powerful cues that stimulate and guide cell migration during wound healing. In diabetic patients, impaired wound healing is one of the most challenging complications in diabetes management. A fundamental gap in knowledge is whether diabetic wounds have abnormal electric signaling. Here we used a vibrating probe to demonstrate that diabetic corneas produced significantly weaker wound electric signals than the normal cornea. This was confirmed in three independent animal models of diabetes: db/db, streptozotocin-induced and mice fed a high-fat diet. Spatial measurements illustrated that diabetic cornea wound currents at the wound edge but not wound center were significantly weaker than normal. Time lapse measurements revealed that the electric currents at diabetic corneas lost the normal rising and plateau phases. The abnormal electric signals correlated significantly with impaired wound healing. Immunostaining suggested lower expression of chloride channel 2 and cystic fibrosis transmembrane regulator in diabetic corneal epithelium. Acute high glucose exposure significantly (albeit moderately) reduced electrotaxis of human corneal epithelial cells *in vitro*, but did not affect the electric currents at cornea wounds. These data suggest that weaker wound electric signals and impaired electrotaxis may contribute to the impaired wound healing in diabetes.

Delayed or non-healing wounds pose an immense health and economic problem, affecting the quality of life of millions of patients globally. The World Health Organization estimated that the global prevalence of diabetes in 2014 was 9% and that it will be the 7th leading cause of death in 2030[1]. Impaired wound healing in diabetic patients results in adverse pathological changes such as chronic foot ulceration which affects approximately 15% of diabetic patients[2]. This burden is growing rapidly due to increasing health care costs, an aging population, and a sharp rise in the incidence of diabetes and obesity worldwide[3,4]. Diabetic patients may also suffer from corneal recurrent erosions/ulcerations[5] which are difficult to treat and may result in significant ocular morbidity and visual impairment[6,7]. The mechanisms underlying wound healing defects in diabetic patients are not fully understood, but may include deregulation of the biochemical milieu such as microcirculatory changes, altered growth factors, abnormal cytokine production, genetic or epigenetic changes and inflammatory state[8,9].

Electric fields (EFs) occur naturally at wounds[10]. The corneal epithelium actively generates and maintains an electrical trans epithelial potential (TEP)[11] by active directional pumping of ions between the stroma and tear side[12]. Wounding collapses the local TEP resulting in significant electric potentials and currents between the wound and the surrounding intact epithelium, establishing the cathode at the wound[13]. The existence of these endogenous wound electric currents has been confirmed using different modern techniques[14–16]. We use "electric signals" to denote steady, direct-current EFs that are intrinsically associated with steady fluxes of ions.

[1]Department of Dermatology, University of California, Davis, CA, USA. [2]Bioelectromagnetics Laboratory, Department of Occupational and Environmental Health, School of Public Health, School of Medicine, Zhejiang University, Hangzhou, China. [3]Department of Biology, Centre of Molecular and Environmental Biology (CBMA), University of Minho, Braga, Portugal. [4]Department of Biology, California State University, Northridge, CA, USA. [5]Department of Pharmacology, University of California, Davis, CA, USA. [6]Department of Ophthalmology and Vision Science, University of California, Davis, CA, USA. Correspondence and requests for materials should be addressed to M.Z. (email: minzhao@ucdavis.edu)

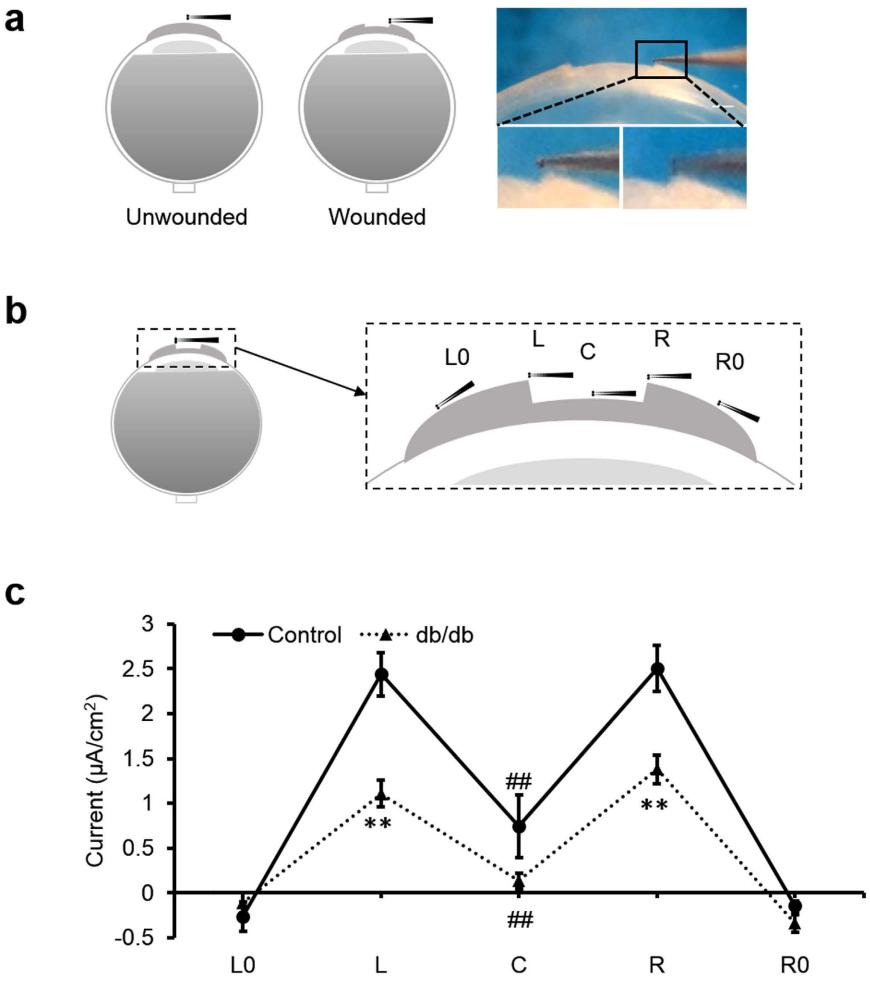

Figure 1. Diabetic corneas generated significantly weaker wound electric signal. (**a**) Schematic diagram of the wound current measurement with the probe positioned at the unwounded center and wound edge. Photographs on the right show the probe in measuring position at the right wound edge. The close-ups below show the probe without vibration for clarity (left) and the probe vibrating (blurred double image) on the right. Scale bar: 250 μm. (**b**) Positions of the vibrating probe when measuring electric current at different places across the wounded cornea: left unwounded position (L0), left wound edge (L), wound center (C), right wound edge (R) and right unwounded positon (R0). (**c**) Electric current profile of wounded control and db/db diabetic corneas. Positive values are outward current (flow of positive charge), negative values are inward. Currents were significantly greater at the wound edges than at the wound center ($p < 0.01$; Student t-test). Currents at the wound edge of diabetic cornea were significantly weaker than in the control group ($^{**}p < 0.01$). Currents at the wound center were not significantly different ($^{\#\#}$NS). Interestingly, currents at the unwounded cornea outside the wound were on average slightly inward. Data are mean ± S.E.M. from 4 independent wounds.

Wound repair is a precise and complex process necessary to recover tissue function after injury. Effective wound healing requires tightly controlled cell movement and tissue growth[17]. Epithelial cells, including corneal epithelial cells (CECs) and skin keratinocytes, respond robustly by directional migration in EFs of strengths that have been measured at wounds *in vivo*[18,19]. The EFs override co-existing directional signals such as free edge and contact inhibition release. Migration of CECs is guided by EFs of physiological strength when applied in a direction opposite to other cues[20]. Applied EFs as low as 12.5 mV/mm guide migration of CECs to the cathode, the same direction of the wound EFs[18]. Electrical stimulation has been approved in the U.S. for treatment of refractory chronic wounds in patients (chronic Stage III or Stage IV pressure ulcers, arterial ulcers, diabetic ulcers and venous stasis ulcers), because of apparent clinical benefits[21–23].

It is, however, not known whether diabetic wounds have abnormal electric signals. Here we tested the hypothesis that diabetic corneas produce weaker electrical signals compared to normal corneas and that the weaker signals may contribute to the impaired wound healing. We also tested whether high glucose affects directional cell migration guided by small-applied electric fields.

Results

Diabetic cornea wounds lost the large electric signal. We used a vibrating probe to measure the intact and wounded cornea electric current (Fig. 1a). To profile the cornea wound current, five different positions inside

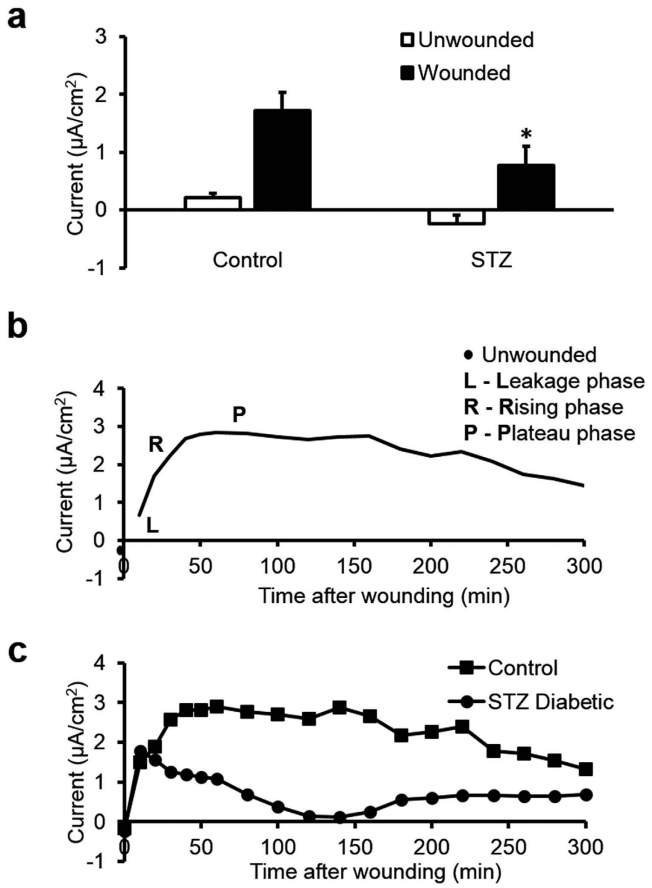

Figure 2. Streptozotocin (STZ) induced diabetic cornea wounds showed an impaired wound electric signal and lost the putative active transport phases. (**a**) STZ diabetic cornea wounds had significantly smaller electric signals. White bars are unwounded current and black bars are wound edge current. Data are mean ± S.E.M. from 6 independent wounds. Control: age-matched vehicle-injected controls. $*p < 0.05$, when compared with the control value, Student *t*-test. (**b**) Three phases of the naturally-occurring electric currents at mouse cornea wound recorded in the hours after wounding. Line is a best fit (rolling average, two period) of the mean control mouse electric current time lapse data. (**c**) Time lapse wound currents in control and diabetic mice measured for five hours after wounding. STZ diabetic cornea lost the rising and plateau phases. Squares are age-matched vehicle-injected control and circles are STZ-induced diabetic.

and outside the wound were measured with the vibrating probe 40 min post-wounding, as this is the approximate time the current reaches maximum (Fig. 1b). In control corneas, currents were maximal at the wound edges and smaller at the wound center (Fig. 1c). Diabetic db/db cornea wounds showed a similar profile: the wound current at the edges were three times larger than that at the wound center ($n = 4$, $p < 0.01$). Currents at the wound center were not significantly different ($n = 4$, $p > 0.05$). However, diabetic cornea wound currents at both the right and left edges displayed significantly weaker electric signals than the control group ($n = 4$, $p < 0.01$). We confirmed this result in a different diabetes model, streptozotocin (STZ)-injected. STZ-induced diabetic cornea wound edges also showed significantly weaker electric signals (Fig. 2a) ($n = 6$, $p < 0.05$).

These wound profile data support our previous hypothesis that the wound edge current depends more on active transport whereas the smaller current at the wound center may be more due to ion leakage[24]. These spatial maps also suggest that the stroma at the wound center does not generate significant ion flux and that diabetic corneas have less active (translocator-mediated) ion flux than control ones. Interestingly, currents outside the wounds were slightly inward, suggesting a circuit of current flowing outward at the wound and inward in the surrounding intact corneal epithelium.

Diabetic cornea wound current lost the rising and plateau phases in the timelapse measurements. We next recorded the time course of the wound electrical signals in control and STZ-induced diabetes. In normal age-matched saline-injected control mice, cornea electric currents showed characteristic dynamic changes after wounding: leakage phase (L), rising phase (R) and plateau phase (P) (Fig. 2b). Electric currents at cornea wounds from STZ-induced diabetic mice lacked these characteristic rising and plateau phases (Fig. 2c). This suggests that ion channels and pumps which generate the cornea electric signals (e.g., TEP and associated wound fields and currents) might be downregulated in diabetes.

We also used the vibrating probe to measure electric current time-course in different diabetes models: db/db and high-fat diet (HFD) diabetic mice. Blood glucose levels were measured before the vibrating probe

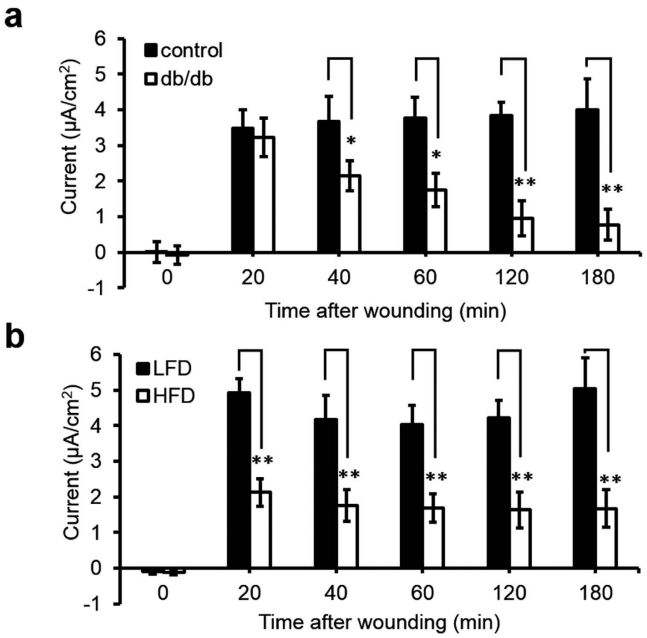

Figure 3. A genetic knockout model of diabetes in mice (db/db) and high-fat diet (HFD) diabetic mice also showed a weaker electric signal at the cornea wound. (**a**) Diabetic db/db cornea wounds generated weaker electric signals. Black bars are the age-matched heterozygous genetic control group and white bars are the diabetic db/db group, n = 6. (**b**) Weaker electric current was also observed in high-fat diet induced diabetic mouse cornea wounds. Black bars are age-matched low fat diet control group (LFD) and white bars are high-fat diet induced diabetic group (HFD), n = 4. Data are mean ± S.E.M. *$p < 0.05$, **$p < 0.01$, when compared with the matched control value, Student *t*-test.

measurement to confirm the diabetic status (Table S1). After wounding, db/db corneas generated weaker currents compared to the age-matched control group (n = 6, $p < 0.05$) (Fig. 3a). Three hours after wounding, the currents at cornea wounds of control mice remained significantly larger ($4.01 \pm 0.86\,\mu A/cm^2$), more than five times larger than in the db/db mice ($0.77 \pm 0.44\,\mu A/cm^2$) (n = 6, $p < 0.01$). Consistently, electric currents at cornea wounds in HFD mice were also significantly smaller than the controls. Electric signal decreased significantly at cornea wounds in HFD-induced mice at 20 min post-wounding and thereafter for up to 3 h (n = 4, $p < 0.01$) (Fig. 3b).

Interestingly, 1 out of 6 corneas of db/db diabetes, 2 out of 6 corneas of STZ-induced diabetes and 1 out 4 corneas of HFD mice had inward wound currents. This was unusual and was never seen in any cornea wound in healthy wild-type mouse, rat or human[25,26], which always show outward cornea wound currents.

Diabetic patients can often have abnormally high levels of glucose in their tears[27]. We tested whether high glucose in the bathing solution altered the cornea wound electric signal. Corneas pre-incubated in high glucose (30 mM) for 3 h prior to wounding did not show significantly different electric currents (unwounded or wounded) when compared with control eyes incubated in normal glucose (5.6 mM) for the same time (Fig. S1). Therefore, diverse diabetes models consistently have weaker cornea wound electric signals compared to matched controls, and it cannot be mimicked by acute exposure to high glucose.

Diabetic cornea wound healing rate correlated with the wound currents. To quantify cornea wound healing, we made similar-sized epithelial wounds in control and diabetic mice (Φ ~1.4 mm) and visualized the wound with fluorescein dye. Wound areas were not significantly different at time zero ($p > 0.5$). Cornea wounds in control mice healed quickly: at 24 h they were more than 50% healed (<½ original area), and by 48 h were almost completely healed (Fig. 4a,b). In contrast, STZ-treated mice wounds healed slowly. There was no healing in the first 24 h and by 48 h they had healed an average of only 42.6% ($p < 0.05$) (Fig. 4a,b). HFD and db/db mice corneas also healed much slower than age-matched control corneas ($p < 0.01$) (Fig. 4a,b).

We used the Pearson correlation analysis to determine the relationship between impaired wound healing and the wound electric currents. The analysis showed that the wound healing rate correlated significantly with the changes in wound electric current (Fig. 4c). Results from two different diabetic mouse models showed a positive correlation between wound current and wound healing. Thus, eyes with small (or even inward) currents showed poor wound healing whereas eyes with larger currents showed better wound healing. Paired analyses of db/db mice (Pearson correlation coefficient, $R = 0.990$) and HFD mice (Pearson correlation coefficient, $R = 0.987$) showed significant correlation (n = 4, $p = 0.010$ and n = 4, $p = 0.013$, respectively) (Fig. 4c).

Decreased expression of CFTR and CLC2 in diabetic corneal epithelium. To test possible changes in ion translocators in diabetic corneas we labeled chloride channel 2 (CLC2) and cystic fibrosis transmembrane conductance regulator (CFTR) because these channels are expressed in corneal epithelium and Cl^- fluxes were

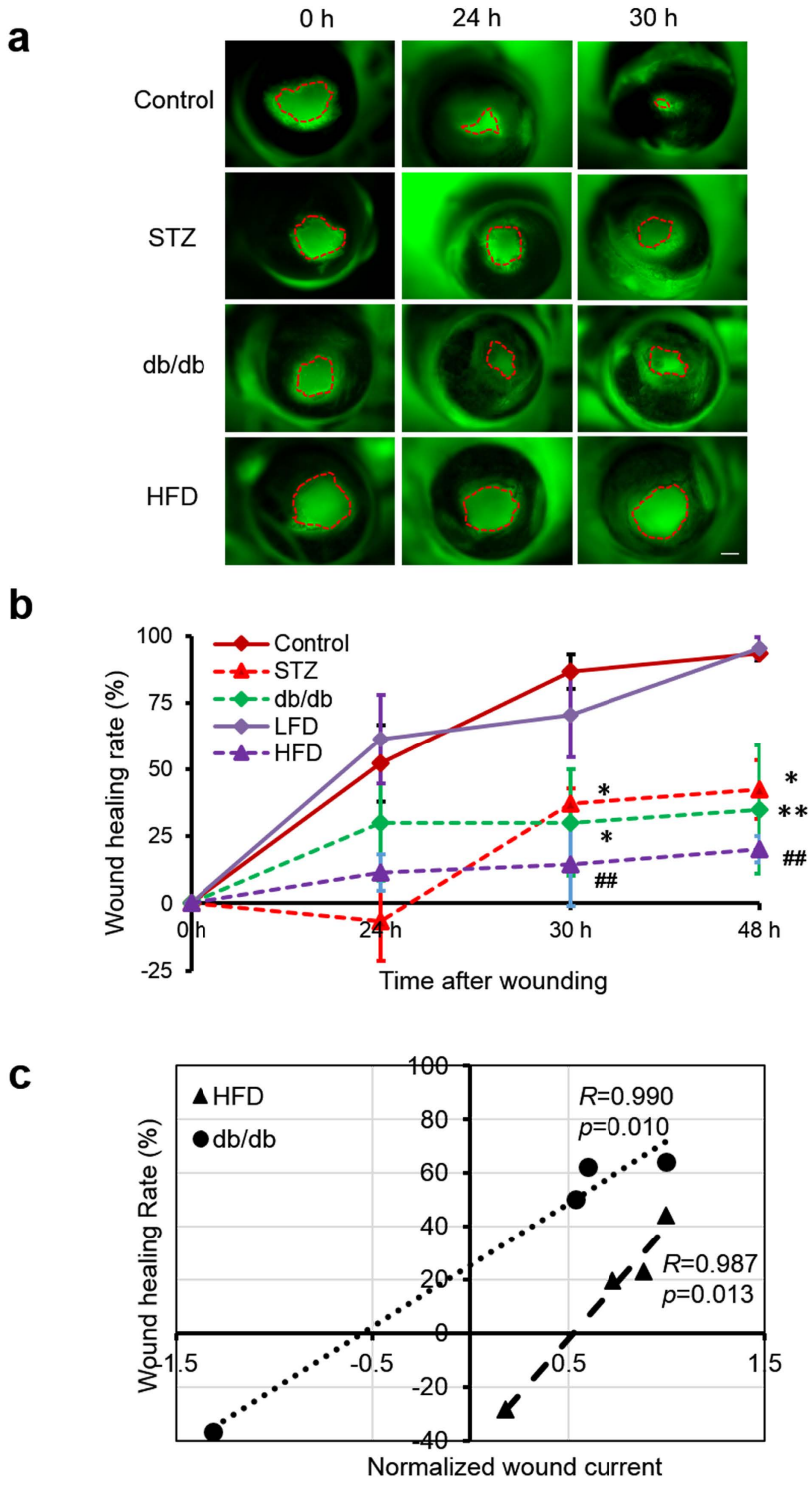

Figure 4. Impaired wound healing in diabetic corneas was correlated significantly with weak wound electric currents. (**a**) Diabetic cornea wounds in three different mouse diabetes models showed significantly slower wound healing than control wounds. Wound areas were not significantly different at time zero ($p > 0.5$). Scale bar: 500 μm. (**b**) Healing rate of cornea wounds in control and diabetic mice. Age-matched control and low fat diet (LFD) wounds (solid lines) healed almost 100% in 48 h. All three diabetic models (dashed lines) healed significantly slower. Values are mean ± S.E.M. from 4 or more independent experiments, $^{*}p < 0.05$, $^{**}p < 0.01$, when compared with the control value, $^{\#\#}p < 0.01$, when compared with low fat diet (LFD) group, Student *t*-test. (**c**) Data from each eye were plotted as wound current *vs* wound healing and the Pearson correlation coefficient calculated. Significant correlation was seen between wound current and wound healing (in paired data) from db/db and high-fat diet (HFD) diabetic mice. Each set of data (HFD and db/db) were normalized so that their maximum wound current was 1 μA/cm^2, so they could be plotted on the same chart. Pearson correlation coefficient (R) and significance value (*p*) value are as shown. db/db, R = 0.990, $p = 0.010$; HFD, R = 0.987, $p = 0.013$.

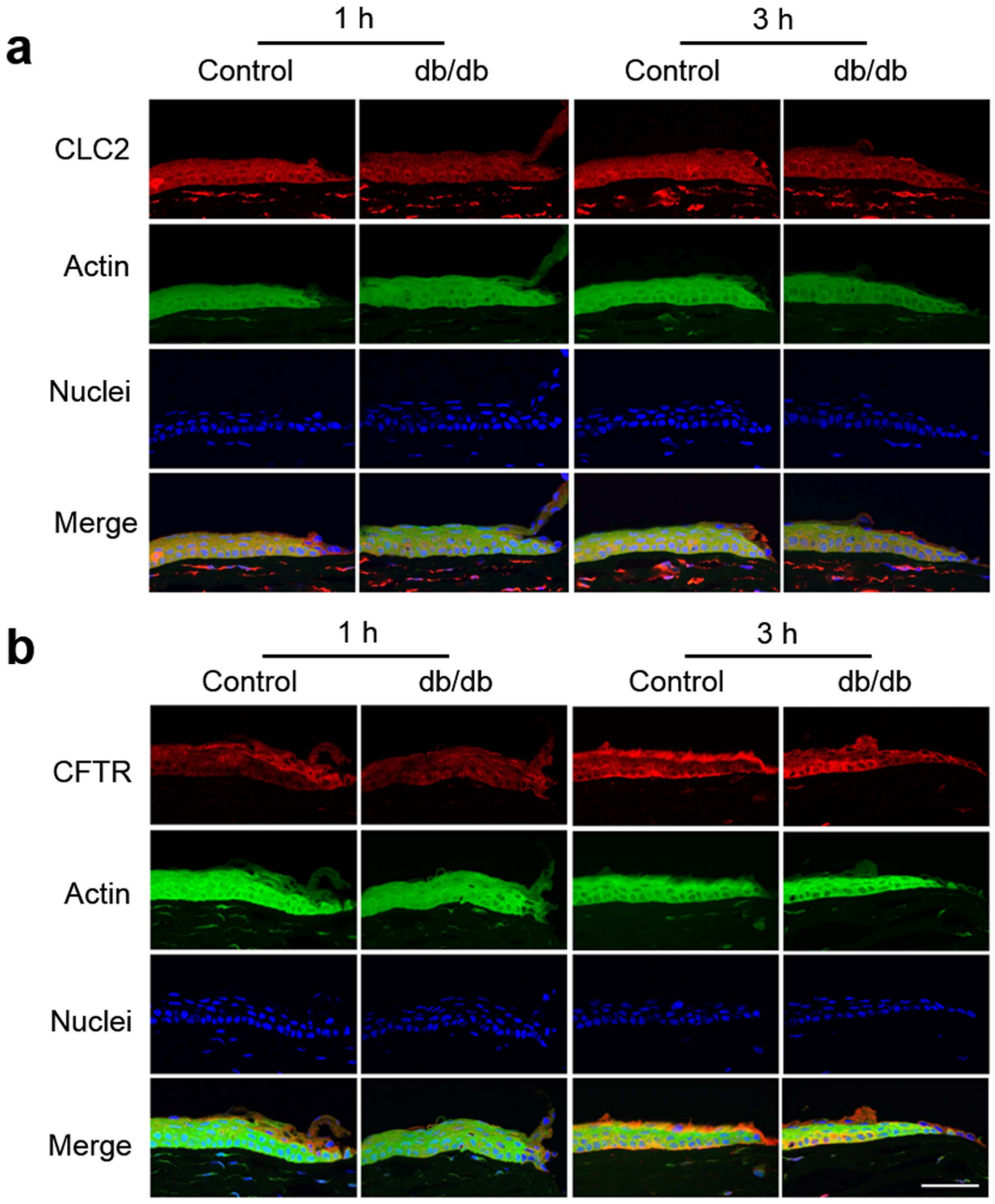

Figure 5. Decreased expression of ion channels CLC2 and CFTR in the diabetic corneal epithelium. Genetic knockout db/db mice showed less CLC2 (**a**) and CFTR (**b**) compared to the control group 1 h and 3 h after wounding. The central, brightly-labeled portion is the corneal epithelium, with the stroma below and tear film above. The epithelial wound edges are to the right in each picture. Scale bar: 50 μm.

proposed to be the major component of the wound electric currents in normal cornea wounds[28,29]. Both CLC2 and CFTR were expressed in the epithelial layers (Fig. 5). CLC2 showed weaker expression in the diabetic cornea wound than in the control cornea wound (Fig. 5a). Three hours after wounding, apical and basal expression of CFTR appeared to increase in the control cornea at the wound edge (Fig. 5b, 3 h post-wounding). These changes seemed to be weaker in the diabetic cornea at the same time. Therefore, fewer of these channels, and concomitantly less flux of Cl^- ions, can in part account for the decreased electric signal in diabetic corneas.

Human corneal epithelial cells in high glucose showed impaired electrotaxis. To determine whether high glucose impairs cell migration, we tested electrotaxis of CECs in EpiLife medium supplemented with 6 mM of D-glucose (total glucose (HG): 12 mM), and EpiLife medium supplemented with 6 mM mannitol to balance the osmolarity (mannitol control is 6 mM glucose plus 6 mM mannitol). In both conditions, cells responded to the applied EF of 100 mV/mm by migrating to the cathode (Fig. 6a,b). Compared to normal

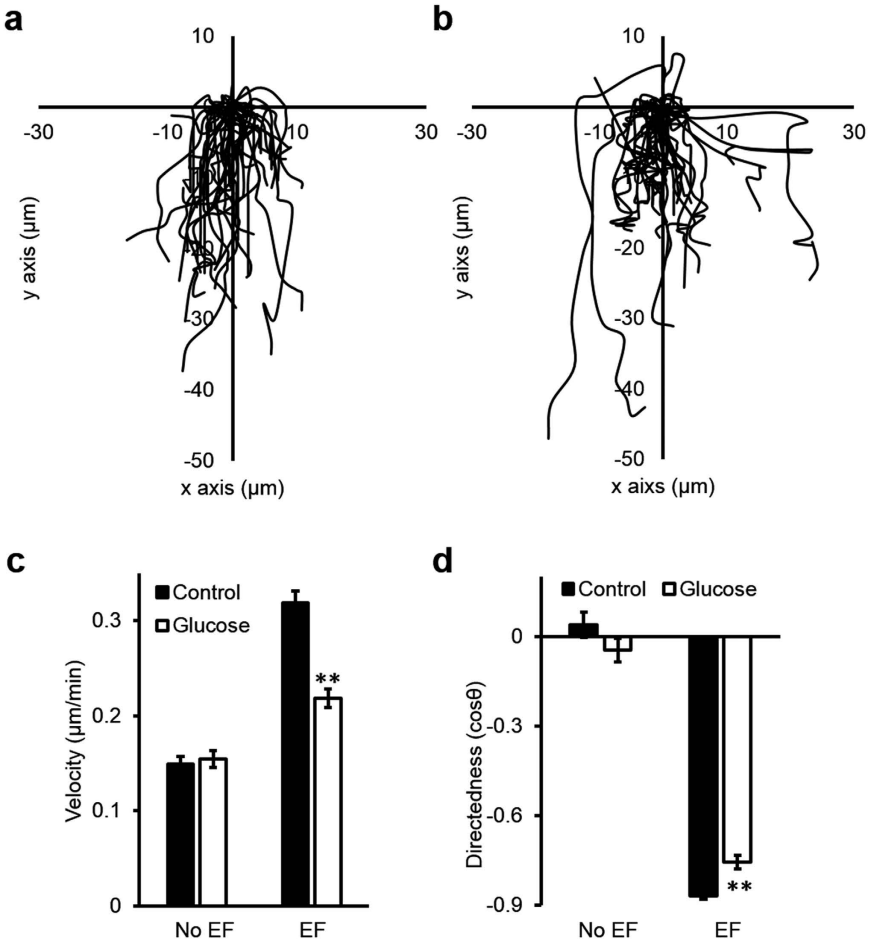

Figure 6. High glucose impaired electrotaxis of human corneal epithelial cells (hCECs). Cell tracks are shown with the position of each cell at the start of the experiment normalized to the origin. The cathode is at the bottom. (**a**) Trajectories of cells in mannitol control group (+6 mM mannitol). (**b**) Trajectories of cells in high glucose group (+6 mM D-glucose). (**c**) Velocity and (**d**) directedness of cells of control and high glucose groups respectively. Cells exposed to high glucose medium for 7 days showed significantly reduced speed and directedness. Data are mean ± S.E.M. from 6 independent experiments. $^{**}p < 0.01$, compared with control, Student *t*-test.

glucose, cells in high glucose migrated slower and with decreased directedness values (n = 6, $p < 0.01$; Fig. 6c,d; **Movie S1**).

Discussion

In this study, we sought to determine whether diabetic wounds generate weaker electric signals relative to normal wounds, and if this in turn correlates with impaired wound healing in diabetes. We hypothesized that cell migration can be deregulated by the abnormal electric signals, leading to impaired healing. In three independent diabetes mouse models, vibrating probe measurements demonstrated that electric signals were significantly impaired at diabetic cornea wounds. Time lapse measurements revealed that the electric currents at diabetic corneas lost the normal rising and plateau phases which are associated with active (translocator-mediated) transport and pumping of ions via the cornea trans epithelial electric potential (TEP). The decreased diabetic electric signals correlated significantly with impaired wound healing. Expression of Cl^- channels CLC2 and CFTR appeared to be lower in diabetic corneas. Short-term high glucose exposure reduced electrotaxis of CECs, but not the electric current at cornea wounds.

Injury induces diverse biochemical and mechanical cues to instigate healing responses[30,31]. EFs at wounds may provide a powerful injury signal to mobilize and guide cells to heal wounds. Electric currents are present at wounds immediately after wounding and persist for hours, days and even weeks[26,32–36]. The negative pole (cathode) is located at the wound center relative to the surrounding intact tissues[32,37]. When stimulated with EFs of the strength that are measured *in vivo*, cells in culture show remarkable enhanced and directional migration towards the cathode[19]. EFs have therefore been proposed as a signal playing an important role in wound healing[20,38]. Neuropathy, micro-circulatory changes, altered growth factors and abnormal cytokine production play important roles in impaired wound healing in diabetes[9,39–41]. With data from three independent diabetic models, we provide the first set of experimental evidence that cornea wounds from diabetic animals had significantly impaired

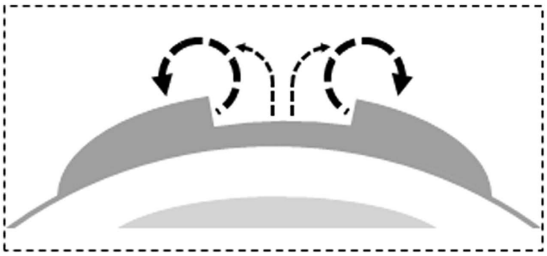

Figure 7. Schematic showing possible path of circulating ion currents at a cornea wound. We measured large outward currents at the wound edges, smaller outward currents at the wound center, and inward currents at the unwounded cornea outside the wound. The currents may therefore circulate out of the wound, flowing through the external solution, and in at the intact cornea, then flowing through the tissue to complete the circuit.

electric signals. Nuccitelli *et al.* found that wound EFs in older individuals were significantly smaller than those of younger adults[42].

Here, quantitative analyses revealed significant correlations between the electric signals and wound healing rate, suggesting that weaker electric currents may contribute to the impaired diabetic healing (Fig. 4c). The correlation between weaker electric signals and the slower rate of wound healing is consistent with previous results showing that pharmacological manipulation of ion pumping to increase or decrease the corneal TEP and wound electric signal increased or decreased, respectively, the wound healing rate[24]. Our results provide experimental evidence supporting the use of electrical stimulation in treatment of refractory chronic wounds[23,43]. Similar to the dynamic time courses of production of cytokines and growth factors following wounding[44], the electric signals following injury also have a dynamic time-course. In control mouse cornea wounds, we observed an initial leakage phase (L), a rising phase (R), and a plateau phase (P) (Fig. 2), as is also seen at cornea wounds in rats or human[25,26]. Cornea wounds from db/db, STZ- and HFD- induced diabetes all showed not only significantly smaller wound electric currents, but also lost the rising and plateau phases. We consider that the rising and plateau phases are likely due to an active response following injury. In some diabetic corneas, we even found inward currents. Similar results have been reported in *Pax6* (+/−) mice[45], where the presence of the electric signal rather than the direction of electric fields appeared to correlate with defective healing.

Acute exposure to high glucose for 3 hours did not alter the electric signal at the cornea wounds (Fig. S1), suggesting that short-term exposure to high glucose in our *ex vivo* model was different from the long-term diabetic condition in animal models. This is an important indicator that the defective electric signal at diabetic corneal wounds is not simply due to high glucose in the tear solution for a short period of time, and is likely due to one or more long-term and systemic effects. These may include altered transportation of ions in diabetic corneas, compromise in epithelial junctions, neuropathy, and abnormal metabolism in cells due to direct and/or indirect effects of long-term high glucose exposure. High glucose *in vitro* inhibited electrotaxis of CECs in a small applied EF (100 mV/mm), reducing both migration speed and directedness. Migration speed was down about 25%, but the directedness was reduced to a lesser extent (~10%) (Fig. 6). High glucose in diabetic tears thus may also compromise cell migration and contribute to impaired wound healing. The impaired wound healing (Fig. 4) therefore is likely due to a combination of defective electrotactic cell migration and impaired electric signaling. Their respective contributions warrant further investigation.

Our recent study suggested that the largest ion flux in cornea wounds is Cl^- flux and this ion flux plays a dominant role in generating the cornea wound current[46]. In order to elucidate the mechanisms of Cl^- transport, we studied CLC2 which is expressed abundantly and specifically in corneal epithelium[29], and CFTR which is an anion transporter involved in airway epithelial wound repair[47]. Lower expression of CFTR and CLC2 seen in the epithelia of diabetic cornea wounds may contribute to the weaker diabetic cornea wound current. This data is consistent with the role of CFTR in the initial stages of wound healing *in vitro*[47], and also suggests that Cl^- flux may regulate the impaired wound healing in diabetic patients. Based on the spatial profile of the wounded cornea (Fig. 1c), we postulate a possible simplified two-dimensional circuit of the electric current flow at the wound (Fig. 7). Thus, currents at the wound, especially at the wound edges but also inside the wound, flow outward and through the external solution. The 'circuit' is completed by inward current flow in the intact cornea around the wound.

In conclusion, cornea wounds in diabetes have abnormal electric signals which may contribute to impaired wound healing, possibly via cell electrotactic migration deregulation. Our data suggest a new player – electric signals – which are a potential therapeutic target in management of chronic and non-healing wounds. Management strategies targeting electric signals in combination with other well-established treatments may offer better outcomes for diabetic wounds.

Methods

Animals. This study was carried out in accordance with the National Institutes of Health Guide for the Care and Use of Laboratory Animals. All procedures were approved by the University of California, Davis, Institutional Animal Care and Use Committee (protocols 16766 and 17876).

Diabetic eyes. Eight week old male BKS.Cg-Dock7m +/+ Lepr db/J heterozygous (db/+), homozygous (db/db) mice and streptozotocin (STZ; 50 mg)-induced diabetic mice[48] and saline-injected control mice were

obtained from Jackson Laboratory. C57Bl/6J mice were placed on either a low fat (10% kcal; control) or high-fat (60% kcal) diet (Research Diets Inc., USA) at 5 weeks of age and were sustained for 24–26 weeks. The composition of these diets and the propensity of mice maintained on this high-fat diet to develop type 2 diabetes has been well described previously[49]. The blood glucose levels of the diabetic animals were measured before the ophthalmectomy using an Accu-Chek Aviva Plus blood glucose meter (Roche Diagnostics) (Table S1).

Experiments were performed on isolated whole eyes from male mice or male Sprague-Dawley rats. Animals were euthanized by inhalation of CO_2 and cervical dislocation. Eyes were removed using fine spring scissors (Fine Science Tools, USA) and placed in room temperature (RT) artificial tear solution (BSS+ intraocular irrigating solution; Alcon Laboratories, Inc., USA). Cornea wounds were made by scraping off approximately 1.5–2 mm^2 of epithelium with a 15° ophthalmologic scalpel (Beaver-Visitec, USA). Electric current density was measured with the vibrating probe (see next section *Vibrating probe*) starting at 5 min after wounding at the wound edge, as this is where the maximum wound electric currents are seen[24]. We also did time lapse measurements where we measured the wound edge current for several hours after wounding to establish a dynamic time-course of wound signal generation. To characterize the current density at different positions on the wounded cornea, we waited until 40 min after wounding, because the time lapse data showed that the electric signal reached maximum level 40–50 min after wounding (see Fig. 2a). For high glucose measurements, eyes were pre-incubated for 3 h in Medium 199 (M199) culture medium (Life Technologies, USA) supplemented with 24.4 mM glucose to give a final glucose concentration of 30 mM. Control eyes were pre-incubated in normal M199 (5.6 mM glucose) supplemented with 24.4 mM mannitol, to compensate for osmolality.

Vibrating probe. The vibrating probe technique for non-invasive measurement of endogenous electric current densities has been previously described in detail[26]. Briefly, the probe is an insulated stainless-steel microelectrode (World Precision Instruments, USA) with a platinum ball electroplated to the tip. The probe, mounted on a 3-dimensional micromanipulator (Line Tool Co., USA), is vibrated at high frequency (~200 Hz) in solution approximately 1 tip ball distance from the cornea surface by a piezoelectric bender. If an electric current is present due to ion flux, the charge on the platinum ball fluctuates in proportion to the size of the current. The probe is connected to a lock-in amplifier (SR530; Stanford Research Systems, USA) that locks on to the probe's specific frequency. The probe is calibrated with a current density of 1.5 $\mu A/cm^2$ at the start and end of experiments. The probe is vibrated in solution far from the cornea (>1 cm), where there is no electric current, to establish a baseline. The probe is then moved into measuring position close to the cornea (either intact unwounded cornea or wound center / wound edge; see Fig. 1a).

Wound healing. Wounds were made as in the previous section *Diabetic eyes*. Each eye was placed with the wound facing up in a 35 mm plastic dish containing an 800 μm nylon mesh (nitex mesh). Fluorescein dye was applied to the wound by placing one drop of artificial tear solution onto a Ful-Glo fluorescein sodium ophthalmic strip (Akron, Inc., USA) and then placing the drop onto the eye. Images were taken at 30× magnification using a Zeiss Lumar V12 microscope with Axiocam MRm camera and an EXFO X-cite 120 fluorescent illumination system. Eyes were incubated at 37 °C, 5% CO_2 in 6-well tissue culture plates with 6 ml of culture medium M199 (supplemented with 100 units of penicillin/streptomycin) in each well. Photographs were taken in fresh wounds and at 24, 30 and 48 h. Wound healing was assessed by measuring wound areas using Image J (imagej.nih.gov/ij/). Wound areas were normalized against the original fresh wound area and presented as percentage (%) of wound healing using the formula: ((original wound area − new wound area) ÷ (original wound area)) × 100.

For correlation of wound electric signal and wound healing, individual eyes (n = 4 for db/db and high-fat diet) were wounded and the wound edge electric current measured (for each eye, average of left and right wound edge currents). Then in the same eyes, wound healing was assessed. Data from each eye was plotted as normalized wound current *vs* wound healing (see Fig. 4c) and the Pearson correlation coefficient calculated (see section *Statistics* below). Each set of data (HFD and db/db) were normalized so that their maximum wound current was 1 $\mu A/cm^2$, so they could be plotted on the same chart.

Cells. Human telomerase-immortalized CECs were a gift from the Christopher J. Murphy/Paul Russel laboratory, Departments of Ophthalmology and Surgical and Radiological Sciences, UC Davis. Cells were cultured in EpiLife medium (Life Technologies, USA) containing 6 mM D-glucose as normal control supplemented with EpiLife defined growth supplement (EDGS) and 1% penicillin/streptomycin (Life Technologies, USA). For high glucose experiments the medium was supplemented with additional 6 mM D-glucose (high glucose) or 6 mM D-mannitol (normal glucose balanced for osmolality) (Sigma-Aldrich, USA) for seven days.

Electrotaxis. Methods to study the migration of cells in applied EFs have been described in detail previously[50]. Briefly, a 22 × 10 mm electrotaxis chamber was coated with fibronectin-collagen mix (Athena Environmental Sciences, Inc., USA) for 5 min. Cells were seeded into the chamber for 30 min before the electrotaxis study began. An EF of 100 mV/mm was applied for 1 h via silver/sliver chloride electrodes and agar bridges to prevent artefacts. Cell migration was recorded by time lapse phase contrast on an inverted microscope using Metamorph software. Cell directedness and speed were analyzed by Image J. Cosine θ, defining cell directedness, is the average angle between the EF vector and a straight line connecting the start and end positions of all the cells which migrated in the EF. A cos θ value between −1 and 0 represents migration towards the cathode and 0 to +1 towards anode. Average cos θ of near 0 indicates random cell migration with no directionality. Velocity is accumulated distance migrated divided by time.

Immunofluorescence. Control and db/db mouse corneas with wounds were fixed in 4% paraformaldehyde for 2 h and then immersed in 10% and 30% sucrose solution, successively, for dehydration. Cryosections (8 μm thick) were fixed in cold acetone and permeabilized in 0.2% Triton X-100. After blocking with buffer containing 5%

donkey serum (Sigma, USA) with 1% BSA in 0.1% Triton X-100 PBS for 1 h, sections were incubated overnight with primary antibodies against chloride channel 2 (CLC2) (1:100; Santa Cruz Biotechnology, USA) or cystic fibrosis transmembrane conductance regulator (CFTR) (1:100; Santa Cruz Biotechnology, USA) at 4 °C. Sections were then incubated with Alexa Fluor 594 conjugated donkey anti-rabbit IgG (H+L) secondary antibody (1:200; Life Technologies, USA). Negative controls included no primary antibody or isotype-specific control antibodies along with secondary antibodies. Nuclei and cytoskeleton were labeled with DAPI (Life Technologies, USA) and fluorescein isothiocyanate conjugated phalloidin (Sigma, USA), respectively. Images were obtained using an Olympus FV1000 confocal microscope with a 40x oil objective from comparative experiments.

Statistics. Data analyses, graphs, and statistical calculations were made using Excel (Microsoft) and SPSS V16.0 (SPSS Inc.). Data are expressed as mean ± standard error of the mean (S.E.M.) or mean ± standard deviation (S.D.). Differences between mean values were compared using Student *t*-test. Differences were considered statistically significant if p-value < 0.05. The correlation study was performed by Pearson correlation test. A Pearson correlation coefficient (R) close to one shows a good correlation. The p value gives the significance of the correlation, $p < 0.05$ showing a significant correlation.

References

1. WHO. *Global status report on noncommunicable diseases 2014*. (2014) Available at: http://www.who.int/nmh/publications/ncd-status-report-2014/en/. (Accessed: 12th April 2016).
2. Ramsey, S. D. *et al.* Incidence, outcomes, and cost of foot ulcers in patients with diabetes. *Diabetes Care*. **22,** 382–387 (1999).
3. Singer, A. J. & Clark, R. A. Cutaneous wound healing. *N Engl J Med*. **341,** 738–746 (1999).
4. Fonder, M. A. *et al.* Treating the chronic wound: A practical approach to the care of nonhealing wounds and wound care dressings. *J Am Acad Dermatol*. **58,** 185–206 (2008).
5. Lutty, G. A. Effects of diabetes on the eye. *Invest Ophthalmol Vis Sci*. **54,** ORSF81-87 (2013).
6. Wang, F., Gao, N., Yin, J. & Yu, F. S. Reduced innervation and delayed re-innervation after epithelial wounding in type 2 diabetic Goto-Kakizaki rats. *Am J Pathol*. **181,** 2058–2066 (2012).
7. Ewald, M. & Hammersmith, K. M. Review of diagnosis and management of recurrent erosion syndrome. *Curr Opin Ophthalmol*. **20,** 287–291 (2009).
8. Rafehi, H., El-Osta, A. & Karagiannis, T. C. Genetic and epigenetic events in diabetic wound healing. *Int Wound J*. **8,** 12–21 (2011).
9. Blakytny, R. & Jude, E. The molecular biology of chronic wounds and delayed healing in diabetes. *Diabet Med*. **23,** 594–608 (2006).
10. Du Bois-Reymond, E. *Untersuchungen uber thierische Elektricitat, Zweiter Band, Zweite Abtheilung (Erste Lieferung)*. (Georg Reimer, 1860).
11. Klyce, S. D. Electrical profiles in the corneal epithelium. *J Physiol*. **226,** 407–429 (1972).
12. Song, B., Zhao, M., Forrester, J. V. & McCaig, C. D. Electrical cues regulate the orientation and frequency of cell division and the rate of wound healing *in vivo*. *Proc Natl Acad Sci USA* **99,** 13577–13582 (2002).
13. Chiang, M., Robinson, K. R. & Vanable, J. W. Jr. Electrical fields in the vicinity of epithelial wounds in the isolated bovine eye. *Exp Eye Res*. **54,** 999–1003 (1992).
14. Nuccitelli, R. A role for endogenous electric fields in wound healing. *Curr Top Dev Biol*. **58,** 1–26 (2003).
15. Sta Iglesia, D. D. & Vanable, J. W. Jr. Endogenous lateral electric fields around bovine corneal lesions are necessary for and can enhance normal rates of wound healing. *Wound Repair Regen*. **6,** 531–542 (1998).
16. Levin, M. H. & Verkman, A. S. Aquaporins and CFTR in ocular epithelial fluid transport. *J Membr Biol*. **210,** 105–115 (2006).
17. Chi, C. & Trinkaus-Randall, V. New insights in wound response and repair of epithelium. *J Cell Physiol*. **228,** 925–929 (2013).
18. Zhao, M., Agius-Fernandez, A., Forrester, J. V. & McCaig, C. D. Orientation and directed migration of cultured corneal epithelial cells in small electric fields are serum dependent. *J Cell Sci*. **109** (Pt 6), 1405–1414 (1996).
19. Nishimura, K. Y., Isseroff, R. R. & Nuccitelli, R. Human keratinocytes migrate to the negative pole in direct current electric fields comparable to those measured in mammalian wounds. *J Cell Sci*. **109** (Pt 1), 199–207 (1996).
20. Zhao, M. *et al.* Electrical signals control wound healing through phosphatidylinositol-3-OH kinase-gamma and PTEN. *Nature*. **442,** 457–460 (2006).
21. Aaron, R. K., Ciombor, D. M. & Simon, B. J. Treatment of nonunions with electric and electromagnetic fields. *Clin Orthop Relat Res*. **419,** 21–29 (2004).
22. Junger, M. *et al.* Local therapy and treatment costs of chronic, venous leg ulcers with electrical stimulation (Dermapulse): a prospective, placebo controlled, double blind trial. *Wound Repair Regen*. **16,** 480–487 (2008).
23. Herberger, K. *et al.* Effectiveness, Tolerability, and Safety of Electrical Stimulation of Wounds With an Electrical Stimulation Device: Results of a Retrospective Register Study. *Wounds-a Compendium of Clinical Research and Practice*. **24,** 76–84 (2012).
24. Reid, B., Song, B., McCaig, C. D. & Zhao, M. Wound healing in rat cornea: the role of electric currents. *FASEB J*. **19,** 379–386 (2005).
25. Reid, B., Graue-Hernandez, E. O., Mannis, M. J. & Zhao, M. Modulating endogenous electric currents in human corneal wounds–a novel approach of bioelectric stimulation without electrodes. *Cornea*. **30,** 338–343 (2011).
26. Reid, B., Nuccitelli, R. & Zhao, M. Non-invasive measurement of bioelectric currents with a vibrating probe. *Nat Protoc*. **2,** 661–669 (2007).
27. Sen, D. K. & Sarin, G. S. Tear glucose levels in normal people and in diabetic patients. *Br J Ophthalmol*. **64,** 693–695 (1980).
28. Vieira, A. C. *et al.* Ionic components of electric current at rat corneal wounds. *PloS one*. **6,** e17411 (2011).
29. Cao, L. *et al.* Chloride channels and transporters in human corneal epithelium. *Exp Eye Res*. **90,** 771–779 (2010).
30. Fu, X. & Li, H. Mesenchymal stem cells and skin wound repair and regeneration: possibilities and questions. *Cell Tissue Res*. **335,** 317–321 (2009).
31. Gurtner, G. C., Werner, S., Barrandon, Y. & Longaker, M. T. Wound repair and regeneration. *Nature*. **453,** 314–321 (2008).
32. Mukerjee, E. V. *et al.* Microneedle array for measuring wound generated electric fields. *Conf Proc IEEE Eng Med Biol Soc*. **1,** 4326–4328 (2006).
33. Sta Iglesia, D. D., Cragoe, E. J. Jr. & Vanable, J. W. Jr. Electric field strength and epithelization in the newt (Notophthalmus viridescens). *J Exp Zool*. **274,** 56–62 (1996).
34. Vanable, J. W. Jr. *Intregumentary potentials and wound healing*. (Alan R. Liss, 1989).
35. Foulds, I. S. & Barker, A. T. Human skin battery potentials and their possible role in wound healing. *Br J Dermatol*. **109,** 515–522 (1983).
36. Illingworth, C. M. & Barker, A. T. Measurement of electrical currents emerging during the regeneration of amputated finger tips in children. *Clinical Physics and Physiological Measurement*. **1,** 87 (1980).
37. Barker, A. T., Jaffe, L. F. & Vanable, J. W. Jr. The glabrous epidermis of cavies contains a powerful battery. *Am J Physiol*. **242,** R358–366 (1982).
38. Reid, B., Song, B. & Zhao, M. Electric currents in Xenopus tadpole tail regeneration. *Dev Biol*. **335,** 198–207 (2009).

39. Barsun, A., Sen, S., Palmieri, T. L. & Greenhalgh, D. G. A ten-year review of lower extremity burns in diabetics: small burns that lead to major problems. *J Burn Care Res*. **34,** 255–260 (2013).
40. Falanga, V. Wound healing and its impairment in the diabetic foot. *Lancet*. **366,** 1736–1743 (2005).
41. Bettahi, I. *et al.* Genome-wide transcriptional analysis of differentially expressed genes in diabetic, healing corneal epithelial cells: hyperglycemia-suppressed TGFbeta3 expression contributes to the delay of epithelial wound healing in diabetic corneas. *Diabetes*. **63,** 715–727 (2014).
42. Nuccitelli, R. *et al.* The electric field near human skin wounds declines with age and provides a non-invasive indicator of wound healing. *Wound repair and regeneration : official publication of the Wound Healing Society [and] the European Tissue Repair Society*. **19,** 645–655 (2011).
43. Schaum, K. D. Decision on national coverage of electromagnetic therapy for wounds. *Adv Skin Wound Care*. **17,** 316–317 (2004).
44. Barrientos, S. *et al.* Growth factors and cytokines in wound healing. *Wound Repair Regen*. **16,** 585–601 (2008).
45. Kucerova, R. *et al.* The role of electrical signals in murine corneal wound re-epithelialization. *J Cell Physiol*. **226,** 1544–1553 (2011).
46. Reid, B. *et al.* Specific ion fluxes generate cornea wound electric currents. *Commun Integr Biol*. **4,** 462–465 (2011).
47. Schiller, K. R., Maniak, P. J. & Grady, S. M. Cystic fibrosis transmembrane conductance regulator is involved in airway epithelial wound repair. *American Journal of Physiology - Cell Physiology*. **299,** C912–C921 (2010).
48. Wang, Z. & Gleichmann, H. GLUT2 in pancreatic islets: crucial target molecule in diabetes induced with multiple low doses of streptozotocin in mice. *Diabetes*. **47,** 50–56 (1998).
49. Winzell, M. S. & Ahren, B. The high-fat diet-fed mouse: a model for studying mechanisms and treatment of impaired glucose tolerance and type 2 diabetes. *Diabetes*. **53** Suppl 3, S215–219 (2004).
50. Tai, G., Reid, B., Cao, L. & Zhao, M. Electrotaxis and wound healing: experimental methods to study electric fields as a directional signal for cell migration. *Methods Mol Biol*. **571,** 77–97 (2009).

Acknowledgements

This work was supported by NIH EY019101 to M.Z. This study was supported in part by an Unrestricted Grant from Research to Prevent Blindness, Inc., and an NEI core grant. Y.S. is supported by a fellowship from the China Scholarship Council. F.F. is supported by Fundação para a Ciência e Tecnologia (FCT) grant SFRH/BD/87256/2012. M.F.N. is supported by NIH HL098200 and HL121059. We thank Dr. James Jester (UC Irvine) for the generous gift of hTCEpi cells. We are grateful to Bradley Shibata and Dr. Paul Fitzgerald, Dept. of Cell Biology and Human Anatomy, UC Davis, for help with cornea histology (NEI Core facilities Grant P30 EY012576, PI, John S Werner), and Madeline Nieves, Dept. of Pharmacology, UC Davis, for technical support. We also thank Dr. Vijay Raghunathan (Surgical and Radiological Sciences, UC Davis) for help with cell culture and imaging. We are also grateful to Dr. Rivkah Isseroff and Michelle So (Dermatology, UC Davis) for helpful discussions and initial tissue samples.

Author Contributions

Y.S., T.P., B.R. and F.F. performed the experiments and acquired the data, M.F.N. provided LFD and HFD fed mice and contributed to the revision of the manuscript, Q.Z. provided some financial support and participated in analysis and interpretation of data. J.L. contributed to the revision of the manuscript and analysis of data. M.Z., B.R. and Y.S. conceived and designed the study. Y.S., B.R. and M.Z. wrote the manuscript.

Additional Information

Supplementary information accompanies this paper at http://www.nature.com/srep

Competing financial interests: The authors declare no competing financial interests.

How to cite this article: Shen, Y. *et al.* Diabetic cornea wounds produce significantly weaker electric signals that may contribute to impaired healing. *Sci. Rep.* **6**, 26525; doi: 10.1038/srep26525 (2016).

III. *INFECTION-GENERATED ELECTRIC FIELD IN GUT EPITHELIUM DRIVES BIDIRECTIONAL MIGRATION OF MACROPHAGES*

Publication overview

This study aimed to find whether bioelectric activities underlie the bidirectional migration of macrophages during infection of mouse cecum. Upon *Salmonella* or other bacterial pathogen infection, macrophages shuttle into (immigrate) the gut Peyer's patches to neutralize the attack; however, some pathogens manage to evade death and egress (emigrate) entry site inside macrophages, leading to widespread infection. This study revealed that *Salmonella* infection induced electric fields (coined infection-generated electric fields, IGEF) in gut epithelium *in vivo* and reversed the macrophage electrotactic migration under IGEF-mimicking EF *in vitro*. Further work showed that the cell surface electric properties are altered by infection, leading to the switch of the migration direction of macrophages under electric fields. The findings unveil a mechanism of action for the previously elusive bacterial dissemination. This study has, therefore, important clinical relevance, suggesting a targetable mechanism to hinder systemic infections of life-threatening consequences.

Publication contributions

From publication's equivalent section: "**Conceptualization:** Yaohui Sun, Alex Mogilner, Min Zhao. **Data curation:** Yaohui Sun, Fernando Ferreira, Guillaume Luxardi, Emanual Maverakis. **Formal analysis:** Yaohui Sun, Brian Reid, Fernando Ferreira, Guillaume Luxardi, Kan Zhu, Gege Xu, Yuxin Sun. **Funding acquisition:** Emanual Maverakis, Alex Mogilner, Min Zhao. **Investigation:** Yaohui Sun, Brian Reid, Fernando Ferreira, Guillaume Luxardi, Li Ma, Kristen L. Lokken, Kan Zhu, Gege Xu, Yuxin Sun, Volodymyr Ryzhuk, Min Zhao. **Methodology:** Yaohui Sun, Brian Reid, Carlito B. Lebrilla, Emanual Maverakis, Min Zhao. **Project administration:** Yaohui Sun, Alex Mogilner, Min Zhao. **Resources:** Kristen L. Lokken, Carlito B. Lebrilla, Emanual Maverakis, Alex Mogilner, Min Zhao. **Supervision:** Carlito B. Lebrilla, Emanual Maverakis, Alex Mogilner, Min Zhao. **Validation:** Yaohui Sun, Emanual Maverakis, Alex Mogilner, Min Zhao. **Visualization:** Yaohui Sun, Brian Reid, Fernando Ferreira. **Writing – original draft:** Yaohui Sun. **Writing – review & editing:** Brian Reid, Fernando Ferreira, Betty P. Guo, Emanual Maverakis, Alex Mogilner, Min Zhao."

More specifically, F.F. contributed to the designing of the TEP experiments, performed most of the TEP measurements, and treated the TEP raw data (Fig. 1A,C, S1 Fig. and S2 Fig.). Also, I contributed to the designing and discussion of bioelectric profiling experiments (Fig. 1 and 6, S1-S3 Fig.). I stringently revised and edited the manuscript, and helped in addressing the peer review comments.

Publication reprint

Vide infra.

PLOS BIOLOGY

RESEARCH ARTICLE

Infection-generated electric field in gut epithelium drives bidirectional migration of macrophages

Yaohui Sun[1,2]*, Brian Reid[1], Fernando Ferreira[1,3], Guillaume Luxardi[1], Li Ma[1,4], Kristen L. Lokken[5], Kan Zhu[1], Gege Xu[6], Yuxin Sun[1¤], Volodymyr Ryzhuk[1], Betty P. Guo[7], Carlito B. Lebrilla[6], Emanual Maverakis[1], Alex Mogilner[2]*, Min Zhao[1]*

1 Department of Dermatology, School of Medicine, University of California, Davis, Sacramento, California, United States of America, **2** Courant Institute and Department of Biology, New York University, New York, New York, United States of America, **3** Departamento de Biologia, Centro de Biologia Molecular e Ambiental (CBMA), Universidade do Minho, Braga, Portugal, **4** Skin and Cosmetic Research Department, Shanghai Skin Disease Hospital, Shanghai, China, **5** Department of Microbiology and Immunology, School of Medicine, University of California, Davis, Davis, California, United States of America, **6** Department of Chemistry, University of California, Davis, Davis, California, United States of America, **7** Office of Research, School of Medicine, University of California, Davis, Davis, California, United States of America

¤ Current address: Department of Radiology and Biomedical Imaging, University of California, San Francisco, San Francisco, California, United States of America
* yhsun@ucdavis.edu (YS); mogilner@cims.nyu.edu (AM); minzhao@ucdavis.edu (MZ)

Citation: Sun Y, Reid B, Ferreira F, Luxardi G, Ma L, Lokken KL, et al. (2019) Infection-generated electric field in gut epithelium drives bidirectional migration of macrophages. PLoS Biol 17(4): e3000044. https://doi.org/10.1371/journal.pbio.3000044

Academic Editor: David S. Schneider, Stanford University, UNITED STATES

Received: September 2, 2018

Accepted: March 5, 2019

Published: April 9, 2019

Data Availability Statement: All raw data used to produce the main figures and the supplementary figures are included in spreadsheets as supplementary materials. Matlab codes generated in this work are available on request.

Funding: This work was supported by US Army Research Office grant W911NF-17-1-0417 to A. M., by AFOSR FA9550-16-1-0052 to M.Z. (Program PI: Wolfgang Losert), by inter-department seed grant S-MPIDRGR from UC Davis School of Medicine to M. Z., Y. S. and R.M.Tsolis.

Abstract

Many bacterial pathogens hijack macrophages to egress from the port of entry to the lymphatic drainage and/or bloodstream, causing dissemination of life-threatening infections. However, the underlying mechanisms are not well understood. Here, we report that *Salmonella* infection generates directional electric fields (EFs) in the follicle-associated epithelium of mouse cecum. In vitro application of an EF, mimicking the infection-generated electric field (IGEF), induces directional migration of primary mouse macrophages to the anode, which is reversed to the cathode upon *Salmonella* infection. This infection-dependent directional switch is independent of the *Salmonella* pathogenicity island 1 (SPI-1) type III secretion system. The switch is accompanied by a reduction of sialic acids on glycosylated surface components during phagocytosis of bacteria, which is absent in macrophages challenged by microspheres. Moreover, enzymatic cleavage of terminally exposed sialic acids reduces macrophage surface negativity and severely impairs directional migration of macrophages in response to an EF. Based on these findings, we propose that macrophages are attracted to the site of infection by a combination of chemotaxis and galvanotaxis; after phagocytosis of bacteria, surface electrical properties of the macrophage change, and galvanotaxis directs the cells away from the site of infection.

Author summary

Bacterial pathogens can invade and survive within macrophages and use them as a vehicle to reach important organs of a human body, resulting in life-threatening infections, but

F. F. was supported by Fundaça~o para a Ciência e a Tecnologia. (SFRH/BD/87256/2012). E.M. was supported by an early career award from the Burroughs Wellcome Fund and by NIH 1DP2OD008752. The funders had no role in study design, data collection and analysis, decision to publish, or preparation of the manuscript.

Competing interests: The authors have declared that no competing interests exist.

Abbreviations: BMDM, bone marrow-derived macrophage; CFU, colony-forming unit; Con A, concanavalin A; EF, electric field; FAE, follicle-associated epithelium; FMO, Fluorescence Minus One; GFP, a green fluorescent protein; GNL, Galanthus Nivalis lectin; IGEF, infection-generated electric field; J_I, electric current density; LB, Luria-Bertani; MAL-2, Maackia Amurensis lectin II; MLN, mesenteric lymph node; MOI, multiplicity of infection; nMFI, normalized mean fluorescence intensity; PBS, phosphate-buffered saline; PDMS, polydimethylsiloxane; PI, post infection; PM, peritoneal macrophage; SE, standard error; *S.* Typhimurium, *Salmonella enterica* serotype Typhimurium; SPI-1, *Salmonella* pathogenicity island 1; TEP, transepithelial potential; TLR, Toll-like receptor; WGEF, wound-generated electric field; WT, wild type; cosθ, cosine theta.

the underlying mechanisms are not well understood. Our current understanding is that macrophages are recruited to the infected site by sensing gradients of chemokines and/or cytokines released by damaged cells—a process known as chemotaxis. However, this mechanism does not explain how macrophages containing the pathogens escape the site to reach the bloodstream. Here, we use a disseminated *Salmonella* infection model in mice and detect electric fields (EFs) generated by *Salmonella* infection at the gut epithelium, which can drive unidirectional migration of macrophages towards the anode—a biological process also known as galvanotaxis. We further demonstrate that macrophage galvanotaxis can be reversed to the cathode by phagocytosis of the bacteria. Based on these findings, we propose that macrophages are attracted to the site of infection by a combination of chemotaxis and galvanotaxis; after phagocytosis of bacteria, the electrical properties of the macrophage change, and galvanotaxis directs the cells away from the site of infection allowing the escape of the macrophages that contain pathogens.

Introduction

Common bacterial pathogens such as *Salmonella*, *Shigella*, and *Yersinia* spp. invade the gut epithelial barrier, preferentially by targeting the relatively small number of M cells located in the follicle-associated epithelium (FAE) [1–3]. Disruption of epithelial integrity releases chemokines that attract immune cells such as neutrophils and macrophages—a process known as chemotaxis [4–7]. Subsequent phagocytosis and clearance of these pathogens by immune cells usually stops the infection. However, some of these bacterial pathogens have developed strategies, such as the type III secretion systems in *Salmonella* spp. [8–12], to evade macrophage killing and survive inside the macrophage [13–16], an environment in which the pathogen is hidden from the immune system. Survival within the macrophage allows the pathogen to spread from its entry site to the spleen, liver, bone marrow, and other organs via the bloodstream, resulting in life-threatening consequences [17–19]. Although chemotaxis can explain how macrophages reach an infected site, it cannot explain how macrophages harboring pathogens escape from the bacterial entry site to reach the lymphatic drainage and/or bloodstream, a critical initial step in the dissemination process that is understudied and poorly understood.

Bioelectric signals have been implicated in development [20–23], wound healing [24–26], and regeneration [27,28]. For example, a wound collapses the transepithelial potential (TEP) difference of an intact epithelial barrier, generating laterally oriented endogenous electric fields (EFs) of up to 1.4 V cm^{-1}, as well as local electric current densities (J_I) of several μA cm^{-2}. These bioelectric phenomena actively control wound healing in the skin and cornea [25,29]; however, they are extremely challenging to study in the gut epithelium due to limited accessibility and have never been characterized in vivo during an active infection. Nonetheless, it is generally appreciated that an EF on this scale can drive directional cell migration—a process known as electrotaxis or galvanotaxis [21]. Many cell types, regardless of their origin, respond to an exogenous EF by directional migration toward the cathode [25,30], whereas others, e.g., human keratinocytes (HaCat cells) and bone marrow mesenchymal stem cells, migrate toward the anode [31]. Macrophages and lymphocytes also undergo galvanotaxis in vitro and in vivo [32–34].

In the present study, we have developed an ex vivo mouse cecum model of *Salmonella* infection that enables bioelectricity measurement. We report that *Salmonella* infection generates a directional EF at the bacterial entry sites that can recruit macrophages by galvanotaxis. We demonstrate that primary macrophages reverse galvanotaxis direction upon *Salmonella*

infection by modifying their surface glycan composition, which reduces the negative electric charge on the surface. This directional switch is independent of the *Salmonella* pathogenicity island 1 (SPI-1) type III secretion system, a major virulence determinant responsible for *Salmonella* invasion. Instead, it may require certain glycosidases that are widely conserved in *Salmonella* spp., because cleavage of surface-exposed sialic acids with a potent neuraminidase caused severe defects of macrophage galvanotaxis.

Results and discussion

Development of an ex vivo mouse cecum model of *Salmonella* infection for bioelectric characterization

The mouse is an ideal organism for understanding human infectious diseases and is widely used to study bacterial pathogenesis and mucosal immunity of enteropathogenic bacteria [35–40]. Previously, we have successfully measured bioelectric currents in various tissue and organ cultures using the noninvasive vibrating probe [41–44]; however, measuring bioelectric currents in the mouse small intestinal epithelium is challenging due to limited accessibility [45]. Therefore, we developed a new ex vivo cecum model for measuring bioelectric activity in the gut epithelium (S1 Fig). This model is based on the well-established mouse typhoid model, in which mice orally infected with *Salmonella enterica* serotype Typhimurium (*S*. Typhimurium) develop disseminated infection that mimics human typhoid disease [36]. Although the ileum is the most commonly targeted organ to study pathogen–host interactions in vivo, it is too small for the bioelectrical measurements in our ex vivo experimental setting. Instead, the size of the mouse cecum is anatomically optimal. *Salmonella* invades the cecum in mice and causes acute appendicitis in humans [46]. Furthermore, we can easily identify the FAE under a dissecting microscope, because we found that 90% of C57BL/6 mice have only 1 Peyer's patch around the blind-end apex, containing 6 to 11 lymphatic follicles.

Active bioelectricity pervades the FAE in the healthy murine cecum

Using microelectrodes [28] in the ex vivo mouse cecum model, we measured a TEP of up to 15 mV, lumen-positive in uninfected mice. Notably, the TEP in the FAE was significantly smaller than that of the surrounding villi (Fig 1A). Next, using a vibrating probe to measure the J_I close to the gut surface, we detected outward currents at the FAE and inward currents at the villus epithelium, with a magnitude of around 1 μA cm^{-2} (Fig 1B). Such currents were not detected in the serosal epithelium, despite the presence of a TEP (Fig 1A), nor in formalin-fixed epithelia (Fig 1B), suggesting the existence of active bioelectricity restricted to the mucosal epithelium.

It has been well appreciated that mammalian intestinal mucosa maintains a large transmucosal potential difference [47,48]. In humans, that potential is up to 12 mV, lumen-negative, in the fasting jejunum and ileum [49,50]. Rats, mice, chickens, and fish all maintain a TEP of up to 5 mV in their intestinal epithelium, as measured with Ussing chambers [51–55]; however, these measurements provide no spatiotemporal information [45]. The TEP of control murine ceca (up to 15 mV) that we have measured directly with glass electrodes under microscopic resolution were well within the physiological range described above; however, it differed spatially, i.e., the TEP of the FAE was significantly lower than the TEP of the surrounding villus epithelium (Fig 1A). Using an ultrasensitive vibrating probe, we further detected ionic currents that run in opposite directions between the FAE and surrounding villi (Fig 1B). Together, these findings unveil lateral voltage gradients and/or constant current loops running between these two structurally and functionally distinct epithelia. In the normal gut scenario, such a

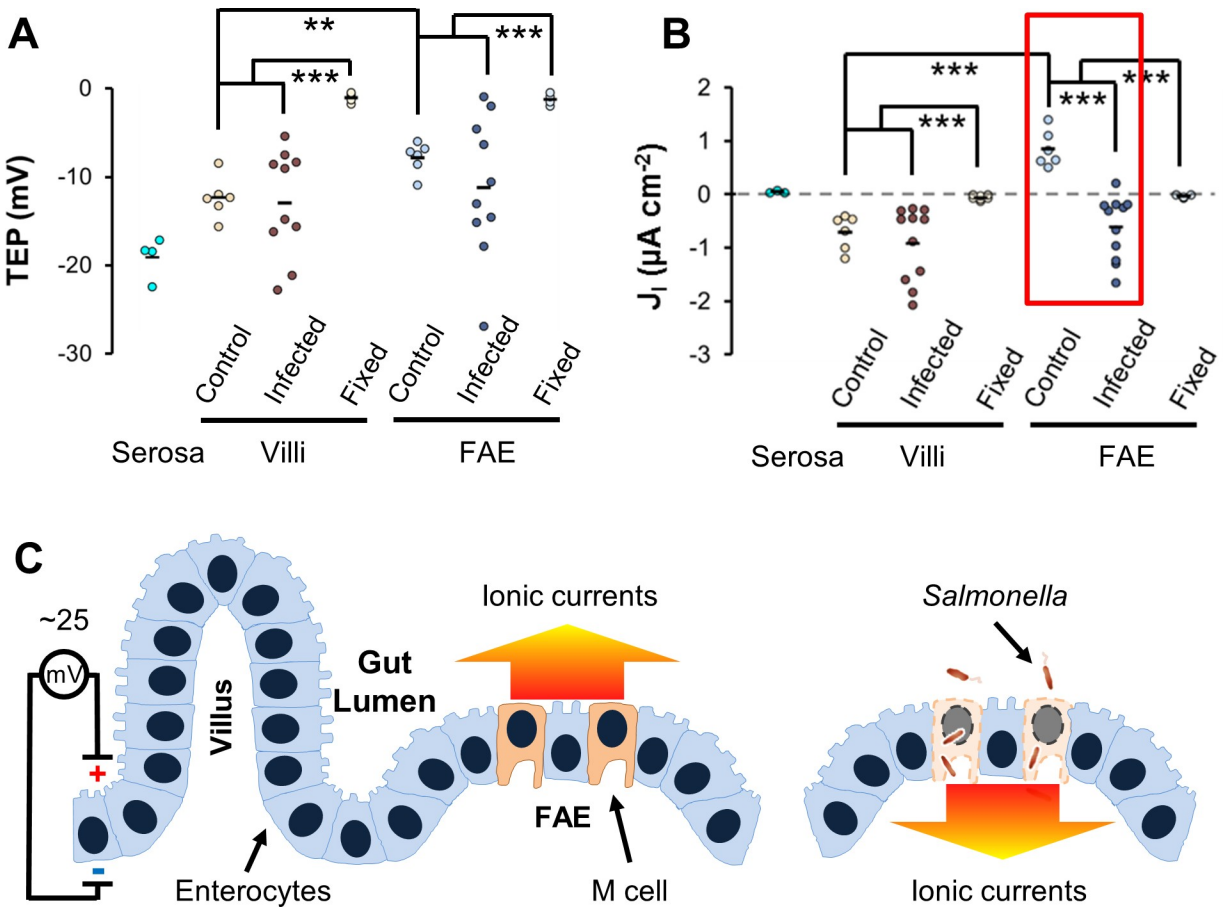

Fig 1. IGEF at gut epithelium. (A) TEP and (B) Peak ionic current density (J_I) in mock-infected mice ("Control") or *Salmonella*-infected mice ("Infected") at 16 to 40 h PI. Each dot represents an average of 3 to 5 FAEs or villus epithelium ("Villi") of each mouse. Serosal epithelia ("Serosa") and formalin-fixed mouse ceca ("Fixed") served as controls. $^{**}P < 0.01$, $^{***}P < 0.001$ by one-way ANOVA with post hoc Tukey HSD test (see S1 Data). The red box highlights *Salmonella* infection-generated current reversal at the FAE. (C) The diagram depicts an IGEF generated by *Salmonella* infection at the gut epithelium in a mouse model of human typhoid fever. TEP of up to 25 mV, lumen-positive, occurs across a single layer of tightly sealed gut epithelium and drives micro-ionic currents running from the epithelial surface to the lumen (color-coded arrow indicates the direction of current flow). *Salmonella* invades and breaks epithelial integrity, preferentially at the FAE, which reverses ionic currents running from the breached epithelium into the deep intestinal wall (color-coded arrow indicates the direction of current flow). FAE, follicle-associated epithelium; HSD, honest significant difference; IGEF, infection-generated electric field; PI, post infection; TEP, transepithelial potential.

https://doi.org/10.1371/journal.pbio.3000044.g001

bioelectrical landscape may prevent commensals from accidentally entering the FAE and enable the pathogens to specifically target M cells via bacterial galvanotaxis [56].

Salmonella infection generates bioelectric fields at the FAE of its entry site

Salmonella invades the intestinal epithelium, preferentially by targeting M cells located at an FAE [1,57]. If a wound disrupting an epithelium can generate a steady EF, one would envisage that similar EFs must be produced at the *Salmonella* entry site because of the breakage of epithelial integrity and subsequent short-circuit of the transmucosal potential difference. This is indeed the case in our model. In mice intragastrically challenged with *S*. Typhimurium, the peak J_I remarkably reversed to become inward in FAE compared to control mice, whereas that of the villus epithelium increased nonsignificantly (Fig 1B). Consistent with this finding, we also detected high variation in TEP from individual *S*. Typhimurium–infected mice (up to 25

mV), still lumen-positive (Fig 1A), which has also been observed in chemically induced colitis in rats [58]. More importantly, penetrating electrodes through disrupted FAE up to 200 μm in depth revealed a stepwise increase in TEP (S2 Fig), suggesting the existence of an electric potential gradient generated by the *S*. Typhimurium infection.

Bacterial invasion and subsequent dissemination to mesenteric lymph nodes (MLNs) and spleen were verified by determination of colony-forming units (CFUs) (S4A Fig), and disruption of FAE was assessed by histological staining (S4B Fig). *S*. Typhimurium was undetectable in some of the MLNs and spleens, indicating that some of the FAE and surrounding villi were either uninfected or mildly infected, which explains the wide distribution of TEP and J_I measured in the *S*. Typhimurium–challenged mice.

Based on these results, we coined the term infection-generated electric field (IGEF) (Fig 1C) to distinguish it from a wound-generated electric field (WGEF) [26]. We demonstrate, for the first time, that *Salmonella* infection generated a steady EF (up to 5 V cm^{-1}, provided an epithelial thickness of 50 μm) that drives minute directional electric currents, running from the breached FAE into the deep intestinal wall in a stepwise manner. Although how the IGEFs are formed is currently unknown, we speculate on a couple of possible mechanisms. First, in order to establish a steady EF, a potential gradient or a circuit must be formed. Even though there are accumulated charges segregated by the epithelium (positive at the apical side), in a healthy gut a circuit is unlikely to be formed by the epithelium itself due to high resistance of the epithelium, which is sealed by tight junctions. However, given that the intestinal lumen is alkaline (more negative in terms of electrogenesis), a micropotential gradient could be developed in close proximity to the apical side of the gut epithelia, which can drive outward ionic currents (Fig 1C). Second, differential expression and asymmetric distribution of ion pumps and channels essential for selective absorption and/or secretion of electrogenic ions by enterocytes and M cells [47,48] are likely to be critical for the generation of the aforementioned bioelectricity. Future studies using specific channel blockers in combination with our bioelectrical experimental model and techniques will help to pinpoint the molecular mechanism of an IGEF by identifying the channel(s) or pump(s) involved. Third, as in the formation of a WGEF [21,59], *Salmonella* preferentially invades and destroys M cells and collapses the epithelial barrier at the FAE (S4B Fig), which short-circuits the TEP. Subsequently, the short-circuited and augmented TEP could then drive inward ionic currents as supported by the measurements of stepwise increase of the TEP (S2B Fig). Fourth, in contrast to the healthy alkaline gut, the microenvironment at the *Salmonella* entry site (i.e., the FAE) is likely to be more acidic (more positive in terms of electrogenesis) because of the local inflammatory responses [60] and metabolic changes [61] induced by *Salmonella* infection. Such a microenvironmental pH switch could be related or attributed to the reversal of ionic current flow as we detected with vibrating probes (Fig 1B). Like the injury currents reported by Sawyer and colleagues in early publications [62–64], IGEF-driving ionic currents could affect small blood vessels in the intestinal wall and mesentery to cause a transvascular potential drop or reversal, resulting in 2 possible consequences: an intravascular occlusion that may benefit transendothelial penetration of immune cells (e.g., monocytes, leukocytes) and/or the creation of a galvanotactic route between the infected epithelium and the electrically impacted vessels [65].

Salmonella reverses the directional migration of IGEF-guided macrophage galvanotaxis in vitro

Although IGEFs may provide a guidance cue for the enterocytes or even local stem cells, contributing to the repair process of damaged epithelium, the major focus of this work is, rather, to investigate its biopathological role in the systemic *Salmonella* infection, specifically during

the initiation of macrophage-driven dissemination. Previous studies have shown that applying an EF in vitro can direct macrophage galvanotaxis to the anode [32–34]. We confirmed this phenotype by demonstrating that the primary mouse peritoneal macrophages (PMs), in response to an exogenous EF tuned to mimic the in vivo IGEF (mathematics in Materials and methods), underwent robust unidirectional migration to the anode (S1 Movie). This unidirectional migration was verified by immunostaining showing that nearly 100% of macrophages were polarized to the anode with a distinct morphology characterized by a leading pseudopodium of dense actin meshwork and a rearward uropod. However, upon challenge with *S.* Typhimurium IR715, the average directionality of EF-induced galvanotaxis decreased significantly, with approximately 41% of the macrophages reversing their migratory direction from the anode to the cathode (Fig 2 and S2 Movie). Although PMs have been widely used in bacterial infection studies [66], likely due to the ease of harvesting, the most commonly used primary murine macrophages are the bone marrow-derived macrophages (BMDMs) because of their high yield and less heterogeneous nature, which makes them phenotypically and functionally different from PMs [67]. To exclude the possibility that the observed bidirectional migration is restricted to PMs, we generated and tested galvanotaxis of BMDMs as we did with PMs. Although both types of macrophages exhibited similar unidirectional migration (mean directionality: −0.98 versus −0.88) to the anode, reversal in BMDMs infected by *Salmonella* IR715 was more robust than in PMs infected by the same *Salmonella* strain (mean directionality: 0.36 versus −0.18) (Fig 2C and S5B Fig). Notably, this phenotype can be reproduced in BMDMs challenged by another 2 virulent *S.* Typhimurium strains, LT2 and SL1344 (S5 Fig), suggesting that directional migration in response to electrical stimuli is an intrinsic hallmark of the macrophages regardless of their origins and that the ability to manipulate and subvert galvanotaxis in these macrophages is conserved in virulent *Salmonella* spp.

If the cells had simply stopped sensing the EF, then we would have observed random migration, as was the case for control macrophages not subjected to an EF (Fig 2E). The observed change in migration pattern can be attributed to *S.* Typhimurium infection for a variety of reasons. First, a gentamycin protection assay confirmed the presence of intracellular bacteria (Fig 2D); second, flow cytometry demonstrated a high *S.* Typhimurium infection rate (approximately 53%) (S6 Fig); and third, high-resolution confocal microscopy revealed that macrophages containing intracellular *S.* Typhimurium switched polarity to the cathode (Fig 2G). Based on these findings, we conclude that *Salmonella*-containing macrophages respond to galvanotaxis stimuli by reversing their primary directional migration.

Infection-dependent directional switch of macrophage galvanotaxis is SPI-1 independent

Macrophages are professional phagocytes that uptake a broad range of substances; meanwhile, pathogenic *Salmonella* has developed several virulence means to evade macrophage killing, with SPI-1 being the major virulence factor responsible for colonization and invasion [10,68]. To better understand whether the directional reversal is phagocytosis dependent or SPI-1 specific, we monitored galvanotaxis under identical conditions in BMDMs challenged with (i) fluorescently labeled microspheres similar in size to bacteria, (ii) *S.* Typhimurium constitutively expressing mCherry, and (iii) a green fluorescent protein (GFP)-expressing Δ*invA* mutant that lacks a functional SPI-1 (unable to inject its effectors into cells) [69] (Fig 3A). Macrophages challenged with microspheres exhibited migratory behavior similar to that of controls, i.e., unidirectional migration to the anode (Fig 3B and S3 Movie). Macrophages challenged with Δ*invA* migrated with a significantly decreased overall directionality close to that of macrophages infected with wild-type (WT) *Salmonella* (Fig 3B), even though the number of

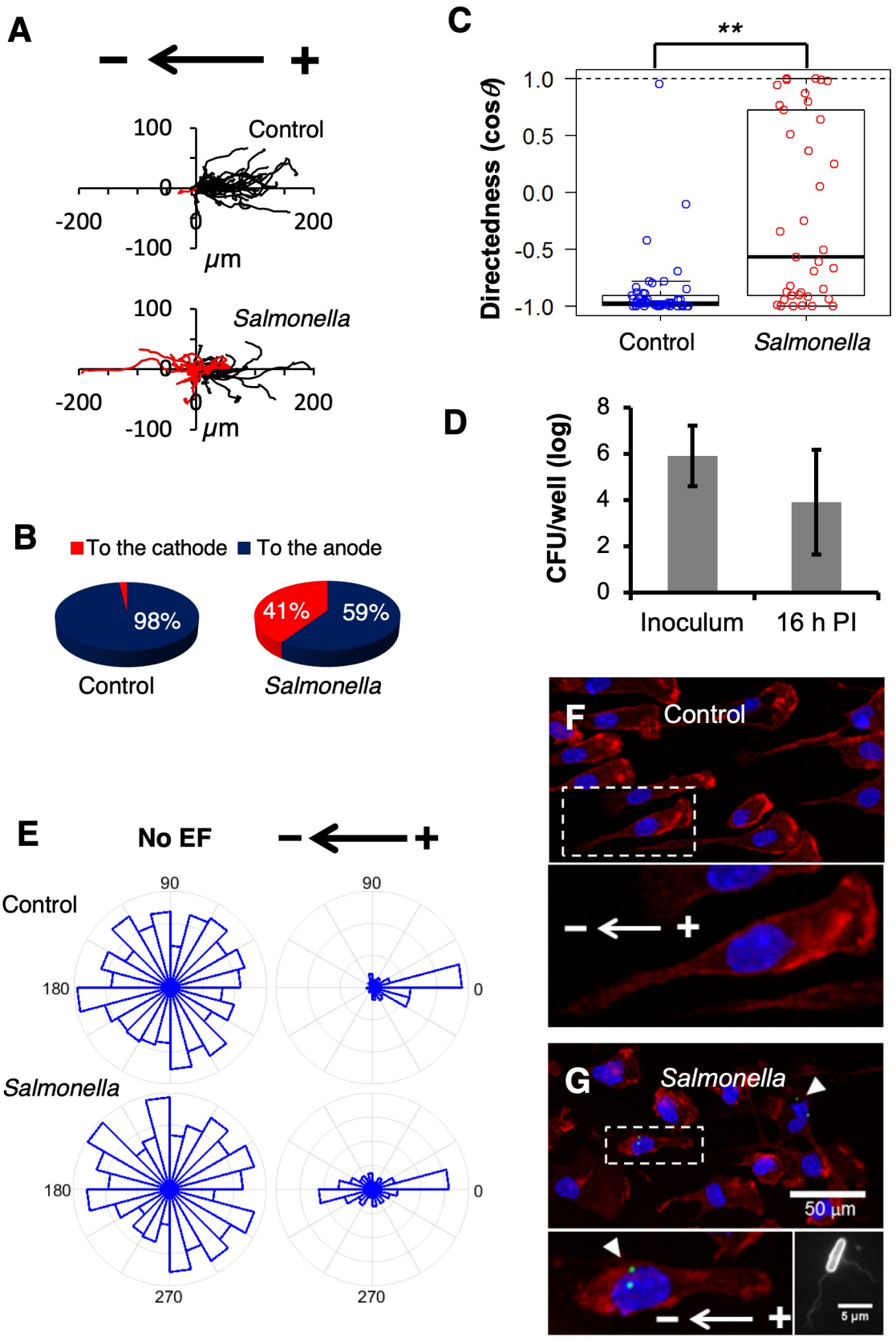
A
100
Control
0
-200
200
-100
μm
100
Salmonella
0
-200
200
-100
μm
B
To the cathode
To the anode
98%
41%
59%
Control
Salmonella
C
**
Directedness (cosθ)
1.0
0.5
0.0
-0.5
-1.0
Control
Salmonella
D
CFU/well (log)
8
6
4
2
0
Inoculum
16 h PI
E
No EF
Control
Salmonella
90
180
0
270
F
Control
G
Salmonella
50 μm
5 μm

Fig 2. *Salmonella* infection switches macrophage galvanotaxis to the cathode. (A) Trajectories of PMs exposed to an IGEF-mimetic EF of 4 V cm^{-1} for 3 h in the indicated orientation before or at 16 h PI. Each line represents one cell's trajectory. (B) Pie charts show percentage of cells migrating to the cathode (red) or to the anode (blue) as demonstrated in panel A. (C) Quantification of overall directionality as directedness. Directedness is calculated as cosθ, in which θ is the angle of each cell traveled corresponding to the applied EF field (positive, to the cathode; negative, to the anode). Data from a representative of multiple independent experiments are represented by jitter plots with boxes indicating the median, the quartile 1/quartile 3, and the minimum/maximum. $^{**}P < 0.01$ by unpaired Student *t* test (see S1 Data). (D) Intracellular bacteria were quantified per gentamycin protection assay in 24-well plates and normalized by inoculum. Data from triplicate wells are presented as mean ± SE. (E) Rose plots show random migration of PMs with no EF, unidirectional migration (to the anode) of control macrophages in response to an EF of 4 V cm^{-1}, and bidirectional migration (either to the anode or the cathode) of cells infected with *Salmonella* exposed to the same EF (see S1 Data). (F) A representative confocal image shows that control PMs were polarized to the anode with a characteristic morphology: massive actin meshwork labeled by Alexa Fluor 555 Phalloidin (red) in the front and a uropod at the rear. Nuclei were labeled by Hoechst 33342 (blue). Bottom panel shows enlargement of the checked area in the indicated field. (G) A representative confocal image showing that macrophages with intracellular *Salmonella* (white arrowheads) were polarized to the cathode. Intracellular *Salmonella* were detected by a specific antibody that recognizes both cell body and flagellae (bottom right panel) and stained with a secondary antibody conjugated with Alexa Fluor 488 (green). Actin and nuclei were stained as in panel F. Bar, 50 μm. Bottom left panel shows enlargement of the checked area in the indicated field. CFU, colony-forming unit; EF, electric field; IGEF, infection-generated electric field; PI, postinfection; PM, peritoneal macrophage; SE, standard error; cosθ, cosine theta.

https://doi.org/10.1371/journal.pbio.3000044.g002

intracellular mutants was indeed lower than that of the WT (Fig 3C). Time-lapse recording captured a marked opposing directional migration pattern: macrophages containing microspheres migrated to the anode, and macrophages with either WT or Δ*invA* bacteria inside migrated to the cathode (Fig 3D and 3E, and S3 Movie), further confirming that the observed directional switch was *Salmonella* infection dependent. There were similar phagocytosis and/or infection rates between the macrophages challenged with microspheres or *Salmonella* in the given multiplicity of infection (MOI; S7A and S7B Fig), as verified by flow cytometry (S6 Fig). Cells containing no or variable microspheres migrated to the anode exclusively (S7C and S7D Fig), ruling out mechanisms solely based on phagocytosis. The fact that cells containing either WT or Δ*invA* migrated to the cathode suggests that the SPI-1 type III secretion system is not required or, at least, is insufficient for the directional switch. These data are in accordance with previous studies that identified an SPI-1-independent pathway contributing to early dissemination of *S*. Typhimurium in the mouse typhoid model [17]. We therefore argue for the existence of a general infection-dependent mechanism that involves phagocytosis and subsequent interplay between the macrophages and internalized bacterial pathogens.

Salmonella but not microspheres decreases surface-exposed sialic acids in macrophages

Charged cell-surface components are critical for EF-induced motility in 3H3 cells [70] and have been implicated in electro-osmosis of concanavalin A (Con A) binding receptors on the surface of myotomal spheres [71]. We hypothesized that the directional switch of macrophage galvanotaxis could result from bacteria-induced modifications to the charged components of the cell surface, which would not occur following microsphere challenge (Fig 4A). To this end, we screened *Salmonella*-infected and control macrophages against a panel of fluorescently labeled lectins (glycan-binding proteins) capable of detecting charged and uncharged cell surface glycans (S1 Table). The normalized mean fluorescent intensity of Maackia Amurensis Lectin II (MAL-2), a lectin that recognizes pathogen-binding sialic acids, was significantly decreased in macrophages infected by *Salmonella* but not in those carrying microspheres (Fig 4B–4D). Marked Galanthus Nivalis Lectin (GNL)- and Con A–binding aggregates were visible within macrophages infected by *Salmonella* (S8 and S9 Figs), raising the possibility that the decrease in MAL-2-binding sialic acids could be the result of bacterial internalization and subsequent degradation.

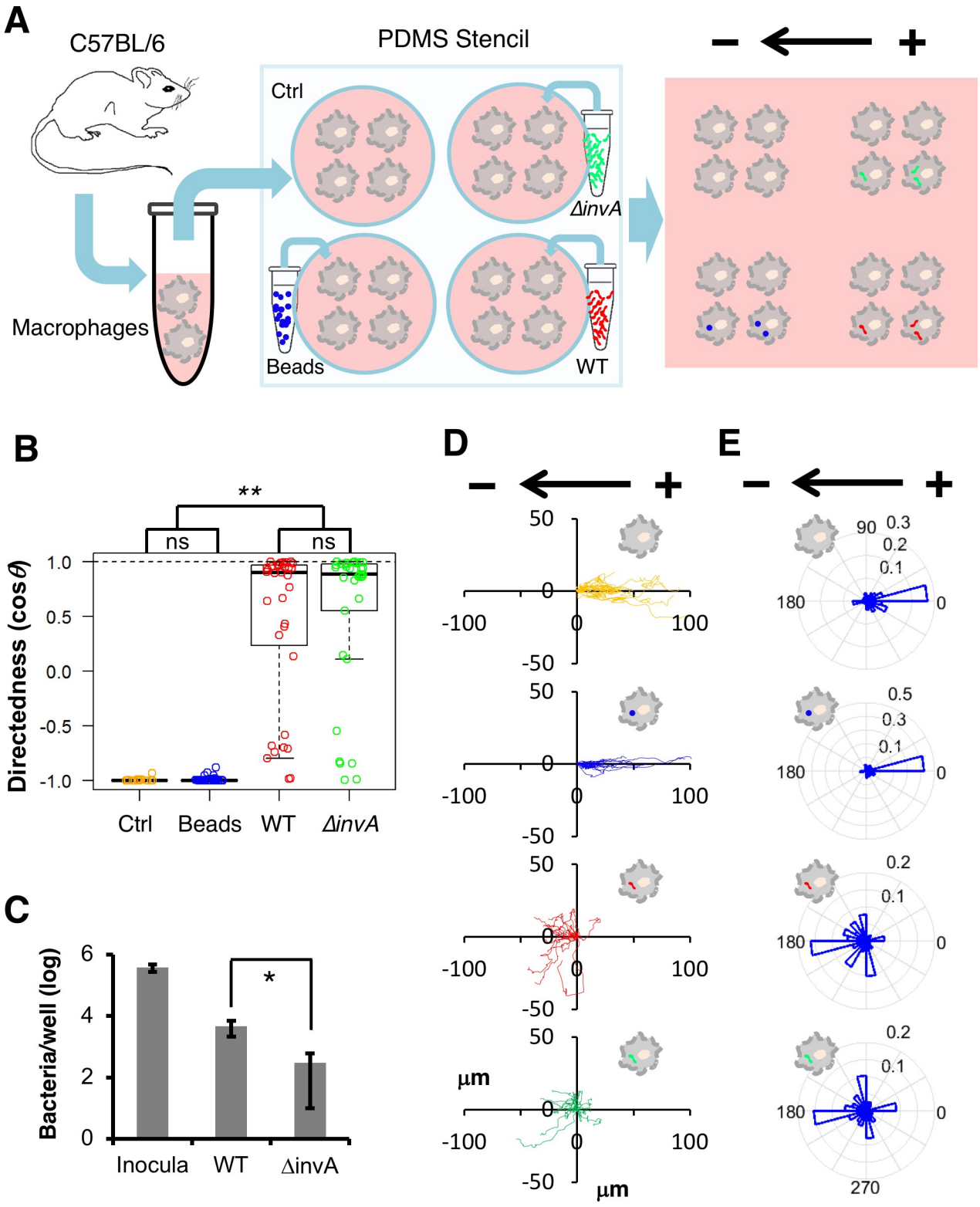

Fig 3. Directional switch mediated by *Salmonella* infection in macrophage galvanotaxis is phagocytosis independent and SPI-1 independent. (A) Schematic of the experimental design. Freshly differentiated mouse BMDMs were seeded in wells engineered with a PDMS stencil. Adhered macrophages were challenged with either blue fluorescent beads ("Beads") or WT *Salmonella* expressing mCherry (WT) or SPI-1 mutants expressing GFP (Δ*invA*) and cultured for 16 h. Unchallenged BMDMs served as the Ctrl. Subsequent migration of macrophages was monitored in the same galvanotaxis chamber under identical conditions after removal of the PDMS stencil. (B) Directedness of macrophages under different challenge

conditions. $^{**}P < 0.01$ by one-way ANOVA with post hoc Tukey HSD test (see S1 Data). (C) Intracellular bacteria were quantified per gentamycin protection assay in 24-well plates and normalized by inoculum. Data from triplicate wells are presented as mean ± SE. $^{*}P < 0.05$ by unpaired Student *t* test. (D) Trajectories of Ctrl macrophages (orange) or macrophages bearing beads (blue) or WT (red) or Δ*invA* (green) exposed to an EF of 4 V cm^{-1} for 3 h in the indicated orientation. (E) Rose plots show opposite galvanotactic behaviors of Ctrl macrophages or macrophages bearing beads (to the anode) or macrophages containing WT or Δ*invA* (to the cathode) (see S1 Data). See also S3 Movie. BMDM, bone marrow-derived macrophage; Ctrl, control; EF, electric field; GFP, green fluorescent protein; HSD, honest significant difference; ns, nonsignificant; PDMS, polydimethylsiloxane; SE, standard error; SPI-1, *Salmonella* pathogenicity island 1; WT, wild type.

https://doi.org/10.1371/journal.pbio.3000044.g003

Cleavage of surface-exposed sialic acids impairs macrophage galvanotaxis via zeta potential

Sialylated cell surface molecules are negatively charged, creating an electronegative zeta potential [72]. Using an electrophoretic light-scattering technique, we determined the zeta potential

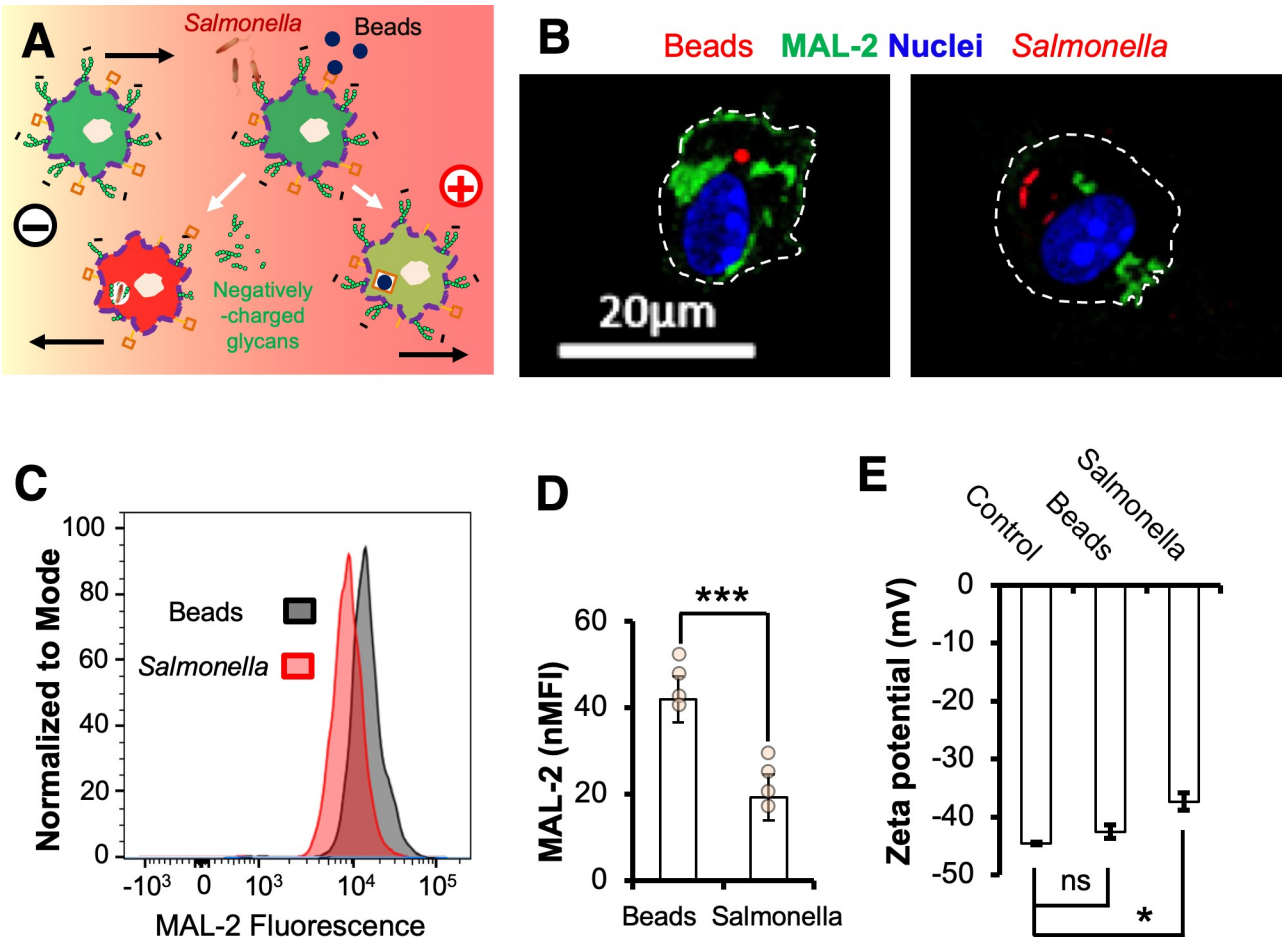

Fig 4. *Salmonella* infection but not challenge by microspheres decreases surface-exposed sialic acids and reduces the negativity of BMDMs. (A) Schematic showing the simplified hypothesis of galvanotaxis in macrophages and a directional switch modulated by *Salmonella* infection. Primary macrophages with sialylated glycoproteins or lipids (small green circles) migrate to the anode. Activated macrophages with reduced negativity, either through enzymatic activities of the *Salmonella* or internalization and/or degradation, switch direction to the cathode, whereas macrophages that phagocytosed beads via nonsialylated surface components (brown squares) still migrate to the anode. (B) Representative confocal images of surface MAL-2 (green) of BMDMs challenged with 1-μm diameter red fluorescent microspheres or *S.* Typhimurium constitutively expressing mCherry (red) at 16 h PI. Nuclei were counterstained with DAPI (blue). Bar, 20 μm. (C) Representative flow cytograms and (D) independent data of standardized MAL-2 fluorescence (green) intensity of BMDMs treated as in panel B. $^{***}P < 0.001$ by Student *t* test. (E) Zeta potential of control BMDMs or BMDMs challenged with beads or *S.* Typhimurium at 16 h PI. Data quantified from a representative of 3 independent experiments are presented as mean ± SE. $^{*}P < 0.05$ by one-way ANOVA with post hoc Tukey HSD test (see S1 Data). BMDM, bone marrow-derived macrophage; HSD, honest significant difference; MAL-2, Maackia Amurensis lectin II; ns, nonsignificant; PI, post infection; SE, standard error; *S.* Typhimurium, *Salmonella enterica* serotype Typhimurium.

https://doi.org/10.1371/journal.pbio.3000044.g004

of BMDMs under various conditions. The negative zeta potential of macrophages infected by *S*. Typhimurium was significantly reduced, i.e., less negative than that of control macrophages ($P < 0.05$) (Fig 4E). By contrast, macrophages challenged with microspheres showed a nonsignificant zeta potential change compared to that of control macrophages (Fig 4E), suggesting that the decrease in surface-exposed sialic acids and subsequent reduction of surface negativity is mediated by active bacterial product(s) [73].

If a decrease of the negatively charged sialic acids of the surface glycoproteins is critical for the directional switch in macrophage galvanotaxis, then cells with their sialic acids enzymatically removed should exhibit a switch or at least a defect in directional migration when exposed to an EF. To test this, we treated freshly isolated mouse BMDMs with a potent neuraminidase (an enzyme that cleaves terminal sialic acid residues from surface-exposed glycoproteins) [74]. Cleavage of sialic acids following enzymatic treatment was confirmed by flow cytometry and confocal microscopy (Fig 5A–5C). As predicted, the zeta potentials of neuraminidase-treated macrophages were significantly reduced (Fig 5D). These cells also lost anodal migration compared to control macrophages monitored in parallel (Fig 5E and 5F, and S4 Movie). Further inspection and morphological quantification of macrophages stained with fluorescently labeled actin and/or lectin revealed that 71% of the macrophages treated with neuraminidase failed to establish a polarity and notably, 12% of the cells were polarized to the cathode whereas nearly all the control macrophages (97%) were polarized to the anode in response to the EF (Fig 5G).

It is well known that a change in the environmental pH can dramatically influence the growth and virulence of *Salmonella* [75,76]. Moreover, by exposure to acidic pH, a condition that is required for activation of several *Salmonella* virulence factors [77–79], it is possible to modify macrophage surface electrical properties [30]. Therefore, to further determine the importance of surface negativity, we incubated BMDMs in medium at pH 5.8 that markedly reduced the zeta potential (S11A Fig), presumably through protonation of the sialylated surface molecules. Similar to the neuraminidase treatment, galvanotaxis of BMDMs under acidic conditions was significantly impaired, resulting in nearly half of the macrophages (47%) losing their directional migration and 14% of the macrophages reversing their polarity to the cathode (S11B-S11D Fig and S5 Movie). Although these data are consistent with our previous studies, showing that low pH abrogates directional migration of epithelial cells in response to an EF [80,81], it also suggests that the acidic environment is not only required for the activation of *Salmonella* but also contributes to triggering dissemination.

How does *Salmonella* infection instruct macrophages to reverse EF-directed migration? Firstly, it is important to note that infecting macrophages with a SPI-1 mutant resulted in a directional switch similar to that of WT, with nearly all the macrophages containing live fluorescent protein-expressing bacteria migrating to the cathode (Fig 3 and S3 Movie). This suggests a general mechanism, independent of this major virulence factor, even though other specific factor(s) may still be involved [82,83]. Previously reported effects have suggested that negatively charged surface glycan moieties are critical for EF-induced cell motility and polarization, which are consistent with our data, and provide a long sought-after mechanism of action. Because macrophages challenged with microspheres did not show a significantly reduced zeta potential (Fig 4E), it is likely that the decrease in surface-exposed sialic acids and reduction of surface negativity is mediated by active bacterial product(s) rather than by metabolic changes in the host itself. It is also important to note that although both *Salmonella* infection and neuraminidase treatment decreased the surface-exposed sialic acids, the latter caused a serious defect in macrophage galvanotaxis without reversing the overall directionality (Fig 5E), in contrast to *Salmonella* infection (Fig 3B). There may be multiple glycosidases involved in surface glycan modification to reverse directionality (Fig 5H) because *Salmonella* possesses

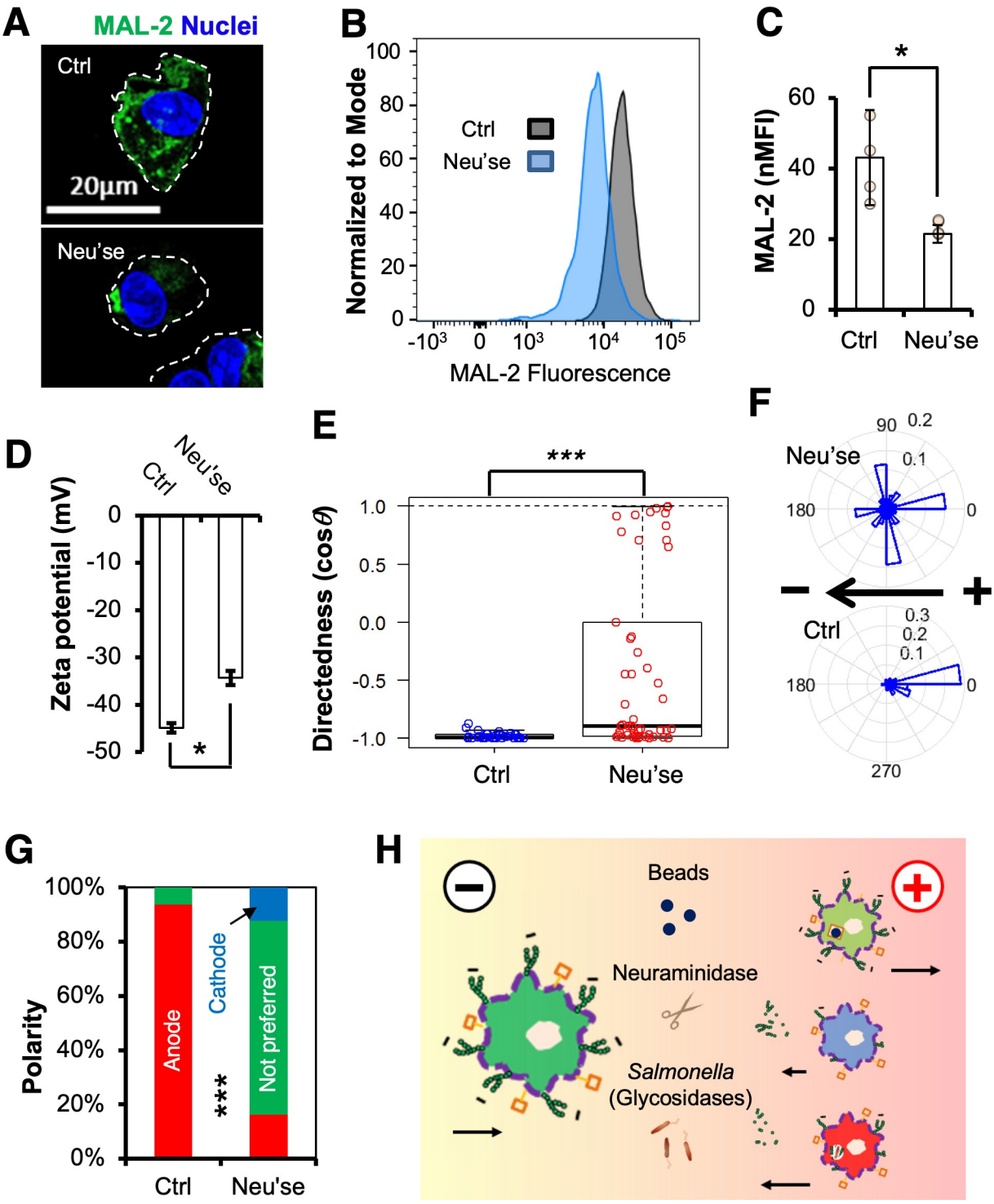

Fig 5. Cleavage of negatively charged sialic acids impairs macrophage galvanotaxis. (A) Representative confocal images of surface MAL-2 (green) of BMDMs incubated with 0 (Ctrl) or 100 mU ml^{-1} Neu'se for 30 min. Nuclei were counterstained with DAPI (blue). Bar, 20 μm. (B) Representative flow cytograms and (C) independent data of standardized MAL-2 fluorescence (green) intensity of BMDMs incubated with 0 or 100 mU ml^{-1} Neu'se for 30 min. $^{*}P < 0.05$ by Student *t* test. (D) Zeta potential of BMDMs incubated with 0 or 100 mU ml^{-1} Neu'se for 30 min. Data were quantified from a representative of 3 independent experiments. $^{*}P < 0.05$ by Student *t* test. (E) Directedness, (F) rose plots, and (G) polarity of BMDMs treated with or without Neu'se, followed by 3 h exposure to an EF of 4 V cm^{-1}. Data were quantified from a representative of 4 independent experiments. $^{***}P < 0.001$ by Student *t* test (Panel E). $^{***}P < 0.001$ by χ^2 test (Panel G) (See S1 Data). (H) Proposed model of *Salmonella*-infection–dependent directional switch in macrophage galvanotaxis. Upon exposure to an IGEF-like EF (marked gradient),

negatively charged (sign with small green circles) macrophages undergo robust directional migration to the anode. Phagocytosing *Salmonella* reduces surface negativity of the macrophage through catalytic activities of certain glycosidases, as exemplified by the cleavage of sialic acids with Neu'se (scissors). Consequently, activated macrophages can either undergo defective directional migration or switch direction to the cathode. Macrophages that phagocytosed beads through binding of nonsialylated surface components (brown squares) still migrate to the anode. Arrows indicate both direction and strength of macrophage galvanotaxis. BMDM, bone marrow-derived macrophage; cosθ, cosine theta; Ctrl, control; EF, electric field; IGEF, infection-generated electric field; MAL-2, Maackia Amurensis lectin II; Neu'se, neuraminidase; nMFI, normalized mean fluorescence intensity; ns, nonsignificant.

https://doi.org/10.1371/journal.pbio.3000044.g005

at least 51 putative glycosidases that likely function in glycan degradation [84]. In fact, a recent study identified several glycosidases, including a putative neuraminidase, as new virulence factors essential for *Salmonella* infection of epithelial cells, which is again independent of the SPI-1 [85]. We are in the process of performing genetic knockouts to identify the factors involved.

It is also possible that modification of surface glycan and reduction of zeta potential were mediated by internalization during phagocytosis of the bacterium itself rather than by bacterial enzymatic activities. For example, macrophages express Toll-like receptors (TLRs) that recognize structurally conserved molecules derived from *Salmonella* and other pathogens. All TLRs contain *N*-linked glycosylation consensus sites, and both TLR2 and TLR4 require glycosylation for surface translocation and function [86,87]. Binding of *Salmonella* to these glycosylated receptors and subsequent internalization may reduce surface negativity of macrophages, leading to directional switch under an EF. This idea is supported by our observations in which the accumulation of certain lectin binding aggregates within macrophages infected by *Salmonella* but not in cells challenged by microspheres (S8 and S9 Figs). It is also possible that a macrophage can uptake microspheres without significantly changing its zeta potential (e.g., through a neutralized receptor) and thus still migrate to the anode.

Disseminated *Salmonella* infection is a major health problem of developing countries, responsible for approximately 433,000 deaths annually [88]. Understanding the mechanisms that trigger dissemination is critical for efforts to target this key process for preventive and therapeutic purposes. We propose that macrophages are attracted to the site of infection by a combination of chemotaxis and galvanotaxis, driving the cells in the same direction. After phagocytosis of bacteria, surface electrical properties of the macrophage change, and galvanotaxis directs the cells away from the site of infection (Fig 6). Our study represents a new perspective for the initiating mechanisms, suggesting that *Salmonella* disseminates through infection-generated bioelectrical control of macrophage trafficking. It is important to emphasize that the demonstrated bidirectional migration of macrophages to the IGEF-like EFs is not a physical electrophoresis (movement of charged particles under direct-current EF) but rather a complex yet poorly understood biological process that requires phosphoinositide 3-kinases and other critical signaling activities, as well as the cellular motility machinery [25,81]. It is also worth emphasizing that the model proposed in this work is not mutually exclusive with respect to chemotaxis but offers an alternative and/or complementary mechanism of directional migration. Both directional cues can coexist and play equally important roles in orchestrating the initial stage of the innate immune response against bacterial infection (Fig 6), although a chemical gradient could be overridden by a strong electrical stimulus [59,89]. Both chemotaxis and galvanotaxis likely share critical signaling pathways as suggested in studies of macrophage-like *Dictyostelium*, which are highly sensitive to cyclic adenosine monophosphate gradients, as well as to electrical potential gradients [90–92]. Future work utilizing transgenic animals and pharmacological perturbations to target specific pathways (known or unknown) will help to pinpoint key molecules mediating the infection-dependent directional reversal (i.e., the molecular mechanisms to initiate disseminated infection) and response to bioelectric signaling.

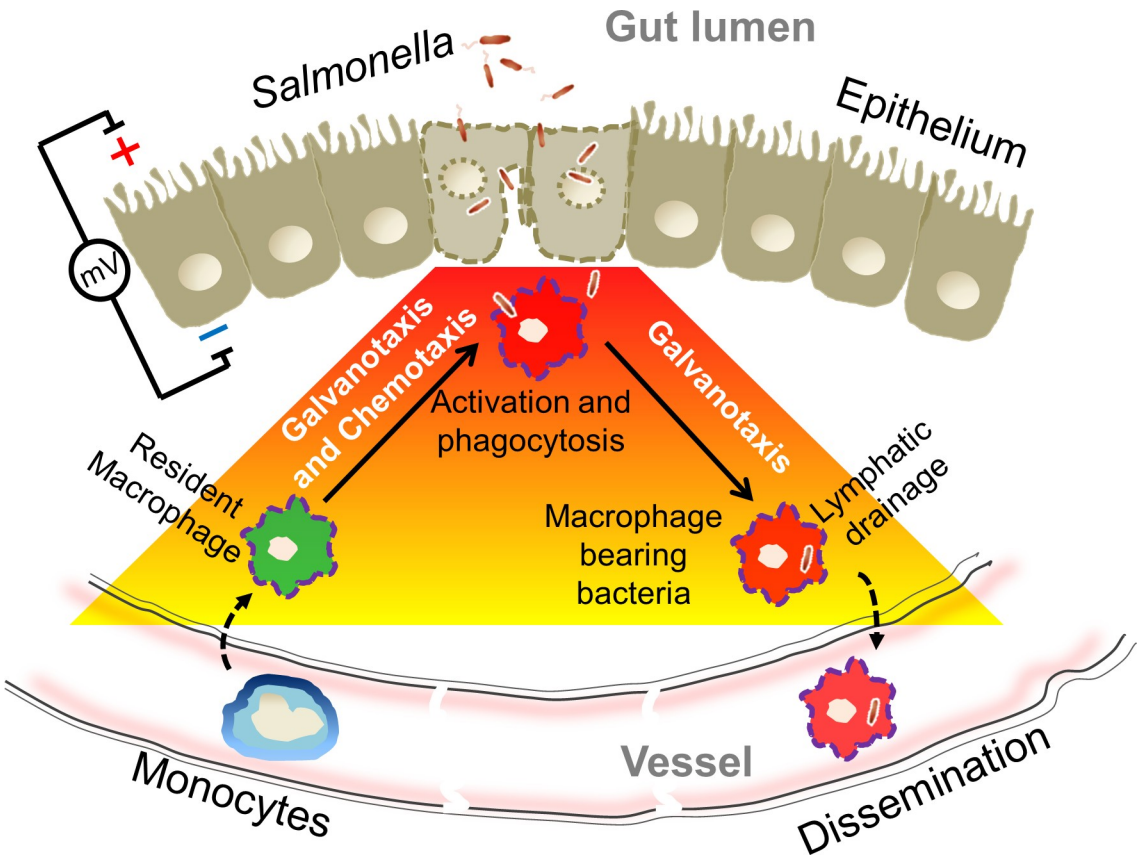

Fig 6. IGEF at gut epithelium and model of macrophage galvanotaxis in initiating dissemination. *Salmonella* invades and disrupts gut epithelial integrity, preferentially at the FAE, generating an IGEF (red to yellow gradient) that recruits resident macrophages to the bacteria entry sites—alone or synergistically with chemotaxis. Macrophages invaded by *Salmonella* revert galvanotaxis direction through the modification of surface electric properties to reach the lymphatic drainage and/or bloodstream, thus initiating dissemination. FAE, follicle-associated epithelium; IGEF, infection-generated electric field.

https://doi.org/10.1371/journal.pbio.3000044.g006

Triggering bacterial dissemination mediated by macrophage galvanotaxis might be a common strategy, not only for pathogenic *Salmonella* but also for other bacterial pathogens that are able to invade macrophages and survive intracellularly. Although the present work deals primarily with gut epithelium and enteric bacteria, the general mechanism that emerged from this work could also apply to other mucous epithelia such as the respiratory tract and its associated pathogens, e.g., *Mycobacterium tuberculosis* (the causative agent of tuberculosis) [93], which is another major public health concern.

Materials and methods

Mice and surgery

The mouse strains used were in a C57BL/6 background (both male and female mice were used in experiments). Mice were purchased from Jackson lab and maintained under a strict 12-h light cycle and given a regular chow diet in a specific pathogen-free facility at University of California (UC), Davis. All animal experiments were performed in accordance with regulatory guidelines and standards set by the Institutional Animal Care and Use Committee of UC Davis. In brief, we dissected mouse cecum following euthanasia and opened longitudinally along the mesenteric attachment remnant to avoid incision damage to the single Peyer's patch

located under the antimesenteric mucosa near the apex (S1A Fig). After thorough washing in mouse Ringer's solution (154 mM NaCl, 5.6 mM KCl, 1 mM $MgCl_2$, 2.2 mM $CaCl_2$, 10 mM glucose, and 20 mM HEPES [pH 7.4]) to remove the luminal contents, we placed the cecum with mucous side facing up, on a 30˚ slope of silicone gel prepared from polydimethylsiloxane (PDMS) in custom-made measuring chambers. The cecum was aligned and immobilized with fine metal (tungsten) pins prior to taking measurements (S1B Fig). This process was usually completed within 5 min.

Measuring TEP with glass microelectrodes

We used glass microelectrodes to directly measure the TEP of intestinal epithelium as previously described [28,94]. TEPs were recorded by microelectrode impalement through the epithelial layers. Microelectrodes (1–2 μm tip diameter; NaCl 3 M electrolyte) had resistances of approximately 1 to 2 MΩ, and the potentials were offset to 0 mV prior to impalement. Cecal FAE and adjacent villus epithelium were discriminated under a dissecting microscope within a Faraday cage on an antivibration table. In some cases, the TEP were measured as follows: first at the epithelial surface (0 μm), then stepwise at 50, 100, and 200 μm in depth, controlled by a micromanipulator (S2A Fig). The potential typically returns to the baseline of 0 mV after microelectrode withdrawal. If the reference baseline was $> \pm 1$ and $\leq \pm 5$ mV, the value was subtracted from the TEP recorded as shown in the equation (S2B Fig); if $> \pm 5$ mV, the trace was rejected. As a control, we measured the TEP of serosa epithelium and the TEP of formalin-fixed mucous epithelium. Measurements were performed at room temperature in mouse Ringer's solution. Data were acquired (saturated sampling at 100 Hz) and extracted using pClamp 10 (Molecular Devices) and analyzed using Excel (Microsoft, Redmond, WA).

Measuring ionic currents with vibrating probes

We used noninvasive vibrating probes to measure the electric current density (J_I) in μA cm^{-2} of mouse cecum epithelium as previously described [28,41,42]. The probes, platinum-electroplated at the tip (approximately 30 μm ball diameter), vibrated at a frequency between 100 and 200 Hz. Prior to measurements, the probe was calibrated to the experimental conditions by an applied J_I of 1.5 μA cm^{-2} (S3C Fig). Under a dissecting microscope, mounted mouse ceca were positioned in the nonconductive measuring chamber (S3A Fig). The plane of probe vibration was perpendicular to the epithelial surface at a distance as close as possible (S3B Fig). J_I was recorded until the plateau peak was reached (<1 min) (S3C Fig). Reference values were recorded with the probe away from the epithelium surface (≫1 mm) (S3A Fig). Measurements were taken at room temperature in mouse Ringer's solution. During calibrations and measurements, a Faraday "wall" (grounded aluminum-wrapped cardboard) covered the microscope. As a control, we measured J_I near the surface of serosal epithelium and formalin-fixed mucous epithelium. Data were acquired and extracted using WinWCP V4 (Strathclyde Electrophysiology Software, University of Strathclyde, Glasgow, United Kindom) and analyzed using Excel (Microsoft, Redmond, WA).

Reagents, plasmids, and *Salmonella* strains

Special reagents used in this work are listed in S2 Table. Plasmids and *Salmonella* strains used in this work are listed in S3 Table. Cultures of *Escherichia coli* (for plasmid extraction) and *S.* Typhimurium were incubated aerobically at 37˚C in Luria-Bertani (LB) broth (per liter: 10 g tryptone, 5 g yeast extract, 10 g NaCl) or on LB agar plates (1.5% Difco agar) overnight. Antibiotics were used at the following concentrations unless stated otherwise: 30 μg ml^{-1}

chloramphenicol, 50 μg ml^{-1} nalidixic acid, 100 μg ml^{-1} ampicillin, 50 μg ml^{-1} kanamycin, and 10 μg ml^{-1} tetracycline.

Construction of *S.* Typhimurium expressing fluorescent proteins

In an effort to monitor live intracellular *Salmonella* during macrophage galvanotaxis we constructed an *S.* Typhimurium strain derived from IR715 that constitutively expresses mCherry coded in its genome [95]. In brief, the *glmS*::*mCherry* allele was transferred to IR715 via P22 transduction from the donor strain *S.* Typhimurium SL1344St (a gift from Leigh Knodler) [96] and selected by chloramphenicol. To remove the FRT-flanked chloramphenicol cassette, the transductant was transformed with pCP20 encoding FLP recombinase. The resulting strain constitutively expressing mCherry encoded by *glmS*::*mCherry*::*FRT* was designated KLL18.

The GFP-expressing SPI-1 mutant Δ*invA* was generated by electroporating pGFT/RalFc into AJB75 [69]. The plasmid pGFT/RalFc was constructed in 2 steps. First, a fragment of a *gfp-mut3* gene under the control of the constitutively active kanamycin-resistance gene *aphA3* promoter was amplified from pJC43 [97] with the primers GFPmut3-F (5′- AGAGCTCCAGC GAACCATTTAAGGTGATAG -3′) and GFPmut3-R (5′- ACTGCAGTTATTTGTATAGTTC ATCCATGCC -3′). This fragment was then digested with SacI/PstI and cloned into pFT/ RalFc, a low–copy-number plasmid based on pBBR1-MCS4 [98].

Oral infection in a mouse model of human typhoid fever

The mouse is a well-established animal model for studying *Salmonella* pathogenesis [35]. C57BL/6 and other mice carrying a mutation in *nramp1* develop disseminated infections when challenged by *S.* Typhimurium, which mimics human typhoid fever [99]. For the mouse infection experiment, we used the hyper-disseminative D23580 strain [100,101]. In brief, D23580 was used to inoculate LB broth and incubated overnight at 37˚C. C57BL/6 mice (6 to 10 wk old, mixed sexes) were intragastrically infected with 10^9 bacteria (actual inoculum was determined by plating) in 0.1 ml LB broth. Uninfected mice used as a control were given 0.1 ml sterile LB broth in place of *Salmonella*.

Mice were euthanized at 16 h and 40 h post infection (PI) by CO_2 asphyxiation followed by cervical dislocation as the secondary method of euthanasia. The 16 h PI was chosen based on previous studies showing that the best-characterized route for the phagocytes harboring *Salmonella* to reach the bloodstream normally requires between 12 and 20 h [17,102]. MLNs and spleens were collected aseptically and homogenized in phosphate-buffered saline (PBS) for CFU enumeration. Ceca were dissected, cleaned, and then either mounted for bioelectrical measurement, prepared for histopathological fixation, or homogenized in PBS for CFU enumeration.

Histology

Ceca were fixed in 10% neutral buffered formalin. After fixation, tissues were routinely processed, embedded in paraffin, sectioned, and stained with hematoxylin–eosin.

Isolation and culture of primary mouse PMs and BMDMs

Both PMs and BMDMs were isolated from C57BL/6 mice (6 to 10 wk old, mixed sex) following standard procedures as previously described [103]. PMs were seeded onto 6-well plates and allowed to adhere to the plastic for 1 to 2 d in DMEM (Invitrogen) with 10% fetal bovine serum (Invitrogen) and 1× antibiotic-antimycotic solution (Invitrogen). BMDMs were cultured in the same medium as described above but supplemented with 20% L-929 conditioned

medium for 6 d (plus an extra feed at day 3), followed by 1-d culture without the conditioned medium. Adherent macrophages were then harvested by gently scraping with a "policeman" cell scraper and used for subsequent experiments accordingly. Cell viability was determined by trypan blue staining and counting.

Our initial galvanotaxis experiments were carried out in PMs. Because we observed better directional switch in BMDMs infected by *Salmonella* (S5 Fig), subsequent experiments were done in BMDMs, unless stated otherwise.

Gentamycin protection assay to determine intracellular bacteria CFU

The gentamycin protection assays were carried out as previously described [104]. In 24-well tissue culture-treated plates, 2×10^5 cells were seeded per well for 5 to 6 h in culture medium (DMEM with 10% fetal bovine serum and no antibiotics). *Salmonella* were grown overnight and used to infect macrophages at an MOI of 20. After 60 min of incubation, cells were gently washed 3× with PBS and further incubated in gentamycin-containing culture media at a final concentration of 50 μg ml^{-1} for an additional 60 min. Afterwards, media were replaced with culture media containing 10 μg ml^{-1} gentamycin for the duration of the experiment. Intracellular CFU was measured at 16 h PI. To measure intracellular CFU, macrophages were lysed using 0.5% Tween 20 for 5 min at room temperature and released by scraping with 1 ml pipette tips. CFUs were enumerated by plating.

Infection, challenge, and treatment of macrophages

Typically, 4×10^4 primary mouse macrophages were seeded per well of engineered silicon stencils sealed in custom-made EF chambers (see "Engineering silicone stencil and EF chamber design" for details) or 96-well glass bottom plates (Nunc) or 2×10^5 cells per well in 24-well tissue culture-treated plates depending on different experiment needs for 5 to 6 h in culture medium. Overnight cultures of *Salmonella* or fluorescently labeled microspheres were used to infect and/or challenge macrophages at an MOI of 20. The rest of the procedures were similar to the gentamycin protection assay. Cells were cultured in medium containing 10 μg ml^{-1} gentamycin for 16 h, and subsequent galvanotaxis experiments were carried out in the same medium containing gentamycin.

For the neuraminidase treatment, cells were incubated in culture medium containing 100 mU ml^{-1} neuraminidase from *Vibrio cholerae* (Sigma-Aldrich) for 30 min at 37˚C [70]. Cells were then washed with culture medium, and subsequent galvanotaxis experiments were carried out in the culture medium containing no neuraminidase.

For the low pH experiments, cells were incubated in culture medium of pH 5.8 buffered with 15 mM MES (Sigma-Aldrich) for 60 min, and subsequent galvanotaxis experiments were carried out in the same media of pH 5.8 [81]. Control experiments were carried out always in parallel in culture medium of pH 7.4 buffered with 14.4 mM HEPES (Invitrogen).

Galvanotaxis assay

1. Engineering silicone stencil and EF chamber design. We have tested cover glass and plastics coated with different substrates and found that macrophages perform robust and consistent galvanotaxis when cultured in tissue culture dishes (Corning). Therefore, our EF chambers were customized based on 100 mm tissue culture dishes. To facilitate group comparability and EF control, we engineered removable and reusable silicone stencils of multiple wells (diameter of 8 mm, thickness of 2.4 mm) to seed the same batch of cells that can be challenged and/or treated with different bacteria and/or substances and monitored under identical

galvanotactic conditions simultaneously [105]. The EF tunnel height is fixed at around 120 μm by double-sided silicone tapes cut by a computer-controlled laser cutter [80].

2. EF application and time-lapse recording. We applied exogenous EF as previously described [42,105–107]. The EF strength is based on the IGEF we measured at the gut epithelium in 2 ways. First, we detected an inward J_I of approximately 1.5 μA cm^{-2} at *Salmonella*-infected FAE. The mouse Ringer's solution we used in the measurement has a resistivity (ρ) of 19.47 mΩ cm, measured with a conductivity meter. A common approximation to the current density assumes that the current is simply proportional to the EF, as expressed by the following equation (derived from Ohm's law):

$$J_I = \frac{E}{\rho}, \quad (1)$$

where E is the EF. Plugging J_I and ρ into the equation, we calculated that a density of 1.5 μA cm^{-2} equals an EF of 0.77 V cm^{-1}. Based on trials in rabbit corneal epithelium, the in vivo J_I is likely 2 to 4 times larger than the ex vivo J_I because of the higher resistances of the tissues and of the higher physiological temperature. Second, we detected a TEP of approximately 25 mV crossing a single layer of *Salmonella*-infected gut epithelium. This generates an EF of 5 V cm^{-1} providing an epithelial cell height of 50 μm. After testing a range around those values, we have empirically chosen an EF of 4 V cm^{-1} because it consistently induced significant directional migration of primary mouse macrophages, although biased directional migration can be achieved by an EF as small as 0.5 V cm^{-1}. Actual EF strengths were measured and determined with a voltmeter before and after each EF application.

Cell migration was monitored with a Carl Zeiss Observer Z1 inverted microscope equipped with a motorized stage and an incubation chamber (37˚C and 5% CO_2). Time-lapse contrast images and/or images of appropriate fluorescence channels were captured using MetaMorph NX program (Molecular Devices). A Retiga R6 (QImaging) scientific CCD camera and long exposure time (approximately 2 s) were used to detect and monitor intracellular *Salmonella* expressing fluorescent proteins. Typically, in each experiment, 2 to 4 fields of each condition under a 10× or a long-distance 20× lens were chosen. Images were taken at 5-min intervals for up to 3 h unless stated otherwise.

3. Image processing and data analysis and/or presentation. Time-lapse images were imported, processed, and assembled in ImageJ (http://rsbweb.nih.gov/ij). To quantify single-cell and population motility, we extracted the trajectory of each cell migration (>30 cells for each condition) using an automatic and/or manual tracking tool [42,81,105]. Directionality as directedness in cosine theta (cosθ), in which θ is the angle that each cell moved with respect to the EF vector, was quantified from the coordinates of each trajectory [108,109]. If a cell moved perfectly along the field vector toward the cathode, the cosine of this angle would be 1; if the cell moved perpendicular to the field vector, the cosine of this angle would be 0; and if the cell moved directly toward the anode, the cosine of this angle would be −1. Dead cells (macrophages killed by *Salmonella*) or cells unresponsive to the EF (due to neuraminidase treatment or acidic conditions) were either washed away or excluded from quantification by migration speed thresholding. The thresholds were estimated from fixed cells recorded in the same optical parameters and experiment setting for the live macrophages. The galvanotaxis assays and quantification of directionality in BMDMs infected with *ΔinvA* and their isogenic WT *Salmonella* were assigned in a double-blinded manner.

To simulate cell migration, each cell was numbered and its x and y coordinates were measured on the first image and on every subsequent image in the image stack, with the x-axis parallel to the applied EF. The (x, y) data of each cell were imported with the ImageJ chemotaxis tool plugin and recalculated based on the optical parameters (lens and camera). Trajectories of

the cells in each group were simulated in a Cartesian coordinate system by placing the first coordinates of each cell in the origin (0, 0).

To plot the rose histograms, we combined θ of each time interval of tracked cells in each group. The vector θ, expressed in radians, was calculated from the coordinates of each trajectory. The distribution of θ in 12 angle bins and their abundance in percentage were plotted in Matlab (Mathworks, Natick, MA) using a custom script (available upon request).

4. Morphological analysis. The polarity of macrophages was determined by the relative distribution of the characterized protrusive lamellipodia front and uropod tail with respect to the applied EF. These were done by visually inspecting a large number of cells (>50 cells in each case) from images taken at 3 h after EF exposure or by quantifying cellular actin intensity of confocal images using ImageJ software with line scan and color function plugins [105].

Immunobiochemistry, lectin staining, and confocal microscopy

Macrophages were seeded in either 96-well glass bottom plates or custom-made EF chambers and infected, challenged, and/or treated by following procedures as described above. The cells were fixed with 4% paraformaldehyde immediately or after EF exposure for 3 h with field orientation marked. *Salmonella* were detected with a polyclonal antibody specific to *Salmonella* spp. (Mybiosource, San Diego, CA) stained by an Alexa Fluor 488-conjugated secondary antibody. F-actin was labeled by Alexa Fluor 555 Phalloidin. Nuclei were labeled by Hoechst 33342.

In the cases of lectin staining, fixed cells were incubated with FITC-labeled lectin (S1 Table) overnight at 4˚C, washed extensively, and then stained with DAPI for 10 min on ice.

Cells were photographed using either an inverted (for cells on cover glass with no EF) or an upright (for cells on plastic EF chambers) Leica TCS SP8 confocal microscope (Leica microsystem). Images were processed using ImageJ. Quantification and comparison of fluorescent intensity were done in images taken in the same batch with the same optical setup and parameters. Lectin binding aggregates stained after permeabilization were quantified by thresholding. Cells were counted using particle analysis function.

Flow cytometry

Infected, challenged, and/or treated macrophages, handled according to the procedures described above, were then incubated with Fc-block (BD, Franklin Lakes, NJ) on ice for 15 min, stained with FITC-labeled lectin (S1 Table) for 1 h on ice, and then stained with Aqua-LIVE/DEAD (Invitrogen, Carlsbad, CA) for 30 min at room temperature. Cells were washed after each step and before being analyzed on a BD Fortessa flow cytometer. Data were analyzed using FlowJo software (Tree Star Inc. Ashland, OR). After gating single cells and live cells, the geometric mean fluorescence intensity and standard error (SE) were collected for each FITC lectin in each condition in addition to Fluorescence Minus One (FMO) for FITC-lectin (no FITC-lectin staining). The geometric mean fluorescence intensity was then standardized across experiments using the following equation:

$$x_{FMO}(MFI) = \frac{x(MFI) - FMO(MFI)}{FMO(SD)}, \quad (2)$$

where $x_{FMO}(MFI)$ is the standardized geometric mean fluorescence intensity of a specific lectin for a specific experiment, $x(MFI)$ is the geometric mean fluorescence intensity of a specific lectin for a specific experiment, $FMO(MFI)$ is the geometric mean fluorescence intensity of the FMO for a specific experiment, and $FMO(SD)$ is the standard deviation of the FMO for a

specific experiment. Standardized geometric mean fluorescent intensities were then plotted and tested for statistical significance (S10 Fig).

Measuring zeta potential

Macrophages were seeded onto 24-well tissue culture plates and infected, challenged, and/or treated following procedures as described above. Cells were fixed in 2% paraformaldehyde and washed with motility buffer (10^{-4} M potassium phosphate buffer at pH 7.0, with 10^{-4} M EDTA) [56]. Cells were then gently collected by scraping with a "policeman" cell scraper, and subsequent measurements were done in motility buffer, except for the macrophages tested for acidic treatment, which were measured in either pH 5.8 medium or pH 7.4 medium as a control. Zeta potential was determined by electrophoretic light scattering at 25˚C with a Zetasizer (Malvern Panalytical Ltd, Malvern, United Kingdom). Zeta potential was calculated in mV, and differences between groups were analyzed by Student *t* test.

Statistics

Galvanotaxis data from representatives of at least 4 independent experiments were routinely presented as mean ± SE, unless stated otherwise. Distributions of macrophage polarity between control and neuraminidase treated or between neutral and acidic conditions were analyzed using χ^2 test. Student *t* test and one-way ANOVA analysis followed by post hoc Tukey HSD test were used for paired or unpaired comparisons among 2 groups or multiple groups (more than 2), respectively.

Supporting information

S1 Table. Selected lectins used in this study.
(DOCX)

S2 Table. Special reagents used in this study.
(DOCX)

S3 Table. Plasmids and *Salmonella* strains used in this study.
(DOCX)

S1 Fig. An ex vivo mouse cecum model for characterization of bioelectrical activities of gut epithelium. (A) Cecum was dissected from C57BL/6 mouse and opened longitudinally along the mesenteric attachment remnant (dotted white line) to avoid incision damage of lymphatic structure that is located under the antimesenteric mucosa near the apex (red circle). (B) Cecum mounted in a custom-made chamber with mucous epithelium facing up on a 30˚ slope of silicone gel and held with the cecum edge with fine metal pins (white arrow heads). (C) Mouse cecal epithelium under a dissecting microscope. FAE—the smooth appearing regions (f), and inter-follicle/surrounding villi (v) are shown. Bar, 5,000 μm. (D) HE stain of a mouse cecum showing the structure of a Peyer's patch. Bar, 200 μm. (E) Magnification of the checked area of panel D showing FAE and inter-follicle and surrounding villi. Double-dotted forks indicate the sites where TEP and J_I were measured. Serosal epithelia served as controls. Bar, 100 μm. FAE, follicle-associated epithelium; HE, hematoxylin–eosin; J_I, electric current density; TEP, transepithelial potential.
(TIF)

S2 Fig. Measuring TEP with microelectrodes. (A) Schematic depicting the microelectrode setup, sites, and procedures of measurement. The measuring microelectrode was impaled through the FAE or surrounding villus epithelial layer (one site at a time), and the circuit was closed by a reference electrode placed in the buffer, representing the lumen. Microelectrode

resistance (S, in which 10 mV equals 1 MΩ) was generated and recorded prior to each impalement to ensure that the tip was neither broken nor obstructed. In some cases, the TEP of infected FAEs were measured as follows: first at the epithelial surface (0 μm), then in stepwise at 50, 100, and 200 μm in depth. The potential typically returns to the baseline of 0 mV after microelectrode withdrawal (W). (B) Two representative traces and a specific equation used to calculate TEP value as a modified mean from S1 Data. In the equation, "a" and "b'"are the early and late values of each impalement in which the electrode was kept in position for at least 60 s. "c" is the reference value immediately after the electrode withdrawal. FAE, follicle-associated epithelium; TEP, transepithelial potential.
(TIF)

S3 Fig. Measuring bioelectric currents using vibrating probes. (A) Schematic of equipment setup and measuring procedures. Under a dissecting microscope, a probe vibrating between 100 and 200 Hz controlled by a micromanipulator is moved from the reference position (R) to the measuring position (M), as close as possible (approximately 20 μm) to the epithelial surface, to detect ionic currents. (B) A picture of a vibrating probe approaching an FAE. (C) Representative traces of bioelectric current measured at the FAE from *Salmonella*-infected or mock-infected control mouse cecum. Probes were calibrated by passing a 1.5 μA cm^{-2} electric current through the measuring buffer in either direction (see S1 Data). By convention, flux of positive charge is used for electric current direction. As in most studies, we used conventional current flow; therefore outward current density is defined as net positive charge leaving the epithelial surface and inward current densities as that entering. Hence, positive values represent net outward current densities, and negative values represent net inward current densities. FAE, follicle-associated epithelium.
(TIF)

S4 Fig. Invasion of cecal epithelium and early dissemination. (A) Ceca, free of contents, MLNs and spleens were dissected in sterile conditions at 16 h or 40 h PI from mice orally infected with *S*. Typhimurium. Bacterial loads were determined by homogenizing each specimen, serial dilution and plating on LB plates. CFUs were calculated by counting bacterial colonies selected with appropriate antibiotics. CFUs lower than the detection limit as indicated by the dotted line were treated as the limit (see S1 Data). (B) HE stain of a cecum section from mice orally infected with *S*. Typhimurium. Disruption of the FAE (arrowhead) and thickened intestinal wall are shown. Bar, 100 μm. CFU, colony forming unit; FAE, follicle-associated epithelium; HE, hematoxylin–eosin; LB, Luria-Bertani; MLN, mesenteric lymph node; PI, post infection; *S*. Typhimurium, *Salmonella enterica* serotype Typhimurium.
(TIF)

S5 Fig. Robust cathodal direction switch in BMDMs infected with different virulent *Salmonella* strains. Mouse BMDMs challenged with 3 virulent *S*. Typhimurium at an MOI of 20, subject to galvanotaxis assay at 16 h PI. EF is 4 V cm^{-1}. Duration is 3 h. (A) Pie charts show percentage of cells migrating to the cathode (red) or to the anode (blue). (B) Overall directionality. $^{**}P < 0.01$ by one-way ANOVA analysis followed by post hoc Tukey HSD test (see S1 Data). (C) Quantification of intracellular bacteria. BMDMs were seeded in 24-well plates and challenged with *S*. Typhimurium at an MOI of 20. Actual inocula were determined by plating and colony counting. Intracellular bacteria at 16 h PI was determined by a gentamycin protection assay. Representative data are presented as log CFU per well, normalized to each inoculum. Bar in SE from triplicate wells (see S1 Data). BMDM, bone marrow-derived macrophage; CFU, colony forming unit; EF, electric field; HSD, honest significant difference; MOI, multiplicity of infection; ns, nonsignificant; PI, post infection; *S*. Typhimurium, *Salmonella enterica*

serotype Typhimurium.
(TIF)

S6 Fig. Determining challenge and/or infection rates by flow cytometry. BMDMs were challenged with 1-μm, red fluorescently labeled polystyrene microspheres or live *S*. Typhimurium IR715 constitutively expressing mCherry at an MOI of 20. Excessive beads and bacteria were removed by washing. Residual extracellular bacteria were killed per gentamycin treatment. (A–E) Representative flow cytograms of a complete experimental design to count target cells using flow cytometry. (A) At 16 h PI, cells were harvested and labeled with Aqua blue and analyzed by flow cytometry. (B) An example of gates used to exclude fragments and cell clumps. (C) Dead cells were excluded by gating Aqua blue signal. Live cells were subject to further cell counting in either PE fluorescence channel for red fluorescent beads (D) or with the dTomato fluorescence channel for *Salmonella* expressing mCherry (E). (F) Representative bar charts showing percentage of macrophages containing intracellular bacteria or beads. BMDM, bone marrow-derived macrophage; MOI, multiplicity of infection; PE, Phycoerythrin; PI, post infection; *S*. Typhimurium, *Salmonella enterica* serotype Typhimurium.
(TIF)

S7 Fig. Phagocytosis (of microspheres) per se does not affect directional migration of macrophages in response to EF. (A) BMDMs were seeded in 96-well glass-bottom plates and challenged with 1-μm microspheres with blue fluorescent at an MOI of 20. Excessive microspheres were removed by washing with medium. At 16 h PI, cells bearing beads (blue) were counted under an epifluorescence microscope. (B) Pie chart of percentage of cells with 0, 1, or up to 5 bead(s) in a typical experiment. (C) Trajectories and (D) directedness of macrophages under an EF of 4 V cm^{-1} in the indicated orientation for 3 h. ns by unpaired Student *t* test (see S1 Data). BMDM, bone marrow-derived macrophage; EF, electric field; MOI, multiplicity of infection; ns, nonsignificant; PI, post infection.
(TIF)

S8 Fig. GNL-binding aggregates in macrophages infected with *Salmonella*. Representative confocal photographs show BMDMs containing red fluorescence-labeled beads or *Salmonella* expressing mCherry (red). Cells were fixed, permeabilized, and stained with DAPI (blue) and FITC-conjugated GNL (green). Cells were outlined in merged photographs (white dashed line). Bar, 20 μm. Note the GNL-binding aggregates inside macrophages containing intracellular *Salmonella* (white arrowhead). BMDM, bone marrow-derived macrophage; FITC, fluorescein isothiocyanate; GNL, Galanthus Nivalis lectin.
(TIF)

S9 Fig. Con A–binding aggregates in macrophages infected by *Salmonella*. (A) Galvanotaxis assays were performed per the rigorous experiment design illustrated in Fig 3A. BMDMs were fixed, permeabilized, and labeled with Alexa Fluor 555 Phalloidin (red) and FITC-conjugated Con A (green), and scanned with an upright confocal microscope. Phagocytosed beads and intracellular bacteria were pseudocolored in yellow. Bar, 20 μm. Control macrophages (left panel) and macrophages challenged with beads (middle panel) were exclusively polarized to the anode with a characteristic morphology: massive actin meshwork in the front and a uropod at the rear. Cells infected with *Salmonella* (right panels) reversed their polarity to the cathode. Note the significant Con A–binding aggregates in macrophages containing intracellular *Salmonella* (white arrowheads). (B) Quantification of macrophages with Con A aggregates. Number of cells counted is indicated inside each bar. $^{***}P < 0.001$ by χ^2 test (see S1 Data). BMDM, bone marrow-derived macrophage; Con A, concanavalin A; FITC, fluorescein isothiocyanate.
(TIF)

S10 Fig. The effects of *Salmonella* infection and neuraminidase treatment on the binding of selected lectins. Box plots showing nMFI of macrophages, either (A) challenged with microspheres and *Salmonella* at 16 h PI or (B) incubated with 0 or 100 mU ml^{-1} neuraminidase for 30 min. Cells were stained with Con A, SNA, GNL, or RCA-1 and analyzed by flow cytometry. Data from 4 independent experiments. ns by unpaired Student *t* test (see S1 Data). Con A, concanavalin A; GNL, Galanthus Nivalis lectin; nMFI, normalized mean fluorescence intensity; ns, nonsignificant; PI, post infection; SNA, Sambucus Nigra lectin; RCA-1, Ricinus Communis Agglutinin I.
(TIF)

S11 Fig. Low pH reduces surface charge and impairs macrophage galvanotaxis. (A) Zeta potential of BMDMs cultured in pH 7.4 or pH 5.8. $^{***}P < 0.001$ by Student *t* test. (B) Rose plots and (C) directedness of BMDMs cultured in pH 7.4 or pH 5.8 exposed to an EF of 4 V cm^{-1} for 3 h. $^{***}P < 0.001$ by Student *t* test. (D) Polarity of BMDMs cultured in pH 7.4 or pH 5.8 and exposed to an EF of 4 V cm^{-1} for 3 h. Data were quantified from a representative of 2 independent experiments. $^{***}P < 0.001$ by χ^2 test (see S1 Data). See also S5 Movie. BMDM, bone marrow-derived macrophage; EF, electric field.
(TIF)

S1 Data. Raw data for graphing.
(XLSX)

S1 Movie. Galvanotaxis of primary mouse macrophages to the anode. Primary mouse PMs migrate to the anode in response to an EF of 4 V cm^{-1} in the indicated orientation for 5 h 50 min. Time-lapse phase contrast images were acquired 1 frame every 5 min. Bar, 50 μm. EF, electric field; PM, peritoneal macrophage.
(AVI)

S2 Movie. Bidirectional galvanotaxis of macrophages challenged with *Salmonella*. Unidirectional migration of PMs to the anode in control (top) (trajectories in highlighted yellow line) and bidirectional migration of macrophages challenged with *S*. Typhimurium (bottom), either to the cathode (trajectories in highlighted red line) or to the anode (trajectories in highlighted yellow line), under an EF of 4 V cm^{-1} in the indicated orientation for 3 h. Time-lapse phase contrast images were acquired 1 frame every 5 min. Bar, 50 μm. EF, electric field; PM, peritoneal macrophage; *S*. Typhimurium, *Salmonella enterica* serotype Typhimurium.
(AVI)

S3 Movie. Infection-dependent directional switch of macrophage galvanotaxis is SPI-1 independent. Galvanotaxis of control macrophages (BMDMs) (top left) or macrophages challenged with microspheres (bottom left) or WT *Salmonella* (bottom right) or SPI-1 mutant *ΔinvA* (top right), under identical conditions at an EF of 4 V cm^{-1} in the indicated orientation for 3 h. Time-lapse phase contrast and fluorescence images were acquired 1 frame every 5 min sequentially and combined using ImageJ. Note the opposite directional migration of macrophages containing beads (blue) or *Salmonella* (red and green) to the anode or to the cathode, respectively. Bar, 50 μm. BMDM, bone marrow-derived macrophage; EF, electric field; SPI-1, *Salmonella* pathogenicity island 1; WT, wild type.
(AVI)

S4 Movie. Treatment with neuraminidase severely impairs macrophage galvanotaxis. Impaired directional migration of BMDMs treated with neuraminidase (left), compared in parallel to the unidirectional migration of control macrophages (right) to the anode under an

EF of 4 V cm^{-1} in the indicated orientation for 2 h 45 min. Time-lapse phase contrast images were acquired 1 frame every 5 min sequentially and combined by using ImageJ. Bar, 100 μm. BMDM, bone marrow-derived macrophage; EF, electric field.
(AVI)

S5 Movie. Low pH impairs macrophage galvanotaxis. Galvanotactic behaviors of BMDMs cultured in acidic condition of pH 5.8 (top) compared, in parallel, to the unidirectional migration of macrophages cultured in pH 7.4 (bottom) to the anode, under an EF of 4 V cm^{-1} in the indicated orientation for 3 h. Time-lapse phase contrast images were acquired 1 frame every 5 min sequentially and combined using ImageJ. Bar, 100 μm. BMDM, bone marrow-derived macrophage; EF, electric field.
(AVI)

Acknowledgments

We are deeply grateful to R. M. Tsolis and A. J. Bäumler for providing the *Salmonella* strains and hosting part of the animal works. We thank S. Hwang and C. Bevins for critical suggestions; V. E. Diaz-Ochoa, B. Young, L. Olney, D. Duo, and I. Brust-Mascher for technical assistance; L. Knodler for sharing an *S*. Typhimurium SL1344 constitutively expressing mCherry; and Robert Heyderman for providing *S*. Typhimurium strain D23580.

Author Contributions

Conceptualization: Yaohui Sun, Alex Mogilner, Min Zhao.

Data curation: Yaohui Sun, Fernando Ferreira, Guillaume Luxardi, Emanual Maverakis.

Formal analysis: Yaohui Sun, Brian Reid, Fernando Ferreira, Guillaume Luxardi, Kan Zhu, Gege Xu, Yuxin Sun.

Funding acquisition: Emanual Maverakis, Alex Mogilner, Min Zhao.

Investigation: Yaohui Sun, Brian Reid, Fernando Ferreira, Guillaume Luxardi, Li Ma, Kristen L. Lokken, Kan Zhu, Gege Xu, Yuxin Sun, Volodymyr Ryzhuk, Min Zhao.

Methodology: Yaohui Sun, Brian Reid, Carlito B. Lebrilla, Emanual Maverakis, Min Zhao.

Project administration: Yaohui Sun, Alex Mogilner, Min Zhao.

Resources: Kristen L. Lokken, Carlito B. Lebrilla, Emanual Maverakis, Alex Mogilner, Min Zhao.

Supervision: Carlito B. Lebrilla, Emanual Maverakis, Alex Mogilner, Min Zhao.

Validation: Yaohui Sun, Emanual Maverakis, Alex Mogilner, Min Zhao.

Visualization: Yaohui Sun, Brian Reid, Fernando Ferreira.

Writing – original draft: Yaohui Sun.

Writing – review & editing: Brian Reid, Fernando Ferreira, Betty P. Guo, Emanual Maverakis, Alex Mogilner, Min Zhao.

References

1. Mowat A.M., Anatomical basis of tolerance and immunity to intestinal antigens. Nat Rev Immunol, 2003. 3(4): p. 331–41. https://doi.org/10.1038/nri1057 PMID: 12669023

2. Jones B.D., Ghori N., and Falkow S., Salmonella typhimurium initiates murine infection by penetrating and destroying the specialized epithelial M cells of the Peyer's patches. J Exp Med, 1994. 180(1): p. 15–23. PMID: 8006579
3. Ohl M.E. and Miller S.I., Salmonella: a model for bacterial pathogenesis. Annu Rev Med, 2001. 52: p. 259–74. https://doi.org/10.1146/annurev.med.52.1.259 PMID: 11160778
4. Shi C. and Pamer E.G., Monocyte recruitment during infection and inflammation. Nat Rev Immunol, 2011. 11(11): p. 762–74. https://doi.org/10.1038/nri3070 PMID: 21984070
5. Serbina N.V., et al., Monocyte-mediated defense against microbial pathogens. Annu Rev Immunol, 2008. 26: p. 421–52. https://doi.org/10.1146/annurev.immunol.26.021607.090326 PMID: 18303997
6. Servant G., et al., Polarization of chemoattractant receptor signaling during neutrophil chemotaxis. Science, 2000. 287(5455): p. 1037–40. PMID: 10669415
7. Devreotes P.N. and Zigmond S.H., Chemotaxis in eukaryotic cells: a focus on leukocytes and Dictyostelium. Annu Rev Cell Biol, 1988. 4: p. 649–86. https://doi.org/10.1146/annurev.cb.04.110188.003245 PMID: 2848555
8. Hensel M., et al., Simultaneous identification of bacterial virulence genes by negative selection. Science, 1995. 269(5222): p. 400–3. PMID: 7618105
9. Ochman H., et al., Identification of a pathogenicity island required for Salmonella survival in host cells. Proc Natl Acad Sci U S A, 1996. 93(15): p. 7800–4. PMID: 8755556
10. Galan J.E., Salmonella interactions with host cells: type III secretion at work. Annu Rev Cell Dev Biol, 2001. 17: p. 53–86. https://doi.org/10.1146/annurev.cellbio.17.1.53 PMID: 11687484
11. Galan J.E. and Curtiss R. 3rd, Cloning and molecular characterization of genes whose products allow Salmonella typhimurium to penetrate tissue culture cells. Proc Natl Acad Sci U S A, 1989. 86(16): p. 6383–7. PMID: 2548211
12. Figueira R., et al., Identification of salmonella pathogenicity island-2 type III secretion system effectors involved in intramacrophage replication of S. enterica serovar typhimurium: implications for rational vaccine design. MBio, 2013. 4(2): p. e00065. https://doi.org/10.1128/mBio.00065-13 PMID: 23592259
13. Celli J., Surviving inside a macrophage: the many ways of Brucella. Res Microbiol, 2006. 157(2): p. 93–8. https://doi.org/10.1016/j.resmic.2005.10.002 PMID: 16364608
14. Chaurasiya S.K. and Srivastava K.K., Downregulation of protein kinase C-alpha enhances intracellular survival of Mycobacteria: role of PknG. BMC Microbiol, 2009. 9: p. 271. https://doi.org/10.1186/1471-2180-9-271 PMID: 20030858
15. Isberg R.R., O'Connor T.J., and Heidtman M., The Legionella pneumophila replication vacuole: making a cosy niche inside host cells. Nat Rev Microbiol, 2009. 7(1): p. 13–24. https://doi.org/10.1038/nrmicro1967 PMID: 19011659
16. Monack D.M., et al., Yersinia signals macrophages to undergo apoptosis and YopJ is necessary for this cell death. Proc Natl Acad Sci U S A, 1997. 94(19): p. 10385–90. PMID: 9294220
17. Vazquez-Torres A., et al., Extraintestinal dissemination of Salmonella by CD18-expressing phagocytes. Nature, 1999. 401(6755): p. 804–8. https://doi.org/10.1038/44593 PMID: 10548107
18. Pagan A.J. and Ramakrishnan L., Immunity and Immunopathology in the Tuberculous Granuloma. Cold Spring Harb Perspect Med, 2015. 5(9).
19. Helaine S., et al., Internalization of Salmonella by macrophages induces formation of nonreplicating persisters. Science, 2014. 343(6167): p. 204–8. https://doi.org/10.1126/science.1244705 PMID: 24408438
20. Shi R. and Borgens R.B., Embryonic Neuroepithelial Sodium-Transport, the Resulting Physiological Potential, and Cranial Development. Developmental Biology, 1994. 165(1): p. 105–116. https://doi.org/10.1006/dbio.1994.1238 PMID: 8088429
21. McCaig C.D., et al., Controlling cell behavior electrically: current views and future potential. Physiol Rev, 2005. 85(3): p. 943–78. https://doi.org/10.1152/physrev.00020.2004 PMID: 15987799
22. Levin M., Pezzulo G., and Finkelstein J.M., Endogenous Bioelectric Signaling Networks: Exploiting Voltage Gradients for Control of Growth and Form. Annu Rev Biomed Eng, 2017. 19: p. 353–387. https://doi.org/10.1146/annurev-bioeng-071114-040647 PMID: 28633567
23. Levin M. and Martyniuk C.J., The bioelectric code: An ancient computational medium for dynamic control of growth and form. Biosystems, 2018. 164: p. 76–93. https://doi.org/10.1016/j.biosystems.2017.08.009 PMID: 28855098
24. Barker A.T., Jaffe L.F., and Vanable J.W., The Glabrous Epidermis of Cavies Contains a Powerful Battery. American Journal of Physiology, 1982. 242(3): p. R358–R366. https://doi.org/10.1152/ajpregu.1982.242.3.R358 PMID: 7065232

25. Zhao M., et al., Electrical signals control wound healing through phosphatidylinositol-3-OH kinase-gamma and PTEN. Nature, 2006. 442(7101): p. 457–60. https://doi.org/10.1038/nature04925 PMID: 16871217

26. Nuccitelli R., A role for endogenous electric fields in wound healing. Curr Top Dev Biol, 2003. 58: p. 1–26. PMID: 14711011

27. Pai V.P., et al., Endogenous gradients of resting potential instructively pattern embryonic neural tissue via Notch signaling and regulation of proliferation. J Neurosci, 2015. 35(10): p. 4366–85. https://doi.org/10.1523/JNEUROSCI.1877-14.2015 PMID: 25762681

28. Ferreira F., et al., Early bioelectric activities mediate redox-modulated regeneration. Development, 2016. 143(24): p. 4582–4594. https://doi.org/10.1242/dev.142034 PMID: 27827821

29. Chiang M.C., Robinson K.R., and Vanable J.W., Electrical Fields in the Vicinity of Epithelial Wounds in the Isolated Bovine Eye. Experimental Eye Research, 1992. 54(6): p. 999–1003. PMID: 1521590

30. Allen G.M., Mogilner A., and Theriot J.A., Electrophoresis of cellular membrane components creates the directional cue guiding keratocyte galvanotaxis. Curr Biol, 2013. 23(7): p. 560–8. https://doi.org/10.1016/j.cub.2013.02.047 PMID: 23541731

31. Zhao Z., et al., Directed migration of human bone marrow mesenchymal stem cells in a physiological direct current electric field. Eur Cell Mater, 2011. 22: p. 344–58. PMID: 22125259

32. Lin F., et al., Lymphocyte electrotaxis in vitro and in vivo. J Immunol, 2008. 181(4): p. 2465–71. PMID: 18684937

33. Moriarty L.J. and Borgens R.B., The effect of an applied electric field on macrophage accumulation within the subacute spinal injury. Restor Neurol Neurosci, 1999. 14(1): p. 53–64. PMID: 12671271

34. Hoare J.I., et al., Electric fields are novel determinants of human macrophage functions. J Leukoc Biol, 2015.

35. Tsolis R.M., et al., Of mice, calves, and men. Comparison of the mouse typhoid model with other Salmonella infections. Adv Exp Med Biol, 1999. 473: p. 261–74. PMID: 10659367

36. Tsolis R.M., et al., How To Become a Top Model: Impact of Animal Experimentation on Human Salmonella Disease Research. Infection and Immunity, 2011. 79(5): p. 1806–1814. https://doi.org/10.1128/IAI.01369-10 PMID: 21343352

37. Mallett C.P., et al., Evaluation of Shigella vaccine safety and efficacy in an intranasally challenged mouse model. Vaccine, 1993. 11(2): p. 190–6. PMID: 8438617

38. Pepe J.C., et al., Pathogenesis of defined invasion mutants of Yersinia enterocolitica in a BALB/c mouse model of infection. Infect Immun, 1995. 63(12): p. 4837–48. PMID: 7591144

39. Heesemann J., Gaede K., and Autenrieth I.B., Experimental Yersinia enterocolitica infection in rodents: a model for human yersiniosis. APMIS, 1993. 101(6): p. 417–29. PMID: 8363822

40. Law R.J., et al., In vitro and in vivo model systems for studying enteropathogenic Escherichia coli infections. Cold Spring Harb Perspect Med, 2013. 3(3): p. a009977. https://doi.org/10.1101/cshperspect.a009977 PMID: 23457294

41. Reid B., Nuccitelli R., and Zhao M., Non-invasive measurement of bioelectric currents with a vibrating probe. Nat Protoc, 2007. 2(3): p. 661–9. https://doi.org/10.1038/nprot.2007.91 PMID: 17406628

42. Sun Y.H., et al., Airway Epithelial Wounds in Rhesus Monkey Generate Ionic Currents That Guide Cell Migration to Promote Healing. J Appl Physiol, 2011.

43. Reid B., et al., Wound healing in rat cornea: the role of electric currents. FASEB J, 2005. 19(3): p. 379–86. https://doi.org/10.1096/fj.04-2325com PMID: 15746181

44. Reid B., Song B., and Zhao M., Electric currents in Xenopus tadpole tail regeneration. Developmental Biology, 2009. 335(1): p. 198–207. https://doi.org/10.1016/j.ydbio.2009.08.028 PMID: 19733557

45. Clarke L.L., A guide to Ussing chamber studies of mouse intestine. Am J Physiol Gastrointest Liver Physiol, 2009. 296(6): p. G1151–66. https://doi.org/10.1152/ajpgi.90649.2008 PMID: 19342508

46. Deutsch A., et al., An uncommon presentation of Salmonella. Pediatr Emerg Care, 1996. 12(4): p. 285–7. PMID: 8858654

47. Tarnawski A. and Ivey K.J., Transmucosal potential-difference profile in rat upper gastrointestinal tract. A simple model for testing gastric effects of pharmacologic agents. Can J Physiol Pharmacol, 1978. 56(3): p. 471–3. PMID: 667721

48. Larsson M.H., et al., Elevated motility-related transmucosal potential difference in the upper small intestine in the irritable bowel syndrome. Neurogastroenterol Motil, 2007. 19(10): p. 812–20. https://doi.org/10.1111/j.1365-2982.2007.00941.x PMID: 17883433

49. Gustke R.F., et al., Human intestinal potential difference: recording method and biophysical implications. J Physiol, 1981. 321: p. 571–82. PMID: 6802960

50. Feil W., et al., Repair of rabbit duodenal mucosa after acid injury in vivo and in vitro. Gastroenterology, 1987. 92(6): p. 1973–86. PMID: 3569771

51. Okada Y., Irimajiri A., and Inouye A., Electrical properties and active solute transport in rat small intestine. II. Conductive properties of transepithelial routes. J Membr Biol, 1977. 31(3): p. 221–32. PMID: 845930

52. Okada Y., et al., Electrical properties and active solute transport in rat small intestine. I. Potential profile changes associated with sugar and amino acid transports. J Membr Biol, 1977. 31(3): p. 205–19. PMID: 845929

53. Wang J.Y., Yuan L.Z., and Wang M.D., [Effects of sodium artesunate on electrical properties and Na+, K(+)-ATPase activities of mouse small intestine]. Zhongguo Yao Li Xue Bao, 1990. 11(4): p. 335–7. PMID: 1966574

54. Amat C., et al., Electrical properties of the intestinal mucosa of the chicken and the effects of luminal glucose. Poultry Science, 1999. 78(8): p. 1126–1131. https://doi.org/10.1093/ps/78.8.1126 PMID: 10472838

55. Sundell K.S. and Sundh H., Intestinal fluid absorption in anadromous salmonids: importance of tight junctions and aquaporins. Front Physiol, 2012. 3: p. 388. https://doi.org/10.3389/fphys.2012.00388 PMID: 23060812

56. Adler J. and Shi W., Galvanotaxis in bacteria. Cold Spring Harb Symp Quant Biol, 1988. 53 Pt 1: p. 23–5.

57. Gebert A., et al., The development of M cells in Peyer's patches is restricted to specialized dome-associated crypts. American Journal of Pathology, 1999. 154(5): p. 1573–1582. https://doi.org/10.1016/S0002-9440(10)65410-7 PMID: 10329609

58. Buch E., et al., Transmucosal potential difference in experimental colitis in rats. Inflammation, 1995. 19(4): p. 445–55. PMID: 7558249

59. Zhao M., Electrical fields in wound healing-An overriding signal that directs cell migration. Semin Cell Dev Biol, 2009. 20(6): p. 674–82. https://doi.org/10.1016/j.semcdb.2008.12.009 PMID: 19146969

60. Santos R.L., et al., Life in the inflamed intestine, Salmonella style. Trends Microbiol, 2009. 17(11): p. 498–506. https://doi.org/10.1016/j.tim.2009.08.008 PMID: 19819699

61. Winter S.E., et al., Gut inflammation provides a respiratory electron acceptor for Salmonella. Nature, 2010. 467(7314): p. 426–9. https://doi.org/10.1038/nature09415 PMID: 20864996

62. Sawyer P.N. and Pate J.W., Electrical potential differences across the normal aorta and aortic grafts of dogs. Am J Physiol, 1953. 175(1): p. 113–7. https://doi.org/10.1152/ajplegacy.1953.175.1.113 PMID: 13114362

63. Sawyer P.N., Pate J.W., and Weldon C.S., Relations of abnormal and injury electric potential differences to intravascular thrombosis. Am J Physiol, 1953. 175(1): p. 108–12. https://doi.org/10.1152/ajplegacy.1953.175.1.108 PMID: 13114361

64. Sawyer P.N., Suckling E.E., and Wesolowski S.A., Effect of small electric currents on intravascular thrombosis in the visualized rat mesentery. Am J Physiol, 1960. 198: p. 1006–10. https://doi.org/10.1152/ajplegacy.1960.198.5.1006 PMID: 14442116

65. Sawyer P.N. and Wesolowski S.A., The electric current of injured tissue and vascular occlusion. Ann Surg, 1961. 153: p. 34–42. PMID: 13746959

66. Kaufmann S.H. and Schaible U.E., Antigen presentation and recognition in bacterial infections. Curr Opin Immunol, 2005. 17(1): p. 79–87. https://doi.org/10.1016/j.coi.2004.12.004 PMID: 15653315

67. Wang C., et al., Characterization of murine macrophages from bone marrow, spleen and peritoneum. BMC Immunol, 2013. 14: p. 6. https://doi.org/10.1186/1471-2172-14-6 PMID: 23384230

68. Valdez Y., Ferreira R.B., and Finlay B.B., Molecular mechanisms of Salmonella virulence and host resistance. Curr Top Microbiol Immunol, 2009. 337: p. 93–127. https://doi.org/10.1007/978-3-642-01846-6_4 PMID: 19812981

69. Baumler A.J., et al., Synergistic effect of mutations in invA and lpfC on the ability of Salmonella typhimurium to cause murine typhoid. Infect Immun, 1997. 65(6): p. 2254–9. PMID: 9169760

70. Finkelstein E.I., et al., Electric field-induced polarization of charged cell surface proteins does not determine the direction of galvanotaxis. Cell Motil Cytoskeleton, 2007. 64(11): p. 833–46. https://doi.org/10.1002/cm.20227 PMID: 17685443

71. McLaughlin S. and Poo M.M., The role of electro-osmosis in the electric-field-induced movement of charged macromolecules on the surfaces of cells. Biophys J, 1981. 34(1): p. 85–93. https://doi.org/10.1016/S0006-3495(81)84838-2 PMID: 6894257

72. Silva Filho F.C., et al., Surface charge of resident, elicited, and activated mouse peritoneal macrophages. J Leukoc Biol, 1987. 41(2): p. 143–9. PMID: 3468193

73. Park D., et al., Salmonella Typhimurium Enzymatically Landscapes the Host Intestinal Epithelial Cell (IEC) Surface Glycome to Increase Invasion. Mol Cell Proteomics, 2016. 15(12): p. 3653–3664. https://doi.org/10.1074/mcp.M116.063206 PMID: 27754876

74. Liu C.K., Wei G., and Atwood W.J., Infection of glial cells by the human polyomavirus JC is mediated by an N-linked glycoprotein containing terminal alpha(2–6)-linked sialic acids. J Virol, 1998. 72(6): p. 4643–9. PMID: 9573227

75. Foster J.W., Acid stress responses of Salmonella and E-coli: Survival mechanisms, regulation, and implications for pathogenesis. Journal of Microbiology, 2001. 39(2): p. 89–94.

76. Foster J.W. and Hall H.K., Adaptive acidification tolerance response of Salmonella typhimurium. J Bacteriol, 1990. 172(2): p. 771–8. PMID: 2404956

77. Allam U.S., et al., Acidic pH induced STM1485 gene is essential for intracellular replication of Salmonella. Virulence, 2012. 3(2): p. 122–135. https://doi.org/10.4161/viru.19029 PMID: 22460643

78. Beuzon C.R., et al., pH-dependent secretion of SseB, a product of the SPI-2 type III secretion system of Salmonella typhimurium. Mol Microbiol, 1999. 33(4): p. 806–16. PMID: 10447889

79. Chakraborty S., Mizusaki H., and Kenney L.J., A FRET-based DNA biosensor tracks OmpR-dependent acidification of Salmonella during macrophage infection. PLoS Biol; 2015:13:4. e1002116. https://doi.org/10.1371/journal.pbio.1002116 PMID: 25875623

80. Cohen D.J., Nelson W.J., and Maharbiz M.M., Galvanotactic control of collective cell migration in epithelial monolayers. Nat Mater, 2014. 13(4): p. 409–17. https://doi.org/10.1038/nmat3891 PMID: 24608142

81. Sun Y., et al., Keratocyte fragments and cells utilize competing pathways to move in opposite directions in an electric field. Curr Biol, 2013. 23(7): p. 569–74. https://doi.org/10.1016/j.cub.2013.02.026 PMID: 23541726

82. McLaughlin L.M., et al., The Salmonella SPI2 effector SseI mediates long-term systemic infection by modulating host cell migration. PLoS Pathog; 2009:5:11: e1000671. https://doi.org/10.1371/journal.ppat.1000671 PMID: 19956712

83. Figueira R. and Holden D.W., Functions of the Salmonella pathogenicity island 2 (SPI-2) type III secretion system effectors. Microbiology, 2012. 158(Pt 5): p. 1147–61. https://doi.org/10.1099/mic.0.058115-0 PMID: 22422755

84. Lombard V., et al., The carbohydrate-active enzymes database (CAZy) in 2013. Nucleic Acids Res, 2014. 42(Database issue): p. D490–5. https://doi.org/10.1093/nar/gkt1178 PMID: 24270786

85. Arabyan N., et al., Salmonella Degrades the Host Glycocalyx Leading to Altered Infection and Glycan Remodeling. Sci Rep, 2016. 6: p. 29525. https://doi.org/10.1038/srep29525 PMID: 27389966

86. Weber A.N., Morse M.A., and Gay N.J., Four N-linked glycosylation sites in human toll-like receptor 2 cooperate to direct efficient biosynthesis and secretion. J Biol Chem, 2004. 279(33): p. 34589–94. https://doi.org/10.1074/jbc.M403830200 PMID: 15173186

87. da Silva Correia J. and Ulevitch R.J., MD-2 and TLR4 N-linked glycosylations are important for a functional lipopolysaccharide receptor. J Biol Chem, 2002. 277(3): p. 1845–54. https://doi.org/10.1074/jbc.M109910200 PMID: 11706042

88. Crump J.A., et al., Part I. Analysis of data gaps pertaining to Salmonella enterica serotype Typhi infections in low and medium human development index countries, 1984–2005. Epidemiol Infect, 2008. 136(4): p. 436–48. https://doi.org/10.1017/S0950268807009338 PMID: 17686194

89. Erickson C.A. and Nuccitelli R., Embryonic fibroblast motility and orientation can be influenced by physiological electric fields. J Cell Biol, 1984. 98(1): p. 296–307. PMID: 6707093

90. Wu L., et al., The G protein beta subunit is essential for multiple responses to chemoattractants in Dictyostelium. J Cell Biol, 1995. 129(6): p. 1667–75. PMID: 7790362

91. Zhao M., et al., Genetic analysis of the role of G protein-coupled receptor signaling in electrotaxis. J Cell Biol, 2002. 157(6): p. 921–7. https://doi.org/10.1083/jcb.200112070 PMID: 12045182

92. Gao R.C., et al., A large-scale screen reveals genes that mediate electrotaxis in Dictyostelium discoideum. Science Signaling, 2015. 8(378).

93. Gordon S.V. and Parish T., Microbe Profile: Mycobacterium tuberculosis: Humanity's deadly microbial foe. Microbiology, 2018. 164(4): p. 437–439. https://doi.org/10.1099/mic.0.000601 PMID: 29465344

94. Luxardi G., et al., Single cell wound generates electric current circuit and cell membrane potential variations that requires calcium influx. Integr Biol (Camb), 2014.

95. Knodler L.A., et al., Dissemination of invasive Salmonella via bacterial-induced extrusion of mucosal epithelia. Proc Natl Acad Sci U S A, 2010. 107(41): p. 17733–8. https://doi.org/10.1073/pnas.1006098107 PMID: 20876119

96. Knodler L.A., et al., Noncanonical inflammasome activation of caspase-4/caspase-11 mediates epithelial defenses against enteric bacterial pathogens. Cell Host Microbe, 2014. 16(2): p. 249–56. https://doi.org/10.1016/j.chom.2014.07.002 PMID: 25121752

97. Celli J., Salcedo S.P., and Gorvel J.P., Brucella coopts the small GTPase Sar1 for intracellular replication. Proc Natl Acad Sci U S A, 2005. 102(5): p. 1673–8. https://doi.org/10.1073/pnas.0406873102 PMID: 15632218

98. de Jong M.F., et al., Identification of VceA and VceC, two members of the VjbR regulon that are translocated into macrophages by the Brucella type IV secretion system. Mol Microbiol, 2008. 70(6): p. 1378–96. https://doi.org/10.1111/j.1365-2958.2008.06487.x PMID: 19019140

99. O'Brien A.D., Rosenstreich D.L., and Taylor B.A., Control of natural resistance to Salmonella typhimurium and Leishmania donovani in mice by closely linked but distinct genetic loci. Nature, 1980. 287 (5781): p. 440–2. PMID: 7001248

100. Okoro C.K., et al., Signatures of adaptation in human invasive Salmonella Typhimurium ST313 populations from sub-Saharan Africa. PLoS Negl Trop Dis. 2015:9:3: e0003611. https://doi.org/10.1371/journal.pntd.0003611 PMID: 25803844

101. Carden S.E., et al., Pseudogenization of the Secreted Effector Gene sseI Confers Rapid Systemic Dissemination of S. Typhimurium ST313 within Migratory Dendritic Cells. Cell Host Microbe, 2017. 21(2): p. 182–194. https://doi.org/10.1016/j.chom.2017.01.009 PMID: 28182950

102. Worley M.J., et al., Salmonella typhimurium disseminates within its host by manipulating the motility of infected cells. Proc Natl Acad Sci U S A, 2006. 103(47): p. 17915–20. https://doi.org/10.1073/pnas.0604054103 PMID: 17095609

103. Zhang X., Goncalves R., and Mosser D.M., The isolation and characterization of murine macrophages. Curr Protoc Immunol, 2008. Chapter 14: p. Unit 14 1.

104. Sun Y.H., et al., virB-Mediated survival of Brucella abortus in mice and macrophages is independent of a functional inducible nitric oxide synthase or NADPH oxidase in macrophages. Infect Immun, 2002. 70(9): p. 4826–32. https://doi.org/10.1128/IAI.70.9.4826-4832.2002 PMID: 12183526

105. Nakajima K., et al., KCNJ15/Kir4.2 couples with polyamines to sense weak extracellular electric fields in galvanotaxis. Nat Commun, 2015. 6: p. 8532. https://doi.org/10.1038/ncomms9532 PMID: 26449415

106. Zhao M., et al., Orientation and directed migration of cultured corneal epithelial cells in small electric fields are serum dependent. J Cell Sci, 1996. 109 (Pt 6): p. 1405–14.

107. Song B., et al., Application of direct current electric fields to cells and tissues in vitro and modulation of wound electric field in vivo. Nat Protoc, 2007. 2(6): p. 1479–89. https://doi.org/10.1038/nprot.2007.205 PMID: 17545984

108. Tai G., et al., Electrotaxis and wound healing: experimental methods to study electric fields as a directional signal for cell migration. Methods Mol Biol, 2009. 571: p. 77–97. https://doi.org/10.1007/978-1-60761-198-1_5 PMID: 19763960

109. Gruler H. and Nuccitelli R., Neural crest cell galvanotaxis: new data and a novel approach to the analysis of both galvanotaxis and chemotaxis. Cell Motil Cytoskeleton, 1991. 19(2): p. 121–33. https://doi.org/10.1002/cm.970190207 PMID: 1878979

IV. *SPATIOTEMPORAL OXYGEN DYNAMICS IN CORNEA CORRELATE WITH WOUND HEALING VIA REACTIVE OXYGEN SPECIES*

Manuscript overview

A spin-off from my preliminary results (partially published in the technical publication (Chapter VI)), this research was carried out by a visiting postdoc who, for two years, developed the study into a publication capable manuscript. Since the manuscript is in preparation for publication, I will only briefly describe its main findings. Using the cutting-edge micro-optrode, this study revealed spatiotemporal oxygen dynamics in intact and wounded corneas that contribute to its physiology and healing. Reactive oxygen species appear to mediate the effect of dynamic oxygen influx in wound healing. O_2 and ROS variations correlate with cell migration and proliferation required for the successful healing. The findings unveil the redox measurement and contribution to corneal wound healing, presenting potential therapeutic implications.

Manuscript contributions

The manuscript has not yet a section detailing the author contributions and since I am not the first author, I will only mention my contribution to it. I helped in the conception of the study an in its designing. My preliminary results were used in the Supplementary information. Also, I contributed to the outline of the manuscript and revise and edit it thoroughly.

Manuscript reprint

Ma, L., Ferreira, F., Reid, B., Guo, L. and Zhao, M. (2019). Optical microsensing reveals spatiotemporal oxygen dynamics in cornea that affect wound healing via reactive oxygen species.

(In preparation; citation subject to change; not reprinted to not compromise journals' criterion for original submission)

V. *ADDENDA* TO THE PUBLICATION *REAL-TIME PHYSIOLOGICAL MEASUREMENTS OF OXYGEN USING A NON-INVASIVE SELF-REFERENCING MICRO-OPTRODE*

Journal cover

Prior to press, we were invited by the journal *Nature Protocols* to submit covers for the issue publishing the paper. The cover was made by the following non-authors: Shooting and post-processing by Shengzhou Shan (Department of Dermatology, Institute for Regenerative Cures, University of California, Davis, CA, USA; Department of Plastic and Reconstructive Surgery, Shanghai Ninth People's Hospital, Shanghai Jiao Tong University School of Medicine, Shanghai, China), and design and shooting by Qin Sun (Department of Dermatology, Institute for Regenerative Cures, University of California, Davis, CA, USA; School of Life Science, Yunnan Normal University, Yunnan, China). Cover awaits selection (if selected, cover will have open access).

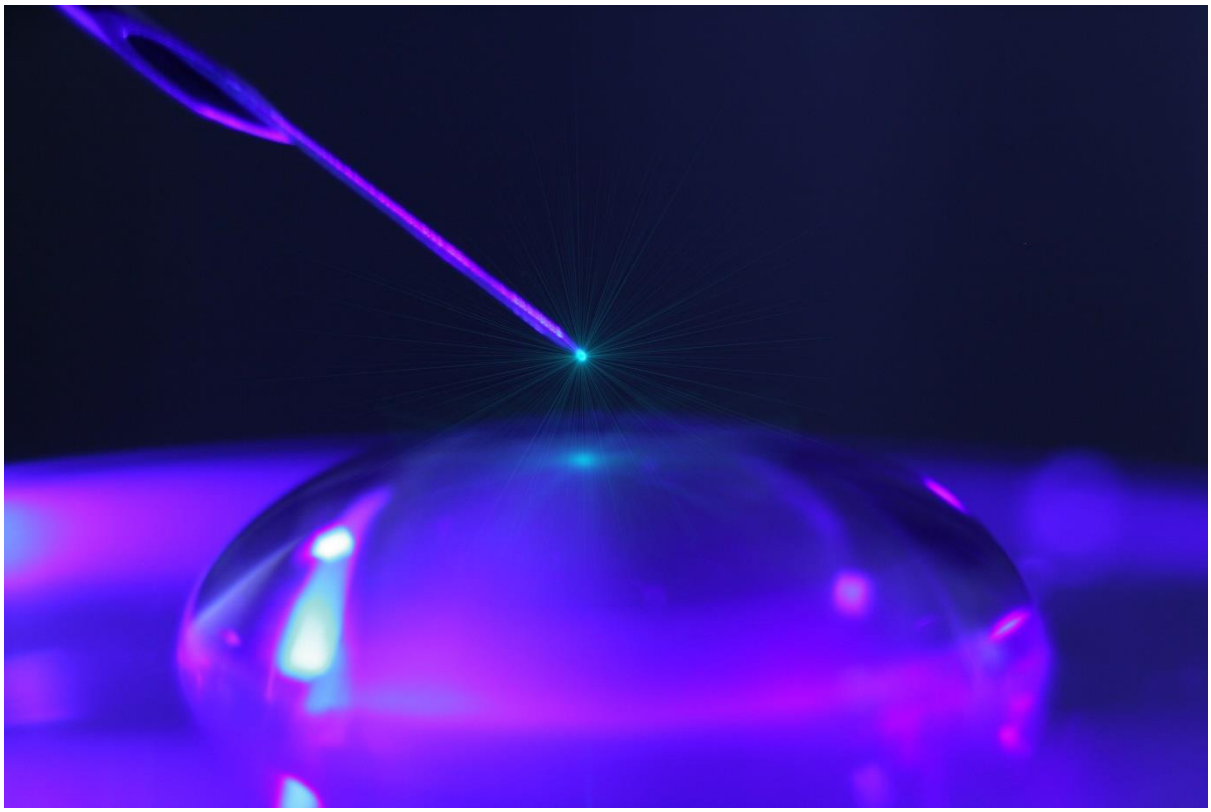

A flashing micro-optrode hangs over a medium drop and is ready to assess oxygen dynamics by fluorescence quenching. Flashing intensity was highlighted using an image manipulation editor, for artistic impression.

Journal editorial summary

Oxygen plays key roles in bioenergetics, metabolism, signalling pathways and developmental biology. This protocol describes how to perform quantitative oxygen flux measurements on cells, *ex vivo* tissues and on various model animals *in vivo*.

Journal transparent peer review

Following the acceptance of the paper, we opted in to the journal's policy on transparent peer review. The reviewers' comments and our point-by-point response and rebuttal are open to provide readers with the discussion undertaken prior to manuscript publication. File will be open access upon publication as supplementary material.

VI. *ADDENDA* TO THE PUBLICATION *EARLY BIOELECTRIC ACTIVITIES MEDIATE REDOX-MODULATED REGENERATION*

Journal cover

After the advance online publication (November 8, 2016) and prior to press, we were invited by the journal *Development* to submit covers (24×23 cm) for the issue (no. 24; December 2016) publishing the paper. I designed and created some variations of a single theme cover and, after comments from all authors, we submitted two covers with the same legend (below). Covers were not selected.

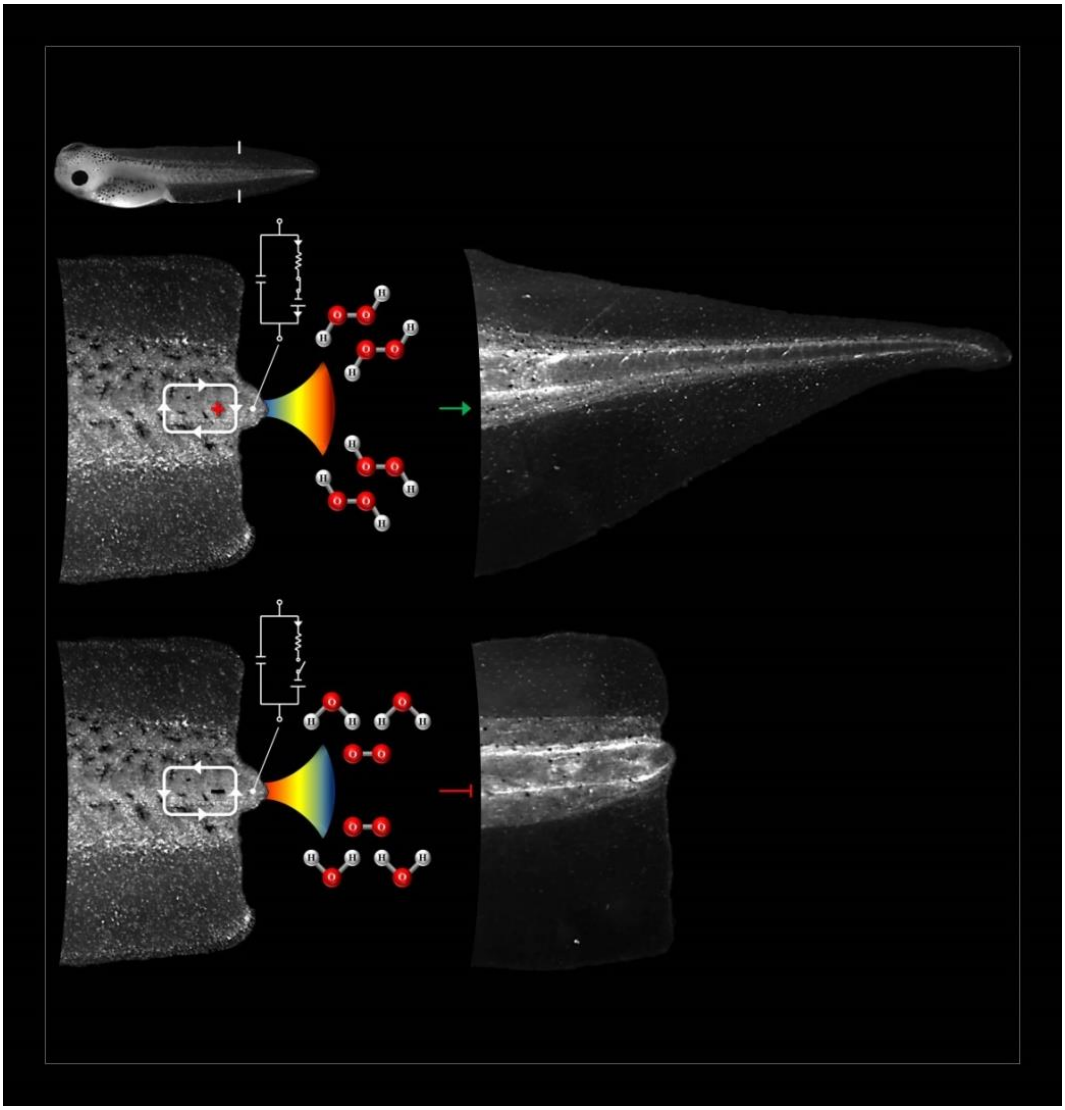

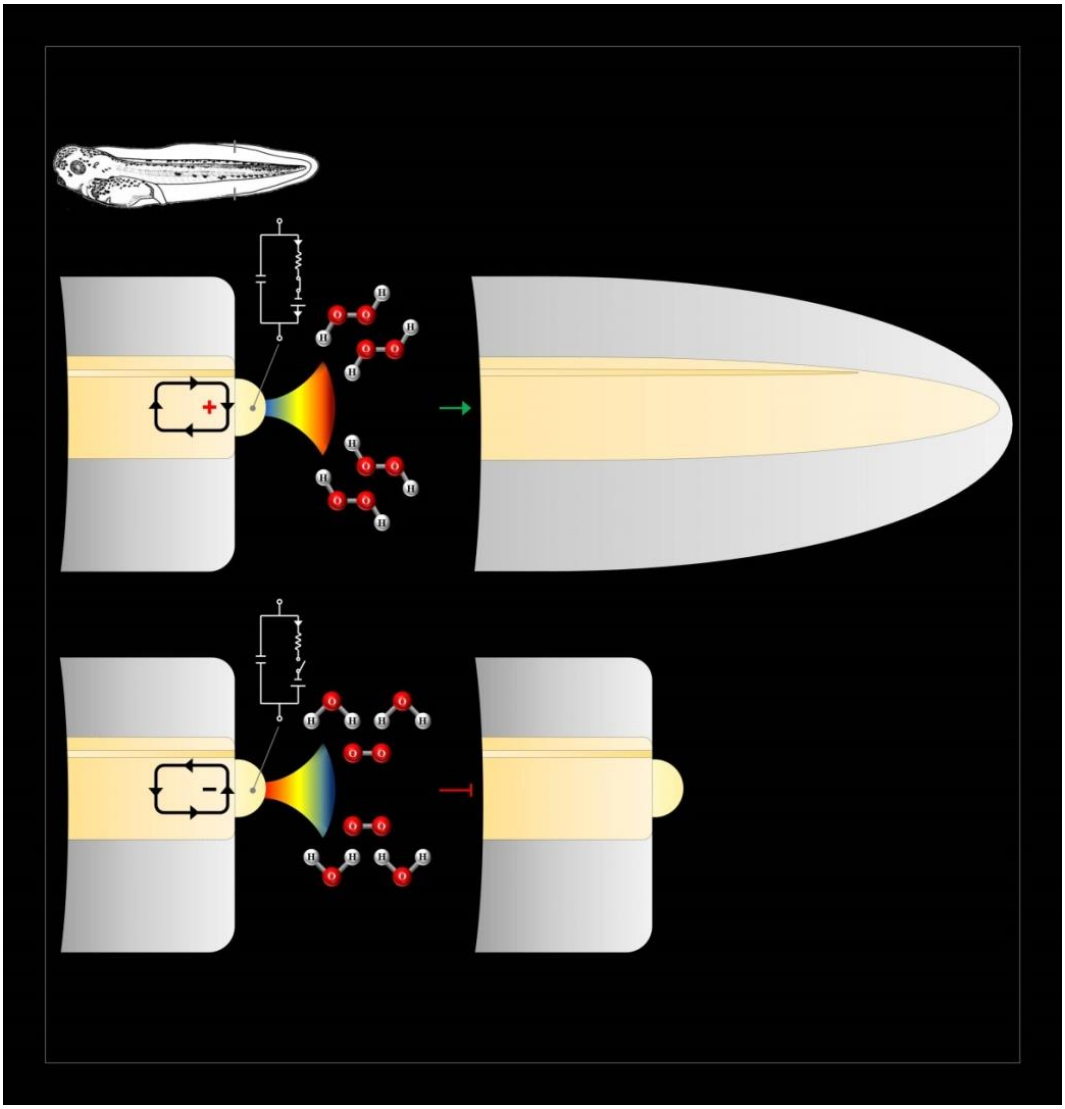

Biochemical and bioelectrical integration during regeneration. Normal redox state or exogenous hydrogen peroxide (H_2O_2) switch electric current (J_I) and field (EF) reversals. Reversals do not occur in suppressed redox state or non-regenerative refractory period. The hallmark H_2O_2-switched J_I reversal modulates regeneration. Heat map, J_I; circuits, EF and electrical equivalent circuit.

Journal editor's highlight

The paper was selected to feature in the 'IN THIS ISSUE' section of the *Development* journal. This section intends to highlight and extract the research findings of the 3-6 selected papers, making them accessible to the broader readership of the developmental and regenerative biology communities. Importantly, the synthesis text is forward to alert other journals and the press media of the content in the forthcoming issue. The piece was written and/or supervised by the journal's executive editor at the time (Katherine Brown) and was revised and slightly edited by the paper authors. The final and printed version is the following:

Sparking regeneration with ROS

URL: http://dev.biologists.org/content/143/24/e2403

During regeneration, multiple signalling pathways act to coordinate the various processes required to regenerate an injured organ or body part. Both reactive oxygen species (ROS) and electric currents have been shown to modulate regeneration, but how they exert their effects, and whether their activities might intersect, is poorly understood. Here (p. 4582), Fernando Ferreira, Min Zhao and colleagues set out to address the potential interplay between ROS and bioelectric phenomena using the *Xenopus* tadpole tail regeneration model. They uncover a dual role for NADPH oxidases in regulating bioelectric activities: NADPH oxidase-driven electron flow induces membrane depolarisation, while the hydrogen peroxide produced leads to activation of sodium channels in cell membranes of the regeneration bud, with consequent effects on transepithelial potential and electric currents that mediate regeneration. Moreover, external application of hydrogen peroxide can induce tail regeneration during the refractory period in the tadpole's life – when regeneration is normally blocked – as well as the formation of ectopic tails at injury sites during the regenerative period. Although the mechanisms by which bioelectric activities might modulate the cellular processes required for regeneration still require further investigation, this work links two previously unconnected regulators of regeneration and provides convincing evidence for redox-bioelectric integration in this context.

Interview with The Node: overview

Following the acceptance of the paper, I and Min Zhao (thesis advisor) were invited for an interview with *The Node* to feature in the series 'The People Behind the Papers', to be published online simultaneously (or very shortly after) with the paper. *The Node*, launched in 2010 and hosted by *Development* journal, is a non-commercial information resource and community news and views site for and by developmental biologists. The publication is focused to highlight and divulge the latest developmental and regenerative biology research in accessible language. 'The People Behind the Papers' is an email-based interview series that generally disclosures the scientific biography of the authors, how they come to meet and to conceive the work, the paper findings, and the future perspectives regarding the study and the authors. The series aims to conduct one interview per issue and associate a link of the interview on the journal's website.

Interview with *The Node*: reprint

The people behind the papers: Fernando Ferreira & Min Zhao

URL: http://thenode.biologists.com/people-behind-papers-8/interview

Posted by the Node Interviews on December 14th, 2016 (Normalized style)

Today's paper comes from the final issue of Development for 2016, and reveals a link between bioelectricity and reactive oxygen species during tail regeneration in *Xenopus*. We caught up with first author Fernando Ferreira and his advisor Min Zhao, Professor in Dermatology at UC Davis.

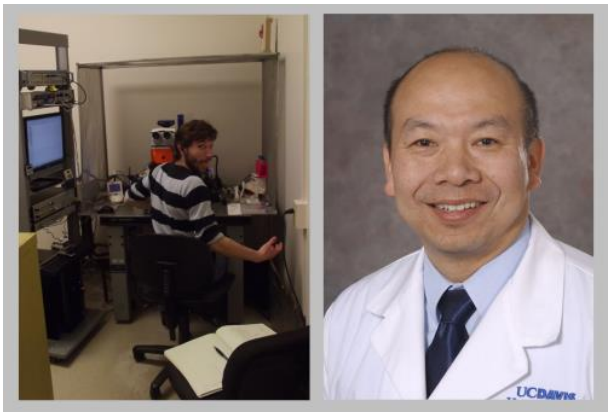

Fernando and Min.

So Min, can you give me the brief history of your lab, and what questions you are interested in?

MZ The main goal of my lab is to electrically heal wounds and regenerate tissues. Demonstrated over one and half centuries ago, the minute electric signals naturally produced at wounds are very poorly understood and appreciated. Epithelial cells and many other types of cells follow the guidance of the electric signals and migrate and grow directionally. We demonstrated that in epithelial sheets, the guidance effect of physiological electric signals overrides other co-existing guidance cues.

I had medical training in trauma with Zhengguo Wang, one of the founding fathers of trauma surgery in China. I then had research training with Geoffrey Burnstock at University College London, and Colin McCaig and John Forrester at University of Aberdeen. I started my lab at the University of Aberdeen with a Welcome Trust University Award and held professor/personal chair and honorary consultant positions at University of Aberdeen and Aberdeen Royal Infirmary (Scotland), before moving to University of California at Davis to take up a professorship in the Department of Dermatology and Department of Ophthalmology.

Supported by grants from NIH, NSF, California Institute of Regenerative Medicine and other federal and state agencies, my lab is interested in answering the following questions:

1. How do cells sense and respond to physiological electric fields?
2. How are the wound electric currents/fields produced and regulated?
3. Can we exploit the "electrical signalling" to enhance wound healing and induce regeneration?

And Fernando, how did you end up in Min's lab?

FF During my Master's degree, my adviser and Min met in an international conference. In the discussion they mentioned me; on arrival, my adviser told me that Min's lab would be willing to host

me and that could be an opportunity that I probably should not let escape. By this time, I already knew and admired much of Min's work and thought it could be an excellent opportunity to test some old and new ideas falling within the framework of his lab. Thus, naturally, I readily set the goal to work with him.

Meanwhile, however, I applied for other closer positions, but I was oddly satisfied or left with a bitter-sweet feeling after receiving no or negative responses; I guess that this proved that I really wanted to join Min's lab. Things aren't straightforward though, and after a considerable despair for not getting a 1 year long Fulbright grant to visit Min's lab, I took a risky move and entered a Ph.D. programme in the Portuguese university (Minho) without funding. I was working in non-scientific part-time jobs to cover the tuition fees and, simultaneously, applied for a studentship grant sponsored by the Portuguese Science and Technology Foundation (FCT). With the Fulbright denial lingering in my mind, I had low expectations. Fortunately, I got the grant and after a way too long "quarantine" process (~8 months), I finally joined the lab in the USA...

It is pressing and fair to recognise that after joining the University of Minho, I received precious encouragement and help from the Ph.D. programme professors and especially my supervisor Andreia Gomes, who accepted me without second thought, always supported me and gifted me with wise advice. All the happiness and sorrow of this journey, allied with the sheer size of the Atlantic Ocean plus the departure delay, made the farewell from family particularly hard; it is a natural cliché to be grateful for family care and support, and undoubtedly I am.

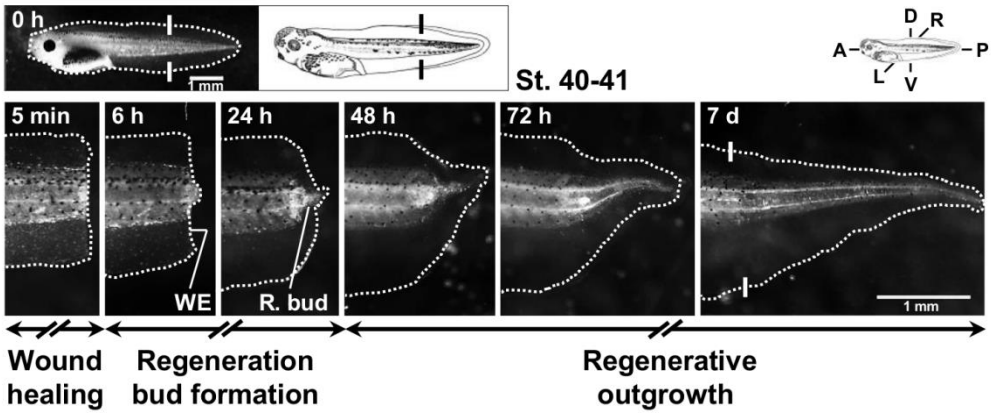

The process of regeneration over time in *Xenopus* tadpoles, from Figure 1 in the paper.

Do you think bioelectricity outside of the nervous system is adequately appreciated in developmental and regenerative biology?

MZ Bioelectricity is not as adequately appreciated in developmental and regenerative biology as I'd wish, which I believe perhaps is due to the following. Research in bioelectricity (not the traditional electrophysiology) was restarted by Lionel Jaffe and his students Richard Borgens, Richard Nuccitelli and Ken Robinson with some wonderful results from the 1960s-1990s. This happened in an era that

coincided with the revolutionary discovery of the double helix and the great advances in biology that ensued. Genetic, molecular and biochemical mechanisms are in the lime light of biology, including developmental and regenerative biology. Great advances in technologies and tools in genetics and molecular biology provided developmental and regenerative biologists with powerful tools to understand some of the most fundamental mechanisms. Research technology in bioelectricity, however, has since stayed virtually unchanged. It is also worthwhile to mention that some "charlatan claims" in bioelectricity have tarnished and discredited this field.

"Great advances in technologies and tools in genetics and molecular biology provided developmental and regenerative biologists with powerful tools to understand some of the most fundamental mechanisms. Research technology in bioelectricity, however, has since stayed virtually unchanged"

Bioelectricity is therefore off the radar of most developmental and regenerative biologists. Very few laboratories have continued the efforts in bioelectricity, for example Michael Levin at Tufts University, USA and Colin McCaig at University of Aberdeen, Scotland. Some of their research has provided very impressive results in combination with genetics and molecular biology.

Was anything known about the connection between reactive oxygen species (ROS) and bioelectricity in regeneration before your paper?

MZ & FF Strictly in regeneration, we couldn't find studies demonstrating a direct connection between redox and bioelectric states. When we started this study we already knew – from decades old evidence – that electric currents were important for a successful regeneration, especially in amphibians; however, no evidence existed about ROS (excluding wound healing in small-scale injuries). Then, a wave of papers came, showing that ROS were also required for regeneration in widespread models, such as *Xenopus* tadpoles and adult zebrafish. The link between ROS and bioelectricity (membrane potential, transepithelial potential (TEP) and electric currents/fields), remained, however, elusive. In the regeneration field, our study thus appeared in a timely fashion to link the fairly old but re-emerging field of bioelectricity with the emergent field of redox biology.

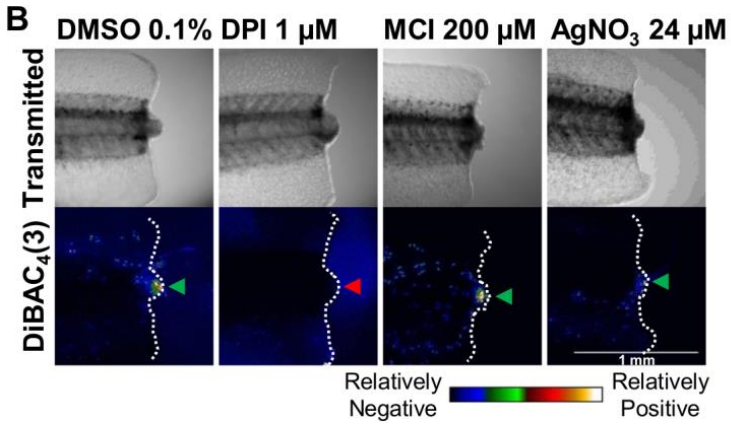

Assaying changes membrane potential following drug treatments, from Figure 2 in the paper.

Could you give us the key results of your paper in a paragraph?

MZ & FF The general take home message is that redox and bioelectric activities interact during regeneration. More specifically, there is a two-way regulation of bioelectric activities by NADPH oxidases: the driven electron flow depolarizes the membrane potential, whereas the produced H_2O_2 increases the magnitude of TEP (positive inside) and switches the direction of electric current (to inward) in the regeneration bud. The depletion of ROS during the regenerative period mimics the abnormally low TEP and non-reversed electric currents measured during the refractory (non-regenerative) period. The external application of H_2O_2 for a short period normalizes the bioelectric activities and, by doing so, rescues and induces regeneration. External H_2O_2 was also inductive enough to form ectopic tails in injuries severing the spinal cord during the regenerative period. Finally and molecularly speaking, H_2O_2 regulates voltage-gated Na^+ channels in order to modulate regeneration.

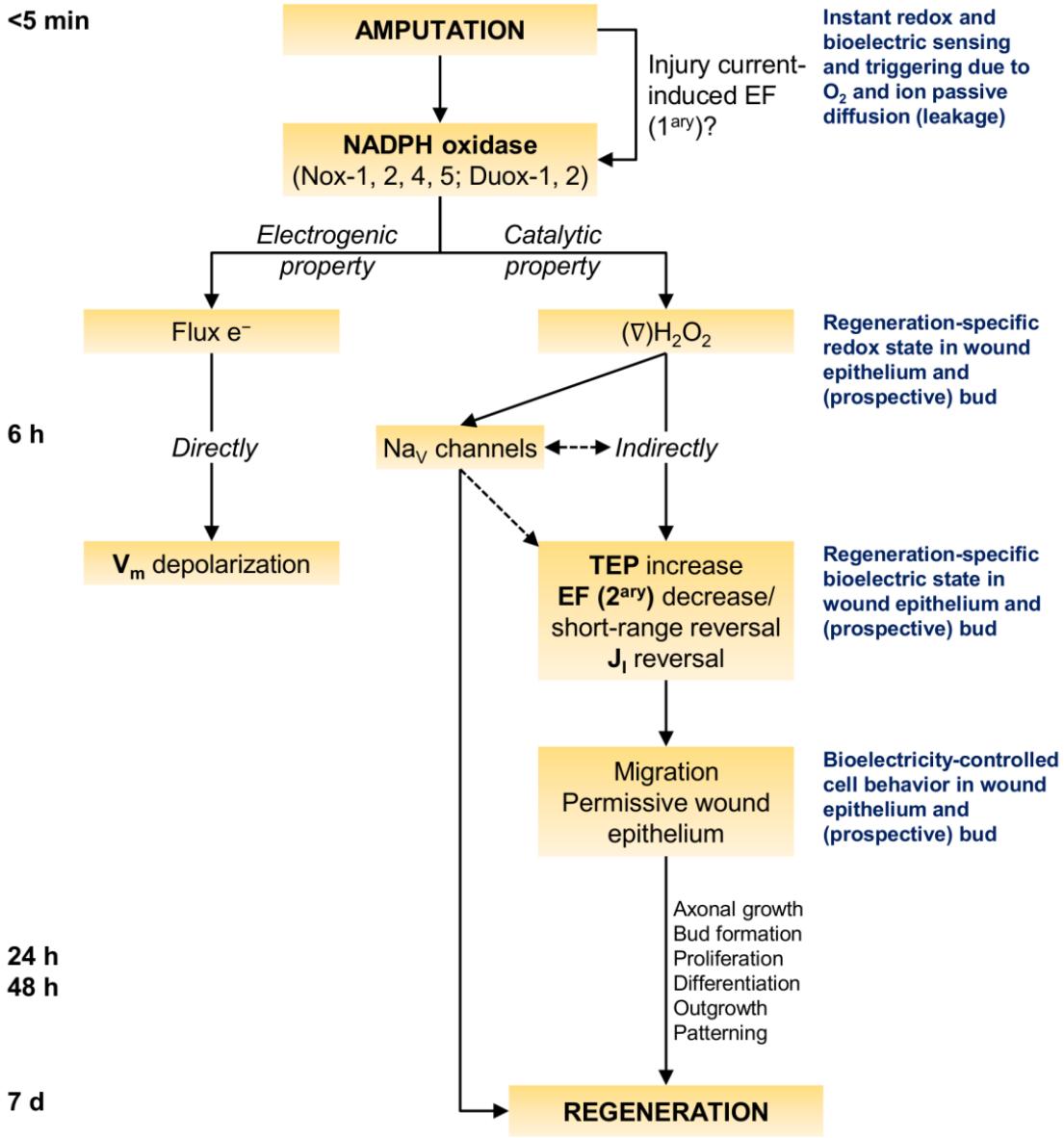

The model from Figure 7 in the paper.

Your paper ends with a model including the proposition that immediately post-amputation, an electrical signal activates the redox signal. How did you come to this hypothesis?

MZ & FF To better understand this hypothesis we need to go back a bit and point out the underlying assumptions. One of the highlights of this study is that ROS are immediately required for regeneration. Those ROS are produced from NADPH oxidases, holoenzymes with complex assembly and regulation; therefore, an ultra-fast signal must activate the enzyme to generate sufficient ROS for the task ahead.

> "One of the highlights of this study is that ROS are immediately required for regeneration... an ultra-fast signal must activate NADPH oxidases to generate sufficient ROS for the task ahead."

An electric short-circuit is an instantaneous response to amputation, which results in the so-called injury current and subsequent electric field. This immediate and automatic electric field is, according to the hypothesis, what activates the NADPH oxidases. In fact, there is some evidence showing that applied electric fields induce production of ROS in cells *in vitro*. We are currently designing experiments to test this hypothesis during regeneration. If true, a redox-bioelectric feedback module would exist in regeneration. This is, the injury-induced electric signals activate the upstream redox signals that regulate downstream electric signals. With caution, we think that the now hypothetical feedback module could be used as theoretical evidence, because it could allow a more tight or efficient regulation of regeneration owing to evolution.

Before speculating or designing more experiments to understand *how* the electric fields would activate the NADPH oxidases, it is more pressing to test *whether* the hypothesis is true.

How do you think your mechanism might relate to the 'canonical' intercellular signalling pathways that are also involved in regeneration?

MZ & FF The integration between ROS and bioelectric activities occurs very early in the regeneration process. Many of the 'canonical' signalling pathways, such as Wnt, BMP and Notch, appear to be activated later on. By itself, this may indicate that those pathways are regulated by ROS and/or bioelectricity, *i.e.*, act downstream. In fact, several studies in the regeneration context have shown that ROS or bioelectricity, independently, regulate some signalling pathways (and also cell behaviours), such as Wnt, FGF and Delta.

Given the high penetrance in regeneration, we think that pathways like the ones already mentioned and others might be affected by redox and bioelectric activities; we also think that follow up studies will unveil this, aiming for a higher level of mechanistic integration in regeneration.

Why do you think the H_2O_2 treatment induced the formation of ectopic tails?

MZ & FF The induction of ectopic tails was a thrilling finding, but it is important to note that the purpose of the assay was to check *whether* H_2O_2 induced ectopic tails and not *why*; the *why* deserves further research. That said, studies found that fin wounds in both *Xenopus* tadpoles and adult zebrafish generate ROS, likely H_2O_2. Unpublished results from us show that blocking the production of ROS impairs healing in *Xenopus* fin wounds. Therefore, we think that a threshold of H_2O_2 could define or tune the morphogenetic outcome, meaning that if the threshold is passed we may get an ectopic tail instead of just healing.

"The induction of ectopic tails was a thrilling finding"

Mechanistically speaking, another study found that Wnt signalling induced ectopic tails in the same model as ours. H_2O_2 could thus regulate Wnt for the same purpose, a pathway that could be mediated by bioelectric activities. Not mutually exclusive, another, maybe more speculative, possibility is an analogy with the accessory limb and blastema formation in axolotls and *Xenopus*, respectively. To induce them, it is required extra neuronal tissue, usually a deviated nerve. The incision we made in the tail severed the spinal cord, therefore, H_2O_2 treatment could, maybe via bioelectricity, affect the neuronal tissue so it becomes inductive.

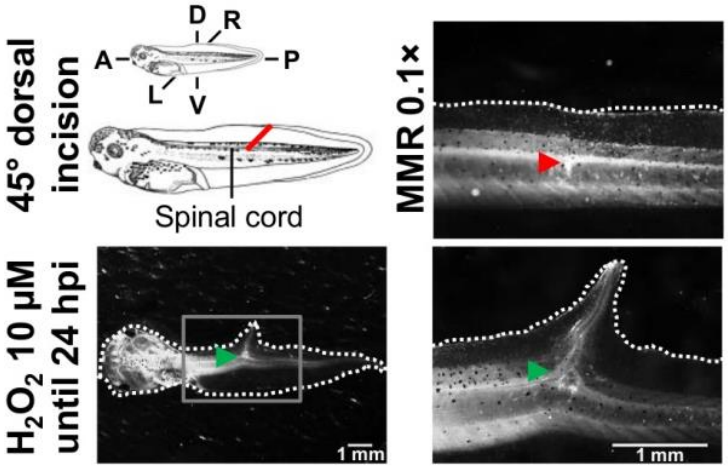

Exogenous hydrogen peroxide induces ectopic tails on severing the spinal cord, from Fig. S15 in the paper.

When doing the research, was there a particularly exciting result or eureka moment that has stayed with you?

FF As many have at one point or another, I had the privilege to experience both life-guiding eureka moments and exciting results. A first eureka-like moment occurred back in my last bachelor year. Anxiously to find what path to follow, I learned about ROS and the caudal regeneration in lizards came to my mind. I had a minor thought experiment: I grabbed a common lizard making it autotomize the tail; with the inner tissues now exposed to the atmosphere, I imagined the oxygen entering the

amputation plane down its chemical gradient and then pictured its transformation into ROS; as the levels rose, ROS alarmed local cells that something went wrong and triggered regeneration without any delay. In my innocence at the time, I let this single moment guide me through science ever since; there is no regret!

A second eureka-like moment occurred just before my arrival in the USA. When analysing a review paper, I read that the NADPH oxidases are *electrogenic*; this triggered a late night chain reaction that led me to the core of this manuscript. As NADPH oxidases work, they transfer electrons through the plasma membrane, so I thought that this was the origin of the membrane depolarization previously shown in regeneration. Then, I thought that since ROS are produced, these would, in turn, affect other facets of the bioelectric phenomena, namely electric currents.

"When analysing a review paper, I read that the NADPH oxidases are *electrogenic*; this triggered a late night chain reaction that led me to the core of this manuscript"

During the research, the exciting moments were when I was performing the critical experiments testing the redox-bioelectric crosstalk during regeneration. I blocked the production of ROS and imaged the membrane potential and measured the electric currents; during experiments, before getting the positive evidence, I was lightly sweating and my hands and belly were shivering. I know that these "symptoms" are analogous of a romantic encounter, guess that made them even more exciting!

Other unforgettable exciting moment was when, in the very first attempt, I saw a well-defined ectopic tail induced by H_2O_2. I was so impressed by it that I was childish enough to call other lab members to see an undisclosed "hopeful monster" in the microscope.

And what about the flipside: any particular moments of frustration and despair?

FF Other than now and then when, by procedural vicissitudes – for example, compromised batches of tadpoles (fungal infection, deficient animals, etc.), or all electrodes ending up breaking when touched, or readings were too noisy or strange because the earth wire was somehow disconnected – or for no obvious reason, experiments didn't work out, I didn't have any moments of frustration or despair worth noting. If you are surprised, so am I; not having major setbacks by the end of this manuscript surprised me and sometimes even "scared" me, since frustrations are a common theme in the research process and I really don't want to think that the hypothesis and experimental design put forth were bullet proof. So, for modesty's sake let's just call it 'beginners luck'; probably, the use of well-established techniques and methods helped. Just to highlight the surprise, we are about to submit a new study, where I had my share of despair moments, which I guess covers their absence in this paper, or at least I joke in that way! In fact, I was fortunate enough to get some serendipitous findings which we might end up following.

And finally, Min: where do you think this work will take you next?

MZ We followed an interdisciplinary approach hoping to merge apparently disparate research fields during regeneration. We think that this approach is important and potentially rewarding, and so several lines of research can be pursued with that in mind. We will have at least two exciting possible directions. One is to detail the molecular mechanisms of the redox-bioelectric interplay and to integrate them with 'canonical' signalling pathways in the *Xenopus* and other regeneration models. To help, we are currently establishing a redox and bioelectric sensor facility in the lab. The other is to take advantage of some of the cutting-edge technologies in wound healing and tissue regeneration in mammals. It appears that we are able to manipulate local electric fields and/or redox activities. A combined approach may provide promising therapies for chronic and non-healing wounds.

"I would be tempted to propose a term, *"electrobiology"*, hoping to suggest that electricity in biology has significant roles"

Evidence is accumulating suggesting bioelectricity as a different layer of mechanism, usually very upstream, together with the fundamental genetics and molecular/cellular processes that orchestrate during development and regeneration. I would be tempted to propose a term, *"electrobiology"*, hoping to suggest that electricity in biology has significant roles, in contrast to the more than the phenomenological nature of the word "bioelectricity".

Selected media coverage: overview

Excluding social and college-associated media, this paper has been covered in the USA-based Public Broadcasting Service (PBS) NOVA Next series (selected in the reprint below). According to their self-description, NOVA Next – launched in 2012 – is an "award-winning digital publication that provides answers from the cutting edge of science and technology". The publication, written in popular science tone, features – quoting series webpage – "articles and commentaries from some of the most respected journalists, scientists, and engineers" in their fields of expertise, exploring "the ideas that are changing the future, from the frontiers of synthetic biology to the politics of personalized medicine". My advisor, Prof. Min Zhao, was interviewed in advance about the paper for this journalistic piece.

Selected media coverage: reprint

Bioelectricity's potential

URL: http://www.pbs.org/wgbh/nova/next/body/bioelectric-potential

By Jyoti Madhusoodanan on Wed, 13 Jun 2018 (Normalized style)

(...)

And other researchers have found electric signals can regulate how human stem cells migrate to repair wounds. Min Zhao, a dermatologist at the University of California, Davis, studies how electrical gradients at wounds—the same currents Reymond detected in his cut finger—direct the process of healing. These gradients guide cells toward injuries that need repair; upending the field makes them migrate away instead. Zhao's team found that cells sense and respond to these electric fields via genetic signals. Last year, they reported that in regenerating tadpole tails, oxygen-containing chemicals that guide cells to repair wounds also help generate electricity, and electric cues trigger the production of these chemicals. "This links these two separate mechanisms to show how they work together," Zhao says. "If you lose either one, regeneration slows down."

A wound-induced electric current—triggered when cells are damaged and ions pour out—starts to flow the instant skin is cut. "It happens faster than any chemical changes," Zhao points out. "When I first started working on this, I thought the electric field would be just another of hundreds of physical and chemical factors. But when we put all these chemical signals together and compared them, we found that the electric field's physiological strength overrides the rest."

(...)

VII. *ADDENDA* TO THE PUBLICATION *EARLY REDOX ACTIVITIES MODULATE* XENOPUS *TAIL REGENERATION*

Journal editor's summary

Reactive oxygen species (ROS) and hypoxia-inducible factors (HIF) mediate regeneration but how is unclear. Here, the authors use an optic-based probe ('optrode') to monitor oxygen (O_2) during *Xenopus* tail regeneration, identifying crosstalk between O_2 influx, ROS production and HIF-1α stabilization.

Journal transparent peer review

Following the acceptance of the paper, we opted in to the journal's policy on transparent peer review. The reviewers' comments and our point-by-point response and rebuttal are open to provide readers with the discussion undertaken prior to manuscript publication. File is open access as 'Electronic supplementary material'.

Selected media coverage: overview

This paper has been covered by the UC Davis Egghead Blog, a college-associated media. By their self-description, "Egghead is a blog about research by, with or related to UC Davis. (...) This blog is created and maintained by UC Davis Strategic Communications, and mostly edited by Andy Fell." My advisor, Prof. Min Zhao, and I were consulted for the elaboration of the text, written in a popular science tone. I prepared the figure accompanying the text.

Selected media coverage: reprint

Exploring the Role of Redox and Bioelectric Players in Tissue Regeneration

URL: https://egghead.ucdavis.edu/2018/11/06/exploring-role-redox-bioelectric-players-tissue-regeneration

By Andy Fell on November 6th, 2018 (Normalized style)

Regeneration of a lost limb is arguably one of the seven wonders of biology. While you can't grow a new arm, a humble tadpole can grow a new tail in a week. Seeking a better understanding of limb regeneration, Min Zhao, professor of dermatology and ophthalmology at the University of California, Davis, and graduate student Fernando Ferreira (also at University of Minho, Portugal) are studying the relationship of redox players, like oxygen and hydrogen peroxide, with bioelectricity, including membrane potential and electric currents, to pinpoint how a tadpole can regrow an amputated tail.

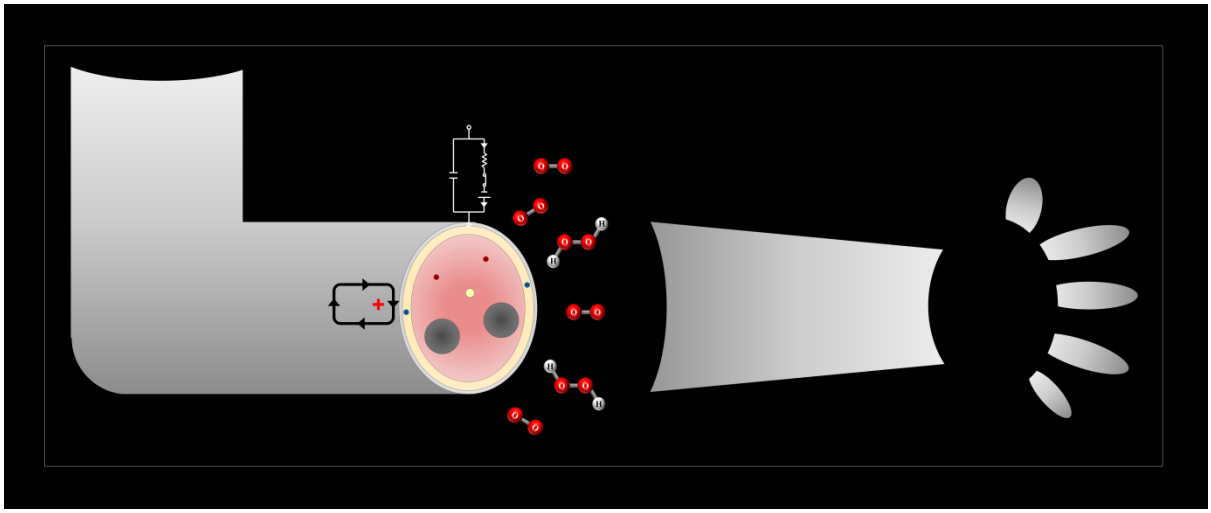

Work from Professor Min Zhao's lab at UC Davis is showing how oxygen molecules and bioelectricity can work together to stimulate regeneration of a new limb in tadpoles.

Previous work by Ferreira and Zhao demonstrated a close interplay between redox and bioelectric activities underlying tail regeneration in tadpoles. In the new study, using the same regeneration model, the researchers detailed the redox component in greater detail, uncovering a complex interaction in the regenerating tail between oxygen, reactive oxygen species and hypoxia-inducible factor.

"When we started this study we already knew – from decades old evidence – that electric currents were important for a successful regeneration, especially in amphibians; however, no evidence existed about ROS (reactive oxygen species) until very recently," Zhao said.

Ferreira used cutting edge technology, an optical based probe called the optrode, that allowed him to measure the flux of oxygen around a wound or amputation. Immediately after injury, oxygen enters the wounded area and fuels the generation of reactive oxygen species, including molecules such as hydrogen peroxide, creating a hypoxic environment, the researchers found. This stabilizes the activity of a molecule called hypoxia-inducible factor, which influences electric currents that control the movement of cells into the wound.

Key results and the future of limb regeneration

According to the Amputee Coalition, there are 2 million people struggling with limb loss in the U.S, with around 185,000 new cases a year. Inductive regeneration, or the stimulation of regrowth and function of the lost limb, would be a near-miraculous treatment for these patients. This possibility is still far away and much more research is needed.

The research conducted by the team has one key and novel takeaway message: redox and bioelectric activities interact during the regeneration process. Tadpoles have a great capacity to regenerate, except during a well-defined period of metamorphosis. Interestingly, fine tuning of the redox and bioelectric states in this refractory period unleashes regeneration, opening hope that regeneration might be induced in mammals as well. The end goal for Zhao's team is to be able to exploit redox and electric

signals, perhaps by topical creams and eye drops, to enhance wound healing and regenerate damaged tissues.

A unique and comprehensive research facility

Zhao's lab at UC Davis is establishing a comprehensive *Redox-Bioelectric Sensing Facility* able to quantitatively measure important redox players – oxygen and hydrogen peroxide – and bioelectric players – namely, minute electric currents, electric fields and ion fluxes (including the fantastic five: sodium, potassium, calcium, chloride and protons). The facility possesses unique ultrasensitive voltage sensing apparatus and other equipment including the optrode that uses light to measure oxygen content and flux. Ferreira was trained in the technique during a summer externship at the Woods Hole Marine Biological Laboratory (MBL). With the optrode, the lab is now uniquely equipped to study redox biology and bioelectricity together, Zhao said.

The work was published on Oct. 16 in the journal *Nature Communications*. Additional authors were Guillaume Luxardi and Kan Zhu, at UC Davis and Vijay Krishna Raghunathan, University of Houston. Financial support was from the NIH, the Air Force Office of Scientific Research and Research to Prevent Blindness, Inc.

VIII. *MAPPING BIOELECTRIC PHENOMENA DURING TAIL REGENERATION IN* XENOPUS LAEVIS *TADPOLES*

Poster overview

The poster was produced after 1 year of laboratorial work in the doctoral program, when critical experiments were successfully performed and completed, namely an extensive spatiotemporal profiling of bioelectric activities and its dynamic correlation with regeneration progression and efficiency. The poster was presented at the Gordon Research Conference *BioElectroChemistry*, under the theme *Cellular and Organismal Responses to Endogenous and Exogenous Fields*. David A. Dean (University of Rochester, Rochester, New York, USA) and Marie-Pierre Rols (CNRS – Université de Toulouse, Institut de Pharmacologie et de Biologie Structurale (Ipbs), Toulouse, France) were the chair and vice-chair of the conference, respectively, which lasted from July 6 to July 11, 2014 and occurred at the University of New England (Biddeford, Maine, USA).

Poster abstract

Epimorphic regeneration is a complex process that requires diverse signalling mechanisms. Bioelectric signals as electric currents at regeneration stump have been implicated in regeneration for the last several decades. These currents have been assumed to be driven by transepithelial potentials (TEP) and altogether generate lateral electric fields (EF). However, to our knowledge, it had not yet been described the TEP and EF dynamic profile during regeneration.

Here we provided a spatiotemporal mapping of the TEP and calculated the associated EFs. After the TEP short-circuit and the exponential recovery in the first 6 hours post-amputation (hpa), more than 75% of TEP recovered at 48 hpa. The EF was very high at 1 hpa (>1500 mV mm^{-1}), but decreases almost exponentially until 6 hpa, reaching a low plateau at 48 hpa.

Since TEP underlie the electric currents, we established the spatiotemporal mapping of the extracellular current density (J_I). After a passive outward current, a characteristic potential reversion occurred at 6 hpa, decreasing to baseline values around 48 hpa.

The refractory period of tadpoles offers an excellent opportunity to discover new players involved in regeneration. Focusing at 6 and 24 hpa in the refractory period, a significant decrease of TEP was measured in both time-points, however without a significant change in the EFs. The potential reversion of J_I was postponed to 24 hpa.

The contrasting differences in TEP and J_I in regenerating or refractory period stages correlated with a regenerative index drop, pointing to a key role of bioelectric phenomena in regeneration.

Poster contributions

F.F., G.L. and M.Z. designed the experiments. F.F. performed the experiments and analysed the results. G.L. and B.R. provided technical training and guidance, and helped to interpret some results. F.F., G.L. and M.Z. outlined the poster. F.F. wrote and produced the poster.

Poster reprint

Vide infra, normalized dimensions.

Universidade do Minho

UCDAVIS UNIVERSITY OF CALIFORNIA

MAPPING BIOELECTRIC PHENOMENA DURING TAIL REGENERATION IN *XENOPUS LAEVIS* TADPOLES

FERNANDO FERREIRA[1,2], GUILLAUME LUXARDI[2], BRIAN REID[2] & MIN ZHAO[2]

[1] CMBA, Departamento de Biologia, Universidade do Minho, 4704 Braga, Portugal; [2] Department of Dermatology and Ophthalmology, University of California, Davis, 95616 CA, USA

INTRODUCTION

Bioelectricity in regeneration

Epimorphic regeneration is a complex process that requires diverse signaling mechanisms. Bioelectric signals as electric currents at regeneration stump have been implicated in regeneration for the last several decades. These currents have been assumed to be driven by transepithelial potentials (TEP) and altogether generate lateral electric fields (EF). However, to our knowledge, it had not yet been described the TEP and EF dynamic profile during regeneration.

METHODS & RESULTS

1. Glass microelectrode measurements of transepithelial potentials (TEP)

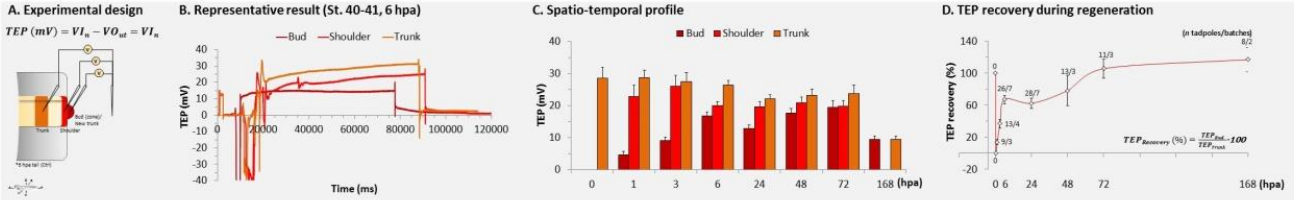

2. Electric fields (EF) calculated from TEP

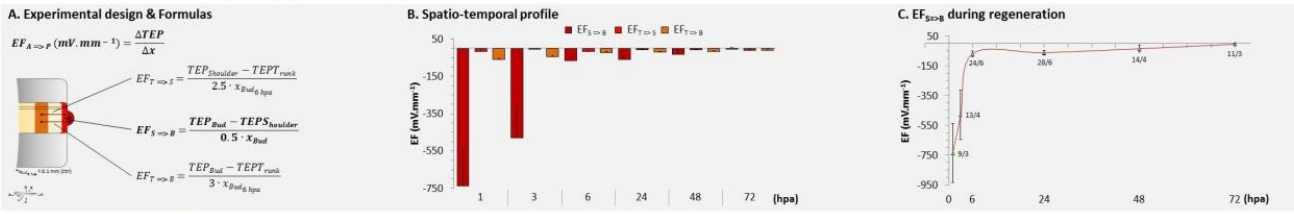

3. Vibrating probe measurements of extracellular current density (J)

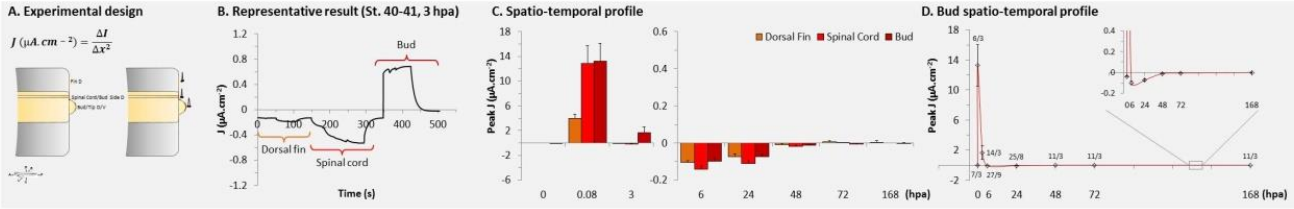

4. Does refractory period (St. 45-47) affect TEP, EFs and J?

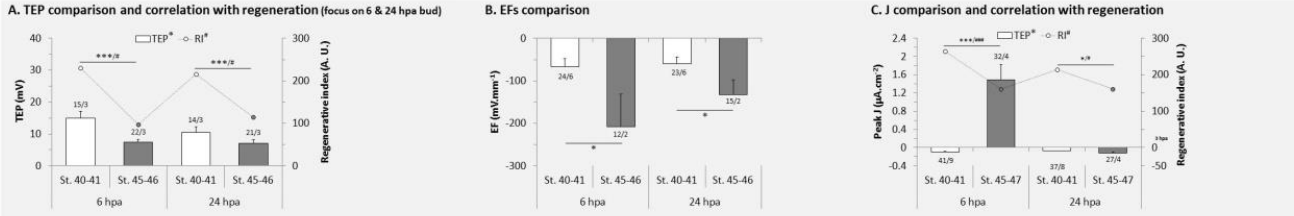

CONCLUSIONS

A bioelectrical model of regeneration

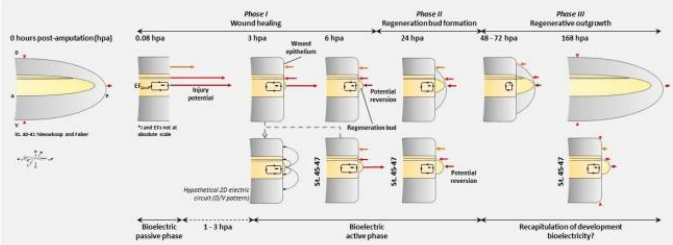

(i) TEP, EFs and J present dynamic profiles that accompany regeneration;

(ii) Significant TEP downregulation and correspondent upregulation of lateral EFs at 6 and 24 hpa in refractory period correlates with a lower regenerative ability;

(iii) Reversion to inward current density at 6 hpa seems necessary to regeneration;

(iv) Recover of the inward current density in refractory period at 24 hpa was not sufficient to recover regeneration, indicating the importance of the time-window around 6 hpa or early regulation;

In conclusion, the contrasting differences observed in refractory period tadpoles points to a key role of bioelectric phenomena in the regulation of regeneration. Since passive and active variations in TEP, EFs and J are immediate responses to amputation they may play a role in cell behavior and cell signaling pivotal to regeneration.

ACKNOWLEDGEMENTS This work was supported by R01EY019101-01A2, also grants from NSF and CIRM and the Ph.D. fellowship SFRH/BD/87256/2012 from Fundação para a Ciência e a Tecnologia (FCT).

IX. *REACTIVE OXYGEN SPECIES REGULATE BIOELECTRIC RESPONSES DURING TAIL REGENERATION OF* XENOPUS LAEVIS *TADPOLES*

Poster overview

The poster was produced after 1.5 year of laboratorial work in the doctoral program, when core results were obtained, demonstrating an interplay between redox and bioelectric activities and the use of that know-how to rescue and to induce regeneration in non-regenerative conditions. The poster essentially presents the research published in the journal *Development* (Chapter VII). The poster was presented at two instances, first in a local symposium and then in an international conference. The symposium is a biennial event of the Department of Dermatology, where work was performed, and occurred in December 10, 2014 at the University of California, Davis. The conference *Oxidants and Antioxidants in Biology* is organized by the Oxygen Club of California and that edition had the theme *Redox Medicine and Nutrition*. The conference was organized by César G. Fraga (Physical Chemistry Institute for Molecular Biochemistry and Molecular Medicine, University of Buenos Aires, Argentina), Patricia Oteiza (Department of Nutrition, University of California, Davis) and Helmut Sies (Institute of Biochemistry and Molecular Biology I, Heinrich-Heine-University Düsseldorf, Düsseldorf, Germany), lasted from May 4 to May 6, 2016 and occurred at the University of California, Davis.

Poster abstract

Symposium

Complex mechanisms orchestrate to regulate tissue regeneration. Regeneration of *Xenopus* tadpole tail for example requires BMP and Notch signalling pathways, Wnt and FGF pathways, and reactive oxygen species (ROS). A very different signalling – bioelectric cue – was proposed over half a century. Recent experiments suggest an important role for this much less understood mechanism. Regenerating stump and refractory (non-regenerative) stumps have electric current signature. Transient induction of sodium current, manipulation of H^+ pump and membrane potential are sufficient to induce *Xenopus* tail regeneration.

How the biochemical and bioelectric signals interact to regulate regeneration is very poorly understood.

Here we determined the roles of ROS in regeneration and the effects of ROS manipulation on bioelectric responses in regeneration of *Xenopus laevis* tadpole tail. We found that: (i) Inhibition of the ROS production, scavenging of ROS, or blocking entry of ROS in cells significantly inhibited regeneration; (ii) Exposure to exogenous hydrogen peroxide (H_2O_2) of low concentrations for short term (first 24 hours) rescued tail regeneration and regained regeneration in refractory stumps; (iii) Exogenous H_2O_2 resulted in significant increase in ectopic (abnormal or extra) tail induction following dorsal incision severing down to the spinal cord (inclusive); (iv) Depolarization of cell membrane

potential (V_m), recovery of transepithelial potential (TEP), and the patterns of stump current density (J_I) predicted whether a stump regenerate or not; (v) Manipulation of ROS significantly affected cell membrane potential (V_m), transepithelial potential (TEP), and density (J_I) and patterns of the stump currents during regeneration; (vi) Changes in ROS levels correlated very well with the unique reversal of stump electric currents; (vii) The ROS-modulated bioelectric phenomena mimic the refractory period altered bioelectric phenomena.

Therefore, for the first time we unveil evidence that NADPH oxidase and ROS modulation regulates bioelectric phenomena – V_m, TEP and J_I – which are necessary for regeneration, and suggest a new mechanism by which redox phenomena control regeneration. In addition, this study provides important new insights into the interplay between biochemical and biophysical signalling during wound healing and regeneration.

Conference

Multiple signalling mechanisms have been shown to modulate regeneration. Biochemical signals such as reactive oxygen species (ROS) and biophysical signals such as electric currents were, independently, shown to participate in this process. However, the interplays between biochemical and biophysical signals during regeneration remain poorly understood.

Here, we take advantage of the fluctuating regenerative abilities of *Xenopus laevis* tadpole tail, that fail to regenerate only at specific developmental stages (refractory period), to investigate the interactions between redox and bioelectric activities during regeneration.

We show that inhibition of NADPH oxidases-mediated production of ROS, scavenging or blocking their diffusion into cells impair regeneration and consistently regulate the dynamics of membrane potential (V_m), transepithelial potential (TEP) and electric current densities (J_I) during regeneration. Depletion of ROS mimics the refractory period altered TEP and J_I. Short-term application of hydrogen peroxide (H_2O_2) rescues (from depleted ROS) and gains (from refractory period) regeneration, TEP increase and J_I reversal. H_2O_2 is thereby necessary for and sufficient to induce regeneration and to regulate TEP and J_I. The unique early J_I reversal in regeneration bud is therefore switched on by H_2O_2 and robustly correlates with regeneration efficiency.

In conclusion, this study unveils interplays between biochemical and biophysical signals during regeneration, suggesting a novel mechanism mediating regeneration: early H_2O_2-switched J_I reversal. It also highlights the opportunities of interdisciplinary integration of apparently disparate states that may reserve promising advances for translational medicine.

Poster contributions

F.F., G.L. and M.Z. designed the experiments. F.F. performed the experiments and analysed the results. G.L. and B.R. provided technical training and guidance, and helped to interpret some results. F.F., G.L. and M.Z. outlined the poster. F.F. wrote and produced the poster.

Poster reprint

Vide infra; normalized dimensions.

REACTIVE OXYGEN SPECIES REGULATE BIOELECTRIC RESPONSES DURING TAIL REGENERATION OF *XENOPUS LAEVIS* TADPOLES

FERNANDO FERREIRA[1,2], GUILLAUME LUXARDI[1], BRIAN REID[1] & MIN ZHAO[1]

[1] Department of Dermatology and Ophthalmology, University of California, Davis, 95616 CA, USA; [2] CMBA, Departamento de Biologia, Universidade do Minho, 4704 Braga, Portugal

QUESTION

Redox and bioelectric states in regeneration

Complex mechanisms orchestrate to regulate epimorphic regeneration. For several decades, bioelectric phenomena such as membrane potential polarization and electric currents have been shown to be necessary and even sufficient for regeneration. More recently, reactive oxygen species (ROS) were also shown to be required for regeneration, possibly by modulation of master signaling pathways such as Wnt. However, to our knowledge, a putative interaction between ROS and bioelectric responses during regeneration has not yet been elucidated. Here we intended to unveil this interaction asking:

Do ROS (especially H_2O_2) regulate regeneration by modulation of some or all of the following bioelectric phenomena: membrane potential (V_m), transepithelial potential (TEP) and extracellular current density (J_i)?

METHODS & RESULTS

1. ROS production, availability and diffusion regulate regeneration

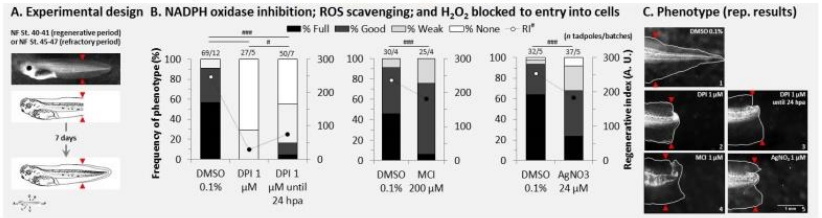

2. ROS on V_m: NADPH oxidase activity, not ROS, depolarizes cell membrane in bud at 6 hpa

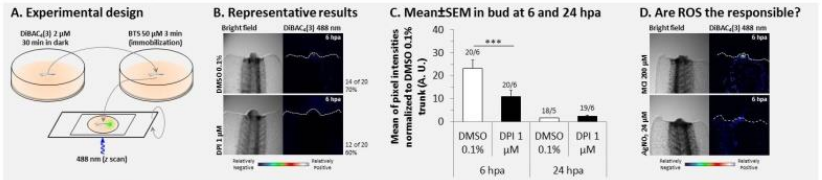

3. ROS on TEP: ROS (H_2O_2) downregulates TEP in bud mainly at 6 hpa

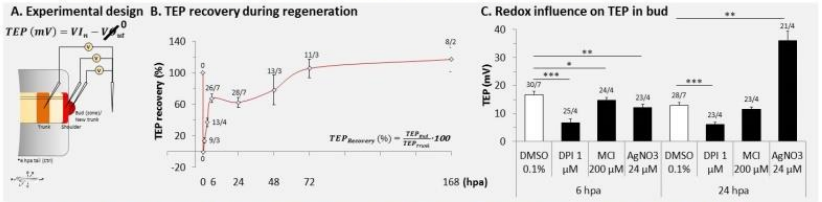

4. ROS on J_i: ROS (H_2O_2) postpones important current density reversion in bud at 6 hpa

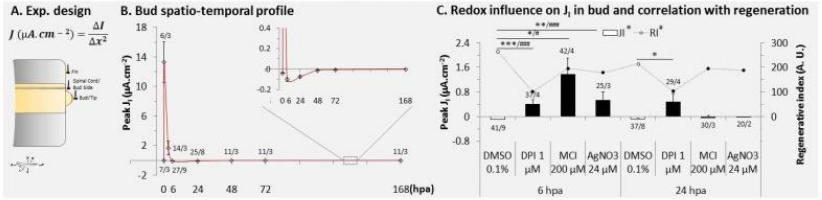

5. ROS-modulated bioelectricity mimic the refractory period altered bioelectric phenomena

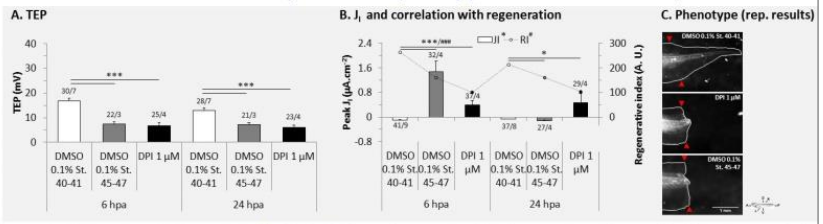

6. Exogenous H_2O_2 rescues/gains TEP, J_i and regeneration in regenerative and refractory period

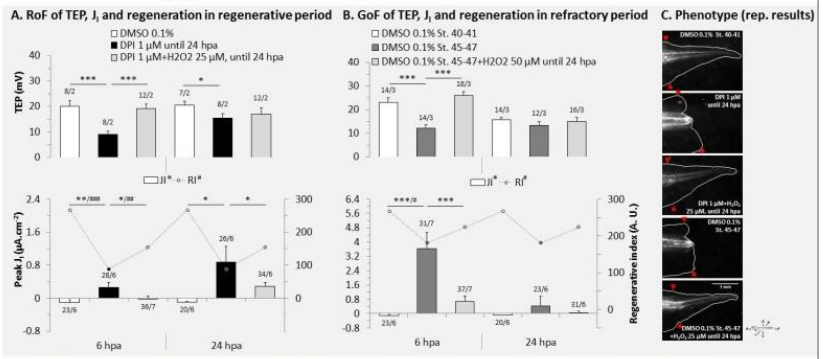

7. Exogenous H_2O_2 increases the frequency of ectopic (abnormal or extra) tails induction

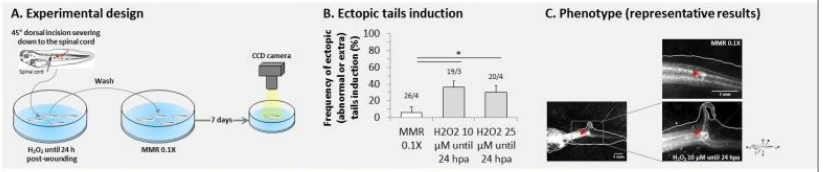

...schematic representation of the H_2O_2 "life cycle" in bioelectricity and regeneration

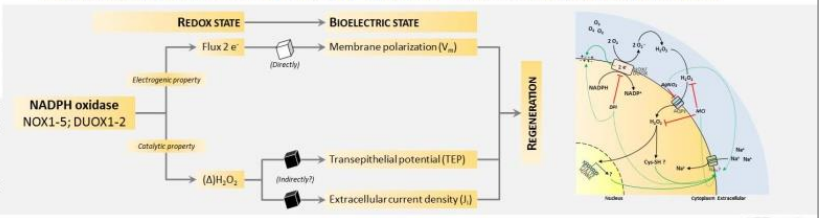

CONCLUSIONS

Final remarks, synthesis and...

In conclusion, for the first time we unveil evidence that NADPH oxidase and ROS (H_2O_2) modulation regulate bioelectric phenomena – V_m, TEP and J_i – know to be required for regeneration. Specifically, we showed that NADPH oxidase activity *per se* generates membrane depolarization and that ROS (H_2O_2) availability and diffusion into cells significantly affects TEP and J_i.

Therefore, these results suggest a new mechanism by which redox phenomena control regeneration.

In addition, this study provides important new insights into the interplay between biochemical and biophysical signaling during wound healing and regeneration.

ACKNOWLEDGEMENTS This work was supported by R01EY019101-01A2, also grants from NSF and CIRM and the Ph.D. fellowship SFRH/BD/87256/2012 from Fundação para a Ciência e a Tecnologia (FCT).

X. *EARLY HIF-1A STABILIZATION, POTENTIALLY ROS-DEPENDENT, MODULATES REGENERATION*

Poster overview

The poster was produced after 3 years of laboratorial work in the doctoral program, when the crucial part of a second research phase was successfully performed and completed, showing a dynamic correlation of O_2 flux with regeneration progression and efficiency, as well as the requirement and sufficiency of HIF-1α stabilization for and to induce regeneration. The poster presents a very significant part of the research published in the journal *Nature Communications* (Chapter VIII). The poster was presented at the local Department of Dermatology symposium, as the previous one (Appendix IX), where poster holders had the unprecedented opportunity to give a pitch (without discussion) highlighting the findings of the research and appealing to attendees' curiosity to see more by the poster (*Vide infra* pitch presentation). The pitch was a mini-oral presentation of a single slide that lasted no more than one minute. The symposium occurred in June 22, 2016 at the University of California, Davis.

Poster abstract

Reactive oxygen species (ROS) levels increase upon amputation and are required for regeneration. Hypoxia is being associated with stem cells niches and mesenchymal condensations, like cancer. The master transcription factor HIF-1α is stabilized under hypoxia. Amputation breaks the epithelial barrier possibly leading to an influx of oxygen (O_2), down its chemical gradient. This putative influx of exogenous O_2 might facilitate local ROS production and pO_2 changes. However, the O_2 influx has not been experimentally demonstrated, neither its effect on ROS and HIF-1α during regeneration.

We used an emergent optic-based probe (micro-optrode) to profile the spatiotemporal O_2 fluxes during tail regeneration in *Xenopus laevis* tadpoles. We find an increased and steady O_2 influx upon amputation, which correlates with the progression and efficiency of regeneration. Inhibition of NADPH oxidases-mediated production of ROS decreases O_2 influx. ROS might therefore regulate the pO_2 environment and consequent HIF-1α stabilization in the regeneration bud. Inhibition of HIF-1α impaired regeneration and stabilization of HIF-1α slightly gained regeneration in the non-regenerative refractory period. Thereby, HIF-1α is necessary for and sufficient to induce regeneration. Inhibition of HSP90 impaired regeneration in exposure conditions similar to HIF-1α. This might indicate that HSP90 acts downstream of HIF-1α.

Altogether, these results suggest a novel mechanism for regeneration via the orchestration of O_2 influx, ROS production and HIF-1α stabilization. Redox state players and dynamics might thus reserve important targets for regenerative medicine.

Poster contributions

All authors designed the experiments. F.F. performed the experiments and analysed the data and results. VK.R. and G.L. helped to interpret the results. F.F. and M.Z. outlined the poster. F.F. wrote and produced the poster.

Poster reprint

Vide infra; normalized dimensions.

Early HIF-1α stabilization, potentially ROS-dependent, modulates regeneration

FERNANDO FERREIRA[1,2], VIJAYKRISHNA RAGHUNATHAN[3], GUILLAUME LUXARDI[1] & MIN ZHAO[1,4]

[1]Department of Dermatology, University of California, Davis, CA, USA; [2]CMBA, Departamento de Biologia, Universidade do Minho, Braga, Portugal;
[3]Department of Surgical&Radiological Sciences, University of California, Davis, CA, USA; [4]Department of Ophthalmology, University of California, Davis, CA, USA.

Introduction

Reactive oxygen species (ROS) levels increase upon amputation and are required for regeneration. Hypoxia is being associated with stem cells niches and mesenchymal condensations, like cancer. The master transcription factor HIF-1α is stabilized under hypoxia. Amputation breaks the epithelial barrier possibly leading to an influx of oxygen (O_2), down its chemical gradient. This putative influx of exogenous O_2 might facilitate local ROS production and pO_2 changes. **However, the O_2 influx has not been experimentally demonstrated, neither its effect on ROS and HIF-1α during regeneration.**

Methods & Results

1. O_2 flux dynamically correlates with regeneration.

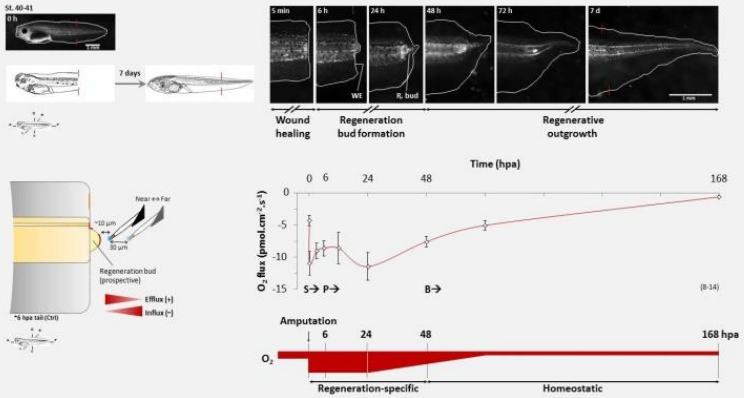

2. O_2 flux prognosticates regeneration efficiency.

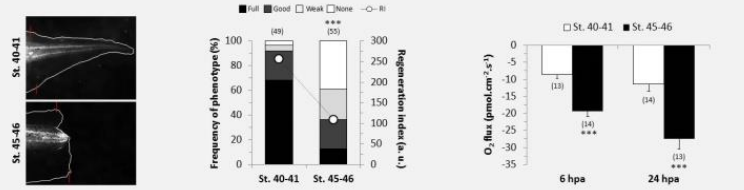

3. ROS production regulates O_2 influx that might stabilize HIF-1α.

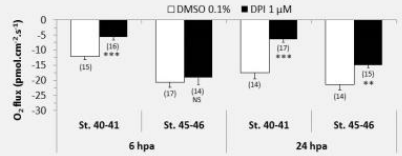

Ongoing...

Protein quantification to test whether:

- .: ROS affect HIF-1α stabilization;
- .: Refractory period *per se* affect HIF-1α stabilization.

4. HIF-1α is immediately necessary for and sufficient to induce regeneration.

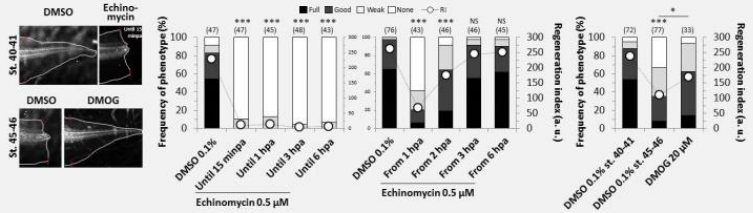

5. HSP90 might act downstream of HIF-1α to modulate regeneration.

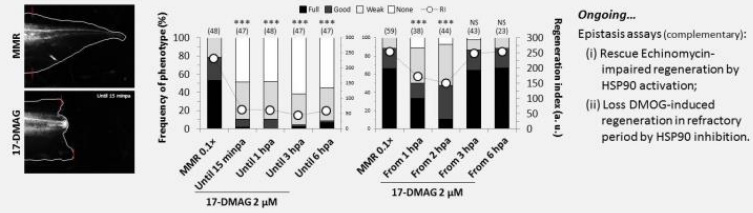

Ongoing...

Epistasis assays (complementary):

- (i) Rescue Echinomycin-impaired regeneration by HSP90 activation;
- (ii) Loss DMOG-induced regeneration in refractory period by HSP90 inhibition.

Discussion & Conclusion

The newly described O_2 flux profile upon amputation correlates with the progression and efficiency of regeneration. Exogenous O_2 fuels ROS production, implying ROS as a potential regulator of the pO_2 environment and consequent HIF-1α stabilization in the regeneration bud. HIF-1α is immediately necessary for and slightly sufficient to induce regeneration. HSP90 is required for regeneration in the same time-window (until 2 hpa) of HIF-1α, suggesting that HSP90 might act downstream of HIF-1α.

In conclusion, we propose a novel mechanism for regeneration *via* the orchestration of O_2 influx, ROS production and HIF-1α stabilization. Redox state is thus targetable for regenerative medicine.

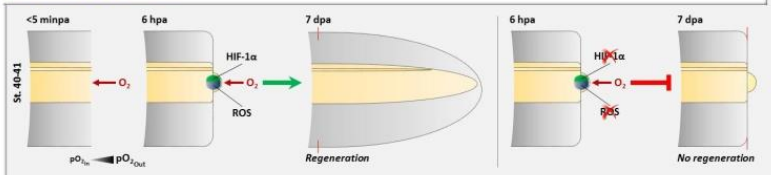

Acknowledgements

We are grateful to Prof. Ph.D. Andreia Gomes (CMBA, UMinho) and Zhao Lab members for helpful comments. This work was supported by UC Davis Bridging fund and NIH grant EB015737 and, in part, by an Unrestricted Grant from Research to Prevent Blindness, Inc., UC Davis Ophthalmology. F.F. was supported by Fundação para a Ciência e Tecnologia (FCT) studentship SFRH/BD/87256/2012.

Pitch presentation

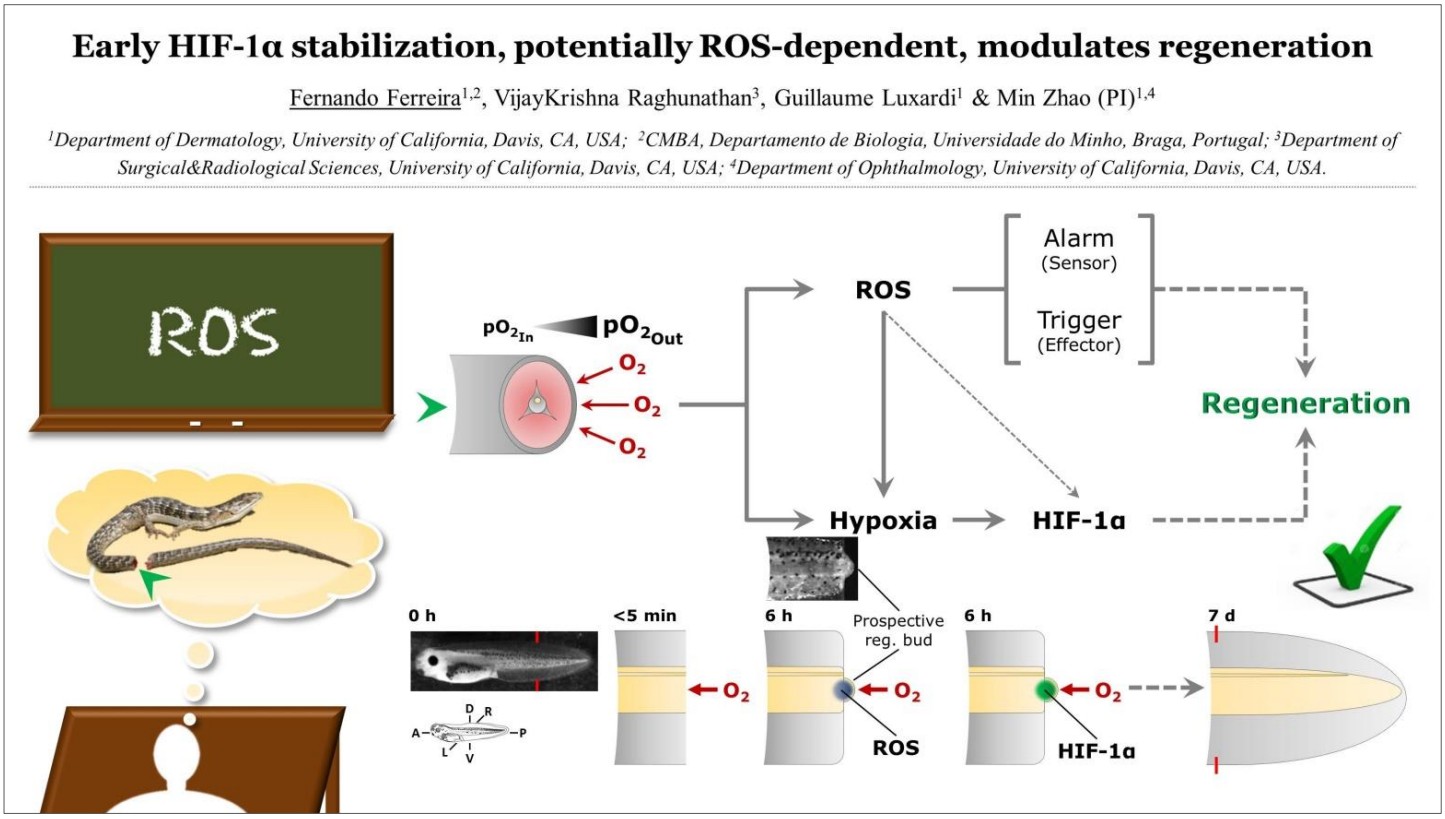

Pitch transcript

When I learned about reactive oxygen species, it came to my mind the caudal autotomy in lizards. The barrier breaking should lead to oxygen influx due to the gradient, which could instigate and/or fuel local ROS production. *[Click]* ROS could alarm that something went wrong and trigger regeneration.

Following up this seminal idea, we noticed that hypoxia and its master player, the hypoxia-inducible factor one alpha, are a common theme in mesenchymal condensations and are pivotal for stemness. *[Click]*

The regeneration bud is a mesenchymal-like structure responsible for de novo tail formation. *[Click]* Therefore, we hypothesize that the putative oxygen influx and ROS production set up a permissive redox microenvironment in the bud – this is, a hypoxia – that stabilizes HIF one alpha. *[Click]* HIF, in turn, modulates regeneration somehow.

All this rationale is speculative... *[Move away from microphone and, then, be back]* until today. *[Click]* Thank you.

XI. *REDOX AND BIOELECTRIC PROBING: HARNESSING THE SENSING POWER OF PHOTONS AND ELECTRONS*

Poster overview

The poster was produced after 3 years of laboratorial work in the doctoral program and is also derived from collaborations and previously published data by the laboratory. The goal was to highlight a prospective *Bioelectric and Redox Sensor Facility*. For that, the poster presents a medley of wound healing and regeneration research using the techniques established in the laboratory that comprise the would-be facility. The poster presents the core techniques used in the research of the thesis, one of them – micro-optrode – published in the journal *Nature Protocols* (Chapter VI). A technique not used in the thesis – ion-selective microelectrode – was published in the *Journal of visualized experiments (JoVE)* (Appendix I). Unfortunately, by room availability issues, poster display was cancelled and instead authors presented a pitch of the poster content. Presentation occurred at the local Department of Dermatology symposium, as the previous ones (Appendix IX, X), where the pitch was followed by discussion with interested attendees. The pitch was a mini-oral presentation of two slides in two minutes (*Vide infra*). The symposium occurred in November 15, 2017 at the University of California, Davis.

Poster abstract

The harnessing and tinkering of redox and bioelectric phenomena by evolution led to a massive complexification of multicellular life. Of the prominent redox signals and cues, partial pressure and flux of oxygen (pO_2 and J_{O_2}, respectively), NADPH oxidases, reactive oxygen species (ROS), hypoxia, and hypoxia-inducible factors (HIF) are pervasive and essential for a comprehensive understanding of the biochemistry and signalling of life processes and behaviours. Similarly, pervasive and essential are the following prominent bioelectric signals and cues: membrane and transepithelial potentials (V_m and TEP, respectively), electric current density (J_I), ion fluxes such as potassium (J_{K^+}) or chloride (J_{Cl^-}), and electric fields (EF).

Recently, we unveiled the interplay between redox and bioelectric activities in the context of vertebrate regeneration. Specifically, NADPH oxidases and ROS regulated V_m, TEP, EF, J_I and probably J_{Na^+}. To build on that finding, it was required the employment of an emergent, cutting-edge, technique – micro-optrode – on the top of established techniques – vibrating probe and glass microelectrode. The technological integration made it possible to establish a prospective *Bioelectric and Redox Sensor Facility* in the laboratory. This facility – currently under remodelling and expansion – aims to be a cornerstone to reliably and accurately study the dynamics of discrete and/or integrative redox and bioelectric phenomena.

Poster contributions

Authors provided data of their previously published data. F.F. performed the experiments of the unpublished data. F.F. and M.Z. outlined the poster. F.F. wrote and produced the poster.

Poster reprint

Vide infra; normalized dimensions.

Redox and bioelectric probing: harnessing the sensing power of photons and electrons

FERNANDO FERREIRA[1,2], BRIAN REID[1], GUILLAUME LUXARDI[1], LI MA[1,3] & MIN ZHAO[1,4]

[1]Department of Dermatology, University of California, Davis, CA, USA; [2]CMBA, Departamento de Biologia, Universidade do Minho, Braga, Portugal; [3]Skin and Cosmetic Research Department, Shanghai Skin Disease Hospital, Shanghai, China; [4]Department of Ophthalmology, University of California, Davis, CA, USA.

Abstract

The harnessing and tinkering of redox and bioelectric phenomena by evolution led to a massive complexification of multicellular life. Of the prominent redox signals and cues, partial pressure and flux of oxygen (pO_2 and J_{O_2}, respectively), NADPH oxidases, reactive oxygen species (ROS), hypoxia, and hypoxia-inducible factors (HIF) are pervasive and essential for a comprehensive understanding of the biochemistry and signaling of life processes and behaviors. Similarly pervasive and essential are the following prominent bioelectric signals and cues: membrane and transepithelial potentials (V_m and TEP, respectively), electric current density (J_I), ion fluxes such as potassium (J_{K^+}) or chloride (J_{Cl^-}), and electric fields (EF).

Recently, we unveiled the interplay between redox and bioelectric activities in the context of vertebrate regeneration. Specifically, NADPH oxidases and ROS regulated V_m, TEP, EF, J_I and probably J_{Na^+}. To build on that finding, it was required the employment of an emergent, cutting-edge, technique – optrode – on the top of established techniques – vibrating probe and glass microelectrode. The technological integration made it possible to establish a prospective redox and bioelectric sensor facility in the laboratory. This facility – currently under remodeling and expansion – aims to be a cornerstone to reliably and accurately study the dynamics of discrete and/or integrative redox and bioelectric phenomena.

Glass microelectrode | Vibrating probe | Ion-selective probe | Optrode

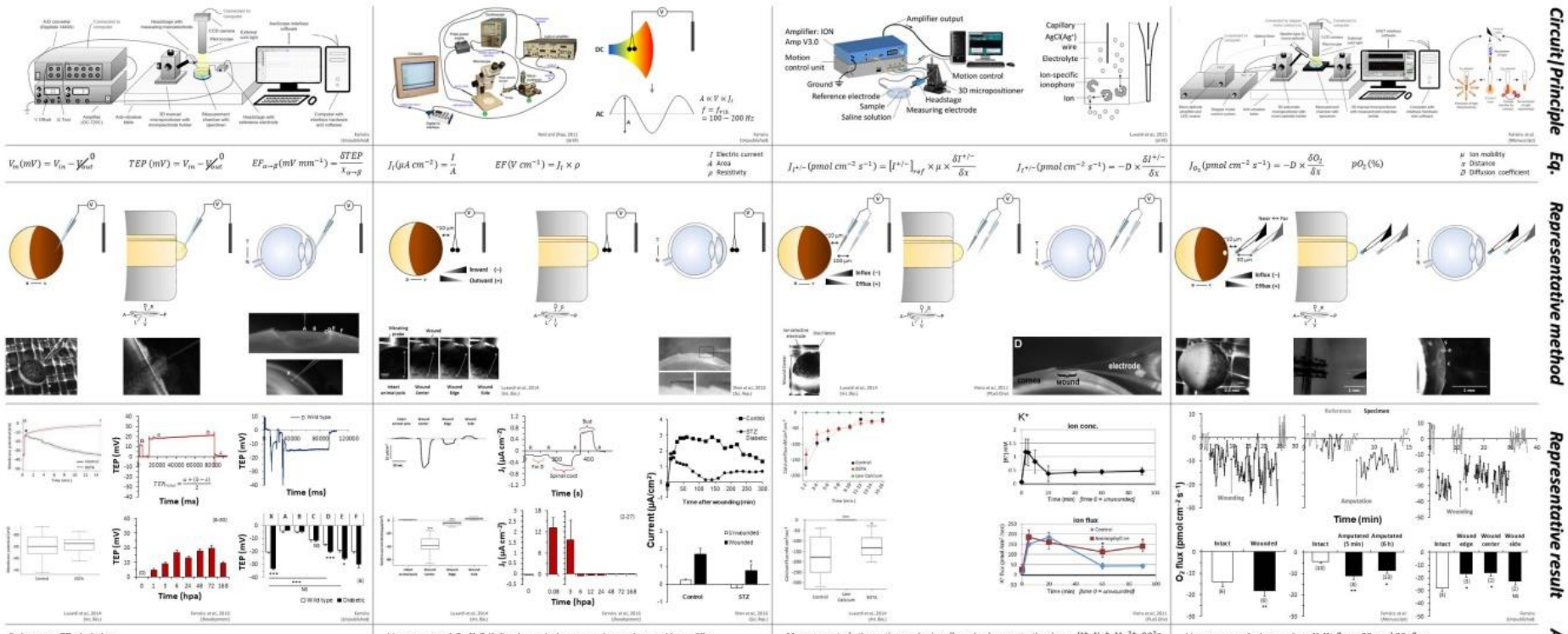

$V_m(mV) = V_{in} - V_{out}^0$ $\quad TEP(mV) = V_{in} - V_{out}^0$ $\quad EF_{\alpha\to\beta}(mV\ mm^{-1}) = \frac{\delta TEP}{x_{\alpha\to\beta}}$

$J_I(\mu A\ cm^{-2}) = \frac{I}{A}$ $\quad EF(V\ cm^{-1}) = J_I \times \rho$

$J_{I^{+/-}}(pmol\ cm^{-2}\ s^{-1}) = [I^{+/-}]_{ref} \times \mu \times \frac{\delta I^{+/-}}{\delta x}$ $\quad J_{I^{+/-}}(pmol\ cm^{-2}\ s^{-1}) = -D \times \frac{\delta I^{+/-}}{\delta x}$

$J_{O_2}(pmol\ cm^{-2}\ s^{-1}) = -D \times \frac{\delta O_2}{\delta x}$ $\quad pO_2(\%)$

I Electric current; A Area; ρ Resistivity; μ Ion mobility; x Distance; D Diffusion coefficient

Ap.

Endogenous *EF* calculation
Dual measurements possibility (with other microelectrode, or vibrating probe or optrode)

Measurement of O_2, H_2O_2 if vibrating probe is connected to a polarographic amplifier
Dual measurements possibility (with other vibrating probe, or microelectrode or optrode)

Measurement of other cations and anions fluxes (and concentrations), *e.g.*, $H^+, Na^+, Mg^{2+}, CO_3^{2-}$
Dual measurements possibility (with other microelectrode, or vibrating probe or optrode)

Measurement of other species: pH, H^+ flux, pCO_2 and CO_2 flux
Dual measurements possibility (with other optrode, or microelectrode or vibrating probe)

Conclusion

The newly described probing capabilities of the on development redox and bioelectric sensor facility do not exhaust its intended full operationally. These close-by, highly integrated techniques to quantify redox and bioelectric activities are user-friendly (exception made for the ion-selective probe), relatively low cost, and can be customized and upgraded to measure more signals in widespread biological models. In a quick comparison among techniques, optrode does not require reference probe and is insensitive to electromagnetic interference, thus dispensing the use of a Faraday cage or wall. Most techniques are automated and centralized using a single software interface, which makes the system ideal for dual measurements studies.

Acknowledgements

We are grateful to Prof. Ph.D. Andreia Gomes (CMBA, UMinho) and Zhao Lab members for helpful comments. This work was supported by UC Davis Bridging fund, NIH (EB015737 and EY019101), AFOSR (FA9550-16-1-0052), and, in part, by an Unrestricted Grant from Research to Prevent Blindness, Inc. to UC Davis Eye Center. F.F. was supported by Fundação para a Ciência e Tecnologia (FCT) studentship SFRH/BD/87256/2012. We are also grateful to Mr. Christopher A. Shipley, owner of Applicable Electronics, LLC, for having the courtesy to loan a SMOT system to the Zhao lab.

2017

Redox and bioelectric probing: harnessing the sensing power of photons and electrons

Fernando Ferreira[1,2], Brian Reid[1], Guillaume Luxardi[1], Li Ma[1,3] & Min Zhao (PI)[1,4]

[1]Department of Dermatology, University of California, Davis, CA, USA; [2]CMBA, Departamento de Biologia, Universidade do Minho, Braga, Portugal;
[3]Skin and Cosmetic Research Department, Shanghai Skin Disease Hospital, Shanghai, China; [4]Department of Ophthalmology, University of California, Davis, CA, USA.

Glass microelectrode

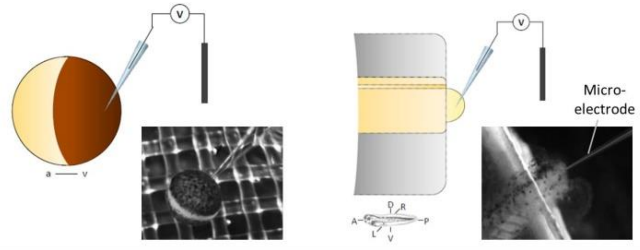

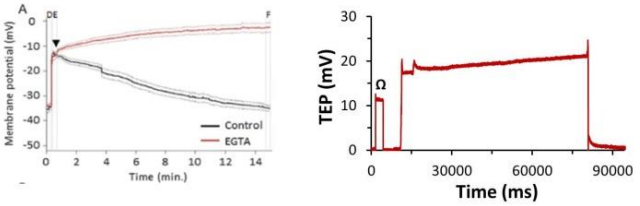

Luxardi *et al.*, 2014 (*Int. Bio.*) Ferreira *et al.*, 2016 (*Development*)

$$V_m \text{ or } TEP(mV) = V_{in} - \cancel{V_{out}}^{0} \qquad EF_{\alpha\to\beta}(mV\ mm^{-1}) = \frac{\delta TEP}{x_{\alpha\to\beta}}$$

Vibrating voltage probe

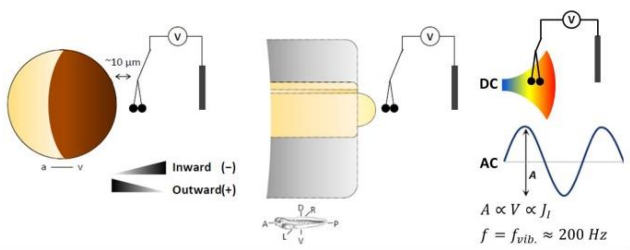

$$A \propto V \propto J_I \qquad f = f_{vib.} \approx 200\ Hz$$

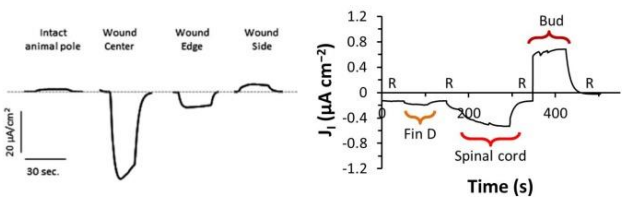

Luxardi *et al.*, 2014 (*Int. Bio.*) Ferreira *et al.*, 2016 (*Development*)

$$J_I(\mu A\ cm^{-2}) = \frac{I}{A} \qquad EF(V\ cm^{-1}) = J_I \times \rho$$

Redox and bioelectric probing: harnessing the sensing power of photons and electrons

Ion-selective microelectrode

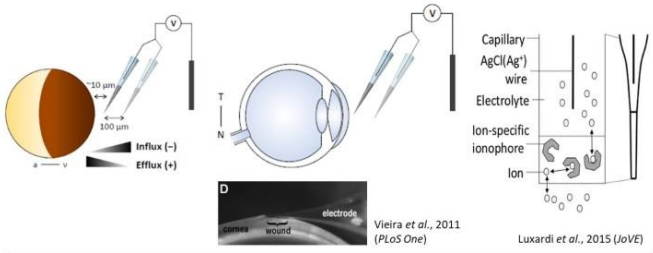

Vieira *et al.*, 2011 (*PLoS One*) Luxardi *et al.*, 2015 (*JoVE*)

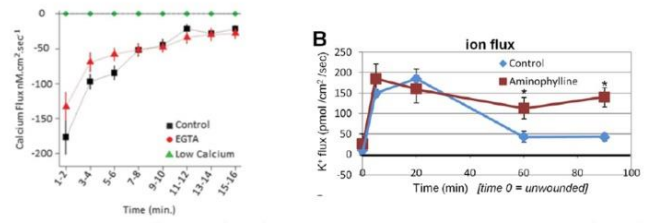

Luxardi *et al.*, 2014 (*Int. Bio.*) Vieira *et al.*, 2011 (*PLoS One*)

$$J_{C^+ or\ A^-}(pmol\ cm^{-2}\ s^{-1}) = [C^+ or\ A^-]_{ref} \times \mu \times \frac{\delta C^+ or\ \delta A^-}{\delta x}$$

Optrode

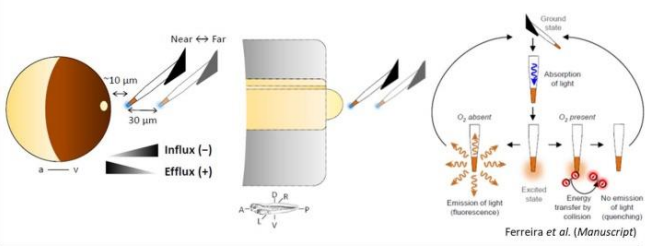

Ferreira *et al.* (*Manuscript*)

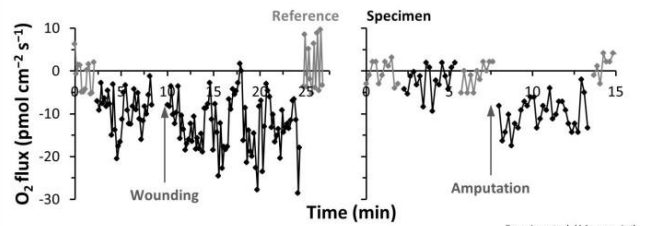

Ferreira *et al.* (*Manuscript*)

$$J_{O_2}(pmol\ cm^{-2}\ s^{-1}) = -D \times \frac{\delta O_2}{\delta x} \qquad pO_2(\%)$$

Pitch transcript

Several techniques have been introduced over the last eight decades to study redox and bioelectric phenomena. I will go over the broad sensing portfolio in the Zhao lab, applied to study mostly wound healing and regeneration in *Xenopus laevis* oocytes and tadpoles and in rodent cornea. *[Click]*

The glass microelectrode, developed in the 40's, basically consists of a liquid salt bridge connecting the specimen with the electrode. Potentials in millivolts are directly measured as redox reactions in the electrode surface. *[Click]* Here are some representative results. *[Click]*

The vibrating probe, introduced in the 70's, consists of a capacitive platinum ball that, when vibrating in an artificial or natural DC voltage gradient, oscillates in an AC sine wave. The amplitude of the wave is proportional to the potential difference at the frequency of the vibration. *[Click]* Here are some representative results of electric currents in the microàmpere range. *[Click]*

The ion-selective microelectrode, first used in the 90's, is an upgrade of the glass microelectrode, where a tip-filled ion-specific ionophore filters the ion of interest and the self-referencing vibration allows accurate flux measurements in the picomole range, after applying Fick's first law. *[Click]* Here are some representative results. *[Click]*

The optic-based self-referencing optrode is an 11 years old technology that uses blue light to excite an oxygen-specific fluorophore. Dissolved oxygen quenches the generated fluorescence allowing its quantification in the picomole range. *[Click]* Here are some representative results. *[Click]*

Thank you.

XII. *INTEGRATION OF EARLY REDOX AND BIOELECTRIC PHENOMENA MODULATES VERTEBRATE REGENERATION*

Poster overview

The poster was produced after 3 years of laboratorial work in the doctoral program, when most thesis results were collected and published or prepared for publication, demonstrating an early interplay between redox and bioelectric activities that was necessary for and sufficient to induce regeneration. The poster presents the core research of the thesis as published in the journals *Development* (Chapter VII) and *Nature Communications* (Chapter VIII). The poster was presented at the Evolutionary and Developmental Biology (BED, Biologia Evolutiva e do Desenvolvimento) symposium with the theme *A decade integrating biology (in) research and training*. The symposium was organized by Élio Sucena (Instituto Gulbenkian de Ciência; Departamento de Biologia Animal, Universidade de Lisboa), Gabriela Rodrigues, Manuela Coelho, Sara Magalhães, Solveig Thorsteinsdottir and Vítor Sousa (Departamento de Biologia Animal, Universidade de Lisboa), and occurred in December 21, 2017 at the Universidade de Lisboa in Portugal.

Poster abstract

Regeneration, or the ability to regain form and function upon large-scale injury, is a complex and multifactorial process. Multiple biochemical and biophysical signalling pathways and cues have been independently shown as important for epimorphic regeneration. Among them, reactive oxygen species (ROS) and electric currents modulate regeneration. However, the mechanisms of and the crosstalk between biochemical and biophysical signals during regeneration remain elusive.

Here, we investigated the interplay between redox (biochemical part) and bioelectric (biophysical part) states during tail regeneration in *Xenopus laevis* tadpoles.

We unveiled a two-way regulation of bioelectric activities by the required NADPH oxidase-mediated production of ROS. NADPH oxidase-driven electron flow (electrogenic property) depolarizes the membrane potential (V_m), while produced ROS (catalytic property) increases the transepithelial potential (TEP) and reverses the electric current density (J_I) during regeneration. Importantly, depletion of ROS levels by inhibition of production, scavenging or blocking their diffusion into cells, mimics the abnormal TEP and J_I observed in the refractory (non-regenerative) period. Crucially, short-term application of hydrogen peroxide (H_2O_2) rescues (from depleted ROS) and induces (from the refractory period) regeneration, TEP increase and J_I reversal. Therefore, H_2O_2 is necessary for and sufficient to induce regeneration and to regulate TEP and J_I. Searching for specific ion translocators, epistasis assays show that voltage-gated Na^+ channels (Na_V) act downstream of H_2O_2 to modulate regeneration.

Further study of the redox state revealed an increased and steady O_2 influx (O_2 sink) immediately upon amputation that correlates with progression and efficiency of regeneration. Inhibition of ROS

production, but not their scavenging, decreases the magnitude of O_2 influx. Therefore, ROS production accounts for most of the motive force driving O_2 flux. Both O_2 and ROS likely regulate the local partial pressure of O_2 and consequent HIF-1α stabilization in the regeneration bud. Notably, blocking HIF-1α activity abrogates regeneration, while stabilizing its activity induces regeneration in the refractory period.

Altogether, these results unveil the orchestration of redox and bioelectric activities and integrate them, discretely and in conjugation, during the regeneration of a composite vertebrate structure. These novel findings might be harvested to attempt to induce epimorphic regeneration in the poor regenerating human body, probably one of the or even the ultimate goal of regenerative medicine.

Poster contributions

F.F., G.L., VK.R. and M.Z. designed the experiments. F.F. performed the experiments and analysed the data and results. G.L., VK.R. and B.R. provided technical training and guidance, and helped to interpret some results. F.F. outlined, wrote and produced the poster.

Poster reprint

Vide infra; normalized dimensions.

Integration of early redox and bioelectric phenomena modulates vertebrate regeneration

FERNANDO FERREIRA[1,2], GUILLAUME LUXARDI[1], VIJAYKRISHNA RAGHUNATHAN[3], BRIAN REID[1] & MIN ZHAO[1,4]

[1]Department of Dermatology, University of California, Davis, CA, USA; [2]CMBA, Departamento de Biologia, Universidade do Minho, Braga, Portugal; [3]The Ocular Surface Institute, College of Optometry, University of Houston, TX, USA; [4]Department of Ophthalmology, University of California, Davis, CA, USA.

Introduction

Regeneration, or the ability to regain form and function upon large-scale injury, is a complex and multifactorial process. Multiple biochemical and biophysical signaling pathways and cues have been independently shown as important for epimorphic regeneration. Among them, reactive oxygen species (ROS) and electric currents modulate regeneration.

However, the mechanisms of and the crosstalk between biochemical and biophysical signals during regeneration remain elusive. Here, we investigated the interplay between redox (biochemical part) and bioelectric (biophysical part) states during tail regeneration in *Xenopus laevis* tadpoles.

Methods

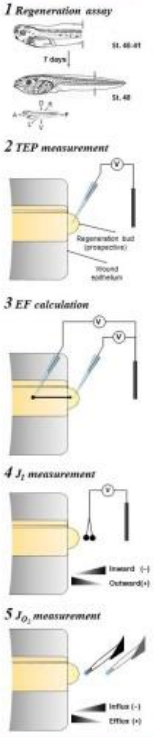

Results

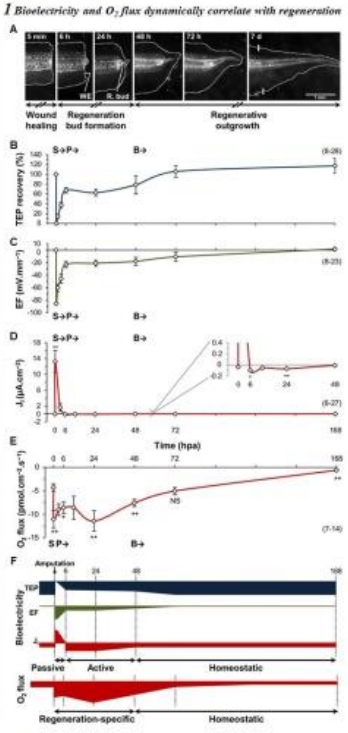

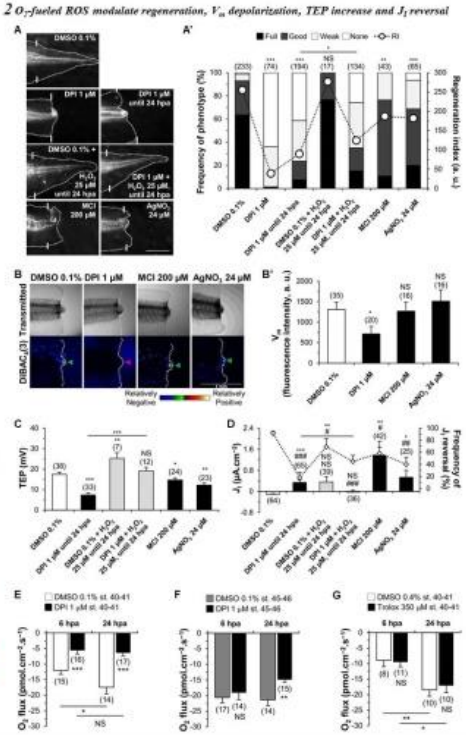

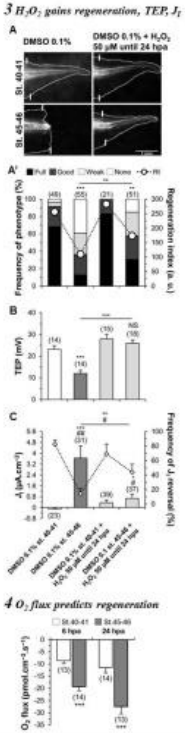

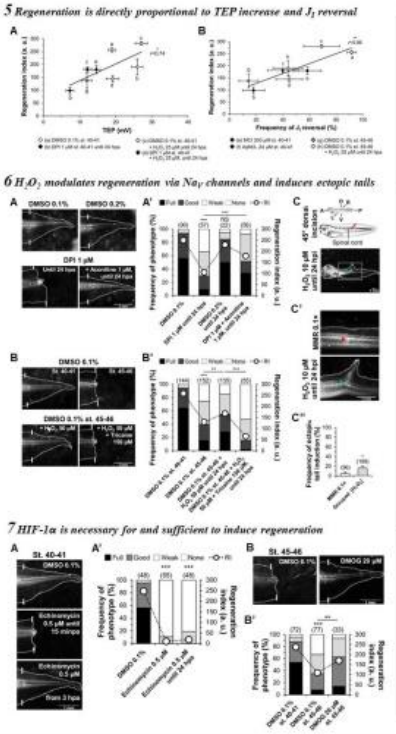

Discussion

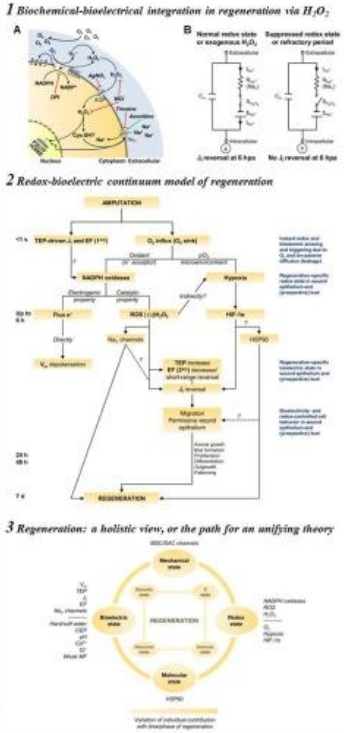

Conclusion

Altogether, the results unveil the orchestration of redox and bioelectric activities and integrate them, discretely and in conjugation, during the regeneration of a composite vertebrate structure.

These novel findings might be harvested to attempt to induce epimorphic regeneration in the poor regenerating human body, probably one of the or even the ultimate goal of regenerative medicine.

References

Ferreira, F., Luxardi, G., Reid, B. and Zhao, M. (2016). Early bioelectric activities mediate redox-modulated regeneration. *Development*. **143**, 4582–4594.
Ferreira, F., Raghunathan, V., Luxardi, G. and Zhao, M. Early redox activities modulate vertebrate regeneration. (In revision for *Nature Communications*)
Ferreira, F., Luxardi, G., Reid, B., Ma, L. and Zhao, M. Real-time physiological measurements of oxygen using a non-invasive self-referencing micro-optrode. (Manuscript ready for submission to *Nature Protocols*)

Acknowledgements

We are grateful to Prof. Ph.D. Andreia Gomes (CMBA, UMinho) and Zhao Lab members for helpful comments. This work was supported by UC Davis Bridging fund, NIH (EB015737 and EY019101), AFOSR (FA9550-16-1-0052), and, in part, by an Unrestricted Grant from Research to Prevent Blindness, Inc. to UC Davis Eye Center. F.F. was supported by Fundação para a Ciência e Tecnologia (FCT) studentship SFRH/BD/87256/2012. We are also grateful to Mr. Christopher A. Shipley, owner of Applicable Electronics, LLC, for having the courtesy to loan a SMOT system to the Zhao lab.

2017

XIII. STEPWISE PROTOCOLS OF ROUTINE METHODOLOGY

Protocols overview

The purpose and fundament of routine and classic methodology – Western blotting, immunohistochemistry and flow cytometry – are too well established to require further description; nonetheless, hereby we present detailed stepwise protocols for scientific and educative transparency and clarity, also facilitating future reproducibility.

Protocols contributions

F.F. based Western blotting protocol on VK.R.'s established protocol with additional help from K.Z. F.F. developed immunohistochemistry protocol based on literature and with advices from L.M. F.F. established flow cytometry protocol together with G.L. F.F. outlined and wrote all protocols.

Protocols reprints

Ferreira, F., Raghunathan, VK. and Zhu, K. (2018). Western blotting (Protocol optimized for HIF-1α staining). (University of California, Davis)

(*Vide infra*; not peer reviewed and unpublished)

Ferreira, F. and Ma, L. (2018). Immunohistochemistry (Protocol optimized for hypoxia and HIF-1α staining). (University of California, Davis)

(*Vide infra*; not peer reviewed and unpublished)

Ferreira, F. and Luxardi, G. (2018). Flow cytometry (Protocol optimized for hypoxia FACS). (University of California, Davis)

(*Vide infra*; not peer reviewed and unpublished)

Western blotting

Protocol optimized for HIF-1α staining (2018)

A. Sample lysate

1. Amputate 30 tails per experimental condition, 1 per min.
2. Recut tails 0.5 mm proximal to amputation plane (1 at a time).
3. Pipette (precut tip and set 2.5 µl) 15 tail explants (1 at a time) to 37.5 µl cold lysis buffer (RIPA) with protease inhibitor mix (Halt cocktail 3× + EDTA 1× + Calpain inhibitor I 260 µM + MG-132 5 µM) in maximum 20 s, with minimal possible volume transfer.
4. Repeat previous step for the other 15 tail explants.
5. For positive experimental control, pipette 5 whole tadpoles (precut tip and set 50 µl) to 100 µl RIPA with protease inhibitor cocktail as before.
6. Lyse tail fragments (15 or 5/1.5 ml tube) on ice using a homogenizer (Pellet Pestle Motor) for up to 1 min.
7. Incubate on ice for 30 min.
8. Centrifuge samples at 14,000 rpm at 4 °C for 2 min, re-homogenize as in step A6 and centrifuge for additional 15 min.
9. Dilute 1:10 the whole tadpole tubes (10 µl sample to 90 µl RIPA with protease inhibitor mix).
10. Pipette supernatant to new tube.

! Pause *Store at −20 °C.*

B. Electrophoresis

11. Normalize loading volumes with the DC protein assay for all samples.
    a. Prepare working reagent A' adding 20 µl reagent S per ml reagent A needed.
    b. Prepare protein standards diluting BSA 2 mg ml^{-1} in RIPA buffer in 0.25 increments, from 0 to 2 mg ml^{-1}, for final 100 µl. Store at −20 °C.
    c. Label a 96 well plate: BSA standard triplicates (vertical) and sample triplicates (horizontal).
    d. Add 25 µl reagent A' into each well.
    e. Add 5 µl standard or sample to respective wells.
    f. Add 200 µl reagent B into each well.
    g. Mix and eliminate air bubbles in balanced plate mixer at 1,000 rpm at RT for 10 min.
    h. Incubate at RT for 15 min (time starts in previous step).
    i. Read absorbance within 1 h at 750 nm using Gen5 microplate reader.
    j. Acquire data using Gen5 software and export data to Excel.
        i. New experiment > Protocol > DC protocol > Procedure > Plate Costar 96 flat bottom.
        ii. Remove 15 min incubation > Plate layout > Fill blank/standards/samples.
        iii. Read plate > Ok > Export to Excel > Calculate using template file.
    k. Calculate sample protein concentration from standard curve and average triplicates.

! Note *≥1 mg ml^{-1} is good total protein concentration for samples.*

    l. Normalize loading volume of each sample for 40 µg protein:

$$V_{Sample}(\mu l) = \frac{40\ \mu g \times 1{,}000\ \mu l}{Sample\ \mu g} = \frac{40\ \mu g}{Sample\ mg}.$$

12. Prepare loading buffer for 60 µl total.
    a. Add ultra-pure H_2O that complete volume into labelled 0.5 ml tubes.
    b. Add calculated sample volumes into respective tubes.
    c. Mix by pipetting up and down (do this with each new addition).
    d. Add 15 µl LDS (lithium dodecyl sulfate, 4x, at 4 °C) buffer into each tube. Vortex LDS precipitates prior to pipetting.
    e. Add 6 µl DDT (dithiothreitol, 10x, reducing agent, at −20 °C) into each tube.

! Tip *To expedite, mix required LDS and DDT volumes and load 21 µl of the solution.*

    f. Denature at 95 °C for 20 min in hot plate. Half fill wells with H_2O for uniform heating.
13. Centrifuge samples to eliminate air bubbles.

! Pause *Store at −20 °C, directly from 95 °C.*

14. Assemble electrophoresis apparatus (XCell SureLock) and run gel.
    a. Remove anode (+) protection strip from gel (Novex 4-12%, 10 wells) cassette and connect into apparatus.
    b. Repeat for the second gel cassette place or use a blank cassette. Combs face inside.
    c. Pour running buffer (500 ml: 25 ml MOPS SDS running buffer 20× and 475 ml dH_2O; add 500 µl antioxidant) between cassettes until top and confirm water tightness.
    d. Pour remaining running buffer around cassettes up to ½ apparatus.
    e. Remove gel cassettes combs.
    f. Load samples onto wells: 1st well, 2.5 µl protein ladder (colorimetric, at −20 °C); 2nd well, 2.5 µl HIF-1α lysate (5 µg; technical control); following wells, 60 µl/each experimental control(s) and treatment samples.
    g. Plug apparatus lid and cables and turn on power supply at 75 mA (~150 V) until first gel cassette lane and at 100 mA after (mostly kept continually at 75 mA).

! Note *Method for gradient gels, due smaller pore downwards. If bands run with a slope in 100 mA return to 75 mA.*

    h. Turn off when reached last gel cassette lane, usually 45 min per one or 1 h per two gels.
15. Disassemble electrophoresis apparatus and break and carefully open gel cassette.
16. Cut and discard gel wells (top) and gel thickness (bottom).

C. Membrane transfer

17. Wet nitrocellulose (NC) membrane and filter papers (2 new and 2 used (if not yellowish)) in 25 ml 1-Step transfer buffer for at least 5 min (or while gel runs).

! Tip *Use 1000 µl tip box lids to wet membrane and gel hereafter.*

18. Wet gel briefly (5 min) in 5 ml 1-Step transfer buffer.
19. Assemble transfer cassette for semi-dry protein transfer.
    a. Take cathode (−) of transfer device (Pierce G2 Fast Blotter) and make gel "sandwich" onto it: Filter papers (used > new) > Gel > NC membrane > Filter papers (new > used).

! Tip *With wet fingertips bend filter papers and membranes grabbing their sides and first touch the center of cathode (−) or previous layer and then slowly lay them down. For gel, do not bend it, first touch on the side of filter paper and then slowly lay it down.*

    b. Roll over softly all filter papers and membrane to eliminate non-conductive air bubbles.
    c. Membrane must face anode (+) for transfer.

! Note *Membrane cannot be moved once on top of gel to prevent distortion of bands.*

d. Absorb excess liquid around sandwich.

20. Lock transfer cassette with anode (+) and slide onto transfer device.
21. Select transfer method (single costume created: constant 25 V, limit 2.5 A) and wait 8.5 min.

! Note *Transfer only 1 gel per time. Up to 4 gels can be transferred simultaneously, but efficiency decreases.*

22. Disassemble transfer cassette and wash gel and membrane in dH_2O for up to 5 min.

! Tip *If gel and membrane are too dry and thus sticky, use dH_2O drops to hydrate and facilitate separation without breaking the gel.*

23. Confirm protein transfer.
    a. Stain membrane with reversible Ponceau red at RT for 5 min with agitation.
    b. Confirm bands presence and take photograph *(Optional)*.
    c. Save Ponceau red and wash membrane with dH_2O flush until red bands disappear.
24. Use gel protein remains to bands normalization (if no ubiquitous protein control used) or to infer putative candidate proteins. *(Optional)*

! Note *For more accurate candidate screen, crop and trypsinize gel and identify proteins using mass spectrometry.*

    a. Stain gel with irreversible Coomassie blue at RT for 2-4 h with agitation.
    b. Save Coomassie blue and wash membrane with dH_2O flush and then o/n with agitation.
    c. Image gel (top up).
        i. Turn equipment on ½ h in advance, remove black cover and plug cable of white base.
        ii. Open UVP software > Acquisition > Camera.
        iii. Take 15-20 ms exposure or autoexposure in transillumination.
        iv. Image > Histogram (to adjust C&B).
        v. Further adjust on a case basis.
        vi. Crop and rotate > Multi-image Action > Extract > Save as .tiff.

! Tip *For time efficiency, image at the time of membrane imaging (step E).*

D. Immunoblotting

25. Block membrane in 15 ml blocking solution (FBS 10%, SuperBlock 10%, fish gelatin 3%, sodium azide 0.02%, in PBS, pH 7.4, at 4 °C) for at least 1 h at 37 °C. Cover with plastic film.
26. Drain blocking solution and move membrane to a plastic pouch, trim excess and heat-seal sides.
27. Add primary antibody diluted in 2 ml blocking solution.
    a. HIF-1α (at −20 °C): 8 µl for 1:250 (rabbit anti-HIF-1α polyclonal; Abcam, cat. no. ab2185).
    b. β-actin (at 4 °C): 1 µl for 1:2,000 (mouse IgG_1 anti-actin monoclonal; Invitrogen, cat. no. MA5-11869).
28. Heat-seal top and label.
29. Incubate membrane o/n at 4 °C (or at RT for 2 h) with agitation.

! Pause *Resume next day if incubation at 4 °C.*

30. Pipette antibody and wash membrane 3× in TBST (15 ml) for 5 min/wash with agitation.

! Save $ *Diluted primary antibodies can be reused up to 3 times. Store at 4 °C for short-term or at −20 °C for long-term.*

31. Add secondary antibody (horseradish peroxidase-conjugated) diluted in 15 ml blocking solution.
    a. HIF-1α (at −20 °C): 15 µl for 1:1,000 (goat anti-rabbit IgG (H+L); Abcam, cat. no. ab205718).
    b. β-actin (at 4 °C): 1.5 µl for 1:10,000 (goat anti-mouse IgG (H+L); KPL, cat. no. 474-1806).

! Note *During optimization only add anti-β-actin after HIF-1α detection, so bands are only of target protein.*

32. Incubate membrane with secondary antibody at 37 °C for 1 h with agitation (70 rpm). Cover with plastic film.
33. Drain antibody and wash membrane 2× in TBST and 1× in TBS (15 ml) for 5 min/wash with agitation.

! Save $ *Diluted secondary antibodies can be reused in the same day. Store at 4 °C.*

E. Detection

34. Mix 1:1 ECL components 1 and 2 (at 4 °C) for a total 2 ml (~0.1 ml cm−2 membrane) in Al-wrapped tube.
35. Put membrane onto open plastic sheet protector inside the X-ray device.
36. Pipette mix all over membrane, cover with the plastic and allow substrate to react for 2 min.
37. Develop membrane (top up) by exposure to X-ray film.
    a. Turn equipment on ½ h in advance and remove black cover.
    b. Open UVP software > Acquisition > Camera > On chip
    c. Take initial short exposure or autoexposure photograph to confirm bands presence.
    d. Image > Histogram (to adjust C&B).
    e. Set exposure up to 1.5 min and take final photograph. Typically select ½ min exposure.
    f. Further adjust on a case basis.
    g. Take epi light photograph using autoexposure to see ladder bands.
    h. Crop and rotate > Multi-image Action > Extract > Save as .tiff.
    i. Count normalized pixels using this software or ImageJ.
38. Wash 1× in TBS (15 ml) for 5 min with agitation and store membrane inside heat-sealed plastic pouch in 2 ml PBS at 4 °C.

F. Reblotting *(Optional)*

39. Wash membrane 1× in TBS (15 ml) for 5 min with agitation.
40. Strip membrane in 15 ml Striping blot for 15 min with agitation.
41. Wash membrane 2× in TBST and 1× in TBS for 5 min/wash with agitation.
42. Repeat step E to attest for bands absence.
43. Repeat steps D and E.

Immunohistochemistry

Protocol optimized for hypoxia and HIF-1α staining (2018)

A. Sampling

1. Amputate 3 (+2 backup) tails per experimental condition.
2. Incubate tadpoles in hypoxia marker pimonidazole HCl 300 µM (in PBS) for 1 h (counting back from fixation time) at a density of 1 tdp ml^{-1} (in a 24 well plate). *(For hypoxia staining only)*
3. Fix tadpoles on PFA 4% for 2 h at 4 °C (use an intermediate dish with PFA 4%).

! Tip *Thawed PFA 4% from −20 °C can be reused when saved at 4 °C for up to 2 weeks.*

4. Wash 3× in PBS for 5 min each and save o/n in PBS at 4 °C.

! Pause *Store at 4 °C for up to 1 week.*

! Tip *Adjust time in PBS so all conditions enter the next steps simultaneously.*

B. Frozen sectioning

5. Incubate tadpoles in sucrose 30% (in PBS) o/n (~24 h) at 4 °C.
6. Place tadpoles (2 at a time) in a low-cost microscope slide (or glass plate) and absorb the most sucrose possible (use pipette and Kimwipe tissue).
7. Fill a top labeled and side trimmed biopsy cryomold (10×10×5 mm) with OCT (freezing medium).
8. Coat each tadpole with 1 drop of OCT and transfer gently to individual cryomolds with forceps.

! Tip *Let OCT drop slip into cryomold by tilting the slide, this almost avoids need for forceps.*

9. Position gently the tadpole laterally in the bottom with an obliquus orientation using forceps.
10. Snap freeze with dry ice.

! Tip *For a uniform freezing of the OCT and specimen, simply put cryomold over a flat block of dry ice. Complete freezing typically takes up to 2 min. Use of minced dry ice alone or with ethanol100% speed up freezing to up to 1 min but curves the tadpole body (A/P axis) due to a faster freezing in borders than in center of the cryomold, rendering specimen virtually incompatible for longitudinal sectioning.*

11. Put blocks into a labeled 50 ml tube and save at −80 °C.

! Pause *Storage of blocks (cryomold removal is optional) in 50 ml tubes or zip bags or other container (or wrap in aluminum foil) avoids desiccation of the tissue (due to the drying out of the blocks). Store up to several months.*

12. Proceed to cryosectioning.
    a. Transfer cryomolds to a −20 °C freezer and let blocks equilibrate temperature for 15 min.
    b. Transport cryomolds in gel ice packs and transfer them to cryotome, after adjusting its chamber and cutting temperatures to −20 °C.
    c. Let blocks stabilize to chamber temperature for a final 5 min and freeze block holders.
    d. Release (meanwhile) block by pushing cryomold base and glue it to the holder with OCT.
    e. Mount holder onto cryotome and adjust position so block is perpendicular to blade.
    f. Set working width to 5 µm and trim block with decreasing widths (50>30>10 µm) until almost reached desired position (tail tip or amputation edge) by naked eye.
    g. Touch RT microscope slide onto slice and check on microscope. If necessary, trim further.

! Tip *Optionally, when sample slices fold too much, microscope slide can be kept inside cryotome at −20 °C to allow slice unfolding using brushes.*

    h. Center 3 slices per labelled slide and acquire 3-6 slides per tadpole.

i. Mark best slides to proceed for staining with an *.
j. Dry slides at RT for up to 2 h and save in a slide box at −80 °C.

! Pause *Optionally, store at −20 °C for short-term and −80 °C for long-term before staining.*

B'. Paraffin sectioning

13. Drop samples to Bradley (NEI's imaging core) for paraffin-embedded sectioning.

! Pause *Wait for the microscope slides with samples and store (long-term) them at 4 °C before staining.*

! Note *Frozen sections appear to have stronger staining in optimization experiments; thus, paraffin sectioning was deferred in favor of frozen sectioning.*

C. Deparaffinization *(For paraffin-embedded sections only)*

14. Select the one or two best slides (6 sections; marked with an *) per condition, plus two slides for negative technical controls (no primary and no secondary antibodies).
15. Immerse slides in Clear Rite 3 2× for 10 min each, using a slide staining rack and dish.

! Note *Use 200 ml of liquid in the slide staining dish for full immersion of slides.*

16. Drain slides (slide rack) in tissue paper.

! Tip *Fold tissue papers into a plastic container, such as the cover box of well plates.*

! Note *Repeat this step after every subsequent immersion.*

17. Immerse slides in ethanol 100% 2× for 10 min each.
18. Immerse slides in ethanol 95% 2× for 5 min each.
19. Immerse slides in ethanol 80% 2× for 5 min each.
20. Wash slides by immersion in dH_2O 2× for 5 min each.

D. Rehydration and permeabilization

21. Select one or two * marked slides per condition, plus two slides for negative technical controls and thaw slides at RT up to 1 h or o/n. *(For frozen sections only)*
22. Absorb liquid around sections (with a Kimwipe tissue) and draw a hydrophobic border with a PAP pen (alternatively, it could be used polish nail).

! Tip *Make a belly-shaped contour in the slide's down right corner to facilitate liquid drain in the subsequent steps.*

23. Let ink dry for 1-2 min (polish nail needs 15-20 min).
24. Transfer slides to staining box with humidified atmosphere (wet tissue paper on the slide box bases).
25. Pipette 200 µl of wash buffer (TBST: TBS 1× with Tween 20 0.1%) into each slide for 10 min.

E. Antigen (heat-induced epitope) retrieval *(Optional)*

26. Rehydrate slides instead by immersion in wash buffer (200 ml) for 10 min.

! Note *When antigen retrieval is performed, PAP pen (or polish nail) cannot be used due to the high temperature used (step E28); thus, for rehydration it is used immersion technique instead.*

27. Set the water bath to 90 °C and pre-heat 200 ml of the antigen retrieval buffer (sodium citrate 10 mM, Tween 20 0.05%, pH 6).

! Note *Use little water for faster heating.*

28. Immerse slides in the heated buffer and incubate at 90 °C for 5 min (frozen sections) or for 20 min (paraffin-embedded sections).

29. Cool slides at RT for 20 min.

! Note *Meanwhile, remove all possible hot water and add tap water to the water bath using the device lid. This allows a timely cooling to 37 °C for the blocking incubation (step G37).*

30. Wash slides by immersion in TBST 2× for 2 min each.

! Save $ *Reuse TBST of rehydration (step E26).*

31. Perform steps D22-24.

! Note *Since non-retrieved antigen staining was robust, step E was not performed after protocol optimization; however, it is kept here in case other antibodies used in future require it.*

F. Blocking peroxidases *(For immunoperoxidase only)*

32. Pipette 200 µl of H_2O_2 3% (in PBS) into each slide.

! Note *Make fresh solution (1:10 dilution of bulk H_2O_2 30%) every time.*

33. Incubate at RT for 5 min in the dark.
34. Remove solution in all slides by pipetting. Tilt slide and pipette liquid in the belly corner.

! Note *Repeat this step before a new solution is applied into slides. Alternatively, absorb liquid or turn over slide so liquid drains.*

35. Wash slides by pipetting 200 µl of TBST 2× for 2 min each.

G. Blocking non-specific binding

36. Pipette 200 µl of blocking solution (goat serum 10% with Tween 20 0.1%, in PBS) or adapted blocking solution (goat serum 10% with Triton X-100 0.3% (from 20% stock), in PBS) *(For immunofluorescence of HIF-1α only)* into each slide.

! Note *Make fresh blocking solution every time.*

37. Incubate at 37 °C for 1 h.

! Note *Check for evaporation at 30 min and, if necessary, pipette more blocking solution. For this, keep 2 ml of blocking solution in a tube in the water bath.*

H. Immunostaining

38. Pipette 100 µl of primary (mouse IgG_1 anti-pimonidazole FITC-conjugated monoclonal) antibody (FITC-MAb1; Hypoxyprobe, cat, no. HP2-100Kit) 1:50 (in blocking solution) *(For immunoperoxidase of hypoxia only)* or 1:500 *(For immunofluorescence of hypoxia only)* into each slide, except the no 1^{ary} Ab control slide.

! Note *Slides were not washed out, so residual protein block solution is left on the sections.*

! Note *Depending on the hydrophobic contour size and antibody price/availability, a range between 50 to 200 µl of diluted antibody can used; 100 µl is a standard volume.*

! Note *Antibody dilutions generally start at 1:50, but then might be increased or decreased depending on signal.*

39. Pipette 100 µl of primary (rabbit anti-HIF-1α polyclonal) antibody (Abcam, cat. no. ab2185) 1:500 (in adapted blocking solution) into each slide, except the no 1^{ary} Ab control slide. *(For immunofluorescence of HIF-1α only)*
40. Incubate at RT for 1 h in the dark *(For immunoperoxidase and immunofluorescence of hypoxia only)* or at 4 °C o/n in the dark *(For immunofluorescence of HIF-1α only)*.

! Note *Hereafter always in the dark.*

! Tip *Check fluorescence signal at 488 nm (positive experimental control) in the quicker fluorescence microscope.*

41. Let slides stabilize to RT for 20 min. *(For immunofluorescence of HIF-1α only)*
42. Wash slides by pipetting 200 µl of TBST 2× for 2 min each *(For immunoperoxidase and immunofluorescence of hypoxia only)* or 3× for 5 min each *(For immunofluorescence of HIF-1α only)*.
43. Pipette 100 µl of secondary (rabbit anti-FITC HRP-conjugated) antibody 1:50 (in blocking solution) into each slide, except the no 2^{ary} Ab control slide. *(For immunoperoxidase of hypoxia only)*
44. Pipette 100 µl of secondary (goat anti-rabbit IgG (H+L) Alexa Fluor 488-conjugated) antibody (Jackson ImmunoResearch Laboratories, cat. no. 111-545-144) 1:200 (in adapted blocking solution) into each slide, except the no 2ary Ab control slide. *(For immunofluorescence of HIF-1α only)*
45. Incubate at RT for 30 min *(For immunoperoxidase of hypoxia only)* or at RT for 1 h *(For immunofluorescence of HIF-1α only)*.
46. Wash slides by pipetting 200 µl of TBST 2× for 2 min each *(For immunoperoxidase of hypoxia only)* or 3× for 5 min each *(For immunofluorescence of HIF-1α only)*.

! Pause *If necessary, a pause can be made in last wash for* ca. *1 h.*

I. Chromogenic reaction *(For immunoperoxidase only)*

47. Mix the 2 DAB reagent tablets into 5 ml dH_2O.
48. Pipette 200 µl of DAB solution into each slide.
49. Incubate at RT for up to 10 min.
50. Detect staining intensity in the dissecting microscope and stop DAB reaction with dH_2O flushes when appropriate.

! Note *Staining should be well visible at 3 min.*

! Note *Owing to enhanced clarity, immunoperoxidase staining (DAB detection) using bright filed microscopy was deferred in favor of immunofluorescence staining (FITC detection) using confocal microscopy.*

J. Counterstaining

51. Pipette 200 µl of hematoxylin *(For immunoperoxidase)* or 100 µl of DAPI (1:1,000; in PBS) *(For immunofluorescence)* into each slide.
52. Incubate at RT for 30 s *(For immunoperoxidase)* or at RT for 5 min *(For immunofluorescence)*.
53. Wash slides by pipetting 200 µl of TBST 1× for 5 min *(For immunofluorescence only)*.
54. Wash and clean slides with dH_2O flushes.

K. Mounting

55. Immerse slides in Clear Rite 3 2× for 10 s each to remove PAP pen ink (not required step if polish nail used). Alternatively, use a tissue paper (Kimwipe) wet with Clear Rite 3 to remove PAP pen. *(For paraffin-embedded sections only) (Optional)*
56. Drain slide in tissue paper and absorb liquid (with a Kimwipe tissue).
57. Coat each section with a drop of CC/Mount *(For immunoperoxidase only)* or Fluoromount-G *(For immunofluorescence only)* and cover with a coverslip (22×50 mm, no. 1)
58. Dry at RT o/n.

59. Save slides in a labelled slide box at 4 °C.

! Pause *Store at 4 °C* ad aeternum.

L. Imaging *(For immunoperoxidase only)*

60. Put slide and rotate camera so tail is at A/P axis at the left side of the photomicrograph.
61. Take bright field photomicrographs in 2 magnifications (200 and 400×), using NEI's microscope.
62. Light intensity is 8 and 9 points for 200 and 400×, respectively.
63. Photomicrographs occupy ½ of the picture size.
64. Adjust on a case basis.

L'. Imaging *(For immunofluorescence only)*

65. Invert slide and adjust rotation manually so tail is at A/P axis at the left side of the photomicrograph.
66. Take FITC and DAPI fluorescent and bright field photomicrographs in 2 magnifications (200 and water's 400×), using Tupper's Olympus confocal microscope.
67. Confocal settings typically are:
    a. DAPI: Laser 1%; HV 650; Offset 30.
    b. FITC: Laser 5%; HV 650; Offset 30.

! Tip *In FITC (AlexaFluor 488) channel, laser was and can be optimized from 1 to 10% and HV from 550 to 750.*

68. Photomicrographs occupy ½ of the picture size.
69. Adjust on a case basis.

Flow cytometry

Protocol optimized for hypoxia FACS (2018)

A. Sample cell dissociation

1. Amputate 20 tails per experimental condition.

! Note *10 and 15 tail explants can alternatively be used, especially for pilot experiments. 20 tails can generate more than 35,000 cells for analysis, while 10 tails generate ~20,000 cells. ~10,000 cells are a good lower limit for FACS.*

2. Incubate tadpoles in hypoxia marker pimonidazole HCl 300 µM (in PBS) for 1 h (counting back from recut time) at a density of 1 tdp ml^{-1} (in a 6 well plate).
3. Recut tails 0.5 mm proximal to amputation plane (1 at a time).
4. Pipette (precut tip and set 2.5 µl) 20 tail explants (1 at a time) to 1 ml dissociation solution (DNase I 100 U ml^{-1} and Liberase 0.25 mg ml^{-1}, in PBS) in maximum 20 s, with minimal possible volume transfer.
5. Incubate at 28 °C (water bath) for ~30 min.
6. Every 15 min help explant dissociation by pipetting up and down using a P200 set to 200 µl.
7. Pass dissociated samples through a 35 µm cell strainer (FACS tubes). *(Optional)*

! Note *Although commonly done in established FACS protocols, this cell filtering step was not performed here but only prior to cell analysis (step E22).*

8. Centrifuge cells (1.5 ml tubes) at 1,200 rpm at RT (22 °C) for 5 min and discard supernatant.

! Tip *Hereafter always leave ~50 µl solution behind to prevent (or greatly minimize) cell removal during pipetting.*

9. Wash cells 1× by resuspending in FACS buffer (BSA 1% in PBS, at 4 °C) 1 ml and repeating previous step.

! Tip *Alternatively, use a 96 well plate that only requires 200 µl of volume for every step. As a further benefit, well plate increases cell survival; untreated 1.5 ml tubes may stick cells to its wall, increasing death rate.*

! Note *FACS buffer stored at 4 °C can be used until a discernible contamination occurs in the solution.*

B. Live/Dead staining

10. Resuspend cells in 200 µl of Aqua stain (Life Technology, cat no. L34965) 1:200 in FACS buffer.

! Note *Aqua stain good for a few hours after dye reconstitution with DMSO; longer storage at −20 °C.*

11. Incubate at RT for 30 min in the dark.

! Note *Hereafter always in the dark.*

12. Wash cells by repeating step A9.

! Tip *Just add FACS buffer 1 ml and centrifuge; no need to remove staining solution.*

C. Cells fixation

13. Resuspend cells in 200 µl of FA 3.7% (1:10 of FA 37%) in PBS.
14. Incubate at RT for 10 min in the dark.
15. Wash cells 2× by repeating step A9.

! Tip *Just add FACS buffer 1 ml twice and centrifuge; no need to remove fixating solution.*

16. Resuspend cells in FACS buffer 500 µl and save o/n at 4 °C. *(Optional; if done just wash 1× in previous step)*

! Pause *Store o/n to synchronize immunostaining with additional sample collection for cross comparison. With the shipment of young and old tadpoles allowing a priori staging optimization, this step was not performed.*

D. Immunostaining

17. Resuspend cells in 200 µl of antibody (mouse IgG_1 anti-pimonidazole FITC-conjugated monoclonal; FITC-MAb1; Hypoxyprobe, cat, no. HP2-100Kit) 1:50 (in FACS buffer).
18. Incubate at RT for 1 h in the dark.
19. Wash cells by repeating step A9.

! Tip *Just add FACS buffer 1 ml and centrifuge; no need to remove staining solution.*

20. Resuspend cells in FACS buffer 500 µl and save o/n at 4 °C.

! Pause *Resume next day.*

E. FACS

21. Take tubes on ice to IRC's Flow cytometry facility.
22. Transfer cells to FACS tubes by passing them through the 35 µm cell strainer.
23. Turn on and set up the flow cytometer equipment (BD LSRFortessa) and software (FACSuite).
    a. Follow the mandatory instructions pinned to equipment and in locally available user manual for the turning on and initial setting up of the flow cytometer.
    b. Make panels for live/dead staining and hypoxia immunostaining.
    c. Make panels for fluorescence compensation using appropriate commercial beads.
    d. Repeat steps b and c for all conditions analyzed.
    e. Optimize acquiring fluorescence settings by using sample with the expected strongest signal.
    f. Kept settings for all acquisitions.
24. Run samples.
    a. Start with dH_2O and then with sample.
    b. Repeat sequence in all samples and compensation controls.
    c. Analyze 20,000 to 25,000 cells in samples and default (by acquisition software) numbers in fluorescent bead.
    d. In the end, run bleach 10% to clean system.
25. Close software and turn of equipment as per instructions.

F. Data analysis

26. Open FlowJo and set compensations.
27. Gate live (from dead) single (from agglomerates) cells (from debris).
28. Generate appropriate flow cytograms (discriminated cells or histograms) for live/dead staining and hypoxia immunostaining.
29. Merge control and treatment flow cytograms for visual cross comparison.
30. Get the geometric mean fluorescence intensities (MFI) per condition.
31. Standardize MFI using the in-house developed (by PhDs G. Luxardi and P. Maillard) equation: $x_{FMO}(MFI) = \frac{x(MFI) - FMO(MFI)}{FMO(SD)}$.
32. Calculate the standardized MFI (final used value) per condition.

XIV. UNPUBLISHED WORK: SIDE PROJECTS AND COLLABORATIONS

Overview

During the thesis many serendipity discoveries allied with previous or emergent research interests, made me carry on many side projects. Likewise, being in a research group, several opportunities appeared to collaborate with work colleagues within and without the group.

Some of the following work was presented in conferences and symposia where I was mentioned. However, non-first author posters or oral communications are excluded from appendixes of this thesis.

Side projects

In addition to the published projects (Chapter VI–VIII), several unpublished side projects were performed. Below it follows the tables summarizing most of those projects.

Table A.X.1 Summary of side project no. 1

Project	*Does regeneration depend on the type and level of amputation?*
Aim	Test the effect of different geometric amputations on regeneration efficiency
Experimental design	Perform anterior (75% tail removal), posterior (25% tail removal), podium-like and diagonal (towards dorsal and ventral axes) amputations
	Compare against control amputation (50% tail removal)
	Follow up regeneration and photograph tails at 7 dpa
Preliminary results	Too much (>75%) anterior amputations seemed to impair regeneration. Anterior amputations did not seem to affect regeneration and indeed had an accelerated regeneration (as it occurs, for instance, in zebrafish and newts amputations)
	Posterior and diagonal amputations did not impair regeneration
	Interestingly, ventral fins typically did not regenerate in towards dorsal diagonal amputations (6 out of 14 or 43%). However, same seemed to occur in control (straight) amputations, where ventral fin was much more likely to not regenerate
	Congruently, towards ventral diagonal also had failed dorsal fin regeneration (5 out of 16 or 31%)
	Podium-like amputations also seemed to impair regeneration, showing that fin and trunk must crosstalk for efficient regeneration
Conclusion	Type and level of amputation seem to affect regeneration outcome and velocity
	Further experiments are required for statistical power and more robust conclusions
Status	Halted

Table A.X.2 Summary of side project no. 2

Project	*Salinity effect on regeneration, V_m and J_I*
Aim	Test the effect of different media salinities on regeneration efficiency, V_m and J_I
Experimental design	Follow amputated tadpoles in hard (MMR 1×), control (MMR 0.1×) and soft (MMR 0.01×) water conditions
	Refresh daily
	Photograph tails at 7 dpa
	Image V_m using $DiBAC_4(3)$ 2 μM
	Measure J_I using the vibrating probe technique
Preliminary results	Hard water impaired regeneration and soft water seemed to enhance regeneration (*n*=2-9)
	Hard water increased V_m depolarization at both 6 and 24 hpa (*n*=5-8), while soft water decreased depolarization (*n*=2-4)
	Hard water almost doubled the injury current, while soft water almost eliminated it (*n*=2)
	Hard water precluded J_I reversal at 6 hpa, maintaining a steady and large outward current (*n*=2)
Conclusion	Salinity affect regeneration, V_m and J_I
	V_m outcome might be explained by the increase/decrease in K^+ levels, which congruently modulate V_m
	Absent J_I reversal at 6 hpa might explain the impaired regeneration in hard water
	Further experiments are required for statistical power and more robust conclusions
Status	Halted

Table A.X.3 Summary of side project no. 3

Project	*pH effect on regeneration*
Aim	Test the effect of pH on regeneration efficiency
Experimental design	Follow amputated tadpoles in acidic (pH 4), neutral (7; control) and basic (pH 10) conditions
	Refresh daily
	Photograph tails at 7 dpa
Preliminary results	Buffer (HEPS 0.5 mM) absence did not impair regeneration
	Tadpoles' culture or breathing or tail regeneration neutralized pH. *E.g.*, at 28 hpa, pH 4 shifted to 6.2 and pH 10 to 7.5
	pH 4 slightly impaired and pH 10 slightly enhanced regeneration; area at 72 hpa was significantly lower for pH 4
Conclusion	pH might affect regeneration
	Further experiments are required for statistical power and more robust conclusions
Status	Halted

Table A.X.4 Summary of side project no. 4

Project	*Ca^{2+} effect on regeneration*
Aim	Test the effect of extracellular and intracellular Ca^{2+} on regeneration efficiency
Experimental design	Follow amputated tadpoles in no extracellular Ca^{2+} ($CaCl_2$ 0 μM and EGTA 200 μM (Ca^{2+} chelator)) and in no intracellular Ca^{2+} (2-APB 0.5-1.5 μM (internal stores blocker)) conditions
	Refresh daily
	Photograph tails at 7 dpa
Preliminary results	Ca^{2+} absence for more than 24 hpa was lethal (drugs commonly used until 24 hpa)
	Extracellular Ca^{2+} did not seem to significantly affect RI
	Internal stores Ca^{2+} release was slightly required for regeneration
Conclusion	Intracellular availability of Ca^{2+} might affect regeneration
	Further experiments are required for statistical power and more robust conclusions
Status	Halted

Table A.X.5 Summary of side project no. 5

Project	*Cl^- effect on regeneration*
Aim	Test the effect of Cl^- ion and channels on regeneration efficiency
Experimental design	Follow amputated tadpoles in general Cl^- channels inhibitor DIDS and in specific Ca^{2+}-activated Cl^- channels (CaCC) inhibitor mefloquine conditions
	Refresh daily
	Photograph tails at 7 dpa
Preliminary results	DIDS dramatically impaired regeneration when used at a high dose (200 μM), but low exposure (until 6 or 24 hpa)
	Higher doses of and exposures to DIDS were lethal
	CaCC inhibition did not impair regeneration, at least using mefloquine
	However, owing to mefloquine toxicity, drug dose could not be raised over 50 μM
Conclusion	Cl^- ion and channels are required for regeneration
	CaCC did not seem to be the specific Cl^- channels, which remains undefined
	Further experiments are required for statistical power and more robust conclusions
Status	Halted

Table A.X.6 Summary of side project no. 6

Project	*EF effect on migration and regeneration**
Aim	Test the effect of exogenous EF on *in vivo* cell migration and regeneration efficiency
Status	Halted
	To be followed up (in a research project and/or for grant proposal)

* This side project was partially delegated to an undergraduate student (Mr. Garrett Chan), trained and supervised by me.

Table A.X.7 Summary of side project no. 7

Project	*Mechanobiology on regeneration*
Aim	Test the effect of stretch-activated channels (mechanosensitive channels; MSC) on regeneration efficiency and J_I
Status	Halted
	To be followed up (in a research project and/or for grant proposal)

Collaborations

In addition to the collaborations published or in preparation for publication (Appendix I–IV), several unpublished collaborations with more or less contributions were performed. Below follow the tables summarizing most of those collaborations. Part of these collaborations is halted projects; the other part is grant and manuscripts under preparation or even submitted, therefore some details are omitted and what is shown is circumscribed to my part in the work.

Table A.X.8 Summary of collaboration no. 1

Project	*Translocators in corneal wound healing*
Aim	Profile the Cl^- flux in wounded mouse cornea (*ex vivo*), control and genetic knock out (homozygote and heterozygote)
Experimental design	Measure Cl^- flux using the ion-selective microelectrode technique in a costume made chamber to hold the *ex vivo* eyes. Measure in artificial tear solution
	Calculate ion fluxes
Preliminary results	High magnitude Cl^- influx detected up to 1 hpa in all conditions
Conclusion	Wound induces a large Cl^- influx
	Inconclusive regarding translocator knock out effect
	Further experiments are required for statistical power and more robust conclusions
Status	Finalized

Table A.X.9 Summary of collaboration no. 2a

Project *Bioelectric profiling of corneal wound healing: TEP and EF*

Status Finalized

Table A.X.10 Summary of collaboration no. 2b

Project *Bioelectric profiling of corneal wound healing: solving the TEP paradox*

Status Halted

Table A.X.11 Summary of collaboration no. 3a

Project *Bioelectric profiling in angiogenesis of chicken eggs*

Status Finalized

Data to be used in a future manuscript

Table A.X.12 Summary of collaboration no. 3b

Project *Bioelectric profiling in primitive streak formation of chicken eggs*

Status Finalized

Data to be used in a future manuscript

Table A.X.13 Summary of collaboration no. 4

Project *Bioelectric profiling of a translocator knocks out in zebrafish*

Status Halted

Table A.X.14 Summary of collaboration no. 5

Project *Bioelectric profiling of Peyer's patch in rat ileum**

Status Finalized

* Collaboration with a researcher outside the group.

Table A.X.15 Summary of collaboration no. 6

Project *Bioelectric profiling of Peyer's patch in mouse cecum*

Status Finalized

Data to be used in a future manuscript

Table A.X.16 Summary of collaboration no. 7

Project	*Biophysical profiling of subcutaneous tumour induced in mouse*
Status	Finalized
	Data collected for use in an interdisciplinary multi-group grant submission

In many of the aforementioned projects, the experimental design, preliminary results and conclusions were not disclosed, in order to not compromise the novelty of the study (a key criterion of the peer-reviewed journals), the usage in grant proposals and to safeguard the interests of the other co-authors involved, especially in the collaborations cases.

Other minor collaborations and technical consulting were performed but they are not relevant enough or are too preliminary to deserve note.

XV. COMPLETED ACKNOWLEDGMENTS

Research should be a reflexion of Nature's beauty; as it, however, research has painful but enlightening thorns from lovely roses. Despite the truism, I shall not dwell into whinging!, as that would be quite cynical. I was longing to experiment (with) Nature! From hubris-free, class-born lucid dreams to bench side conquest and turmoil, a decade has permeated through me. The quest was lengthy but not lonely... and here and now the due respects shall emerge.

I truly want to acknowledge my pedagogic supervisor and, specially, my scientific advisor.

It all commenced in the now distant 2011, when Prof. Andreia Gomes (Departamento de Biologia, Universidade do Minho) accepted to be the pedagogic supervisor of an (odd) project that she (oddly) trusted. You were my link to Universidade do Minho, you guided me in the early steps of the Ph.D., especially through the theoretical year and with all academic bureaucratises. For that and for the friendly and scientific advices and for much more, Obrigado!

I'm also grateful to the professors that lecturer and head(ed) the doctoral programme and head(ed) the Departmento of Biologia and Escola de Cências for the helping in the bureaucratic paperwork and for important advices.

The rose could never bloom if it wasn't for the role of my scientific advisor, Prof. Min Zhao (Departments of Dermatology and Ophthalmology, University of California (UC), Davis). Sprouting ideas is a hurting valence if no one believes on them. And you believed... and even nurtured! You provided me with all the time, soil and fertilizers I needed to mature abstract ideas into concrete knowledge. Your guidance and mentorship through the meanders of research helped me to harvest more than I dreamed from fields still awaiting the deserving attention. Importantly, you endured my naïve science and expanding discussions with remarkable patient! I surely will follow your soft touch towards daring students and the kind words to motivate them in times of apparent despair, when the crops simply degenerate. For all of that and for supporting me to attend international conferences and for welcoming me among your peers, Lab members, staff and even family (I miss the Thanksgiving gatherings with ping-pong!) and for so much more, Thank you!

I'm also grateful to my master's advisor Catarina Certal, who recommended me to Prof. Min Zhao.

Beyond the mentorship of Prof. Min, three researches helped and worked with me the most.

Guillaume Luxardi was, essentially, my Ph.D. guide in the first times, when he introduced me to the laboratory, and trained me on the animal models and exquisite techniques. When you left the lab, I went through hardships; but you were an excellent teacher and I managed to be independent because of you. Fortunately, you didn't go far and we kept collaborating for the remaining of the Ph.D. work. For that and for sharing science excitement and for being my friend and for much more, Gui, Thank you!

For some time, I and the resident researcher Brian Reid were virtually alone in the Davis Lab, but then we welcomed researchers and students in our midst. We cultivated a scientific and personal partnership further grounded on "Game of Thrones" (please forgo the series finale!) discussions. Being

an expert of electrode-based techniques, you provided me with fundamental training. For that and for the native English proof-reading and for being my friend and for much more, Brian, Thank you!

Regarding the third researcher, VijayKrishna Raghunathan, although "Game of Thrones" also played a role, the most important thing was our enthusiastic science debates, which always left a sense of watering for more. Your full-time-readiness to discuss science fascinated me! Not least, were the very helpful guidance and tips on the Western blotting and other techniques, and on general Lab-related work. For that and for the excellent manuscript editing and for much more, Vijay, Thank you!

As immediate but rather great lab companions and friends, who shared the ventures of the bench side idiosyncrasies and helped each other, I want to say Thank you! to Li Ma, Yunyun Shen and Kan Zhu.

A friendly word too for those with whom I collaborated and/or shared the bench or office at times: Yan Li, Trisha Pfluger, Liang Guo, Yawei Yu and Yao-Hui Sun.

A kind word to all Zhao Lab members (past and present) for helpful comments; and to Garrett Chan, whom I supervised for a side project.

Another appreciation word to the administrative personnel associated with the UC Davis and the Zhao Lab, for making my life, not only in the Lab but also in the USA, much easier.

Special thanks to Alan Shipley, whom, for whatever reason, never stopped helping and supporting and, most enigmatically, believing in me! Al, I couldn't have achieved my lucid dream without you and the techniques and sustained encouragement you handled to me. For that and for being my friend and for much more, I'm eternally grateful. Another special word to Eric Karplus, who helped me consistently in the operation and math behind the novel SMOT technique.

The key time for kick-starting the work of my second publication was my externship at the Marine Biological Laboratory (MBL), in Woods Hole; and I can't ever let pass how welcome and happy I was there. For that I should thank, first and foremost, Al, for the invitation and making it logistically feasible (hosted me in the lovely Donna's house!); second, Andrew Miller, for accepting me in his summer programme; third, visiting students and local staff, for helping with Lab work and logistics; and fourth, Prof. Min Zhao, for covering the travel expenses.

Final thanks to Elias Barriga for providing me with a daring challenge for the future and giving me space for the completion of this work.

Forgiveness is requested in advance for those omitted.

(More research-related Acknowledgments are in the publication's equivalent section.)

***

Na língua fortunamente herdada, os agradecimentos são devidos à família nuclear, à minha sobejamente querida e aos amigos do lado de cá.

O imenso interlúdio oceânico encerrou, em si, semelhante volume de saudade, esse sentimento inerentemente português, trespassador da alma. O ácido do lar e o doce do laboratório gerou aquele agridoce, constante no meu palato. Dizer que foi dificil é somente exercitar a redundância retórica. A família leva-se no coração, essa fortaleza resiliente às milhas náuticas. Aos pai Manuel e mãe Rosa, seis irmãos e oito irmãs, seis cunhados e cinco cunhadas, doze sobrinhos (um deles afilhado) e doze sobrinhas (uma delas afilhada), e, até, um sobrinho-neto!, o meu Obrigado!

Na bruma da escrita surgiu-se-me, numa brecha, a minha sobejamente querida. De seu nome Gena, diva da mente humana, das teclas musicais e do canto, com paixão mútua por Jardins, desenvencilhou-me do – como o apelida – esfolamento do rabo da cabra. Num gesto assaz, refugiou-me numa ermida de escriba onde, satisfeito o essencial, imergi nas letras da ciência e na ciência das letras, e findei, enfim, a Tese de Doutoramento! A ermida não continha somente paredes (bem) reforçadas, tinha vivalmas que permeavam o espaço em respeito pela obra em curso. Assim, o meu Obrigado! à mãe Lúcia, irmã, futuro cunhado, avó e prima-afilhada da Gena.

Tormentas negras ribombaram no decorrer da escrita – ao que dedico a tese –, e o céu permaneceu plúmbeo. A tese, como a vida, desvaneceu-se; a vontade de escrever foi golpeada por um relâmpago atroz, e esfumou-se. Mas o fado reservou-me alguém sobejamente querida que me amparou primeiro e atiçou depois a continuar após um interregno sanador. A cura passou por exprimirmo-nos na arte verde com nuances digitais, no Festival Internacional de Jardins de Ponte de Lima. Sob o tema "Jardins do Fim do Mundo", demos ênfase à emergência climática atual com o nosso Jardim metafórico, de seu título *Vertigem (ir)reversível*... ou, um almejo onírico concretizado!

Agradeço também à demais família, aos colegas e aos amigos que se aguentaram durante as minhas presenças e, sobretudo, ausências.

Findo os Agradecimentos com um Bem-haja! a todos os que me ajudaram de algum modo; espero que tenha feito por merecê-lo!

XVI. NOTES

Translation of quotations

[1]From *The Internet Classics Archive*, URL: http://classics.mit.edu/Aeschylus/prometheus.html.

[2]From the *Perseus Digital Library*, URL: http://www.perseus.tufts.edu/hopper/text?doc=Hes.+Th.

[3] *If we presume sometimes to raise ourselves higher, let it be with that wise circumspection which befits so feeble an understanding as ours.*
Jean d'Alembert *in* Encyclopaedia, or a systematic dictionary of the sciences, arts, and crafts (Preliminary Discourse to the Encyclopaedia of Diderot) (1751).

From *The Encyclopaedia of Diderot & d'Alembert Collaborative Translation Project*, URL: http://hdl.handle.net/2027/spo.did2222.0001.083.

[4] *The times change, the desires change, and who*
we are, and what we trust, keeps changing with them;
the whole world is composed of change's rhythm,
forever shifting qualities anew.

Luís de Camões *in* Rimes (The times change, the desires change) (1595; *postumus*).

From book *Lisbon Poets – Camões, Cesário, Sá-Carneiro, Florbela, Pessoa* (2015).

[5] *Hereupon I was fired with incredible zeal and desire of having the same experience, and of bringing to light whatever might be concealed in the phenomenon. (...) [It] always occurred in the same manner: violent contraction in individual muscles of the limbs, just as if the prepared animal had been seized with tetanus, were induced at the same moment of time in which sparks were discharged.*

Luigi Galvani *in* Commentary On The Effect Of Electricity On Muscular Motion (1791).

From the *Internet Archive*, URL: https://archive.org/details/AloysiiGalvaniD00Galv (Original in Latin); https://archive.org/details/commentaryonthee002243mbp (Translated in English).

[6] *The first [precept] was never to accept anything for true which I did not clearly know to be such; that is to say, carefully to avoid precipitancy and prejudice, and to comprise nothing more in my judgment than what was presented to my mind so clearly and distinctly as to exclude all ground of doubt.*

René Descartes *in* Discourse on the Method of Rightly conducting one's reason and of seeking truth in the sciences (1637).

From *Project Gutenberg*'s eBook #59, URL: http://www.gutenberg.org/files/59/59-h/59-h.htm.

[7] *In the divine boldness of my youth,*
in this fortune-quelling pagan ecstasy,
this quivering thrill of anticipation,
I give you my body, betrothed to death!

Florbela Espanca *in* Heath in Bloom (Voluptuousness) (1931; *postumus*).

From book *Lisbon Poets – Camões, Cesário, Sá-Carneiro, Florbela, Pessoa* (2015).

[8] *When some of us feel the temptation to despise our fellows too much, to reconcile with them it is enough to contemplate a library like this, full of monuments elevated by the grandeur of man.*
Arturo Pérez-Reverte *in* Good men (2015).

From an autonomous translation of the book's Portuguese edition.

[9] *All things are nourished together without their injuring one another.*

Confucius *in* Doctrine of the Mean, Zisi (*ca.* 500 B.C.E.).

From *The Internet Classics Archive*, URL: http://classics.mit.edu/Confucius/doctmean.html.

And do remember, knowledge is not what one thinks to know, but what one knows to ignore.

Fernando Ferreira (2018)

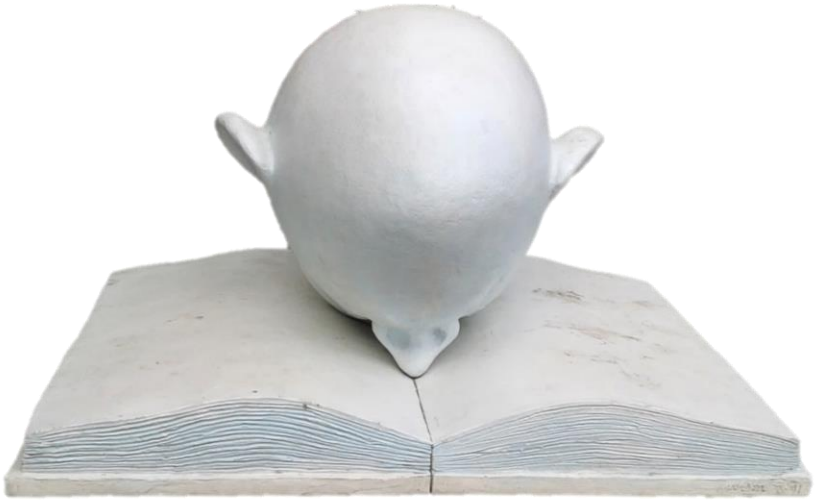

Bookhead **(The Egghead Series)**
University of California, Davis
Robert Arneson (1991)

Pro Passion, Pro Pulchritae

∞